U.S. Department
of Transportation
Federal Railroad
Administration

Office of Research,
Development and Technology
Washington, DC 20590

Mitigation of Differential Movement at Railway Transitions for U.S. High-Speed Passenger Rail and Joint Passenger/Freight Corridors

DOT/FRA/ORD-24/21

Final Report | May 2024

REPORT DOCUMENTATION PAGE

Form Approved
OMB No. 0704-0188

1. REPORT DATE *(DD-MM-YYYY)*	**2. REPORT TYPE**	**3. DATES COVERED** *(From - To)*
September 2022	Technical Report	February 2020

4. TITLE AND SUBTITLE

Mitigation of Differential Movement at Railway Transitions for U.S. High-Speed Passenger Rail and Joint Passenger/Freight Corridors

5a. CONTRACT NUMBER
DTFR53-11-C-00028

5b. GRANT NUMBER

5c. PROGRAM ELEMENT NUMBER

6. AUTHOR(S)

Erol Tutumluer 0000-0003-3945-167X
Debakanta Mishra 0000-0003-2354-1312
James H. Hyslip xxx
Huseyin Boler 0000-0002-4087-6088
Wenting Hou 0000-0001-5321-4684

5d. PROJECT NUMBER

5e. TASK NUMBER

5f. WORK UNIT NUMBER

7. PERFORMING ORGANIZATION NAME(S) AND ADDRESS(ES)
University of Illinois Urbana-Champaign
1901 South 1st Street, Suite A
Champaign, IL 61820-7473

8. PERFORMING ORGANIZATION REPORT NUMBER

9. SPONSORING/MONITORING AGENCY NAME(S) AND ADDRESS(ES)
U.S. Department of Transportation
Federal Railroad Administration
Office of Railroad Policy and Development
Office of Research, Development, and Technology
Washington, DC 20590

10. SPONSOR/MONITOR'S ACRONYM(S)

11. SPONSOR/MONITOR'S REPORT NUMBER(S)
DOT/FRA/ORD-24/21

12. DISTRIBUTION/AVAILABILITY STATEMENT
This document is available to the public through the FRA eLibrary.

13. SUPPLEMENTARY NOTES
COR: Cameron D. Stuart

14. ABSTRACT
To address the need to minimize differential movement at railway transitions for joint high-speed passenger and freight routes in the U.S., this research study identified and studied three problematic bridge approaches near Chester, PA, along Amtrak's Northeast Corridor line and another two on the N-Line mainline of Norfolk Southern near Ingleside, WV. The field instruments installed included multi-depth deflectometers for measuring track substructure layer deformations and rail strain gauges for measuring vertical wheel loads and quantifying tie support conditions. Analyses of both the track settlement and transient response data established the ballast layer to be the primary source of differential movement. Excessive vibrations within the ballast layer and significant gaps underneath the instrumented crossties recorded at the Amtrak bridge locations were linked to high-impact loads on the ballast as indicated by the significant negative displacements and the resulting crosstie oscillatory motion. The applied rehabilitation techniques included: (1) polyurethane grout injection and stabilization of existing ballast, (2) use of stone-blowing to add a thin layer of clean stone to the ballast under tie, and finally, (3) use of under tie pads to decrease pressure on the ballast and hence improve seating and load transfer beneath the tie.

15. SUBJECT TERMS
Railway transitions, bridge approach, differential movement, high-speed passenger rail, freight rail, ballast, tie-ballast gap, settlement, transient response, numerical modeling

16. SECURITY CLASSIFICATION OF:			**17. LIMITATION OF ABSTRACT**	**18. NUMBER OF PAGES**	**19a. NAME OF RESPONSIBLE PERSON**
a. REPORT	**b. ABSTRACT**	**c. THIS PAGE**			**19b. TELEPHONE NUMBER** *(Include area code)*
Unclassified	Unclassified	Unclassified		272	

METRIC/ENGLISH CONVERSION FACTORS

ENGLISH TO METRIC	METRIC TO ENGLISH
LENGTH (APPROXIMATE)	**LENGTH (APPROXIMATE)**
1 inch (in) = 2.5 centimeters (cm)	1 millimeter (mm) = 0.04 inch (in)
1 foot (ft) = 30 centimeters (cm)	1 centimeter (cm) = 0.4 inch (in)
1 yard (yd) = 0.9 meter (m)	1 meter (m) = 3.3 feet (ft)
1 mile (mi) = 1.6 kilometers (km)	1 meter (m) = 1.1 yards (yd)
	1 kilometer (km) = 0.6 mile (mi)
AREA (APPROXIMATE)	**AREA (APPROXIMATE)**
1 square inch (sq in, in^2) = 6.5 square centimeters (cm^2)	1 square centimeter (cm^2) = 0.16 square inch (sq in, in^2)
1 square foot (sq ft, ft^2) = 0.09 square meter (m^2)	1 square meter (m^2) = 1.2 square yards (sq yd, yd^2)
1 square yard (sq yd, yd^2) = 0.8 square meter (m^2)	1 square kilometer (km^2) = 0.4 square mile (sq mi, mi^2)
1 square mile (sq mi, mi^2) = 2.6 square kilometers (km^2)	10,000 square meters (m^2) = 1 hectare (ha) = 2.5 acres
1 acre = 0.4 hectare (he) = 4,000 square meters (m^2)	
MASS - WEIGHT (APPROXIMATE)	**MASS - WEIGHT (APPROXIMATE)**
1 ounce (oz) = 28 grams (gm)	1 gram (gm) = 0.036 ounce (oz)
1 pound (lb) = 0.45 kilogram (kg)	1 kilogram (kg) = 2.2 pounds (lb)
1 short ton = 2,000 pounds (lb) = 0.9 tonne (t)	1 tonne (t) = 1,000 kilograms (kg) = 1.1 short tons
VOLUME (APPROXIMATE)	**VOLUME (APPROXIMATE)**
1 teaspoon (tsp) = 5 milliliters (ml)	1 milliliter (ml) = 0.03 fluid ounce (fl oz)
1 tablespoon (tbsp) = 15 milliliters (ml)	1 liter (l) = 2.1 pints (pt)
1 fluid ounce (fl oz) = 30 milliliters (ml)	1 liter (l) = 1.06 quarts (qt)
1 cup (c) = 0.24 liter (l)	1 liter (l) = 0.26 gallon (gal)
1 pint (pt) = 0.47 liter (l)	
1 quart (qt) = 0.96 liter (l)	
1 gallon (gal) = 3.8 liters (l)	
1 cubic foot (cu ft, ft^3) = 0.03 cubic meter (m^3)	1 cubic meter (m^3) = 36 cubic feet (cu ft, ft^3)
1 cubic yard (cu yd, yd^3) = 0.76 cubic meter (m^3)	1 cubic meter (m^3) = 1.3 cubic yards (cu yd, yd^3)
TEMPERATURE (EXACT)	**TEMPERATURE (EXACT)**
[(x-32)(5/9)] °F = y °C	[(9/5) y + 32] °C = x °F

QUICK INCH - CENTIMETER LENGTH CONVERSION

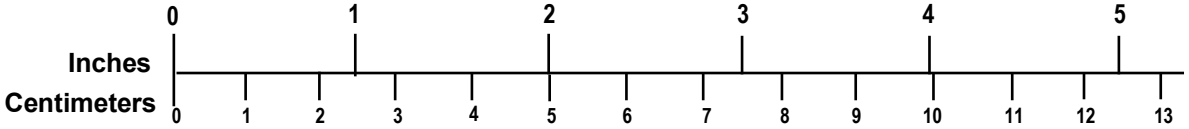

QUICK FAHRENHEIT - CELSIUS TEMPERATURE CONVERSIO

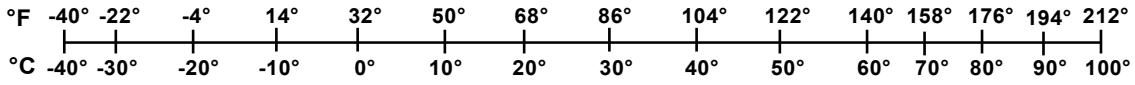

For more exact and or other conversion factors, see NIST Miscellaneous Publication 286, Units of Weights and Measures. Price $2.50 SD Catalog No. C13 10286

Updated 6/17/98

Acknowledgements

This research project was supported by the Federal Railroad Administration (FRA). The authors would like to acknowledge the vision, leadership, and research support of Cameron Stuart of the FRA Office of Research, Development and Technology. The valuable support and guidance provided by Gary Carr, Hugh Thompson, and Dr. Ted Sussmann was also greatly appreciated. Several individuals contributed significantly to the successful completion of this project. The authors have attempted to name those essential to the report; without their contributions, completing this project would not have been possible.

First and foremost, the authors would like to express their heartfelt gratitude to Mike Tomas of Amtrak, who supervised the design and development of all instrumentation components in this project and led the instrumentation and data acquisition efforts at the Amtrak bridge approaches. Marty Perkins and Carl Walker of Amtrak contributed significantly throughout these tasks. Dr. Steve Chrismer (formerly with Amtrak, now with LTK Engineering) served as the project liaison with Amtrak and facilitated all field instrumentation and remedial measure implementation activities. It was Dr. Chrismer's vision and interest in understanding track transition behavior that helped the research team accomplish several of the tasks. Thanks to Michael Trosino, Dave Staplin, and Joe Smak for providing the research team access to the test sites.

Brad Kerchof, Director of Research and Tests for Norfolk Southern (NS) Corporation, helped coordinate all the instrumentation and data acquisition activities at the Ingleside, WV, bridge approaches. Thanks to Dr. Dingqing Li of Transportation Technology Center, Inc. (TTCI) for sharing past test data for the NS N-Line mainline and Eastern Megasite locations.

Special thanks go out to the faculty and staff of the Rail Transportation and Engineering Center, established at the University of Illinois at Urbana-Champaign (UIUC) under the direction of Dr. Chris Barkan, Riley Edwards, and Tim Gress, who contributed to the management of this project. Mr. James Pforr and Dr. Aaron Coenen, formerly research engineers at the Illinois Center for Transportation (ICT), helped significantly with field instrumentation and data collection activities. Mr. James Meister, senior research engineer at ICT, was a constant source of support throughout this project. Hasan Kazmee, graduate student at UIUC, played an integral role throughout all instrumentation tasks at the Amtrak and NS bridge approaches. In addition, Drs. Maziar Moaveni and Yu Qian helped with ballast characterization and discrete element modeling tasks.

Mike Wnek and Liang Chow, (former) graduate students in the Civil and Environmental Engineering (CEE) department at UIUC, helped with the field instrumentation work. Dr. Aaron Judge of HyGround Engineering played an integral part in the instrumentation activities at the NS N-Line mainline bridge approaches. Dr. Judge and Mike LaValley of HyGround Engineering constantly provided help respecting reduction and interpretation of track geometry data. Tim Prunkard, Darold Marrow, and Marc Killion of the UIUC Civil Engineering machine shop helped with the manufacturing of all instrumentation components. Rehabilitation activities were supported by: Tom Planert of Substrate Testing, Inc. (formerly Ssesco, Inc.) for the polyurethane grout injection into ballast; Kevin Hansen of Harsco Rail for stone-blowing; and Bill Moorhead and Jeff Marty of Pandrol CDM Track for the under tie pad installation.

The research team also acknowledges the contributions of Dr. Timothy D. Stark, Professor in the CEE Department at UIUC and co-principal investigator of this research project, as well as his graduate student Steve Wilk.

The opinions expressed in this report are solely those of the authors and do not represent the opinions of the sponsored research agency.

Contents

Executive Summary 1

1. Introduction 3
   1.1 Background 3
   1.2 Objectives 3
   1.3 Overall Approach 3
   1.4 Scope 4
   1.5 Organization of the Report 6

2. Review of Published Literature 9
   2.1 Bridge Approaches as the Most Significant Track Transition Type 9
   2.2 Summary of Past Track Transition Instrumentation Efforts 11
   2.3 Analytical and Numerical Modeling of Railroad Track Transitions 12
   2.4 Remedial Measures to Mitigate Differential Movement at Track Transitions 16
   2.5 Summary 21

3. Instrumentation of Selected Bridge Approaches 22
   3.1 Identification of Problematic Sites for Instrumentation 22
   3.2 Instrumentation Plan 31
   3.3 Equipment Installation 36
   3.4 Summary 47

4. Performance Monitoring of Instrumented Bridge Approaches 49
   4.1 Monitoring Settlement Trends with Time 49
   4.2 Transient Response under Train Loading 56
   4.3 Load Distribution Characteristics as an Indicator of Support Conditions 74
   4.4 Dynamic Amplification of Load at Bridge Approaches 79
   4.5 Ballast Layer as the Primary Contributor for Transient Displacement at Bridge Approaches 80
   4.6 Summary 83

5. Advanced Analyses of Field Instrumentation Data and Numerical Modeling 84
   5.1 Digital Filter for Analyzing Transient Response Data 84
   5.2 Numerical Differentiation to Calculate Accelerations from Displacement Time-History and Comparison with Accelerometer Results 88
   5.3 Fourier Transform to Convert Data from Time to Frequency Domains 90
   5.4 Transient Response of the Tie-Ballast Interface at Railroad Track Transitions 90
   5.5 Interpretation of Track Substructure Layer Accelerations in Time and Frequency Domains 105
   5.6 Estimating Track Substructure Layer Moduli Using GeoTrack 117
   5.7 Summary 128

6. Implementation of Remedial Measures and Performance Monitoring of Remediated Bridge Approaches 129
   6.1 Selection of Bridge Approaches for Remedial Measure Implementation 129
   6.2 Chemical Grouting 130

6.3 Stone-blowing 146
6.4 Under Tie Pads 160
6.5 Summary 166
7. Numerical Modeling of Track Transitions 168
7.1 Development of a 3D FEM 169
7.2 Validation of the 3D FEM Model 179
7.3 3D FEM Model to Predict Performances of Remedial Measures 186
7.4 Modeling for Moving Wheel Loads 192
7.5 Development of an Integrated Approach for Analyzing Track Transition Behavior 195
7.6 Summary 206
8. Conclusion 207
8.1 Study Highlights and Key Findings 208
8.2 Recommendations for Improved Bridge Approach Designs and Future Research. 211
9. References 214

Illustrations

Figure 2.1: The Bump (left) and Dip (right) at End of Railway Bridge (Nicks, 2009) 10

Figure 2.2: Dual-Element Shear Strain Gauges Installed at the Rail Neutral Axis for Wheel Load and Tie Reaction Measurements 11

Figure 2.3: MDD Installed to Measure Vertical Deformation Contributed by Each Layer of a Multi-Layer Strata (Weinmann et al., 2004) 12

Figure 2.4: Discretely Supported Track Model (Huang et al., 2010) 13

Figure 2.5: Train and Track Interaction Model (Varandas, 2013) 14

Figure 2.6: Degradation of Track Transition Zone (Wang et al. 2015) 15

Figure 2.7: Polyurethane Grouting of Ballast – Injected Grout Seen From Underneath Tie 18

Figure 2.8: Schematic Analytical Model GroundVib (Johansson et al., 2008) 20

Figure 2.9: Stone-Blowing Procedure (Selig and Waters, 1994) 21

Figure 3.1: Track Geometry Data for Bridge Over Madison Street Near Chester, PA 23

Figure 3.2: Track Geometry Data for Bridge Over Hinkson Street Near Chester, PA 23

Figure 3.3: R^2 Example (From Hyslip, 2002) 24

Figure 3.4: (a) GPR Scans, (b) MCO Data, and (c) Space Curve for Track 3 at Upland Street Bridge Approach (MDD Positions: 4.6 m and 18.3 m From North Abutment) 25

Figure 3.5: (a) GPR Scans, (b) MCO Data, and (c) Space Curve for Track 2 at Madison Street Bridge Approach (MDD Positions: 3.0 and 18.3 m From South Abutment) 26

Figure 3.6: (a) GPR Scans, (b) MCO Data, and (c) Space Curve for Track 3 at Caldwell Street Bridge Approach (MDD Positions: 24.4 m From South Abutment) 27

Figure 3.7: Relative Locations of the Two Bridge Approaches Selected for Instrumentation at NS East Mega Site 28

Figure 3.8: Longitudinal Track Substructure Profile for BR352.2 – East Approach 29

Figure 3.9: Longitudinal Track Substructure Profile for BR352.2 – West Approach 30

Figure 3.10: Longitudinal Track Substructure Profile for BR352.8 – East Approach 30

Figure 3.11: Vertical Surface Roughness Trends for NS N-Line MP352.2 and MP352.8 Bridges and Their Approaches 31

Figure 3.12: Schematic of Track Substructure Profile with MDD Modules at Individual Layer Interfaces 32

Figure 3.13: (a) Schematics and Detailed Components of an MDD Assembly; and (b) Photograph Showing an LVDT Module 33

Figure 3.14: Schematic Showing the Concept of MDD Installation Using the Independent Anchoring Concept (Not to Scale) 34

Figure 3.15: Photographs Showing (a) an Assembled MDD Module Along With the LVDT and Inner Core; and (b) MDD Module Mounted in the Insertion Tool Ready for Installation Into the Drilled Hole..... 35
Figure 3.16: Photographs Showing Different Steps During the Installation of Strain Gauges 36
Figure 3.17: Photographs Showing Different Stages of Drilling for MDD Installation..... 37
Figure 3.18: Photographs Showing Different Stages of Ballast Stabilization During Drilling.... 38
Figure 3.19: Substructure Layer Profile for Upland Street 15 ft From the North Abutment (Track 3) 40
Figure 3.20: Substructure Layer Profile for Upland Street 60 ft From the North Abutment (Track 3) 40
Figure 3.21: Substructure Layer Profile for Madison Street 12 ft From the South Abutment (Track 2)..... 42
Figure 3.22: Substructure Layer Profile for Madison Street 60 ft From the South Abutment (Track 2)..... 42
Figure 3.23: Substructure Layer Profile for Caldwell Street 80 ft From the South Abutment (Track 3; West End of Tie) 43
Figure 3.24: Substructure Layer Profile for Caldwell Street 80 ft From the South Abutment (Track 3; East End of Tie) 43
Figure 3.25: Track Substructure Layer Profile at Bridge MP352.8 East Approach 44
Figure 3.26: Track Substructure Layer Profile at Bridge MP352.2 West Approach..... 45
Figure 3.27: Installing Cable Duct Underneath Adjacent Tracks..... 47
Figure 4.1: (a) DAQ Cable Connected to Wayside DAQ Box; and (b) HBM Amplifier and Laptop Setup Used for DAQ..... 49
Figure 4.2: (a) Layer Settlement Trends With Time and (b) Track Substructure Layer Profiles for the Upland Street Bridge Approach – Near-Bridge Location (15 ft From North Abutment)50
Figure 4.3: (a) Layer Settlement Trends With Time and (b) Track Substructure Layer Profiles for the Upland Street Bridge Approach – Open-Track Location (60 ft From North Abutment) 52
Figure 4.4: (a) Layer Settlement Trends With Time and (b) Track Substructure Layer Profiles for the Madison Street Bridge Approach – Near-Bridge Location (12 ft From South Abutment) 53
Figure 4.5: (a) Layer Settlement Trends With Time and (b) Track Substructure Layer Profiles for the Madison Street Bridge Approach – Open-Track Location (60 ft From South Abutment) 54
Figure 4.6: (a) Layer Settlement Trends With Time and (b) Track Substructure Layer Profiles for the Caldwell Street Bridge Approach (80 ft From South Abutment; West End of Tie)..... 55
Figure 4.7: (a) Layer Settlement Trends With Time and (b) Track Substructure Layer Profiles for the Caldwell Street Bridge Approach (80 ft From South Abutment; East End of Tie)..... 55

Figure 4.8: Example Transient Deformation Time-History Recorded Under Train Loading at the Upland Street Bridge Approach (Near-Bridge Location) 56
Figure 4.9: (a) Dual-Element Shear Strain Gauges Installed at the Rail Neutral Axis for Wheel Load and Tie Reaction Measurements; (b) Load Time-History of an Acela Express Train Recorded by the Wheel Load Strain Gauge Circuit 57
Figure 4.10: Load Time-History Recorded at Upland Street Bridge Approach; Data Collected in August 2012; Train 1 59
Figure 4.11: Displacement Time-History Recorded at Upland Street Bridge Approach; Data Collected in August 2012; Train 1 59
Figure 4.12: Load Time-History Recorded at Upland Street Bridge Approach; Data Collected in August 2012; Train 2 (Acela Express) 60
Figure 4.13: Displacement Time-History Recorded at Upland Street Bridge Approach; Data Collected in August 2012; Train 2 (Acela Express) 60
Figure 4.14: Ballast Transient Displacements Recorded at the Upland Street Bridge Approach Under the Passage of Acela Express Trains Over Time (Normalized to a Load of 100 kN) 62
Figure 4.15: Load Time-History Recorded at the Madison Street Bridge Approach; Data Collected in August 2012; Train 1 63
Figure 4.16: Displacement Time-History Recorded at the Madison Street Bridge Approach; Data Collected in August 2012; Train 1 64
Figure 4.17: Load Time-History Recorded at the Madison Street Bridge Approach; Data Collected in August 2012; Train 2 (Acela Express) 64
Figure 4.18: Displacement Time-History Recorded at the Madison Street Bridge Approach; Data Collected in August 2012; Train 2 (Acela Express) 65
Figure 4.19: Ballast Transient Displacements Recorded at the Madison Street Bridge Approach Under the Passage of Acela Express Trains Over Time (Normalized to a Load of 100 kN) 65
Figure 4.20: Load Time-History Recorded at the Caldwell Street Bridge Approach; Data Collected in August 2012; Train 1 (Acela Express) 66
Figure 4.21: Displacement Time-History Recorded at the Caldwell Street Bridge Approach; Data Collected in August 2012; Train 1 (Acela Express) 67
Figure 4.22: Load Time-History Recorded at the Caldwell Street Bridge Approach; Data Collected in August 2012; Train 2 (Acela Express) 67
Figure 4.23: Displacement Time-History Recorded at the Caldwell Street Bridge Approach; Data Collected in August 2012; Train 2 (Acela Express) 68
Figure 4.24: Ballast Transient Displacements Recorded at the Caldwell Street Bridge Approach Under the Passage of Acela Express Trains Over Time (Normalized to a Load of 100 kN) 68
Figure 4.25: Load Time-History Recorded at the MP352.2 Bridge Approach – Near-Bridge Location; Data Collected in November 2013; Train 1 69
Figure 4.26: Displacement Time-History Recorded at the MP352.2 Bridge Approach – Near-Bridge Location; Data Collected in November 2013; Train 1 70

Figure 4.27: Load Time-History Recorded at the MP352.2 Bridge Approach – Open-Track Location; Data Collected in November 2013; Train 1 70
Figure 4.28: Displacement Time-History Recorded at the MP352.2 Bridge Approach – Open-Track Location; Data Collected in November 2013; Train 1 71
Figure 4.29: Comparing the Load-Transient Displacement Relationships for the Ballast Layer at the Near-Bridge and Open-Track Locations for Bridge MP352.2; Data Collected in November 2013 71
Figure 4.30: Load Time-History Recorded at the MP352.8 Bridge Approach – Near-Bridge Location; Data Collected in November 2013 72
Figure 4.31: Displacement Time-History Recorded at the MP352.8 Bridge Approach – Near-Bridge Location; Data Collected in November 2013 72
Figure 4.32: Load Time-History Recorded at the MP352.8 Bridge Approach – Open-Track Location; Data Collected in March 2014 73
Figure 4.33: Displacement Time-History Recorded at the MP352.8 Bridge Approach – Open-Track Location; Data Collected in March 2014 73
Figure 4.34: Example Cases for Vertical Wheel Load and Tie Reaction Values Measured Using Strain Gauges: (a) Instrumented Tie Carries 50 Percent of the Applied Wheel Load; (b) Instrumented Tie Carries No Load (Hanging Tie Condition) 75
Figure 4.35: Change with Time in Percent Wheel Load Carried by the Instrumented Tie at the Upland Street Bridge Approach 76
Figure 4.36: Change with Time in Percent Wheel Load Carried by the Instrumented Tie at the Madison Street Bridge Approach 77
Figure 4.37: Change with Time in Percent Wheel Load Carried by the Instrumented Tie at the Caldwell Street Bridge Approach 77
Figure 4.38: Change with Time in Percent Wheel Load Carried by the Instrumented Tie at the MP352.2 Bridge Approach (NS N-Line Mainline) 78
Figure 4.39: Change with Time in Percent Wheel Load Carried by the Instrumented Tie at the MP352.8 Bridge Approach (NS N-Line Mainline) 78
Figure 4.40: Load Amplification at Upland Street Bridge Approach 79
Figure 4.41: Load Amplification at Madison Street Bridge Approach 80
Figure 4.42: Contribution of the Ballast Layer Toward Total Transient Deformations Under Train Loading at the Upland Street Bridge Approach 81
Figure 4.43: Contribution of the Ballast Layer Toward Total Transient Deformations Under Train Loading at the Madison Street Bridge Approach 81
Figure 4.44: Contribution of the Ballast Layer Toward Total Transient Deformations Under Train Loading at the Caldwell Street Bridge Approach 82
Figure 4.45: Contribution of the Ballast Layer Toward Total Transient Deformations Under Train Loading at the MP352.2 Bridge Approach (NS N-Line Mainline) 82

Figure 5.1: Acela Locomotive and Passenger Cars Axle Spacing..... 85

Figure 5.2: Magnitude Multipliers Corresponding to Different Frequencies for a 30 Hz, 6-Pole, Low-Pass Butterworth Filter..... 86

Figure 5.3: Results from FFT of Displacement Time-Histories: (a) Madison Street Bridge Approach – Acela Express – June 2013; (b) MP352.2 – Near-Bridge Location – Freight Train – November 2013..... 87

Figure 5.4: Magnitude Multipliers Corresponding to Different Frequencies for a 5 Hz, 6-Pole, Low-Pass Butterworth Filter..... 88

Figure 5.5: Verification of the Numerical Differentiation Approach to Calculate Layer Acceleration Values From Displacement Time-Histories: (a) Instrumentation Set-Up Used for Verification; (b) Comparing the Acceleration Values Recorded Using Accelerometers With Those Calculated From Displacement Time-Histories..... 89

Figure 5.6: Hanging Tie Conditions Created at Railroad Track Transitions Due to Uneven Settlement of the Track Substructure Layers..... 92

Figure 5.7: Existence of Void Affecting the Load-Carrying Behavior of Railroad Tracks (Illustration Borrowed From Li et al., 2016, and Ebersöhn and Selig, 1994)..... 92

Figure 5.8: Quantification of Gaps at the Tie-Ballast Interface Using a Progressive Load Threshold Approach..... 94

Figure 5.9: Relative Location of the Strain Gauge Circuits With Respect to the Instrumented Tie..... 94

Figure 5.10: Transient Load-Deformation Behavior of the Ballast Layer Approximated Using a Straight Line..... 95

Figure 5.11: Transient Deformations of the Ballast Layer Calculated Through Subtraction of Tie-Gaps From LVDT 1 Measurements – Madison Street Bridge Approach..... 97

Figure 5.12: Transient Deformations of the Ballast Layer Calculated Through Subtraction of Tie-Gaps From LVDT 1 Measurements – Upland Street Bridge Approach..... 98

Figure 5.13: Transient Deformations of the Ballast Layer Calculated Through Subtraction of Tie-Gaps From LVDT 1 Measurements – Caldwell Street Bridge Approach..... 98

Figure 5.14: Load and Deformation (LVDT 1) Time-Histories Under the Passage of an Acela Express Train at the Madison Street Bridge Approach – Near-Bridge Location (Data Collected in June 2013)..... 99

Figure 5.15: Load and Deformation (LVDT 1) Time-Histories Under the Passage of an Acela Express Train at the Upland Street Bridge Approach – Near-Bridge Location (Data Collected in July 2014)..... 101

Figure 5.16: Maximum and Minimum Transient Displacements Recorded for the Instrumented Tie – Madison Street Bridge Approach..... 103

Figure 5.17: Maximum and Minimum Transient Displacements Recorded for the Instrumented Tie – Upland Street Bridge Approach..... 104

Figure 5.18: Maximum and Minimum Transient Displacements Recorded for the Instrumented Tie – Caldwell Street Bridge Approach 104
Figure 5.19: Load and Acceleration Time-Histories for the Madison Street Bridge Approach (Data Collected in August 2012) 106
Figure 5.20: Layer 1 Accelerations for the Madison Street Bridge Approach Presented in the Frequency Domain (Data Collected in August 2012) 107
Figure 5.21: Summary of Peak Accelerations Recorded at the Madison Street Bridge Approach Under the Passage of Acela Express Trains 107
Figure 5.22: Load and Acceleration Time-Histories for the Upland Street Bridge Approach (Data Collected in August 2012) 108
Figure 5.23: Layer 1 Accelerations for the Upland Street Bridge Approach Presented in the Frequency Domain (Data Collected in August 2012) 109
Figure 5.24: Summary of Peak Accelerations Recorded at the Upland Street Bridge Approach Under the Passage of Acela Express Trains 109
Figure 5.25: Load and Acceleration Time-Histories for the Caldwell Street Bridge Approach (Data Collected in August 2012) 110
Figure 5.26: Layer 1 Accelerations for the Caldwell Street Bridge Approach Presented in the Frequency Domain (Data Collected in August 2012) 111
Figure 5.27: Summary of Peak Accelerations Recorded at the Upland Street Bridge Approach Under the Passage of Acela Express Trains 111
Figure 5.28: Time and Frequency Domain Representation of Layer Accelerations at the MP352.2 Bridge Approach – Near-Bridge Location (Data Collected in November 2013) 112
Figure 5.29: Time and Frequency Domain Representation of Layer Accelerations at the MP352.2 Bridge Approach – Open-Track Location (Data Collected in November 2013) 113
Figure 5.30: Time and Frequency Domain Representation of Layer Accelerations at the MP352.8 Bridge Approach – Near-Bridge Location (Data Collected in November 2013) 113
Figure 5.31: Time and Frequency Domain Representation of Layer Accelerations at the MP352.8 Bridge Approach – Open-Track Location (Data Collected in March 2014) 114
Figure 5.32: Displacement and Acceleration Time-Histories for Layer 1 at the Madison Street Bridge Approach Under the Passage of an Acela Express Train (Data Collected in June 2013) 115
Figure 5.33: Frequency Domain Representation of Layer 1 Accelerations at the Madison Street Bridge Approach Under the Passage of an Acela Express Train (Data Collected in June 2013) 115
Figure 5.34: Displacement and Acceleration Time-Histories for Layer 1 at the Upland Street Bridge Approach Under the Passage of an Acela Express Train (Data Collected in July 2014) 116

Figure 5.35: Frequency Domain Representation of Layer 1 Accelerations at the Upland Street Bridge Approach Under the Passage of an Acela Express Train (Data Collected in July 2014) 117

Figure 5.36: Track Elements in GeoTrack Model (Reproduced from Chang et al., 1980) 118

Figure 6.1: Schematic Layout of Selected Bridge Approaches and Relative Locations of Remedial Measures 130

Figure 6.2: (a) Grout Injection Adjacent to the Tie Using a Proprietary Injection System; (b) Excavation of Ballast Around Crossties to Confirm Adequate Permeation of Grout Into the Ballast Layer; (c) Grout Extruding Out From Injection Locations After Expansion 131

Figure 6.3: Layer Settlement Trends for the Upland Street Bridge Approach - Near-Bridge Location (15 ft From the North Abutment; Track 3) 132

Figure 6.4: Space Curve and Running Roughness Data for the Upland Street Bridge Approach (North Approach; Track 3) Showing the Effect of Chemical Grouting 133

Figure 6.5: Effect of Chemical Grouting on (a) Ballast Transient Deformations and (b) Track Space Curve at the Upland Street Bridge Approach 134

Figure 6.6: Displacement Time-Histories Recorded at the Upland Street Bridge Approach; Data Collected on July 22, 2014; Train 1 (Acela Express) 135

Figure 6.7: Displacement Time-Histories Recorded at Upland Street Bridge Approach; Data Collected in January 2015; Train 1 136

Figure 6.8: Displacement Time-Histories Recorded at Upland Street Bridge Approach; Data Collected in May 2015; Train 1 (Acela Express) 136

Figure 6.9: Ballast Transient Displacements Recorded at the Upland Street Bridge Approach Under the Passage of Acela Express Trains on Different Dates of Data Acquisition (Normalized to a Load of 100 kN) 137

Figure 6.10: Contribution of the Ballast Layer Toward Total Transient Deformations Under Train Loading at the Upland Street Bridge Approach 138

Figure 6.11: Load Amplification at Upland Street Bridge Approach After Chemical Grouting 138

Figure 6.12: Load and Acceleration Time-Histories for the Upland Street Bridge Approach (Data Collected on July 22, 2014) 140

Figure 6.13: Layer 1 Accelerations for the Upland Street Bridge Approach Presented in the Frequency Domain (Data Collected on July 22, 2014) 140

Figure 6.14: Load and Acceleration Time-Histories for the Upland Street Bridge Approach (Data Collected in January 2015) 141

Figure 6.15: Layer 1 Accelerations for the Upland Street Bridge Approach Presented in the Frequency Domain (Data Collected in January 2015) 142

Figure 6.16: Load and Acceleration Time-Histories for the Upland Street Bridge Approach (Data Collected in May 2015) 142

Figure 6.17: Layer 1 Accelerations for the Upland Street Bridge Approach Presented in the Frequency Domain (Data Collected in May 2015) 143

Figure 6.18: Summary of Peak Accelerations Recorded at the Upland Street Bridge Approach Under the Passage of Acela Express Trains – After Chemical Grouting 143

Figure 6.19: Maximum and Minimum Transient Displacements Recorded for the Instrumented Tie – Upland Street Bridge Approach – After Chemical Grouting 144

Figure 6.20: Space Curve and Running Roughness Data for the Morton and Potter Streets Bridge Approach..... 146

Figure 6.21: Different Steps Involved in the Stone-blowing Process..... 147

Figure 6.22: (a) Measurement of Voids Underneath Ties Using Void Meters; (b) Design of Target Track Elevation Using Stone Injection at the Madison Bridge Approach 148

Figure 6.23: Different Steps Involved in the Stone-blowing Process..... 149

Figure 6.24: Layer Settlement Trends for the Madison Street Bridge Approach – Near-Bridge Location (12 ft From the South Abutment; Track 2)..... 150

Figure 6.25: Space Curve and Running Roughness Data for the Madison Street Bridge Approach (South Approach; Track 2) Showing the Effect of Stone-blowing..... 151

Figure 6.26: Effect of Stone-Blowing on (a) Ballast Transient Deformations and (b) Track Space Curve at Madison Street Bridge Approach (South Approach; Track 2)..... 152

Figure 6.27: Displacement Time-Histories Recorded at the Madison Street Bridge Approach; Data Collected in January 2015; Train 1 153

Figure 6.28: Displacement Time-Histories Recorded at the Madison Street Bridge Approach; Data Collected in May 2015; Train 1 (Acela Express)..... 153

Figure 6.29: Ballast Transient Displacements Recorded at the Madison Street Bridge Approach Under the Passage of Acela Express Trains on Different Dates of Data Acquisition (Normalized to a Load of 100 kN)..... 154

Figure 6.30: Contribution of the Ballast Layer Toward Total Transient Deformations Under Train Loading at the Madison Street Bridge Approach (South Approach; Track 2)..... 154

Figure 6.31: Load Amplification at the Madison Street Bridge Approach After Stone-blowing155

Figure 6.32: Load and Acceleration Time-Histories for the Madison Street Bridge Approach (Data Collected in January 2015) – After Stone Injection (Acela Express) 156

Figure 6.33: Layer 1 Accelerations for the Madison Street Bridge Approach Presented in the Frequency Domain (Data Collected in January 2015) – After Stone Injection..... 157

Figure 6.34: Summary of Peak Accelerations Recorded at the Madison Street Bridge Approach Under the Passage of Acela Express Trains – After Stone Injection..... 158

Figure 6.35: Maximum and Minimum Transient Displacements Recorded for the Instrumented Tie – Madison Street Bridge Approach – After Stone Injection 159

Figure 6.36: Newly Manufactured Concrete Ties Mounted with UTPs..... 161

Figure 6.37: Final View of the New Tie Panel After Installation..... 161

Figure 6.38: Space Curve and Running Roughness Data for the Upland Street Bridge Approach (South Approach; Track 2) Showing the Effect of UTP Installation..... 162

Figure 6.39: Schematic of Instrumentation Layout to Measure Transient Response of Ties Fitted With UTPs 163
Figure 6.40: Instrumentation Types and Locations to Measure Track Transient Response Under Loading 164
Figure 6.41: Force and Displacement Time-Histories Measured at Upland Street Bridge – Track 2 South Approach; Data Collected in August 2015; Train 1 (Acela Express) 165
Figure 6.42: Acceleration Time-Histories Calculated from Transient Displacement Measurements at Upland Street Bridge – Track 2 – South Approach; Data Collected in August 2015; Train 1 (Acela Express)..... 165
Figure 6.43: Tie Accelerations for Upland Street Bridge – Track 2 – South Approach – Presented in the Frequency Domain (Data Collected in August 2015)..... 166
Figure 7.1: FEM Model Size Developed by Kim et. al. (2009)..... 170
Figure 7.2: Plan View of the 3D FE Model..... 171
Figure 7.3: Depth of the 3D FE Model..... 171
Figure 7.4: GeoTrack Half Tie Load Assignment 172
Figure 7.5: Half Tie Segment Loading Arrangement in the Model..... 172
Figure 7.6: Ties 1, 5, and 6 GeoTrack Loading Configuration..... 173
Figure 7.7: Ties 1, 2, and 6 GeoTrack Loading Configuration..... 174
Figure 7.8: Abaqus FE Mesh and the Boundary Conditions 175
Figure 7.9: Abaqus FEM Model Zoomed to Indicate GeoTrack Loading Assembly 176
Figure 7.10: Element Types: (a) C3D8 Element; (b) C3D20 Element..... 176
Figure 7.11: Plan View of the FE Mesh 177
Figure 7.12: Y-Z View of the FE Mesh..... 177
Figure 7.13: 3D View of the FE Mesh: (a) Geometry; (b) Zoomed View of the Model..... 178
Figure 7.14: Deformation View of Abaqus FEM Model Subjected to Tie 1, 5, and 6 Loading Configuration 179
Figure 7.15: Upland 15 ft Predicted Layer Deformations and Percent Differences..... 180
Figure 7.16: Upland 60 ft Predicted Layer Deformations and Percent Differences..... 181
Figure 7.17: Madison 12 ft Predicted Layer Deformations and Percent Differences..... 182
Figure 7.18: Madison 60 ft Predicted Layer Deformations and Percent Differences..... 183
Figure 7.19: Caldwell West End of Tie Predicted Layer Deformations and Percent Differences: (a) Caldwell West – November 2012; (b) Caldwell West – January 2013; (c) Caldwell West June 2013 185
Figure 7.20: Caldwell East End of Tie Predicted Layer Deformations and Percent Differences: (a) Caldwell East November 2012; (b) Caldwell East January 2013; (c) Caldwell East June 2013..... 186

Figure 7.21: Adjusted Tie Segments in the New 3D FEM Model to Include Rails and Ties..... 187
Figure 7.22: 3D View of Half Tie Created 188
Figure 7.23: 3D View of the FEM Model Showing Half Ties and Rail Assembly 188
Figure 7.24: Loads Applied on Rail by an Acela Locomotive Bogie..... 189
Figure 7.25: Predicted Layer Deformations and Percent Differences – Before and After Polyurethane Injection (Upland 15 ft) 190
Figure 7.26: Layer 1 Ballast Deformations – Before and After Polyurethane Injection (Upland 15 ft)..... 191
Figure 7.27: Predicted Layer Deformations and Percent Differences – After Stone-blowing (Madison 12 ft, May 2015) 191
Figure 7.28: New 3D FEM Model Created with 21 Ties to Simulate Quasi-Static Moving Wheel Loads..... 192
Figure 7.29: Predicted Layer Deformations from the Moving Wheel Load Simulation and the Field Measurements (Upland 60 ft August 2012); (a) Abaqus Prediction for the Front Axle/Wheel Location (Upland 60 ft August 2012 Acela); (b) Field MDD Measurements (Layer 1 with ~ 0.3435 mm Tie-Gap)..... 194
Figure 7.30: Predicted Layer Deformations from Moving Wheel Load Simulation (After Considering Tie-Gap) and Field Measurements (Upland 60 ft August 2012); (a) Abaqus Prediction for the Front Axle/Wheel Location (Upland 60 ft August 2012 ACELA) – Using Lower Ballast Layer Modulus Due to Tie-Gap; (b) Field MDD Measurements (Layer 1 with ~ 0.3435 mm Tie-Gap) 195
Figure 7.31: Schematic Representation of Fully Coupled 3D Track Model Used in the Current Study (Model Developed by Huang et al. 2014) 199
Figure 7.32: Load Levels Applied on the Ballast Layer as Predicted by the Fully Coupled 3D Dynamic Track Model 200
Figure 7.33: Particle Size Distribution of Ballast Material Used on Site 201
Figure 7.34: Steps Involved in Creating 3D Polyhedrons for Individual Ballast Particles to be Used in DEM of Railroad Track Structures..... 202
Figure 7.35: Half-Track Model Generated Using DEM..... 202
Figure 7.36: Comparing the Particle Acceleration Levels at Different Positions Within the Ballast Layer: (a) 15 cm Below Bottom of Tie – Position 1; (b) 15 cm Below Bottom of Tie – Position 2; (c) 20 cm Below Bottom of Tie; (d) 30 cm Below Bottom of Tie 204
Figure 7.37: Vector Plot Showing Vertical Load Concentration Underneath the Rail as Predicted From the Discrete Element Simulation..... 205

Tables

Table 3.1: Instrumented Borehole Locations and Achieved Depths 39

Table 3.2: Track Substructure Layer Profiles Established During Drilling and Instrumentation at the Amtrak NEC Bridge Approaches 41

Table 3.3: Track Substructure Layer Profiles Established During Drilling and Instrumentation at the NS N-Line Mainline Bridge Approaches..... 46

Table 4.1: Summary Dates of Data Collection for Amtrak NEC Bridge Approaches and Number of Days Since Instrumentation..... 50

Table 5.1: Gap Quantification at the Tie-Ballast Interface Using the Progressive Load Threshold Approach: Madison Street Bridge Approach..... 95

Table 5.2: Gap Quantification at the Tie-Ballast Interface Using the Progressive Load Threshold Approach: Upland Street Bridge Approach..... 96

Table 5.3: Gap Quantification at the Tie-Ballast Interface Using the Progressive Load Threshold Approach: Caldwell Street Bridge Approach 96

Table 5.4: Time Difference Between Peak Load and Subsequent Initiation of Tie Lift-Off Phenomenon – Madison Street Bridge Approach – Near-Bridge Location (Data Recorded in June 2013)..... 100

Table 5.5: Time Difference Between Registering Peak Load, and Subsequent Initiation of Tie Lift-Off Phenomenon – Upland Street Bridge Approach – Near-Bridge Location (Data Recorded in July 2014) 102

Table 5.6: Track Substructure Layer Thicknesses for the Instrumented Amtrak NEC Bridge Approaches Established through Merging of Intermediate Layers 105

Table 5.7: Inherent Features and Assumptions of the GeoTrack Program..... 118

Table 5.8: Typical Track Parameters Used During GeoTrack Analysis 120

Table 5.9: General Information for the Example Case Madison 12 ft, August 2012..... 121

Table 5.10: Track Substructure Layer Modulus Values for the Madison Street Bridge Approach Estimated Through Iterative Analysis Using GeoTrack – Before Correcting for Contributions Due to Tie-Gaps..... 122

Table 5.11: Track Substructure Layer Modulus Values for the Caldwell Street Bridge Approach Estimated Through Iterative Analysis Using GeoTrack – Before Correcting for Contributions Due to Tie-Gaps..... 122

Table 5.12: Track Substructure Layer Modulus Values for the Upland Street Bridge Approach Estimated Through Iterative Analysis Using GeoTrack – Before Correcting for Contributions Due to Tie-Gaps..... 123

Table 5.13: Corrected Layer 1 Deformations for the Madison Street Bridge Approach Calculated by Subtracting the Tie-Gap Magnitudes from Transient Deformations Recorded by the Top-Most LVDT..... 124

Table 5.14: Corrected Layer 1 Deformations for the Caldwell Street Bridge Approach Calculated by Subtracting the Tie-Gap Magnitudes from Transient Deformations Recorded by the Top-Most LVDT 125

Table 5.15: Corrected Layer 1 Deformations for the Upland Street Bridge Approach Calculated by Subtracting the Tie-Gap Magnitudes from Transient Deformations Recorded by the Top-Most LVDT 125

Table 5.16: Track Substructure Layer Modulus Values for the Madison Street Bridge Approach Estimated Through Iterative Analysis Using GeoTrack – After Correcting for Contributions Due to Tie-Gaps 126

Table 5.17: Track Substructure Layer Modulus Values for the Caldwell Street Bridge Approach Estimated Through Iterative Analysis Using GeoTrack – After Correcting for Contributions Due to Tie-Gaps 127

Table 5.18: Track Substructure Layer Modulus Values for the Upland Street Bridge Approach Estimated Through Iterative Analysis using GeoTrack – After Correcting for Contributions Due to Tie-Gaps 127

Table 6.1: Gap Quantification at the Tie-Ballast Interface Using the Progressive Load Threshold Approach: Upland Street Bridge Approach (After Chemical Grouting) 139

Table 6.2: Track Substructure Layer Modulus Values for the Upland Street Bridge Approach Near-Bridge Location Estimated Through Iterative Analysis Using GeoTrack – After Chemical Grouting 145

Table 6.3: Gap Quantification at the Tie-Ballast Interface Using the Progressive Load Threshold Approach: Madison Street Bridge Approach (After Stone-blowing) 156

Table 6.4: Track Substructure Layer Modulus Values for the Madison Street Bridge Approach Near-Bridge Location Estimated Through Iterative Analysis Using GeoTrack – After Stone Injection 159

Table 7.1: Tie Segment Contact Pressures Using Ties 1, 5, and 6 Loading Configuration 173

Table 7.2: Tie Segment Contact Pressures Using Ties 1, 2, and 6 Loading Configuration 174

Table 7.3: Predicted Layer Deformations Compared for the Applied Tie Load Sequences 175

Table 7.4: Predicted Layer Deformations Compared for Different Meshing and Elements 177

Table 7.5: Upland Street Near-Bridge Track Location Elastic Layer Modulus Values Back calculated Using GeoTrack 179

Table 7.6: Upland Street Open-Track Location Elastic Layer Modulus Values Back calculated Using GeoTrack 181

Table 7.7: Madison Street Near-Bridge Track Location Elastic Layer Modulus Values Back calculated Using GeoTrack 182

Table 7.8: Madison Street Open-Track Location Elastic Layer Modulus Values Back calculated Using GeoTrack 183

Table 7.9: Caldwell Street West End of Tie Track Location Elastic Layer Modulus Values Back calculated Using GeoTrack 184

Table 7.10: Caldwell Street East End of Tie Track Location Elastic Layer Moduli Values Back calculated Using GeoTrack 184

Table 7.11: Upland Street Near-Bridge Track Location after Polyurethane Remedial Measure – Elastic Layer Modulus Values Back calculated Using GeoTrack 189

Table 7.12: Madison Street 12 ft (Near-Bridge Location) after Stone-blowing Remedial Measure May 2015 – GeoTrack Backcalculation Results 191

Table 7.13: Concentrated Point Load Locations 193

Table 7.14: Upland Street Open-Track Location Elastic Layer Modulus Values Back calculated Using GeoTrack 194

Executive Summary

Railway transitions experience differential movements due to differences in track system stiffness, impact loads and vibration, track damping characteristics, foundation type, ballast settlement from fouling and/or degradation, as well as fill and subgrade settlement. This differential movement at the "bump," or transition, is especially problematic for high-speed rail infrastructure and is accentuated at high speeds. The identification of different factors contributing to this differential movement, as well as development of design and maintenance strategies to mitigate the problem, is imperative for the safe and economical operation of both freight and passenger rail networks.

To address the need to minimize differential movement at railway transitions on joint high-speed passenger and freight routes in the U.S., the University of Illinois at Urbana-Champaign (UIUC) executed this Federal Railroad Administration (FRA)-supported research study in collaboration with several railroad and industry research partners. The main objectives of the project were to identify major causes of differential movement at track transitions and to develop design methodologies for new railway transitions and maintenance or rehabilitation strategies for existing transitions to improve high-speed operation, safety, and passenger comfort.

Project researchers identified and studied three problematic transition zones close to bridge approaches near Chester, Pennsylvania, along Amtrak's Northeast Corridor (NEC) line and two other bridges on the Norfolk Southern (NS) N-Line mainline near Ingleside, West Virginia. The field instruments used were multi-depth deflectometers (MDDs) for measuring track substructure layer deformations and strain gauges mounted on the rail for measuring the vertical wheel loads and quantifying tie support conditions. The MDD systems, installed through crossties, were successful in recording both permanent (plastic) and transient deformations of individual track substructure layers. Strain gages mounted on the rail were effective in measuring vertical wheel loads applied during the passage of a train and monitoring the support conditions underneath the instrumented crossties.

Analyses of the track settlement (permanent deformation) data from these bridge approaches established the ballast layer as the source of differential movement and the primary contributor to the recurrent settlement and track geometry problems at these locations. Transient layer deformations recorded under train passage were also higher in the ballast layer than in any of the other substructure layers at both the Amtrak and NS sites. Both the transient displacements and wheel loads recorded at the Amtrak NEC Upland Street and Madison Street locations were consistently higher than those at the open-track locations. The wheel loads carried by the instrumented ties were similar at both the near-bridge and the open-track locations of the NS instrumented bridge approaches.

UIUC observed excessive vibrations within the ballast layer and significant gaps underneath the instrumented crossties at the Amtrak Upland and Madison Street near-bridge locations. Tie-gaps consistently increased with time, leading to a loss of support under the ties. From advanced transient data analyses, certain high acceleration magnitudes and higher frequency vibration modes were measured only at the near-bridge locations. Researchers observed significant amounts of peak negative transient displacements and tie lifting in these near-bridge locations, followed by an impact load on the ballast as the rail-tie system was pushed downward under the next axle/wheel load, thereby causing an oscillatory motion.

The research team used the GeoTrack software program as a tool for applying an iterative process to back calculate track substructure layer moduli based on the field-measured transient layer deformation results collected at the Amtrak bridge approaches. UIUC developed a 3-dimensional numerical analysis model, based on the finite element method (FEM), to analyze the problematic bridge approaches. The model was validated for prediction accuracy using the GeoTrack back calculated layer moduli as inputs for transient repose predictions. The estimated substructure layer moduli were particularly useful for comparing the effectiveness of the remedial measures. UIUC also introduced an integrated approach to dynamic analysis of the railway track transitions behavior using the field instrumentation, analytical modeling, and numerical simulations of ballast deformation behavior using the discrete element method (DEM). The research emphasized the importance of modeling the ballast layer as a particulate medium, and successfully demonstrated the particle-to-particle nature of load transfer within the ballast layer.

The rehabilitation techniques selected for the Amtrak bridge approaches focused primarily on the problematic ballast layer and included: (1) polyurethane grout injection and stabilization of existing ballast; (2) use of stone-blowing to add a thin layer of clean stone to the ballast under tie, and finally; (3) use of under-tie pads (UTPs) glued under new ties to decrease pressure on the ballast in order to improve seating and load transfer beneath the tie. Chemical grouting of the ballast proved to be effective in the short term, but its effectiveness as a remedial measure diminished rapidly after a few months. Close inspection of the track conditions indicated that excessive fouling of the ballast layer may have led to inadequate bonding between the grout and individual ballast particles. Grout application at another bridge approach with a clean ballast layer exhibited better performance. Both stone-blowing and the installation of UTPs proved to be effective remedial measures for mitigating differential movement at the track transitions. Better support conditions at the tie-ballast interface could be ensured through these remedial measures, which in turn led to significantly improved track response and stable track geometry profiles.

Finally, the following factors were identified as contributing to the development of a bump at the instrumented railway bridge approaches: (1) tie-ballast contact condition and gap, (2) train speed, (3) impact loads and vibration, and (4) ballast material. All remedial measures should aim to reduce the tie-ballast gap and train/crosstie vertical acceleration at the transition zones. Maintaining proper ballast contact underneath the crosstie will improve performance and track performance.

1. Introduction

University of Illinois at Urbana-Champaign (UIUC) executed this Federal Railroad Administration (FRA)-supported research study to address the need to minimize differential movement at railway transitions on joint high-speed passenger and freight routes. The research was conducted between September 2011 and December 2015 and included monitoring and numerically modeling existing transitions to develop cost-effective design and mitigation solutions. The research concerns and directions included in the research effort were gathered from conversations with railroad industry experts in the field of track design and performance, FRA, Amtrak, Norfolk Southern (NS) Class I freight railroad, engineering consultants, and track geotechnology solution providers. Many of these experts were cost-share partners in this research effort. The research results are expected to facilitate the advancement of infrastructure component design and performance for high-speed passenger rail operations.

1.1 Background

Railway transitions, such as bridges and grade crossings, experience differential movement due to differences in track system stiffness, impact loads and vibration, track damping characteristics, foundation type, ballast settlement from fouling and/or degradation, as well as settlement of the approach embankment fill and the native soils underlying the approach fill. This differential movement is especially problematic for high-speed rail infrastructure because an elevation difference, often described as a "bump" at the transition, is accentuated at high speeds and can lead to unacceptable geometry, bridge damage, and poor ride quality. The individual components causing the differential settlement must be identified and controlled to improve high-speed safety and passenger comfort. Reducing differential movement at railway transitions is also beneficial for freight lines operating in joint corridors since heavy loads from long freight trains can exacerbate the situation.

1.2 Objectives

The main objectives of this project were to identify major causes of differential settlement at track transitions and to develop design technologies for new railway transitions as well as maintenance or rehabilitation for existing transitions to improve high speed operation, safety, and passenger comfort.

1.3 Overall Approach

To achieve the project objectives, researchers monitored several new and rehabilitated railway transitions to better understand the location and magnitude of the differential movement at railway transitions and developed numerical models that accurately predict the monitored field performances. UIUC undertook tasks involving state-of-the-art field monitoring, field investigation, and numerical modeling of new and problematic railway transitions. The monitoring data developed was intended to guide new design and rehabilitation methodologies to ensure better performance of bridge-embankment and other track transitions. Further, these new design and rehabilitation methodologies were investigated to ensure safer railways, faster speeds, lower life-cycle costs, lengthened maintenance intervals, increased capacity to operate trains, less frequent and shorter track outages, and reduced annual operating costs for high-speed and intercity passenger rail systems.

1.4 Scope

The scope of this project provides the following deliverables: (1) results of field monitoring of new and rehabilitated railway transitions – using multi-depth deflectometers (MDDs) for measuring track substructure layer deformations and rail strain gauges for recording wheel loads – and determining the location and cause of differential movement at railway transitions; (2) an understanding of the dynamic load and vibration effects, tie-ballast contact, and major causes of differential movement at railway transitions; (3) a summary of currently used design and rehabilitation techniques to minimize and mitigate, respectively, differential movement of railway transitions; (4) development of calibrated numerical models for railway transitions that can accommodate various design and rehabilitation techniques; and (5) a final report on field monitoring and improved (and optimized) design and rehabilitation techniques for railway transitions, including construction implications, to be implemented by railroads and for future research needs statements.

This project includes four major phases defined herein as work packages: (1) monitor railway transitions to locate and identify causes of differential movement; (2) identify major factors causing differential movement at railway transitions; (3) numerical modeling of monitored railway transitions; and (4) planning, management, reporting, and communications.

1.4.1 Work Package 1 – Monitor Railway Transitions to Locate and Identify Causes of Differential Movement

UIUC conducted field monitoring of new and rehabilitated railway transitions to better understand the materials and factors that contribute to differential movement and the effectiveness of current design and rehabilitation techniques. Care was taken during the selection of candidate transitions to include sites where different mechanisms were likely to contribute toward the differential movement problem. Control sections were also selected for instrumentation and monitoring for comparison purposes.

Detailed analyses of Amtrak's Northeast Corridor (NEC) track performance records of problematic Chester, PA, track transitions identified three bridge approaches (over Upland, Madison, and Caldwell streets) as primary locations for instrumentation and monitoring. Based on field testing and modeling of substructure layer settlement, the sources of most of these settlements at the bridge approaches could be instability at the tie-ballast interface, ballast degradation, and possibly fill or subgrade deformation. To determine the relative contributions of the substructure layers to the observed settlement, MDDs were installed to measure the elastic/transient deformations and permanent settlement of the substructure layers at different depths. Each site selected was different with regards to the design or rehabilitation technique used to obtain actual performance data for current design and rehabilitation techniques.

Field monitoring was also targeted for two rehabilitated railway transitions at the NS Eastern Mega Site. Historical evidence indicated that these open-deck bridges and their approaches experience track geometry degradation (both in the vertical as well as horizontal directions), requiring frequent surfacing work. One of the bridges was modified from an open-deck to a ballast-deck structure in the fall of 2007 to remediate the recurrent track geometry problem, but this change appeared to have solved only part of the transition problem. Track geometry records indicated that there was still a vertical differential movement problem at the site. Monitoring of

this site would provide important data on the performance of open-deck and ballast-deck structures.

The movements of the selected bridge approaches and transitions were monitored using MDD and strain gauge instrumentation and survey equipment. Materials and factors that contribute to differential movement at the instrumented railway transitions were studied. More importantly, the data were used to clarify the location of the differential movement at the railway transitions (e.g., ballast settlement or degradation, fill settlement, or subgrade movement). Field monitoring, field investigation, and numerical modeling were then conducted on these sites.

UIUC conducted field investigations to obtain data necessary to model the railway transition and better understand the factor(s) that contributed to the differential movement. The field investigations measured the layer substructure details, height of fill, type of fill, type of foundation, type of bridge structure, embankment soil type and compaction specifications, and drainage conditions. In addition, the bridge approaches were surveyed by railroad personnel to quantify the current magnitude of differential movement. UIUC compared the survey results with as-built data to determine the magnitude and pattern of the movement. Field testing was conducted to characterize the fill and subgrade materials underlying the ballast.

The results from the field investigations were used to develop input parameters for a numerical model of the field conditions. The input parameters, along with the measured movements of the transition over time, were used to develop calibrated numerical models that could be used to assess the effectiveness of various design and rehabilitation techniques for the type of transition and field conditions encountered.

1.4.2 Work Package 2 – Identify Major Factors Causing Differential Movement at Railway Transitions

Work Package 2 of this project identified the materials and major factors that resulted in significant differential movement at the instrumented railway transitions. This was accomplished with the data collected from the field investigation sites highlighted in Work Package 1 and through an extensive literature review. In addition, UIUC reviewed problematic bridge approach cases identified throughout the country and from international literature to establish a synthesis report to prioritize root causes of differential movements at transitions. With proper understanding of the problematic materials and major factors, correct materials and design recommendations could be made to increase the life and performance of railway transitions. These major factors were then prioritized so design procedures and field maintenance/rehabilitation techniques could be developed and/or revised to address the most important materials and factors.

UIUC used the MDDs, rail strain gauges, and surface survey measurements to identify the location and pattern of differential movement and to assess the performance of the ballast rehabilitation. In addition, UIUC examined impact loads, vibration effects and other important considerations, such as tie-ballast contact, to understand the mechanical behavior and transient response of railway transitions under dynamic loading. This Work Package also included the application of three selected remedial measures (i.e., polyurethane grout injection, stone-blowing and under tie pads glued to newly installed ties) to the bridge approaches of the selected Amtrak transition sites and monitoring and reporting of their effectiveness.

1.4.3 Work Package 3 – Numerical Modeling of Monitored Railway Transitions

Work Package 3 focused on numerical modeling of the monitored railway transitions to develop calibrated numerical models and to predict the performance of other design or rehabilitation techniques for railway transitions. Several numerical tools were used, including GeoTrack multi-layered elastic solution (Chang et al., 1980), Abaqus with 3-dimensional (3D) finite element modeling (FEM) approach, dynamic track models such as the Sandwich and the 3D fully coupled models by Huang et al. (2014), and the use of discrete element method (DEM) for modeling deformation behavior of the particulate nature of ballast.

The individual layer deformations for both transient response and time dependent settlement were obtained from the installed MDDs. The wheel loads applied on the instrumented tie were determined from the installed strain gauges. With these inputs from the field instrumentation, track substructure individual layer moduli were back calculated for selected locations using the GeoTrack layered elastic analysis program. Stresses and deformations were calculated as a function of multi-axle loads, properties of rails and ties, properties of substructure layers, and geometry of ties and underlying layers (Li and Selig, 1998). Later, these layer moduli were used to develop 3D Abaqus FEM models to consider transient responses in relation to tie-ballast gaps and predict responses of the rehabilitated bridge approaches.

For the dynamic track model, wheel load and transient layer deformation values collected from the instrumented bridge approaches under train loading were first used to calibrate a fully coupled three-dimensional train-track-soil model developed by Huang et al. (2014). This model characterizes the subgrade as a three-dimensional plane stress finite element mesh. Additionally, the rail was modeled as a Euler beam discretely supported at points corresponding to the tie locations. Each rail-pad, tie, and ballast system were modeled using a combination of mass, spring, and damper. The train was modeled as a simplified Type I vehicle with both primary and secondary suspensions having 10 degrees of freedom.

UIUC's BLOKS3D DEM program was used to generate a model of the mass of typical railroad ballast as well as model the dynamic deformation and vibration behavior of the ballast under the instrumented tie. The BLOKS3D program uses rigid but random shaped 3D polyhedrons as basic elements to realistically simulate interactions, such as the interlocking aggregate particles. The development of the ballast DEM model was intended to provide a quantitative track performance simulation capability to conduct field applications and investigate various aspects of railroad ballast designs and behavior.

1.4.4 Work Package 4 – Planning, Management, Reporting, and Communications

Work Package 4 included all necessary planning and management tasks for this project as well as reporting and communications between UIUC, railroad and industry partners, subcontractors, and FRA. Additionally, research findings from this project were disseminated to the railroad community and researchers through journal papers, conference proceedings, and presentations at railroad, construction, materials, and transportation-related conferences.

1.5 Organization of the Report

Section 2 of this report presents a summary of the literature review. Definition, types, and performance records of track transitions are presented. Special attention is given to the bridge approach, which is one of the most common track transitions. The section includes a summary of

past track transition instrumentation efforts and a review of the current numerical and analytical modelling efforts of railway track systems, including track transition zones. Finally, this section lists common remedial measures to mitigate differential movement at track transition zones, including under tie pads, chemical grouting, and stone-blowing.

Section 3 presents a detailed effort to identify the problematic track transitions. The details of instrumentation and performance monitoring activities are summarized. Two different classes of bridge approaches were instrumented, including track transitions that predominantly experience passenger traffic and those that are carrying predominantly freight traffic. Details of the site selection, instrumentation, and performance monitoring of the problematic bridge approaches are presented.

Section 4 includes an analysis and discussion of the field data. The periodic data acquired to monitor changes in permanent (plastic) and transient deformations of track substructure layers over time are analyzed together with the strain gage data also collected to determine wheel load on the instrumented tie and tie reaction. This section highlights several site to record Linear Variable Differential Transformer (LVDT) offset values as well as transient response under train loading. The time-history of bridge approach performance is discussed using the track substructure layer deformation (both permanent and transient) as well as wheel load data collected under train loading, and the root causes of poor performance are identified.

Section 5 presents an analysis of the transient response data and conclusions regarding tie support conditions and accelerations induced in different substructure layers due to train loading. Several mathematical and data analysis tools used for in-depth analyses of the track transient response data are introduced in the beginning of the section. The GeoTrack program is introduced as a tool to estimate track substructure layer moduli from the transient response data. This is followed by discussions of the transient response of the tie-ballast interface at railroad track transitions. A new method is proposed to quantify the size of the gaps (if any) existing between the bottom of the tie and the top of the ballast layer based on the transient deformation data collected using the MDDs. Upward movement of the rail-tie system between the applications of consecutive wheel loads is also analyzed, and an effort is made to correlate this phenomenon to support conditions underneath the instrumented ties. Individual track substructure layer accelerations are also calculated from the displacement time-histories, and inferences are made concerning the dynamic response of the track system.

Section 6 presents the three types of remedial measures adopted at instrumented sites, including chemical grouting, stone-blowing, and installation of under tie pads. Detailed implementation procedures for the selected remedial measures are presented. Tie-gaps and layer moduli after selected remedial measures are re-estimated. Performance monitoring of remediated bridge approaches discussed in this section includes layer settlement trends, geometry data, and transient responses under train loading.

Section 7 presents numerical modeling efforts which concentrate first on developing a calibrated 3D FEM model to accurately predict the instrumented tie responses using the GeoTrack back calculated layer moduli. This also validates the developed 3D FEM model for the elastic transient response analysis and helps to establish a proper finite element mesh for studying other bridge approach site specific conditions such as those of the quasi-static moving wheel load considerations as well as rehabilitated transition design. Finally, an integrated approach to dynamic analysis of railway track transitions is presented with the application of the track

deformation and load data from the instrumented bridge approaches to calibrate a fully coupled 3D track dynamic model. Loading profiles generated from this model are used as input for the BLOKS3D DEM program to predict individual particle accelerations within the ballast layer.

Section 8 provides the summary and conclusions of this project. Major causes of differential settlement and transient response trends under train loading are summarized first according to the field instrumentation results and advanced analyses of the field data from the monitored bridge approach sites. Performances of the selected remedial measures applied to the instrumented bridge approaches are then discussed with inferences made on their effectiveness for mitigating differential movement. Finally, recommendations based on the project findings are offered for improved bridge approach designs and future research needs.

2. Review of Published Literature

Differential settlement at railroad track transitions has been a global problem for both track maintenance personnel and passengers. The Association of American Railroads (AAR) reported an annual expenditure of approximately $200 million to maintain track transitions (Sasaoka et al., 2005; Hyslip et al., 2009), and more than $110 million was spent annually on transition zones in Europe by 1999 (Hyslip et al., 2009; ERRI, 1999). Examples of railway track transitions include tunnels, special track work, highway/rail at-grade crossings, and the most common, transitions encountered at bridge approaches.

Railway track transitions present a significant challenge for track profile maintenance of the track profile (Woodward et al., 2007; Banimahd et al., 2012). Due to the sudden change in track stiffness, the "stiff" side of a track transition experiences lower deformations under loading, compared to the "less stiff" side. This differential movement often results in the formation of a "bump" in the track profile. Bridge approaches qualify as an ideal example of track transitions, with the approach track on either side of the bridge abutment being much less stiff compared to the bridge deck that is often supported by deep foundations. Differences in track system stiffness and/or damping characteristics, settlement of the ballast layer due to degradation and/or fouling, and settlement of the subgrade and/or fill layers are some of the factors commonly reported as mechanisms contributing to the differential movement at track transitions. Proper understanding of different mechanisms contributing to this phenomenon requires the combined application of field instrumentation with analytical and numerical track modeling.

2.1 Bridge Approaches as the Most Significant Track Transition Type

Bridge approaches have been investigated by many researchers. The bump and "dip" formations at the end of a railroad bridge were illustrated by Nicks (2009) as shown in Figure 2.1. Due to drastic differences in substructure and loading conditions, the tracks on a bridge deck undergo significantly lower deformations under loading compared to the approach tracks. This sudden change in track deformation behavior at the transition point results in an extreme loading condition and ultimately leads to the rapid deterioration of the track and bridge structural components. This structural damage often manifests as a track geometry defect. Differential movement at bridge approaches often results in the development of a bump, usually within 15 m from the bridge end (Plotkin and Davis, 2008).

A survey of railroads in north America, Australia, and Europe conducted in 2006 indicated that approximately 50 percent of bridge approaches developed a low approach, usually 6 to 102 mm in depth and 1.2 to 15.2 m in length, that adversely affected ride quality (Briaud et al., 2006). Development of sudden dips adjacent to the bridge deck increases the dynamic impact loads significantly. Koch (2007) reported vertical dynamic loads about twice the static wheel load level for coal gondolas at track transitions. Read and Li (2006) concluded that the bump problem at track transitions was more significant as a train moves from a high-stiffness track to a low-stiffness track. According to Read and Li (2006), the problem of differential movement was more critical at the exit end of a bridge, whereas the sudden track stiffness increase at the bridge entrance led to rail surface fatigue, tie deterioration, and rail seat pad deterioration.

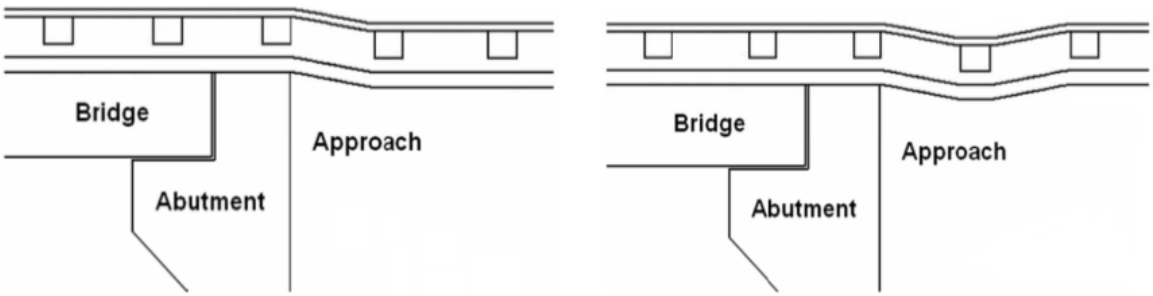

Figure 2.1: The Bump (left) and Dip (right) at End of Railway Bridge (Nicks, 2009)

The differential movement at track transitions is particularly problematic for high-speed rail infrastructure, as bumps are accentuated at high speeds. The issue is even more critical for shared corridors carrying both freight and high-speed lines. Transitions along shared corridors need to be maintained to satisfy the high ride quality requirements associated with high-speed trains and to withstand the heavy loads imposed by slow-moving freight trains. With the current impetus for development of high-speed lines in the U.S and the challenges associated with shared corridors for operation of passenger trains at increased speeds, preventing and mitigating the problem of differential movement at bridge approaches and other track transitions has become more significant.

Researchers do not always agree about the root causes and major influential factors affecting bridge approach problems. From the investigation of four bridge approaches with concrete ballast-deck bridges and concrete ties, Li and Davis (2005) reported inadequate ballast and sub-ballast layer performance to be the primary cause of track geometry degradation. Using settlement rods installed in the test sections, they observed no significant subgrade movements, but instead reported significant track geometry deterioration for a site with cement-stabilized backfill. On the other hand, Selig and Li (1994) identified subgrade stiffness to be the most influential parameter affecting the moduli of ballasted tracks. As track transition problems are often related to the stiffness of the approach trackbed, this would indicate that the subgrade layer plays the most significant role in governing the differential movement at track transitions. Recent field data, to be discussed in detail in this report, clearly identifies the ballast layer as the primary contributor to the differential movement problem (Mishra et al., 2012; Tutumluer et al., 2012; and Mishra et al., 2014). As the ballast breaks down and consolidates under repeated train loading, ballast movement and degradation often lead to recurrent ballast settlement at the transition zones.

Sasaoka and Davis (2005) attributed track transition problems to three primary factors: (1) differential settlement, (2) differences in stiffness characteristics, and (3) discrepancies in track damping properties between adjacent sections. Similarly, Li and Davis (2005) listed (1) track stiffness change, (2) ballast settlement, and (3) geotechnical issues as the major causes of bridge approach problems. Nicks (2009) listed the following 10 factors identified by researchers as contributing to bump development at railway bridge approaches: (1) differential track modulus, (2) quality of approach fill, (3) impact loads, (4) ballast material, (5) drainage, (6) damping, (7) abutment type, (8) bridge joint, (9) traffic considerations, and (10) quality of construction. Note that although most researchers list “track stiffness difference” as an important factor influencing the differential movement and other track deterioration problems at transitions, Plotkin and

Davis (2008) used five different analysis methods to conclude that stiffness differences did not play an important role in track behavior and ride quality at track transitions.

2.2 Summary of Past Track Transition Instrumentation Efforts

Several attempts have been made to characterize bump development at track transitions. For instance, strain gauges (see Figure 2.2) are widely used for measuring wheel loads on the rail. Namura and Suzuki (2013) used axle box acceleration data to evaluate the wheel load on vehicles and placed strain gauges on rail webs to measure the wheel loads on the rail. These field data were compared with analytical model results to validate effectiveness of the modeling approach. Mitigation methods were then proposed for minimizing the track geometry degradation at track transitions. Sakurai et al. (2013) adopted a set of instruments for monitoring performance of pre-stressed ballast track (PSB). The PSB track sleepers were pulled down against ballast by tie rods fixed to the anchors laid under trackbed. Strain gauges were placed on the tie rod to measure reactions (Sakurai et al., 2013). Similarly, Hayano et al. (2013) investigated the effect of ballast thickness and tamping repair approaches on the settlement characteristics of ballasted tracks using a one-fifth scale model developed in the laboratory, with displacement gauges installed to measure settlement of footing under cyclic loading. Computer vision techniques, such as 3D images, were also used by researchers to measure soil mass density of ballast material (Hayano et al., 2013).

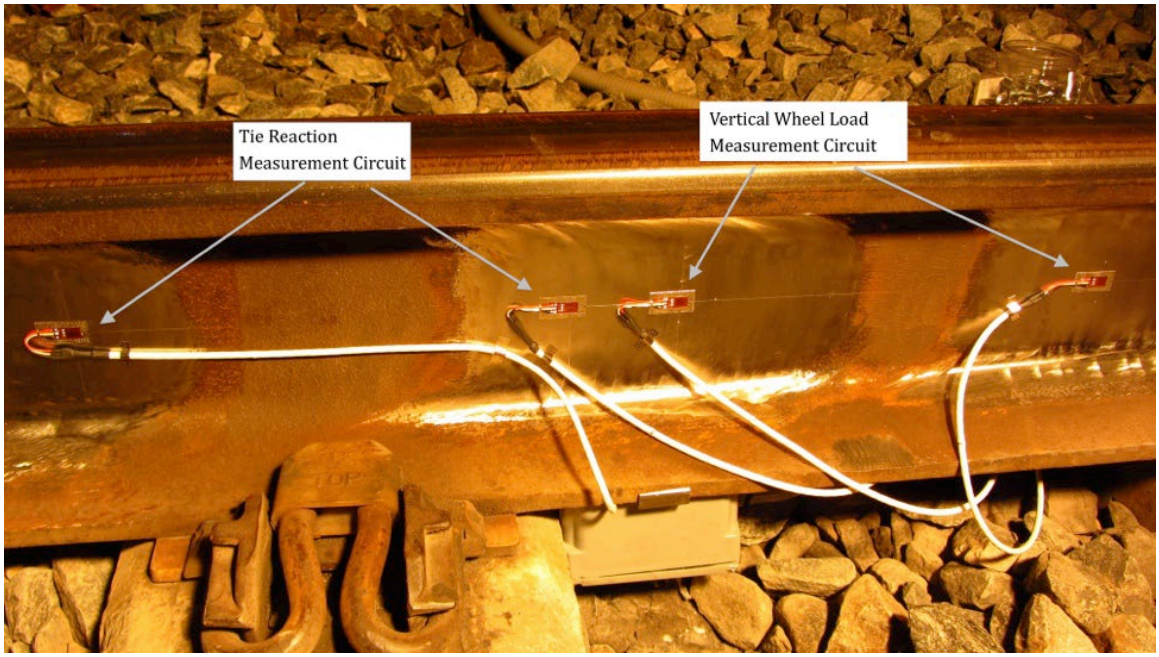

Figure 2.2: Dual-Element Shear Strain Gauges Installed at the Rail Neutral Axis for Wheel Load and Tie Reaction Measurements

MDDs, which are employed in this research effort, have been used to measure track substructure layer deformations. The MDD technology was first developed in South Africa in the early 1980s to measure individual layer deformations in highway pavements (Scullion et al., 1989). MDDs typically consist of up to six LVDTs installed vertically at preselected depths in a small-diameter (typically 45 mm) hole to measure the displacements of individual substructure layers with respect to a fixed anchor buried deep in the ground (DeBeer et al., 1989). Although several

studies in the U.S. have used MDDs to measure layer deformations in highway and airfield pavements, their use in railroad applications has been limited. Two studies in the U.S. (Sussmann and Selig, 1998; Bilow and Li, 2005) used MDDs to monitor the deformations in railway track substructure layers.

It is noteworthy that the use of MDDs to monitor railway track performance has been extensively pursued in South Africa (Grabe and Shaw, 2010; Priest et al., 2010; Vorster and Grabe, 2013). The vertical deformations are measured from a reference head near the top surface to predetermined depths in a borehole with the overall vertical deformation referenced to a fixed anchor in the subgrade (see Figure 2.3). Coelho et al. (2011) studied typical transition zones in the Netherlands. In their research, accelerations and velocities of the track, soil, and approach slabs in response to passenger trains were measured for the calculation of displacements. In addition, track settlements and pore water pressures were monitored over a 1-year period.

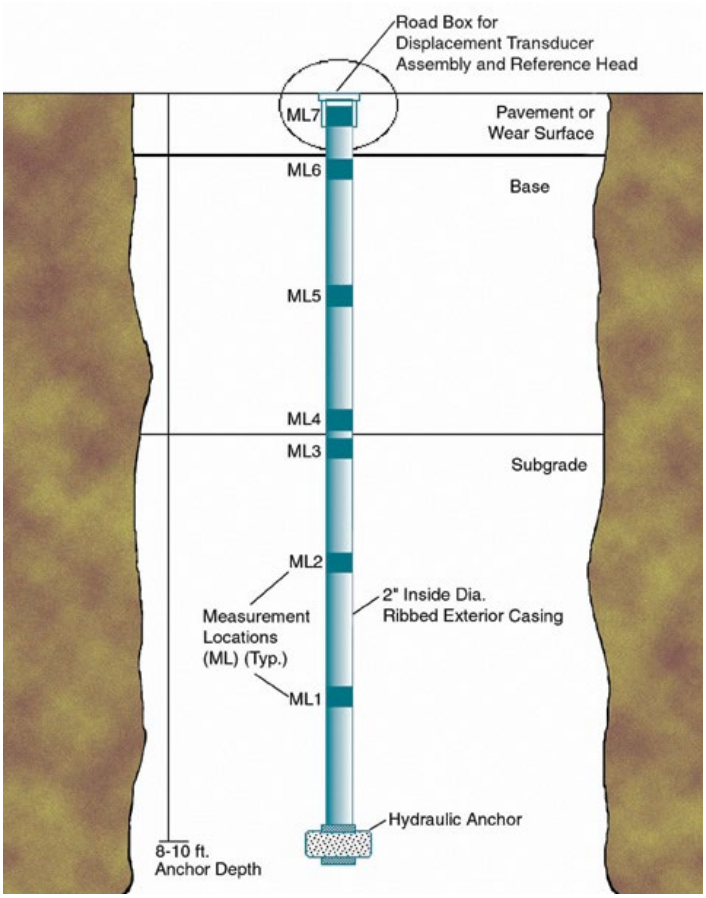

Figure 2.3: MDD Installed to Measure Vertical Deformation Contributed by Each Layer of a Multi-Layer Strata (Weinmann et al., 2004)

2.3 Analytical and Numerical Modeling of Railroad Track Transitions

There have been various mathematical models developed to interpret and predict the dynamic response of railroad track. Early examples were one- or two-dimensional models composed of a beam on a Winkler foundation under a moving force. Mise and Kunii (1956) developed a theoretical framework for the vibrations of a flexible beam supporting a moving locomotive. In their simplified model, only a beam under a moving force was considered. Kalker (1996)

introduced discretely supported rails under a travelling vertical point load to better represent the irregular discrete support of the sleepers. Closed-form solutions were derived for the dynamic response of a simple beam under high-speed trains (Yang et al., 1997). Huang et al. (2010) developed the analytical solution of a railroad track model under moving loads with an asphalt trackbed used underneath the ballast layers (see Figure 2.4). Basu and Rao (2013) studied the steady state responses of an infinite beam resting on a viscoelastic foundation where shear resistance of soil was also included in the analysis.

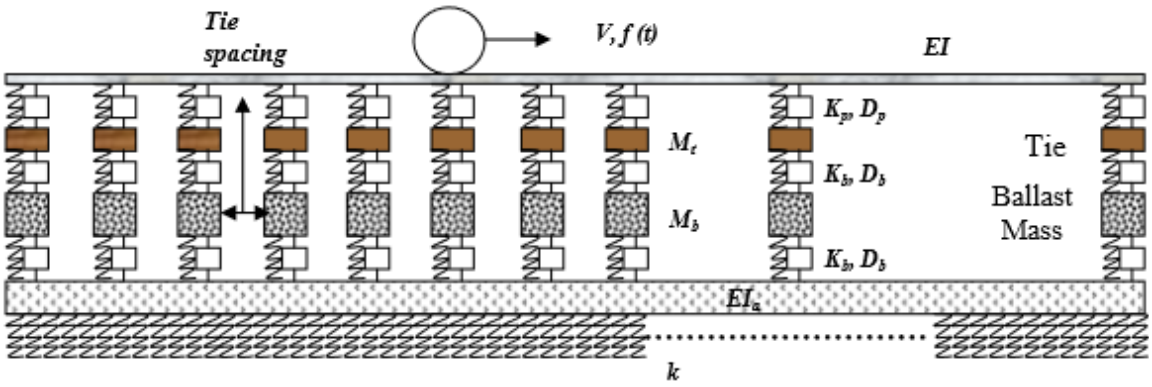

Figure 2.4: Discretely Supported Track Model (Huang et al., 2010)

Rail track and substructure can be represented as a discretely supported rail system with the coupling of soil's shear resistance. However, these models do not include the mass of the train and the interacting force between the wheel and track or the irregularity of the track profile. The work of Lee (1998) introduced the dynamic response of a Timoshenko beam on a Winkler foundation subjected to a moving mass load and showed the limitation of neglecting inertial effects of the mass when only an equivalent moving force was considered. Furthermore, Lei and Noda (2002) developed a computational model for the vehicle and track coupling system where the system was divided into two parts. The upper structure was a whole locomotive with two layers of a spring, and a damping system in which vehicle and bogie were involved. The lower structure was a railway track where rails were considered as beams rested on a double-layer continuous elastic foundation. Random irregularity of the track vertical profile was also simulated in their work. Zhai and Sun (1994) also investigated a model for vertical interaction between a vehicle and track. The vehicle subsystem was modeled as a multi-body system with 10 degrees of freedom (DOFs) running on the track with a constant velocity, and the track substructure as an infinite Euler beam supported on a discrete continuous elastic foundation consisting of the three layers of rail, sleeper, and ballast. Lei and Rose (2008) analyzed track vibration by Fourier transform technique with random irregularity of track vertical profile.

Note that the above analytical models do not include the 3D dynamic wave field generated in the ground due to the passage of a train. Therefore, they are restricted to cases where the velocity of the train is much smaller than a critical velocity (Krylov, 1995). Krylov (1995) studied ground vibrations generated by superfast trains theoretically. He found that superfast railway trains moving with speeds approaching or exceeding the Rayleigh wave velocity in the ground could cause very large increases in ground vibration levels when compared to those generated by conventional trains. The most typical Rayleigh wave velocity values for soils are 250–500 m/s. Holm et al. (2002) confirmed that "critical speed" is the speed at which trains induce a large

resonant response in the track with soft ground conditions, resulting in excessive vertical vibrations. Based on these theories, 3D models on the soil considering ground vibrations were proposed. Bian et al. (2008) conducted a simulation of high-speed train-induced ground vibrations using a 2.5D finite element method. The train-induced track and ground vibrations have been studied using analytical-numerical combined method. Later, a fully coupled 3D train track soil model was also introduced by Huang et al. (2014), where 3D soil parts were included.

Most of the developed analytical models are linear in nature and therefore limited when nonlinear aspects become significant, i.e., when there is an unsupported tie. To avoid this limitation, Tanabe et al. (2003) built a 3D numerical analysis model where nonlinear springs and dampers were employed. Nielson and Oscarsson (2004) expanded their previous model to account for state-dependent track properties separated into linear contributions corresponding to an unloaded track, and non-linear contributions that are dependent on the time-variant state of the different track components due to the dynamic loading from a moving train model.

There are very few analytical solutions for the track transition problem. Frohling et al. (1996) developed a mathematical model to study the influence of spatially varying track stiffness on the performance of the wheel and the track at low frequencies. Biondi et al. (2005) investigated the 2D dynamic interaction among a running train, a track structure, and a supporting bridge where both rails and bridge were modeled as Bernoulli Euler beams. Similarly, Zhai et al. (2013) established a model for the analysis of train-track-bridge dynamic interactions which also accounts for the continuity problem. The work of Coelho et al. (2009) showed the importance of hanging sleepers in the transition zone due to the large settlement of the embankment and the higher dynamic impact forces induced by passing trains on these areas. Varandas (2013) and Varandas et al. (2011) confirmed the main cause for the higher displacement amplitudes registered on the transition zone was the existence of a group of consecutive hanging sleepers. They presented a model (see Figure 2.5) which is nonlinear for the interaction between force and displacement of springs and considers the unloaded position of track and ballast (including hanging distances). The model can simulate when the wheels move onto the trough existing after the culvert as a lever effect lifts the rail/sleepers (ties) system before the culvert.

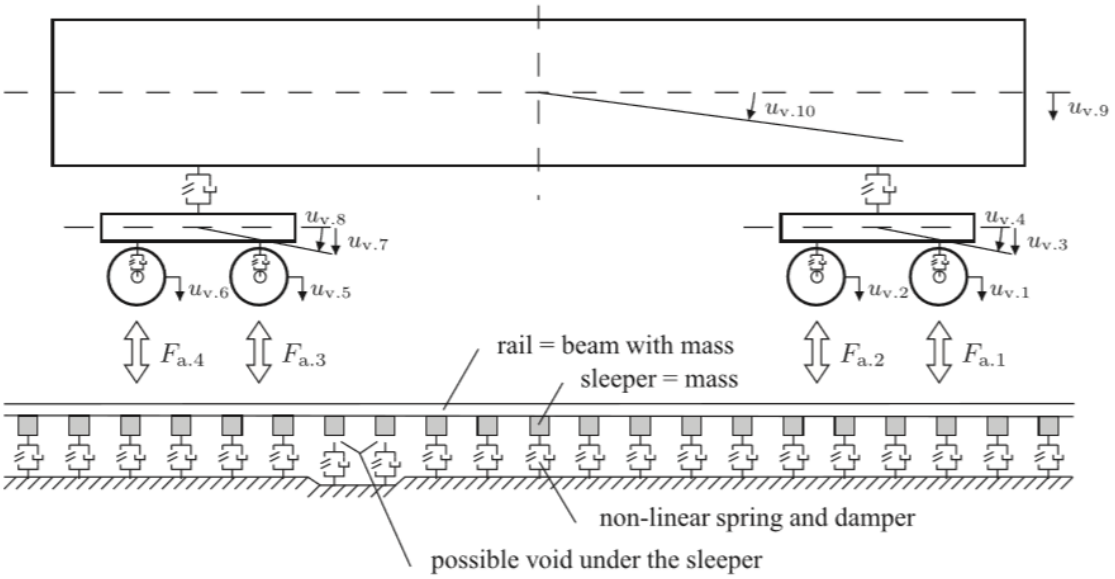

Figure 2.5: Train and Track Interaction Model (Varandas, 2013)

2.3.1 Numerical Modeling Approaches

Laboratory scale experiments and field testing are not always the best choices for studying the behavior railway track systems because of the long test durations and costs involved. However, analytical models, such as the methods discussed in the previous section, are not always accurate for the specific details and different geometries involved. GeoTrack (Chang et al., 1980) is a layered elastic system program that has been validated and widely used for track structural analysis. In GeoTrack, stresses and deformations are calculated as a function of multi-axle loads, properties of rails and ties, properties of substructure layers, and geometry of ties and underlying layers (Li et al., 1998). KENTRACK (Huang et al., 1984) is a finite, element-based trackbed structural design program that can be used to analyze responses of granular ballast trackbed as well as asphalt trackbed and slab track. Of course, these models also come with certain assumptions and several limitations such that in some situations they may not be appropriate. For instance, they do not consider the dynamic response behavior of the track system.

To study the time-dependent behavior of track under dynamic loading, the FEM has been adopted and used by researchers (Feng, 2011; Smith et al., 2006). Feng (2011) used FEM to simulate different track systems with various analytical formulations and complexities, such as the beam on discrete support model, the track with ballast mass model, and the rail on sleeper on continuum model. For individual cases, the displacements of the trackbed were evaluated. Numerical solutions indicated that rail pad stiffness considered in the model had a major effect on the resonance frequency.

At track transitions in which unsupported, hanging ties are common (see Figure 2.6), tracks sometimes experience impact loading conditions and nonlinear track behavior. However, only a few numerical models include these features (Smith et al., 2006; Kaewunruen et al., 2011; Giner et al., 2012; Wang et al., 2015). Smith et al. (2006) conducted a parametric study using a finite difference program, FLAC3D, considering the effects of velocity and stiffness of substructure materials. The limitation of this model is that the train load was not distributed through the rail and ties. Kaewunruen et al. (2011) used a nonlinear solver in STRAND7 to conduct numerical FEM simulations of track and focused on the hanging tie problem due to a lack of support or excessive track settlement. The model was able to evaluate the effect of voids on the dynamic responses of concrete sleepers. The negative dynamic bending moments were enlarged by hanging ties and could cause the ballast to wear out sooner. Yin and Wei (2013) developed an FEM of railway bridge transition zone using Abaqus commercial software. The model included vehicle modeling, bridge modeling, and open-track modeling. Track irregularity was also included in the model. More recently, a dynamic FEM model using an explicit integration of the track transition zone was developed (Wang et al., 2015) to model transition zones with differential settlement or hanging ties. This model was validated through field measurements on a ballasted track.

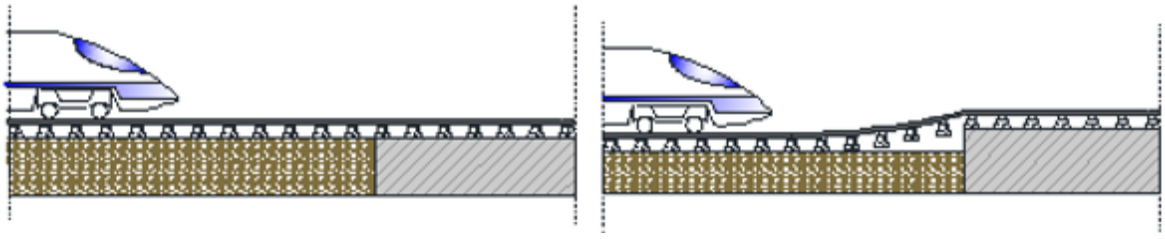

Figure 2.6: Degradation of Track Transition Zone (Wang et al. 2015)

2.4 Remedial Measures to Mitigate Differential Movement at Track Transitions

Although the problem of bump development at highway bridge approaches has been extensively studied (Zaman et al., 1991; Briaud et al., 1997; White et al., 2005; Puppala et al., 2009), few research studies have focused on mitigating the differential movement at railway track transitions. Studies investigating track transition problems have primarily focused on preselected mitigation techniques and have presented test section and parametric analysis results on the effectiveness of these remedial measures (Sasaoka et al., 2005; Read and Li, 2006; Nicks, 2009).

Several different remedial measures have been suggested by researchers to mitigate differential movement problems at track transitions. Nicks (2009) divided the remedial measures into the following interrelated categories: (1) reduce approach settlement, (2) decrease modulus on bridge deck, (3) increase modulus on approach track, (4) reduce ballast wear and movement, and (5) increase damping on the bridge deck. Kerr and Moroney (1993) concluded that most problems at track transitions arise from rapid changes in the vertical acceleration of wheels and cars in the transition zone. Accordingly, they recommended that all remedial measures should aim to reduce the train vertical acceleration at the transition zones. Solutions can be arranged into the following three categories (Kerr and Moroney, 1993): (a) smoothing the track stiffness (often represented as "k") distribution on the "soft" side of the transition; (b) smoothing the transition by increasing the bending stiffness of the rail-tie structure on the "soft" side, in close vicinity of the transition point; and (c) reducing the vertical stiffness on the "stiff" side of the transition. Remedial measures under category (a) include use of oversized ties, reduced tie spacing, ballast reinforcement using geogrids, hot-mix-asphalt (HMA) underlayment, and use of approach slabs. The most known method under category (b) was developed by the German Federal Railways (DB) and involves attaching four extra rails (two inside and two outside the running rails) to the crossties (Kerr and Bathurst, 2001). Finally, the primary approach in category (c) involves the installation of tie pads and/or ballast mats on ballast-deck bridges to reduce the track stiffness on the "stiff" side of a transition point.

Using analytical procedures, Kerr and Moroney (1993) engineered rail pad stiffness to match the track running over the bridge. A later study (Kerr and Bathurst, 2001) installed these "matched pads" on three different open-deck bridges near Chester, PA, Catlett, VA, and Philadelphia, PA. Field test results after the installations indicated significant improvements in track geometry near the bridge abutments. Sasaoka and Davis (2005) tried different methods to alter the track stiffness and damping characteristics on bridge approaches. Installing ties made of different materials, they reported that plastic ties on a concrete span ballasted-deck bridge effectively reduced the stiffness difference at track transitions. Through parametric analyses using the GeoTrack multi-layered elastic program, they concluded that subgrade improvement in the approach and altering tie pad properties on the bridge deck were the most effective methods to minimize track stiffness differences at bridge approaches. Similarly, from dynamic analyses using NUCARS, they concluded that providing extra dampers on the bridge deck could improve the impact attenuation at the transition by up to 30 percent. Li and Davis (2005) concluded that remedies intended to strengthen the subgrade were not effective for sites where ballast/sub-ballast layers were primarily responsible for the differential movement. In such cases, mitigation techniques such as rubber pads under the concrete ties or rubber mats on the concrete bridge deck had to be used to reduce the track stiffness and enhance the damping characteristics.

Rose and Anderson (2006) presented asphalt underlayment trackbeds as an effective method for improving the performance of track transitions at tunnels, bridge approaches, special trackwork

(i.e., crossing diamonds, crossovers, and turn-outs), and at rail/highway at-grade crossings. Placement of a thicker HMA underlayment adjacent to the bridge and a thinner section close to the existing all-granular trackbed reportedly improved the performance of both open-deck and ballast-deck bridges. Rose and Anderson (2006) reported on four bridge approaches that were rehabilitated using this technique along a Kentucky mainline with over 50 million gross tons (MGT) annual tonnage and a line speed of 80–96 km/h. Over 5 years since the renewal of these approaches, no resurfacing was needed to correct track geometry.

Apart from the above-listed remedial measures, researchers have also suggested converting open-deck bridges to ballast-decks (Hyslip et al., 2009), constructing approach slabs (Sharpe et al., 2002), and applying chemical grouting (Woodward et al., 2007; Hyslip et al., 2009) and stone-blowing (Chrismer, 1990; McMichael and McNaughton, 2003) as alternatives to mitigate track transition problems. Bridge approach slabs have been used as a semi-structural method to ease the transition from approach embankments to the fixed bridge structure (Sharpe et al., 2002). However, concrete approach slabs require a good connection at the abutment and good support conditions away from the abutment to be effective, so they are not widely used. Hyslip et al. (2009) proposed chemical grouting as a conceptual solution for bridge transition improvement. Among the above proposed remedial measures, chemical grouting, under tie pads, and stone-blowing were chosen in this study as remedial measures to investigate the field-instrumented bridge approach locations.

2.4.1 Chemical Grouting

Ballast provides structural support and stability to the track. It also contributes considerably to track settlement. Chemical grouting, also known as polyurethane stabilization (see Figure 2.7), has been successfully used to reduce excessive ballast vibrations and long-term, permanent deformations. Polyurethanes, aka polymers, are extremely large, complex molecules, produced by combining a large number of simpler molecules called monomers. The lower the closed-cell content in polyurethanes, the more the material acts like a flexible foam. In the case of a rigid-foam, where mechanical properties such as high strength and stiffness are needed, a high-content, closed-cell foam is preferred. Polyurethane ballast stabilization is an economical solution due to its quick curing period. It can be applied without taking the track out of service. When properly applied, chemical grouts can bind the ballast particles together, thus reducing excessive vibrations and particle migration (Woodward et al., 2007). Moreover, it is reported that polyurethane chemical grouting does not adversely affect the drainage ability of the ballast layer.

There has been extensive laboratory testing and evaluation of polyurethane-stabilized ballast. Dersch et al. (2010) evaluated the effectiveness of elastomer polyurethane coating of ballast through a direct shear box test. Polyurethane-coated ballast samples formed rigid blocks and resulted in a two- to three-fold increase in the shear strength of the ballast, while the amount of ballast breakdown during testing decreased due to less particle movement and reorientation under shear loading (Dersch et al., 2010; Boler, 2012). Boler (2012) further studied ballast aggregates treated with polyurethane with an image-aided particle shape model and particle packing simulations using the DEM. The results showed that the shear strength increase of the polyurethane-coated ballast assembly was significantly influenced by the bond strengths of the particle contacts. Keene et al. (2012) tested specimens of polyurethane-stabilized ballast under repeated loading. The results showed that polyurethane-stabilized ballast had good resistance to the accumulation of plastic strain compared to untreated substructure materials. Also, flexural

strength tests conducted on polyurethane-stabilized ballast were close to that of cement-stabilized soils. However, the flexural modulus of polyurethane-stabilized ballast was much lower than that of cement-stabilized soils.

Figure 2.7: Polyurethane Grouting of Ballast – Injected Grout Seen From Underneath Tie

Researchers also conducted field and full-scale tests. Woodward et al. (2012) evaluated the polyurethane ballast reinforcement technique through laboratory tests under cyclic loading and a case study in Grovehill Tunnel, UK. With proper injection of polyurethane to achieve the desired stiffness, strength, and penetration depths, gauge clearances on ballasted railway track could be maintained. Full-scale testing was conducted by Kennedy et al. (2013) to compare traditional ballast and polyurethane-reinforced ballast behavior trends for up to a maximum of 500,000 load cycles at different loading levels. Significant reductions in track settlement were achieved with the polyurethane reinforcement. Polyurethane-treated ballast railway track provided performance similar to slab track.

Recently, Warren (2015) used an expanding rigid polyurethane foam to reinforce an in-service railroad track in Illinois, where track settlement and progressive shear failure presented problems. The study mainly focused on a life-cycle cost analysis and the analyses related to maintenance cycles of both the stabilized ballasted track and traditional track. Results showed that over a 10-year period, polyurethane injections could save significant maintenance costs.

2.4.2 Under Tie Pads

Under tie pads (UTPs) can be used to maintain a smooth transitional stiffness between regular track and a bridge deck and to slow down track deterioration at the bridge approach (Lundqvist

et al., 2006). UTPs are resilient pads attached to the bottom surface of ties to provide an elastic layer between ties and ballast. They have been used in track structures for almost 25 years. According to Lundqvist et al. (2006), UTPs control stiffness and thus minimize rail-tie-ballast contact force variations.

UTPs have been tested in laboratory by many researchers and practitioners (Pen et al., 2015; Grabe et al., 2015). It is believed that with the use of UTPs on concrete ties, the contact area between tie and ballast can be increased from approximately 3 percent to 10–35 percent depending on the pad type. French and Austrian installations demonstrated that tamping can be reduced and therefore maintenance cost is greatly reduced (Fimor, 2015). Grabe et al. (2015) conducted a full tie test and a half tie test of UTPs under various loading conditions such as static, dynamic, and cyclic loading, and used tactile surface sensors to measure the pressure under the tie. The results showed that the use of UTPs can provide a reduction in settlement by approximately 27–44 percent, an increase of contact area by 10–33 percent, a reduction of contact pressure by 70 percent, and a reduction of ballast breakdown by 10–40 percent (Grabe et al., 2015).

Field installations of UTPs have generally been successful. Li and Davis (2005) conducted preliminary investigations on the benefits of using rubber pads under concrete ties in a section of test track at the Transportation Technology Center (TTC) in Pueblo, Colorado. The altering of track modulus and damping showed that UTPs not only reduced track stiffness but also increased track damping. UTPs can also reduce impacts between ballast particles and concrete ties or bridge surfaces. Two different types of rubber pads used as UTPs were tested by Sasaoka and Davis (2005). The pads were adhered to the bottom of concrete ties and installed on both a concrete span bridge and a steel beam span bridge. They concluded that both types of pads were successful at lowering the bridge modulus to below that of the approach track as well as providing damping for the bridge structure. Full-scale field tests were conducted in Switzerland to investigate the influence of UTPs (Schneider et al., 2011). The UTP-installed track typically generated higher rail and sleeper accelerations but lower strains levels. UTPs can also slow down geometry degradation. Li and Maal (2015) reported the performance of UTPs installed on a ballast deck concrete tie bridge in 2007. The bridge has not required repair or major track maintenance since 2007. Moreover, high-amplitude vibrations were significantly reduced. Pen et al. (2015) used geophones (velocity transducers) to measure track substructure responses in a UK site to conclude that the potential benefits of UTPs: (1) increase the number and area of contact; (2) reduce the rate of plastic settlement; (3) reduce the support stiffness and spread the load along a greater length of track; and (4) add a consistent increment to the track deflection and reduce support stiffness variation.

UTPs usually consist of two layers, one elastic spring layer and a geotextile to protect the spring layer. Numerical models have been developed to study their properties and effectiveness. For example, a parametric study was conducted by Johansson et al. (2008) with different combinations of dynamic stiffness properties of rail pads, under tie pads, and ballast materials using two numerical models. A schematic drawing of one of the analytical models, known as GroundVib, is shown in Figure 2.8. Results showed that UTP stiffness influenced only the lower part of the frequency spectrum (below 250 Hz). Higher under tie pad stiffness was found to lead to lower rail bending moment and lower vertical rail displacement and velocity. No clear relationship between under tie pad stiffness and rail acceleration was found. However, higher UTP stiffness would also lead to higher load on the tie from the ballast interface.

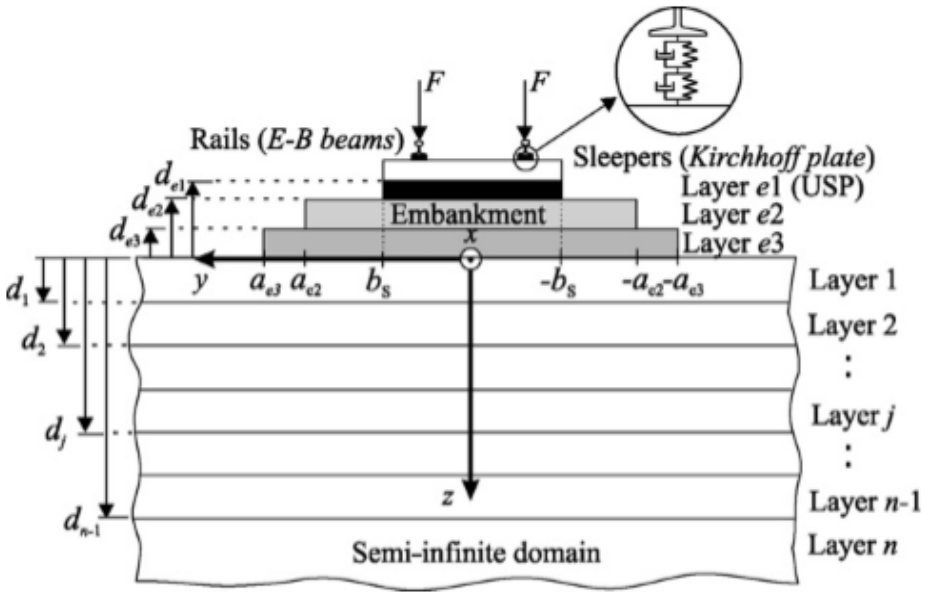

Figure 2.8: Schematic Analytical Model GroundVib (Johansson et al., 2008)

Witt (2008) examined the influence of UTPs using FEM. Three types of UTPs (stiff, medium, and soft) were used. Results showed that stiff UTPs did not influence transition area load; the peak load caused by a hanging sleeper could even increase when using stiff UTPs as compared to using no pads. Similarly, when using soft UTPs, the force on the transition area did not exhibit a large difference compared to areas with no pads. The best results came from using medium-stiffness UTPs. Small variations of contact forces occurred, and the peak caused by the transition area disappeared. Insa et al. (2011) also performed simulations to study the effectiveness of using UTPs. The results showed that UTPs contributed significantly to stiffness reduction by lowering the vertical stiffness of track on a bridge. Ribeiro et al. (2015) used FEM modeling to show that soft UTPs would amplify rail displacement and tie accelerations and reduce abrupt variations in track vertical stiffness.

Despite many successful installations of UTPs in different countries and field applications, some researchers emphasize the need for more research to understand the their behavior. Variations in UTP stiffness and quality are crucial to track settlement (Witt, 2008; Ribeiro et al., 2015). Paixao et al. (2015) reported their findings of two monitored transitions which had similar box culverts. UTPs were added in one of the transitions. Comparison results indicated that the UTPs influenced dynamic behavior by increasing vertical flexibility and amplifying both rail displacements and sleeper accelerations. The installation of UTPs, contrary to the original expectation, did not provide a smoothing stiffness of transition (Hence, Paixao et al., 2015). UTPs have a significant influence on track dynamic behavior that must be understood to properly apply these devices.

2.4.3 Stone-Blowing

Stone-blowing is the addition of ballast to the surface of an existing ballast layer such that any gap between the tie bottom and ballast layer is closed. Originally developed by British Railways, the process of stone-blowing involves the following steps (Selig and Waters, 1994): (1) The geometry of the existing track is measured; (2) the precise track lift required at each crosstie to

restore it to an acceptable geometry is calculated; (3) the volume of stone that needs to be blown beneath the sleeper to achieve such a lift is deduced from the known relationship between the volume of added stone and residual lift; and (4) stone is blown under the ties. The target elevation during stone injection is always set "higher" than the desired elevation so that enough space is provided to have the stones adequately distributed under the tie and to account for settlement. This leads to a smooth transition between the bridge approach and the bridge deck. The stone matrix achieves a stable configuration through particle rearrangement and packing. It is therefore common for the track profile to gradually move down with loading immediately after stone-blowing until a stable configuration is attained. The procedure is illustrated in Figure 2.9.

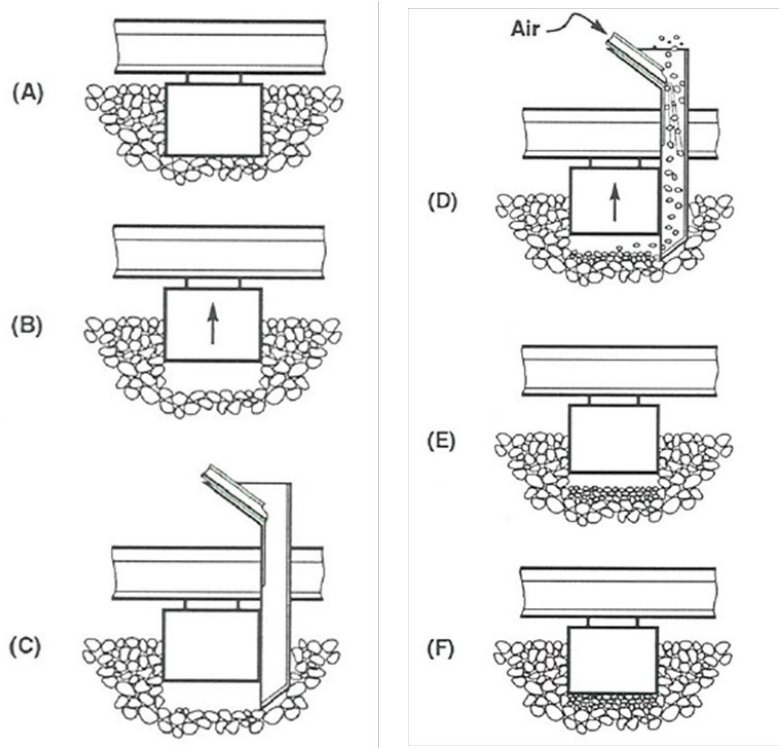

Figure 2.9: Stone-Blowing Procedure (Selig and Waters, 1994)

2.5 Summary

Track geometry problems at railway transitions have been well recognized. Design standards, including the European Rail Research Institute (ERRI), UIC code 719, Design Standards for Railway Structures and Commentary, and AREMA, all involve the design of the transition zone (Muramoto, 2013). Although tunnels, special track work, and highway/rail at-grade crossings are all examples of railway track transitions, the most common transition problems are often encountered at bridge approaches. Due to drastic differences in substructure and loading conditions, the tracks on a bridge deck undergo significantly lower deformations under loading compared to the approach tracks. This sudden change in track deformation behavior at the transition point results in extreme dynamic loading conditions which leads to the rapid deterioration of the track and bridge structural components. Mitigation solutions, including chemical (polyurethane) grouting, under tie pads, and stone-blowing, can be effective at reducing the effect of transition on track condition. These remedial measures are a focus of this research project.

3. Instrumentation of Selected Bridge Approaches

The first task in this research project involved the identification of problematic track transitions experiencing recurrent differential movement problems for instrumentation and performance monitoring. Inputs from railroad industry partners established that bridge approaches consistently ranked as the most problematic track transitions, with the frequency and severity of bump development at bridge approaches being significantly higher than other track transitions (i.e., culverts, tunnels, and grade crossings). Therefore, the instrumentation, performance monitoring, and numerical modeling activities in the current study primarily focused on bridge approaches. Two classes of bridge approaches were instrumented in this research project. The first category represented track transitions that predominantly experience passenger traffic, and the second category comprised track transitions carrying predominantly freight traffic. This section presents details on the site selection, instrumentation, and performance monitoring of the selected problematic bridge approaches.

3.1 Identification of Problematic Sites for Instrumentation

Track geometry records for bridge approaches requiring frequent maintenance were obtained from railroad industry partners and were analyzed to identify locations for instrumentation. The track geometry data used for the site selection were taken from 2009 to 2011. The following subsections present details on the sites selected to study root causes of differential settlements often experienced at those bridge approaches.

3.1.1 Amtrak Northeast Corridor

There are several closely spaced bridges with recurring differential movement problems on Amtrak's NEC near Chester, PA. The NEC is primarily a high-speed railway with occasional freight traffic, carrying high-speed passenger trains operating up to a maximum speed of 241 km/h (150 mph). The NEC near Chester comprises four tracks, with Tracks 2 and 3 maintained for high-speed Acela Express passenger trains operating at 177 km/h (110 mph). The predominant direction of traffic along Track 2 is northbound whereas Track 3 primarily carries southbound traffic.

Preliminary analysis of track geometry data resulted in the selection of two bridge approaches (over Madison and Hinkson streets) as candidate locations for instrumentation and performance monitoring. Figure 3.1 and Figure 3.2 present examples of track geometry data for the two bridges. Tracks 2 and 3 were resurfaced in July 2011 and track geometry data were collected on August 10–24, 2011.

Track geometry undulation was apparent at both Madison and Hinkson Street bridge locations. The bridge over Madison Street was surfaced seven times since 2009 and rapidly developed an abrupt 1 in (~25 mm) dip off the north end shortly after the resurfacing. Similarly, the bridge over Hinkson Street had been surfaced four times since 2009, and the original dipped profile returned after 2–3 weeks following the resurfacing. The recurring dip formations at these two bridge approaches were believed to primarily result from excessive ballast deformations.

Historical track geometry data were obtained from Amtrak spanning the 60-month period from January 2005 to January 2010. Vertical profiles of Tracks 2 and 3 were analyzed using an 18.9 m (62 ft) mid-chord offset and associated data from the vertical space curve. Ground penetrating

radar (GPR) scanning of the tracks was conducted to identify significant substructure features. Detailed analyses of track geometry data led to the discovery that Madison and Hinkson Street bridge approaches were not the most problematic transitions in terms of recurring differential movement. Subsequently, three other bridge approaches (bridges over Upland, Madison, and Caldwell streets) were selected for instrumentation and performance monitoring.

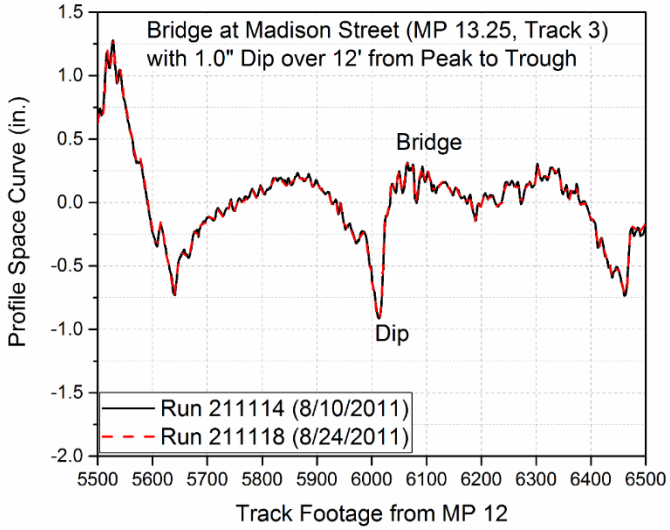

Figure 3.1: Track Geometry Data for Bridge Over Madison Street Near Chester, PA

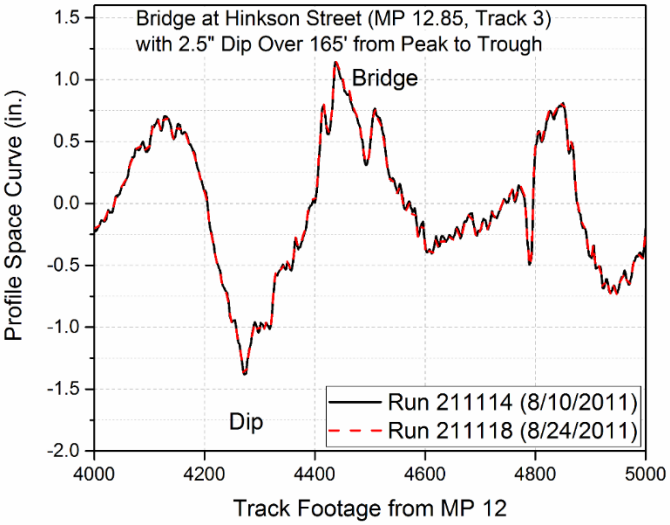

Figure 3.2: Track Geometry Data for Bridge Over Hinkson Street Near Chester, PA

The fundamental indicator of track condition is track geometry, and in most cases, poorly performing track geometry is the condition indicating the need for track quality improvement. Track geometry data from the track geometry measurement vehicle (TGMV) provide an objective indication of the roughness of the track and is useful in distinguishing the sections of track. Also, comparing quantified geometry data for different sections of track can be used to rank the track sections for maintenance prioritization. Track geometry patterns, in particular vertical profile (surface) patterns, are influenced by ballast fouling, changing drainage condition,

and variable subgrade condition. The track geometry analysis focused on the vertical profile geometry channel since this is the channel most influenced by track substructure condition.

Running roughness (R^2) (Ebersöhn and Selig, 1994) was used to quantify the vertical surface mid-chord offset (MCO) track geometry data. R^2 is a mean square statistical calculation that provides a magnitude analysis of the geometry measurements. It is essentially an average of the deviations squared, within a specific moving window, i.e.,

$$R^2 = \frac{\sum_{i=1}^{n} d_i^{\,2}}{n} \tag{3.1}$$

where

d_i = MCO deviation,

n = number of measurements in the length of track under consideration.

Figure 3.3 presents an example of R^2 as applied to vertical profile MCO data. The 62 ft MCO data is shown along with R^2 computed in a 200 ft moving window. It is apparent that the R^2 values are greatest in areas where there are relatively large magnitude MCO deviations. For the Amtrak Chester bridge data, a 60 ft moving window was used. Once the geometry MCO data was converted to R^2, the individual successive runs of track geometry data were aligned to each other and to track features.

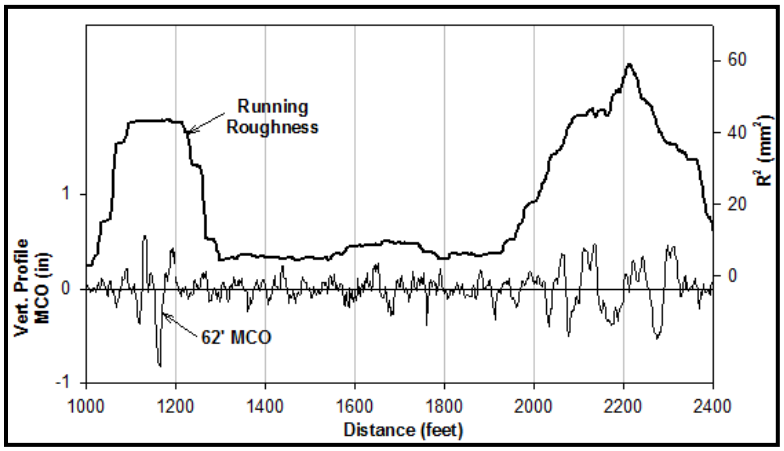

Figure 3.3: R^2 Example (From Hyslip, 2002)

Figure 3.4 through Figure 3.6 present GPR scans, R^2 of MCO data, and space curve plots for the three bridge approaches selected for instrumentation (Upland, Madison, and Caldwell streets). Although the MCO and space curve data represent the time-history of track performance spanning the 60-month period, the GPR scans at all three bridge approaches were conducted in June 2012. The figures also show the geometry profiles of Upland Street (Track 3), Madison Street (Track 2), and Caldwell Street (Track 3) bridges, respectively. As shown in Figure 3.4, the north approach of Upland Street bridge clearly indicated recurrent bump problems over the 60-month period. The vertical axis in Figure 3.4(b) represents time in months, whereas the

horizontal axis represents distance along the track. Significant deviations in the vertical profile are represented by red color, whereas blue-colored patches indicate smooth profiles. As shown in Figure 3.4(b), the north approach of the Upland Street bridge showed recurrent red colored patches representing frequent deviations in the surface profile. Similarly, Figure 3.4(c) shows bumps in the space curve at distances of 4.6 m (15 ft) and 18.3 m (60 ft) from the north abutment. Accordingly, these two locations have been marked and indicated in Figure 3.4 by dashed black lines as the locations for instrumentation.

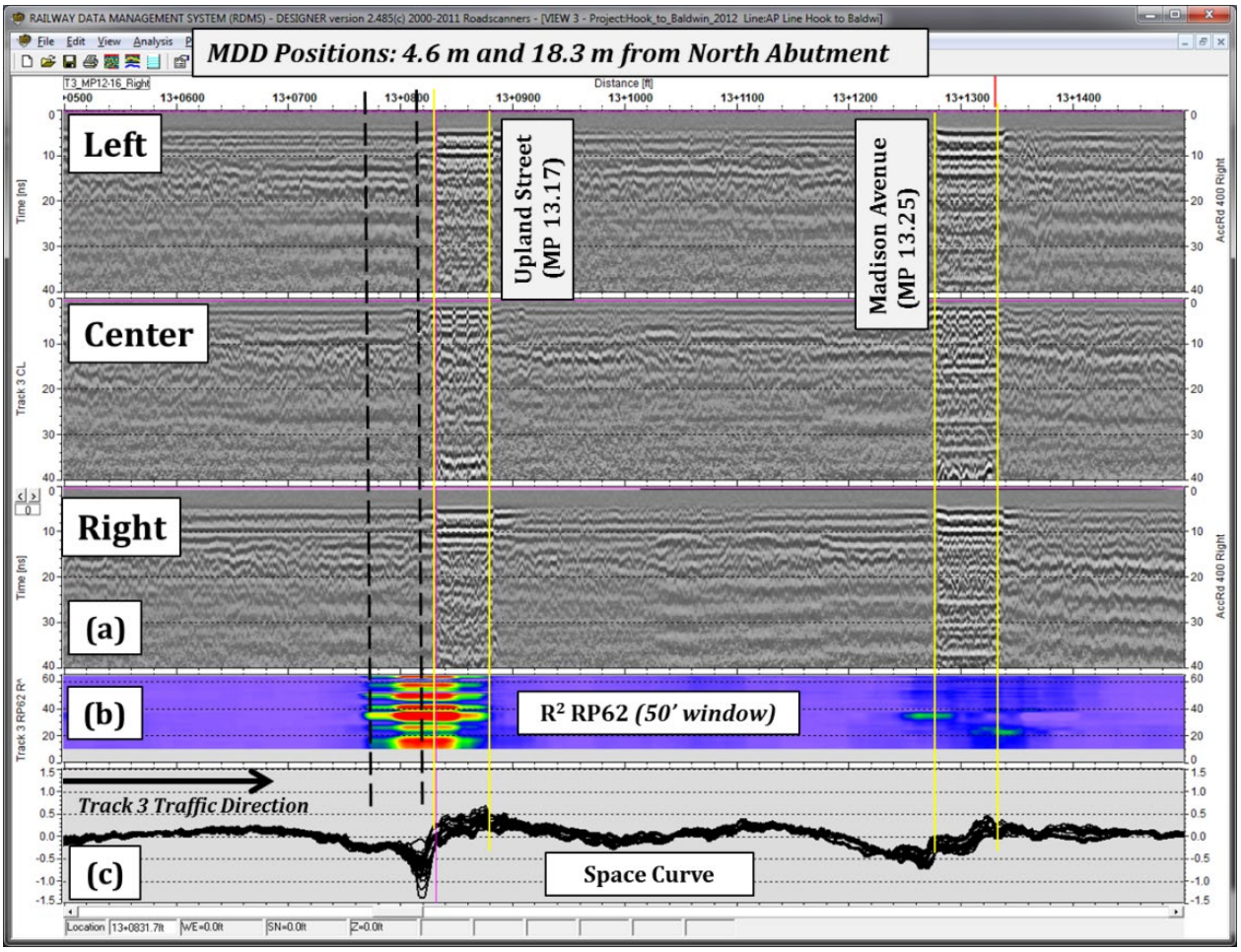

Figure 3.4: (a) GPR Scans, (b) MCO Data, and (c) Space Curve for Track 3 at Upland Street Bridge Approach (MDD Positions: 4.6 m and 18.3 m From North Abutment)

Figure 3.5 shows similar plots for Track 2 near the Madison Street bridge. The south abutment of Madison Street bridge showed recurrent bump problems over the 60-month period represented by the recurrent red colored patches in Figure 3.5(b). The vertical space curve in Figure 3.5(c) shows significant bumps at distances of 3.0 m (10 ft) and 18.3 m (60 ft) from the south abutment. Accordingly, these two locations have been marked and indicated in Figure 3.5 by dashed black lines as locations for instrumentation.

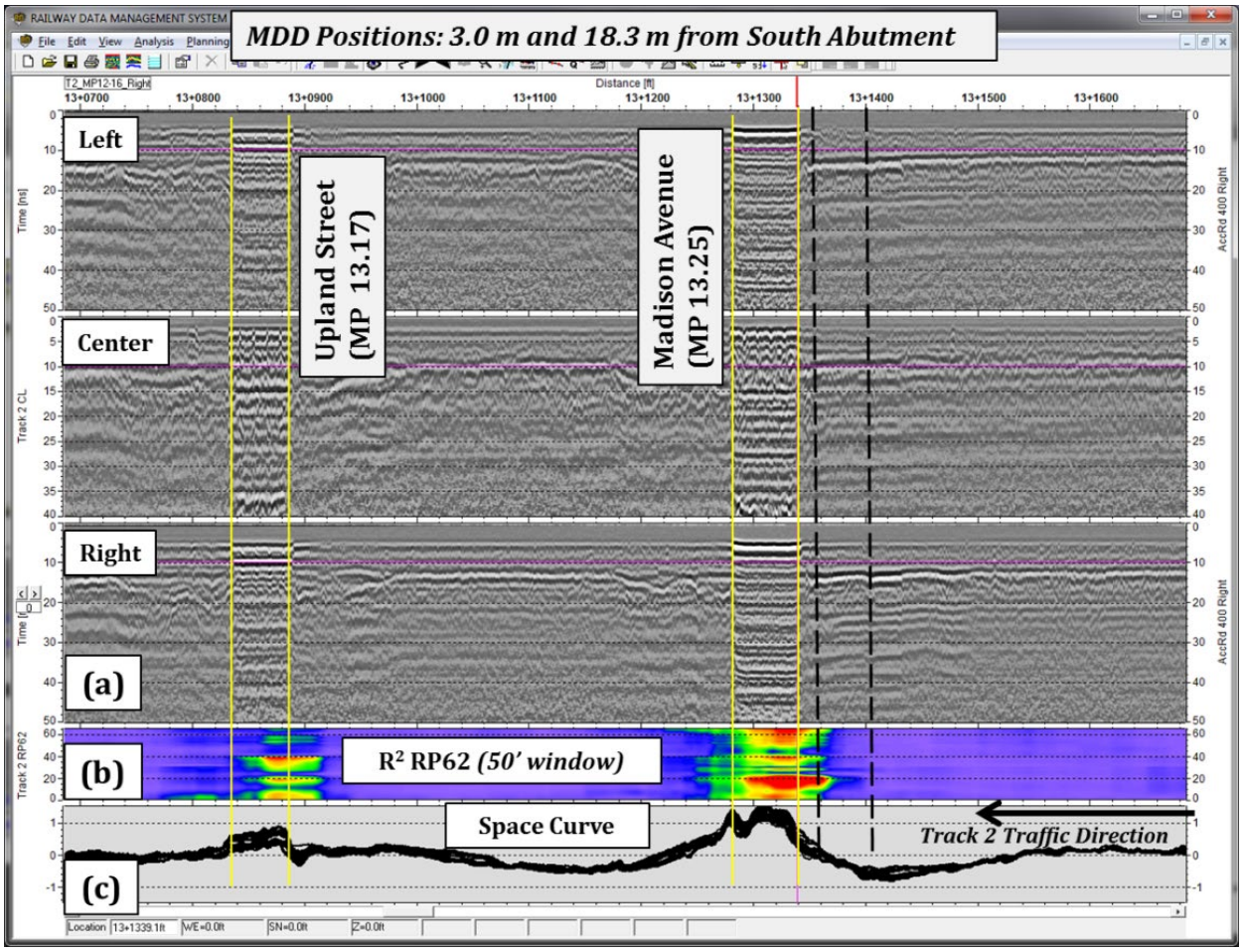

Figure 3.5: (a) GPR Scans, (b) MCO Data, and (c) Space Curve for Track 2 at Madison Street Bridge Approach (MDD Positions: 3.0 and 18.3 m From South Abutment)

As shown in Figure 3.4 and Figure 3.5, the entrance sides of the bridge approaches (train moving from the approach to the bridge) were selected for instrumentation at both the Upland as well as Madison Street bridge locations. For selecting the third bridge approach for instrumentation, the objective was then to identify an approach with recurrent differential movement problems on the exit side of an approach (train moving from the bridge to the embankment). Accordingly, Figure 3.6 shows the track geometry data for Track 3 at the Caldwell Street bridge location. As highlighted in Figure 3.6(c), the space curve shows a significant dip at 24.4 m (80 ft) from the south abutment. To evaluate the uniformity of settlement at either end of a crosstie, researchers decided to instrument both sides of a single crosstie at 24.4 m (80 ft) from the south abutment.

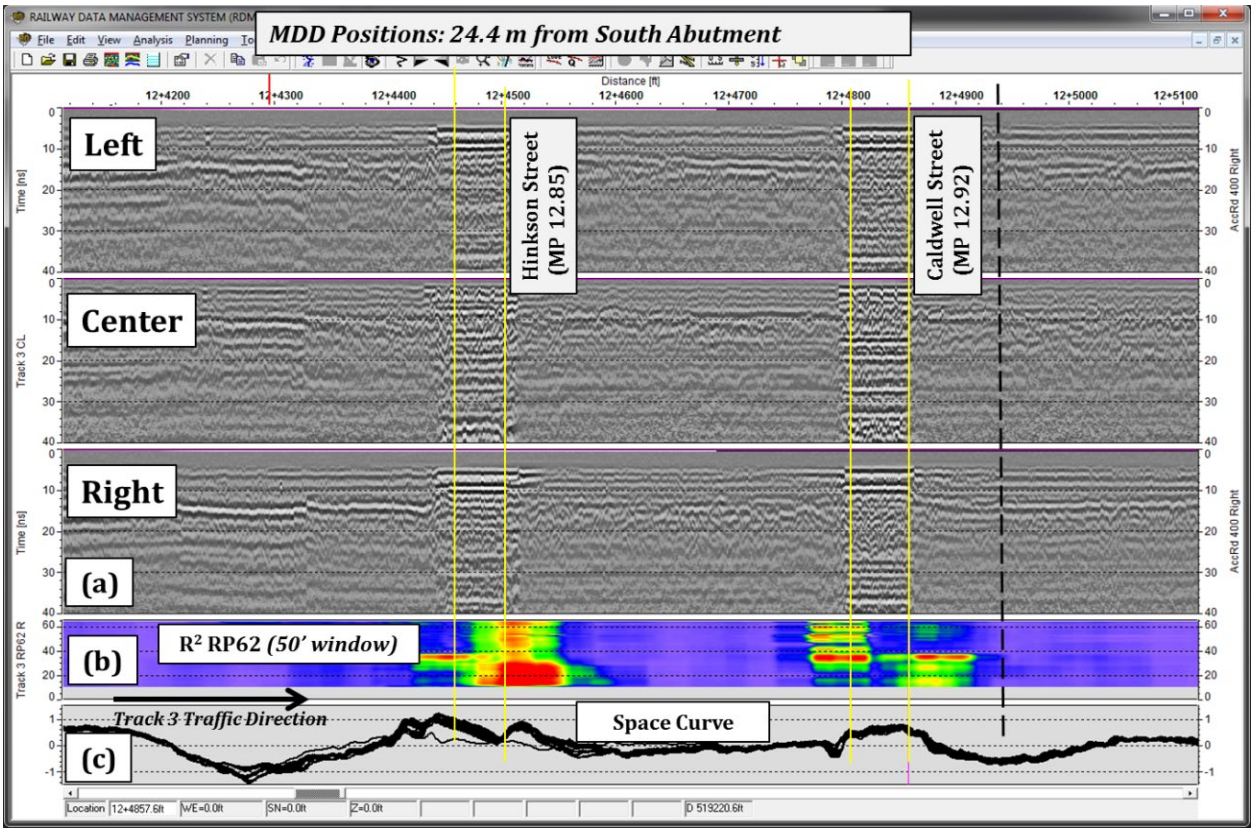

Figure 3.6: (a) GPR Scans, (b) MCO Data, and (c) Space Curve for Track 3 at Caldwell Street Bridge Approach (MDD Positions: 24.4 m From South Abutment)

3.1.2 NS N-Line Mainline

In general, higher-speed passenger trains limit the effects of wheel load-induced stress waves to the upper portion of the track substructure. To get a more thorough understanding of the differential movement problem at locations where the loads and the associated stress waves are likely to penetrate deeper into the track substructure layers, it was important to instrument track sections that represented different loading and operating conditions. The research team selected another set of bridge approaches that predominantly support slower-moving freight trains. This was accomplished in collaboration with NS. As a railroad industry partner, NS reported and provided data concerning recurrent track geometry defects from two problematic undergrade bridges along their N-Line mainline in West Virginia.

The two selected NS undergrade bridges were located at mileposts (MP)352.2 and MP352.8 between Norfolk, VA and Bluefield, WV. The MP352.2 bridge is located in a 10-degree curve and on a 1.1 percent grade. The MP352.8 bridge is located in a 9.7-degree compound curve on a 0.9 percent grade. The track speed is 25 mph (40 km/h) on this line as loaded trains move downhill from west to east with full dynamic brake and often with air brakes applied. Figure 3.7 shows relative locations of the two bridges along the track. This section of track is subjected to heavy axle load train operation with an annual tonnage of approximately 55 MGT.

Historical data shows that these open-deck bridges and their approaches have repeatedly experienced track geometry degradation (both in vertical as well as horizontal directions), and

therefore have required frequent tamping and alignment work. As a potential remediation to the recurrent track geometry problems, Bridge (BR)352.2 was modified from an open-deck to a ballast-deck structure in the fall of 2007.

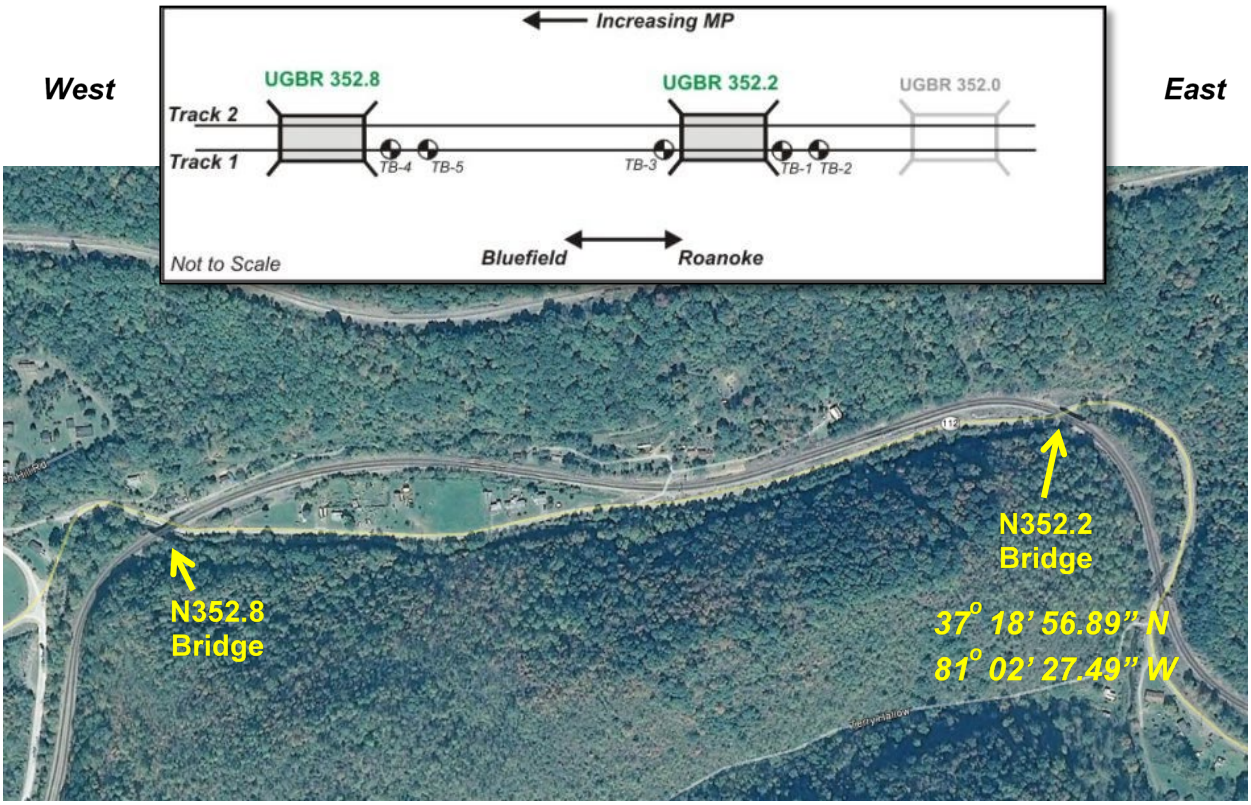

Figure 3.7: Relative Locations of the Two Bridge Approaches Selected for Instrumentation at NS East Mega Site

As part of the east Mega Site research program funded by AAR and FRA, engineers from the Transportation Technology Center, Inc. (TTCI), HyGround Engineering, and NS investigated in 2008 to determine the causes of recurrent track geometry deterioration problems. The investigation included site inspection, vertical track modulus tests using a Track Loading Vehicle (TLV), subgrade strength testing using TLV-equipped cone penetrometer test (CPT), gage restraint testing using FRA's Gage Restraint Measurement System (GRMS) test vehicle, and standard test borings (penetration tests and sampling).

Hyslip et al. (2009) used the results from the field testing to develop longitudinal profiles for the approaches to the two bridges (both east and west approaches for BR352.2, and east approach for BR352.8). Figure 3.8, Figure 3.9, and Figure 3.10 show schematics of the longitudinal track substructure profiles for approaches at BR352.2 east, BR352.2 west, and BR352.8 east, respectively. All three bridge approaches comprise significantly thick clay and/or silt layers in the track substructure immediately adjacent to the abutments. These clay/silt layers are likely to undergo permanent deformation under the slow-moving, heavy-haul traffic, leading to significant differential movements immediately adjacent to the abutment. These two bridge approaches were therefore selected for instrumentation in this research study to identify the movements in individual track substructure layers.

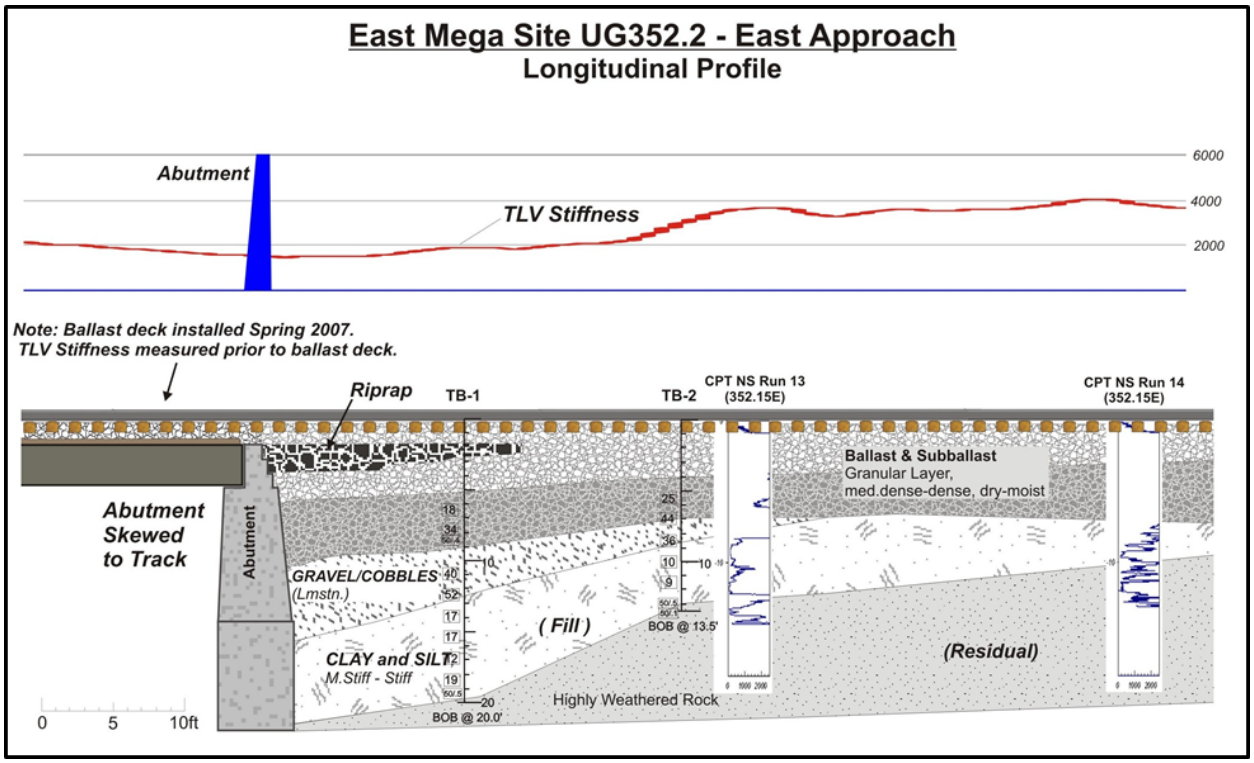

Figure 3.8: Longitudinal Track Substructure Profile for BR352.2 – East Approach

Hyslip et al. (2009) initially analyzed the track geometry data at these two bridge locations from August 2005 and July 2008 to identify the frequency and severity of track geometry deterioration. Their initial analyses showed that converting the bridge at MP352.2 from open deck to ballast deck in the fall of 2007 initially helped reduce the surface roughness (Hyslip et al., 2009). Figure 3.11 shows the surface roughness (i.e., the maximum roughness values at each end of the undergrade bridges) data with time. Although the surface roughness reduced immediately after converting the open deck to ballast deck, the roughness values have consistently increased since January 2010. This indicates that converting the bridge from open deck to ballast deck was most likely not a sufficient remedial solution to mitigate the differential movement problem. Figure 3.11 also shows a similar plot for the bridge at MP352.8. As shown in the figure, the bridge at MP352.8 also experienced recurrent surface roughness problems, particularly at the east approach. Note that BR352.8 was not converted to a ballast deck. Instrumentation and performance monitoring of these two bridges was carried out to identify the primary factors contributing to the recurrent track geometry problems, which could aid in the selection of appropriate remedial measures.

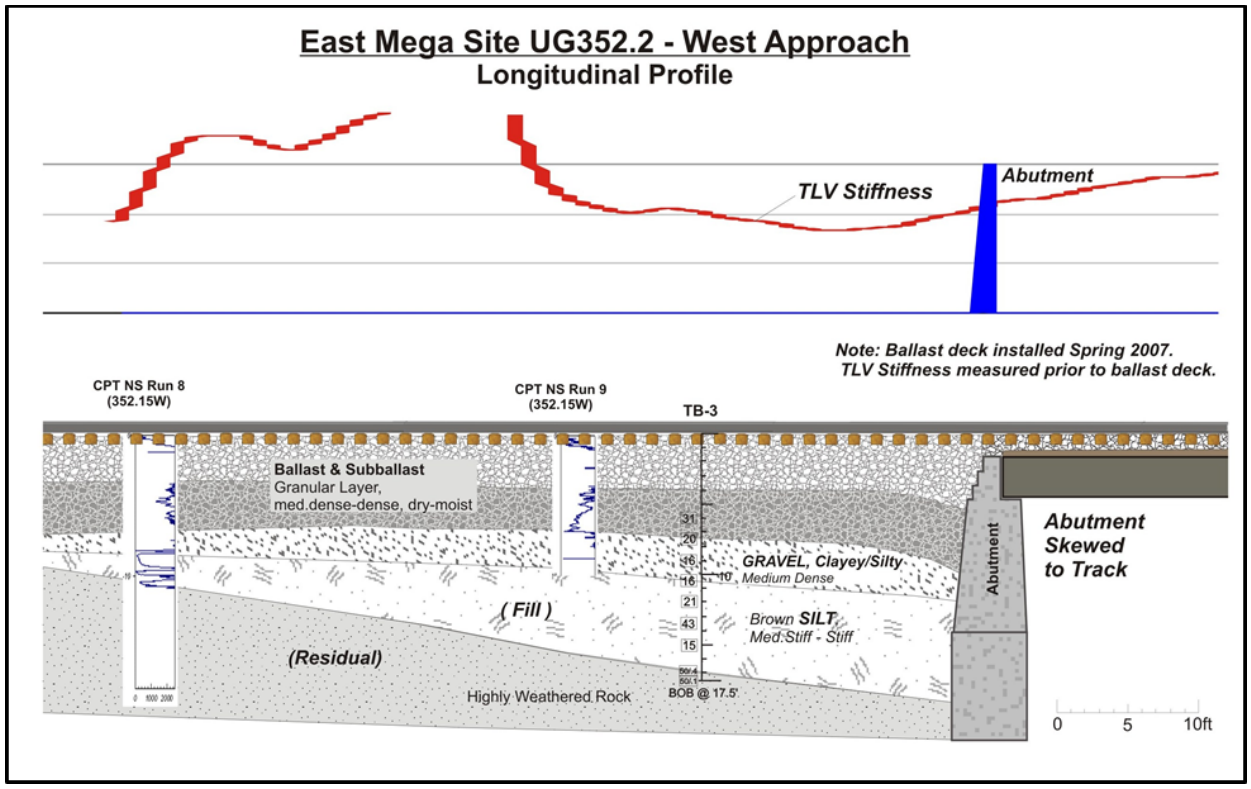

Figure 3.9: Longitudinal Track Substructure Profile for BR352.2 – West Approach

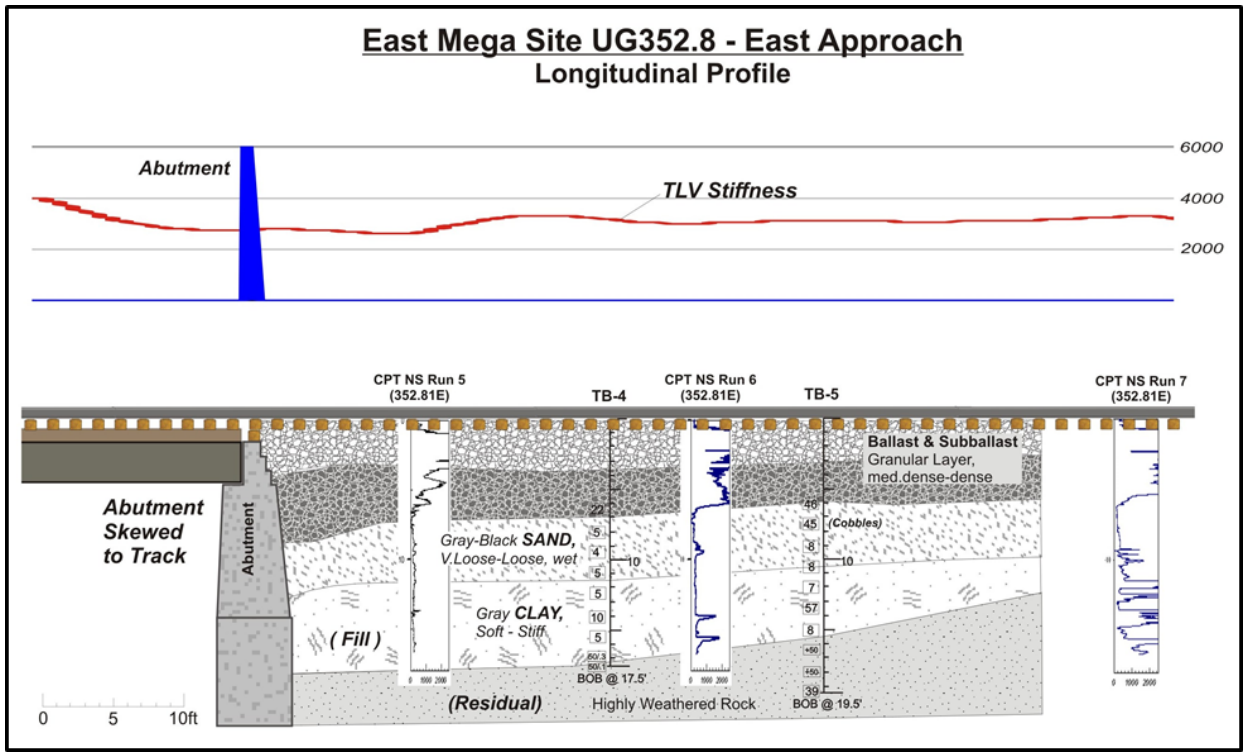

Figure 3.10: Longitudinal Track Substructure Profile for BR352.8 – East Approach

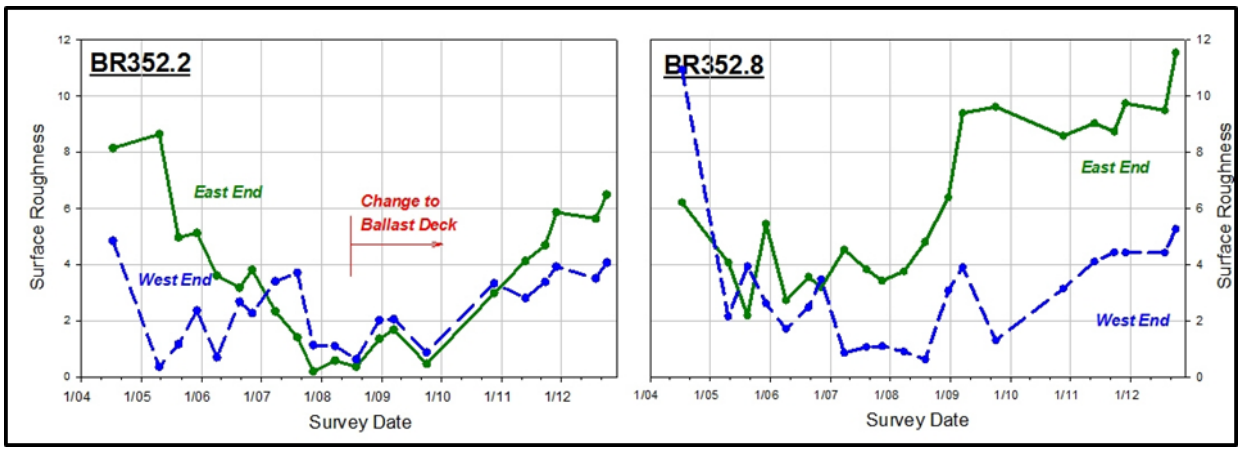

Figure 3.11: Vertical Surface Roughness Trends for NS N-Line MP352.2 and MP352.8 Bridges and Their Approaches

3.2 Instrumentation Plan

The first task in investigating the different factors contributing to differential movement at the selected bridge approaches involved the development of an instrumentation plan using the "systematic approach" recommended by Dunnicliff (1993). Note that not all steps suggested by Dunnicliff (1993) were relevant to the current research study. No detailed construction records for the selected bridge approaches could be obtained from Amtrak. However, through discussions with track maintenance personnel, it was discovered that the bridges have been in service for approximately 100 years. As detailed subsurface exploration prior to the instrumentation was not possible, the research team relied on the subsurface layer configuration information obtained during the instrumentation process. Preliminary information on the native subgrade soil at this location was obtained from the United States Department of Agriculture, Natural Resources Conservation Service county soil report.

3.2.1 Layer Deformation Measurement Using MDD

MDDs were selected to monitor the movement of individual track substructure layers. Figure 3.12 shows the schematic of a track structure with LVDT modules shown at individual substructure layer interfaces. Note that the anchor is placed well below ground level and is assumed to be rigid. All analyses of MDD data assume that the anchor is rigid and does not move with time or under loading. It is therefore important to ensure that the anchor is installed sufficiently below the track surface to limit the train-induced stress levels applied to the soil around the anchor. Under these conditions, the assumption of a "fixed" anchor can be reasonably accurate. In the original form of MDD installation as described by DeBeer et al. (1989), the displacements of LVDT modules used in a MDD system were recorded with respect to the anchor.

Figure 3.13(a) shows the schematics of individual components that constitute a single LVDT module used in the MDD system. Figure 3.13(b) shows a photograph of an individual LVDT module fitted inside a brass enclosure ready for installation. The MDD systems used in the current study comprised five or six such modules, depending on the depth of the borehole. The anchor was placed at a depth of 3.05 m (10 ft) below the top of the tie for the Amtrak NEC bridge approaches, whereas the anchor depth varied between 3.6 m (12 ft) and 5.5 m (18 ft) for

the NS N-Line mainline locations. Note that the primary assumption associated with measurement of layer deformations using MDDs is that the deformations (both elastic and plastic) corresponding to the depth of the anchor is zero. Accordingly, the accuracy of deformation measurements using MDDs depends to large extent on ensuring that the anchor is at a sufficient depth with negligible deformations.

The instrumented bridge approaches along the Amtrak NEC have been in service for more than 100 years. It was assumed that the soil layers at a depth of 3.05 m (10 ft) below the track surface have been fully consolidated, therefore justifying the assumption of a fixed anchor at that depth. The anchor depths for the bridge approaches along NS's N-Line mainline were set to depths where the presence of stiff layers prohibited further drilling. The current study used a modified form of the MDD technology, referred to as the *independent anchoring system,* where each LVDT module in a MDD string functioned as the "anchor" for the module immediately above it.

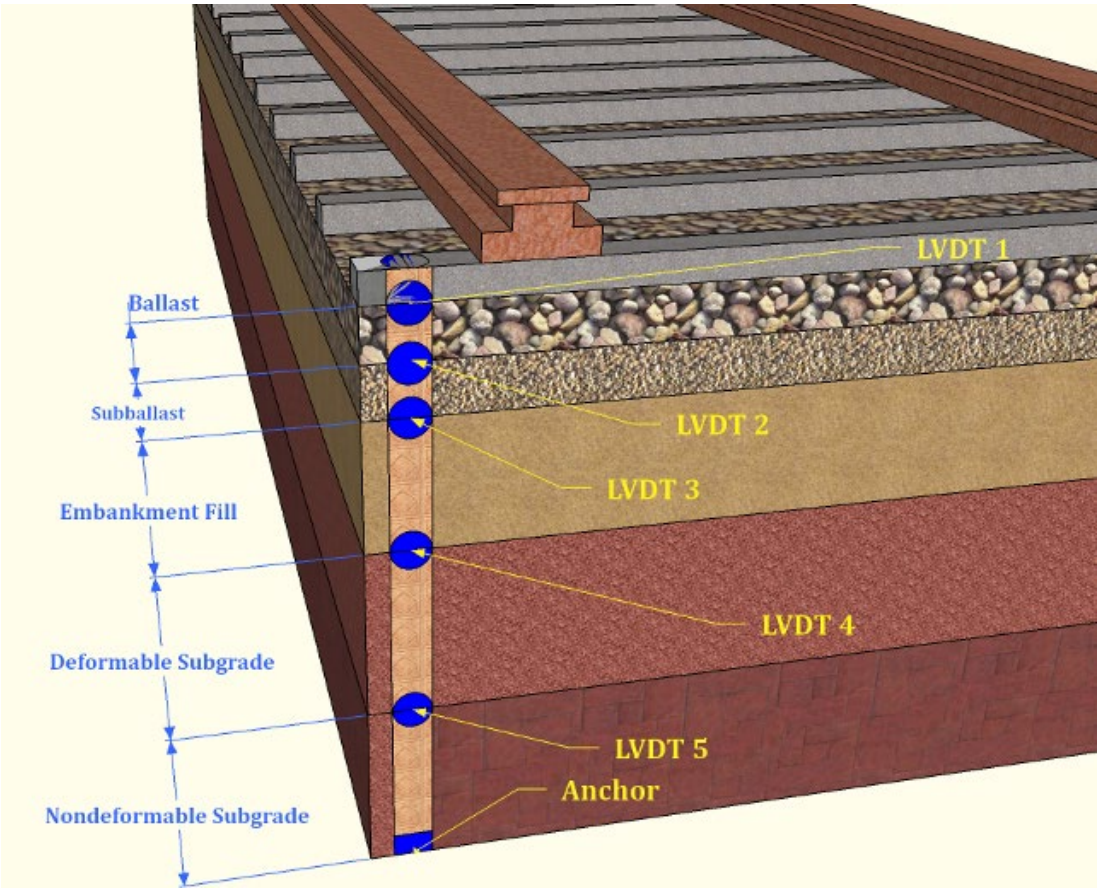

Figure 3.12: Schematic of Track Substructure Profile with MDD Modules at Individual Layer Interfaces

The displacement transducers (LVDTs) were 4 mm full range and were specially developed for MDD usage. Similar transducers have been extensively used by the South African railroad in its MDD deployments. As LVDTs use an alternating current (AC) excitation voltage, standard signal conditioning equipment do not have the capabilities of range selection, offset storage, and other programming features needed. As a result, signal conditioners manufactured by Hottinger Baldwin Messtechnik (HBM) were selected which can accommodate inductive displacement transducers. The displacement transducers developed for this instrumentation effort can only be

used on HBM inductive modules. The displacement transducer units were developed to withstand submersion and have a V-cup on the lower end to find the active core on insertion, with all components manufactured from stainless steel. The transducers have an accuracy of better than 1 percent (typically better than 0.5 percent) over the full range. Although specified at 4 mm, the transducers can measure displacements up to 5 mm, where the error within the last 1 mm of the stroke can be as high as 1 percent. LVDT modules installed near the top of the hole where higher deformations (both elastic and plastic) are expected, were designed with a maximum stroke length of 10 mm.

Part #	Description
1	Core Adaptor for LVDT above
2	Top Nut used for Expanding Rubber Washer
3	Top Washer
4	Rubber Washer with Steel Balls used for Gripping Against Side Walls
5	LVDT Module Body
6	LVDT Body
7 A	LVDT Core
7 B	LVDT Core Attached to Anchor to Core Adaptor
8	Anchor to Core Adaptor
9	Anchor Extension Rod
10	Bottom Anchor

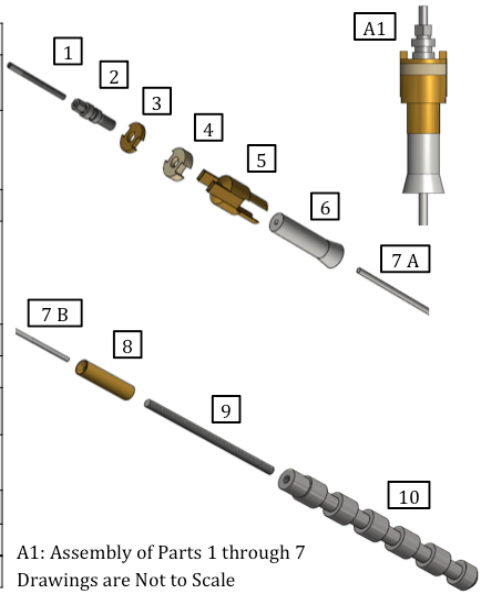

(a)

(b)

Figure 3.13: (a) Schematics and Detailed Components of an MDD Assembly; and (b) Photograph Showing an LVDT Module

This research used the concept of "independent anchoring" for measuring individual track substructure layer deformations using MDDs. In the independent anchoring configuration, each MDD module functions as the anchor for the LVDT immediately above it. This concept is schematically represented in Figure 3.14. The inner core for the bottom-most LVDT (LVDT No. 5 in the illustration; attached to MDD module No. 5) is mounted directly to the bottom anchor.

Subsequently, the core for LVDT No. 4 (attached to MDD No. 4) is directly mounted on module No. 5. This pattern is repeated for LVDTs 3, 2, and 1. Therefore, except for the bottom-most MDD, all other MDDs have "movable" anchor points. Accordingly, the deflection value measured by each LVDT represents the deflection in that particular layer. For example, the voltage induced in LVDT No. 3 will correspond to the deformation of the third layer (d_3), as shown in the schematic in Figure 3.14.

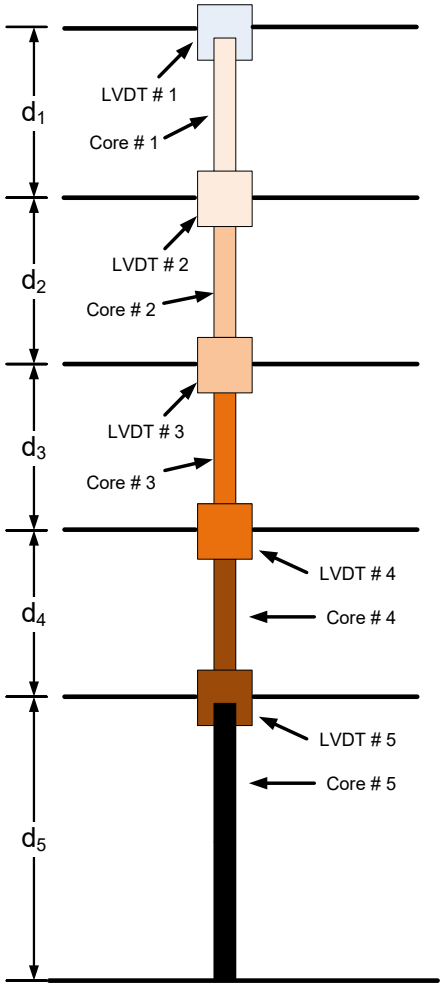

Figure 3.14: Schematic Showing the Concept of MDD Installation Using the Independent Anchoring Concept (Not to Scale)

Figure 3.15 shows photographs of (a) an assembled MDD module along with its LVDT and inner core, and (b) an MDD module mounted inside the insertion tool ready for installation. Note that the top two MDD modules are likely to be within the influence zone of tamping and other track surfacing activities. It is therefore important to protect these instruments by removing them prior to the maintenance operations. The independent anchoring system used in the current project allowed for such removal and reinstallation of the top two MDD modules. All instrumentation components as well as installation tools used in the current study were manufactured at the University of Illinois Civil Engineering Machine Shop under the guidance of Michael Tomas of Amtrak.

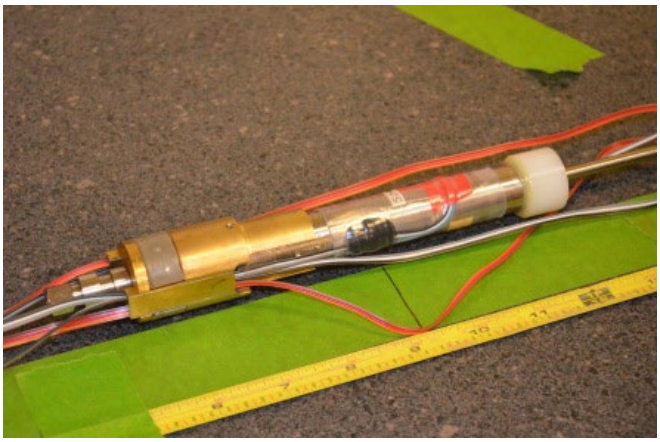

(a)

(b)

Figure 3.15: Photographs Showing (a) an Assembled MDD Module Along With the LVDT and Inner Core; and (b) MDD Module Mounted in the Insertion Tool Ready for Installation Into the Drilled Hole

3.2.2 Measurement of Wheel Loads Using Strain Gauges

Strain gauges were mounted on the rail to measure vertical wheel loads applied during the passage of a train and to monitor the support conditions underneath the instrumented crossties. Dual-element 350 ohm shear gauges mounted on a stainless shim were welded on the rail at the neutral axis for this purpose. Specific dimensions of the rail sections were used to identify and mark the rail neutral axis in the field. The strain gauges were pre-harnessed for vertical load measurements. A calibration frame was used to correlate applied vertical load levels to the voltages induced in the strain gauges using a Wheatstone bridge circuit. Figure 3.16 shows the different installation stages.

(a) (b)

(c) (d)

(e) (f)

Figure 3.16: Photographs Showing Different Steps During the Installation of Strain Gauges

3.3 Equipment Installation

The team instrumented the NEC bridge approaches during July-August 2012. The NS bridges were instrumented between October 15 and November 1, 2013. A special drill-rig was manufactured at the University of Illinois to complete the drilling process. The drill rig includes a tripod base and was mounted on a wooden-triangular base which in turn was clamped to the rails. The rig was mounted with a mechanical winch to facilitate the movement of the hammer drill along two vertical shafts. The drilling was carried out in small increments of 75–100 mm, and the bit was repeatedly extracted from the hole to remove accumulated soil and to clean the drilled hole using compressed air and a high-capacity vacuum cleaner. Drilling in such small

increments ensured that the substructure layer boundaries could be identified up to a resolution of approximately 25 mm. Layer boundaries were identified when the team noticed significant differences in the material type being removed from the drilled hole. Soil samples were collected from different depths during the drilling process for subsequent testing and characterization in the laboratory. Embankment and subgrade soil properties were used as inputs into the numerical models developed to predict the track transition performance trends under different rehabilitation measures. Figure 3.17 shows photographs of different drilling stages.

(a) (b) (c) (d) (e) (f)

Figure 3.17: Photographs Showing Different Stages of Drilling for MDD Installation

After achieving the desired depths, each MDD hole was lined with a flexible tube, and individual MDD modules were installed at pre-determined depths. A custom-designed tool was used to

install the individual MDD modules, and the voltages recorded by each LVDT were monitored throughout the installation process.

A total of six MDD strings (two at each instrumented approach) were installed at the Amtrak NEC bridge approaches. Four MDD "strings" were installed at the NS bridge approaches. Each string comprised five or six LVDT modules, depending on the depth of the hole.

The primary challenge while drilling the MDD holes was drilling through the ballast layer while keeping loose ballast particles from falling into the hole. Expandable polyurethane foam was used to stabilize the ballast for subsequent drilling using a coring drill bit. Photographs of different steps involved in the stabilization of ballast during drilling are presented in Figure 3.18. Figure 3.18(c) and Figure 3.18(d) show the expansion of the polyurethane foam within the drilled hole. Covering the top of the hole during this process ensures the expansion of the urethane foam into the ballast layer, which bonds the ballast particles together and results in a cohesive mass. Field boring logs created during the drilling process helped establish the different soil types encountered and the corresponding layer interfaces. This information was subsequently used to fix the positions of individual LVDT modules inside the drilled hole. Details of individual borehole locations drilled at the Amtrak NEC and NS N-Line mainline sites and corresponding borehole depths are listed in Table 3.1. No instrumentation could be placed on the east side of NS BR352.2 due to repeated damage to drill rod extensions (a total of five drill rod extensions were broken during this drilling effort).

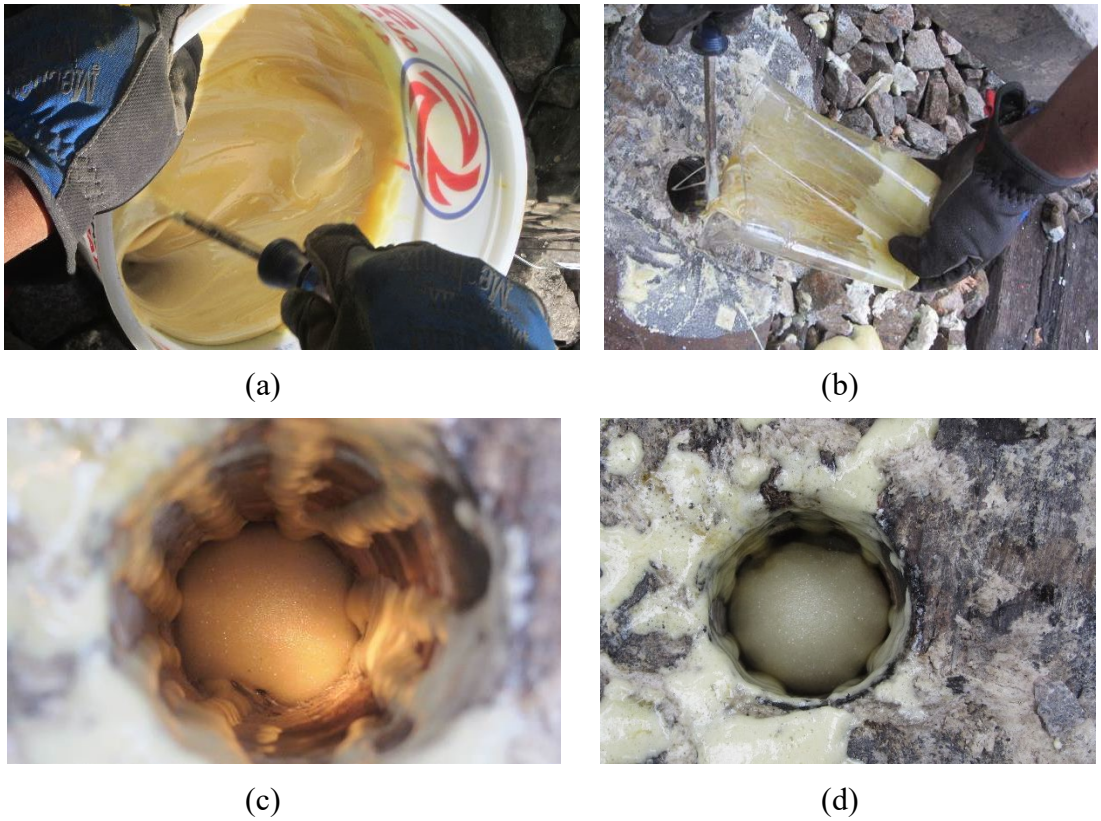

(a) (b)

(c) (d)

Figure 3.18: Photographs Showing Different Stages of Ballast Stabilization During Drilling

Table 3.1: Instrumented Borehole Locations and Achieved Depths

Site Designation	Bridge Approach	Borehole Designation	Distance from Wing Wall (m / ft)	Depth of Borehole (m / ft)
Amtrak NEC near Chester, PA	Upland Street	Near-Bridge	4.6 / 15	3.05 / 10
		Open Track	18.3 / 60	3.05 / 10
	Madison Street	Near-Bridge	3.7 / 12	3.05 / 10
		Open Track	18.3 / 60	3.05 / 10
	Caldwell Street	West	24.4 / 80	3.05 / 10
		East	24.4 / 80	3.05 / 10
NS N-Line mainline near Ingleside, WV	BR352.8-East	352.8-Near	3.33 / 10.9	5.55 / 18.3
		352.8-Far	8.74 / 28.7	5.55 / 18.3
	BR352.2-West	352.2-Near	3.98 / 4.7	3.81 / 12.5
		352.2-Far	9.54 / 31.3	3.81 / 12.5

3.3.1 Amtrak Track Substructure Layer Configurations and Locations of MDDs

One of the primary tasks during the drilling process was to identify the locations of track substructure layer interfaces. This would facilitate the mounting of individual LVDT modules at the layer interfaces to measure the deformations of individual track substructure layers. This section presents the layer interfaces at the different boreholes as established through visual inspection of soil samples in the field.

Figure 3.19 lists the different layer types encountered while drilling the holes for MDD installation at the three Amtrak bridge approaches. The layer interfaces corresponded to installation depths of the MDD modules with respect to the top of the tie. Note that the top-most module (LVDT 1) was installed inside the tie. The tie was assumed to move as a rigid body, so the depth of the top-most LVDT from the top of the tie was not considered important. Figure 3.19 through Figure 3.23 show schematics of the substructure layer profiles established for the Amtrak NEC bridge approaches during drilling.

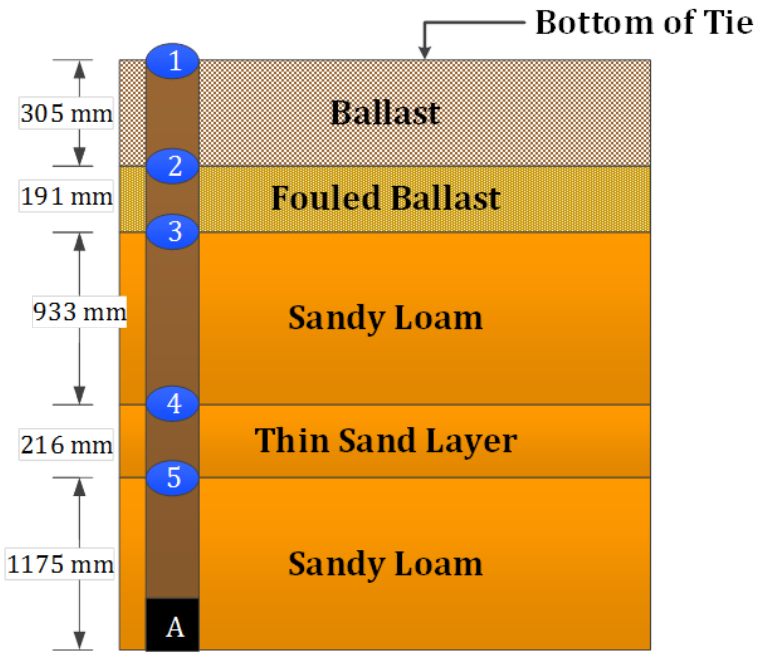

Figure 3.19: Substructure Layer Profile for Upland Street 15 ft From the North Abutment (Track 3)

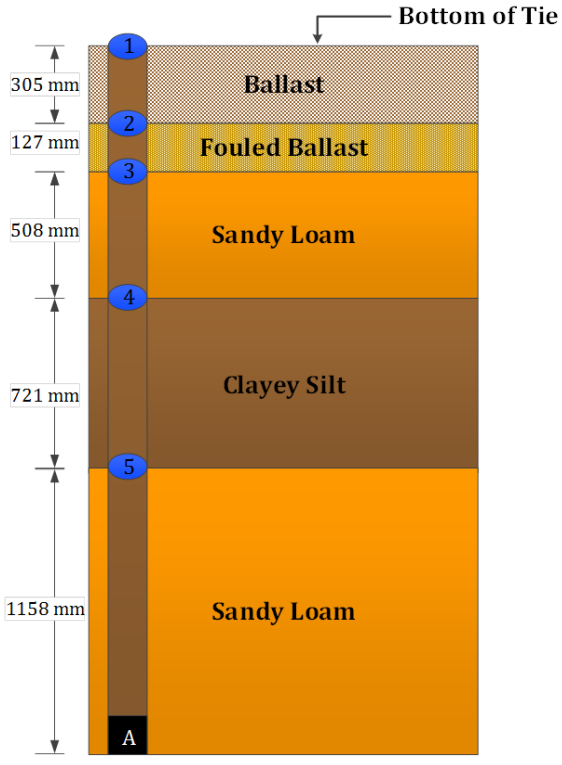

Figure 3.20: Substructure Layer Profile for Upland Street 60 ft From the North Abutment (Track 3)

Table 3.2: Track Substructure Layer Profiles Established During Drilling and Instrumentation at the Amtrak NEC Bridge Approaches

Bridge Approach	Location of MDD Modules (Depths Measured from Top of the Tie)		
	LVDT Number	*Depth (in)*	*Layer Interface*
Upland Street Bridge (60 ft from North Abutment)	1	N/A	Within Tie
	2	19	Clean Ballast–Fouled Ballast
	3	24	Sandy Loam
	4	44	Clayey Silt
	5	72 3/8	Top of Anchor
Upland Street Bridge (15 ft from North Abutment)	1	N/A	Within Tie
	2	19	Clean Ballast-Fouled Ballast
	3	26.5	Sandy Loam
	4	63 ¼	Thin Concrete Layer
	5	71 ¾	Top of Anchor
Madison Street Bridge, Track 2 (12 ft from South Abutment)	1	N/A	Within Tie
	2	18	Clean Ballast-Fouled Ballast
	3	23 ½	Hard Pan
	4	46	Gray Sandy Loam + Cinder
	5	73 1/8	Top of Anchor
Madison Street Bridge, Track 2 (60 ft from South Abutment)	1	N/A	Within Tie
	2	20	Clean Ballast-Fouled Ballast
	3	39	Water Table
	4	53 3/8	Fat Clay, Very Wet
	5	67 ½	Top of Anchor
Caldwell Street, Track 3 (80 ft from South Abutment, West End of Tie)	1	N/A	Within Tie
	2	19	Clean Ballast-Fouled Ballast
	3	25	Brown Silty Sand
	4	38	Silty Clay
	5	74	Top of Anchor
Caldwell Street, Track 3 (80 ft from South Abutment, East End of Tie)	1	N/A	Within Tie
	2	19.5	Clean Ballast-Fouled Ballast
	3	27.5	Possible Thin HMA Layer
	4	36	Clay
	5	73 ¾	Top of Anchor

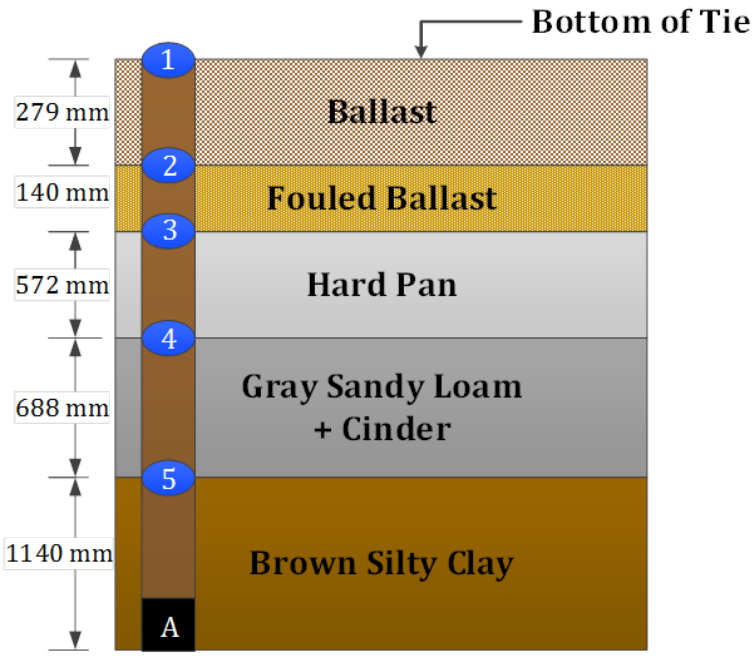

Figure 3.21: Substructure Layer Profile for Madison Street 12 ft From the South Abutment (Track 2)

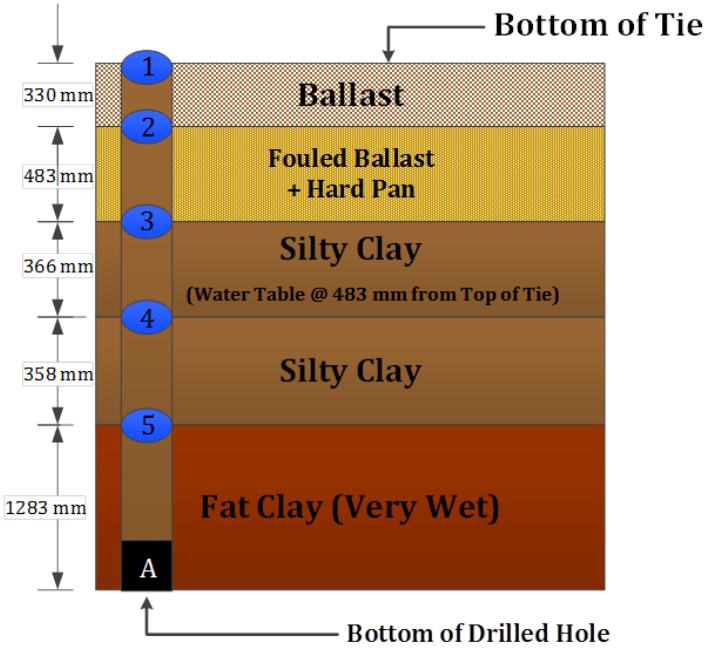

Figure 3.22: Substructure Layer Profile for Madison Street 60 ft From the South Abutment (Track 2)

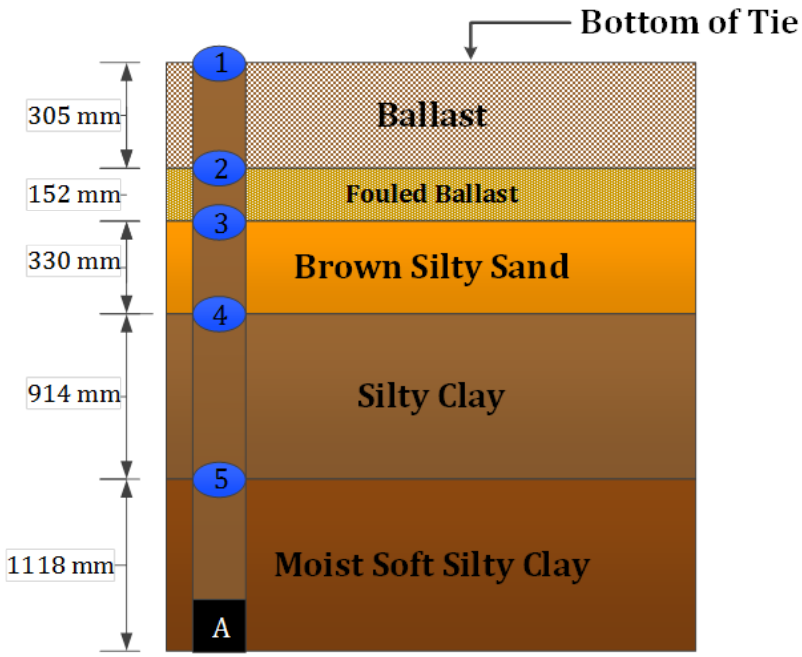

Figure 3.23: Substructure Layer Profile for Caldwell Street 80 ft From the South Abutment (Track 3; West End of Tie)

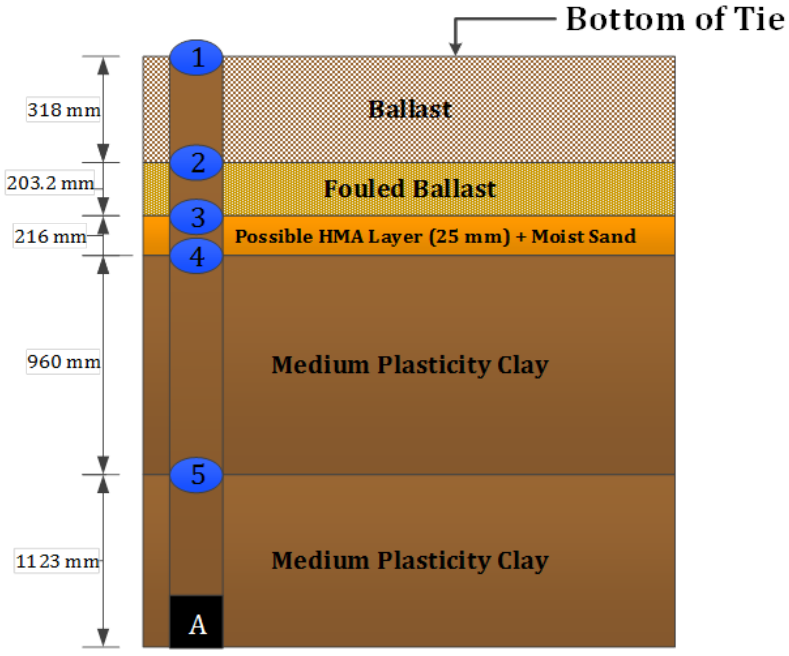

Figure 3.24: Substructure Layer Profile for Caldwell Street 80 ft From the South Abutment (Track 3; East End of Tie)

3.3.2 NS Track Substructure Layer Configurations and Locations of MDDs

Figure 3.25 and Figure 3.26 show the substructure layer interfaces developed for the four instrumented ties at the NS N-Line mainline bridge approaches. Note that these field logs were established following the ASTM D 2488 Visual-Manual Soil Classification procedure and graphed first to identify major substructure layers and depths of layer boundaries. The individual LVDT modules installed are also presented in Figure 3.25 and Figure 3.26.

Table 3.3 lists the different layers established for the MDD installations at the four bridge approach locations. The reported layer interfaces also corresponded to installation depths of the MDD modules with respect to the top of the tie. Note that due to the large layer thicknesses, two to three LVDT modules were sometimes needed for installation into one layer. The top-most module (LVDT 1) was installed inside the tie.

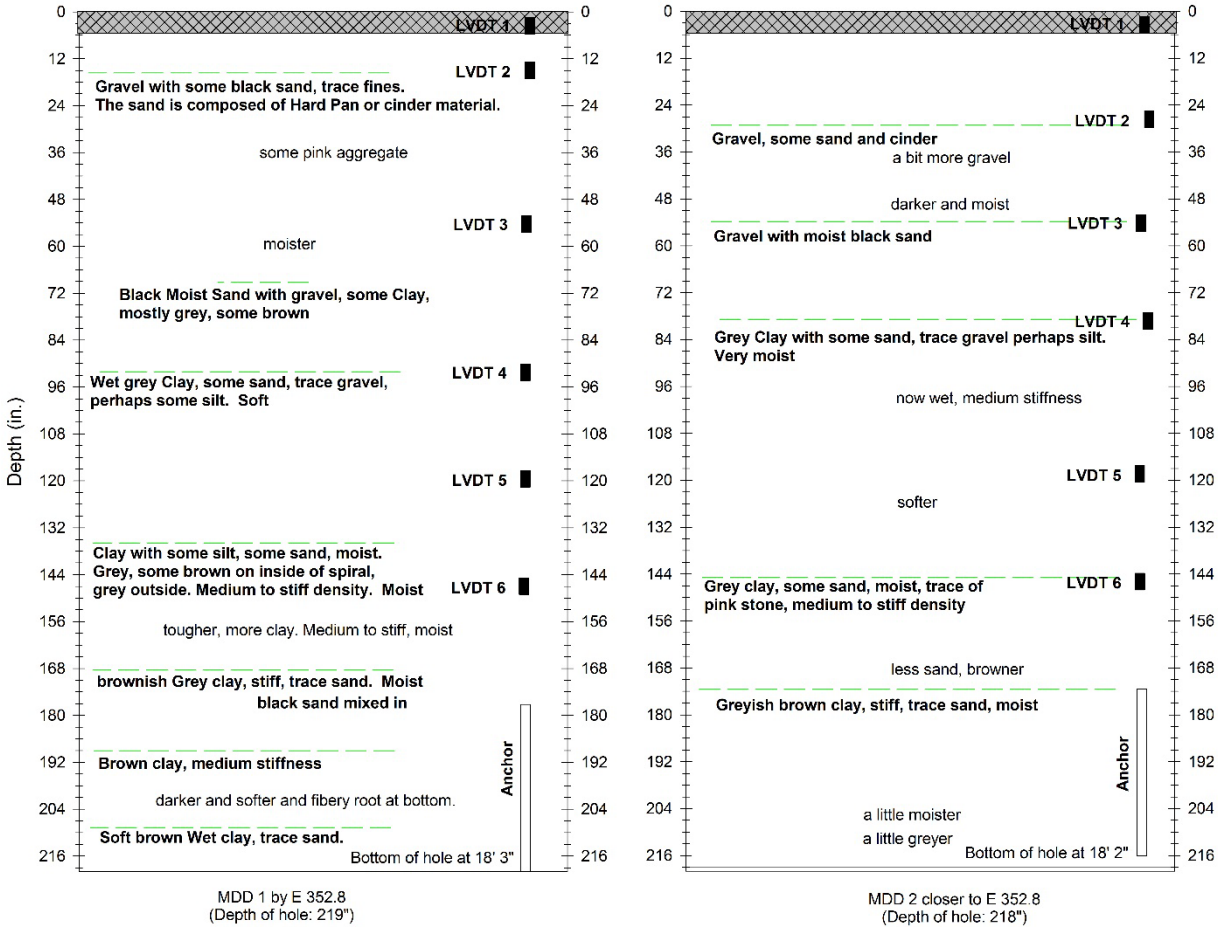

Figure 3.25: Track Substructure Layer Profile at Bridge MP352.8 East Approach

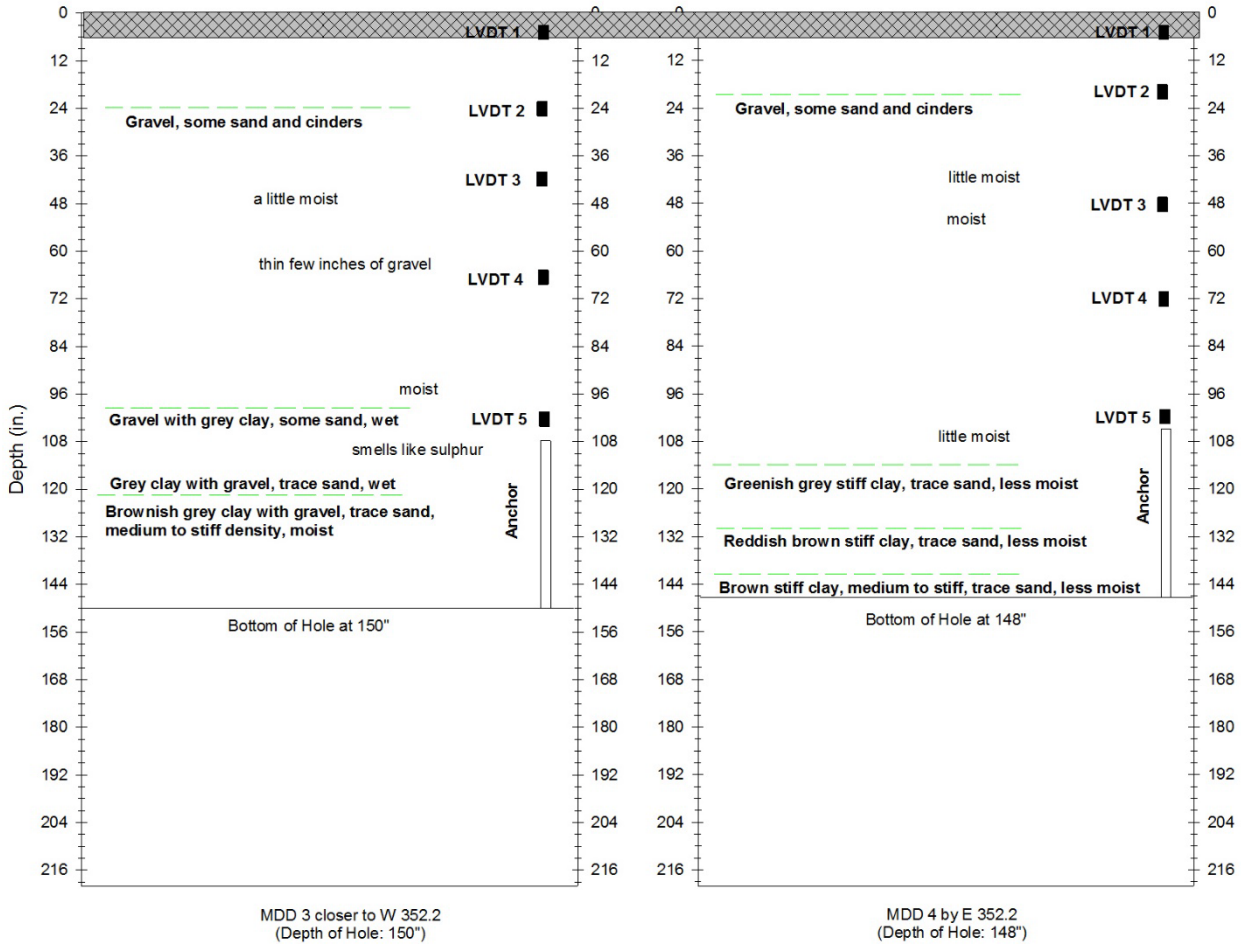

Figure 3.26: Track Substructure Layer Profile at Bridge MP352.2 West Approach

Table 3.3: Track Substructure Layer Profiles Established During Drilling and Instrumentation at the NS N-Line Mainline Bridge Approaches

Bridge Approach	Location of MDD Modules (Depths Measured from Top of the Tie)		
	LVDT Number	Depth (in)	Layer Interface
Mile Post 352.8 Open Track Location (28' 7" from Wingwall edge, 19th tie)	1	N/A	Within the tie
	2	15	Gravel with some black sand
	3	54	Some pink aggregate, moist
	4	93	Wet grey clay, some silt and sand, trace gravel
	5	120	Wet grey clay, some silt and sand, trace gravel
	6	144	Top of anchor
Mile Post 352.8 Near Bridge Location (131" from Wingwall edge, 8th tie)	1	N/A	Within tie
	2	29	Gravel, some sand and cinder
	3	54	Gravel with moist black sand
	4	79	Grey clay, some silt and sand, trace gravel
	5	120	Grey clay, some silt and sand, trace gravel
	6	144	Top of anchor
Mile Post 352.2 Open Track Location (375.5" from Wingwall edge, 20th tie)	1	N/A	Within tie
	2	20	Gravel, some sand and cinders
	3	48	Gravel, some sand and cinders
	4	72	Gravel, some sand and cinders
	5	100	Top of Anchor
Mile Post 352.2 Near Bridge Location (156.5" from Wingwall edge, 11th tie)	1	N/A	Within Tie
	2	24	Gravel, some sand and cinders
	3	42	Gravel, some sand and cinders
	4	66	Gravel, some sand and cinders
	5	100	Top of Anchor

3.3.3 Wayside Data Acquisition System

Cables from the instrumentation were connected to wayside data acquisition boxes installed by the side of the tracks. Special care was taken to bundle all the cables from one instrumentation location into a single duct pipe, which was then laid underneath the adjacent tracks and connected to the wayside data acquisition box. Figure 3.27 shows a photograph of the cable duct being laid underneath adjacent tracks and eventually connected to the wayside data acquisition boxes.

Figure 3.27: Installing Cable Duct Underneath Adjacent Tracks

3.3.4 Modification of Instrumentation Components to Accommodate Greater Instrumentation Depths

All the drilling and instrumentation equipment used in this research study was originally developed with a target drilling depth of 3.05 m (10 ft). This is the standard borehole depth used for MDD installations. As the Amtrak NEC bridges have been in operation for more than 100 years, it was assumed that soil layers at a depth of 10 ft were relatively rigid. Track substructure layer profiles of the NS bridge approaches indicated the presence of soft clay layers at an approximate depth of 18 ft below the track surface (see Figure 3.25). To ensure placement of the MDD anchor in a relatively fixed layer, it was necessary to modify all drilling and instrumentation tools to achieve borehole depths of 18 ft.

3.4 Summary

This section presented details on the instrumentation activities carried out in this research effort to monitor the performances of problematic bridge approaches experiencing recurrent differential movement problems. MDDs and strain gauges were installed at the selected bridge approaches to quantify deformations of individual track substructure layers under loading (elastic or transient component) as well as with time (plastic or permanent component). The principle underlying measurement of layer deformations using MDDs was presented in this section, followed by an

introduction to the concept of independent anchoring system. All instrumentation components were manufactured at the University of Illinois Civil Engineering Machine Shop in consultation with Mike Tomas of Amtrak. Finally, track substructure layer profiles established through visual inspection of soil samples obtained during drilling were presented to mark the locations of individual LVDT modules at the layer interfaces. The track substructure layer deformation trends (both under loading and with time) established for the instrumented bridge approaches will be presented in Section 4.

4. Performance Monitoring of Instrumented Bridge Approaches

The next task in the research study involved periodic data acquisition from the instrumented bridge approaches to monitor changes in permanent (plastic) and transient deformations of track substructure layers over time. This required periodic visits to the instrumented sites to record LVDT offset values as well as transient response under train loading. Track substructure layer deformation (both permanent and transient) as well as wheel load data collected under train loading are presented in this section.

4.1 Monitoring Settlement Trends with Time

The settlement trends of individual substructure layers were monitored at regular intervals (1–2-week intervals immediately after instrumentation and 1-month intervals thereafter) by collecting data from the offset position of each LVDT module with respect to the initial (zero) position. For the Amtrak NEC bridge approaches, this task was performed in coordination with Amtrak, as it was not possible for the research team members to visit the site at such frequent intervals. The NS bridge approach data was collected four times, when members of the research team traveled back to Ingleside, WV. Data collection during each data acquisition (DAQ) trip was accomplished by connecting an amplifier and a laptop computer to the wayside DAQ boxes containing all the instrumentation cables. Figure 4.1(a) and Figure 4.1(b) show photographs of the wayside DAQ box and the amplifier and laptop computer setup, respectively.

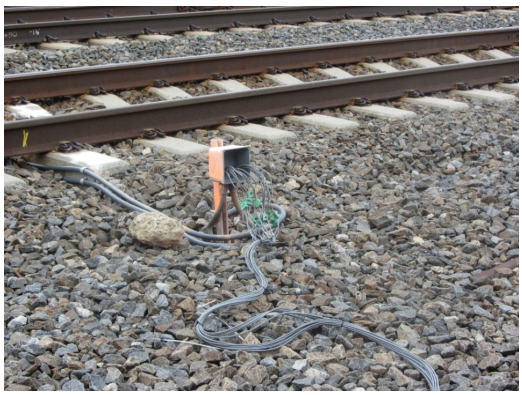

(a)

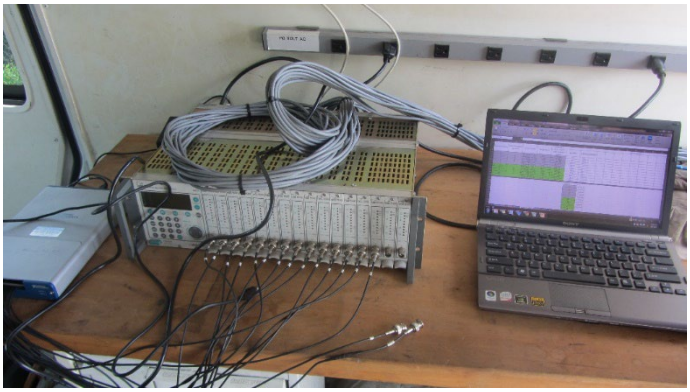

(b)

Figure 4.1: (a) DAQ Cable Connected to Wayside DAQ Box; and (b) HBM Amplifier and Laptop Setup Used for DAQ

Table 4.1: Summary Dates of Data Collection for Amtrak NEC Bridge Approaches and Number of Days Since Instrumentation

Year	Dates of Data Collection	Days Since Instrumentation
2012	2 August, 3 August, 7 August, 9 August, 20 August, 28 August, 4 September, 11 September, 28 September, 15 October, 23 October, 5 November, 20 November, 10 December	0, 1, 5, 7, 18, 26, 33, 40, 57, 74, 82, 95, 110, 130
2013	29 January, 25 February, 11 March, 1 April, 16 April, 25 June, 17 July, 15 August, 4 September, 16 October, 18 December	180, 207, 221, 242, 257, 327, 349, 378, 398, 440, 503
2014	2 April, 18 June, 22 July, 9 September, 17 December, 30 December	608, 685, 719, 768, 867, 880
2015	2 April, 20 May, 10 September	973, 1021, 1134

4.1.1 Track Settlement Trends – Amtrak Northeast Corridor

Table 4.1 lists the dates of data collection for Amtrak NEC bridge approaches and the days since the instrumentation was installed. Figure 4.2(a) shows the settlement trends of individual track substructure layers with time for the Upland Street bridge approach, 15 ft from the north abutment (also referred to as the *near-bridge location*). Individual lines in the figure correspond to the "offset" voltages registered by individual LVDT modules. Figure 4.2(b) represents the track substructure layer profile for this location established during the instrumentation effort. Voltage changes registered by LVDT 1 represented movements in the ballast layer. Similarly, movements registered by LVDTs 2, 3, 4, and 5 correspond to movements within the Fouled Ballast, Sandy Loam (upper), Thin Sand, and Sandy Loam (lower) layers, respectively. Note that the MDD corresponding to the near-bridge location at the Upland and Madison Street bridge approaches was marked as "MDD1." Similarly, the MDD installed at the open-track location (60 ft from the north abutment at the Upland Street bridge approach; 60 ft from the south abutment at the Madison Street bridge approach) was labeled as "MDD2" for illustration purposes.

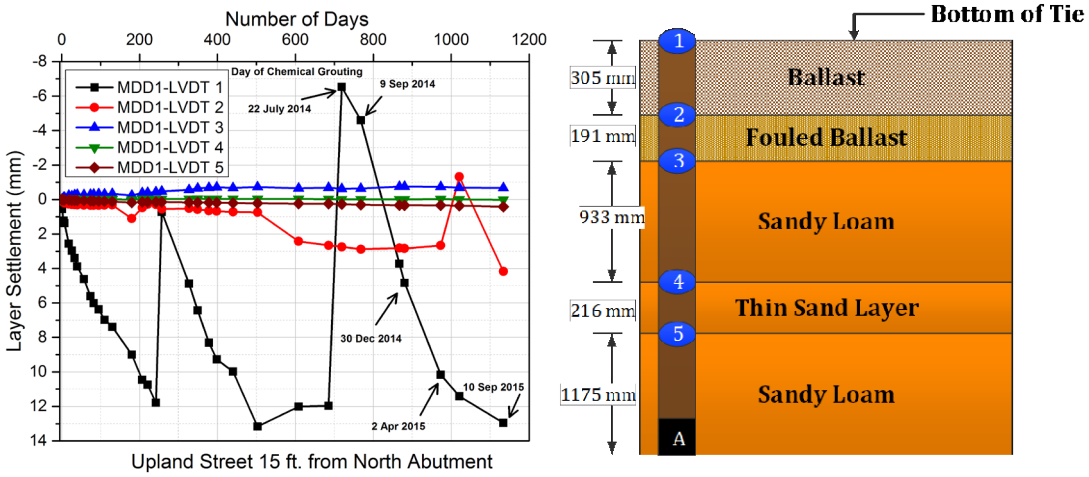

(a) (b)

Figure 4.2: (a) Layer Settlement Trends With Time and (b) Track Substructure Layer Profiles for the Upland Street Bridge Approach – Near-Bridge Location (15 ft From North Abutment)

Downward movement (compression) of the layers has been plotted as positive numbers while upward movement (indicative of expansion) are negative. The following observations are made from the data presented in Figure 4.2(a):

1. LVDT 1 had significantly higher voltage fluctuations over time compared to the other four LVDTs. This indicated that the movement within the ballast layer was significantly higher than that within the other substructure layers.
2. The upward movement of the LVDT 1 line (see Figure 4.2(a)) was due to track re-surfacing (tamping) activities. As LVDT 1 was located inside the crosstie, lifting of the tie during tamping registered a decrease in the offset voltage. Accordingly, the first resurfacing activity at the Upland Street bridge location was undertaken approximately 250 days after instrumentation. The ballast layer had undergone a settlement of approximately 12 mm before the resurfacing activity, and the tie position was restored to its original level (the same level as at the time of the instrumentation).
3. The effect of tamping on ballast settlement rate can be assessed by comparing the slope of the LVDT 1 line immediately after the instrumentation (number of days = 0) and immediately after the resurfacing (number of days = 250). The slopes of the two lines are very similar.
4. The next major track resurfacing activity was undertaken approximately 700 days after instrumentation. This was the date the chemical grouting was applied as a remedial measure. More details on the implementation of the remedial measures and their effects on track response and performance will be presented in Section 6. It is interesting to note that the rate of settlement accumulation within the ballast layer was relatively low immediately after implementation of the remedial measure. However, the settlement rate increased significantly after the data point corresponding to September 9, 2014.
5. Settlement rates in layers 2 through 5 were significantly lower than those recorded in the ballast layer.
6. Layer 2 did not register any significant settlement for the first 500 days after instrumentation. However, the rate of settlement increased after that time, with the maximum layer settlement reaching a value of 3 mm.
7. The upward shift in the line corresponding to LVDT 2 after April 2, 2015, appeared to represent an anomaly in the recorded voltage. First, no track resurfacing activity was undertaken around that time. Second, as LVDT 2 was 305 mm below the bottom of the tie, the position of the LVDT should not have been affected by any track resurfacing activity.
8. Layers 3 through 5 had negligible settlement rates.

Figure 4.3(a) and Figure 4.3(b) present the settlement trends and substructure layer profiles for the open-track location (60 ft from the north abutment) at the Upland Street bridge approach, respectively. Following are the primary observations made from the data presented in Figure 4.3:

1. Settlement in ballast layer (LVDT 1) for the open-track location (MDD2) was significantly lower than that for the near-bridge location. This demonstrated the severity of the differential movement problem adjacent to the bridge deck compared to locations that are farther away from the effects of the rigid bridge.

2. The track resurfacing activity carried out approximately 250 days after the instrumentation did not have any effect on the LVDT 1 reading 60 ft from the bridge abutment. This was because the low settlement in the ballast layer at the open-track location 250 days after the instrumentation (~1.5 mm) did not warrant raising the track.
3. Like the near-bridge location, layers 2 through 5 had negligible settlement rates.
4. The LVDT 1 reading at the open-track location showed a sudden spike approximately 1,000 days after the instrumentation. Interestingly, this happened on the exact same day as the LVDT 2 spike reported for the near-bridge location (see Figure 4.2(a)). As no track resurfacing activity was reported around this date, this spike can be attributed to noise in that particular data channel.
5. Comparing Figure 4.2 and Figure 4.3 leads to the primary conclusion that settlement in the ballast layer was much more significant for the near-bridge location compared to the open-track location.

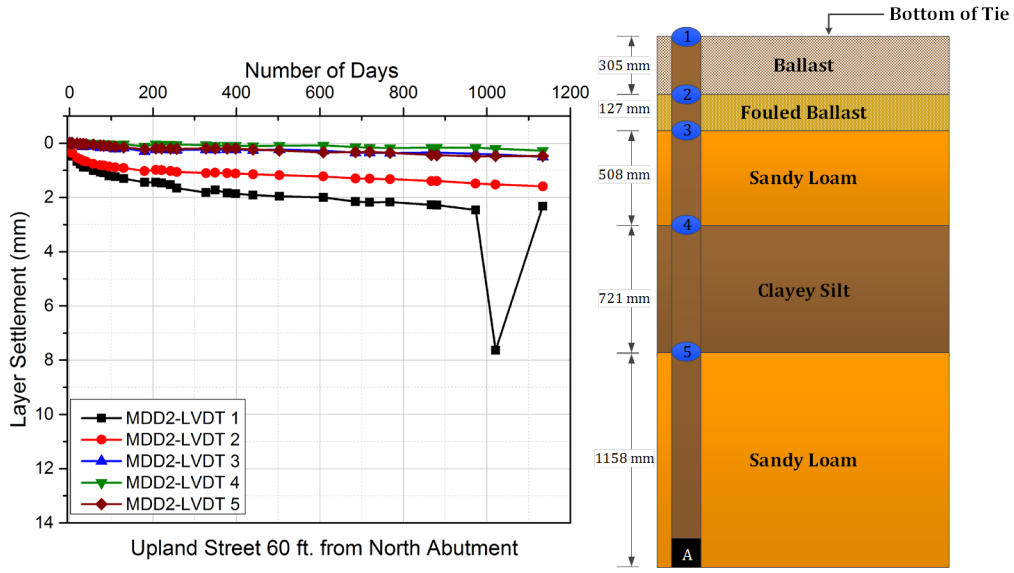

(a) (b)

Figure 4.3: (a) Layer Settlement Trends With Time and (b) Track Substructure Layer Profiles for the Upland Street Bridge Approach – Open-Track Location (60 ft From North Abutment)

Figure 4.4(a) and Figure 4.4(b) present the settlement trends and substructure layer profiles for the near-bridge location (12 ft from the south abutment) at the Madison Street bridge approach, respectively. Like the Upland Street near-bridge location, the near-bridge location at Madison Street exhibited significant movements within the ballast layer. Interestingly, the ballast settlement at this location accumulated rapidly, reaching a value of approximately 6 mm within the first 20 days after instrumentation. This was followed by a resurfacing (tamping) activity that is reflected through an upward movement of the LVDT 1 line in Figure 4.4(a). The settlement rate after the tamping was significantly lower than the initial rate, and the settlement level did not reach 6 mm till about 200 days after the instrumentation. The next major resurfacing activity was undertaken approximately 375 days from the date of instrumentation. However, this time the LVDT was not raised to its original position corresponding to zero displacement.

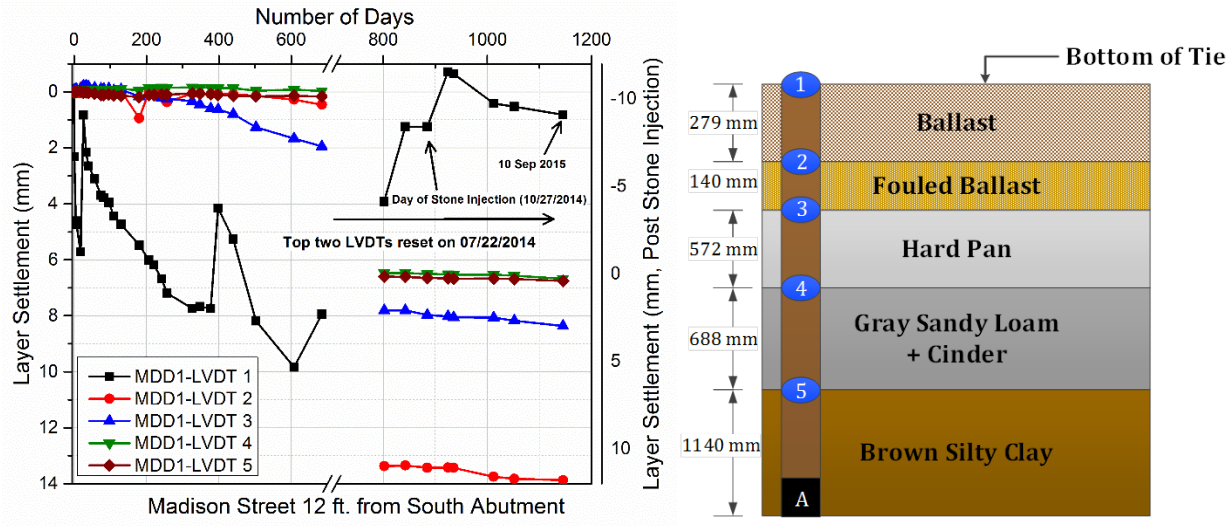

(a) (b)

Figure 4.4: (a) Layer Settlement Trends With Time and (b) Track Substructure Layer Profiles for the Madison Street Bridge Approach – Near-Bridge Location (12 ft From South Abutment)

As will be discussed in Section 6, stone injection was employed as a remedial measure at the Madison Street near-bridge location in October 2014. To accommodate the excessive movement of the tie and within the ballast layer during the stone injection process, the top two LVDTs at this location were reset on July 22, 2014. This changed the "zero position" of the top two LVDTs, therefore all data after July 22, presented in Figure 4.4(a), require the use of a secondary vertical axis to interpret (secondary vertical axis is shown on the right side of the plot).

Figure 4.4(a) shows a crest in the LVDT 1 trace immediately after stone injection (October 27, 2014), which indicated the introduction of an "upward bump" in the track profile through the stone-injection process. This was primarily a result of manual jacking of the track to attain a desired profile prior to blowing the stone. As discussed in Section 6, an "over-lift" was built into the track profile to account for settlement. As shown in Figure 4.4(a), this artificially introduced crest in the vertical track profile gradually dissipated to achieve a stable configuration. Like the Upland Street bridge approach, layers 2 through 5 at the Madison Street near-bridge location did not exhibit excessive movements with time. Interestingly, layer 3 (hardpan) at this location showed higher settlement values compared to those from layer 2. Nevertheless, the total settlement was less than 2 mm, which was insignificant compared to the permanent deformation experienced by the ballast layer.

Figure 4.5(a) and Figure 4.5(b) present similar data for the open-track location at the Madison Street bridge approach (60 ft from the south abutment). As with the previous two cases, the ballast layer accounted for a major portion of the total track settlement. The settlement at the open-track location was not as drastic as at the near-bridge location. For example, the settlement within the ballast layer (MDD2-LVDT 1) before the first track resurfacing activity (corresponding to 20 days after the instrumentation) was approximately 4 mm (compared to 6 mm for the near-bridge location). Similarly, the total ballast layer settlement did not reach a value of 6 mm until about 400 days after the instrumentation. This indicated a slower rate of settlement accumulation for the open-track location compared to the near-bridge location.

Moreover, no sudden change in the settlement rate was observed for the open-track location, unlike the near-bridge location. The stone-injection activity undertaken at the near-bridge location approximately 900 days after the instrumentation did not have any noticeable effect on the LVDT positions for the open-track position. Like the previous two cases, the settlements of layers 2 through 5 were insignificant.

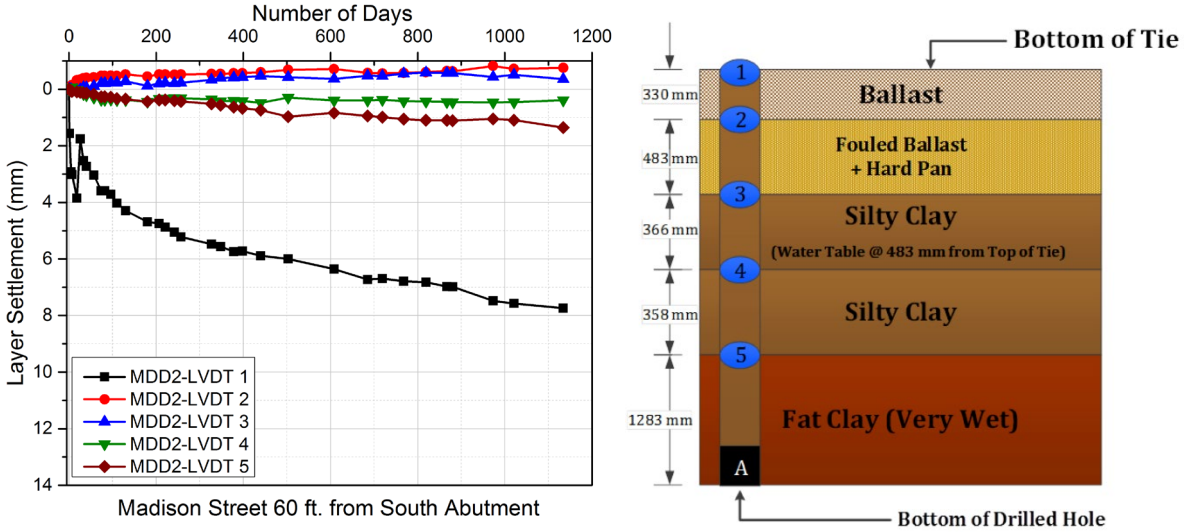

(a) (b)

Figure 4.5: (a) Layer Settlement Trends With Time and (b) Track Substructure Layer Profiles for the Madison Street Bridge Approach – Open-Track Location (60 ft From South Abutment)

Figure 4.6 and Figure 4.7 present similar information for the Caldwell Street bridge approach. Just one crosstie, located 80 ft from the south abutment, was instrumented at this location, with the two MDDs being drilled on west and east ends of the tie. Figure 4.6 presents information for the west end of the tie, whereas Figure 4.7 presents the layer settlement trends and track substructure layer profiles for the east end of the tie. As shown in the figures, the two ends of the tie exhibited similar behavior, with the ballast layer again contributing to a major portion of the total track settlement. The total settlement within the ballast layer from both MDDs was approximately 9 mm, indicating uniform settlement across the tie. Note that no track resurfacing (tamping) activity was recorded at this location. Although the total settlement within the ballast layer reached 8 mm, the relatively far distance (80 ft) of this location from the bridge abutment most likely resulted in the differential movement magnitudes not being reported as significant by track geometry measurement vehicles. Despite being farther away from the bridge abutment compared to the other instrumented locations, a major portion of the track settlement at the Caldwell Street location still originated from movement within the ballast layer.

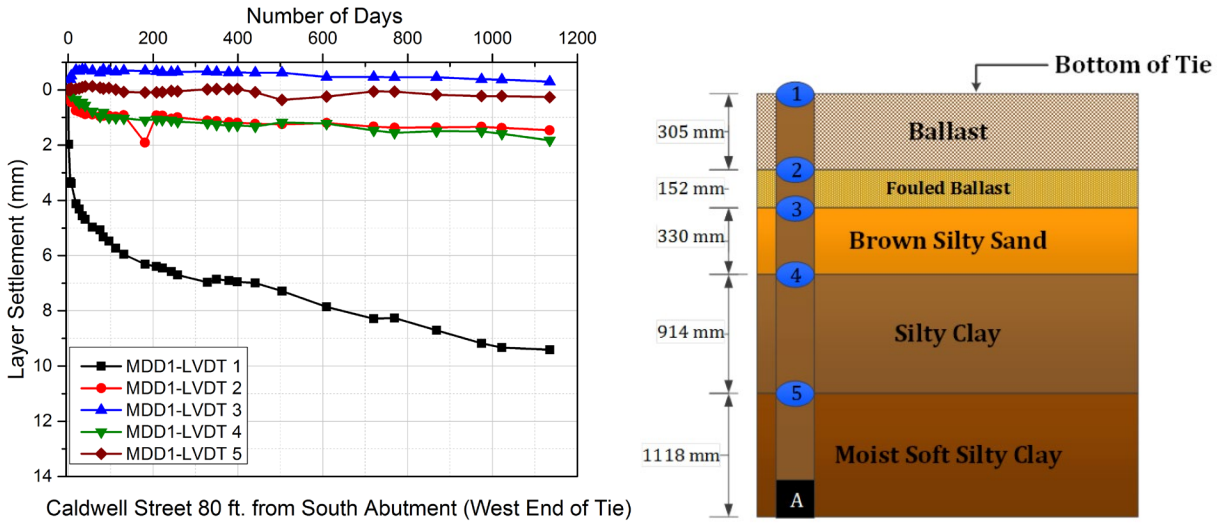

(a) (b)

Figure 4.6: (a) Layer Settlement Trends With Time and (b) Track Substructure Layer Profiles for the Caldwell Street Bridge Approach (80 ft From South Abutment; West End of Tie)

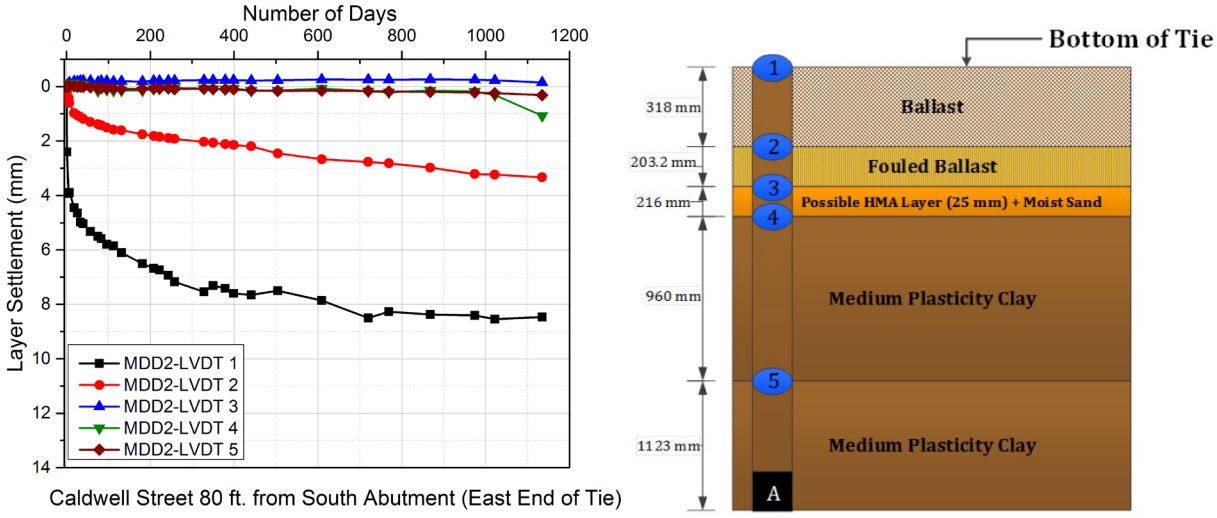

(a) (b)

Figure 4.7: (a) Layer Settlement Trends With Time and (b) Track Substructure Layer Profiles for the Caldwell Street Bridge Approach (80 ft From South Abutment; East End of Tie)

4.1.2 Summary of Observations from Track Settlement Trends

Settlements and movements within the ballast layer were the primary contributing factors to the differential movement at all three instrumented bridge approaches along Amtrak's NEC near Chester, PA. Therefore, selection and implementation of remedial measures to mitigate this problem of recurrent bump development should target the stabilization of the ballast layer.

4.2 Transient Response under Train Loading

Transient response of the instrumented locations was also measured to learn about the "elastic bounce-back" behavior of the substructure layers under loading. This required connecting a laptop computer to the signal conditioner amplifier and acquiring data from the individual channels as a train passed over the instrumented ties. The DAQ setup used a National Instruments analog/digital signal converter connected to a laptop computer running the CMS continuous DAQ software. Figure 4.8 shows an example of the transient deformation time-history recorded by individual LVDT modules under a passing train. LVDT 1, mounted within the tie, registers the highest transient deformations. Peaks corresponding to the passage of each wheel over the instrumented tie are quite distinguishable. It is important to note that all the substructure layers register finite amounts of transient deformation under train loading. This indicates the propagation of dynamic loads and associated stress waves generated by the passing train all the way down to the bottom LVDT module. The measurement of the transient deformation response within each substructure layer is essential in evaluating the long-term performance of the instrumented bridge approaches under loading.

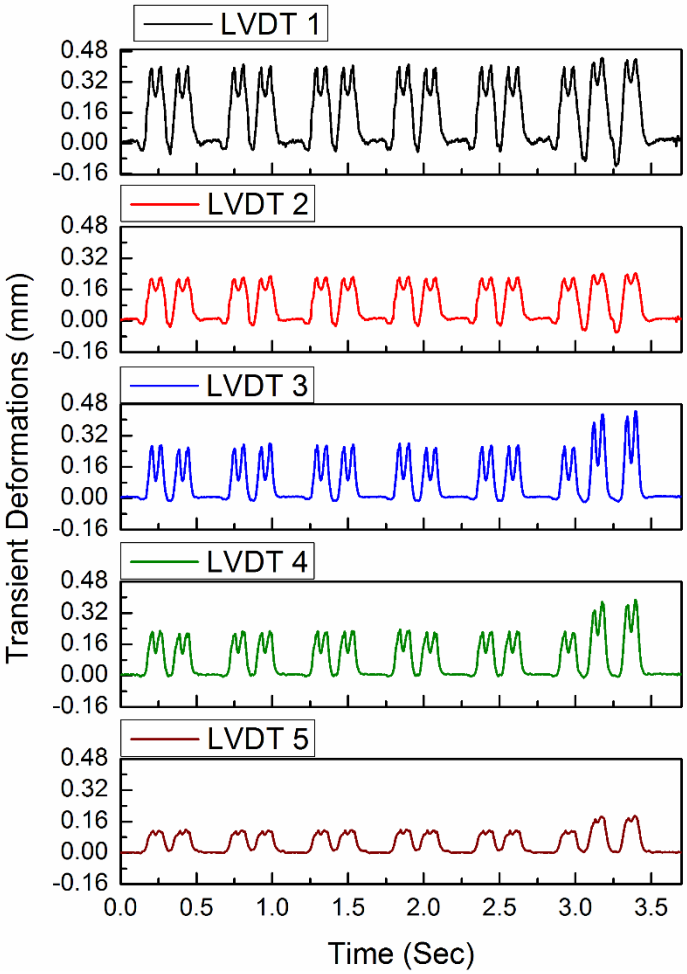

Figure 4.8: Example Transient Deformation Time-History Recorded Under Train Loading at the Upland Street Bridge Approach (Near-Bridge Location)

4.2.1 Measurement of Vertical Wheel Loads and Tie Support Conditions

Dual-element 350 ohm shear gauges mounted on a stainless shim were welded on the rail at the neutral axis to monitor the applied vertical wheel loads as well as tie support conditions. Specific dimensions of the rail sections were used to identify and mark the rail neutral axis in the field. Before installation, the strain gauges were pre-harnessed for vertical load measurements and made ready for mounting on the rail with connection to a signal cable. A calibration frame was used after installation of the strain gauges to correlate applied vertical load levels to the voltages produced by the strain gauge circuit. Figure 4.9(a) shows a photograph of the strain gauges spot-welded to the web of the rail at the neutral axis.

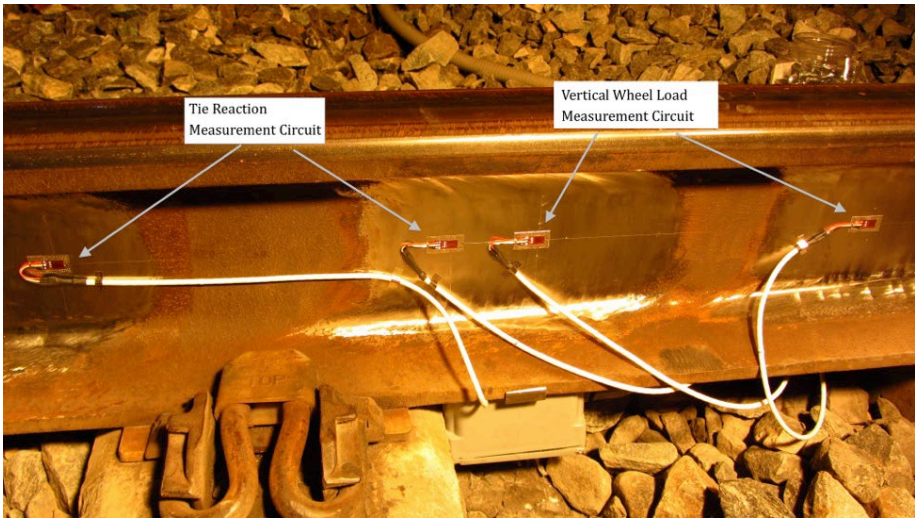

(a)

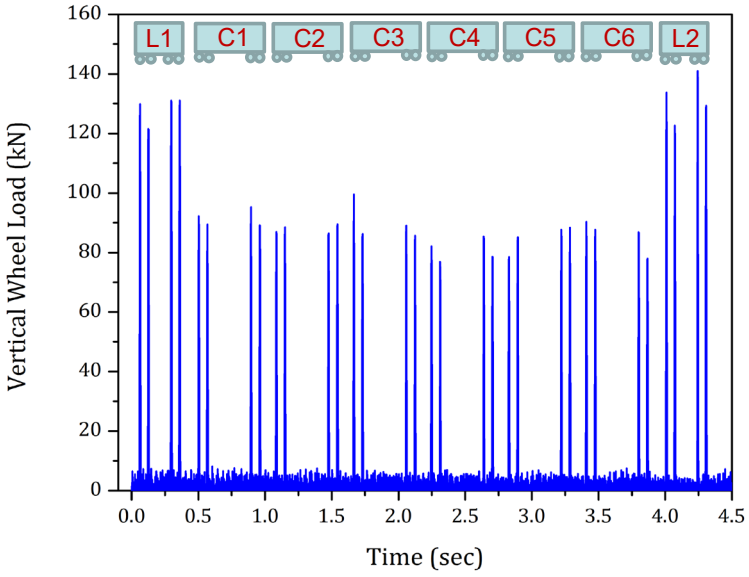

(b)

Figure 4.9: (a) Dual-Element Shear Strain Gauges Installed at the Rail Neutral Axis for Wheel Load and Tie Reaction Measurements; (b) Load Time-History of an Acela Express Train Recorded by the Wheel Load Strain Gauge Circuit

Figure 4.9(b) shows an example load time-history recorded for an Acela Express passenger train passing one of the instrumented ties. The strain gauge circuit clearly registered 32 peaks, corresponding to the 32 wheels in an Acela Express train operating along the NEC with two locomotives (one each at the front and rear ends of the train) and 6 passenger cars. Individual wheels corresponding to each peak in the load time-history record are annotated in Figure 4.9(b). As expected, the front and rear locomotives registered significantly higher load levels compared to the passenger cars. The maximum wheel load registered by this train was 140 kilonewtons (kN). The strain gauge circuits do not make any distinction between static and dynamic components of wheel loads. Therefore, the vertical wheel load values included contributions from both the static weight of the train and dynamic loading, with components introduced by track irregularities and/or mechanical defects such as wheel flats. Measurement of vertical wheel loads is particularly important to gain a better understanding of the track substructure layer response to varying load levels.

4.2.2 Amtrak Transient Displacements

The figures in this section correspond to the time-histories of transient displacements recorded at the instrumented bridge approaches along Amtrak's NEC. Transient displacement time-histories of both the near-bridge and open-track locations are presented under the passage of the same train for comparison. The load-deformation response of the substructure layers corresponding to both the near-bridge and open-track locations for the Amtrak NEC bridge approaches are presented in this section by listing the magnitudes of LVDT-based displacement with the registered load magnitudes. The transient deformations registered by LVDT 1 (mounted inside the crosstie) were often significantly higher than those recorded by LVDTs 2 through 5. Time-histories for LVDT 1 are also plotted in separate sub-figures. Accordingly, the four sub-figures in a figure (refer to Figure 4.11 as an example) represent the following:

- Top-Left: Displacement time-history for layer 1 at near-bridge location
- Top-Right: Displacement time-history for layer 1 at open-track location
- Bottom-Left: Displacement time-histories for layers 2 through 5 at near-bridge location
- Bottom-Right: Displacement time-histories for layers 2 through 5 at open-track location

Upland Street Bridge Approach

Figure 4.10 and Figure 4.11 present the first set of load and displacement time-histories, respectively, collected at the Upland Street bridge approach in August 2012 immediately after the instrumentation effort and under the passage of a southbound regional commuter train. Similar data under the passage of a second train (southbound Acela Express) are presented in Figure 4.12 and Figure 4.13. Note that the wheel load time-histories in Figure 4.10 and Figure 4.12 present data from two different strain gauge circuits, marked in the figures as "Wheel Load Measurement between Ties" and "Wheel Load Measurement on Top of the Tie." The two different strain gauge circuits were installed with the intention to quantify the support conditions underneath individual instrumented ties. Detailed discussions on the approach to evaluate the support conditions underneath individual instrumented ties will be presented later in this section.

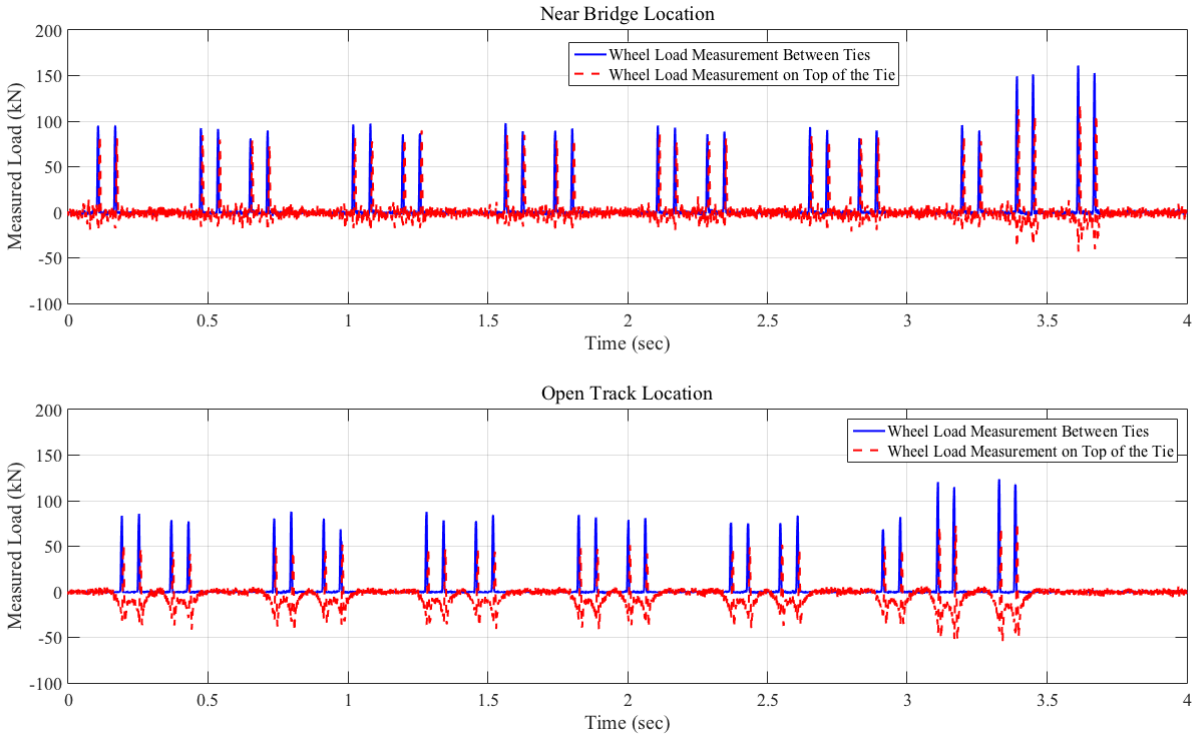

Figure 4.10: Load Time-History Recorded at Upland Street Bridge Approach; Data Collected in August 2012; Train 1

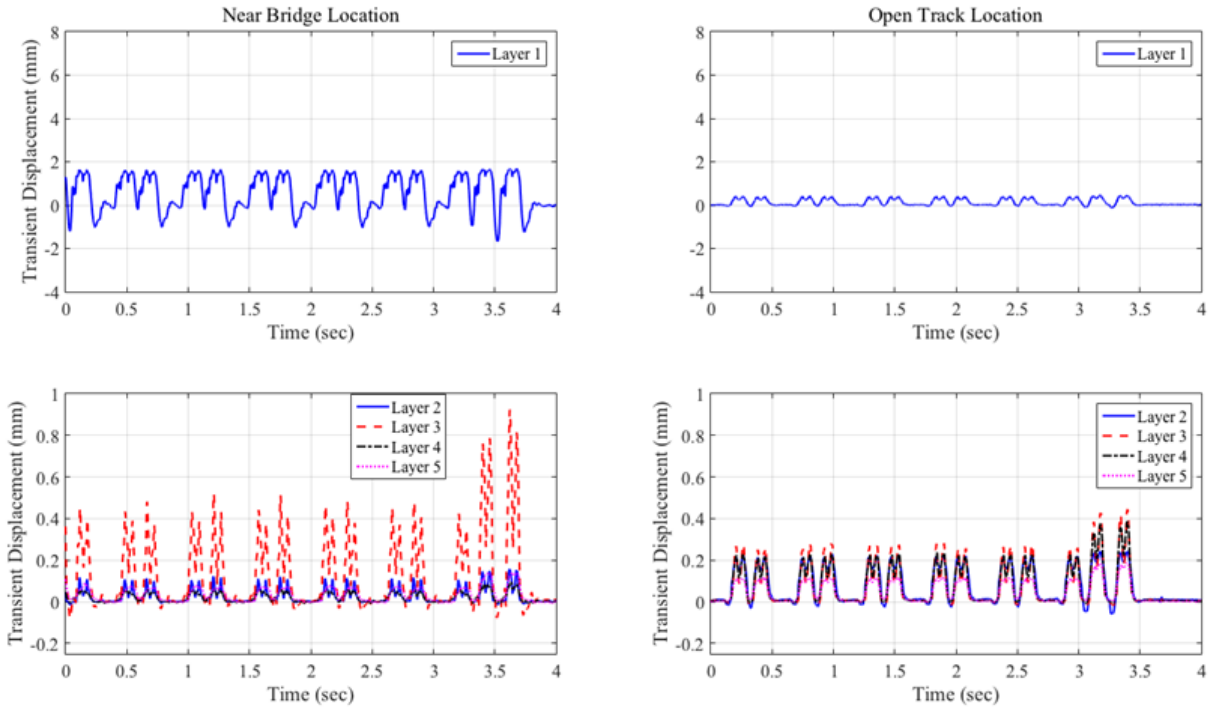

Figure 4.11: Displacement Time-History Recorded at Upland Street Bridge Approach; Data Collected in August 2012; Train 1

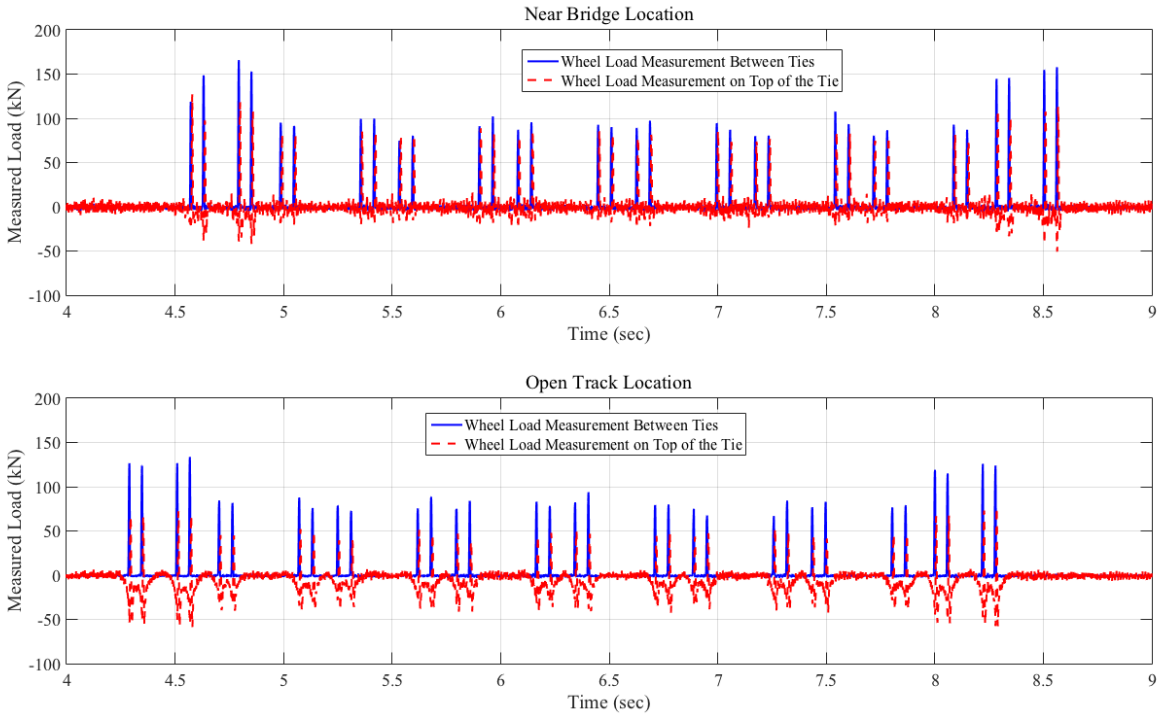

Figure 4.12: Load Time-History Recorded at Upland Street Bridge Approach; Data Collected in August 2012; Train 2 (Acela Express)

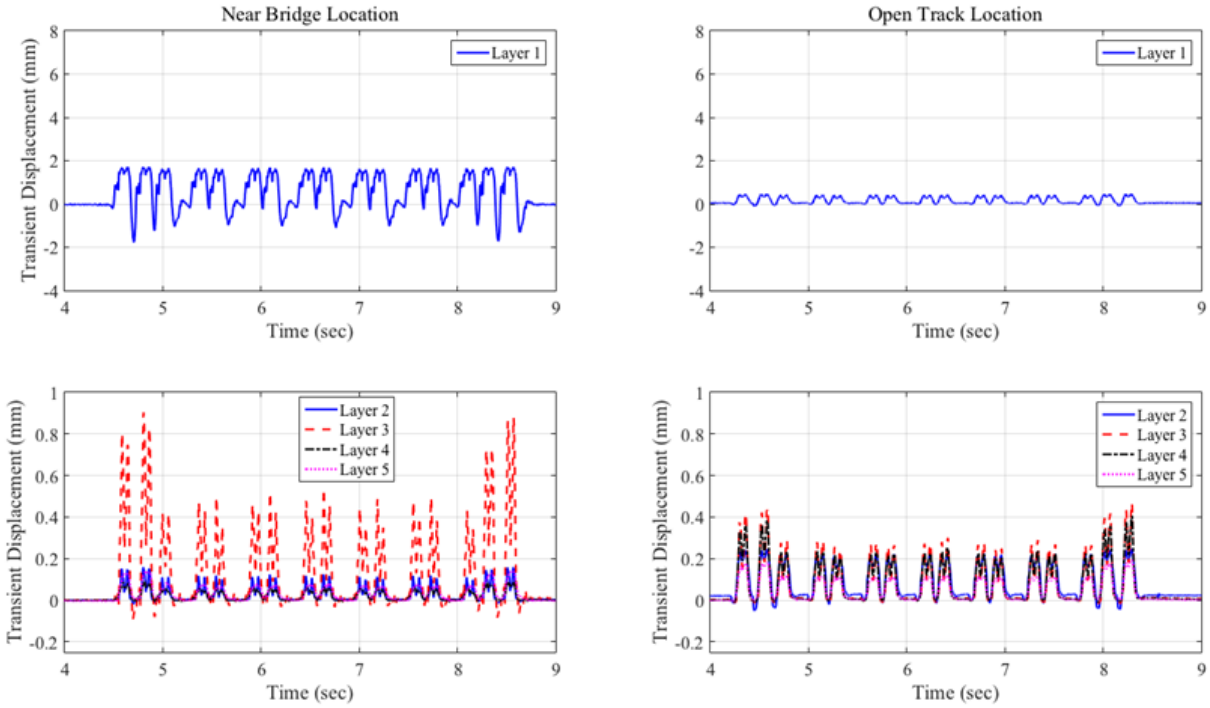

Figure 4.13: Displacement Time-History Recorded at Upland Street Bridge Approach; Data Collected in August 2012; Train 2 (Acela Express)

The following conclusions can be drawn from Figure 4.10 through Figure 4.13:

- Load levels recorded at the near-bridge location were consistently higher than those recorded at the open-track location. For example, the very last wheel of the train (last peak in the load time-history) registered as 150 kN at the near-bridge location, whereas the same wheel was recorded as ~125 kN at the open-track location. This can be attributed to the dynamic amplification induced at the near-bridge location compared to the open-track location.
- Layer 1 registered significantly higher transient deformations compared to layers 2 through 5 for both the near-bridge and open-track locations, as shown in Figure 4.11 and Figure 4.13. (Note the difference between the Y-axis scale for the top and bottom row of sub-figures.)
- Transient deformations registered in the top layer at the near-bridge location were significantly higher than those registered at the open-track location.
- The displacement of layer 3 at both the locations was higher than that of layer 2. This can be attributed to the thin, fouled ballast layers (191 mm thick at the near-bridge location; 127 mm thick at the open-track location) encountered at this bridge approach. The total deformations in the thin fouled ballast layer were lower in magnitude compared to other, thicker layers. As shown in the figures, layer 3 (Sandy Loam) registers higher deformations at both the near-bridge and open-track locations.
- Similar trends were observed for both trains recorded on that particular day.
- Detailed data for other trains recorded at this site are presented in Appendix A-1.

Transient deformations recorded in the ballast layer were significantly higher than those recorded in the other substructure layers. The displacements recorded by LVDT 1 represent deformation of the ballast layer *only when* there was full contact between the tie and the underlying ballast layer. This was not always the case, as ballast migration and settlement underneath the ties often resulted in "hanging tie" conditions, leaving a gap between the tie and the ballast layer. Transient displacements registered by LVDT 1 in such a case includes both (1) the movement of the tie before it comes in contact with the underlying ballast layer and (2) deformation of the ballast layer. Any displacement of the tie before it comes in contact with the underlying ballast layer needs to be subtracted from total displacements recorded by the top-most LVDT to get an accurate estimate of the transient deformation of the ballast layer. A novel approach to quantify the gap (if any) underneath the crosstie was developed in this research, to be described in detail in Section 5. All discussions in this section are based on the total deformation recorded by LVDT 1 under train loading.

To assess the change in bridge approach conditions over time, the transient displacements recorded by LVDT 1 at the Upland Street bridge location are plotted in Figure 4.14. To ensure that all measured displacements can be compared considering a standard load magnitude, the wheel loads recorded under each train have been normalized to a standard value of 100 kN using the equation below. For example, if the transient displacement recorded under a load of 150 kN was 1.5 mm, this value has been scaled down to 1.0 mm, corresponding to a normalized load of 100 kN for plotting and comparison purposes.

$$\textit{Normalized Displacement} = (\textit{Recorded Displacement} / \textit{Recorded Load}) * 100$$

Note that this normalization approach does assume that the transient displacement varies linearly with the applied load levels, which is not necessarily correct considering the stress-hardening nature of unbound granular materials such as railroad ballast. However, such normalization can prove to be very effective when comparing the trends in track substructure layer deformations. This has been the simple approach to compare the load deformation responses over time.

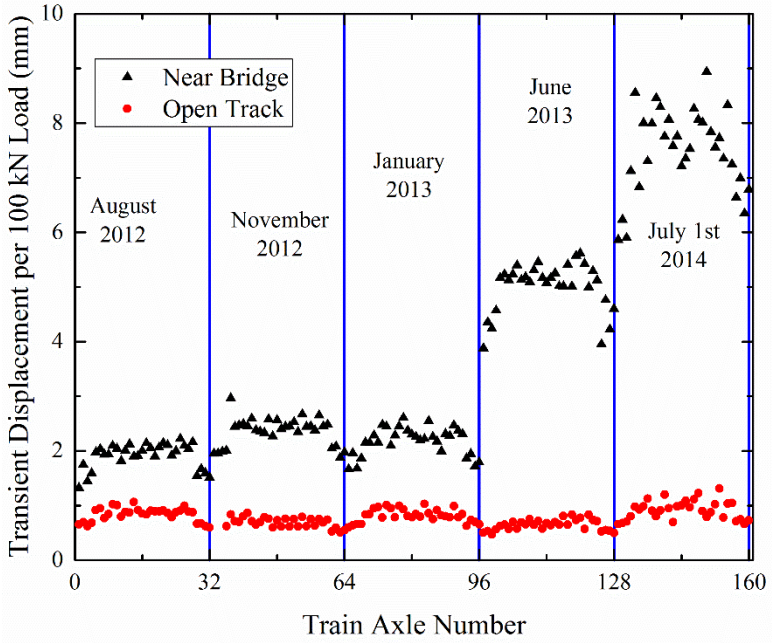

Figure 4.14: Ballast Transient Displacements Recorded at the Upland Street Bridge Approach Under the Passage of Acela Express Trains Over Time (Normalized to a Load of 100 kN)

As shown in Figure 4.14, transient displacements recorded at the near-bridge locations were consistently higher than those at the open-track location. The transient displacement, per 100 kN of load, at the near-bridge location increased significantly from August 2012 to July 2014. This indicates a gradual deterioration in the ballast layer condition over time. No such deterioration was observed for the open-track location, where the transient displacement in the ballast layer remained more or less constant between August 2012 and July 2014. Just like the track substructure layer settlement trends presented earlier in this section, the near-bridge location showed significantly more rapid deterioration compared to the open-track location.

Madison Street Bridge Approach

Figure 4.15 through Figure 4.18 present the load and displacement time-histories for the first two trains recorded at the Madison Street bridge approach in August 2012. The first train was a regional commuter train and the second train was a northbound Acela Express train. Only 30 wheels for the Acela Express were recorded by the open-track location (see Figure 4.17 bottom sub-figure) because of a delay in the triggering of the DAQ software. The wheel load magnitudes recorded at the open-track location were not significantly lower than those recorded at the near-bridge location. Note that the space curve and geometry data indicate no bump at the open-track location. Based on the space curve and direction of traffic, the near-bridge loading may have been low due to the train "launching over" the near-bridge instrumented tie.

This theory is supported by the displacement time-histories for the first two trains recorded at the Madison Street bridge approach (see Figure 4.16 and Figure 4.18). The layer 1 displacements recorded at the open-track location were surprisingly higher than those recorded at the near-bridge location. However, layers 2 through 5 registered higher transient displacement values at the near-bridge location compared to the open-track location. This indicates the presence of inadequate support conditions underneath the instrumented tie at the open-track location

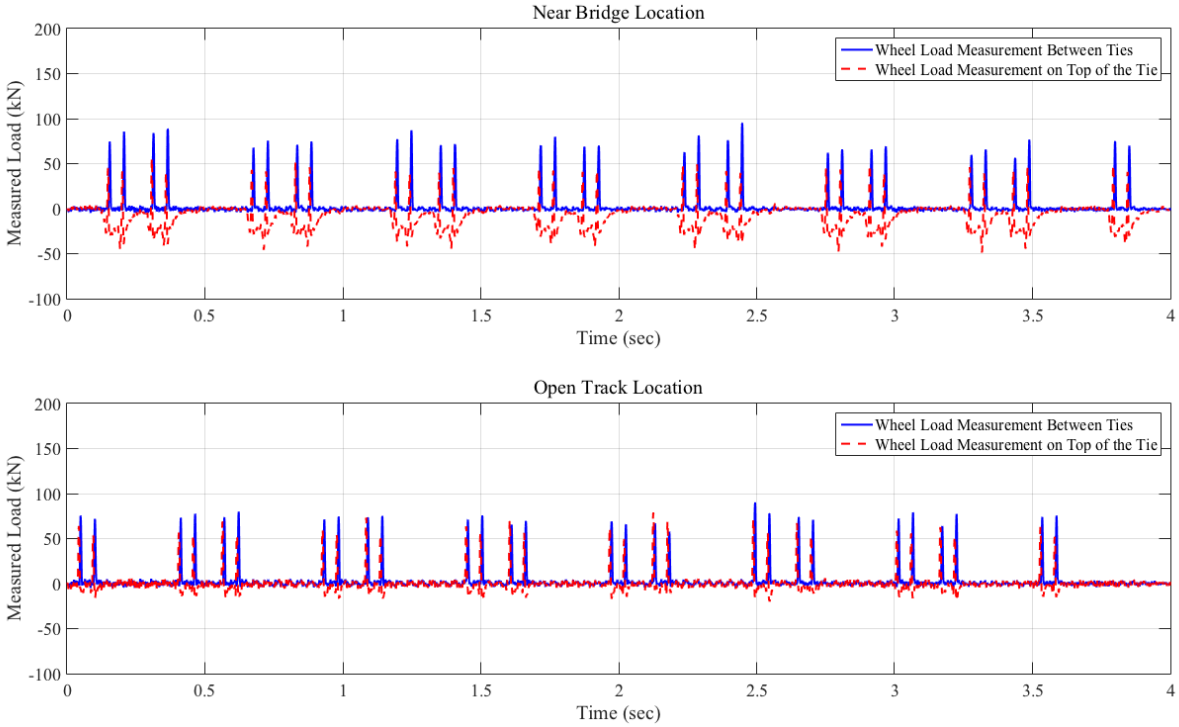

Figure 4.15: Load Time-History Recorded at the Madison Street Bridge Approach; Data Collected in August 2012; Train 1

Figure 4.19 shows the peak transient deformation magnitudes registered by LVDT 1 on different days of DAQ to compare the transient deformation trends at the Madison Street bridge approach near-bridge and open-track locations. The peak transient displacements recorded by layer 1 at the open-track location were consistently higher than those at the near-bridge location in August 2012. However, the trend was reversed for all other data collection dates, with the near-bridge location registering higher transient deformation values under a normalized load magnitude of 100 kN. Tie-gap estimation calculations, to be discussed in detail in Section 7, proved that the gap between the tie and the ballast layer was indeed higher for the open-track location in August 2012 (1.12 mm) when compared to the near-bridge location (0.54 mm). However, the tie-gap values measured in November 2012, January 2013, and June 2013 were higher at the near-bridge location compared to the open-track location.

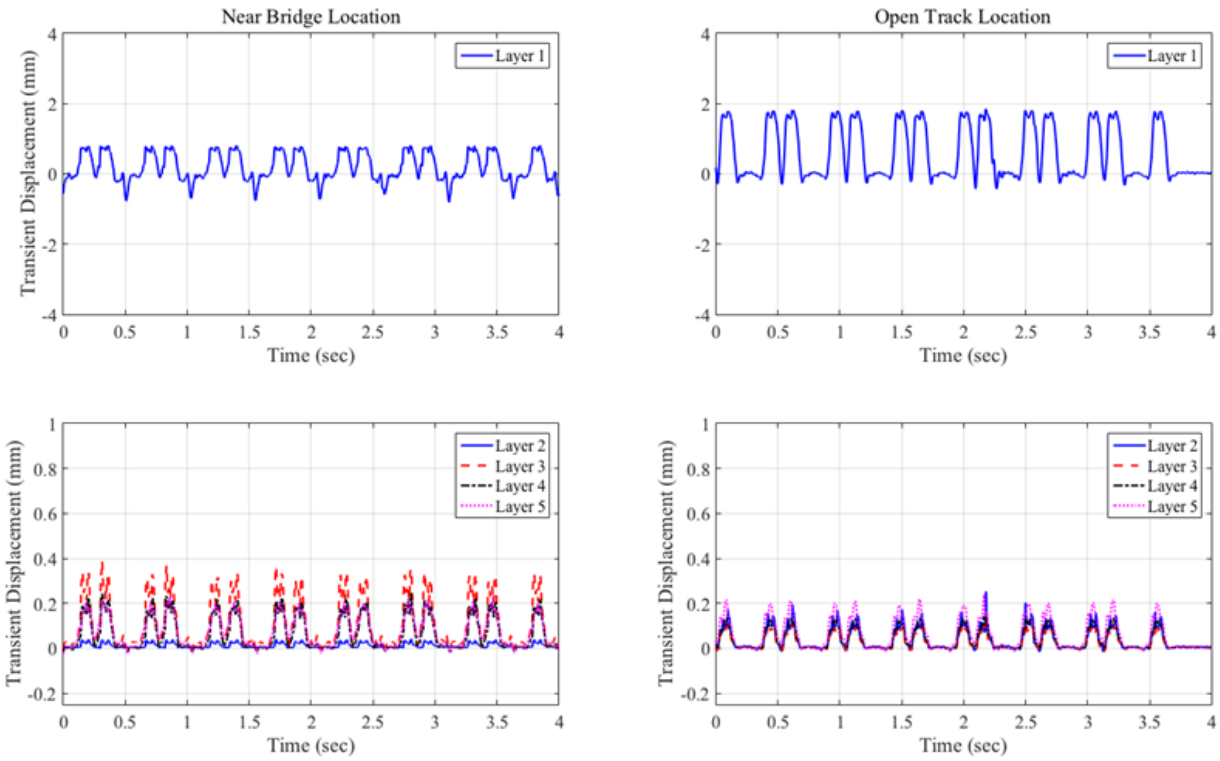

Figure 4.16: Displacement Time-History Recorded at the Madison Street Bridge Approach; Data Collected in August 2012; Train 1

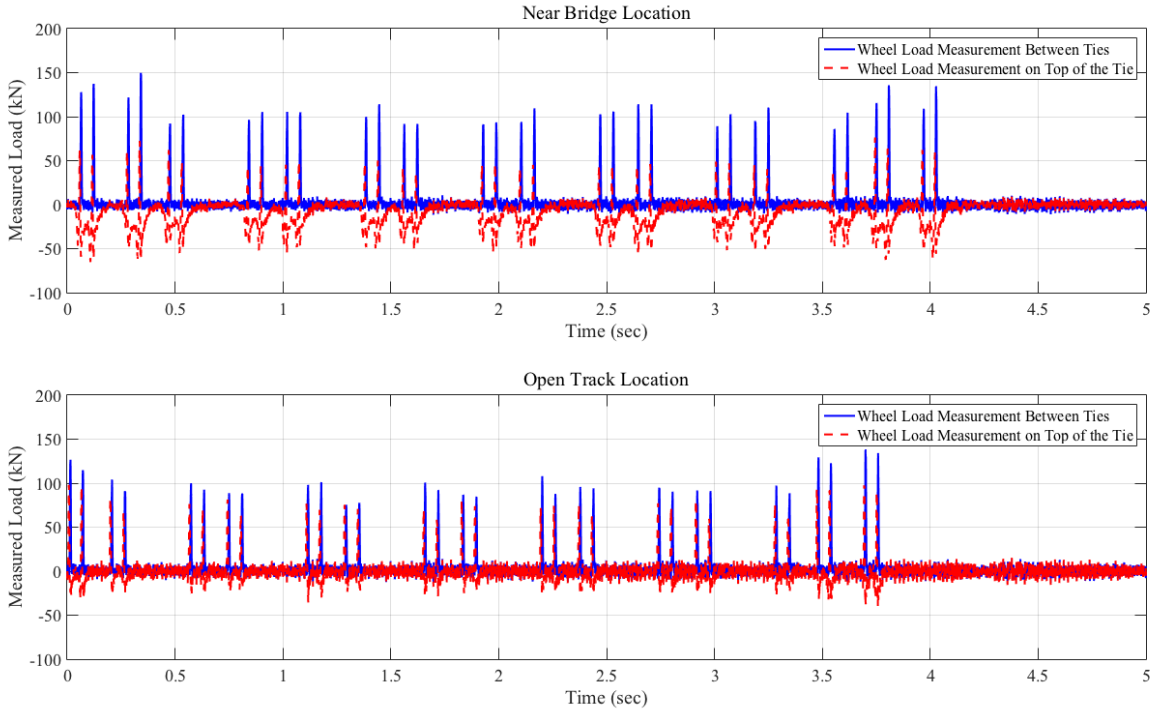

Figure 4.17: Load Time-History Recorded at the Madison Street Bridge Approach; Data Collected in August 2012; Train 2 (Acela Express)

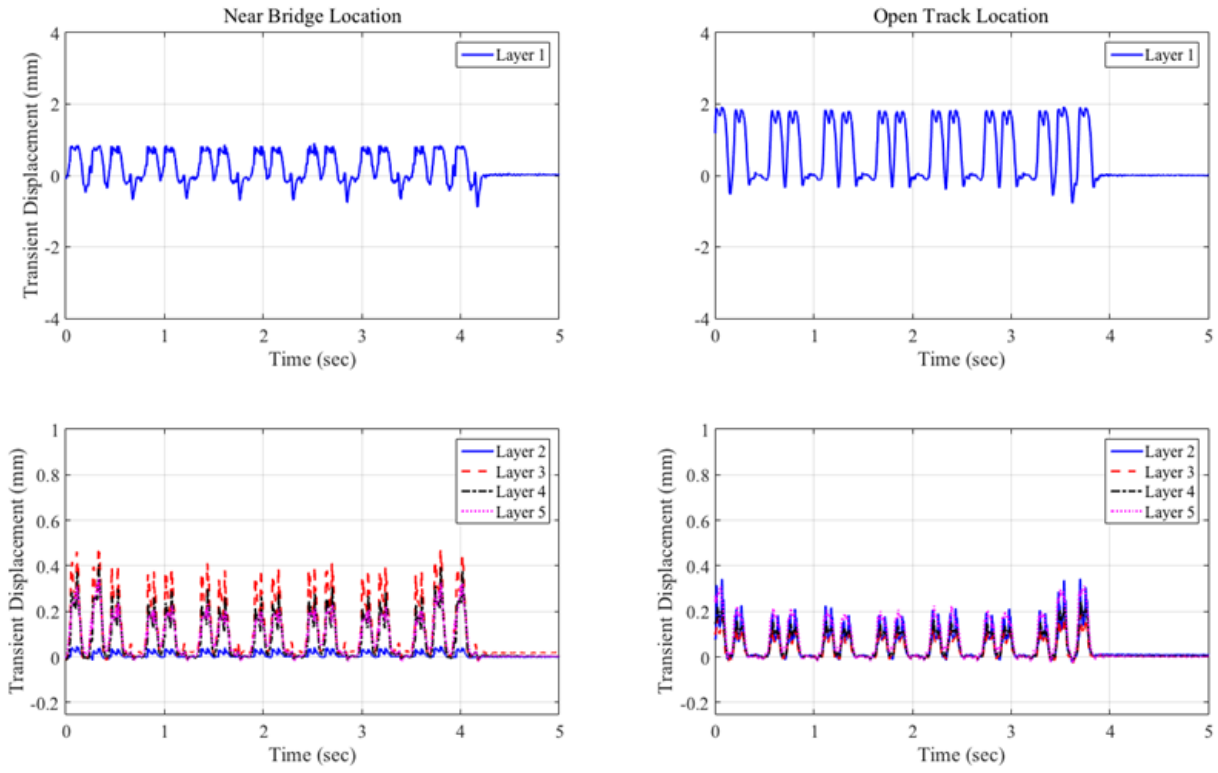

Figure 4.18: Displacement Time-History Recorded at the Madison Street Bridge Approach; Data Collected in August 2012; Train 2 (Acela Express)

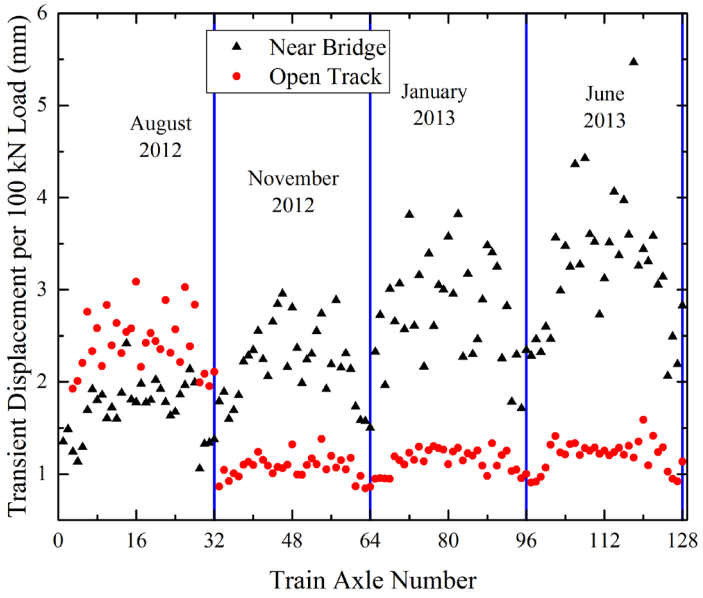

Figure 4.19: Ballast Transient Displacements Recorded at the Madison Street Bridge Approach Under the Passage of Acela Express Trains Over Time (Normalized to a Load of 100 kN)

Caldwell Street Bridge Approach

MDDs and strain gauges were installed 24.4 m (80 ft) from the south abutment at the Caldwell Street bridge on Track 3 which predominantly carries southbound traffic. Unlike the Upland and Madison Street bridge approaches, the Caldwell Street bridge approach was monitored for track response under loading as trains moved from the bridge deck onto the approach embankment. Transient displacement data under train loading was collected since the initial instrumentation in August 2012. As will be discussed in Section 6, no remedial measure was applied at the Caldwell bridge location, therefore all data collected through May 2015 represents the response under loading of the original bridge approach configuration. Unlike the Upland and Madison Street bridge locations, the two MDDs at the Caldwell Street location were installed on two ends of a single crosstie. The objective was to assess any differences in the tie support conditions between the two ends of the tie.

Figure 4.20 through Figure 4.23 present the load and displacement time-histories of the first two trains recorded in August 2012. Comparing the load magnitudes recorded by strain gauges on the east versus the west end of the tie, it is apparent the west end recorded consistently higher load magnitudes compared to the east end for the same wheel loads. This indicates the presence of higher dynamic amplification on the west end of the tie compared to the east end. This theory can be corroborated from the displacement time-histories for layer 1 presented in Figure 4.21 and Figure 4.23, which clearly show higher transient deformations of the ballast layer on the west end of the tie. It is safe to hypothesize that the presence of a larger gap between the tie and the ballast layer on the west end of the tie led to higher dynamic load amplifications and higher layer 1 displacements recorded under train loading. A validation of this hypothesis can be obtained from the tie-gap calculations presented in Section 7, which clearly show the gap underneath the west end of the tie to be 1.36 mm, compared to 0.74 mm for the east end of the tie.

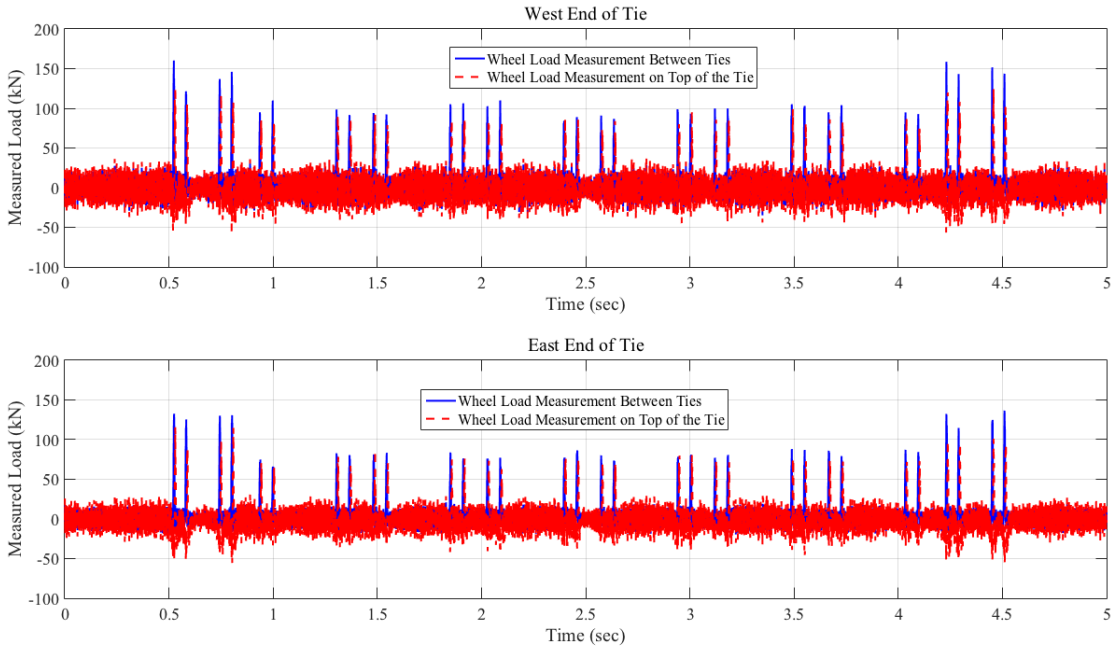

Figure 4.20: Load Time-History Recorded at the Caldwell Street Bridge Approach; Data Collected in August 2012; Train 1 (Acela Express)

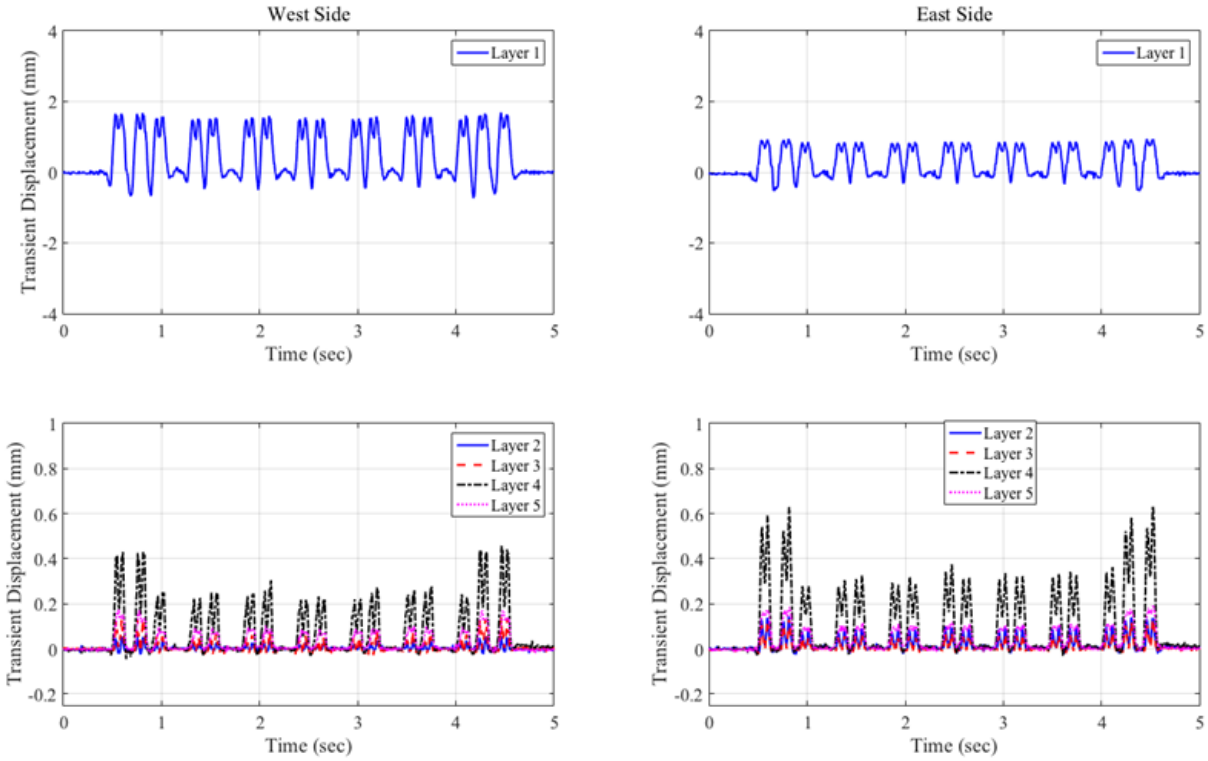

Figure 4.21: Displacement Time-History Recorded at the Caldwell Street Bridge Approach; Data Collected in August 2012; Train 1 (Acela Express)

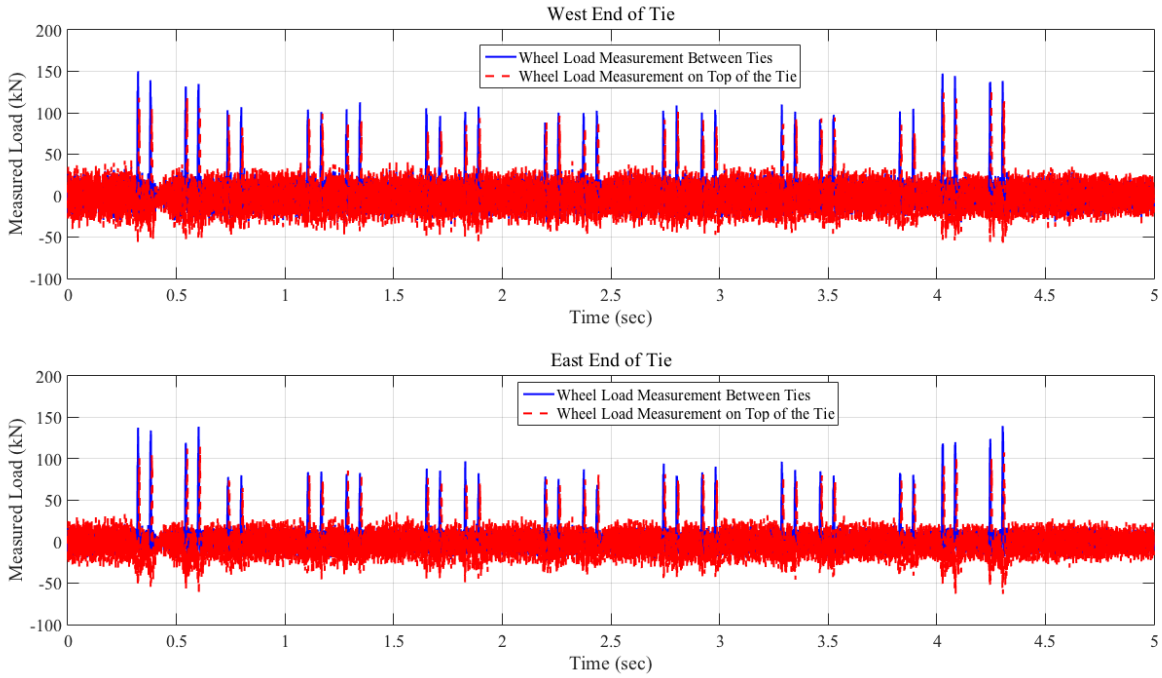

Figure 4.22: Load Time-History Recorded at the Caldwell Street Bridge Approach; Data Collected in August 2012; Train 2 (Acela Express)

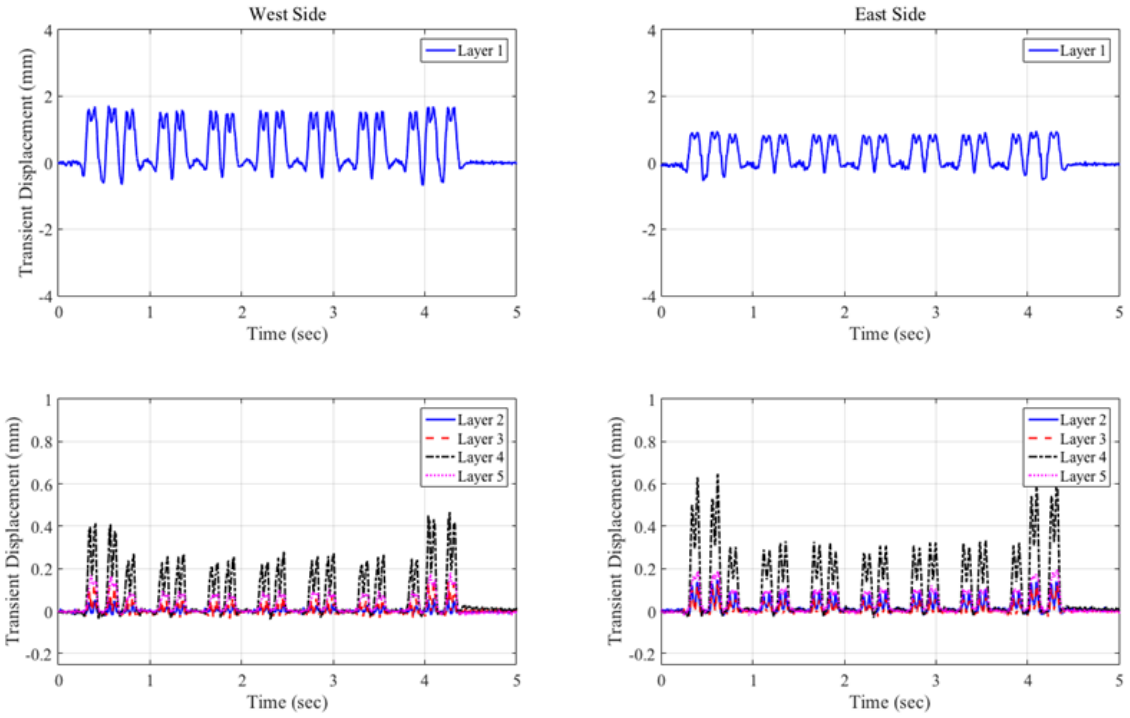

Figure 4.23: Displacement Time-History Recorded at the Caldwell Street Bridge Approach; Data Collected in August 2012; Train 2 (Acela Express)

Figure 4.24 plots the peak transient displacement values recorded for the ballast layer at the Caldwell Street bridge approach under the passage of Acela Express trains. As before, all displacement values have been normalized to a standard load of 100 kN. As shown in the figure, there is no significant difference between the normalized displacement values calculated for the west end and the east end of the tie. The data points corresponding to the west end of the tie appear to be slightly higher than those for the east end, which can be correlated to the presence of a higher gap between the tie and the ballast layer.

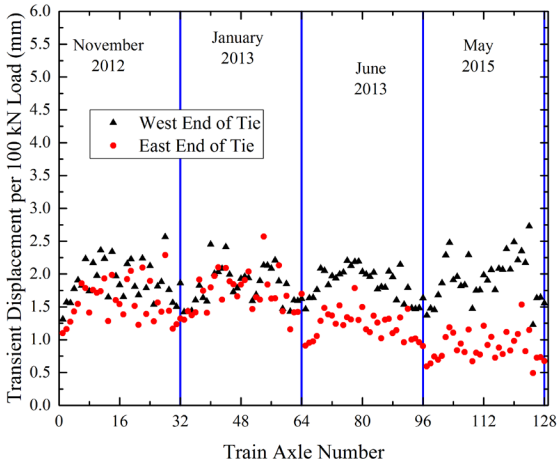

Figure 4.24: Ballast Transient Displacements Recorded at the Caldwell Street Bridge Approach Under the Passage of Acela Express Trains Over Time (Normalized to a Load of 100 kN)

It is interesting to note that due to the instrumented location being far away from the bridge abutment (80 ft), the ballast layer condition did not deteriorate with time, as was the case for the Upland and the Madison Street bridge approaches (see Figure 4.14 and Figure 4.19).

4.2.3 NS Transient Displacements

Load and displacement time-histories recorded at the NS N-Line mainline bridge approaches are presented in this sub-section. The NS N-Line mainline bridge approaches primarily carried freight trains moving at a maximum speed of 25 mph. Data acquisition was carried out by connecting the signal conditioner/amplifier and a laptop to the DAQ box mounted to the bottom of the rail. Only eight independent channels were available on the amplifier unit, so the response under the same train could not be collected for both the near-bridge and open-track locations. Therefore, data collected at individual instrumented crossties at these bridge approaches correspond to different trains.

Bridge MP352.2

Figure 4.25 and Figure 4.26 present the first set of load and displacement time-histories, recorded at the MP352.2 bridge approach, near-bridge location. As before, the displacement time-history for the ballast (layer 1) has been plotted as a separate sub-figure (top), whereas the transient displacements for all other substructure layers are given in the bottom sub-figure. From Figure 4.25 it is apparent that the train comprised both loaded and empty cars leading to the registration of high and low measured load values, respectively. Simultaneous inspection of Figure 4.25 and Figure 4.26 establishes that the loaded cars led to higher transient deformations in the track substructure layers compared to empty cars. Like the Amtrak NEC bridge approaches, the ballast layer contributed a large portion of the total track transient deformations at the near-bridge location.

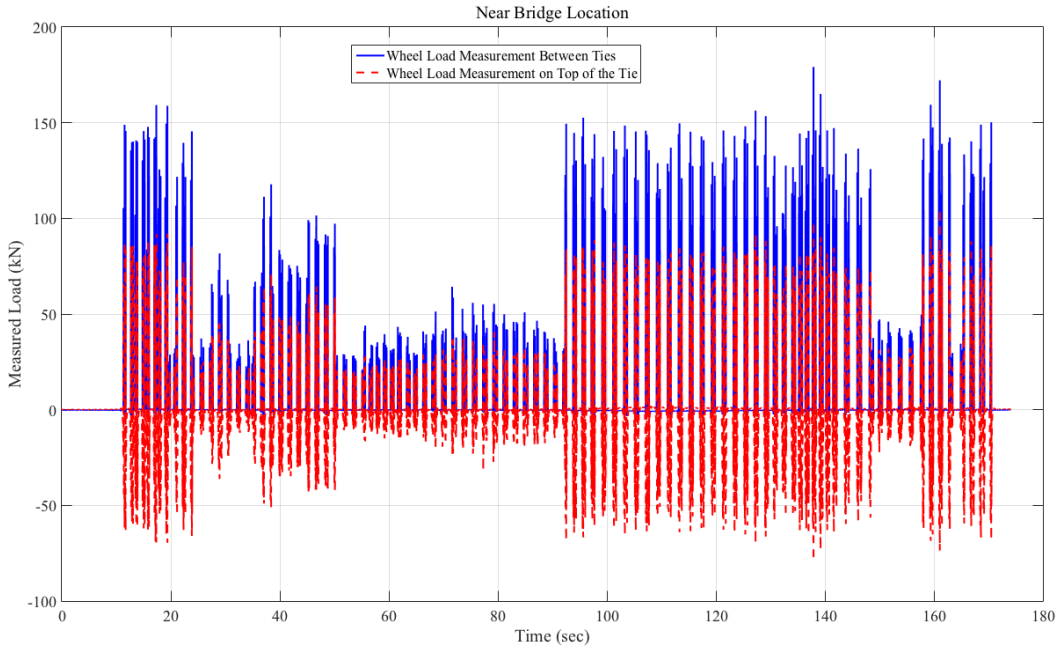

Figure 4.25: Load Time-History Recorded at the MP352.2 Bridge Approach – Near-Bridge Location; Data Collected in November 2013; Train 1

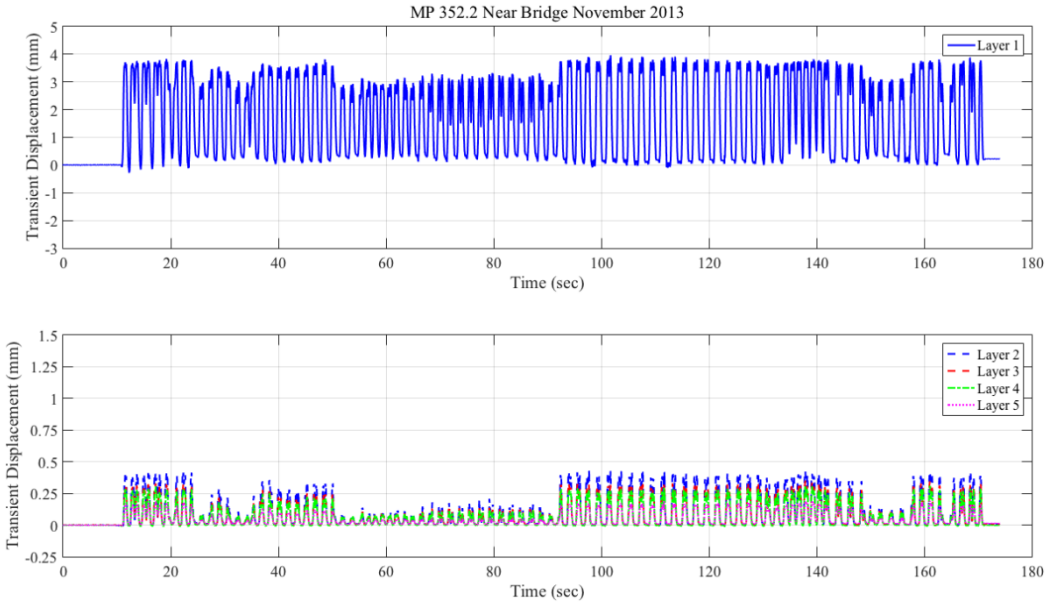

Figure 4.26: Displacement Time-History Recorded at the MP352.2 Bridge Approach – Near-Bridge Location; Data Collected in November 2013; Train 1

Figure 4.27 and Figure 4.28 present the load and transient displacement time-histories, respectively, recorded at the open-track location of the same bridge (MP352.2). As evident from Figure 4.27, this train comprised loaded cars only, with all wheel loads recorded as approximately 150 kN. This led to uniform transient deformations recorded in the substructure layers across the entire length of the train. Note that the difference between the transient deformations recorded for the ballast layer and the other substructure layers was less significant for the open-track location compared to the near-bridge location. In fact, the transient displacements registered by the LVDT in layer 2 at the open-track location were of comparable magnitude to those registered by the ballast layer (LVDT 1).

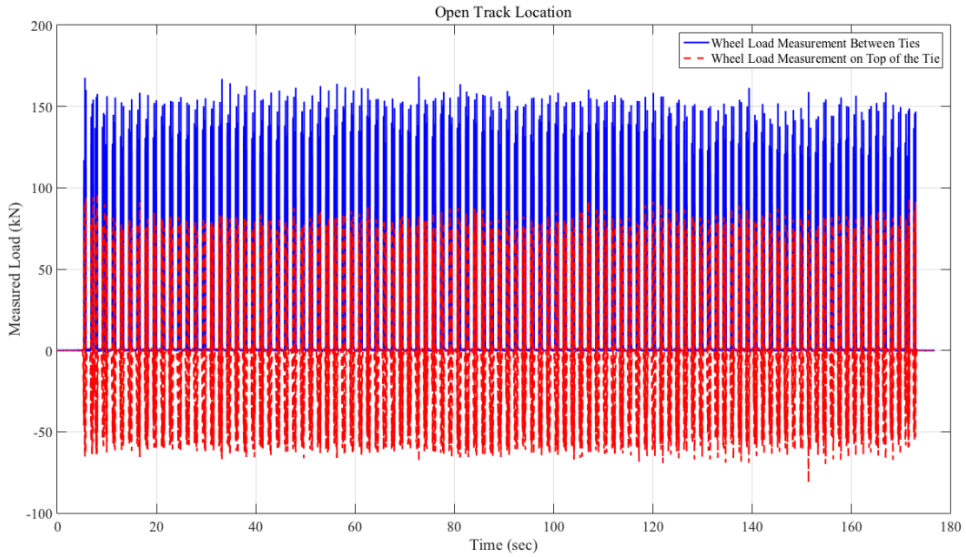

Figure 4.27: Load Time-History Recorded at the MP352.2 Bridge Approach – Open-Track Location; Data Collected in November 2013; Train 1

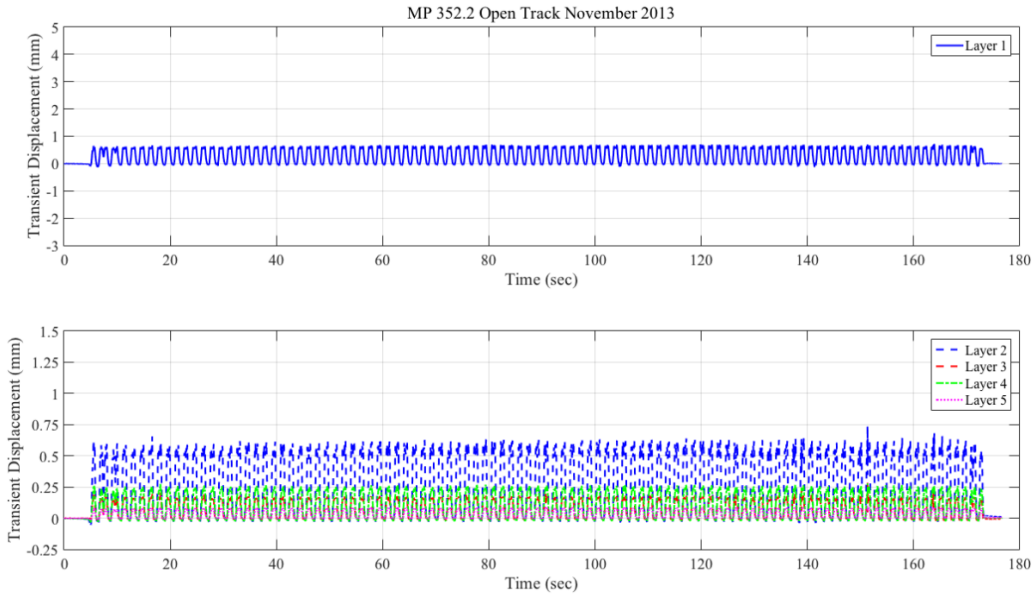

Figure 4.28: Displacement Time-History Recorded at the MP352.2 Bridge Approach – Open-Track Location; Data Collected in November 2013; Train 1

The load-transient deformation trends for the ballast layer corresponding to the near-bridge and open-track locations at bridge MP352.2 are presented in Figure 4.29. For a given wheel load, the ballast layer at the near-bridge location had significantly higher transient deformation values compared to the open-track location. This indicates that even for the slower moving freight trains, the stress wave reflections from the bridge abutment resulted in significantly higher ballast deformations for the near-bridge locations compared to the open-track locations. Additional load and displacement time-histories recorded for this bridge approach can be found in Appendix A-1.

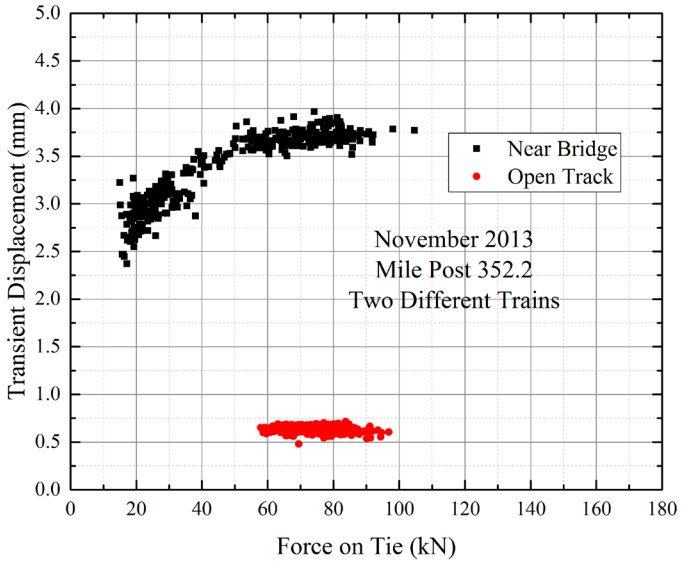

Figure 4.29: Comparing the Load-Transient Displacement Relationships for the Ballast Layer at the Near-Bridge and Open-Track Locations for Bridge MP352.2; Data Collected in November 2013

Bridge 352.8

Figure 4.30 and Figure 4.31 present the load and displacement time-histories, respectively, recorded at the MP352.8 near-bridge location in November 2013. As evident from the load time-history, this train was comprised primarily of empty cars that registered significantly lower wheel load magnitudes compared to the locomotive. Transient deformations recorded for the ballast layer (layer 1) were significantly higher (approximately 2-3 times in magnitude) compared to those recorded for layers 2 and 3.

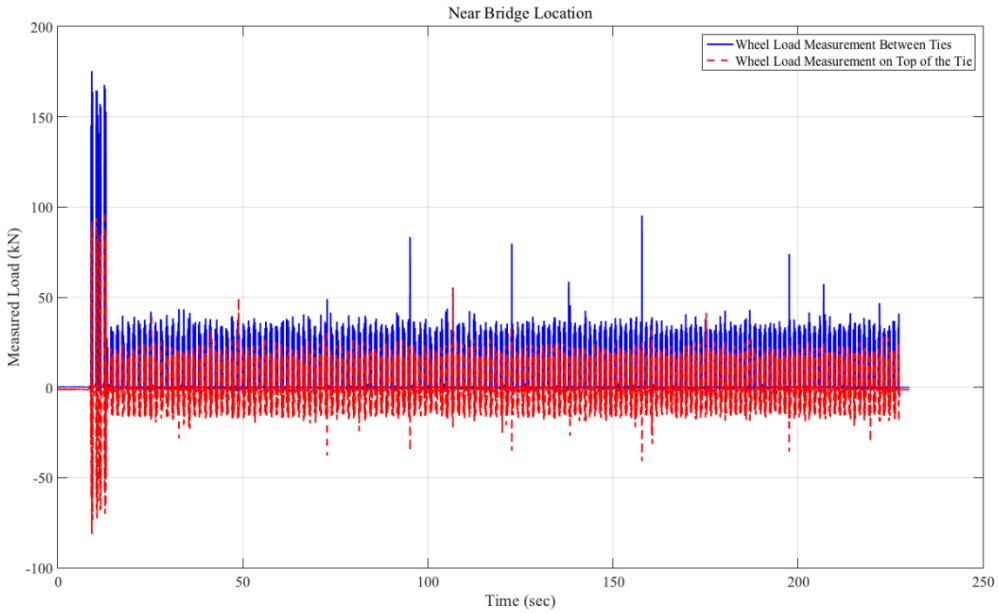

Figure 4.30: Load Time-History Recorded at the MP352.8 Bridge Approach – Near-Bridge Location; Data Collected in November 2013

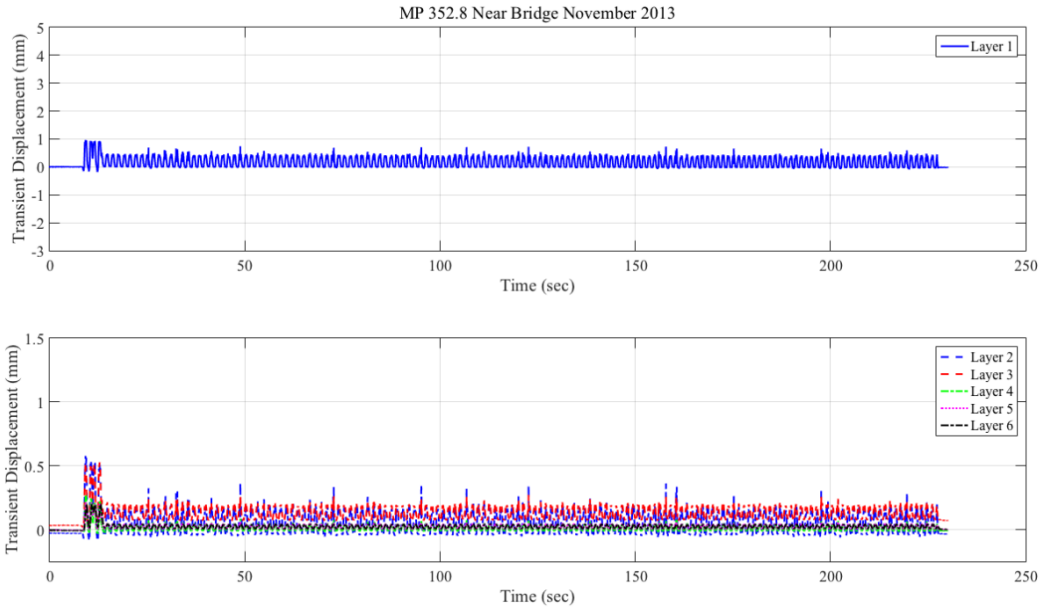

Figure 4.31: Displacement Time-History Recorded at the MP352.8 Bridge Approach – Near-Bridge Location; Data Collected in November 2013

Due to scheduling conflicts, transient response at the bridge MP352.8 open-track location could not be collected in November 2013. Accordingly, Figure 4.32 and Figure 4.33 present the load and displacement time-histories, respectively, recorded at the open-track location of bridge MP352.8 in March 2014. Once again, the recorded train primarily comprised empty cars that led to uniform transient layer deformations across the entire length of the train. Like the near-bridge location, the ballast layer at the open-track location registered transient displacements that were 2–3 times higher in magnitude compared to those for layer 2.

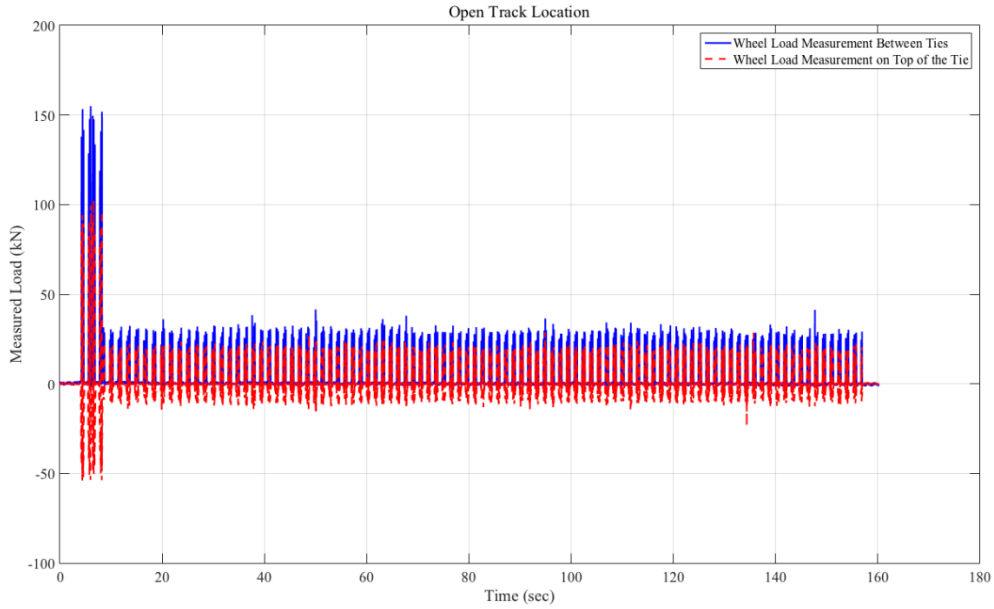

Figure 4.32: Load Time-History Recorded at the MP352.8 Bridge Approach – Open-Track Location; Data Collected in March 2014

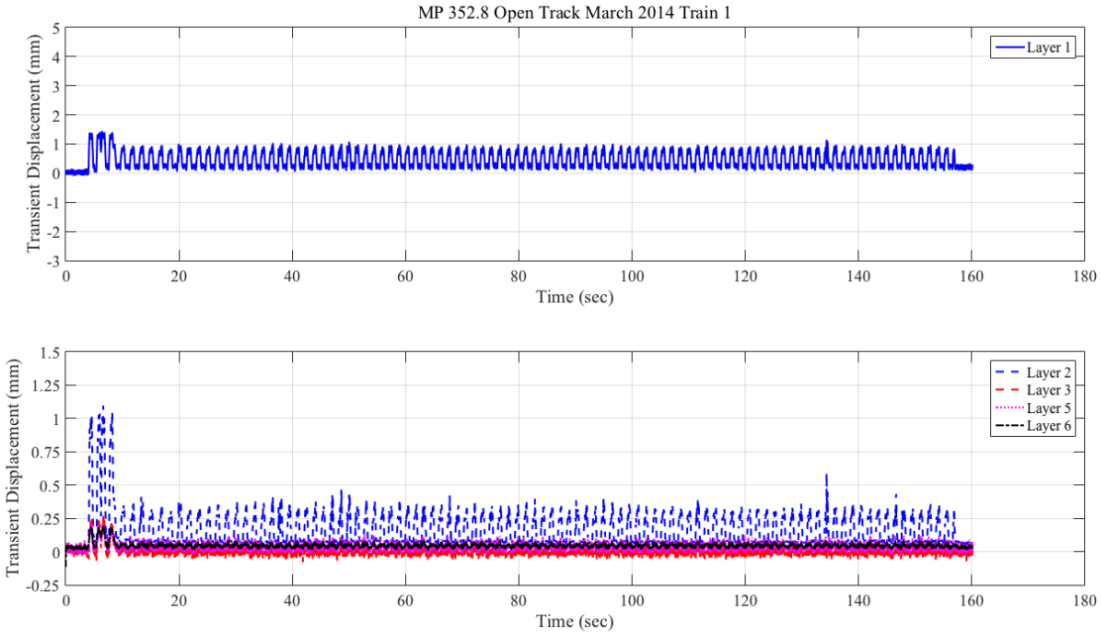

Figure 4.33: Displacement Time-History Recorded at the MP352.8 Bridge Approach – Open-Track Location; Data Collected in March 2014

4.3 Load Distribution Characteristics as an Indicator of Support Conditions

This section presents a novel approach to assess the tie support conditions based on wheel loads recorded by the dual-element strain gauges mounted at the neutral axis of the rails. A total of eight strain gauges were installed near each instrumented tie to measure the vertical wheel load and tie reaction values under train loading. Four of the eight strain gauges were mounted on the rail over the crib area (two on either face of the rail web) and formed the vertical wheel load measurement circuit. The remaining four strain gauges (two on either face of the rail web) were mounted on either side of the instrumented tie and formed the tie reaction circuit. A brief explanation of the theory of operation behind the tie reaction measurement circuit is given below. The analysis method used was originally developed by Michael Tomas of Amtrak.

Two adjacent strain gauges corresponding to the vertical wheel load circuit, or the tie reaction circuit, were separated by 254 mm (10 in). As the load was applied on top of the vertical wheel load circuit, the rail underwent bending, and a corresponding level of shear stress was induced in the rail section. The dual-element shear gauges mounted on the neutral axis detected the shear stresses, oriented at 45° to the rail neutral axis, and the corresponding vertical wheel loads were calculated using a calibration factor established during the installation of the strain gauges.

The distance between adjacent tie reaction circuit strain gauges was identical to that for the vertical wheel load circuit. The only difference was that the two adjacent strain gauges for the tie reaction circuit (on a given side of the rail web) were mounted on either side of the instrumented tie, as opposed to being mounted in the crib area as in the vertical wheel load circuit. Considering an extreme case where the instrumented tie is fully supported by rigid underlying layers, it was expected that the rail section immediately above the tie would not undergo any bending upon loading. No bending-induced shear stress was recorded. The portion of the vertical load carried by the instrumented tie can be calculated by subtracting the tie reaction circuit load levels from the vertical wheel load circuit levels.

A hypothetical, extreme condition can occur when the instrumented tie has no support underneath, and hence is “hanging” in the air. In such a case, no differences exist between the bending-induced shear stress levels in the rail sections above the crib and the sections immediately above the instrumented tie. The vertical wheel load circuit and the tie reaction circuit will register identical load levels. Subtracting the two values will indicate that the instrumented tie does not support any fraction of the applied vertical load.

Support conditions for in-service ties are usually expected to be intermediate between these two extremes. A well-maintained track with good support conditions can be idealized as an elastic foundation, and the vertical wheel loads can be assumed to be distributed among the several adjacent ties. One common assumption is that 40 percent of the vertical wheel load is carried by the center tie, with the next two ties on either side carrying 20 percent and 10 percent of the load, respectively.

Two examples of vertical wheel load and tie reaction values recorded from the instrumented bridge approaches are presented in Figure 4.34. The top graphs in both Figure 4.34 (a) and (b) show the vertical wheel load levels and the center graphs show the values recorded by the tie reaction circuits. For graphing purposes, the vertical wheel load is referred to as “Wheel Load Measurement between Ties” and the loads recorded by the tie reaction channel are referred to as “Wheel Load Measurement on Top of the Tie.” The bottom graphs show the differences between the two and represent the loads supported by the instrumented ties. In Figure 4.34(a), the

maximum detected vertical wheel load was approximately 140.5 kN, and the corresponding tie reaction circuit value was 66.7 kN. Accordingly, the load carried by the instrumented tie can be calculated as 140.5 – 66.7 = 73.8 kN, which is about 52.5 percent of the applied wheel load. Figure 4.34(b) presents an extreme condition where a lack of adequate support underneath the instrumented tie resulted in a hanging tie condition, with no load being supported by the instrumented tie. These data were used to evaluate and quantify seasonal changes in track support conditions.

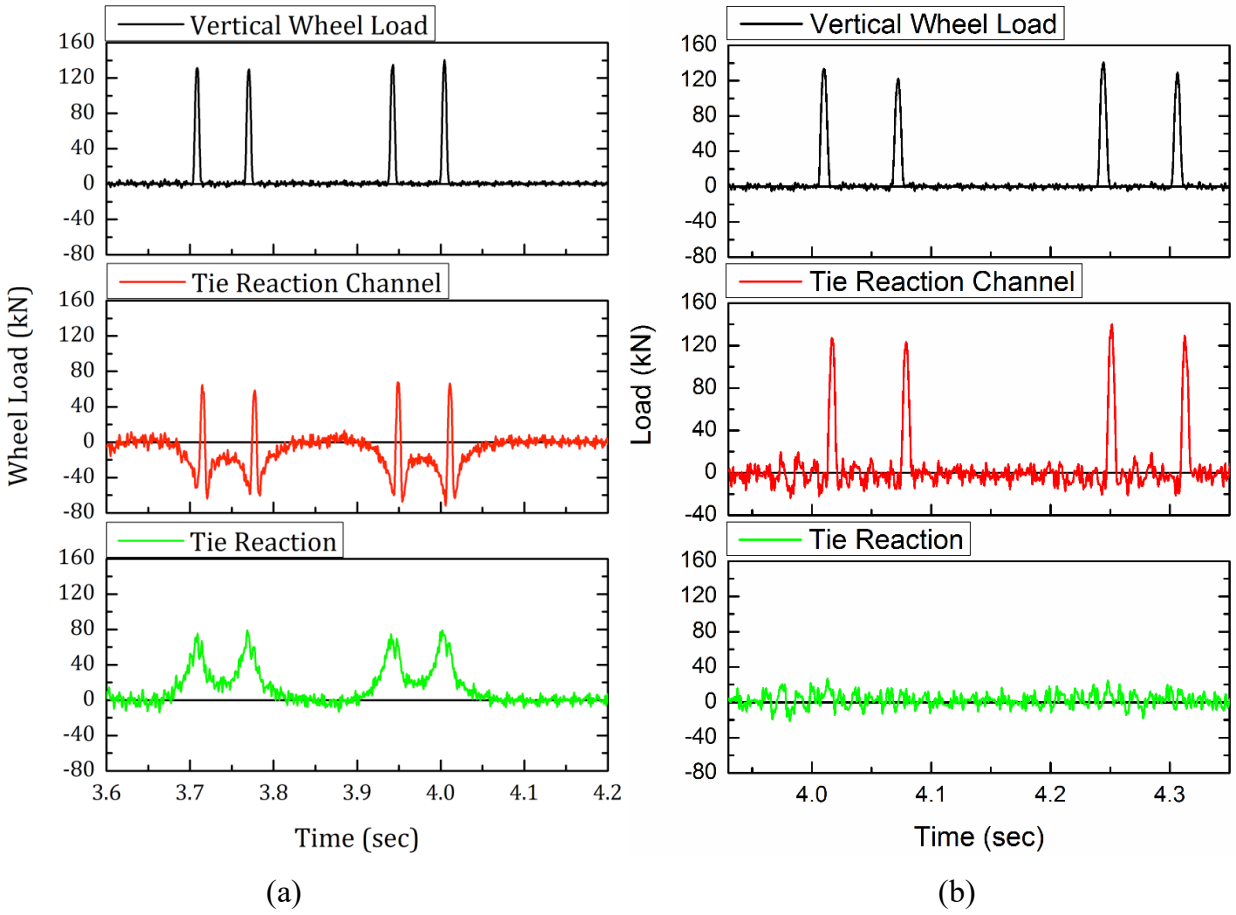

Figure 4.34: Example Cases for Vertical Wheel Load and Tie Reaction Values Measured Using Strain Gauges: (a) Instrumented Tie Carries 50 Percent of the Applied Wheel Load; (b) Instrumented Tie Carries No Load (Hanging Tie Condition)

The percentage of wheel load supported by the instrumented tie was monitored for each of the instrumented bridge approaches to assess the support conditions and possible change in the support conditions over time. Data collected under each wheel load at the instrumentation locations were compiled and graphed in the form of box plots in the figures below. The mean value is shown as a data point and the median value as a horizontal line in each box that represents an interquartile range for the minimum and maximum data values highlighted by the vertical line.

Trends in the percentage of wheel load carried by the instrumented ties at the Amtrak NEC and NS N-Line mainline bridge approaches were analyzed. Figure 4.35 shows the trends in tie support conditions at the Upland Street bridge approach. Note that the figure includes data from

both the near-bridge (NB) and open-track (OT) locations. As shown in the figure, the percentage of load carried by the instrumented tie at the OT location was consistently higher than those for the NB location. A well-supported tie usually carries approximately 40–50 percent of the wheel load, which is the exact range where the mean values for the open-track location lies. From Figure 4.35, it is clear that the tie support conditions at the NB location exhibit significantly more variation with time compared to those at the OT condition. Close inspection of the percentage of wheel load carried by the instrumented tie for the NB location indicates that the mean percentage values were less than zero, corresponding to the November 2012 measurement. This essentially means that the loads recorded by the tie reaction channel (measured over the instrumented tie) were higher than those recorded by the vertical wheel load channel (measured between ties). This was a result of complex dynamic loading conditions that resulted from certain ties losing contact with the underlying ballast, which can lead to the significant dynamic amplification of the loads. The strain gauge circuits used in this study did not distinguish between static and dynamic loading conditions, and hence impact loads (if any) resulting from the change in track profile or wheel flats, etc. could be recorded as an increase in the wheel load. The support conditions at the NB location were restored to approximately 35 percent (mean value), as indicated by the January 2013 measurement. This corresponds to the tamping and track resurfacing that was carried out at this location approximately 200 days after the original instrumentation (see Figure 4.2).

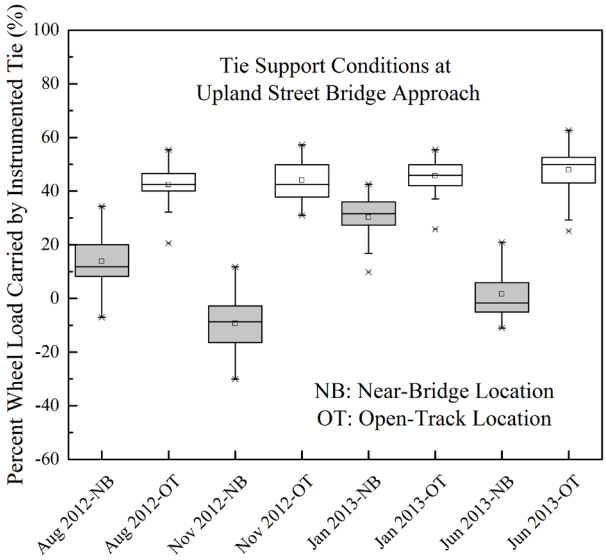

Figure 4.35: Change with Time in Percent Wheel Load Carried by the Instrumented Tie at the Upland Street Bridge Approach

Figure 4.36 presents similar data for the Madison Street bridge approach. This location shows that a higher percentage of the wheel load was carried by the instrumented tie at the near-bridge location compared to the open-track location (represented in the figure as NB and OT, respectively). Further, the dynamic action of the train could have been causing quite different applied loads at near-bridge and open-track locations. Data for the open-track location at the Madison Street bridge approach indicates that 10–20 percent (mean value) of the wheel load was carried by the instrumented tie. This phenomenon can be attributed to the larger gaps underneath the ties present at the open-track location compared to the near-bridge location for this bridge approach (discussed later in Section 5). Essentially, part of the wheel load was used to bring the

tie back in contact with the ballast layer, and the remaining portion of the load was supported by the tie once it was in contact with the underlying ballast layer.

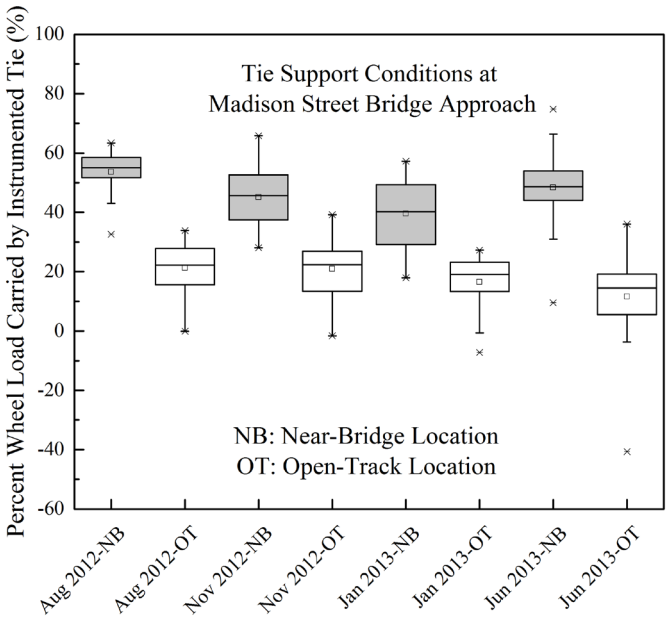

Figure 4.36: Change with Time in Percent Wheel Load Carried by the Instrumented Tie at the Madison Street Bridge Approach

Figure 4.37 shows the tie support condition data collected at the Caldwell Street bridge approach. No significant difference existed between the tie support conditions at the east and west ends of the instrumented crosstie. Moreover, no significant change in the support conditions was observed over time. This illustrates the relatively stable and consistent support conditions underneath this tie.

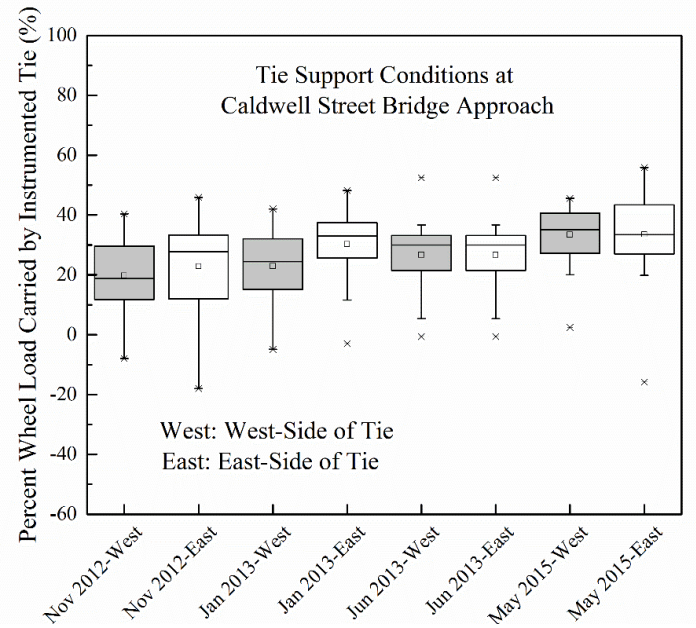

Figure 4.37: Change with Time in Percent Wheel Load Carried by the Instrumented Tie at the Caldwell Street Bridge Approach

Similar plots for the NS N-Line mainline bridge approaches are presented in Figure 4.38 and Figure 4.39. As shown in Figure 4.38, the support conditions for the bridge at MP352.2 remained relatively consistent over time. Although the difference between the support conditions at the near-bridge and the open-track location was not as drastic as that observed for the Amtrak NEC bridge approaches, the near-bridge location exhibited slightly lower percent load carried when compared to the open-track location. However, this trend was reversed for the MP352.8 bridge approach, where the near-bridge location showed slightly higher values for the percentage of wheel load carried by the instrumented tie.

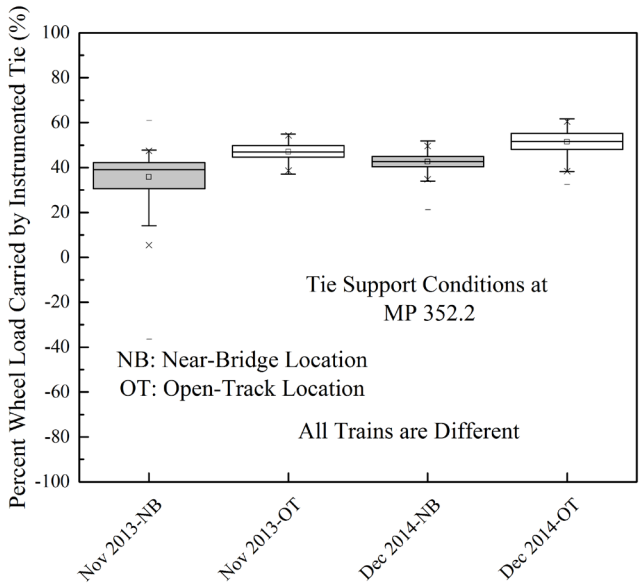

Figure 4.38: Change with Time in Percent Wheel Load Carried by the Instrumented Tie at the MP352.2 Bridge Approach (NS N-Line Mainline)

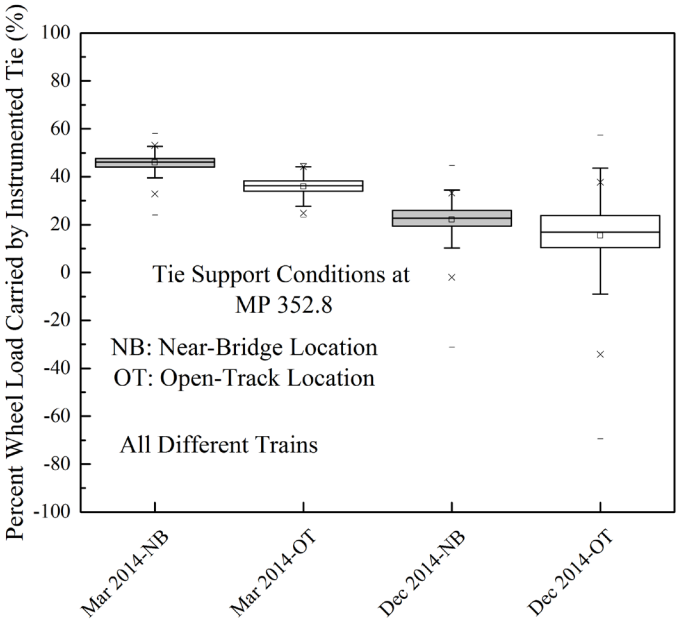

Figure 4.39: Change with Time in Percent Wheel Load Carried by the Instrumented Tie at the MP352.8 Bridge Approach (NS N-Line Mainline)

4.4 Dynamic Amplification of Load at Bridge Approaches

Differential movement at bridge approaches often results in higher dynamic forces under train loading. These magnified loads in turn lead to rapid layer deformations, further deteriorating the tack geometry profile. To assess the extent of dynamic amplification of wheel loads caused by the differential movement at the instrumented bridge approaches, wheel loads measured by the strain gauge circuits at the near-bridge and open-track locations were compared for the Amtrak NEC Upland and Madison Street bridge approaches. Percent amplification in the wheel loads was calculated using the following formula:

$$PA\ (\%) = \frac{P_{NB} - P_{OT}}{P_{OT}} \times 100$$

where

PA = Percent Amplification

P_{NB} = Registered Load at the Near-Bridge Location

P_{OT} = Registered Load at the Open-Track Location

Figure 4.40 shows the percent load amplification at the Upland Street bridge approach. Both the loads measured between the ties (vertical wheel load channel) and the load measured on top of the tie (tie reaction channel) were used to calculate the percent amplification values. As shown in the figure, wheel loads measured in the crib area are amplified by approximately 20 percent at the bridge approach. The percent amplification values calculated for the force measured on top of the tie were significantly greater, often exceeding 100 percent. This means the same wheel imparted double the load on the rail at the near-bridge location compared to the open-track location. This can be related to the dynamic effect of the train suspension, which may have been excited by the inadequate support conditions at the near-bridge location. These amplified loads on top of the ties were likely to cause excessive vibrations, settlement, and migration of ballast particles surrounding the tie, leading to severe hanging tie conditions. This mechanism can work in a negative-feedback loop, causing continued deterioration of the track support conditions and track geometry.

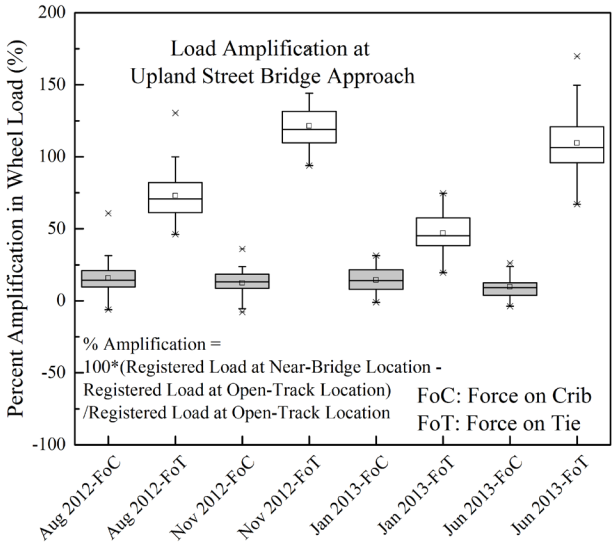

Figure 4.40: Load Amplification at Upland Street Bridge Approach

Figure 4.41 presents similar load amplification data for the Madison Street bridge approach. The percent amplification values calculated for the Madison Street bridge approach were significantly lower than those for the Upland Street bridge approach. Negative percent amplification values calculated at the Madison Street bridge approach for the force on top of the tie indicates that lower loads were recorded at the near-bridge location compared to the open-track location. Again, this was the result of gaps underneath the ties. Details of the tie-gap estimation procedure and the resulting effects will be presented in Section 7.

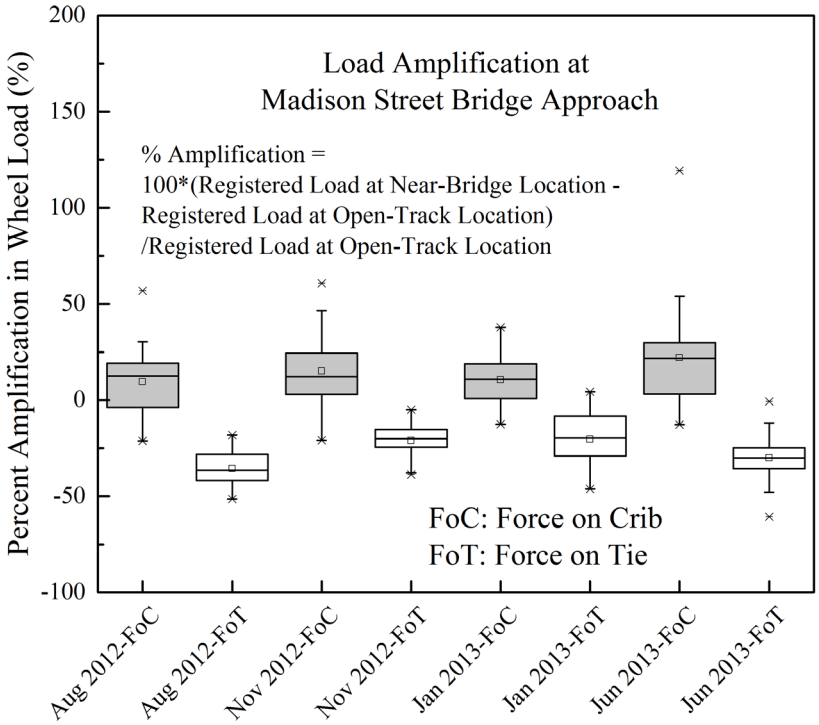

Figure 4.41: Load Amplification at Madison Street Bridge Approach

4.5 Ballast Layer as the Primary Contributor for Transient Displacement at Bridge Approaches

To quantify the contributions of individual substructure layers to the total track deformation, transient deformations registered by individual LVDT modules were expressed as a percentage of the total track transient deformation under applied wheel loading. Figure 4.42 shows the contributions, in percentage, of the ballast layer toward the total track transient deformations for the Upland Street bridge approach. As evident from the figure, the ballast layer accounted for a major portion of the transient deformations, with the value ranging from 55–95 percent for the near-bridge location, and 20–35 percent for the open-track location. Such high deformations recorded by the top LVDT should not be treated as indicators of very low modulus ballast layers, as a major portion of the transient deformations probably occurred before the tie came in full contact with the underlying ballast layer. Nevertheless, the ballast layer contributions to the total deformation were consistently higher than the underlying substructure layers.

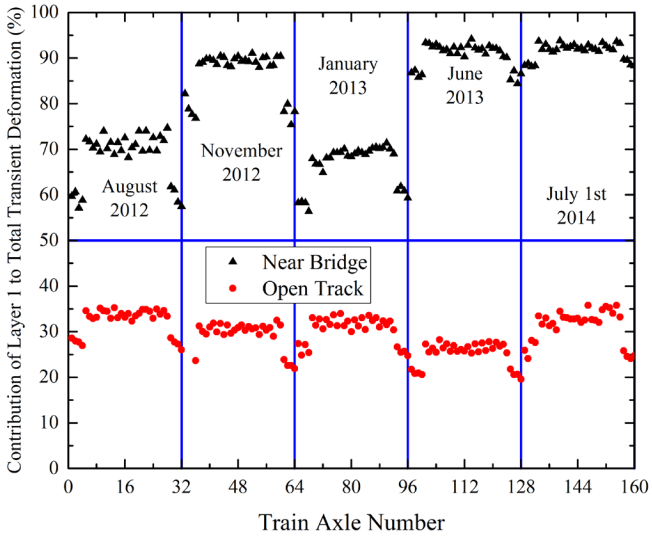

Figure 4.42: Contribution of the Ballast Layer Toward Total Transient Deformations Under Train Loading at the Upland Street Bridge Approach

Figure 4.43, Figure 4.44, and Figure 4.45 present similar data for the Madison Street, Caldwell Street, and MP352.2 bridge approaches, respectively. As shown in the figures, the ballast layer accounted for a major portion of the total transient displacements at all locations. No significant difference between percent contributions due to the ballast layer was observed between near-bridge and open-track locations at the Madison Street bridge approach (see Figure 4.43). Measurements taken in August 2012 indicated that the ballast layer at the open-track location contributed to a higher percentage of the total transient deformations compared to the near-bridge location. This can be related to the larger gaps underneath the tie in the open-track location. Subsequent measurements showed that the ballast layer at the near-bridge location contributed to a higher percentage of the total transient deformation compared to the open-track location. Nevertheless, it is important to note that both locations indicated more than 50 percent of the total transient deformations were consistently accounted for by the ballast layer.

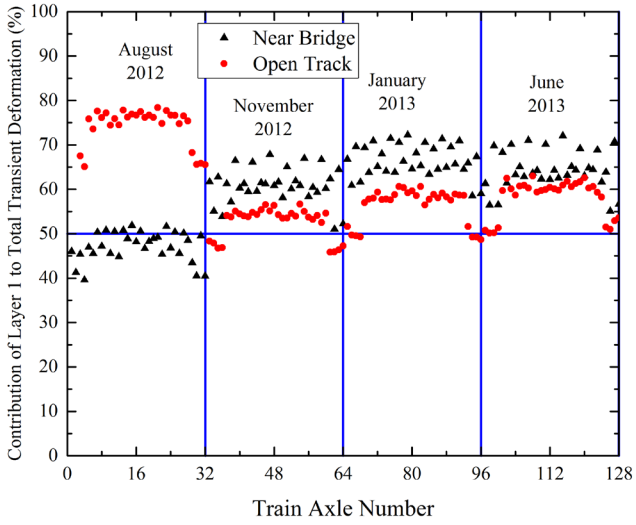

Figure 4.43: Contribution of the Ballast Layer Toward Total Transient Deformations Under Train Loading at the Madison Street Bridge Approach

Although the Caldwell Street bridge approach conditions were not as severe as the Upland and Madison Street bridge approaches, the ballast layer still accounted for up to 80 percent of the total transient displacements at this bridge approach (see Figure 4.44). Note that the contribution of the ballast layer for the east end of the tie was consistently lower than that for the west end of the tie. This is directly correlated with the tie-gaps calculated in Section 7 for this bridge approach. A larger gap was present between the bottom of the tie and the top of the ballast layer at the west end of the tie compared to the east end of the tie.

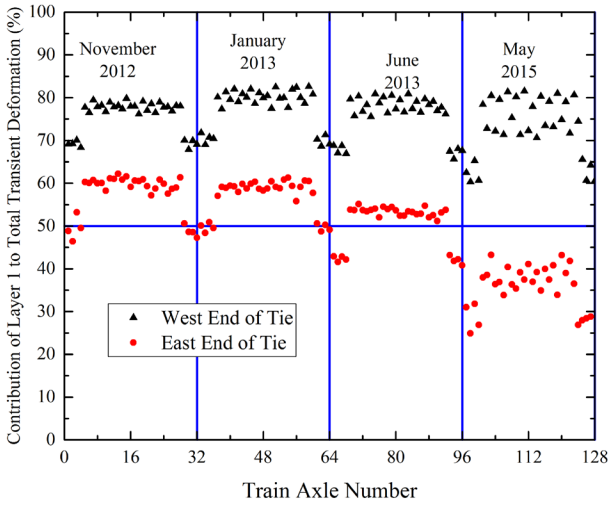

Figure 4.44: Contribution of the Ballast Layer Toward Total Transient Deformations Under Train Loading at the Caldwell Street Bridge Approach

A similar plot for the MP352.2 bridge approach (see Figure 4.45) clearly shows that ballast deformation was still the primary contributing factor even under slow-moving freight trains. Ballast transient deformation was a much more significant component at the near-bridge location, contributing up to 70–95 percent of the total transient deformation values. This value was significantly lower (~40 percent) at the open-track location.

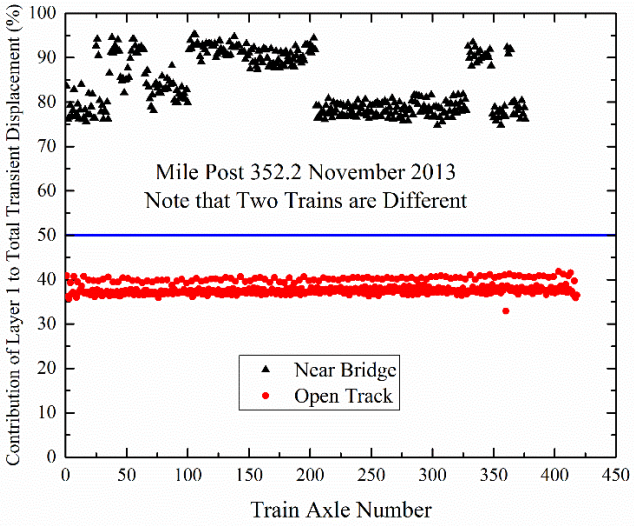

Figure 4.45: Contribution of the Ballast Layer Toward Total Transient Deformations Under Train Loading at the MP352.2 Bridge Approach (NS N-Line Mainline)

The dynamic load-generated stress wave reflections from the bridge abutment can be linked to significant ballast movements at the near-bridge locations. Higher loads could also be applied at top of rail due to train dynamic loading. This was observed even under slow-moving freight trains. For passenger trains moving at higher speeds, the transient deformation of the ballast layer could be significant even for open-track locations as observed at the Caldwell Street location (see Figure 4.44).

4.6 Summary

This section presented data obtained from the instrumented bridge approaches along Amtrak's NEC near Chester, PA, and NS's N-Line mainline near Ingleside, WV. Trends in individual track substructure layer settlements were presented, highlighting the significant contribution of deformations within the ballast layer toward total track settlement. Transient response of the instrumented bridge approaches was subsequently presented with emphases on both the load-displacement histories and contributions of individual track substructure layers to the total elastic (transient) track deformation.

A novel approach was then presented to assess the support conditions underneath crossties using data from strain gauges mounted on the rails. Analyzing the contributions of the ballast layer toward total transient deformations, researchers observed that near-bridge locations accumulated much higher deformations under train loading than the open-track sites. When a train is entering the bridge, applied dynamic loads can cause significant ballast movements at near-bridge locations. As a result, high-speed train traffic and the reflection of stress waves from bridge abutments present the worst combination as far as movements within the ballast layer are concerned. The reflection of stress waves played a significant role at the near-bridge locations even under slow-moving freight train traffic. However, movements within the ballast layer were significantly reduced for open-track locations exposed to slow-moving train traffic. The next section will present analyses of transient response data obtained from the instrumented bridge approaches.

5. Advanced Analyses of Field Instrumentation Data and Numerical Modeling

This section presents the detailed analyses of the transient response data and conclusions regarding tie support conditions and accelerations induced in the different layers from train loads. Several mathematical and data analysis tools used for in depth analyses of the track transient response data are introduced in the beginning of the section, followed by discussions of the transient response of the tie-ballast interface at the track transitions. A new methodology is proposed to quantify the size of the gaps (if any) that existed between the bottom of the tie and the top of the ballast layer-based data collected using MDDs. Upward movement of the rail-tie system is analyzed, and an effort is made to correlate this phenomenon to support conditions underneath the instrumented ties. Individual track substructure layer accelerations were calculated from the displacement time-histories, and conclusions were made concerning the dynamic response of the track system. Finally, the team used the GeoTrack software program to estimate the track substructure layer moduli from the transient response data. Primary trends and mechanisms observed from data analyses were used to select and implement remedial measures to mitigate the problem of differential movement at track transitions.

5.1 Digital Filter for Analyzing Transient Response Data

Transient response data collected at the instrumented bridge approaches included a variety of information related to track geometry, wheel or rail defects, and noise from AC or other signal noise imposed on the data. The team used two common approaches to eliminate or reduce the noise associated with any data collection activity. The first approach involves the elimination of noise with algorithms and filters built into the data acquisition equipment. This approach can be quite effective and can greatly simplify data post-processing and analysis efforts; however, data acquisition equipment comprising filtering capabilities are expensive. A more commonly used approach to eliminate or reduce noise from field data uses digital signal processing techniques during post-processing of the data. Selection of appropriate filters can often eliminate unwanted noise.

Paixão et al. (2015) used an 80 hertz (Hz) low pass filter to eliminate any noise caused by wheel and track defects to allow easier analyses of displacements obtained from field measurements. After optical measurement of railway track displacements under a train moving at 220 km/h, Pinto et al. (2015) reported that dominant frequencies of displacement signals were below 30 Hz, and these frequencies were sensitive to the train's axle spacing. Priest et al. (2010) observed that dominant ground velocities obtained from geophone measurements under the passage of a coal train moving at 50 km/h corresponded to frequencies around 1, 2, and 6 Hz, and concluded that the frequencies corresponded to axle spacings and distance between consecutive bogies (trucks)[1]. Auersch (2006) reported that vibrations due to wheel passage were not observed at frequencies over 50 Hz; any vibrations observed at frequencies between 50 Hz and 125 Hz could be related to wheel and rail anomalies. Namura and Suzuki (2007) stated that unsupported sleeper

[1]A bogie (truck) is an assembly of four or six wheels forming a pivoted support at either end of a railway coach that provides flexibility on curves.

information could be discovered using train axle acceleration, and that they corresponded to frequencies between 10 and 20 Hz.

The first step to extract relevant information concerning dynamic track response from the measured transient data involves the design of a suitable digital filter that can isolate the information of interest. This task considered the geometry of the trains. Acela Express trains are the predominant traffic at the instrumented Amtrak NEC bridge approaches. The operating speed near the instrumented bridge approaches is 177 km/h (110 mph, or 49,166.7 mm/sec). Axle and wheel spacing data for the Acela Express trains are presented in Figure 5.1. The minimum distance of interest during the passage of an Acela Express train is 2,844.8 mm, which represents the distance between two wheels on a particular bogie of the locomotive. Considering a speed of 49,166.7 mm/sec, it takes the train 0.06 seconds to travel a distance equivalent to the spacing of the two wheels. The corresponding loading frequency can be calculated as:

$$f = \frac{1}{0.0578} = 17.3 \text{ Hz.} \tag{5.1}$$

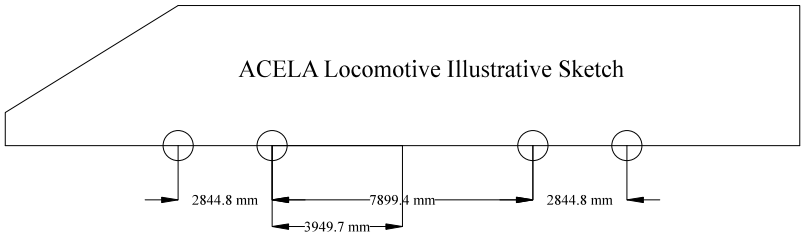

(a) ACELA Locomotive Illustrative Sketch

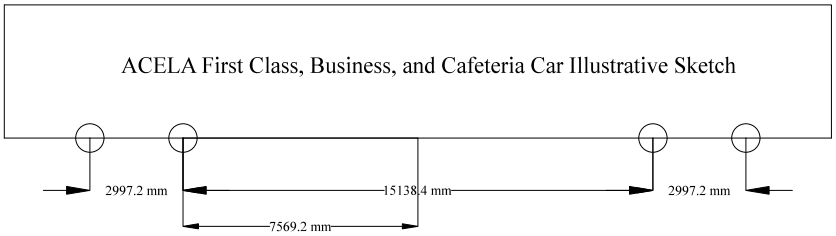

(b) First Class, Business Class and Cafeteria Car Illustration

Figure 5.1: Acela Locomotive and Passenger Cars Axle Spacing

Therefore, the maximum frequency of interest during the passage of an Acela Express train over the instrumented bridge approaches was 17.3 Hz. To address speed variations, the data analysis efforts in the current study focused on all frequencies lower than 20 Hz. To isolate all information pertaining to signals with a frequency of 20 Hz from the recorded displacement time-histories, a 30 Hz, 6-pole, low-pass filter was applied to all transient displacement data. The magnitude multiplier at different frequencies for this filter is plotted in Figure 5.2. As seen from the figure, this low-pass filter retained all signal information corresponding to frequency levels below 20 Hz (indicated by a magnitude multiplier value of 1.0). Therefore, the use of this signal filter was justified during the analyses of transient response data from the Amtrak NEC bridge approaches.

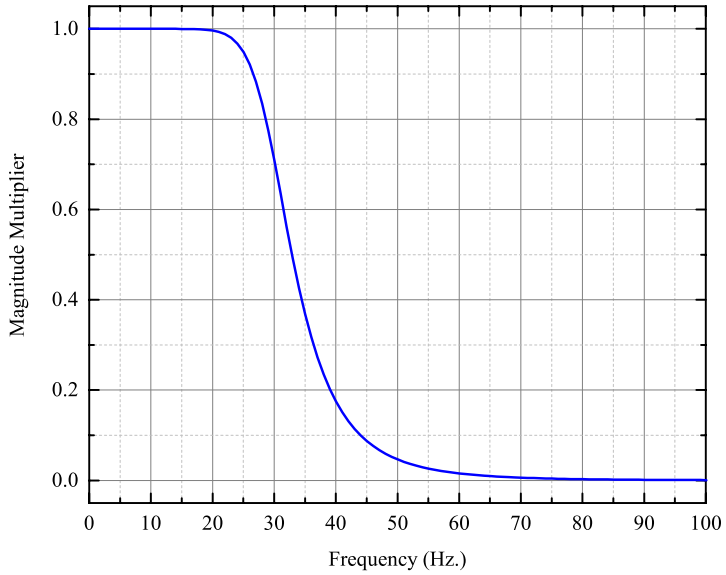

Figure 5.2: Magnitude Multipliers Corresponding to Different Frequencies for a 30 Hz, 6-Pole, Low-Pass Butterworth Filter

The freight trains at the instrumented bridge approaches along NS's N-Line mainline have an operating speed in the range of 40 km/h (25 mph). Therefore, the use of 30 Hz, low-pass filters would not isolate the data of interest. As detailed information concerning the axle geometry for these freight trains was not available, the use of fast Fourier transform (FFT) helped to identify dominant frequencies inherent to the displacement time-history records. As an example, Figure 5.3(a) shows results from the FFT of displacement time-history data recorded at the Madison Street bridge approach under the passage of an Acela Express train (data collected in June 2013). The X-axis in the plot represents different frequencies and the Y-axis represents the waveform amplitudes corresponding to the different frequency levels. As expected, all contributing waveforms corresponded to frequency values lower than 20 Hz, corroborating the basic calculations presented above. Similar results for the bridge at NS MP352.2 (near-bridge location) are plotted in Figure 5.3(b). All major contributing waveforms corresponded to frequency values lower than 2.5 Hz. Therefore, a 5 Hz, 6-Pole, low-pass filter was successfully used for analyzing the transient response data collected under the passage of freight trains. Magnitude multipliers at different frequencies for this filter are shown in Figure 5.4.

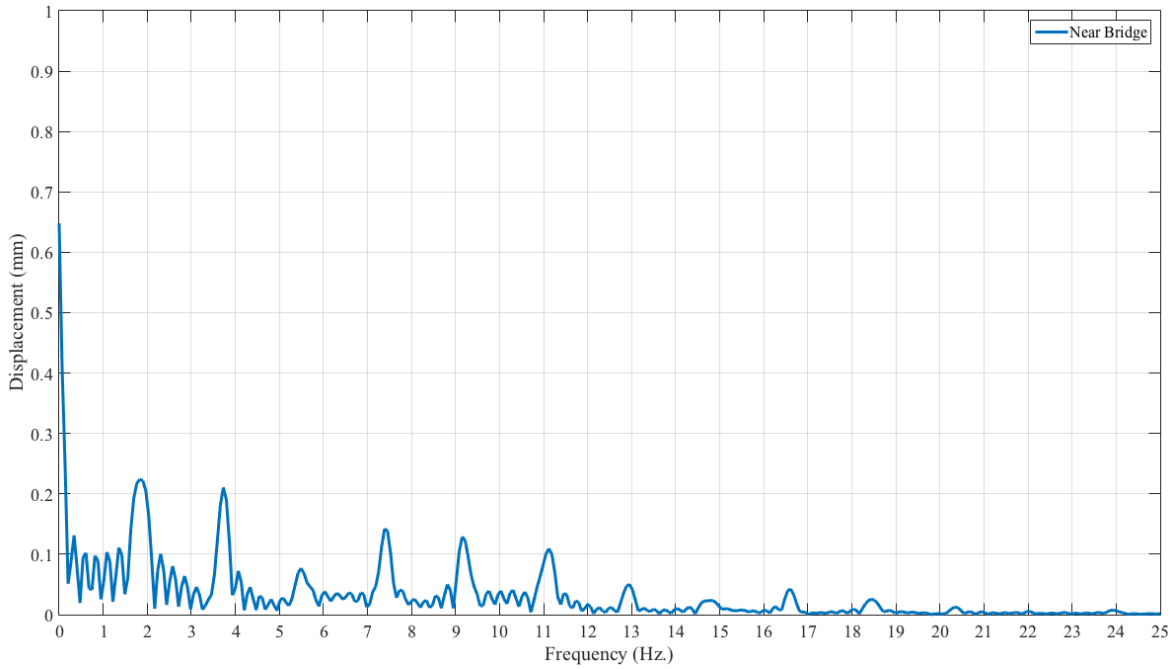

(a)

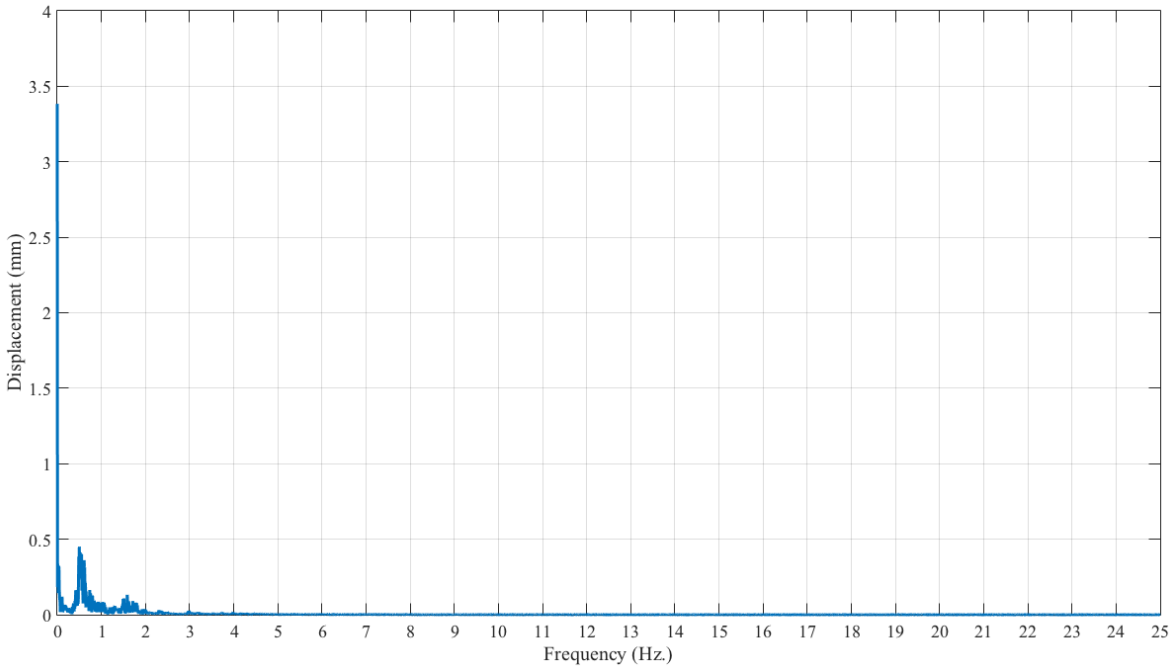

(b)

Figure 5.3: Results from FFT of Displacement Time-Histories: (a) Madison Street Bridge Approach – Acela Express – June 2013; (b) MP352.2 – Near-Bridge Location – Freight Train – November 2013

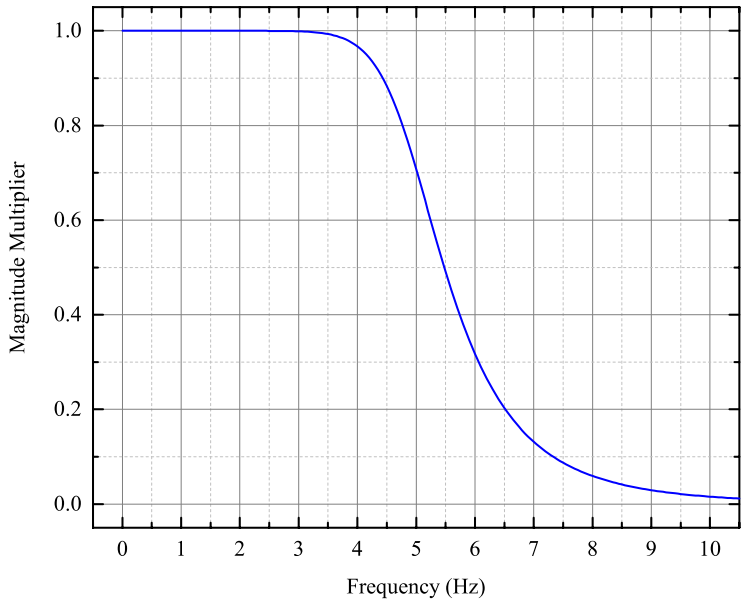

Figure 5.4: Magnitude Multipliers Corresponding to Different Frequencies for a 5 Hz, 6-Pole, Low-Pass Butterworth Filter

5.2 Numerical Differentiation to Calculate Accelerations from Displacement Time-History and Comparison with Accelerometer Results

To calculate individual substructure layer accelerations from the displacement time-histories, a sixth order central finite difference approach (see equation below) was used.

$$\ddot{u}_i = \frac{2u_{i-3} - 27u_{i-2} + 270u_{i-1} - 490u_i + 270u_{i+1} - 27u_{i+2} + 2u_{i+3}}{180 \times \Delta t^2} \tag{5.2}$$

where

$\ddot{u}_i$ is vertical acceleration calculated corresponding to data point i;

u_i is vertical deformation collected for data point i; and

Δt is time step.

Although this approach had the disadvantage of losing three data points each at the beginning and end of the data set, the use of sufficiently high sampling frequencies (2000 Hz for passenger trains, 1000 Hz for freight trains) reduced the impact of this loss. Note that the filtered displacement time-histories were used to calculate the layer accelerations.

The use of accelerometers is very common for monitoring railroad track response under loading. However, the number of studies involving direct measurement of substructure layer displacements using MDDs is limited. A verification effort was undertaken in this study to compare acceleration values recorded using accelerometers to those calculated through numerical differentiation of the filtered displacement time-history data.

Figure 5.5(a) shows a photograph of the setup used during this verification effort. Acceleration and displacement time-histories were recorded for the same crosstie during the passage of an Acela Express train. The displacement measurements during this verification effort were

accomplished using a metal strip mounted with strain gauges. One end of the metal strip was glued to the crosstie and the other mounted on a metal anchor buried approximately 610 mm (2 ft) below the top of the ballast layer. Movement of the crosstie under loading caused bending of the metal plate, which was recorded by the strain gauges. A pre-established calibration curve was used to relate the voltages recorded by the strain gauge circuit to deflection of the tip of the metal strip. Tie accelerations measured by the two approaches matched reasonably well (see Figure 5.5(b)), thus validating the use of the numerical differentiation approach to calculate track substructure layer accelerations from the displacement time-histories. Slight differences in the two acceleration traces presented in Figure 5.5(b) can be attributed to the fact that the accelerometer captured all ground movements, whereas the strain gauge-mounted plate captured displacements with respect to its anchor point, 610 mm below the top of the ballast layer. Moreover, as seen in the photograph (Figure 5.5(a)), the two instrumentation types were not mounted exactly at the same point of the crosstie, and hence may have recorded different responses. Nevertheless, acceleration time-histories established by the two methods were reasonably close to each other, and therefore could be used satisfactorily for data analysis purposes without introducing significant errors into the analysis process.

(a)

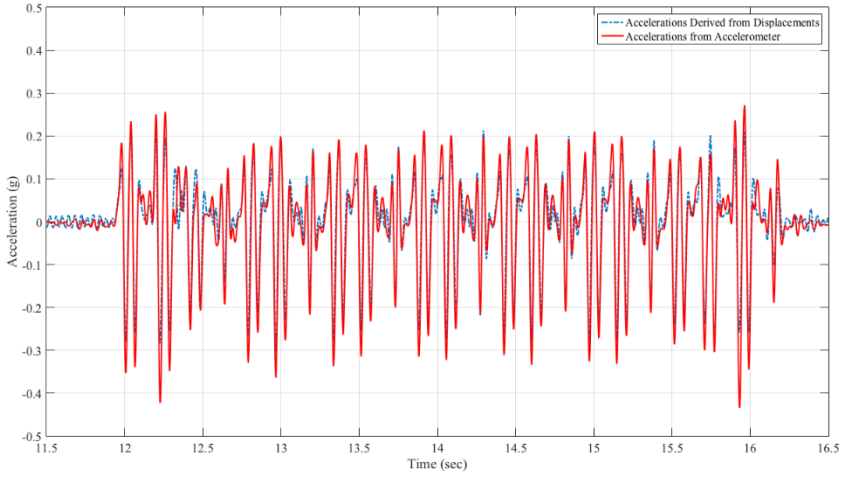

(b)

Figure 5.5: Verification of the Numerical Differentiation Approach to Calculate Layer Acceleration Values From Displacement Time-Histories: (a) Instrumentation Set-Up Used for Verification; (b) Comparing the Acceleration Values Recorded Using Accelerometers With Those Calculated From Displacement Time-Histories

5.3 Fourier Transform to Convert Data from Time to Frequency Domains

Fourier transform is a mathematical method to transform a signal from time domain to frequency domain to identify the frequencies corresponding to the major contributing waveforms. To achieve this, the discrete Fourier transform (DFT) equation used is as follows (Rao et al., 2010):

$$X_k^F = \sum_{n=0}^{N-1} X_n^T \, e^{-2*\pi*i/N} \tag{5.3}$$

where

X_k^F is a vector of complex number that represents signal in frequency domain. Sub-index k stands for kth element of vector X^F.

X_n^T is a vector that contains magnitude of signal in time domain. It is a one-dimensional vector that only has magnitudes of signal. For an acceleration signal, for instance, it would only have components of acceleration values. Sub-index n stands for nth element of vector X^n.

N represents the length of the signal.

Due to the quadratic nature of the above equation, the associated computational times are proportional to the square of the signal length, rendering this approach computationally inefficient for large signals. FFT, on the other hand, is the general name of algorithms to calculate DFT more efficiently (Rao et al., 2010).

The following steps have been taken in this research effort to convert track response time-histories (displacement or acceleration) to frequency domains using FFT. Discussions on the transformed signals, and corresponding inferences will be presented later in this section.

1. Transient displacement time-histories collected from the field were filtered using a 30 Hz low pass filter.
2. A 5-second period of the signal corresponding to passage of the Acela Express was extracted from the full-length filtered signal.
3. This truncated (5-second long) signal was numerically differentiated to obtain the corresponding acceleration time-histories.
4. The acceleration time-histories were converted to a frequency domain using a commercially available software (SeismoSignal™; SeismoSoft, 2016).

Note that SeismoSignal™ is limited to 32,768 data points to perform Fourier transform. The number of data points collected from each freight train is higher than this maximum limit. Therefore, MATLAB's fft() function was used for analyzing freight train signals instead.

5.4 Transient Response of the Tie-Ballast Interface at Railroad Track Transitions

The tie-ballast interface is a critical component governing the load transfer mechanism on railroad tracks. Proper characterization of the load-deformation behavior at the tie-ballast interface is therefore critical to achieving a detailed understanding of track substructure response under loading. This is particularly important at track transitions such as bridge approaches, as

complex dynamic interaction leads to drastic changes in the tie-ballast interface behavior under loading. This section uses transient response data collected using the MDDs and strain gauges to investigate the load-deformation behavior of the tie-ballast interface.

5.4.1 Effect of Gaps at Tie-Ballast Interface on Track Response under Loading

Uniform contact between the bottom of the tie and the top of the ballast layer ensures the adequate distribution of loads applied during train passage and is critical to ensuring sufficient reduction in the stress levels to protect the weak, underlying layers such as sub-ballast or subgrade. Uniform contact between the ties and the underlying ballast layers is usually ensured during construction and/or resurfacing of ballasted railroad tracks. However, differences in loading conditions and changes in track support conditions (such as those observed at track transitions) can sometimes lead to uneven settlement of the ballast layers under loading. Such uneven settlement of ballast layers often leads to the creation of gaps at the tie-ballast interface. These gaps significantly affect the load transfer mechanism. As the crossties are attached to the rail using fastener systems, it is possible for a tie to be suspended in the air even if settlement of the underlying ballast layer has resulted in the creation of a void space immediately underneath that particular tie. In track sections where the ballast settlement remains relatively uniform as the train moves longitudinally along the track, all crossties settle uniformly to the new level, thus resulting in a vertical shift in the track surface curve. Although such uniform settlements result in overall track geometry defects and hence ultimately require maintenance and resurfacing, all ties along the track are still uniformly supported by the underlying ballast layer. Thus, no gaps exist at the tie-ballast interface in these situations. However, railroad track transitions, such as bridge approaches, present a situation where the settlement of the ballast layer is not uniform, thus leading to differential settlements along the track. Such differential settlements often lead to hanging tie conditions, where the tie is not uniformly supported by the underlying ballast layer. Figure 5.6 shows a schematic of hanging tie conditions resulting from the uneven settlement of substructure layers at railroad track transitions.

The top-most LVDT in an MDD system is placed inside the crossties; it measures the movement of the tie with time (permanent deformation) or due to train passage (transient deformation). For a particular LVDT to accurately represent deformations of the ballast layer, full contact at the tie-ballast interface must be assumed. If a gap exists at the tie-ballast interface, the tie needs to first undergo a certain amount of deflection corresponding to the magnitude of the gap before full contact with the ballast layer is established. Therefore, the deformation magnitudes recorded by the top-most LVDT in an MDD system comprises contributions due to the existence of gaps at the tie-ballast interface and deformations of the ballast layer. The use of the total LVDT measurement in response analysis may lead to a serious underestimation of the ballast layer modulus. Therefore, it is crucial to determine the gap under the instrumented tie and subtract it from the deformations recorded by the top-most LVDT in an MDD system. A new approach was developed in this study to quantify the gap (if any) at the tie-ballast interface. Note that this approach is conceptually identical to the phenomenon described by Sussmann and Selig (2000), and as illustrated in Figure 5.7 (adapted from Li et al., 2016, and Ebersöhn and Selig, 1994).

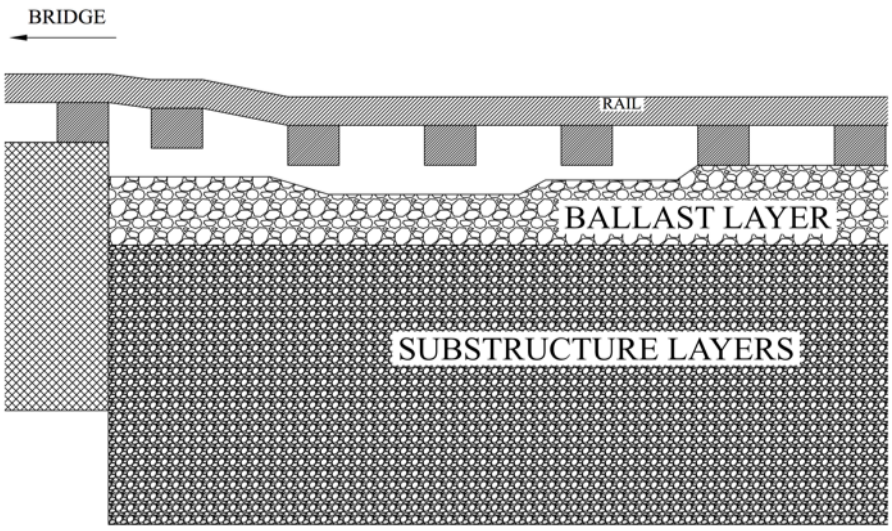

Figure 5.6: Hanging Tie Conditions Created at Railroad Track Transitions Due to Uneven Settlement of the Track Substructure Layers

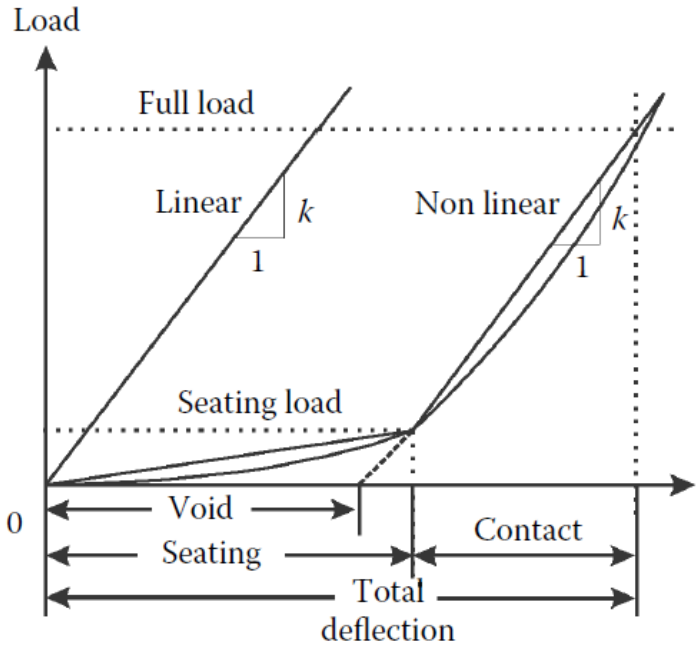

Figure 5.7: Existence of Void Affecting the Load-Carrying Behavior of Railroad Tracks (Illustration Borrowed From Li et al., 2016, and Ebersöhn and Selig, 1994)

5.4.2 Tie-Gap Estimation from Multi-depth Deflectometer Data

This section presents the steps to quantify the gaps at a tie-ballast interface based on the transient response data recorded through the MDD systems. The procedure is conceptually identical to that proposed by Sussmann and Selig (2000) and is based on the premise that the slope of the load-deflection curve changes drastically depending on whether there is full contact at the tie-ballast interface. As illustrated in Figure 5.7, establishing full contact between the tie and the ballast (marked as "seating" in Figure 5.7) absorbs part of the load. The remaining portion of the

load produces deformations in the track substructure layers. Considering that the MDD system enables recording the full time-history of transient responses under train loading, the load (recorded using strain gauges) and deflection data can be easily used to quantify the gaps underneath the instrumented ties. As the current research effort comprised the measurement of transient response at different times between 2012 and 2015, monitoring the change in tie-gaps with time can present a good perspective to indicate the gradual deterioration (if any) of tie support conditions at track transitions. The steps followed in the current study to quantify the gaps at the tie-ballast interface are listed below:

1. Compile the transient responses recorded due to the passages of multiple trains on a particular day at a particular location into one dataset.
2. Extract the loads recorded by the strain gauge circuit mounted on top of the instrumented tie and the corresponding layer transient deformations recorded by the top-most LVDT (mounted inside the instrumented tie).
3. Delete negative load values (induced by negative bending of the rail and often observed due to dynamic effects relevant to track transitions) recorded by the strain gauge circuit and the deformations recorded by the top-most LVDT.
4. Plot the recorded loads versus the corresponding deflections measured by the top LVDT (see Figure 5.8).
5. Gradually increase the threshold load level assumed to establish full contact between the tie and the underlying ballast layer until a clear trend for the load-deflection behavior of the ballast layer is observed. This phenomenon is illustrated through different sub-figures in Figure 5.8. As shown in Figure 5.8(a), the initial value for the load threshold was assumed to be zero. This shows two distinct regions in the load-deflection curve: the horizontal portion corresponding to the seating of the tie and the inclined portion representing deformation (under loading) of the ballast layer. To exactly identify the magnitude of the gap and the corresponding load required to ensure complete "seating" of the tie, the threshold load level was gradually increased to 15, 25, and 28 kN (see Figure 5.8(b), 5.8(c), and 5.8(d), respectively). As shown in the figure, a clear inclined portion for the load-deflection curve was obtained corresponding to a load threshold level of 28 kN and a tie-gap of approximately 6.5 mm.
6. Once a clear inclined portion for the load-deflection curve is obtained, extract the five smallest transient deformation values, and calculate the tie-gap as the mean of those five values.

Several different alternatives to this approach were considered. For example, the first alternative involved the use of wheel loads measured in between two consecutive crossties rather than wheel loads measured directly on top of the instrumented tie. This approach was inadequate because the distance between the strain gauge circuit (between two consecutive ties) and the top LVDT (installed within the instrumented tie) resulted in a time lag in the load and deformation time-histories. This presented a significant challenge regarding the identification of wheel loads and the corresponding deflections. Moreover, as the tie-reaction channel (strain gauge channel mounted directly on top of the instrumented tie) measured the load-induced bending directly on top of the instrumented tie, correlating the load magnitudes to the corresponding deflection measurements was relatively straightforward. Relative locations of the two strain gauge channels

with respect to the instrumented tie are shown in Figure 5.9. Note that viscosity effects inherent to the track structure resulted in a slight time lag between the load and corresponding transient deformation measurements. However, exact quantification of this time lag was prohibitively difficult, and therefore ignored in this study.

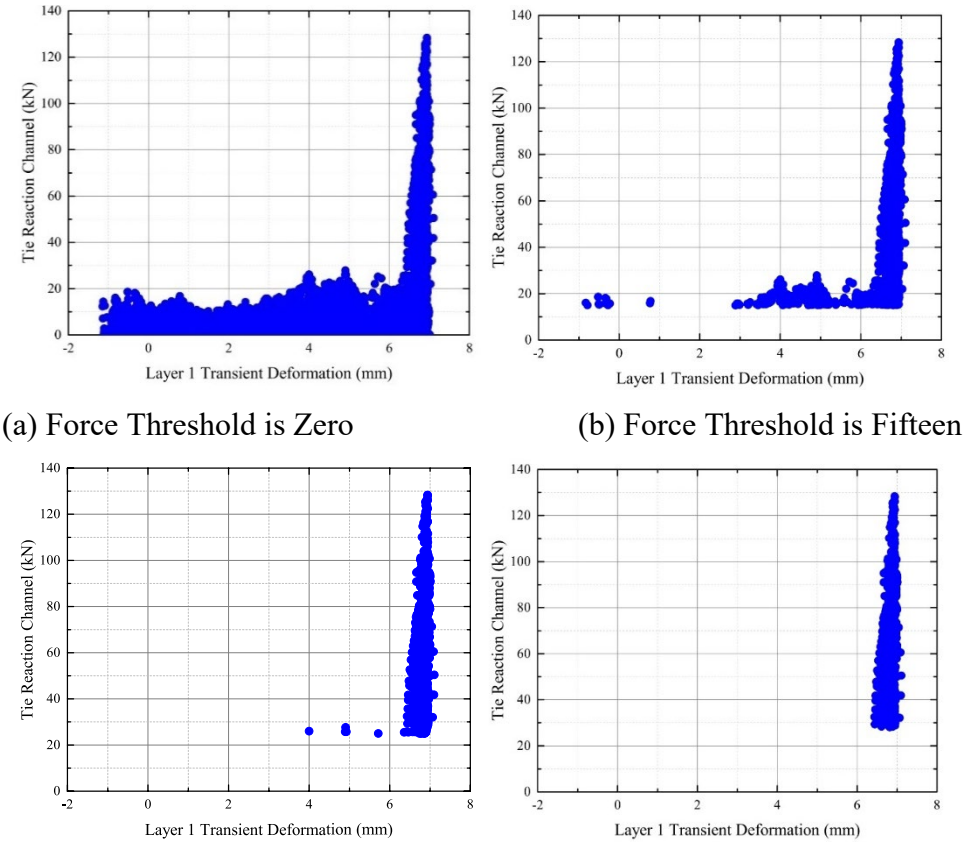

(a) Force Threshold is Zero

(b) Force Threshold is Fifteen

(c) Force Threshold is Twenty-Five

(d) Force Threshold is Twenty-Eight

Figure 5.8: Quantification of Gaps at the Tie-Ballast Interface Using a Progressive Load Threshold Approach

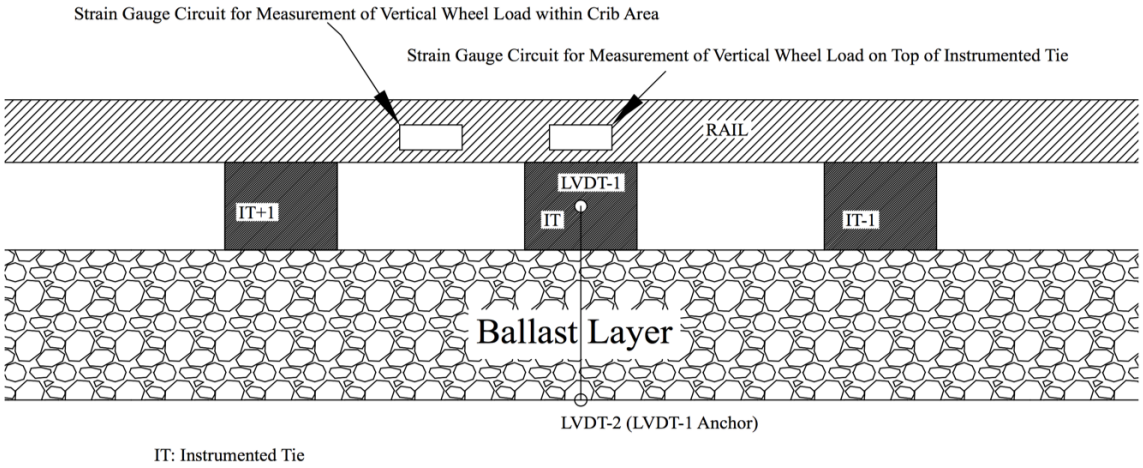

Figure 5.9: Relative Location of the Strain Gauge Circuits With Respect to the Instrumented Tie

Another approach used polynomial equations to represent the load-deformation behavior. Once such a straight line is plotted (as was done by Sussmann and Selig in 2000, see Figure 5.7), its intercept with the deformation axis can be used as an estimate of the tie-gap. This approach is summarized in Figure 5.10. Note that unlike in Figure 5.7 and Figure 5.8, Figure 5.10 shows the load values plotted along the x-axis. Nevertheless, the coefficient of determination (R^2) values resulting from such a linear fit were significantly low (see Figure 5.10). Therefore, using a linear relationship to represent the load-deformation behavior did not seem logical. Researchers decided to use the average of the five smallest transient deformation values (corresponding to the inclined portion of the load-deflection curve) as an estimate of the gap at the tie-ballast interface. Tie-gaps calculated using the above-listed steps for the instrumented bridge approaches along Amtrak's NEC are listed in Table 5.1-Table 5.3.

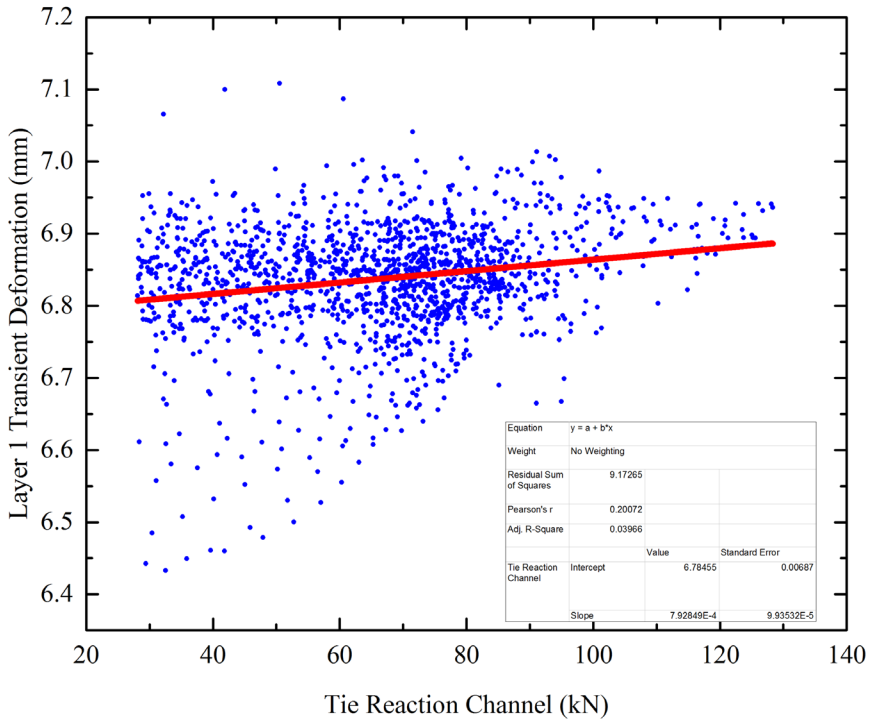

Figure 5.10: Transient Load-Deformation Behavior of the Ballast Layer Approximated Using a Straight Line

Table 5.1: Gap Quantification at the Tie-Ballast Interface Using the Progressive Load Threshold Approach: Madison Street Bridge Approach

	12 ft from South Abutment		60 ft from South Abutment	
	Gap (mm)	Load Threshold (kN)	Gap (mm)	Load Threshold (kN)
August 2012	0.55	10	1.12	16
November 2012	0.92	13	0.59	25
January 2013	1.37	25	0.61	23
June 2013	1.43	12	0.76	17

Table 5.2: Gap Quantification at the Tie-Ballast Interface Using the Progressive Load Threshold Approach: Upland Street Bridge Approach

	15 ft from North Abutment		60 ft from North Abutment	
	Gap (mm)	Load Threshold (kN)	Gap (mm)	Load Threshold (kN)
August 2012	1.53	17	0.34	8
November 2012	1.98	28	0.24	14
January 2013	1.32	47	0.28	39
June 2013	3.86	16	0.22	11
July 2014	6.45	28	0.22	17

Table 5.3: Gap Quantification at the Tie-Ballast Interface Using the Progressive Load Threshold Approach: Caldwell Street Bridge Approach

	West End of Tie (80 ft from South Abutment)		East End of Tie (80 ft from South Abutment)	
	Gap (mm)	Load Threshold (kN)	Gap (mm)	Load Threshold (kN)
August 2012	1.36	44	0.74	36
November 2012	0.98	28	0.71	23
January 2013	0.93	48	0.72	40
June 2013	1.00	40	0.62	32
May 2015	0.77	31	0.18	27

As listed in Table 5.1, tie-ballast interface gap for the near-bridge location (12 ft from the south abutment) increased consistently from August 2012 to June 2013. This indicated a gradual deterioration of the tie support conditions at this location, which can in turn result in increased dynamic load magnitudes. Note that even the resurfacing activity at this location shortly after the initial instrumentation in August 2012 did not prevent the tie-gap from increasing between August and November 2012. The open-track location (60 ft from the south abutment) at the Madison Street bridge approach, on the other hand, showed a significant reduction in the tie-gap between August and November 2012. This indicated that the resurfacing activity in August 2012 resulted in better support conditions underneath the instrumented tie at this location. Interestingly, the tie-gap at this location remains relatively unchanged between November 2012 and June 2013.

Table 5.2 presents similar data for the Upland Street bridge approach. For the near-bridge location (15 ft from the north abutment), a slight reduction in the tie-gap was observed through

the measurement efforts in January 2013. However, the tie-gap increased significantly thereafter, reaching a magnitude of 6.45 mm in July 2014. Just like the permanent deformation data presented in Section 4, the near-bridge location at the Upland Street bridge approach exhibited the highest degree of deterioration in tie support conditions.

Estimated tie-ballast interface gaps for the Caldwell Street location are presented in Table 5.3. The tie support conditions were not uniform at both ends of the tie, and the west end exhibited higher gaps compared to the east end. Note that the tie-gaps calculated at the Caldwell Street location were similar in magnitude to those calculated for the open-track locations at the Madison and Upland Street bridge approaches. In conclusion, the tie-gaps for open-track locations for bridge approaches were not affected by the predominant direction of train traffic.

The next task involved re-calculating the transient deformations of the ballast layer by subtracting the tie-gap values from the total deformations recorded by the top-most LVDT in the MDD system. This was particularly important for the accurate representation and interpretation of ballast layer conditions at the instrumented bridge approaches. For example, a relatively stiff ballast layer can be misinterpreted as undergoing large transient deformations under loading if a large gap exists at the tie-ballast interface. Accordingly, Figure 5.11 through Figure 5.13 show the ballast layer transient responses calculated for the Madison, Upland, and Caldwell Street bridge approaches, respectively, by subtracting the calculated tie-gaps from the LVDT 1 measured responses. All the instrumented locations, except for the Madison Street open-track location, exhibited relatively consistent ballast transient deformation magnitudes under train loading. As all the data points presented in Figure 5.11 through Figure 5.13 correspond to the measurements taken during the passage of Acela Express trains, it is safe to assume that the load magnitudes remained relatively constant across time. Thus, most of the track geometry deterioration at the instrumented bridge approaches can be linked to the loss of support underneath the ties and does not necessarily indicate the deterioration of the ballast layer.

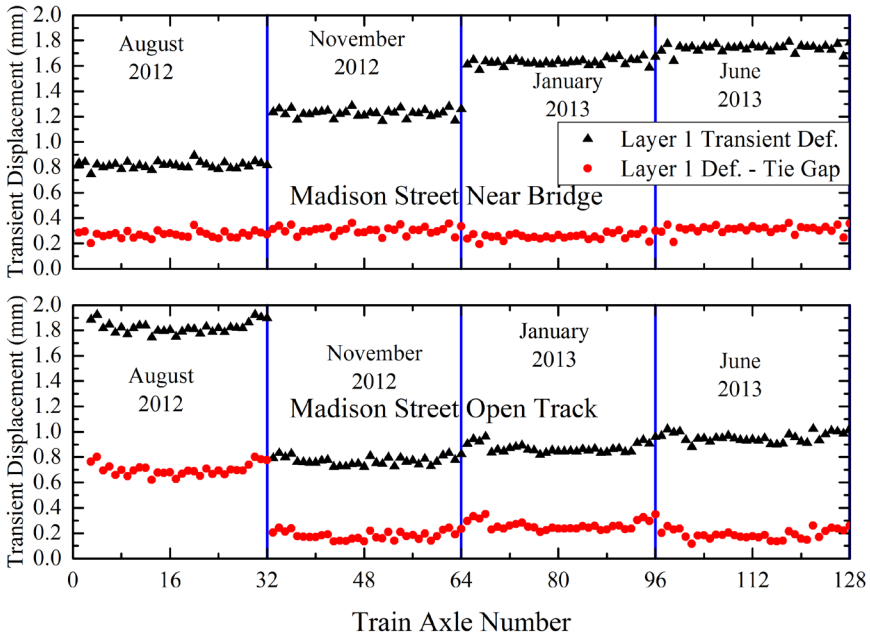

Figure 5.11: Transient Deformations of the Ballast Layer Calculated Through Subtraction of Tie-Gaps From LVDT 1 Measurements – Madison Street Bridge Approach

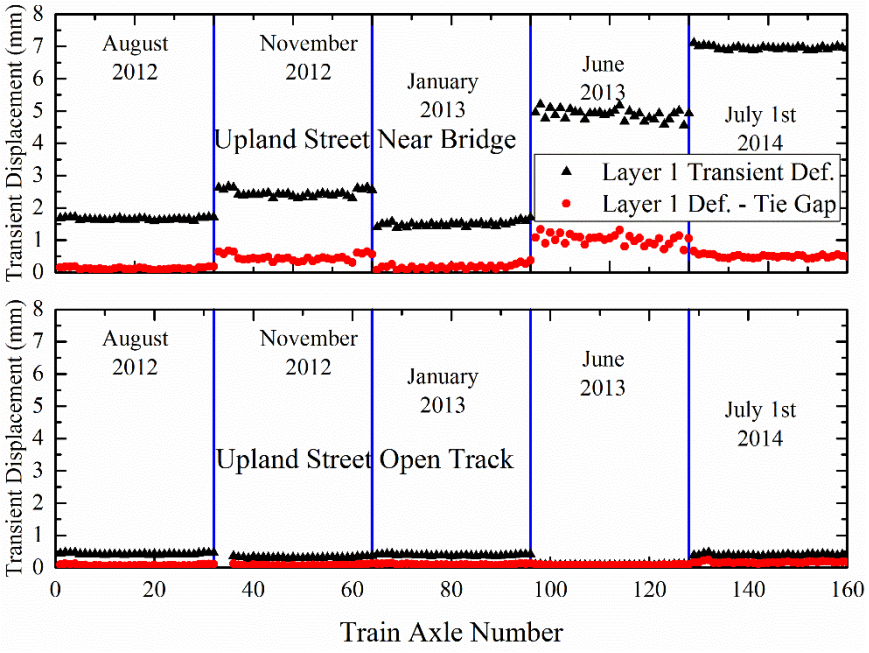

Figure 5.12: Transient Deformations of the Ballast Layer Calculated Through Subtraction of Tie-Gaps From LVDT 1 Measurements – Upland Street Bridge Approach

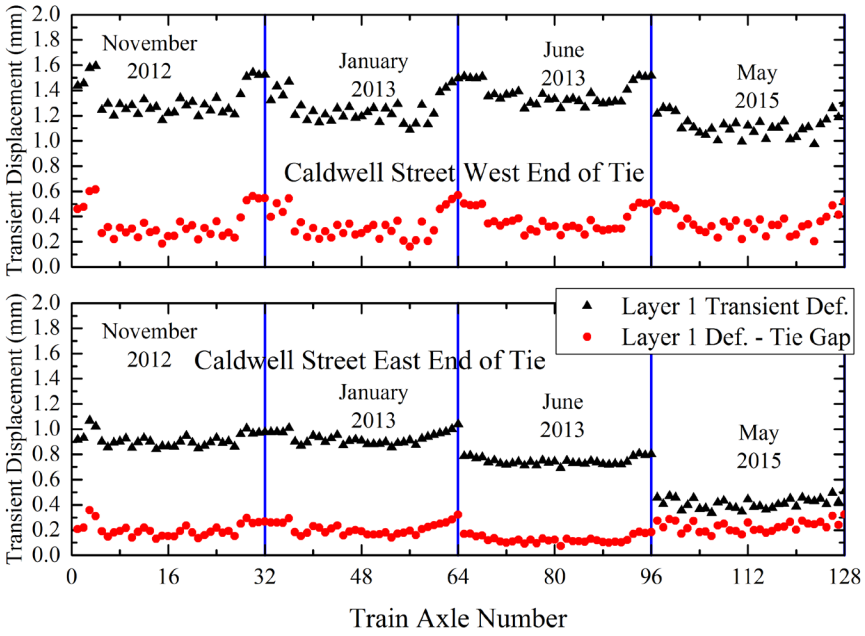

Figure 5.13: Transient Deformations of the Ballast Layer Calculated Through Subtraction of Tie-Gaps From LVDT 1 Measurements – Caldwell Street Bridge Approach

5.4.3 Negative Displacement (Lifting) of Ties at Track Transitions

One of the interesting trends observed in transient deformation time-histories presented in Section 4 involved negative transient deformation values recorded by the top-most LVDT (mounted within the crosstie). As already mentioned, any movements registered by the top-most LVDT in the MDD system comprise contributions due to movement of the tie independent of the

ballast layer, as well as movement of tie-ballast system as a unit. The particulate nature of the ballast layer renders it incapable of supporting tensile forces. Accordingly, any upward "pull" on a crosstie leads to its separation from the ballast layer and results in a void at the tie-ballast interface. Any subsequent downward force first compensates for this newly created void, before inducing any deformations in the underlying ballast layer. This sub-section investigates this "tie lifting" phenomenon using the load-deformation data collected at the Madison and Upland Street bridge approaches.

An Acela Express train operating in Amtrak's NEC comprises a total of eight cars – two locomotives and six coach cars between the locomotives. The 8 cars consist of 16 bogies with 2 axles on each bogie. Therefore, the train comprises a total of 32 axles that register as 32 peaks on the load time-history recorded by strain gauges mounted on the rail. Figure 5.14 shows the load and displacement time-histories (LVDT 1) recorded under the passage of an Acela Express train at the Madison Street bridge approach (data collected in June 2013). Note that downward movements of the tie (compression of the substructure) are represented as positive numbers in Figure 5.14. Accordingly, negative displacements represent tie-lifting and separation of the tie from the underlying ballast layer.

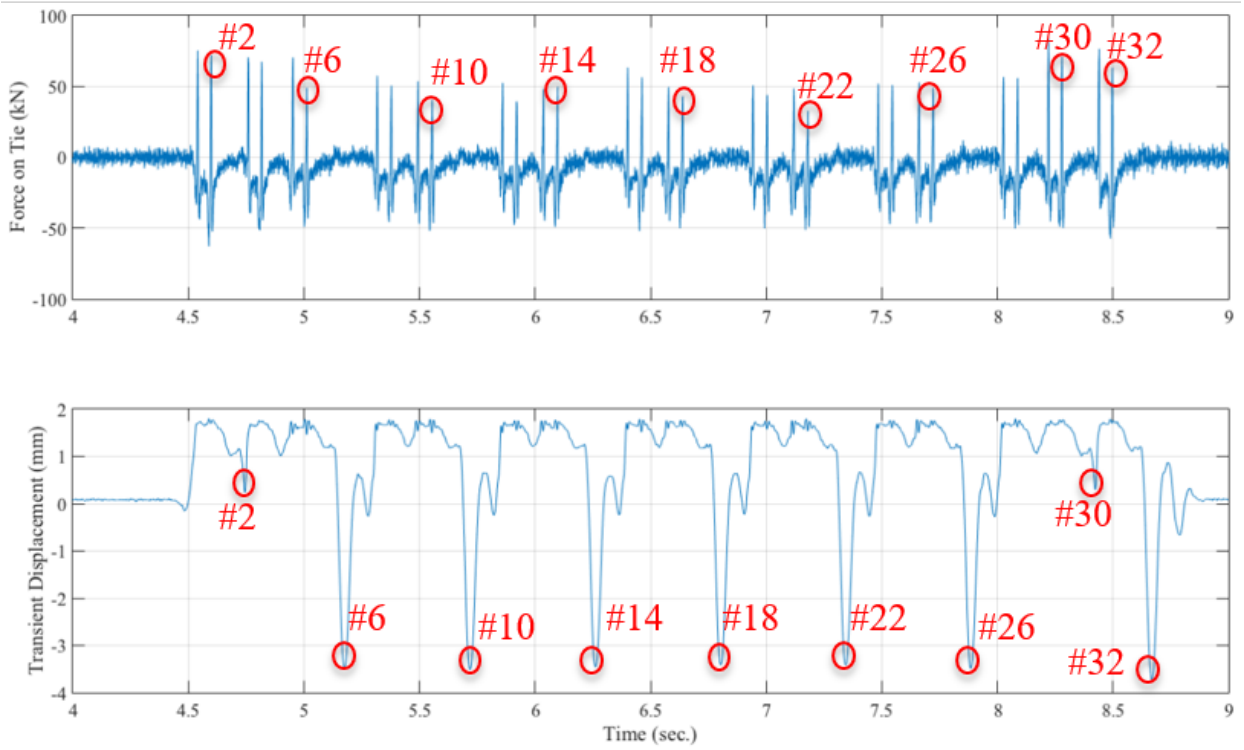

Figure 5.14: Load and Deformation (LVDT 1) Time-Histories Under the Passage of an Acela Express Train at the Madison Street Bridge Approach – Near-Bridge Location (Data Collected in June 2013)

As shown in Figure 5.14, significant amounts of tie lifting (negative transient displacements) were recorded at this location under the passage of an Acela Express train. The peak negative displacements and the peak loads recorded immediately before the negative displacements are both highlighted in Figure 5.14 using small red circles. As indicated in the figure, the first instance of tie lifting is observed immediately after load peak number 2. Note that load peak 2

corresponds to the passage of the second axle of the leading bogie of the locomotive. In other words, a lifting tendency for the tie is observed immediately after passage of the first bogie of the leading locomotive and before the trailing bogie reaches the location of the instrumented tie. It is also important to note that although the "lift-off" tendency of the tie is clearly apparent from the downward movement of the displacement time-history curve, the displacement value recorded by LVDT 1 for peak 2 is still greater than zero (> 0). The tie showed a tendency to "bounce-back" from its compressed position under passage of the leading bogie, but the position of the tie did not cross its original (zero) position. As a particular wheel passed over the instrumented tie, the compressed rail-tie-ballast system relaxed and attempted to restore to its original position through upward movement. Momentum gained during this upward movement carried the rail-tie system past its original (zero) position, thereby causing an oscillatory motion. This motion was interrupted by the arrival of the next wheelset and the rail-tie system was pushed downward. This mechanism led to significant impact loads on the ballast layer, thus accelerating layer settlement.

Subsequent tie lift-off events for the data presented in Figure 5.14 are marked as the values 6, 10, 14, 18, 22, 26, 30 (between the two bogies of the trailing locomotive), and 32 (immediately after departure of the train). The times corresponding to the occurrence of the load peaks and initiation of the tie lifting phenomenon are listed in Table 5.4. It is important to note that the third column in the table lists the instant when the tie lifting phenomenon started and not the instant corresponding to the maximum magnitude of tie lifting observed. By using the difference between these two instances (instant of peak load, and instant of initiation of tie lifting), one can calculate the approximate distance traveled by the train during that period. Note that an operating speed of 177 km/h (110 mph) was assumed for the Acela Express trains operating along this section of the NEC.

Table 5.4: Time Difference Between Peak Load and Subsequent Initiation of Tie Lift-Off Phenomenon – Madison Street Bridge Approach – Near-Bridge Location (Data Recorded in June 2013)

Peak No.	Force Peak Time (sec)	Lifting Starts (sec)	Distance Traveled (m)
2	4.60	4.72	5.88
6	5.01	5.13	5.95
10	5.56	5.67	5.75
14	6.10	6.21	5.73
18	6.64	6.76	5.80
22	7.18	7.30	5.93
26	7.72	7.84	5.78
30	8.28	8.40	5.90
32	8.50	8.62	6.00

As listed in the fourth column of Table 5.4, a particular axle traveled approximately 5.8 meters from the instrumented tie before the lifting occurred. The downward transient displacement values recorded immediately prior to the initiation of the tie lifting process ranged between 1.1 mm and 1.4 mm, indicating delayed propagation of the compression wave even after passage of a wheel set. Like peak 2, the lifting corresponding to peak 30 did not register a negative number

on LVDT 1. This phenomenon can be explained by close inspection of train dimensions and the effect of distance between two consecutive bogies on negative rail bending as shown in Figure 5.1.

As shown in Figure 5.1, the distance between the bogies for the locomotives (7899.4 mm) was less than that for the coach cars (15138.4 mm). This time "headway" (time difference between the instants of arrival at a particular point) between the leading and trailing bogies for a locomotive was shorter than that for a coach car. Accordingly, the upward movement of the rail-tie system was interrupted by the arrival of the trailing bogie after a shorter time gap for the locomotives as compared to the coach cars. The negative (upward) movement of the tie was interrupted by the trailing bogie of the locomotive before it crosses its original (zero) position, whereas the full negative (upward) movement of the tie is seen underneath coach cars.

Similar data for the Upland Street bridge approach (near-bridge location) recorded in July 2014 is presented in Figure 5.15. Table 5.5 lists the distance traveled by the train between the departure of a particular wheel and the initiation of the corresponding tie lift-off event. Although the overall tie lift-off trends observed at the Madison and the Upland Street locations were similar to each other, two main differences that were worth highlighting are as follows:

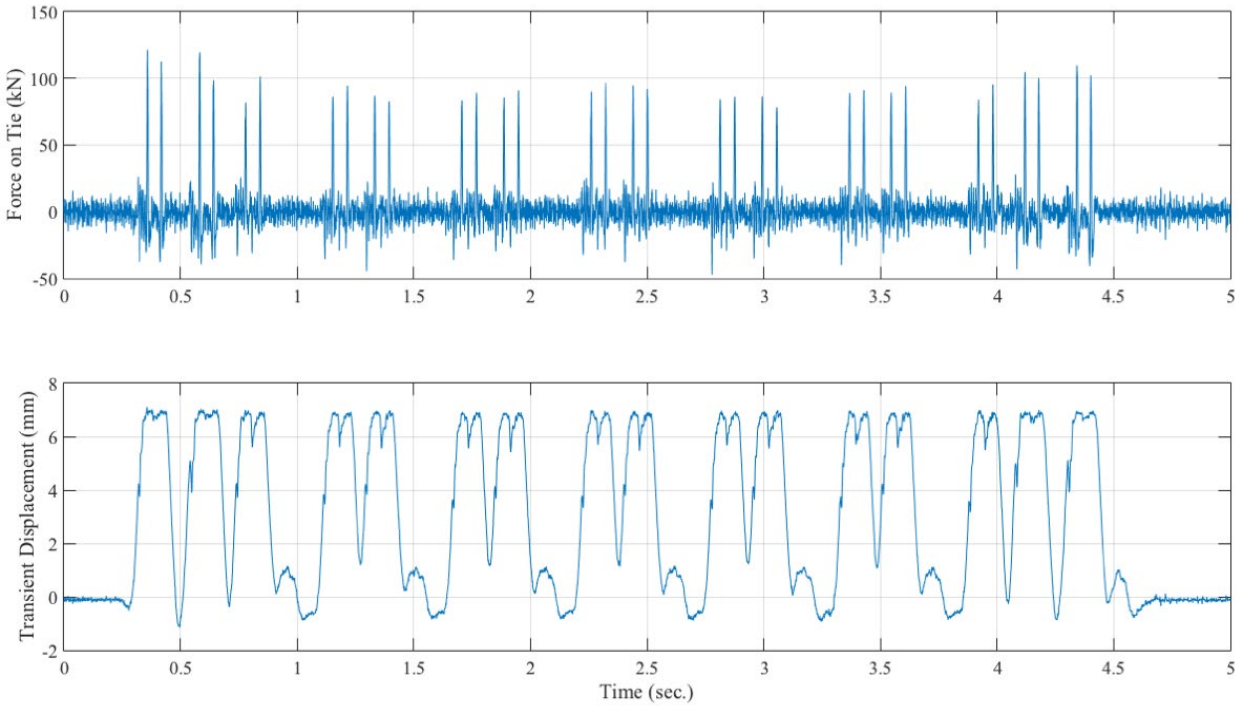

Figure 5.15: Load and Deformation (LVDT 1) Time-Histories Under the Passage of an Acela Express Train at the Upland Street Bridge Approach – Near-Bridge Location (Data Collected in July 2014)

1. Absolute values of the negative displacements recorded at the Upland Street location (~ 1 mm) were lower than those for the Madison Street location (~ 3.5 mm). This can be explained by comparing the magnitudes of downward transient displacements recorded at these two locations. Transient downward displacements recorded at the Madison Street bridge approach (near-bridge location) were on the average 2 mm, whereas the values recorded for the Upland Street bridge approach (near-bridge location) were

approximately 7 mm. In other words, the rail-tie system needed to "bounce back" through a longer distance at the Upland Street bridge approach compared to the Madison Street bridge approach. As more time was required for the rail-tie system to restore back to its original position, the upward movement was interrupted before significant levels of negative displacements (tie lift-offs) were mobilized. The relatively smaller downward transient displacement at the Madison Street bridge approach left more time for mobilization of the negative displacement before the upward motion was interrupted by the arrival of the trailing bogie.

2. No significant difference was observed between the negative displacements associated with the locomotive and the coach cars. In both cases, negative displacements with magnitudes of approximately 1 mm were mobilized.

Table 5.5: Time Difference Between Registering Peak Load, and Subsequent Initiation of Tie Lift-Off Phenomenon – Upland Street Bridge Approach – Near-Bridge Location (Data Recorded in July 2014)

Peak No.	Force Peak Time (sec)	Lifting Starts (sec)	Distance Traveled (meters)
2	0.42	0.44	1.11
6	0.84	0.96	5.71
10	1.40	1.51	5.65
14	1.95	2.07	5.86
18	2.50	2.62	5.73
22	3.06	3.17	5.69
26	3.61	3.72	5.51
30	4.18	4.19	0.69
32	4.40	4.52	5.96

To investigate any potential relationship between the magnitude of the downward transient displacement to the corresponding upward movement, Figure 5.16 shows the maximum upward and downward movements recorded at the Madison Street bridge approach during different data acquisition efforts. As before, downward movements are plotted as positive (+ve) numbers, whereas upward movements have been plotted as negative (-ve) numbers. The following observations can be made from Figure 5.16:

1. Peak negative displacements recorded at the near-bridge location were consistently higher than those for the open-track location. However, the negative displacement observed at the open-track location in August 2012 was comparable to that for the near-bridge location. As discussed in the previous section, the tie-ballast interface gap at the open-track location was greater in August 2012 compared to the near-bridge location. The large gap underneath the tie possibly led to greater negative displacement magnitudes.

2. As shown in Table 5.1, the gap at the tie-ballast interface increased consistently for the near-bridge location. Similarly, negative displacement magnitudes for this location exhibited an increasing trend between August 2012 and June 2013.
3. Negligible negative tie displacements were recorded for the open-track location in November 2012, January 2013, and June 2013. This also corresponded to relatively low tie-gap values (0.59 – 0.76 mm) calculated at this location during these time periods.

Similar data for the Upland Street bridge approach (see Figure 5.17) indicated consistently lower negative tie displacements for the open-track location compared to the near-bridge location. Looking at the corresponding tie-gap values presented in Table 5.2, no particular trend exists between the magnitude of the tie-gap and the magnitude of negative displacement undergone by the tie. Data for the Caldwell Street location (see Figure 5.18) showed consistently higher magnitudes of negative tie displacement at the west end of the tie compared to those measured at the east end of the tie. Note that Table 5.3 presented consistently higher tie-gaps calculated for the west end of the tie compared to the east end. Data from all three instrumented bridge approaches indicated that locations with high gaps at the tie-ballast interface generally exhibited a higher degree of tie lift-off. However, no particular trends relating the magnitudes of the tie-gap and the tie lifting were observed.

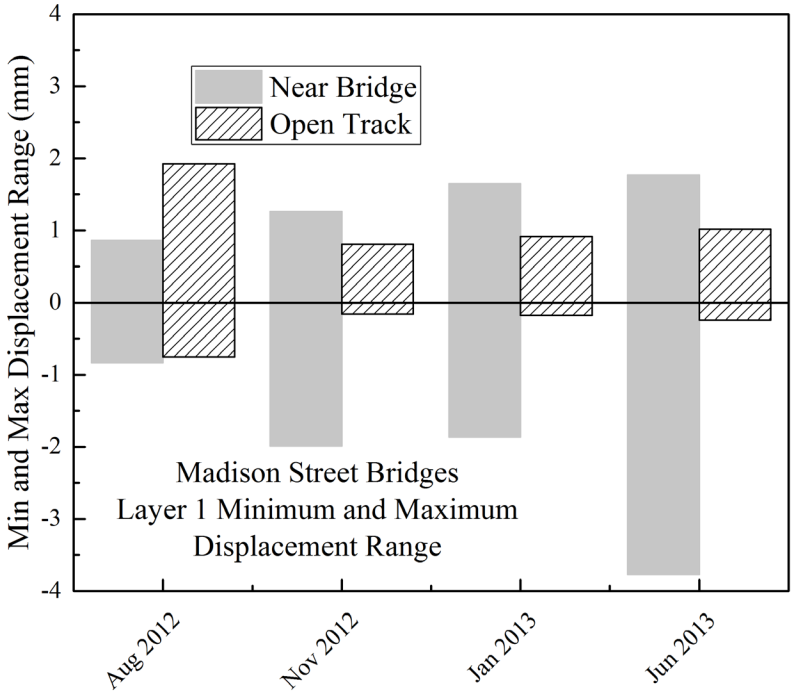

Figure 5.16: Maximum and Minimum Transient Displacements Recorded for the Instrumented Tie – Madison Street Bridge Approach

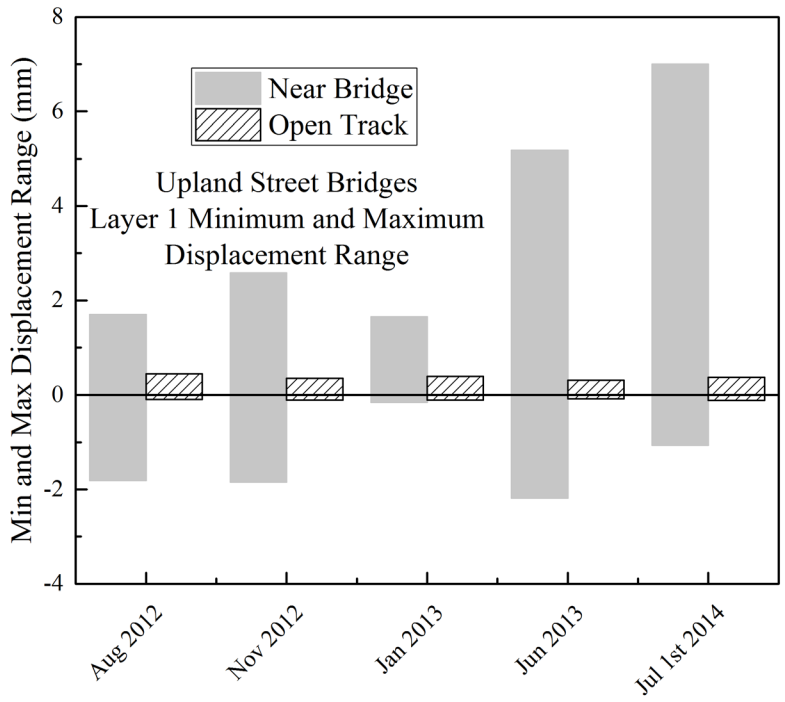

Figure 5.17: Maximum and Minimum Transient Displacements Recorded for the Instrumented Tie – Upland Street Bridge Approach

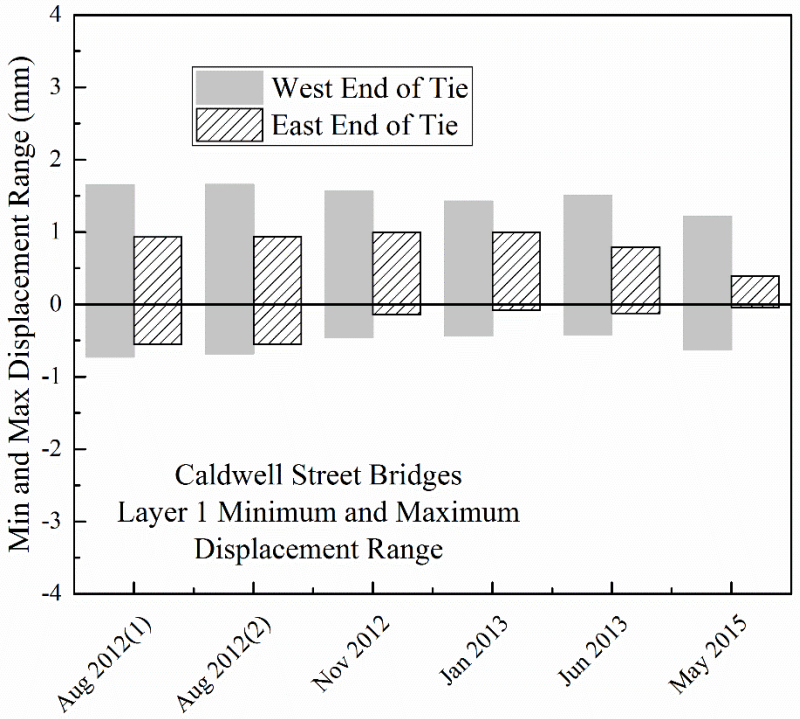

Figure 5.18: Maximum and Minimum Transient Displacements Recorded for the Instrumented Tie – Caldwell Street Bridge Approach

5.5 Interpretation of Track Substructure Layer Accelerations in Time and Frequency Domains

Accelerometers are commonly used for the response monitoring of railroad tracks. Accelerations measured under train loading can be interpreted in time and frequency domains to characterize the track's dynamic response. MDD displacement time-histories were numerically differentiated to calculate the corresponding layer accelerations. These accelerations were in turn used to make inferences concerning the dynamic response of the track under loading. The computed acceleration time-histories were converted from time domain to frequency domain using FFT. Detailed descriptions of this analysis approach and relevant inferences are presented in this sub-section. To compare the substructure layer responses corresponding to the near-bridge and open-track locations, layers 2, 3, and 4 at each instrumentation location were combined into one layer, termed the "intermediate layer." This was necessary because the thicknesses of individual substructure layers were different for each instrumentation location, and a comparison of substructure layer behavior across locations was not possible without such simplifying assumptions. Table 5.6 lists substructure layer thicknesses at the instrumented Amtrak NEC bridge approaches established through the merging of layers 2, 3, and 4. Note that all depth measurements were made with respect to the top of the tie (surface of the ballast layer).

Table 5.6: Track Substructure Layer Thicknesses for the Instrumented Amtrak NEC Bridge Approaches Established through Merging of Intermediate Layers

Madison Street Bridge Approach				
Layer Number	Near-Bridge Location		Open-Track Location	
	Starts at Depth (mm)	Ends at Depth (mm)	Starts at Depth (mm)	Ends at Depth (mm)
1	Surface	279	Surface	330
2 + 3 + 4	279	1679	330	1537
5	1679	2819	1537	2820
Upland Street Bridge Approach				
Layer Number	Near-Bridge Location		Open-Track Location	
	Starts at Depth (mm)	Ends at Depth (mm)	Starts at Depth (mm)	Ends at Depth (mm)
1	Surface	305	Surface	305
2 + 3 + 4	305	1645	305	1661
5	1645	2820	1661	2819
Caldwell Street Bridge Approach				
Layer Number	West End of Tie		East End of Tie	
	Starts at Depth (mm)	Ends at Depth (mm)	Starts at Depth (mm)	Ends at Depth (mm)
1	Surface	305	Surface	318
2 + 3 + 4	305	1701	318	1697.2
5	1701	2819	1697.2	2820.2

5.5.1 Analyses of Substructure Layer Accelerations at the Madison Street Bridge Approach

Track substructure layer accelerations calculated for the Madison Street bridge approach under the passage of an Acela Express train are presented in Figure 5.19 (data collected in August 2012). The data trends corresponding to the near-bridge location are highlighted in the left column of sub-plots, whereas the right column of sub-plots corresponds to data collected at the open-track location. The top row of sub-plots presents the load time-histories recorded during the passage of the Acela Express train, and the bottom row of sub-plots presents the corresponding acceleration time-histories (calculated from numerical double-differentiation of the displacement time-histories).

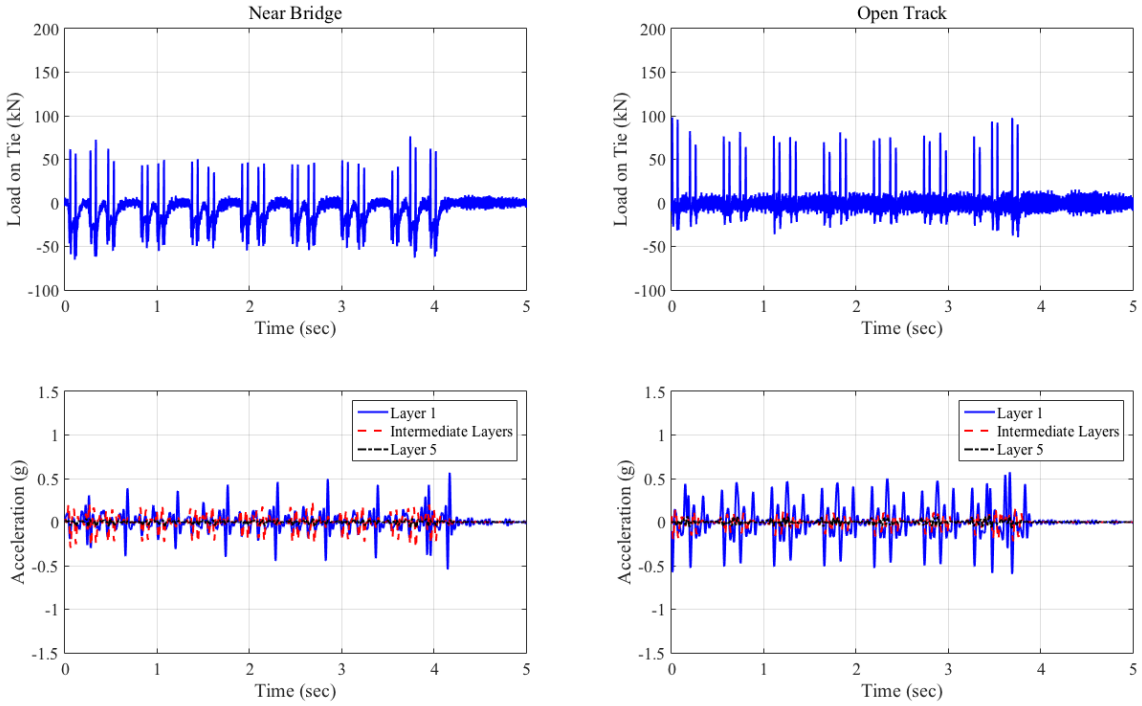

Figure 5.19: Load and Acceleration Time-Histories for the Madison Street Bridge Approach (Data Collected in August 2012)

The near-bridge location at the Madison Street bridge approach exhibited lower transient displacements compared to the open-track location. This was later attributed to the presence of a larger gap underneath the instrumented tie at the open-track location in August 2012 compared to the near-bridge location. Comparison of the acceleration values plotted in Figure 5.19 also indicates slightly higher acceleration values for the open-track location compared to the near-bridge location. A larger gap at the tie-ballast interface enabled the tie to move over a longer distance in a short time, thus leading to higher velocity and acceleration magnitudes.

Figure 5.20 shows layer 1 accelerations for the Madison Street bridge approach presented in the frequency domain. As seen from the figure, predominant waveform contributions for both the near-bridge and open-track locations occur at frequency levels of 11 Hz and 16.5 Hz. Moreover, the near-bridge location comprises contributions from waveforms in the 22 Hz frequency range, whereas such frequencies are missing from the open-track location.

Figure 5.21 shows the acceleration ranges recorded at the Madison Street bridge approach during the four data acquisition events. The detailed acceleration time-histories for the data corresponding to November 2012, January 2013, and June 2013 are given in Appendix A-2. As seen from Figure 5.21, the near-bridge location shows higher acceleration values in November 2012, January 2013, and June 2013 compared to the open-track location. This is because the tie-gaps calculated for the near-bridge location at these time periods were consistently higher than those for the open-track location. No significant trends were observed for the acceleration values calculated for the intermediate layers or layer 5. Different peaks observed during frequency domain analyses of the near-bridge and open-track layer accelerations will be further investigated in the following sections.

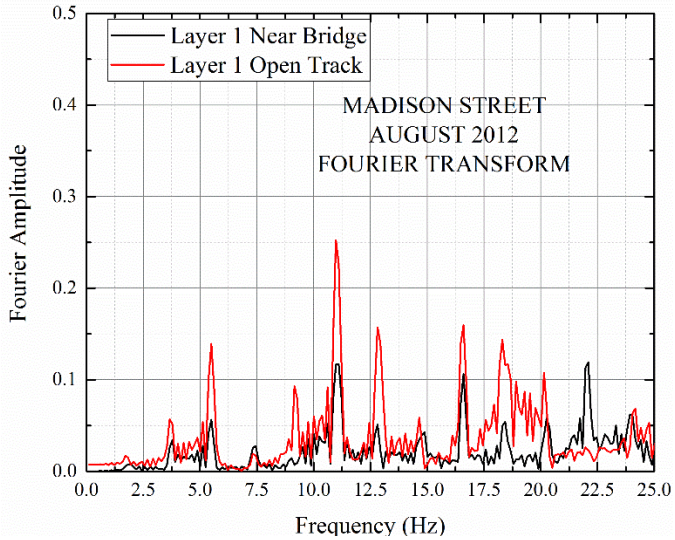

Figure 5.20: Layer 1 Accelerations for the Madison Street Bridge Approach Presented in the Frequency Domain (Data Collected in August 2012)

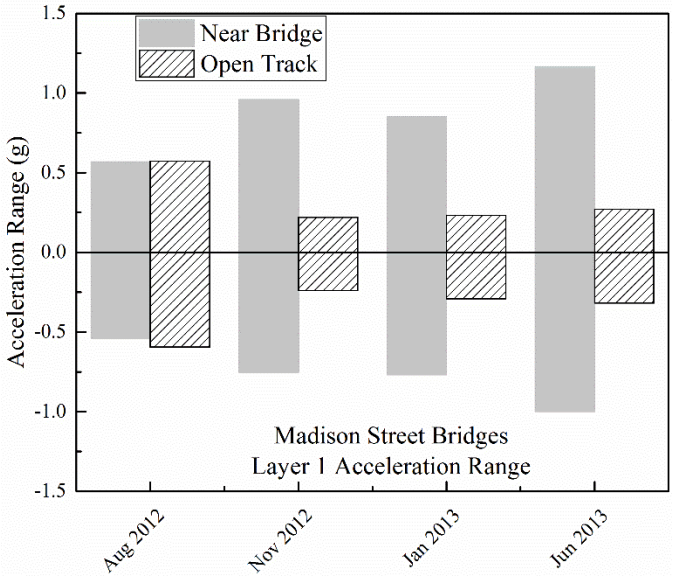

Figure 5.21: Summary of Peak Accelerations Recorded at the Madison Street Bridge Approach Under the Passage of Acela Express Trains

5.5.2 *Analyses of Substructure Layer Accelerations at the Upland Street Location*

Similar data for the Upland Street bridge approach are presented in Figure 5.22 through Figure 5.24. Other detailed measurements corresponding to November 2012, January 2013, June 2013, and July 2014 data collection periods are given in Appendix A-2.

The following conclusions can be drawn from the substructure layer acceleration values calculated for the Upland Street location, as highlighted in Figure 5.22 through Figure 5.24:

1. Layer 1 accelerations calculated for the open-track location were consistently lower than those for the near-bridge location across all data collection events. This can be directly corroborated by the fact that tie-gaps for the open-track location were consistently lower than those for the near-bridge location.
2. Like the Madison Street bridge approach, frequency domain representation of the layer 1 accelerations at the near-bridge location indicated significant contributions at 11 Hz, 16.5 Hz, and 22 Hz frequency levels. One additional peak at 9 Hz was observed for the Upland Street location, which was not apparent at the Madison Street location.
3. Due to very small accelerations calculated for the open-track location at the Upland Street bridge approach, no significant inference can be drawn regarding predominant contributing frequencies.
4. As shown in Figure 5.24, peak accelerations at the open-track location remained relatively unchanged across time, consistent with the relatively unchanged tie-gap values calculated for this location and reported in Table 5.2.

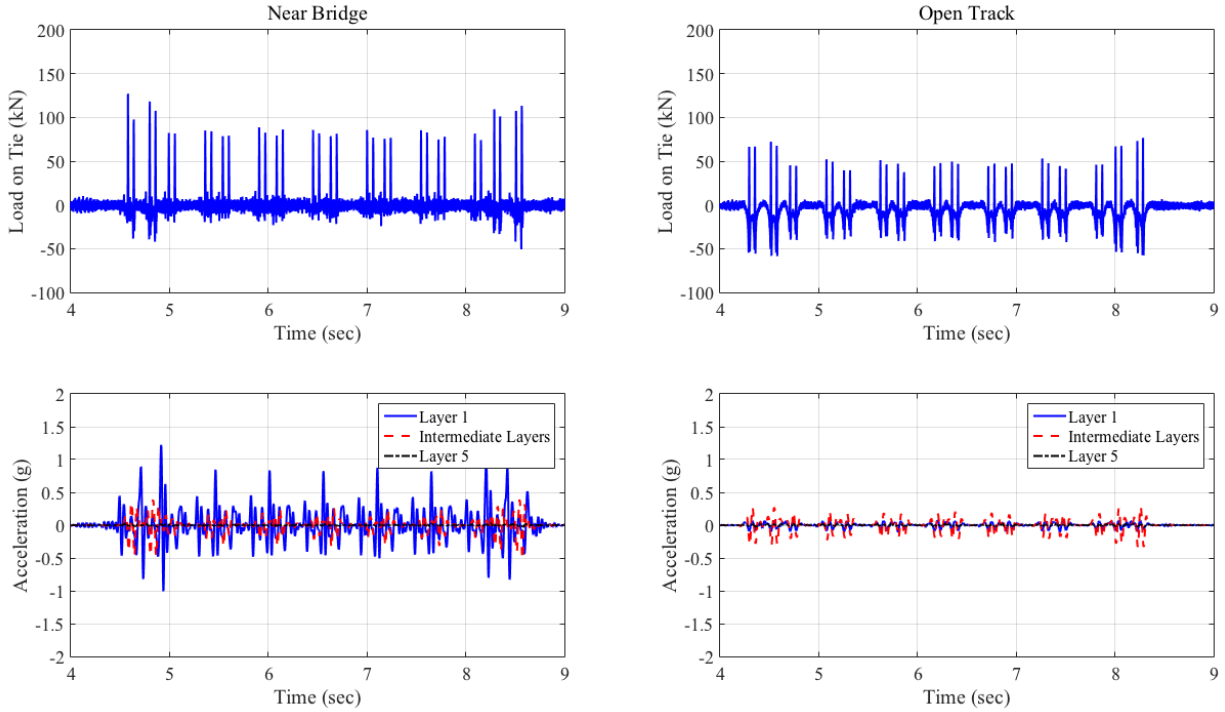

Figure 5.22: Load and Acceleration Time-Histories for the Upland Street Bridge Approach (Data Collected in August 2012)

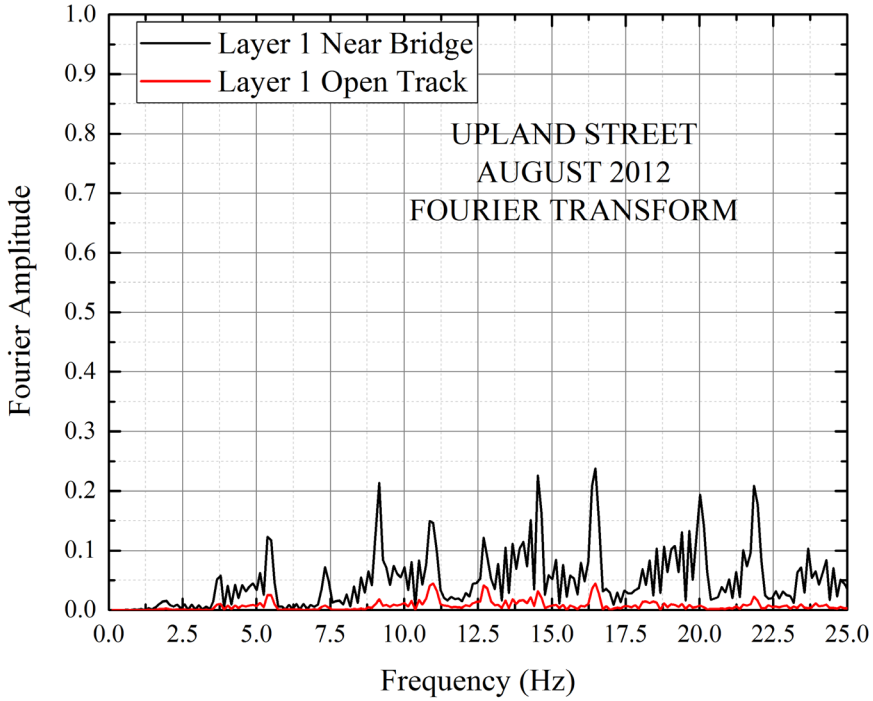

Figure 5.23: Layer 1 Accelerations for the Upland Street Bridge Approach Presented in the Frequency Domain (Data Collected in August 2012)

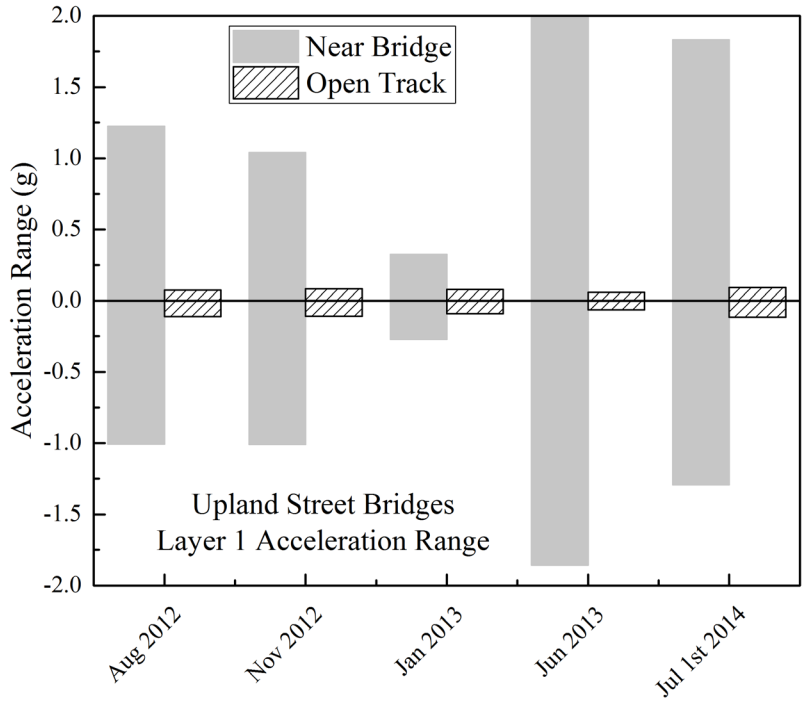

Figure 5.24: Summary of Peak Accelerations Recorded at the Upland Street Bridge Approach Under the Passage of Acela Express Trains

5.4.3 Analyses of Substructure Layer Accelerations at the Caldwell Street Location

Identical data for the Caldwell Street bridge approach are presented in Figure 5.25 through Figure 5.27. As shown in the figures, layer 1 accelerations calculated for the west end of the instrumented tie were slightly higher in magnitude than those calculated for the east end of the instrumented tie. This finding once again corroborated higher tie-gaps calculated for the west end of the tie compared to the east end (see Table 5.3). Dominant contributing waveforms for both ends of the tie were observed at frequency levels of 5.5 Hz, 11 Hz, 12.75 Hz, and 16.5 Hz. The peak accelerations calculated for layer 1 remained relatively unchanged with time (see Figure 5.27), with the accelerations for the west end of the tie being consistently higher than those for the east end.

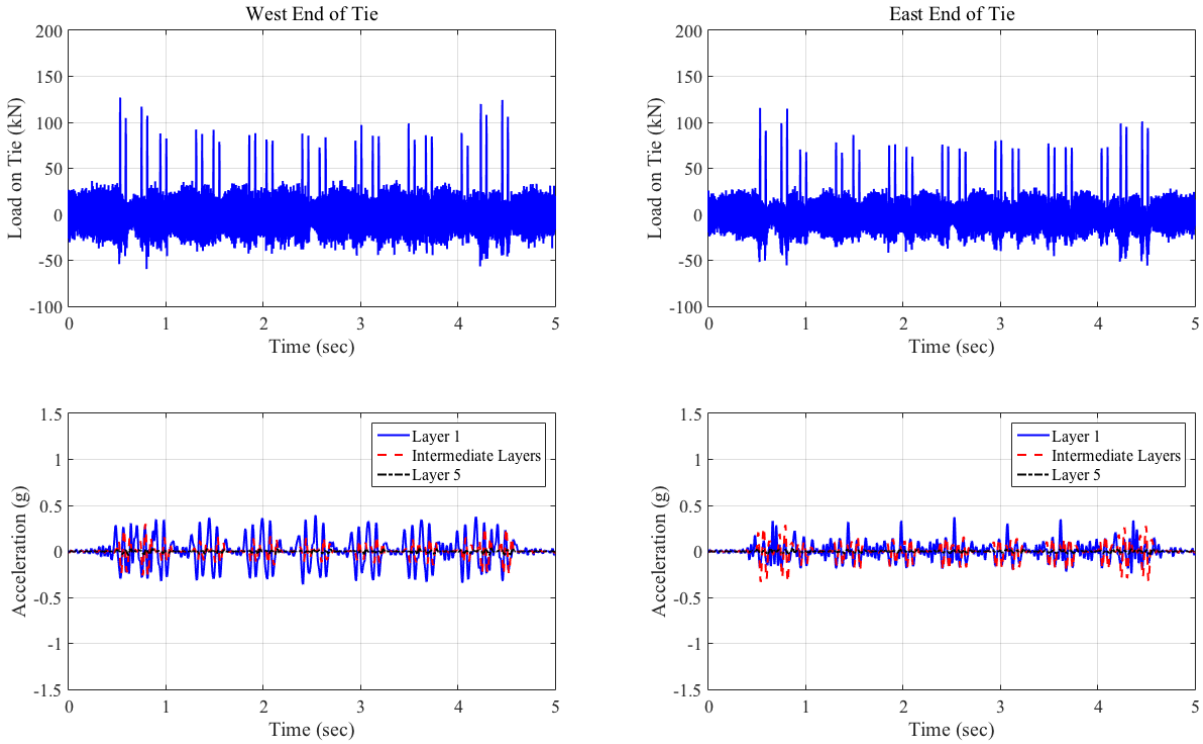

Figure 5.25: Load and Acceleration Time-Histories for the Caldwell Street Bridge Approach (Data Collected in August 2012)

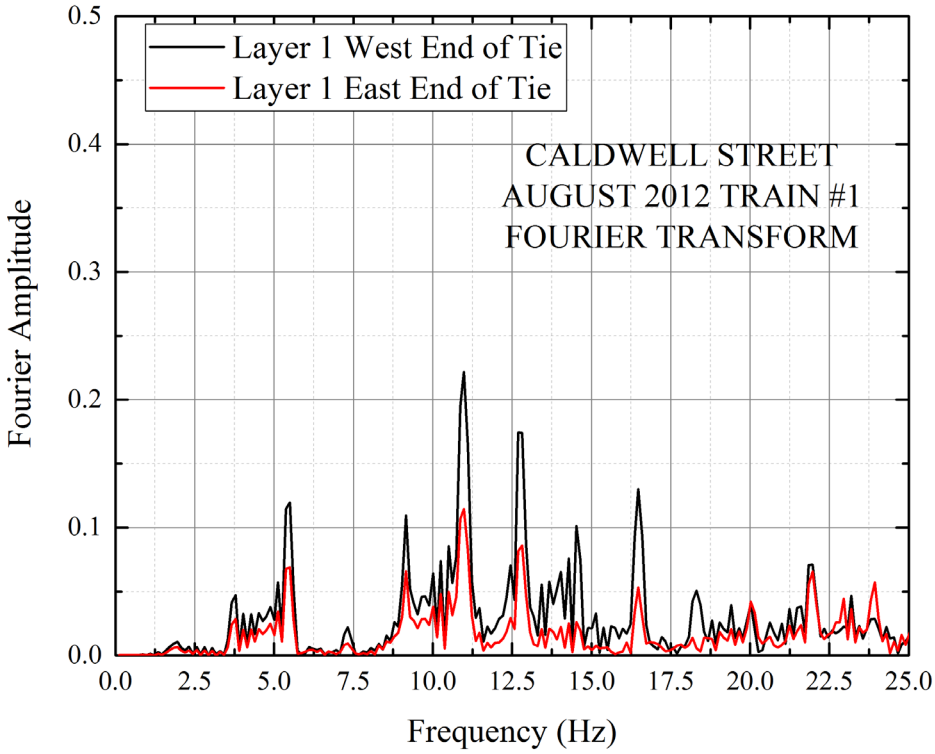

Figure 5.26: Layer 1 Accelerations for the Caldwell Street Bridge Approach Presented in the Frequency Domain (Data Collected in August 2012)

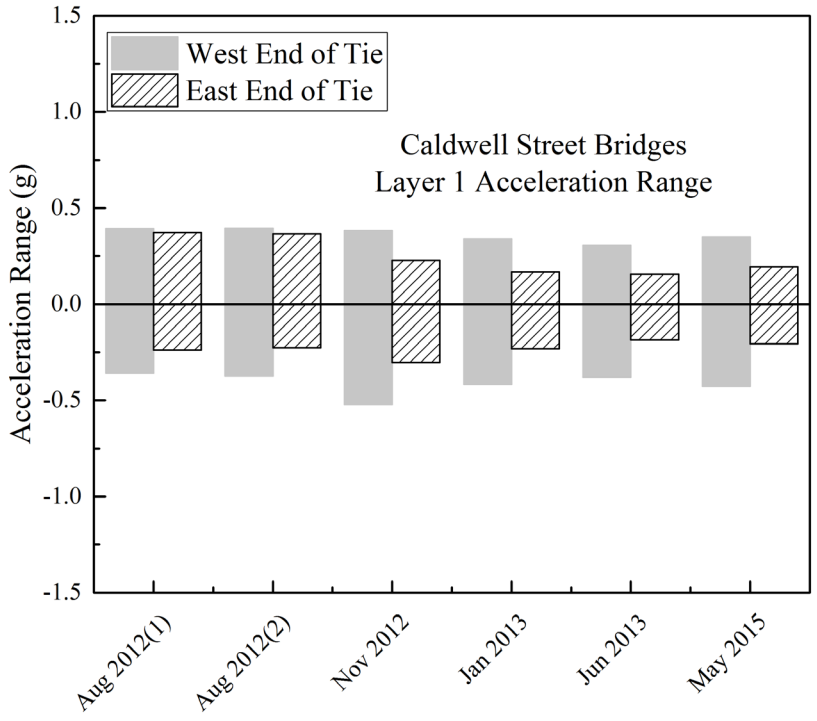

Figure 5.27: Summary of Peak Accelerations Recorded at the Upland Street Bridge Approach Under the Passage of Acela Express Trains

5.4.4 Analyses of Substructure Layer Accelerations at the MP352.2 and MP352.8 Bridges (NS N-Line Mainline)

Transient track response data recorded at the instrumented bridge approaches along NS's N-Line mainline were used to calculate the layer accelerations, which were subsequently transformed to the frequency domain using FFT. Figure 5.28 shows the accelerations calculated for the near-bridge location at the MP352.2 bridge approach plotted in both time and frequency domains. The top row of sub-plots presents the layer acceleration values in the time domain, whereas the bottom row of sub-plots shows frequency domain representation of the calculated layer accelerations. As seen from the figure, very small acceleration values (< 0.05 g) were calculated for layer 1, with even smaller values calculated for the deeper layers. No particular trend was observed concerning the dominant waveform frequencies contributing to the layer accelerations. Figure 5.29 presents similar data for the open-track location at the MP352.2 bridge approach, whereas Figure 5.30 and Figure 5.31 show similar graphs for the MP352.8 bridge approach (near-bridge and open-track locations, respectively). Analysis of the data collected from the instrumented bridge approaches along NS's N-Line mainline conclude that certain trends in track substructure layer accelerations were much more apparent under fast-moving passenger trains compared to slow-moving freight trains.

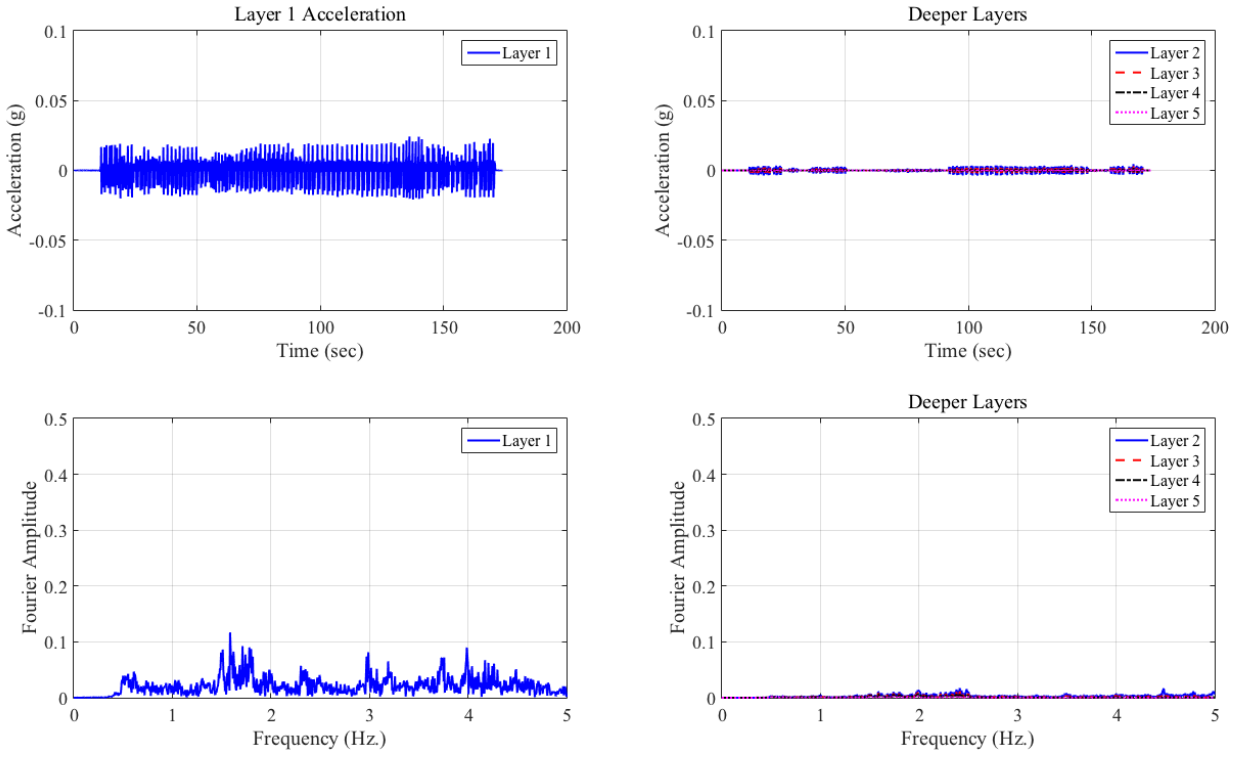

Figure 5.28: Time and Frequency Domain Representation of Layer Accelerations at the MP352.2 Bridge Approach – Near-Bridge Location (Data Collected in November 2013)

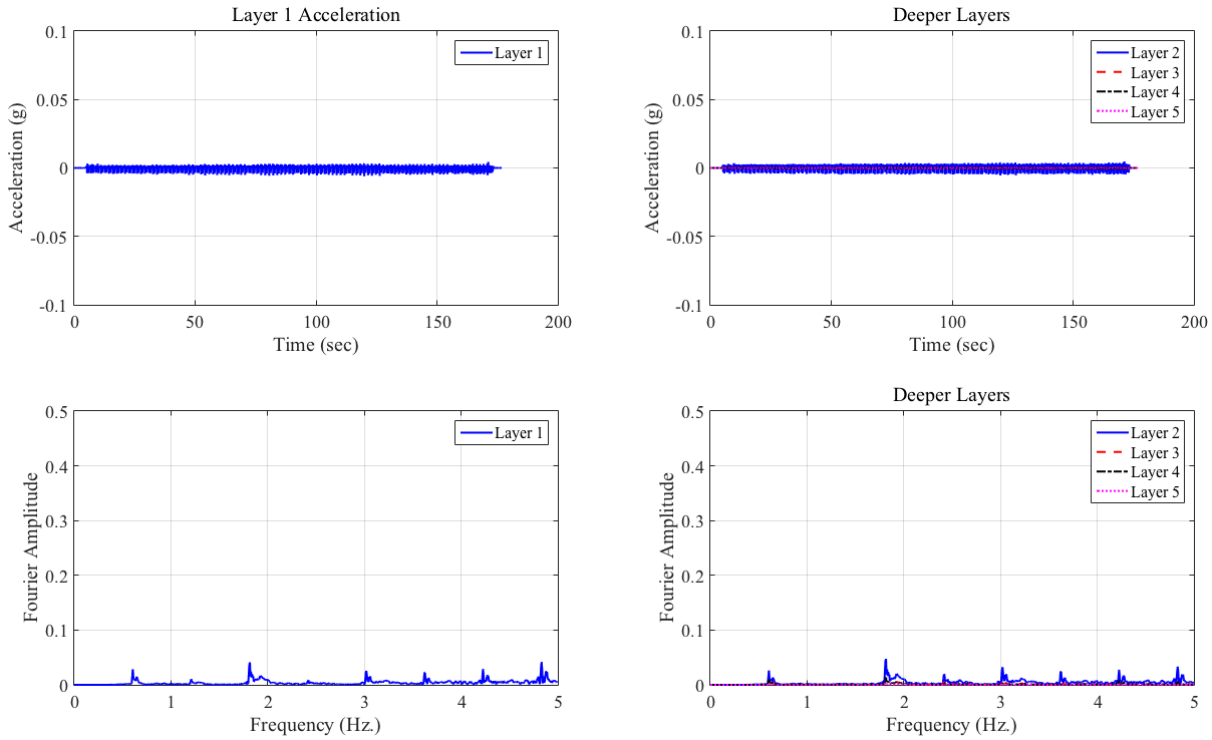

Figure 5.29: Time and Frequency Domain Representation of Layer Accelerations at the MP352.2 Bridge Approach – Open-Track Location (Data Collected in November 2013)

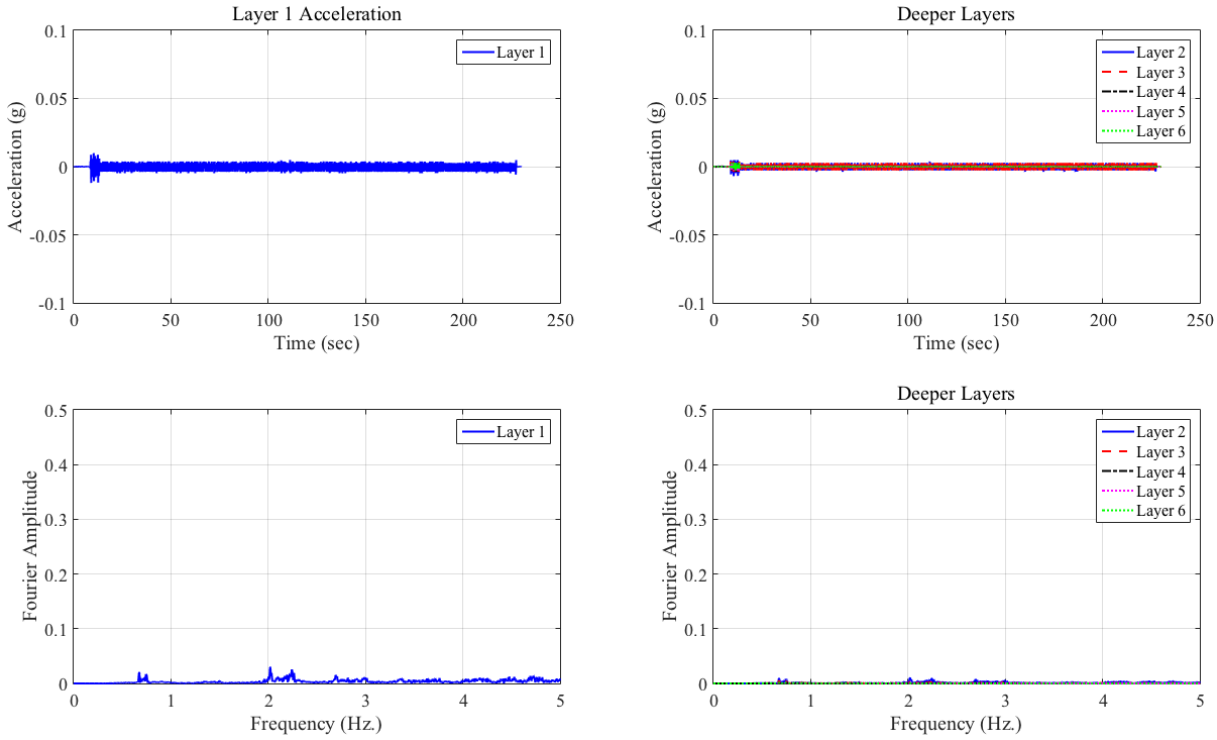

Figure 5.30: Time and Frequency Domain Representation of Layer Accelerations at the MP352.8 Bridge Approach – Near-Bridge Location (Data Collected in November 2013)

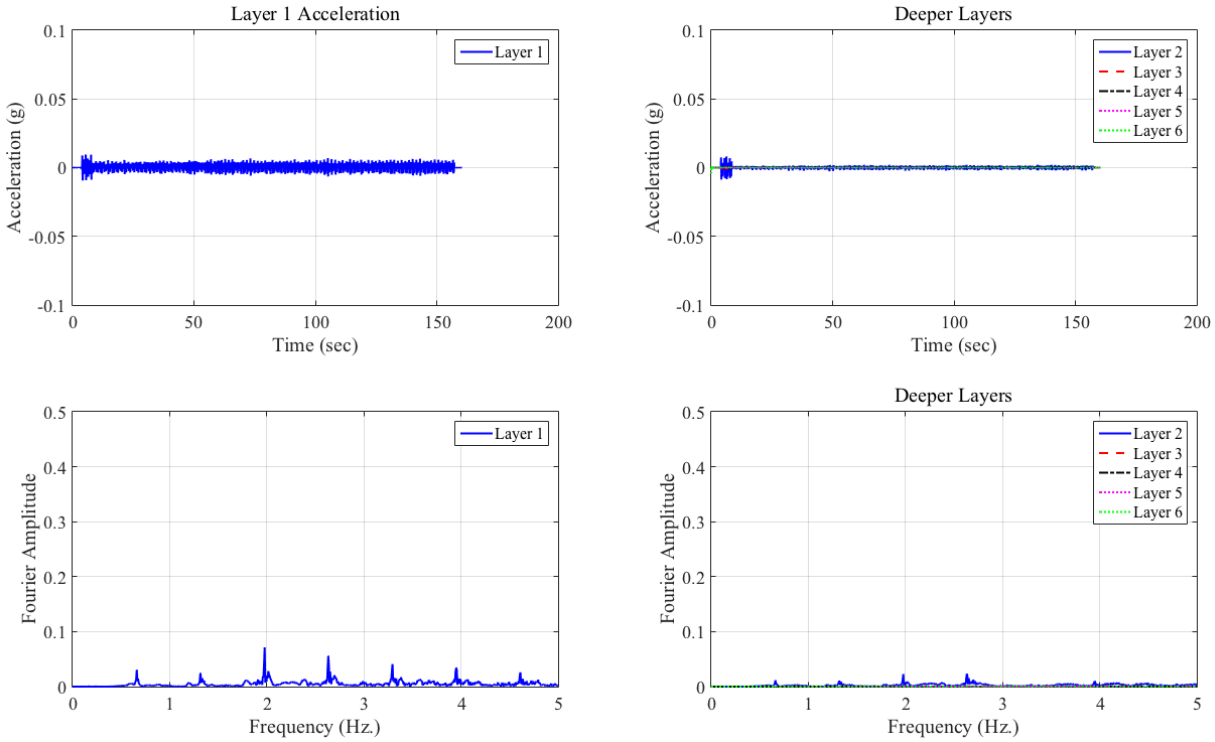

Figure 5.31: Time and Frequency Domain Representation of Layer Accelerations at the MP352.8 Bridge Approach – Open-Track Location (Data Collected in March 2014)

5.4.5 Analyses of Tie Lifting in Acceleration – Time Domain and Frequency Domain

This subsection includes analyses of the tie-lifting phenomenon using tie accelerations in both time and frequency domains. Figure 5.32 presents the displacement and acceleration time-histories for the instrumented tie (as the top-most LVDT is mounted inside the crosstie, accelerations calculated using this LVDT can be referred to as the tie acceleration) at the Madison Street bridge approach (data collected in June 2013) under the passage of an Acela Express train. As shown in the figure, negative displacements (tie lifting) were recorded only for the near-bridge location, with only positive deformations recorded for the open-track location. Varandas et al. (2011) observed similar negative displacement trends at track transition locations. However, in their case the connecting structure was a culvert with a very short span. They reported that these negative displacements at the measured side of the transition zone were caused after the first bogie of a train car passed on to the other side of the connecting structure, thus causing a lifting effect on the side where measurements were being carried out. Note that the bridges in the current study were significantly longer than 15 m; therefore, the lifting mechanism described by Varandas et al. (2011) was not applicable to the current study.

Figure 5.33 shows the tie (layer 1) accelerations for the near-bridge and open-track locations transformed into the frequency domain. Close inspection reveals that the Fourier amplitudes for frequencies between 7.5 Hz to 13 Hz were either greater or slightly smaller than those for frequencies between 16 Hz to 18 Hz, corresponding to the distance between the two wheels of the Acela locomotive. Note that waveforms corresponding to the frequency range of 7.5 Hz to 13 Hz were not observed for the open-track location. This indicated that the waveforms

corresponding to this frequency range were somehow originating from the vicinity of the instrumented tie to the bridge abutment. This can be seen by calculating the time required for the train to move from the instrumented tie (near-bridge location) to the bridge abutment.

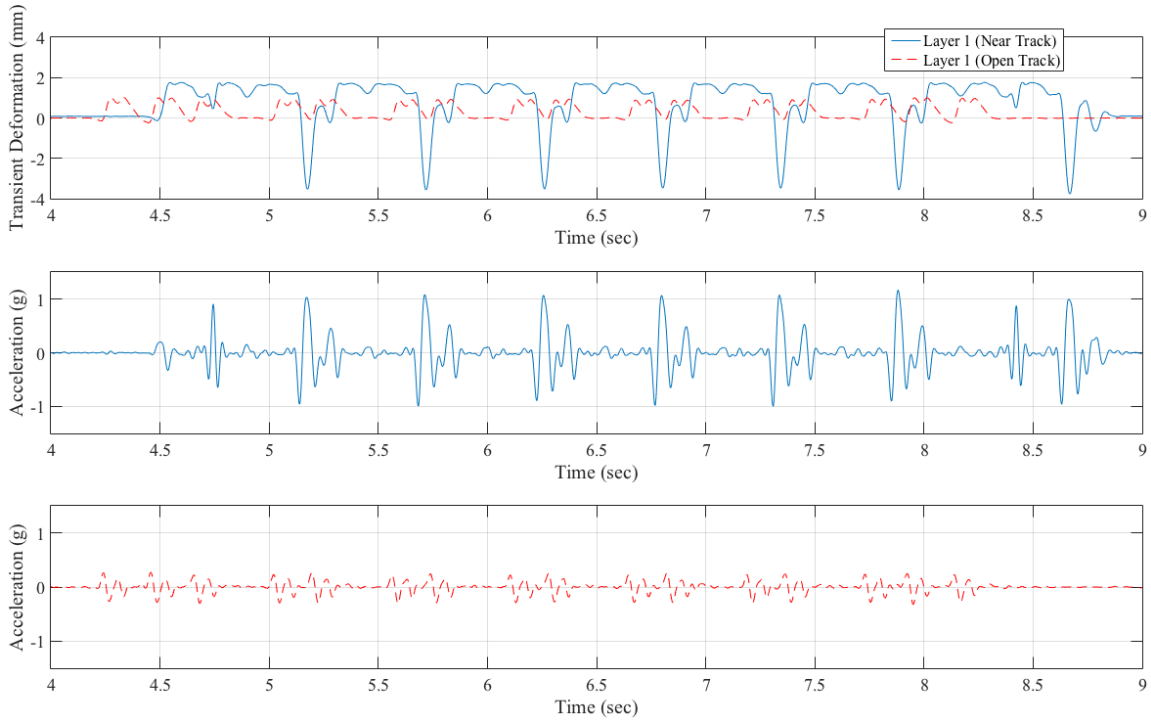

Figure 5.32: Displacement and Acceleration Time-Histories for Layer 1 at the Madison Street Bridge Approach Under the Passage of an Acela Express Train (Data Collected in June 2013)

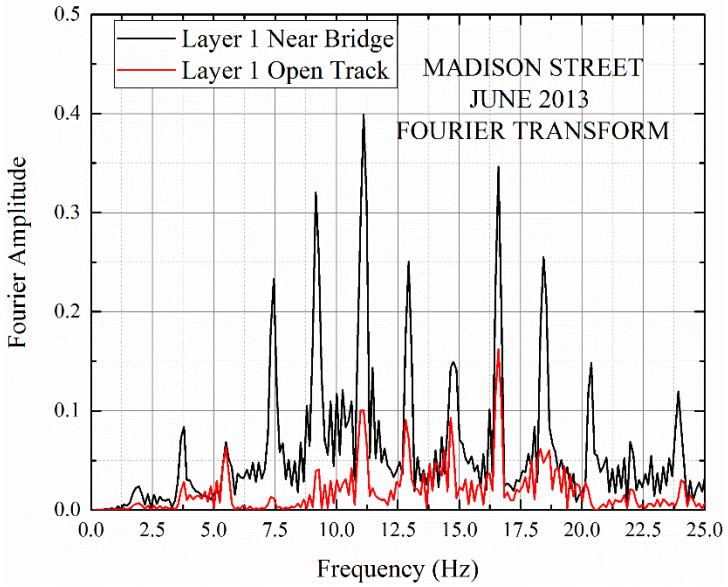

Figure 5.33: Frequency Domain Representation of Layer 1 Accelerations at the Madison Street Bridge Approach Under the Passage of an Acela Express Train (Data Collected in June 2013)

The distance between bridge abutment to the instrumented tie for the Madison Street near-bridge location was approximately 3657.6 mm (12 ft), and that for the Upland Street location was approximately 4572 mm (15 ft). Considering an operating speed of 177 km/h or 49,166.7 mm/sec, it takes the train 0.074 seconds or 0.093 seconds, respectively, to travel over 12 ft or 15 ft. These durations correspond to frequency values of 13.5 Hz or 10.76 Hz, respectively, which coincide with the peaks observed during analyses of the tie accelerations in the frequency domain. Moreover, the distance traveled by the train between the instant of the peak load and the instant corresponding to initiation of the negative tie displacement was approximately 5.8 m. The frequency corresponding to the time taken by the train to travel over 5.8 m can be calculated to be 8 Hz (assuming a train operating speed of 177 km/h), which falls between 7.5 Hz to 13 Hz.

This swinging motion of the tie started immediately after the passage of the first bogie of the locomotive and was interrupted by the arrival of the second bogie, which caused a heavy "hammering" type impact load on the ballast layer. This phenomenon can potentially lead to the rapid breakdown of the ballast particles, causing increased ballast fouling and localized movement associated with tie settlement. Moreover, this hammering effect can also cause damage to the crossties, fastening systems, and the rails, and can be a contributing mechanism for commonly observed track transition problems such as ballast attrition and/or pulverization, mud pumping, differential settlement, and hanging or unsupported crossties (Li and Davis, 2005; Li et. al., 2010). Figure 5.34 and Figure 5.35 present similar data for the Upland Street bridge approach, which corroborate the hypotheses developed from the data collected at the Madison Street bridge approach.

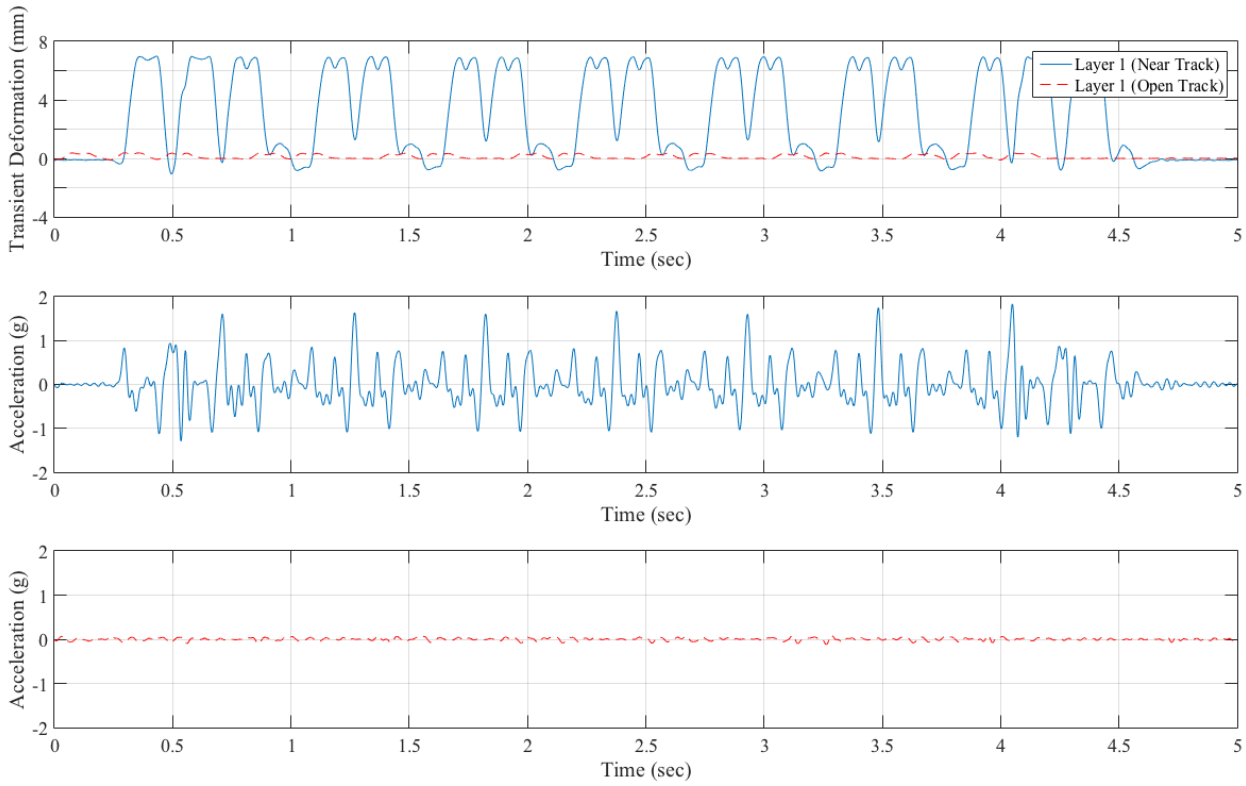

Figure 5.34: Displacement and Acceleration Time-Histories for Layer 1 at the Upland Street Bridge Approach Under the Passage of an Acela Express Train (Data Collected in July 2014)

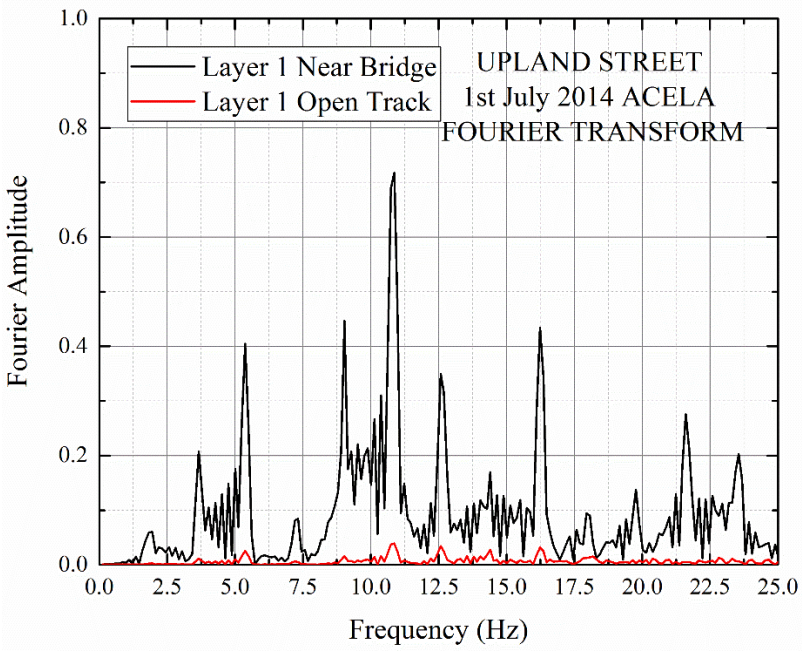

Figure 5.35: Frequency Domain Representation of Layer 1 Accelerations at the Upland Street Bridge Approach Under the Passage of an Acela Express Train (Data Collected in July 2014)

5.6 Estimating Track Substructure Layer Moduli Using GeoTrack

The transient data collected under train passage from the instrumented bridge approaches were used in this study to iteratively estimate the track substructure layer modulus values. A 3D, multi-layer, elastic model GeoTrack was used for this purpose. Originally developed by Chang et al. (1980), the GeoTrack program has been validated by several studies (Stewart and Selig, 1982a/b) to closely match the elastic response of railroad tracks in operation. GeoTrack can determine the elastic response of the track structure using either linear elastic or stress dependent properties for the ballast, sub-ballast, and subgrade materials. It allows the calculation of track deflection, track modulus, and estimates of stresses and displacements in ballast, sub-ballast, and subgrade layers as a function of axle loads, properties of rails, ties, ballast and underlying layers, and geometry of the track structure. An assumption made in GeoTrack is that each wheel load is distributed over 11 ties, 5 on each side of the central tie where load is applied, which means the load is not carried by any tie which is at the sixth or farther position from the central tie.

The rails are represented as linear, elastic beams supported by several concentrated reactions, one at each intersection of tie and rail. These rails span 11 ties that are free to rotate at the ends and at each tie (Chang et al, 1980; Selig and Waters, 1994). The ties are also represented as linear, elastic beams, divided into 10 equal, rectangular segments with underlying ballast reaction represented as concentrated force at the center of each segment. These forces are applied in the form of a uniform pressure over a circular area, calculated from the tie segment dimensions. The connection between the rails and ties is represented by a linear spring, which can take tension as well as compression. The ballast, sub-ballast, and subgrade are represented as series of linear, elastic layers with individual modulus of elasticity and Poisson's ratio properties assigned for each layer. All the layers are assumed to be infinite in the horizontal direction and are placed on a half space, which is infinite in the downward direction. The basic assumptions

and features of the GeoTrack program are listed in Table 5.7. Figure 5.36 shows a schematic of the track structure commonly analyzed by the GeoTrack program.

Table 5.7: Inherent Features and Assumptions of the GeoTrack Program

General	• 3D multilayer • Up to 5 substructure layers • Infinite horizontal extent • No slip at layer interfaces • Only vertical loading considered
Rail	• Linear elastic beams • Spans 11 ties • Free to rotate at ends and at each tie • Linear spring connection between rail and tie
Ties	• Linear elastic beams • Supported at 10 equally spaced circular locations by the underlying ballast

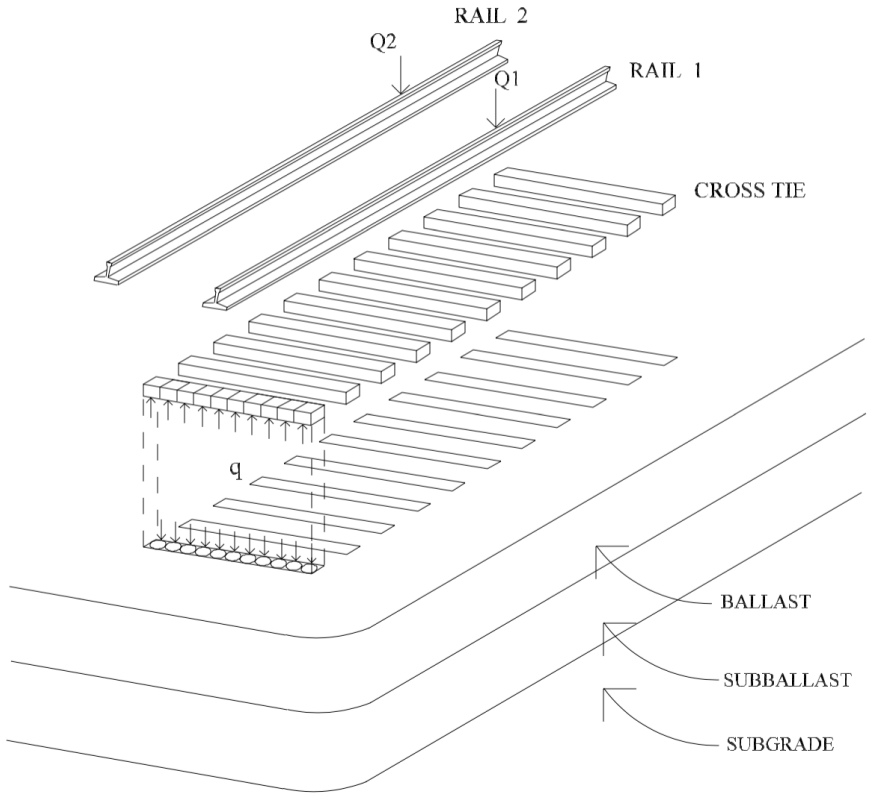

Figure 5.36: Track Elements in GeoTrack Model (Reproduced from Chang et al., 1980)

5.6.1 GeoTrack Input Parameters

The first step during the analysis of a given track structure using GeoTrack is the selection of the relevant input parameters for different track components. Some of the input parameters (e.g., rail, tie, and fastener properties, etc.) remain constant across different sites, whereas other input parameters (e.g., substructure layer properties, etc.) change from one site to another. Table 5.8 lists the typical track parameters used in the current study for GeoTrack analysis of the bridge approach transitions behavior under loading.

5.6.2 Vertical Wheel Load Assignment During GeoTrack Analysis

Peak transient displacements corresponding to the last two wheels on the trailing locomotive were used for estimating the substructure layer modulus values. The corresponding wheel loads measured by the strain gauge circuits were used as inputs in the GeoTrack software. The field-installed strain gauge circuits were based on the principle of measuring the shear strains induced at the neutral axis of the rail and did not distinguish between dynamic and static components of the loads applied to the rail. Therefore, the load levels recorded by strain gauges during the current study included the dynamic components imposed due to track/wheel irregularities. These load levels were used as "static" inputs for the GeoTrack analyses. Peak transient deformations recorded by the individual LVDTs corresponding to the time when the leading wheel of the trailing locomotive was directly on top of the instrumented tie were used as the substructure layer deformations. The position of the second wheel load was determined based on the axle spacing (obtained from the locomotive manufacturers) and tie spacing patterns at the instrumented bridge approaches. For instances where the second wheel location was between two ties, standard force and moment balance methods were used to assign representative vertical load values to individual ties.

The data recorded under the passage of an Acela Express at the Upland Street bridge approach were taken as an example case to illustrate how vertical wheel loads were assigned to different ties for the GeoTrack analysis. Table 5.9 presents the general site information, including tie spacing, axle spacing, and wheel loads measured by the strain gauge circuit installed in the field corresponding to the last two wheels on the trailing locomotive. The two peak loads were assigned on three ties. The first load was assigned to the first tie, and the second load was 2,800 mm away from the first load, which was between the fifth and the sixth tie.

Accordingly, the number of ties between the first load and the second load is calculated by:

$$\frac{2800\ mm}{609.6\ mm} = 4.59$$

The distance from the fifth tie for the second load is:

$$(4.59 - 4) \times 609.6\ mm = 361.6\ mm$$

The distance from sixth tie for the second load is:

$$609.6\ mm - 361.6\ mm = 248\ mm$$

The allocated load on the fifth tie can be determined from the following equilibrium equation:

$$Moment\ (M) = 0$$

$$Load\ on\ 5th\ Tie \times 609.6 = second\ load \times 248$$

$$Load\ on\ 5th\ Tie = 126kN \times \frac{248}{609.6} = 51.26kN$$

Similarly, the allocated load on the sixth tie is calculated as:

$$Load\ on\ 6th\ Tie = 126kN - 51.26kN = 74.74kN$$

Table 5.8: Typical Track Parameters Used During GeoTrack Analysis

Example Case: Madison Street 12 ft, August 2012	
Track variable	Value
(1) Rail Properties	
Spacing (mm)	1,510
Cross sectional area (mm^2)	8,594
E (MPa)	2.07E+05
Weight (kg/m)	67.46
I (mm^4)	3.90E+07
Fastener or sleeper pad stiffness (kN/m)	1.20E+06
(2) Sleeper Properties	
Length (mm)	2591
Center to center sleeper spacing (mm)	609.6
Sleeper width at base of sleeper (mm)	274.3
Sleeper width (mm)	228.6
Sleeper height (mm)	177.8
E (MPa)	2.07E+04
Sleeper weight (kg)	386
No. of sleeper segments having centers between the rails	6
I (mm^4)	2.42E+08
(3) Material Properties	
Unit weight (kN/m^3)	19.5, 19.5, 20.5, 20.5, 20.5
Poisson's ratio	0.35,0.35,0.4,0.4,0.4
Modulus (MPa)	*Need to be backcalculated*
K1 & K2	0
K0	3, 3, 0.7, 0.7, 0.7
Thickness (mm)	*279.4,140,571.5,688.3*
(4) Wheel Load	
Tie number	1,2,6
Magnitude (tonnes)	*8,5.5,10.9*

Table 5.9: General Information for the Example Case Madison 12 ft, August 2012

Test	MAD12-02
Last two peak loads	134 and 126 kN
Tie Spacing	609.6 mm
Axle Spacing	2,800, 7,870, 2,800 mm

5.5.3 Iterative Approach to Layer Modulus Determination

The moduli of individual track substructure layers were determined by a trial-and-error method. A set of seed moduli was first assigned to track substructure layers and GeoTrack was used to calculate deflections at the depths corresponding to the locations of individual MDD modules. Based on comparisons between the calculated and measured deflection values at each depth, adjustments were made to the individual layer modulus values. For example, if the calculated deflections were larger than those measured in the field, the modulus values assigned to the track substructure layers had to be increased for the next iteration. This process was repeated until the deflections measured in the field and those predicted using GeoTrack matched with a tolerance level of less than 5 percent. Some of the simplifying assumptions made during such iterative estimation of track substructure layer moduli using GeoTrack are listed below:

1. The ballast and sub-ballast layers at the Madison Street 12 ft and Caldwell Street west locations were combined into one layer for the analyses.
2. The two silty clay layers (layers 3 and 4) at the Madison Street open-track location (60 ft from the south abutment) were combined into one layer.
3. The sandy loam and sand layers (layers 3 and 4) at the Upland Street near-bridge location (15 ft from the north abutment) were combined into one layer.
4. The tolerance levels between the field-measured and GeoTrack-predicted transient deformations were restricted to less than 5 percent.

5.5.4 Track Substructure Layer Modulus Values Estimated without Correcting LVDT Displacements for Contributions from Tie-Gap

As already discussed, transient deformations recorded by the top-most LVDT in an MDD system comprises contributions from (1) movement of the tie before it comes in contact with the underlying ballast layer, and (2) movement of the tie-ballast system as a unit. Accordingly, taking the transient displacements recorded by the top-most LVDT as representative of the ballast layer deformation can lead to the serious over-estimation of movements within the ballast layer. This in turn leads to the significant under-estimation of the back calculated ballast layer modulus values. To more clearly indicate this, the first set of iterative substructure layer modulus estimations were carried out without eliminating the tie-gap contributions from the LVDT 1 measurements. The resulting back calculated layer modulus values for the Madison, Caldwell, and Upland Street locations are presented in Table 5.10 through Table 5.12.

Table 5.10: Track Substructure Layer Modulus Values for the Madison Street Bridge Approach Estimated Through Iterative Analysis Using GeoTrack – Before Correcting for Contributions Due to Tie-Gaps

	Madison 12 ft (MPa)				Madison 60 ft (MPa)		
Layer	Nov 2012	Jan 2013	June 2013	Layer	Nov 2012	Jan 2013	June 2013
Ballast	21	14	17	Ballast	29	28	25
Fouled Ballast	21	14	17	Fouled Ballast + Hardpan	61	68	63
Hard Pan	77	51	56	Silty Clay	36	39	33
Grey Sandy Loam + Cinder	34	24	26	Silty Clay	40	40	40
Brown Silty Clay	42	39	41	Fat Clay	59	58	59

Table 5.11: Track Substructure Layer Modulus Values for the Caldwell Street Bridge Approach Estimated Through Iterative Analysis Using GeoTrack – Before Correcting for Contributions Due to Tie-Gaps

	Caldwell West (MPa)				Caldwell East (MPa)		
Layer	Nov 2012	Jan 2013	June 2013	Layer	Nov 2012	Jan 2013	June 2013
Ballast	20.5	21	23.5	Ballast	22.5	20	30
Fouled Ballast	20.5	21	23.5	Fouled Ballast + Hardpan	59	40	48
Brown Silty Sand	116	121.5	127	Possible HMA Layer (25 mm) + Moist Sand	72	68	74
Silty Clay	40	42	45	Silty Clay	30.5	27	30
Moist Soft Silty Clay	86.5	92	108	Fat Clay	63.5	55.5	66

Table 5.12: Track Substructure Layer Modulus Values for the Upland Street Bridge Approach Estimated Through Iterative Analysis Using GeoTrack – Before Correcting for Contributions Due to Tie-Gaps

	Upland 15 ft (MPa)				Upland 60 ft (MPa)		
Layer	Aug 2012	Jan 2013	June 2013	Layer	Aug 2012	Jan 2013	June 2013
Ballast	20	15	5	Ballast	48	51	75
Fouled Ballast	40	35	35	Fouled Ballast	19	48	51
Sandy Loam	35	28	31	Sandy Loam	33	30	31
Thin Sand Layer	55	55	55	Clayey Silt	38	31	32
Sandy Load	85	85	85	Sandy Loam	73	60	70

As seen from the tables, assuming uniform contact between at the tie-ballast interface (or assuming no gap underneath the tie) led to the estimation of significantly low ballast layer modulus values (mostly close to 20 megapascal (MPa)). These values were significantly lower than typical ballast layer modulus values reported in the literature (Sussmann and Selig, 2000), and therefore need to be revised through elimination of tie-gap contributions from the LVDT 1 transient deformations. The errors introduced by this assumption of no gap at the tie-ballast interface were primarily due to the estimated ballast and sub-ballast layer moduli; the estimated modulus values for the underlying track substructure layers were more reasonable. For example, estimated modulus values for the underlying substructure layers ranged between 30 MPa to 80 MPa in most cases. The next step in this research effort involved an estimation of the track substructure layer modulus values after eliminating the tie-gap contributions from the transient deformation values recorded by the top-most LVDTs in the MDD system.

5.5.5 Track Substructure Layer Modulus Values Estimated After Correcting LVDT 1 Displacements for Tie-Gap Contributions

To calculate the track substructure layer moduli for a more accurate representation of the field load-deformation behavior of the ballast layer, it was necessary to subtract the tie-gap magnitudes from the transient deformations recorded by the top-most LVDT in an MDD system. Tie-gap values estimated in Section 5.4.1 were subtracted from the peak transient displacements recorded by the top-most LVDTs to calculate the "Corrected Layer 1 Deformation" values, which can be said to represent the ballast layer deformation under train loading. Such corrected layer 1 deformation values for the Madison, Caldwell, and Upland Street bridge approaches are listed in Table 5.13, Table 5.14, and Table 5.15, respectively. Table 5.16 through Table 5.18 present the revised track substructure modulus values estimated using GeoTrack after removal of the tie-gap contributions from LVDT 1 measurements. Figures showing the exact match between the field-measured and GeoTrack-predicted substructure layer deformations using the final set of layer moduli are included in Appendix A-2.

Comparing the estimated track substructure layer modulus values before and after the consideration of the tie-gap magnitudes indicated a significant increase in the estimated ballast and sub-ballast layer moduli for the latter case, which was more representative of values reported in the literature. This iterative approach to estimating track substructure layer moduli using GeoTrack will be used in Section 6 to evaluate the effectiveness of individual remedial measures applied at the Amtrak NEC bridge. The estimated substructure layer moduli were particularly useful as initial modulus estimates during advanced numerical modeling of railroad track transitions, which will be discussed in Section 7 of this report.

Table 5.13: Corrected Layer 1 Deformations for the Madison Street Bridge Approach Calculated by Subtracting the Tie-Gap Magnitudes from Transient Deformations Recorded by the Top-Most LVDT

	Location	Field Measured Layer 1 Deformation (mm)	Tie Gap Estimated (mm)	Corrected Layer 1 Deformation (mm)
Aug 2012	12 FT	0.83962	0.5454	0.29422
	60 FT	1.9038	1.1209	0.7829
Nov 2012	12 FT	1.1875	0.9219	0.2656
	60 FT	0.74028	0.5873	0.15298
Jan 2013	12 FT	1.5979	1.3731	0.2248
	60 FT	0.88728	0.6085	0.27878
June 2013	12 FT	1.7133	1.4275	0.2858
	60 FT	0.96554	0.7637	0.20184

Table 5.14: Corrected Layer 1 Deformations for the Caldwell Street Bridge Approach Calculated by Subtracting the Tie-Gap Magnitudes from Transient Deformations Recorded by the Top-Most LVDT

	Location	Field Measured Layer 1 Deformation (mm)	Tie Gap Estimated (mm)	Corrected Layer 1 Deformation (mm)
Nov 2012	West	1.52	0.978	0.542
	East	0.976	0.7099	0.2661
Jan 2013	West	1.5	0.9252	0.5748
	East	1.04	0.7166	0.3234
June 2013	West	1.51	1.007	0.503
	East	0.794	0.618	0.176

Table 5.15: Corrected Layer 1 Deformations for the Upland Street Bridge Approach Calculated by Subtracting the Tie-Gap Magnitudes from Transient Deformations Recorded by the Top-Most LVDT

	Location	Field Measured Layer 1 Deformation (mm)	Tie Gap Estimated (mm)	Corrected Layer 1 Deformation (mm)
Aug 2012	15 FT	1.712	1.5286	0.1834
	60 FT	0.4537	0.3435	0.1102
Nov 2012	15 FT	2.6261	1.9836	0.6425
	60 FT	0.34659	0.2364	0.11019
Jan 2013	15 FT	1.594	1.3242	0.2698
	60 FT	0.40564	0.2819	0.12374
June 2013	15 FT	4.5513	3.864	0.6873
	60 FT	0.31634	0.2176	0.09874

Table 5.16: Track Substructure Layer Modulus Values for the Madison Street Bridge Approach Estimated Through Iterative Analysis Using GeoTrack – After Correcting for Contributions Due to Tie-Gaps

	Madison 12 ft (MPa)					Madison 60 ft (MPa)			
Layer	Aug 2012	Nov 2012	Jan 2013	June 2013	Layer	Aug 2012	Nov 2012	Jan 2013	June 2013
Ballast	70	94	102	78	Ballast	32	155	96	105
Fouled Ballast	70	94	102	78	Fouled Ballast + Hard Pan	56	80	80	60
Hard Pan	37	51	57	40	Silty Clay	35	39	41	34
Grey Sandy Loam + Cinder	41	60	42	39	Silty Clay	35	39	41	34
Brown Silty Clay	36	36	38	35	Fat Clay	54	50	54	49

Table 5.17: Track Substructure Layer Modulus Values for the Caldwell Street Bridge Approach Estimated Through Iterative Analysis Using GeoTrack – After Correcting for Contributions Due to Tie-Gaps

	Caldwell West (MPa)				Caldwell East (MPa)		
Layer	Nov 2012	Jan 2013	June 2013	Layer	Nov 2012	Jan 2013	June 2013
Ballast	52	57	50	Ballast	80	60	125
Fouled Ballast	52	57	50	Fouled Ballast + Hardpan	60	49	50
Brown Silty Sand	126	130	130	Possible HMA Layer (25 mm) + Moist Sand	65	70	75
Silty Clay	38	39	35	Silty Clay	27	27	27
Moist Soft Silty Clay	80	75	80	Fat Clay	55	50	55

Table 5.18: Track Substructure Layer Modulus Values for the Upland Street Bridge Approach Estimated Through Iterative Analysis using GeoTrack – After Correcting for Contributions Due to Tie-Gaps

	Upland 15 ft (MPa)					Upland 60 ft (MPa)			
Layer	Aug 2012	Nov 2012	Jan 2013	June 2013	Layer	Aug 2012	Nov 2012	Jan 2013	June 2013
Ballast	153	40	100	34	Ballast	184	205	180	230
Fouled Ballast	80	111	87	77	Fouled Ballast	19	57	60	54
Sandy Loam	33	43	39	42	Sandy Loam	31	30	31	31
Thin Sand Layer	33	43	39	42	Thin Sand Layer	37	33	31	32
Sandy Loam	123	110	118	111	Sandy Loam	70	70	64	70

5.7 Summary

This section presented results from advanced analyses of transient response data collected at the instrumented bridge approaches. The objective was to get a better understanding of the load-deformation behavior of railroad track transitions. Several mathematical and data analysis tools were first introduced in this section followed by discussions on the load-deformation behavior of the tie-ballast interface. This included discussions on methods to quantify the gap at the tie-ballast interface as well as mechanisms contributing to the negative displacement (lift-off) of the instrumented tie due to train passage. This was followed by a discussion on the use of individual layer accelerations calculated from the MDD data under transient loading and the displacement time-histories to make important inferences regarding track dynamic response at the instrumented bridge approaches. Finally, the GeoTrack software program was introduced as a tool for applying an iterative process to back calculate track substructure layer moduli based on the field-measured transient layer deformation results. The next section will present findings on the performances of implemented remedial measures to mitigate the problem of recurrent differential movement at track transitions.

6. Implementation of Remedial Measures and Performance Monitoring of Remediated Bridge Approaches

Sections 4 and 5 of this report presented findings based on the performance monitoring of instrumented bridge approaches along Amtrak's NEC and NS's N-Line mainline. Data from the instrumented bridge approaches identified the ballast layer as the major contributor toward differential movement at these bridge approaches. The ballast layer transient deformations increased with excessive vibrations at near-bridge locations, which led to loss of support underneath the ties, creating "hanging tie" conditions. Such inadequate support underneath ties can significantly increase the dynamic loads applied to the track structure, which in turn leads to increased layer settlements with time. To avoid and eliminate this condition and its detrimental consequences, researchers identified remedial measures that would mitigate excessive vibrations within the ballast layer and facilitate better support underneath the ties. After extensive review of the published literature and discussions with railroad industry partners, appropriate remedial measures were selected for implementation on the entrance sides of the bridges over Upland and Madison Streets. Details regarding the installation of these remedial measures are presented in this section. Data collected from the instrumentation as well as through periodic track geometry surveys were used to make conclusions regarding the effectiveness of each remedial measure for mitigating the problem of differential movement at track transitions.

The team assessed the effectiveness of the remedial measures through analysis of track geometry MDD and strain gauge data. The conclusions made regarding the performance of the bridge approaches upon remediation were based on data collected during this project only. It is not the intention of the research team to advocate in favor or against any of the remedial measures. The following sections discuss the effectiveness of individual remedial measures assessed in light of the transient response data and the track geometry car records.

6.1 Selection of Bridge Approaches for Remedial Measure Implementation

Three different remedial measures – (1) chemical (polyurethane) grouting, (2) stone-blowing, and (3) installation of under tie pads (UTPs) – were selected to improve ballast settlement conditions. The objective was to monitor the performances of remediated bridge approaches over a reasonable time period to collect and document engineering data on the effectiveness of each remedial measure. Field performance trends presented in Sections 4 and 5 established that the near-bridge locations at both Upland and Madison Street bridge approaches experienced significant ballast settlement problems leading to a rapid deterioration in track geometry. The Caldwell Street bridge approach did not experience significant track geometry defects and was eliminated as a candidate location for remedial measure implementation.

To facilitate the comparison of a particular bridge approach before and after remediation, it was important that all remedial measures be implemented at approach locations that exhibited similar track substructure conditions and that were exposed to similar train traffic conditions. Drastic changes in the track substructure or traffic conditions may result in different dynamic behavior at the transition, which may not be similar to the trends summarized in Sections 4 and 5 of this report. This phenomenon can be easily explained using the example of Amtrak's NEC near Chester, PA. Track 2 near Chester predominantly carries northbound traffic, whereas the predominant traffic direction for Track 3 is southbound. Therefore, both the Madison (Track 2; south approach) and Upland (Track 3; north approach) Street bridge approaches instrumented

during this project represented “entrance side” traffic conditions, with trains predominantly moving from the “soft” approach embankment to the “stiff” bridge deck. Similar traffic conditions could be observed for the north approach of Madison Street bridge along Track 3 and the south approach of Upland Street bridge along Track 2. Considering the short spans of these bridges, it could safely be assumed that the track substructure conditions did not change drastically from one side of the bridge to the other. It was reasonable to assume that approaches located diagonally across each other on either side of a particular bridge represented similar substructure and traffic conditions.

As all instrumentation were originally placed on the “entrance side” of bridge approaches, the team decided to implement all remedial measures on the entrance sides as well. Accordingly, for the Upland Street bridge approach, the approaches receiving remedial measures were (a) Track 3 on the north approach and (b) Track 2 on the south approach. Corresponding locations for the Madison Street bridge approach were (a) Track 2 on the south approach and (b) Track 3 on the north approach. The inherent assumption in this method was that approaches on either side of a particular bridge exposed to similar traffic conditions exhibited similar long-term and short-term settlement trends. Investigation of the historical track geometry records at the Upland and Madison Street bridge approaches supported this assumption. Figure 6.1 shows a schematic layout of the bridge approaches and locations selected for implementation of the individual remedial measures.

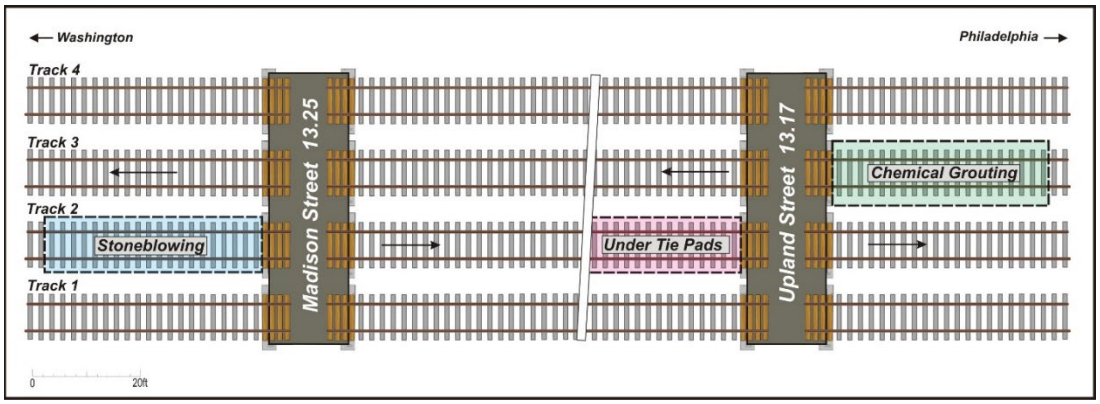

Figure 6.1: Schematic Layout of Selected Bridge Approaches and Relative Locations of Remedial Measures

6.2 Chemical Grouting

Chemical grouting, also referred to here as polyurethane injection, has been successfully used to reduce excessive ballast vibrations and long-term permanent deformations (Woodward et. al, 2007; Banimahd et al., 2011; Woodward et al., 2009). When properly applied, chemical grouts bind the ballast particles together, thus reducing excessive vibrations and particle migration. An engineered polyurethane grouting approach was adopted in this study to reduce frequent ballast settlement tendency and to create better support conditions underneath the crossties. The research team partnered with Thomas Planert of Ssesco Inc. (now with Substrate Testing Inc.) to perform chemical grouting work in this project.

Chemical grouting at the Upland Street bridge north approach (Track 3) was completed July 17, 2014. The grout was a two-part polyurethane and had a density of approximately 240 kg/m^3 (15 pounds per cubic foot or 15 pcf), a compressive strength of 5,516 kPa (800 pounds per square

inch, or psi), and a tensile strength of 1,034 kPa (150 psi). The primary factor governing selection of the grout material was its ability to withstand movement. For example, the compressive strength of 5.5 megapascals (MPa) (800 psi) corresponds to 0 percent strain. The same grout presents a compressive strength of 13.8 MPa (2000 psi) at 10 percent strain. Such resilience of the grout is important to ensure the grouted ballast can withstand vibrations induced upon train loading.

The first step in the process involved conducting a top-of-rail (TOR) survey of the track to identify geometry defect locations and to determine the desired track profile. Once the lift elevations for all ties were determined, the track profile could be plotted to determine the exact location of the bump being addressed. A design profile was set by using a straight line to connect the track elevation on the bridge deck to a point far away from the bridge. Laser markers custom-developed for this project were used to mark the target elevation of the track, and the track was lifted using hand-operated track jacks. Grout was then injected adjacent to the ties to create better support conditions and to hold the ballast particles together. The jacks were removed shortly after injection, as the grout has a relatively short setting time. The research team was able to open the track to train traffic immediately after the grout injection. Multiple injection points were used along the length of the tie to ensure adequate permeation of the grout into the ballast. Injection at a given point was stopped when excessive grout was observed to extrude out from the ballast surface. Photographs showing different steps involved in the chemical grouting process are presented in Figure 6.2.

(a) (b)

(c)

Figure 6.2: (a) Grout Injection Adjacent to the Tie Using a Proprietary Injection System; (b) Excavation of Ballast Around Crossties to Confirm Adequate Permeation of Grout Into the Ballast Layer; (c) Grout Extruding Out From Injection Locations After Expansion

6.2.1 Conclusions Based on Layer Settlement Trends and Track Geometry Records

Settlements or permanent deformations registered by individual track substructure layers were used as the first criterion to assess the effectiveness of the chemical grouting as an applied remedial measure. Figure 6.3 presents the same figure that was presented in Figure 4.2(a), depicting individual layer settlements recorded by the MDD installed at the Upland Street bridge approach, near-bridge location. This figure highlights the ballast layer (LVDT 1) as the primary contributor toward the differential movement accumulation at this particular bridge approach. To make conclusions regarding the effectiveness of chemical grouting as a remedial measure, close attention was paid to the part of the curve showing layer settlement values after approximately 700 days. As annotated in the figure, chemical grouting was performed at this location after approximately 700 days from the day of the first instrumentation effort in July 2012. Note that the slope of the settlement line reduced initially (between July 22, 2014, and September 9, 2014) after the chemical grouting. However, the rate of the settlement increased soon after, and a layer settlement value greater than 10 mm was recorded in April 2015. The effect of chemical grouting was short-lived.

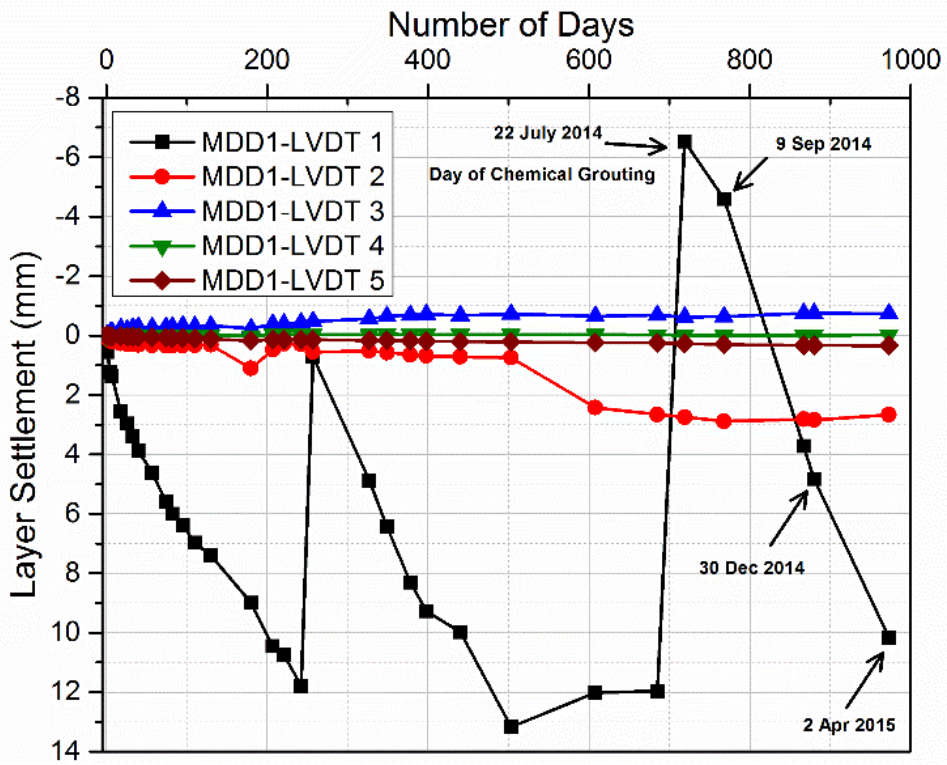

Figure 6.3: Layer Settlement Trends for the Upland Street Bridge Approach - Near-Bridge Location (15 ft From the North Abutment; Track 3)

Track space curve and roughness values for the Upland Street bridge approach are plotted against time in Figure 6.4. Note that the application of chemical grout resulted in an initial reduction in the track roughness and a more consistent track profile (reflected from a smooth space curve). However, the roughness increased significantly after January 2015. Once the chemical grout section was finally surfaced, there was likely quite a bit of urethane fouling the

ballast, and this, combined with its already high degree of fouling, resulted in a short-lived geometry correction.

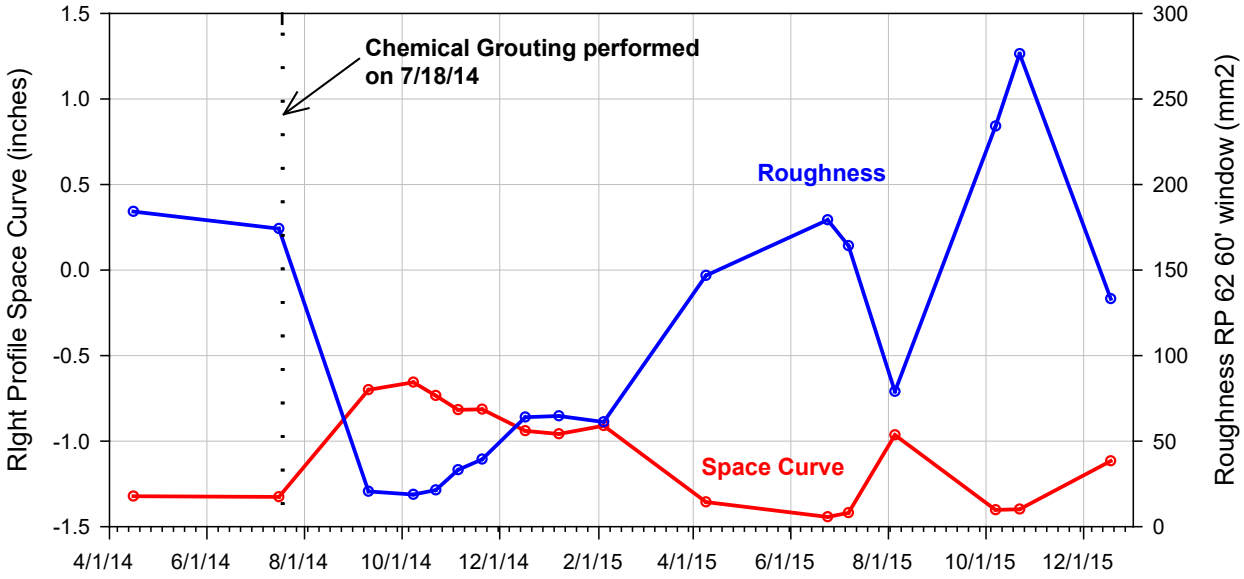

Figure 6.4: Space Curve and Running Roughness Data for the Upland Street Bridge Approach (North Approach; Track 3) Showing the Effect of Chemical Grouting

6.2.2 Inferences Based on Transient Response Data

The transient response data at the Upland Street bridge approach (north approach; Track 3) were collected at three time periods – July 2014, January 2015, and May 2015. Transient responses of the track substructure layers were used to make conclusions regarding any changes in the effectiveness of chemical grouting as a remedial measure to mitigate the problem of differential movement at track transitions.

Figure 6.5(a) shows the ballast transient deformations for the Upland Street bridge approach (15 ft or 4.6 m from the north abutment) before and after chemical grouting. Note that the peak transient displacements recorded by the LVDT mounted at the tie-ballast interface diminished from 7 mm before grouting to 0.25 mm after grouting. This indicated that the grout application significantly improved the support conditions underneath the tie, and also reduced excessive vibrations and particle migration within the ballast layer. Figure 6.5(b) shows the space curve for the same bridge approach established through geometry car data obtained from Amtrak within 3 months of the grouting application. The light gray lines corresponding to location 13+0800 ft indicate the original space curve before implementation of the chemical grout. The space curves collected after grouting show that the dip corresponding to a distance of 13+0800 ft was eliminated during the grouting process, and the "corrected" track profile was maintained for a period of time.

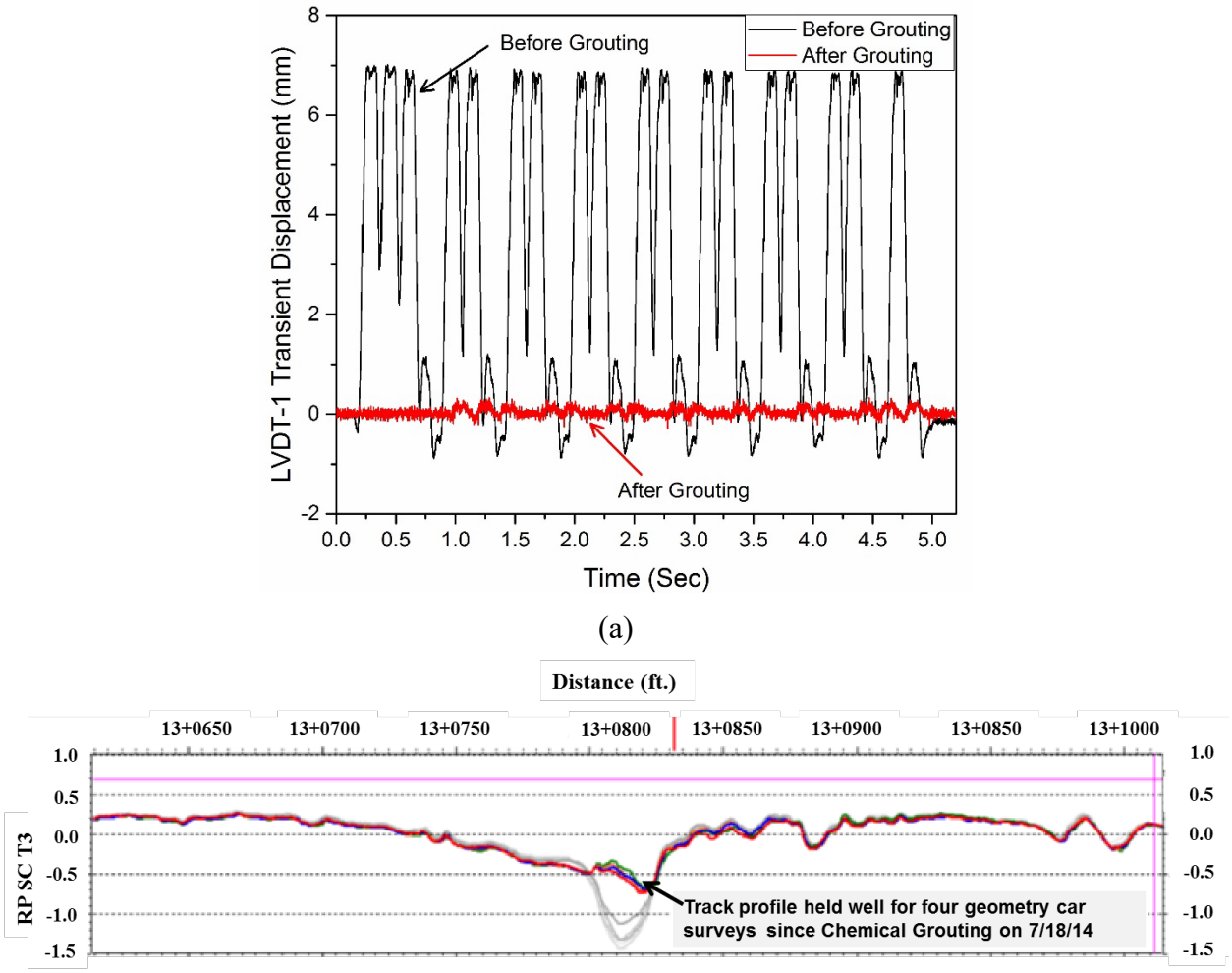

Figure 6.5: Effect of Chemical Grouting on (a) Ballast Transient Deformations and (b) Track Space Curve at the Upland Street Bridge Approach

Figure 6.6 presents the full displacement time-history for an Acela Express train recorded at the Upland Street bridge approach on July 22, 2014. Interestingly, the top LVDT recorded lower transient deformations at the near-bridge location compared to the open-track location. The chemical grouting application extended 40 ft in length from the bridge abutment, and the open-track location was 60 ft from the bridge abutment.

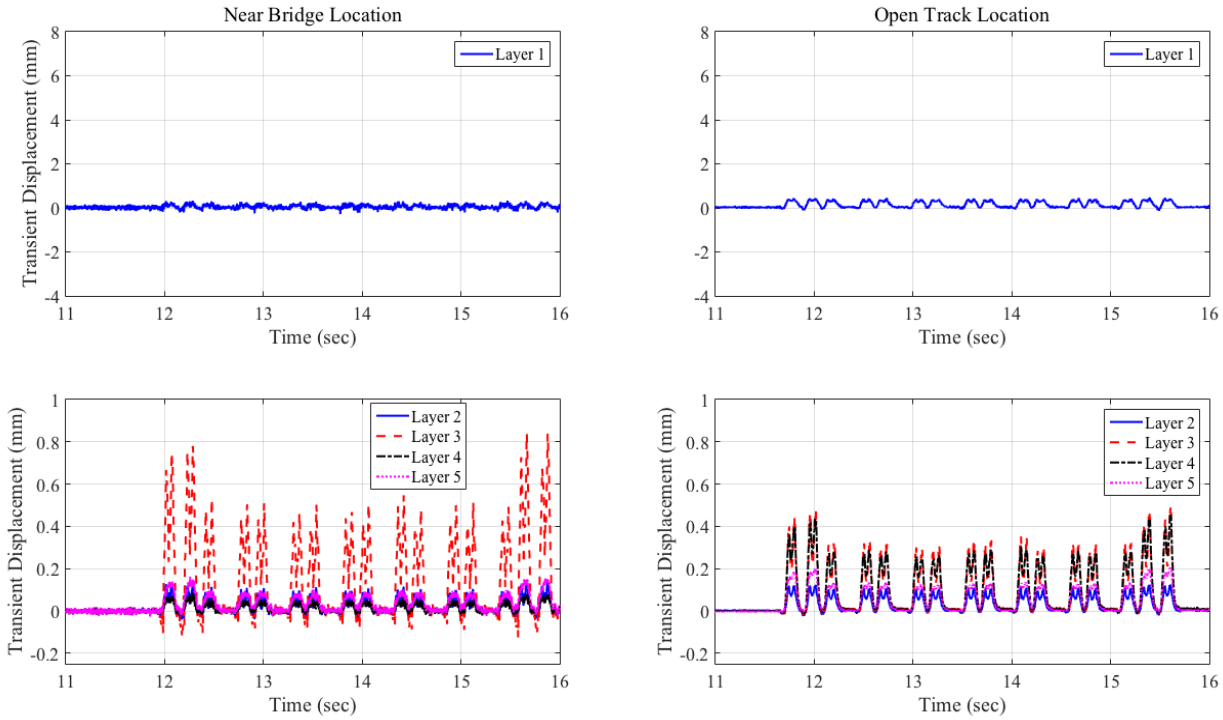

Figure 6.6: Displacement Time-Histories Recorded at the Upland Street Bridge Approach; Data Collected on July 22, 2014; Train 1 (Acela Express)

Although the data collected immediately after the chemical grouting (presented in Figure 6.5 and Figure 6.6) highlighted significant improvements in the track response under loading, this trend was observed to change drastically during subsequent data acquisition activities. Figure 6.7 and Figure 6.8 present displacement time-histories collected at the Upland Street bridge approach in January 2015 and May 2015, respectively. As shown in Figure 6.7, the transient deformation magnitudes recorded by the top-most LVDT (LVDT 1) are significantly higher than those recorded immediately after the grouting (see Figure 6.6) and show maximum values of approximately 3 mm. Layer 1, at the near-bridge location, also showed higher transient deformation values compared to the open-track location, which was different from the trend observed in Figure 6.6. This indicated that the support conditions underneath the tie at the near-bridge location deteriorated significantly between July 2014 and January 2015, thus resulting in transient deformation magnitudes that were higher than those recorded at the open-track location. It is also interesting to note that the layer 1 transient deformations for the open-track location remain relatively unchanged between July 2014 and January 2015. Transient response data collected in May 2015 (see Figure 6.8) showed similar trends when the data from near-bridge and open-track locations were compared. The data from May 2015 also showed significant negative displacement (approximately 3mm) values registered through the top LVDT. As discussed in Section 5, this could have been directly related to poor support conditions underneath the instrumented tie. Time-domain analyses of the transient displacement records therefore clearly established the gradual deterioration in tie support conditions with time for the Upland Street bridge approach (north approach, Track 3) where chemical grouting was performed to stabilize the ballast layer.

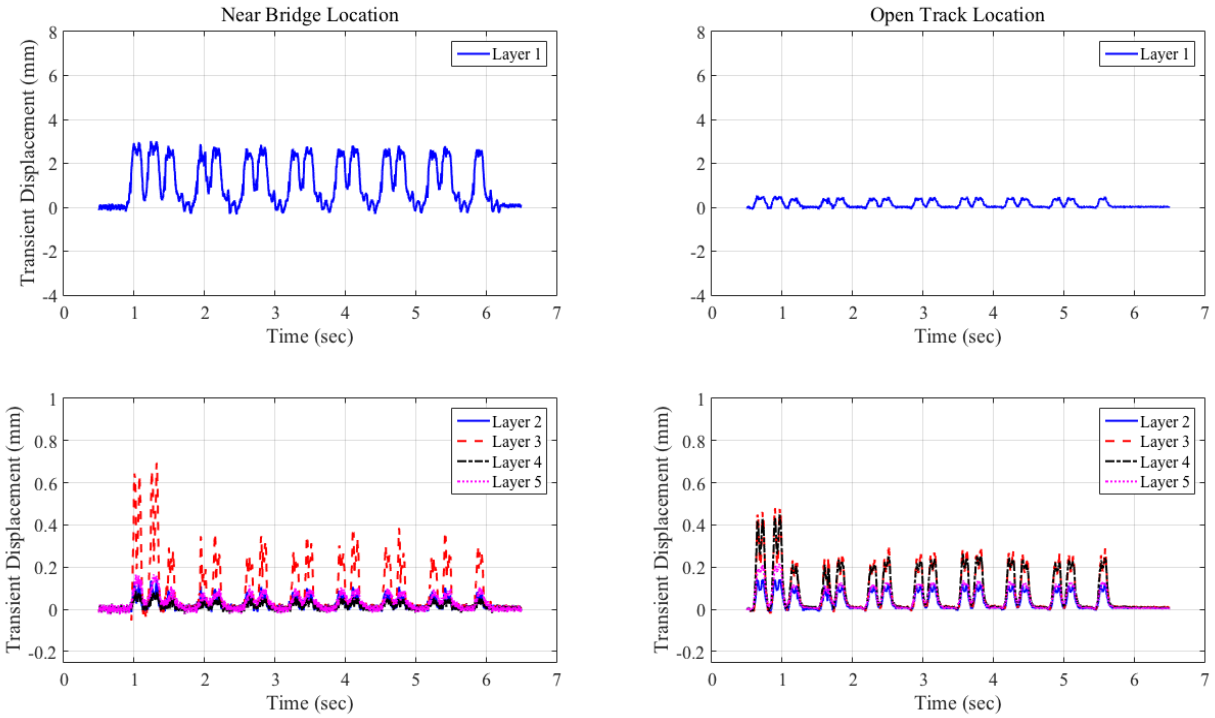

Figure 6.7: Displacement Time-Histories Recorded at Upland Street Bridge Approach; Data Collected in January 2015; Train 1

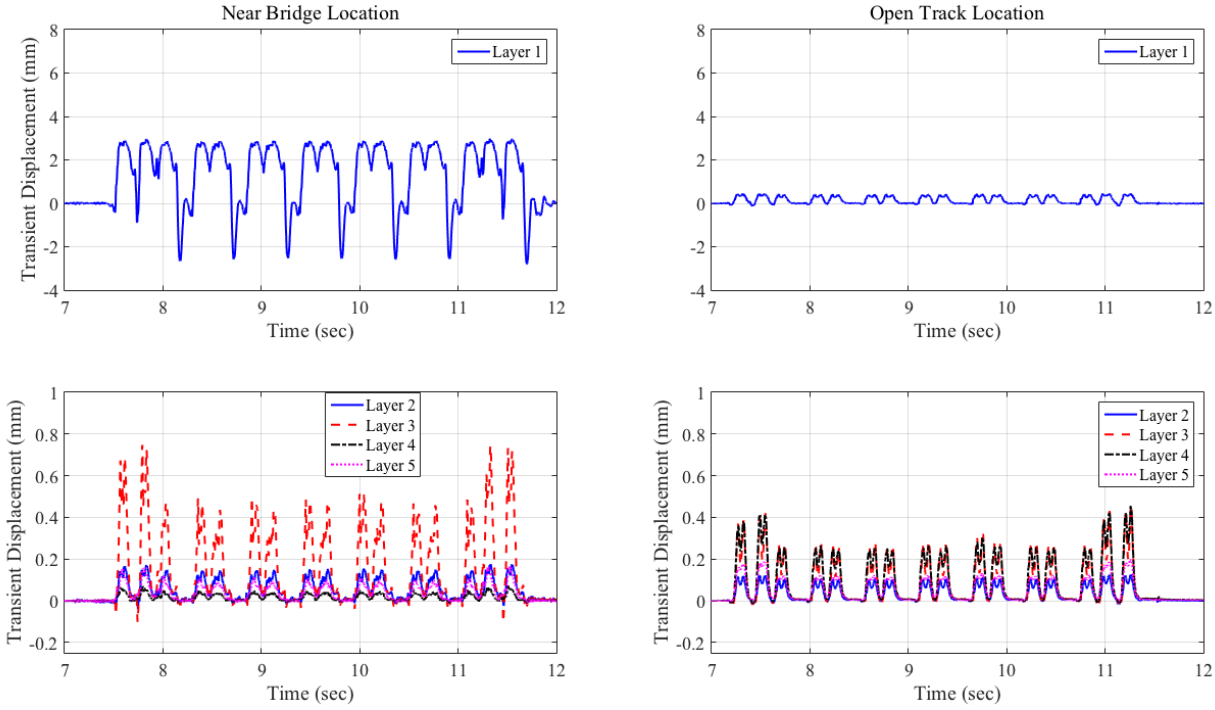

Figure 6.8: Displacement Time-Histories Recorded at Upland Street Bridge Approach; Data Collected in May 2015; Train 1 (Acela Express)

Figure 6.9 shows the normalized transient displacement values recorded by LVDT 1 at the Upland Street bridge approach (all displacements normalized to a load level of 100 kN). This figure is essentially an extension of similar data prior to the implementation of remedial measures, presented in Figure 4.14 of this report. To assess the effectiveness of chemical grouting as a remedial measure, particular attention needs to be paid to the part of the curve showing data after July 1, 2014. The immediate benefit of the chemical grouting effort was highlighted by the significantly reduced ballast layer displacements recorded at the near-bridge location on July 22, 2014. However, the normalized transient displacement value gradually increased since that time until the last set of data acquisition in May 2015. The normalized transient displacement values for the near-bridge location in May 2015 were still lower than the values recorded on July 1, 2014, immediately before the grout application. This may have indicated that although the track conditions had deteriorated significantly after application of the grout, they were still better than the track condition immediately before the grouting. However, no concrete evidence supporting this hypothesis was available. Figure 6.9 clearly shows that the grouting activity did not have any significant effect on the normalized transient response values at the open-track location.

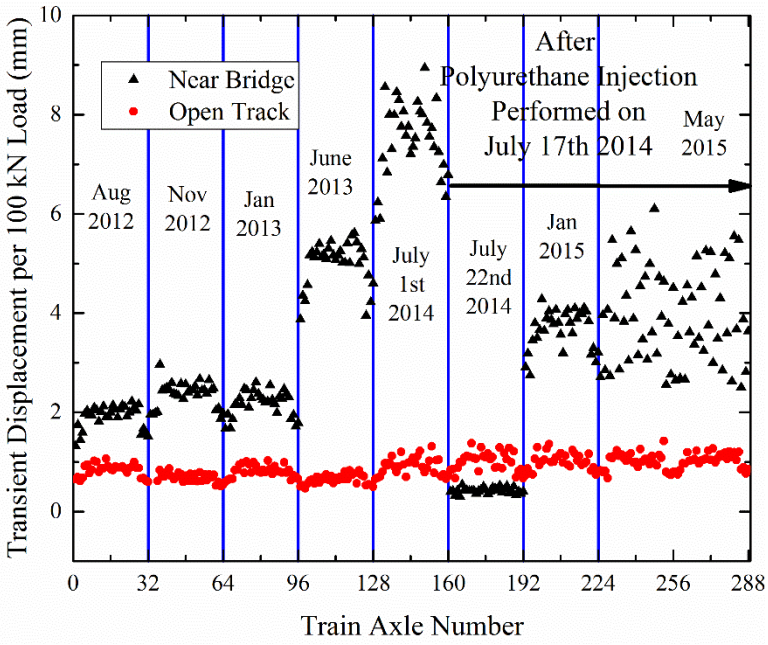

Figure 6.9: Ballast Transient Displacements Recorded at the Upland Street Bridge Approach Under the Passage of Acela Express Trains on Different Dates of Data Acquisition (Normalized to a Load of 100 kN)

Figure 6.10 shows the contributions, in percentage, of the ballast layer toward the total track transient deformations for the Upland Street bridge approach. This figure is an extension of Figure 4.42 and includes data since the chemical grouting effort. Immediately after the grouting, the contribution of the ballast layer toward the total transient deformation reduced significantly, but then showed a gradual increase though May 2015.

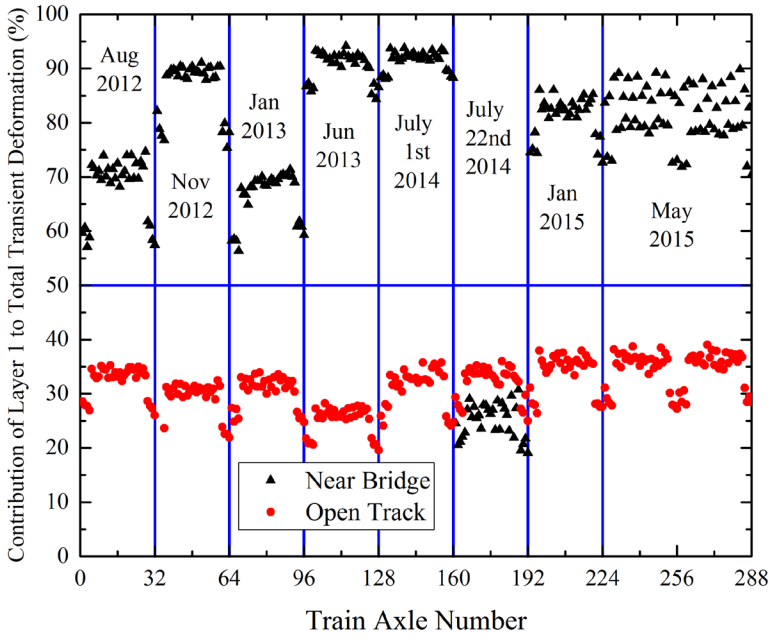

Figure 6.10: Contribution of the Ballast Layer Toward Total Transient Deformations Under Train Loading at the Upland Street Bridge Approach

6.2.3 Effect of Chemical Grouting on Dynamic Load Amplification

The team assessed the effect of chemical grouting on the dynamic load amplification characteristics at the Upland Street bridge approach; Figure 6.11 shows the percent amplification factors for the loads measured between the ties (vertical wheel load channel) and on top of the instrumented tie (tie reaction channel).

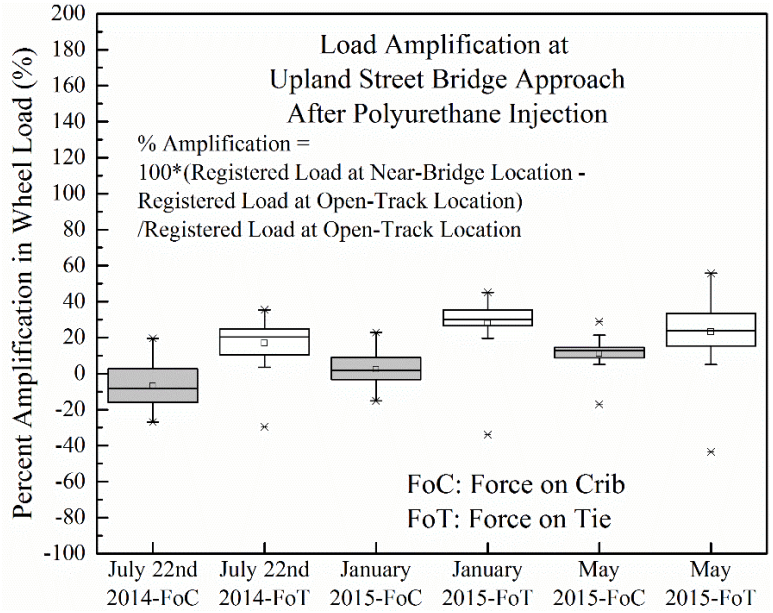

Figure 6.11: Load Amplification at Upland Street Bridge Approach After Chemical Grouting

This figure is an extension of Figure 4.40, and includes data after the chemical grouting effort. As shown in Figure 6.11, the percent load amplification values are consistently lower than 20 percent, which appears to be a significant improvement over the values before chemical grouting presented in Figure 4.40. Interestingly, the percent amplification values remained close to 20 percent even in May 2015, which corresponded to high transient deformations recorded by the top LVDT. This indicated that even though the effectiveness of chemical grouting to reduce transient deformations within the ballast layer diminished with time, it continued to perform adequately as far as its ability to reduce the dynamic load amplifications.

6.2.4 Effect of Chemical Grouting on the Gap at the Tie-Ballast Interface

Table 5.2 lists the gaps at the tie-ballast interface for the Upland Street bridge approach calculated using this new method. As an extension, Table 6.1 lists the gap magnitudes calculated at this location after the application of the chemical grout. For reference, the table also includes the values calculated on July 1, 2014, which was shortly before application of the chemical grout. As indicated in Table 6.1, application of the chemical grout resulted in an immediate reduction (from 6.45 mm to 0.04 mm) in the tie-gap magnitude at the near-bridge location. However, this gap magnitude increased to 2.29 mm in January 2015. Interestingly, the value calculated in May 2015 (1.23 mm) was lower than that in January 2015. No justification for this behavior could be found. Like the trend observed for the transient deformation magnitudes, the gap at the open-track location was not affected by the chemical grouting activity.

Table 6.1: Gap Quantification at the Tie-Ballast Interface Using the Progressive Load Threshold Approach: Upland Street Bridge Approach (After Chemical Grouting)

	15 ft from North Abutment		60 ft from North Abutment	
	Gap (mm)	Load Threshold (kN)	Gap (mm)	Load Threshold (kN)
1 July 2014	6.45	28	0.22	17
22 July 2014	0.04	21	0.26	14
January 2015	2.29	24	0.28	14
May 2015	1.23	22	0.30	11

6.2.5 Effect of Chemical Grouting on Layer Accelerations Analyzed in Time and Frequency Domains

Vertical layer accelerations calculated from the displacement time-histories are presented in Figure 6.12 through Figure 6.17 and allow analysis using time as well as frequency domains to evaluate the effectiveness of chemical grouting as a remedial measure. As shown in Figure 6.12, significantly low layer accelerations were calculated on July 22, 2014, immediately after the grout application. As already observed from the displacement time-histories (see Figure 6.5(a)), no negative displacement (tie liftoff) was observed. Figure 6.13 presents layer 1 accelerations for both the near-bridge and open-track locations, plotted in the frequency domain. As shown in the

figure, no significant contribution in the 7.5 Hz to 13 Hz frequency range was observed. As discussed in Section 5, frequencies between 7.5 Hz to 13 Hz can be directly correlated to negative tie displacements caused when the train leaves the approach embankment and moves onto to the bridge deck.

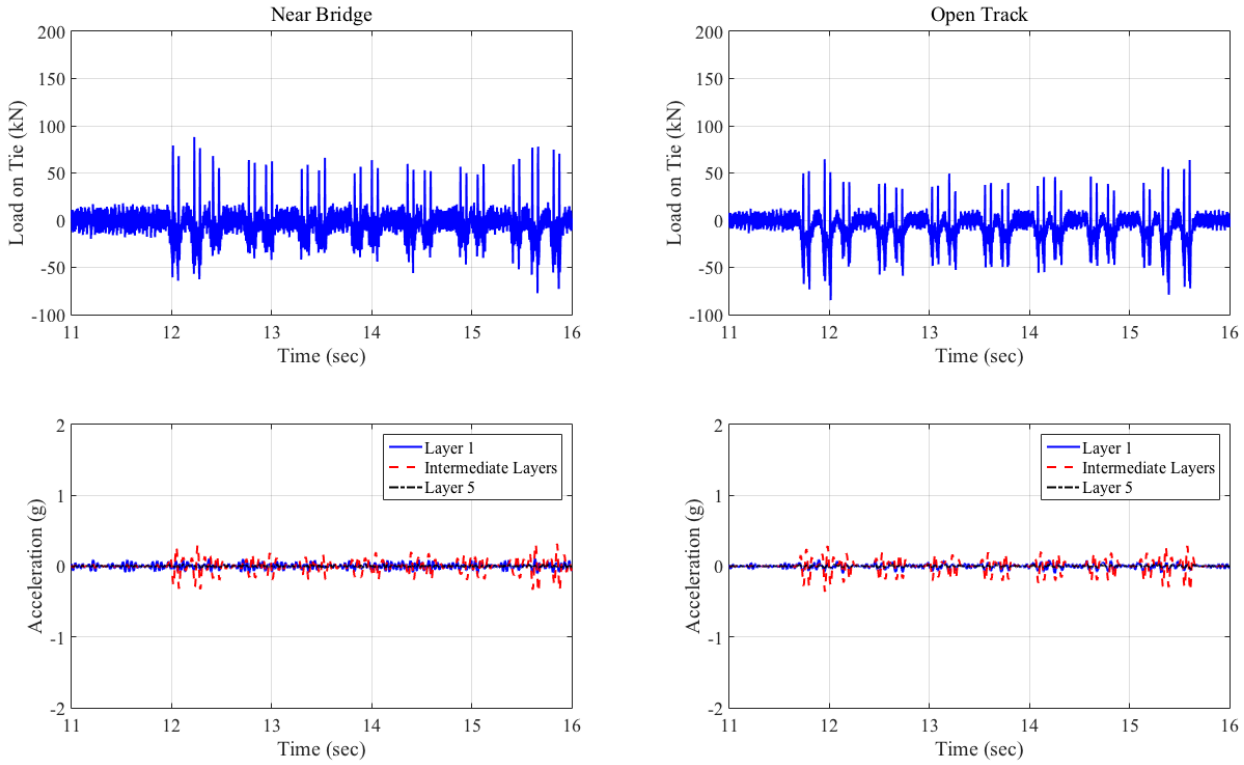

Figure 6.12: Load and Acceleration Time-Histories for the Upland Street Bridge Approach (Data Collected on July 22, 2014)

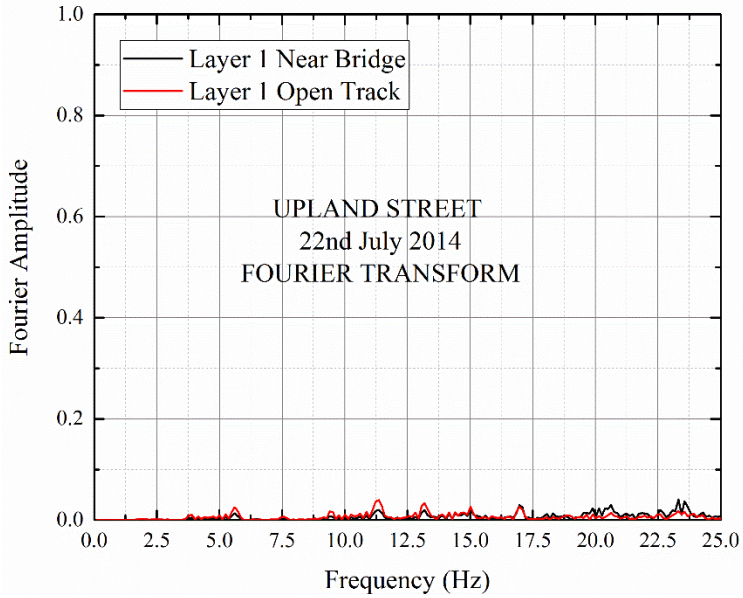

Figure 6.13: Layer 1 Accelerations for the Upland Street Bridge Approach Presented in the Frequency Domain (Data Collected on July 22, 2014)

Figure 6.14 and Figure 6.15 present similar data corresponding to the data collected in January 2015. A significant increase in the layer 1 accelerations at the near-bridge location can be observed compared to the data collected on July 22, 2014 (see Figure 6.12). This indicated a deterioration in the tie support conditions. Even though the acceleration magnitudes increased significantly compared to July 22, 2014, no significant negative displacement (or acceleration) was recorded in January 2015. However, as shown in Figure 6.16 and Figure 6.17, high magnitudes of acceleration and negative displacements were recorded for the near-bridge approach in May 2015. Frequency domain representation of the acceleration data (see Figure 6.17) showed dominant frequencies between 7.5 Hz to 13 Hz, which could have been linked to the excessive swinging motion of the tie. Peak accelerations just before and after the chemical grouting are summarized in Figure 6.18, which show significantly low acceleration values recorded for the near-bridge location on July 22, 2014, immediately after the chemical grouting. However, rapid deterioration of the support conditions was reflected through significantly increased peak acceleration values as recorded in January and May 2015. Note that the peak acceleration values calculated for the open-track location did not exhibit any significant change with time.

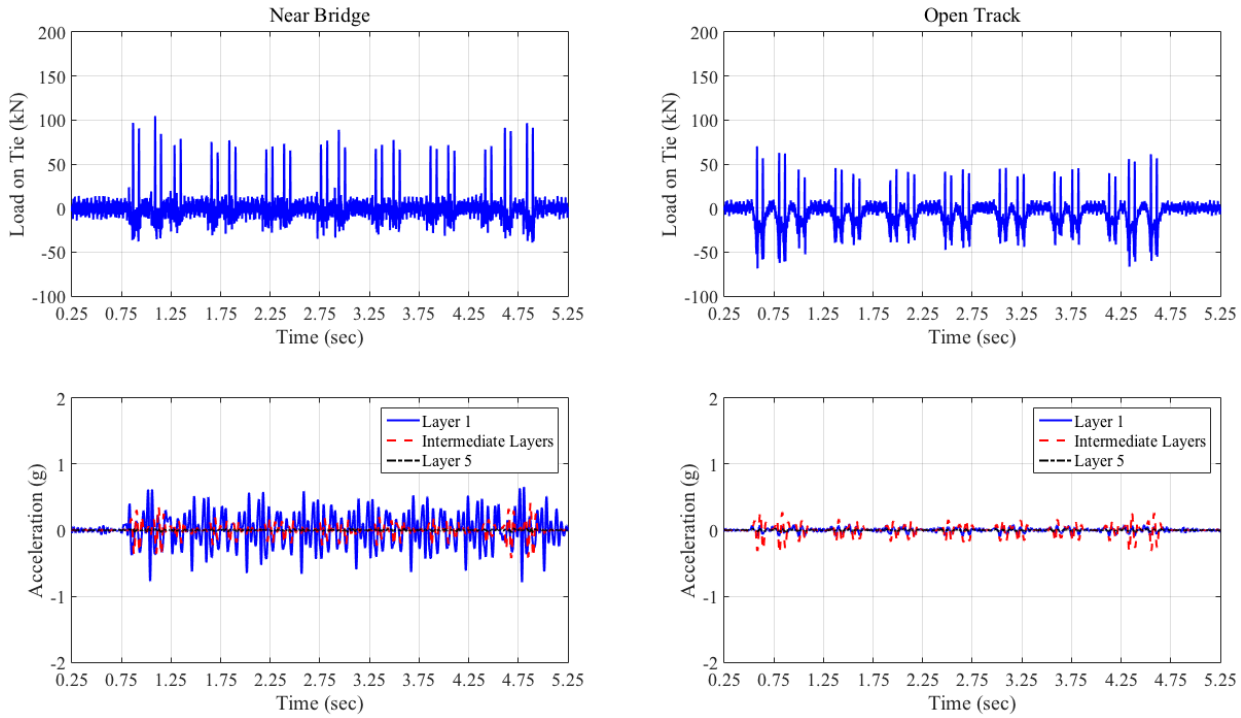

Figure 6.14: Load and Acceleration Time-Histories for the Upland Street Bridge Approach (Data Collected in January 2015)

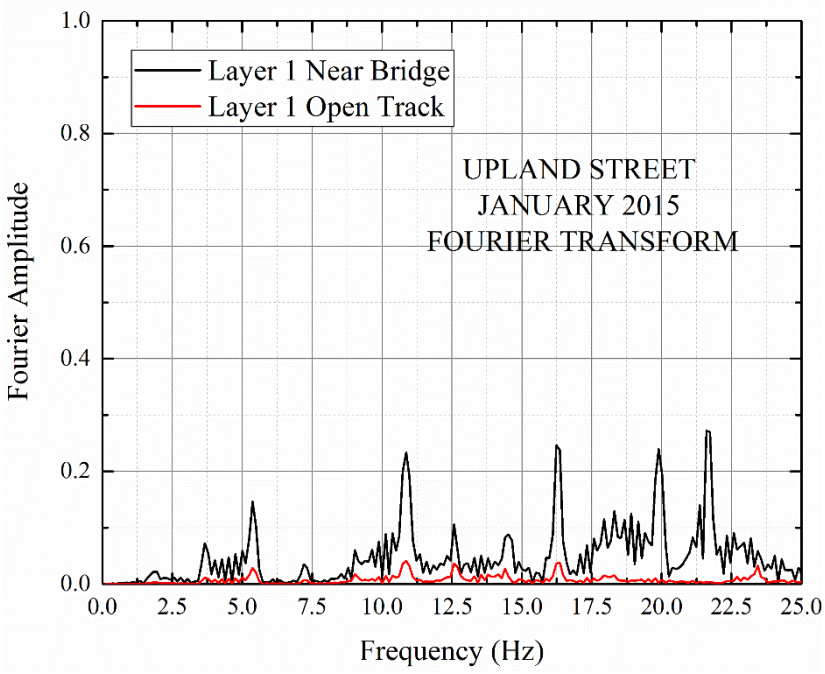

Figure 6.15: Layer 1 Accelerations for the Upland Street Bridge Approach Presented in the Frequency Domain (Data Collected in January 2015)

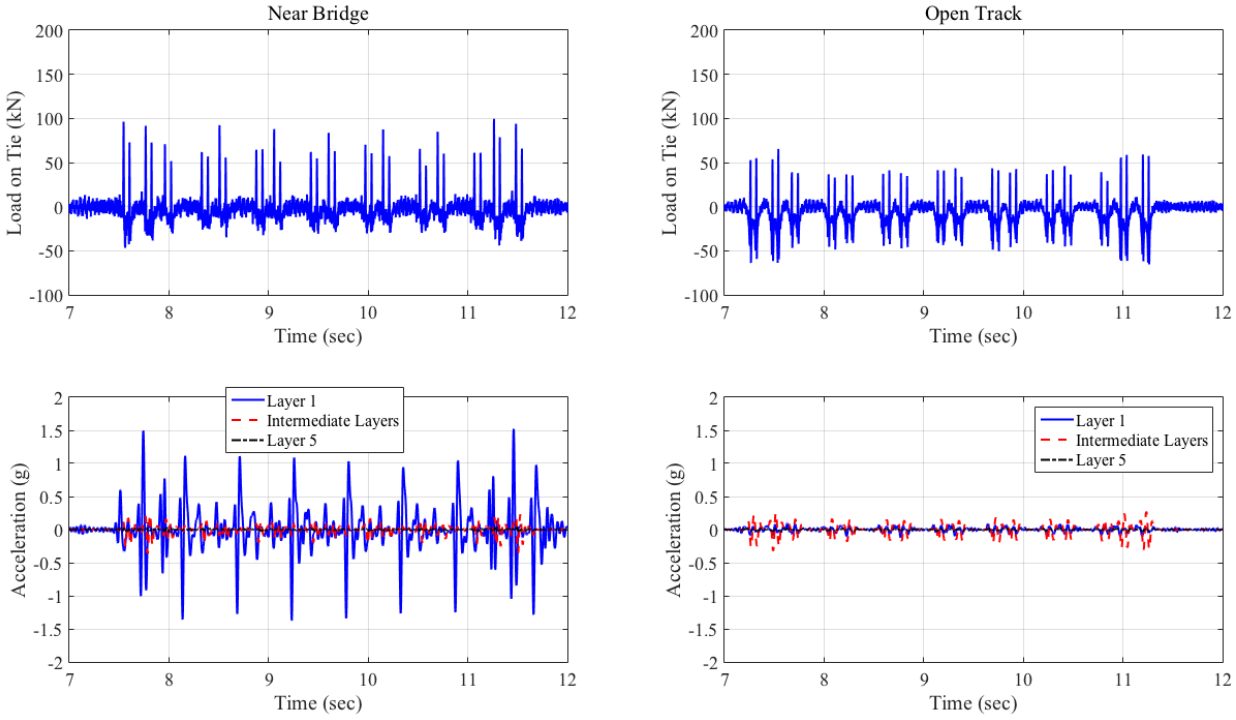

Figure 6.16: Load and Acceleration Time-Histories for the Upland Street Bridge Approach (Data Collected in May 2015)

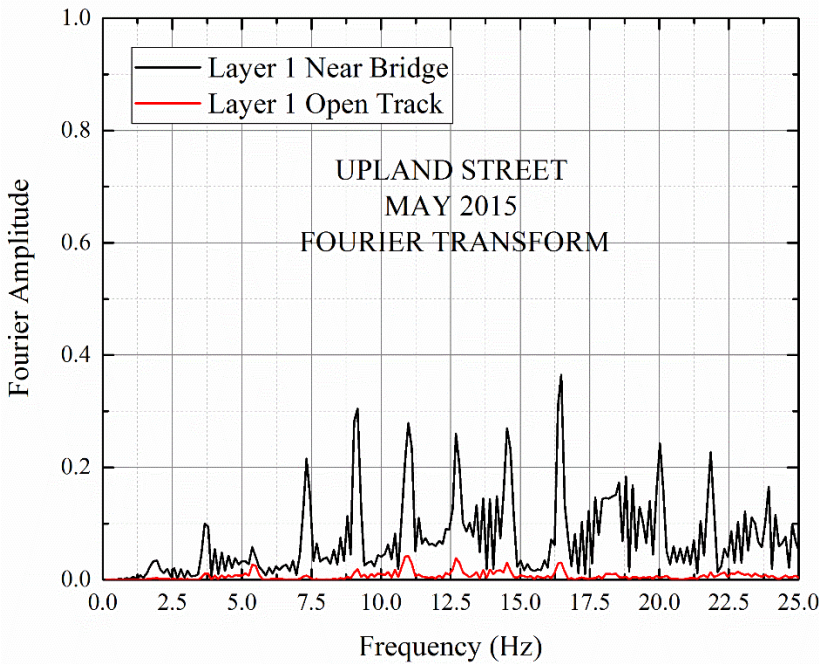

Figure 6.17: Layer 1 Accelerations for the Upland Street Bridge Approach Presented in the Frequency Domain (Data Collected in May 2015)

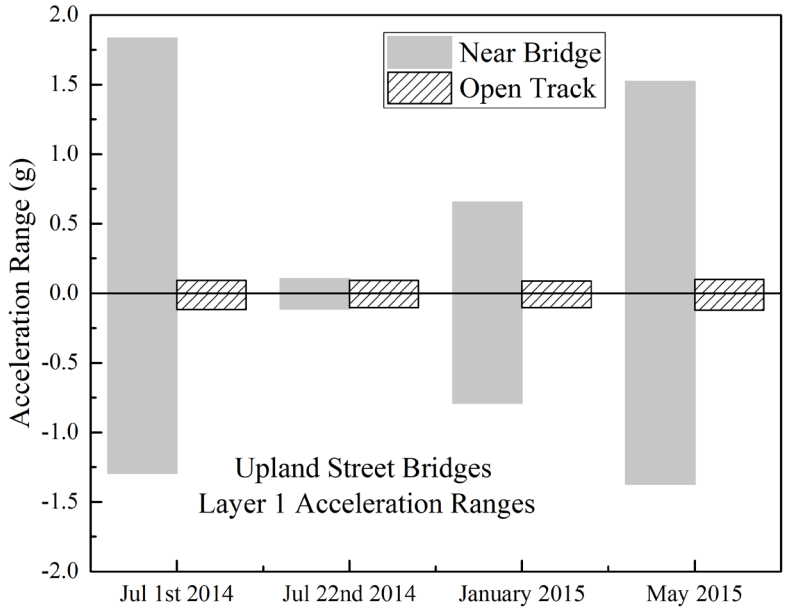

Figure 6.18: Summary of Peak Accelerations Recorded at the Upland Street Bridge Approach Under the Passage of Acela Express Trains – After Chemical Grouting

6.2.6 *Effect of Chemical Grouting on Tie Lift Off (Negative Displacement)*

Section 5.4.2 of this report discussed the negative displacement (lifting) of ties observed at the instrumented bridge approaches. Figure 5.17 presented the maximum and minimum transient displacements recorded for the instrumented tie at the Upland Street bridge approach prior to the implementation of any remedial measure. Figure 6.19 presents similar data after the chemical grouting as well as the last set of data collected (July 1, 2014) before application of the chemical grout. Significant reductions in the positive (downward) and negative (upward) displacements under loading are evident from Figure 6.19, with gradually increasing magnitudes corresponding to subsequent data acquisition efforts. High magnitudes of negative displacements were correlated in Section 5, with poor support conditions underneath the ties. Data presented in the figure can be used to conclude that most of the benefits achieved through chemical grouting of the Upland Street bridge approach (north approach; Track 3) had diminished by May 2015.

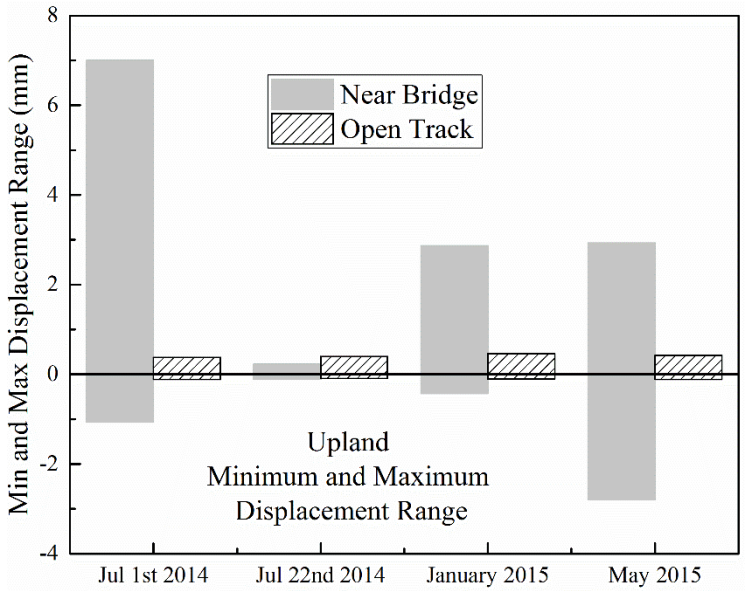

Figure 6.19: Maximum and Minimum Transient Displacements Recorded for the Instrumented Tie – Upland Street Bridge Approach – After Chemical Grouting

6.2.7 *Effect of Chemical Grouting on Track Substructure Layer Moduli*

Transient load and deformation data collected at the instrumented bridge approaches were used to iteratively back calculate individual track substructure layer modulus values using the GeoTrack software. Considering that the primary objective behind implementing the remedial measures was to stabilize the ballast layer, transient data collected after implementation of the remedial measures were used to quantify the increase (if any) in the individual track substructure layer moduli. Table 6.2 lists the back calculated layer modulus values for the Upland Street bridge approach (near-bridge location) after application of the chemical grout. For convenience, the data collected shortly before the grouting effort (data collected on July 1, 2014) is also included in the table.

Table 6.2: Track Substructure Layer Modulus Values for the Upland Street Bridge Approach Near-Bridge Location Estimated Through Iterative Analysis Using GeoTrack – After Chemical Grouting

Layer Number	Backcalculated Layer Moduli (MPa)			
	1 July 2014	22 July 2014	January 2015	May 2015
1	44	90	39	14
2	58	80	84	79
3	40	31	43	80
4	40	31	43	80
5	164	114	150	231

Table 6.2 indicates the modulus of layer 1 increased from 44 MPa to 90 MPa immediately upon application of the chemical grout. This directly corresponded to the drastically low transient deformation values observed just after grouting. Significantly reduced ballast modulus values corresponding to the measurements in January 2015 and May 2015 indicated deteriorated tie support conditions and increased transient deformations recorded by the top LVDT. Note that modulus values for layer 2 back calculated from all three measurements after the grout application were significantly higher than immediately before the grout application (an increase from 58 MPa to ~80 MPa).

6.2.8 Summary

The observed short lifespan of chemical grouting as a remedial measure at the Upland Street bridge approach can be explained by the presence of high amounts of fines (fouling material) in the ballast layer at this location. Presence of the fouling material, predominantly dust from degraded ballast particles, prevented the grout from developing strong bonds with individual ballast particles. This led to the grout-ballast bond breaking upon repeated loading, leading to diminishing effects of the remedial measure; high rates of track settlement resumed. To validate this hypothesis, the research team performed chemical grouting at a second bridge approach (Morton and Potter Street bridge) less than 1 km northeast of the Upland Street bridge. Note that the approach at the Morton and Potter Street bridge also experienced recurrent differential movement problems over the years, although not of the same magnitude as the Upland and Madison Street bridges.

Figure 6.20 shows the space curve and running roughness profiles of the Morton and Potter Streets bridge approach. As shown in the figure, this approach maintained improved roughness and space curve profiles after application of the chemical grouting. Note that the ballast layer at this bridge approach was fairly clean and no sign of significant fouling was observed. Improved performance of this bridge approach since implementation of the chemical grouting supported the research team's hypothesis. Chemical grouting can prove to be an effective remedial measure to mitigate the problem of differential movement at track transitions provided adequate bonding between the grout and the ballast particles is achieved.

The performance of the chemical grout at the Morton and Potter bridge approach has not been monitored over a sufficiently long period. Track geometry at this bridge approach needs to be continuously monitored to accurately assess the effectiveness of chemical grouting as a remedial measure.

Moreover, adverse effects of unsuccessful grout applications on future track maintenance activities have yet to be explored. Track geometry deterioration at locations comprising grouted ballast layers will necessitate tamping and resurfacing activities in the future. However, the "bonded" nature of the ballast at these locations may offer increased resistance against penetration of the tamping tines. Continued performance monitoring of the grouted bridge approaches will provide valuable experience and data on these matters. Advanced numerical modeling approaches such as the DEM can be used to extensively study the inter-particle bond strength achieved through grouting and its comparative magnitude to the force exerted by tamping tines.

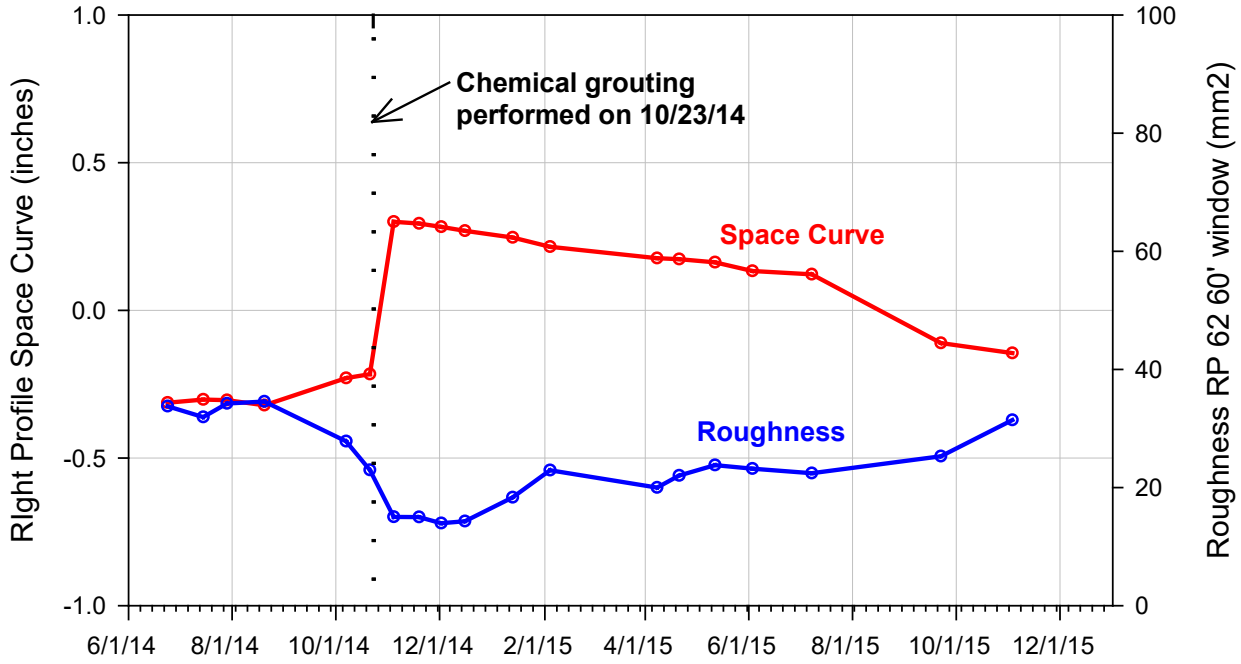

Figure 6.20: Space Curve and Running Roughness Data for the Morton and Potter Streets Bridge Approach

6.3 Stone-blowing

Stone-blowing (also referred to as "stoneblowing" or "stone injection") involves the addition of stone (or ballast) to the surface of existing ballast. Originally developed by British Railways, stone-blowing involves the following steps (Selig and Waters, 1994): (1) The geometry of the existing track is measured; (2) the precise track lift required at each crosstie to restore it to an acceptable geometry is calculated (note that a "designed over-lift" is always incorporated during this step, and will be discussed later in this section); (3) the volume of stone that needs to be blown beneath the sleeper to achieve such a lift is deduced from the known relationship between volume of added stone and residual lift; (4) the track is stone-blown. A schematic showing the steps involved in stone-blowing is presented in Figure 6.21.

Like the chemical grouting process, the first step in stone-blowing is to establish the current TOR profile through digital surveying, and to determine the design track profile. The target elevation during stone injection has to be set higher than the desired elevation to allow for settling. The stone matrix tends to attain a "stable" configuration through particle rearrangement and packing.

It is therefore common for the track profile to gradually "move down" with loading immediately after stone-blowing until a stable configuration is attained. This phenomenon of raising the track to an elevation higher than the final desired elevation is known as "design over-lift."

The amount of injected stone under each rail depends on the amount of lift desired and the support conditions underneath the ties. For instance, any voids underneath ties (hanging tie conditions) will significantly increase the amount of stone required to lift the track by a given amount. Voids under crossties resulting from ballast migration are often not captured during TOR surveying of an unloaded track section.

Void meters were used in this study to measure the amount of voids underneath crossties. Void meters are portable slide gauge-type devices that fit on the base of the rail in the ballast crib. A plastic spacer is pushed tight against the bottom flange of the rail after placement. Subsequent passing wheel loads move the plunger down and up under each axle load. After train loading, a "feeler" gauge is inserted between the spacer and the main bracket to determine the depth of the void. Figure 6.22(a) includes a photograph of a void meter mounted on the rail and a feeler gauge being used to determine the depth of void.

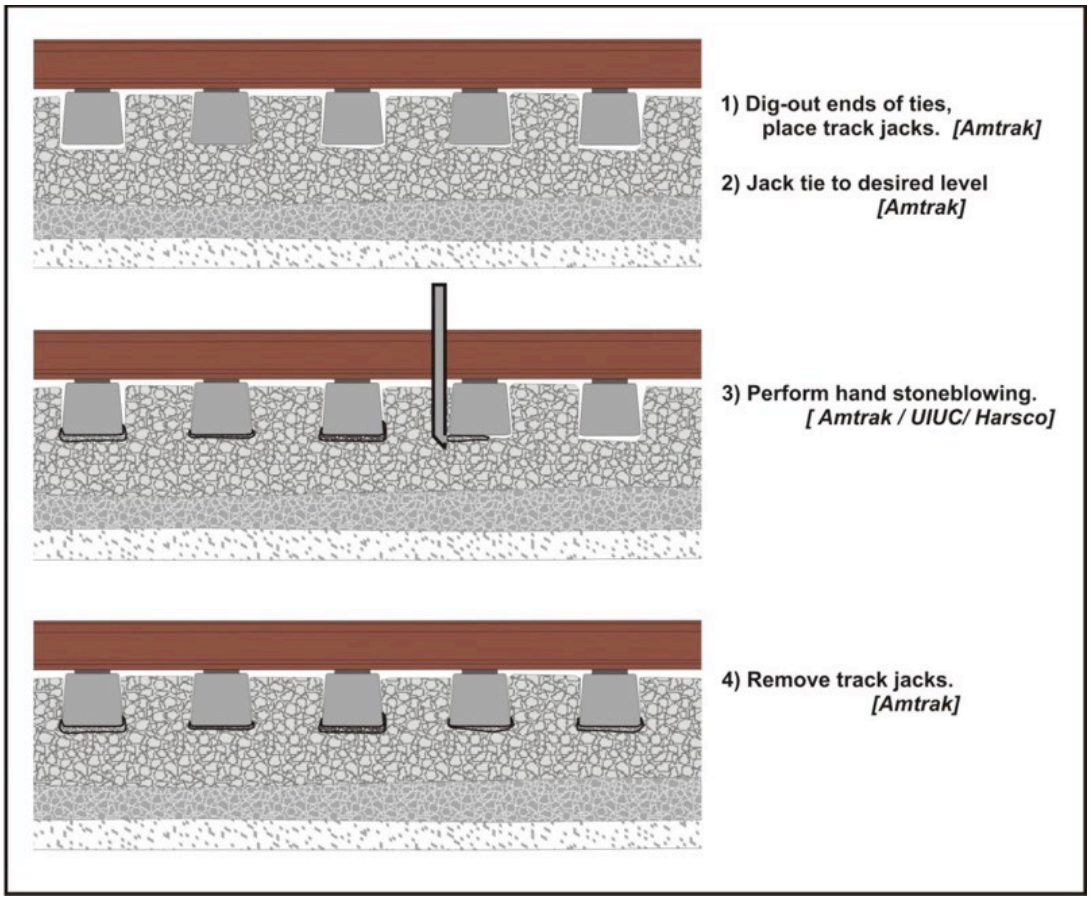

Figure 6.21: Different Steps Involved in the Stone-blowing Process

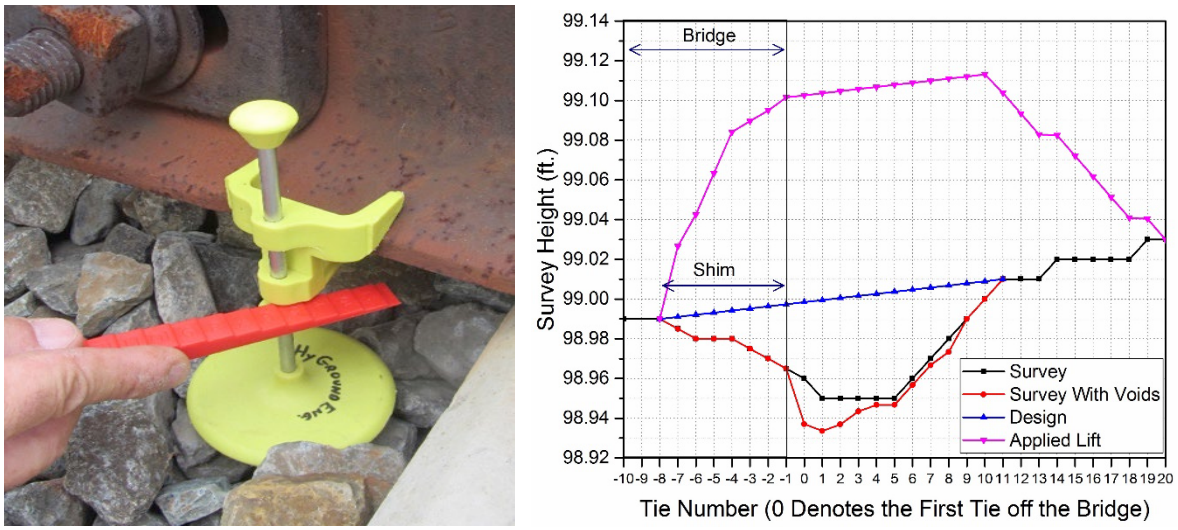

(a) (b)

Figure 6.22: (a) Measurement of Voids Underneath Ties Using Void Meters; (b) Design of Target Track Elevation Using Stone Injection at the Madison Bridge Approach

A pre-calculated amount of design over-lift is incorporated into the stone-blowing process prior to the actual injection of stones. The target track profile is determined using the TOR profile obtained through surveying, void measurements, and design over-lift. Figure 6.22(b) shows example profiles developed during stone injection at the Madison Street bridge approach. Similar to the case of chemical grouting, the target elevations for the track are marked using laser markers and track jacks are used to lift the rail to the desired elevation before stone injection. The injected stone size passes the 19 mm (.75 in) sieve and is retained on the 12.5 mm (.5 in) sieve. The relationship between the weights of 12.5 mm stone to lift the height of one rail is approximately 1 lb for every 1/32 of an inch (or approximately 525 grams for every 1 mm). Usually, two injectors are placed on either side of the rail being lifted. Accordingly, each injector receives half of the predetermined amount of stone.

An impact hammer drives the injector tubes into the crib ballast adjacent to the tie near the tie-rail interface. Only the side of the tube facing the tie has an opening. The injector is driven only so far as to expose a slot height of about 51 mm (2 in) from the tube insert to the bottom of the tie. In this fashion, the tube insert is placed at the same elevation as the ballast bed. The operator drives the tubes snug against the tie until the tie markings on the outside of the tube line up with the top of the tie.

The hand-held injectors are attached to an air compressor and the air enters the tube through a small opening that allows air to attain a high velocity. It is this velocity of air, not the air pressure, which forces the stone under the tie. The high velocity air accelerates the particles with sufficient energy to blow them under the tie into the formation. Examinations have shown that the dimensions of the area of support created through stone injection is approximately 230 mm by 460 mm (9 in by 18 in), approximately the same area affected by tamping tines. Photographs of different steps involved in the stone-blowing process are shown in Figure 6.23.

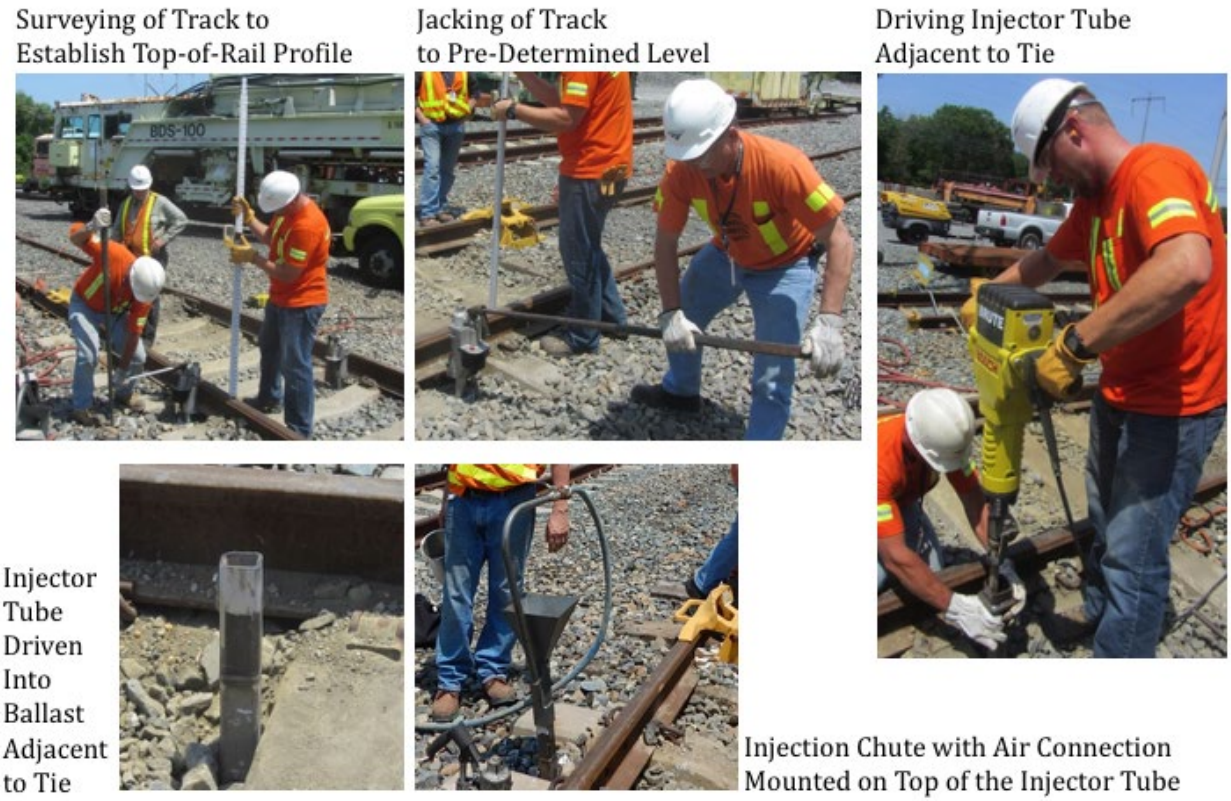

Figure 6.23: Different Steps Involved in the Stone-blowing Process

Stone-blowing at the Madison Street Bridge south approach (Track 2) was completed October 27, 2014. Wooden shims were placed under the tie plates on the bridge to remove the dip that extended onto the bridge and to adjust the target track elevation (see Figure 6.23(b)). The first few bridge timbers were modified (cut) to make a smoother transition to the dip in the approach; after adjusting the dip in the approach, the dip in the bridge timbers required adjustment back to where they should have been originally. In total, 12 ties received stone-blowing.

6.3.1 Conclusions Based on Layer Settlement Trends and Track Geometry Records

Settlements or permanent deformations registered by individual track substructure layers can be used to evaluate the effectiveness of stone-blowing as a remedial measure to mitigate the problem of differential movement at track transitions. Figure 6.24 presents the same data given in Figure 4.4(a) and shows individual layer settlement trends recorded by the MDD installed at the Madison Street bridge approach, near-bridge location (south approach; Track 2). Like the case of the Upland Street bridge approach, the ballast layer at Madison Street was observed to be the primary contributor to the differential movement.

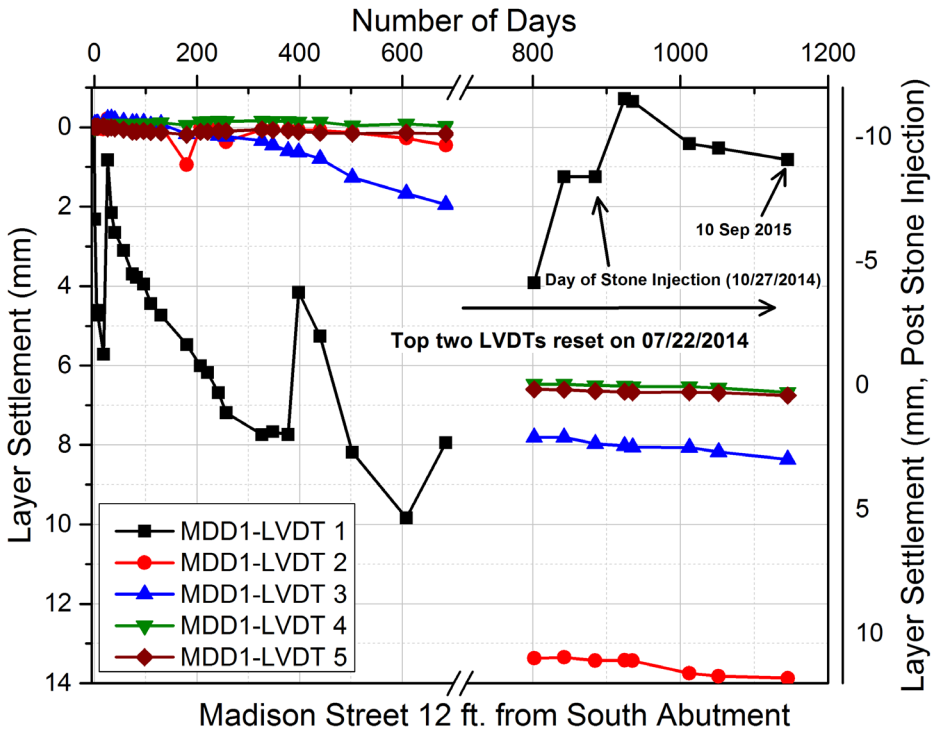

Figure 6.24: Layer Settlement Trends for the Madison Street Bridge Approach – Near-Bridge Location (12 ft From the South Abutment; Track 2)

Stone-blowing as a remedial measure was implemented at the Madison Street near-bridge location in October 2014 to mitigate the recurrent differential movement problem. To accommodate the excessive movement of the tie and within the ballast layer during the stone injection process, the top two LVDTs at this location were reset on July 22, 2014. The resulting change in the "zero position" of the top two LVDTs resulted in plotting all data after this date using a secondary vertical axis (see Figure 6.24).

The crest in the LVDT 1 trace (Figure 6.24) immediately after stone injection indicated the introduction of an "upward bump" in the track profile through the stone injection process. This was primarily a result of manual jacking of the track to attain a desired profile prior to the stone injection. This artificially introduced crest in the vertical track profile gradually dissipated to achieve a stable configuration. The last data collected in September 2015 indicated a relatively "flat" slope of the settlement line. This indicated a relatively low rate of settlement accumulation with time. Unlike the chemical grout, the effectiveness of stone-blowing as a remedial measure did not diminish with time, and improved track performance was observed even 1 year after the stone injection. Figure 6.25 shows the space curve and running roughness data for the Madison Street bridge approach (south approach; Track 2) to illustrate the positive effect of stone-blowing. As annotated in the figure, the stone-blowing application was performed on October 27, 2014, and resulted in an immediate reduction in the roughness value. The data shown until November 2015 did not indicate any drastic change in the running roughness or surface curve traces. This indicated that application of the stone-blowing had achieved a stable configuration and improved track performance.

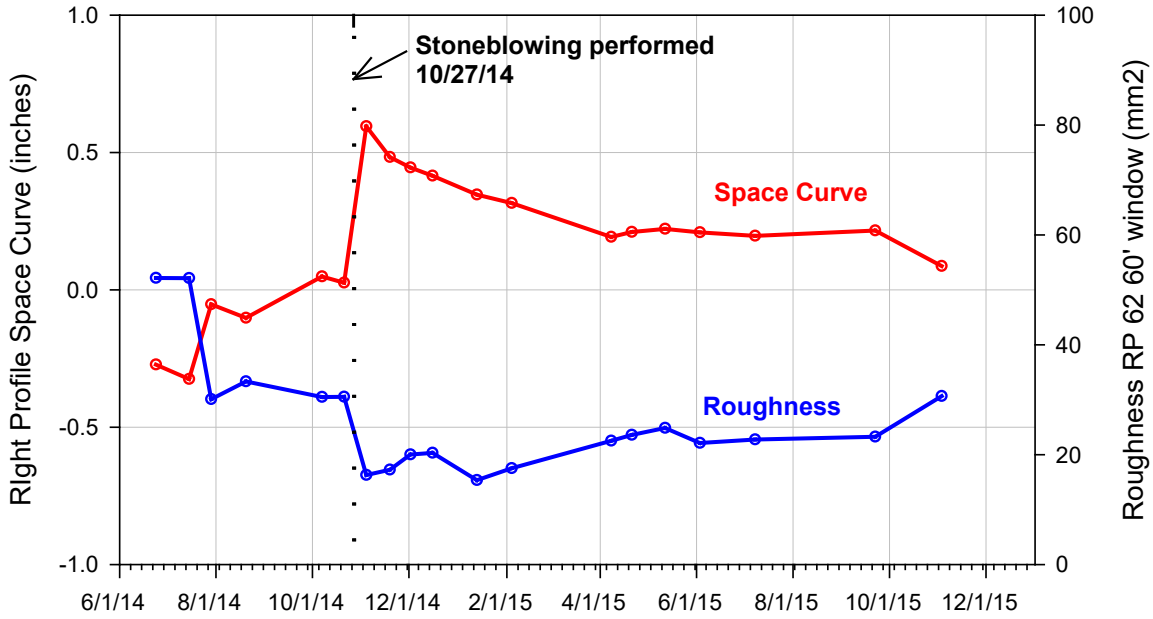

Figure 6.25: Space Curve and Running Roughness Data for the Madison Street Bridge Approach (South Approach; Track 2) Showing the Effect of Stone-blowing

6.3.2 Conclusions Based on Transient Response Data

Figure 6.26(a) presents the transient deformations registered by the top LVDT (LVDT 1) at the Madison Street bridge approach before and after the stone injection. As shown in the figure, the peak transient deformation recorded by the LVDT placed at the tie-ballast interface decreased from 1.7 mm to 0.7 mm upon stone injection. Although this reduction appeared smaller compared to the numbers presented for the Upland Street bridge approach (see Figure 6.5(a)), the peak transient deformations at the Madison Street bridge approach were significantly lower than those at the Upland Street bridge approach even before the implementation of any remedial measure. One interesting observation of the Madison Street bridge approach concerns the significant negative deformation (as high as 1.9 mm) recorded by the LVDT before stone-blowing (shown in Figure 6.26(a)). Note that a significant reduction in this tie lift-off (from 1.87 mm to 0.34 mm) was observed after stone-blowing. This indicated that significantly improved tie support conditions were achieved through the stone injection process.

Figure 6.26(b) shows the space curve for the Madison Street bridge location before and after stone injection. A significant dip in the track profile (concave up portion of the red line) was present before stone injection. Space curves for the same location of the track approximately one, three, and five weeks after the stone injection are also shown in Figure 6.26(b). As indicated in the figure, the design over-lift introduced during stone-blowing appeared as a “hump” in the track exactly at the same location where the dip was located. Gradual dissipation of this “heave” with time can also be seen in the figure. The dip in the space curve did not reappear until at least five weeks after stone-blowing.

Figure 6.27 presents the full displacement time-histories for individual track substructure layers recorded at the Madison Street bridge approach in January 2015 during the passage of a train. Note that the ballast layer (layer 1) displacements recorded at the near-bridge and open-track

locations were comparable to each other. This illustrates the improved tie support conditions achieved through stone-blowing. Underlying layers at the near-bridge location showed higher transient displacement magnitudes compared to the open-track location.

Figure 6.28 presents similar displacement time-histories for the Madison Street bridge approach (near-bridge location) under the passage of an Acela Express train in May 2015. Note that layer 1 displacements recorded for the near-bridge and open-track locations were once again similar in magnitude. Moreover, no significant increase in peak layer 1 transient displacements were observed between January 2015 and May 2015. This indicated that the support conditions underneath the stone-injected crossties did not deteriorate between January 2015 and May 2015. This observation established stone-blowing as a longer-lasting remediation approach compared to the chemical grouting application in this study.

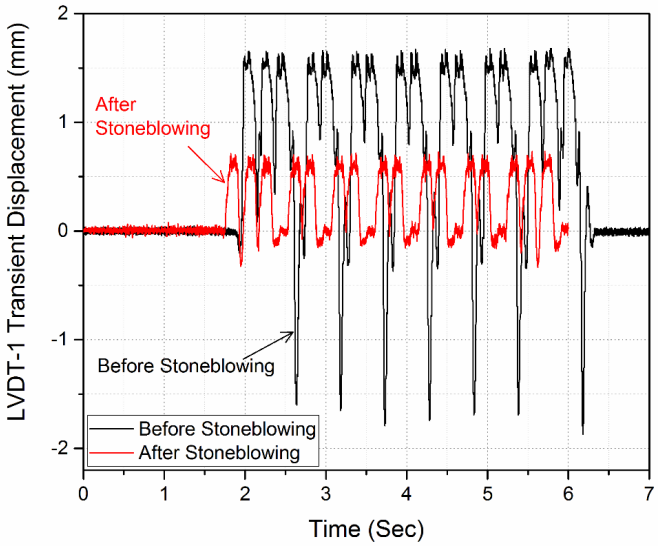

(a)

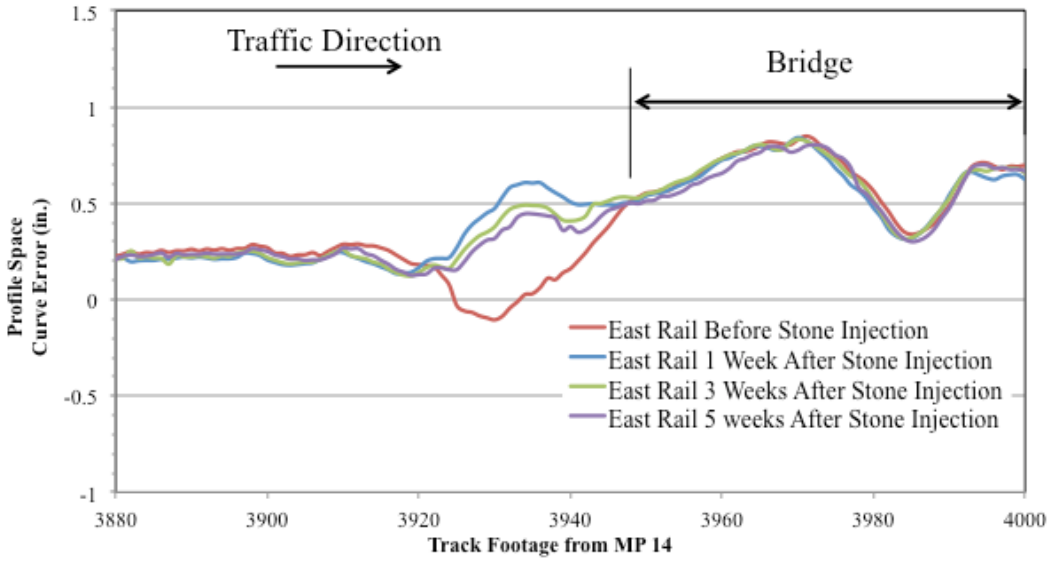

(b)

Figure 6.26: Effect of Stone-Blowing on (a) Ballast Transient Deformations and (b) Track Space Curve at Madison Street Bridge Approach (South Approach; Track 2)

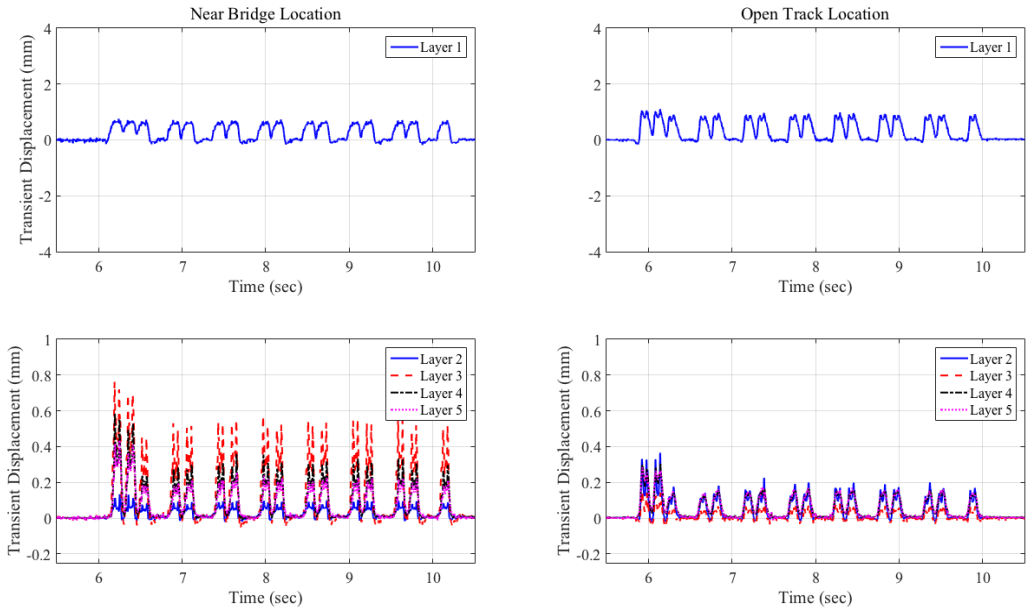

Figure 6.27: Displacement Time-Histories Recorded at the Madison Street Bridge Approach; Data Collected in January 2015; Train 1

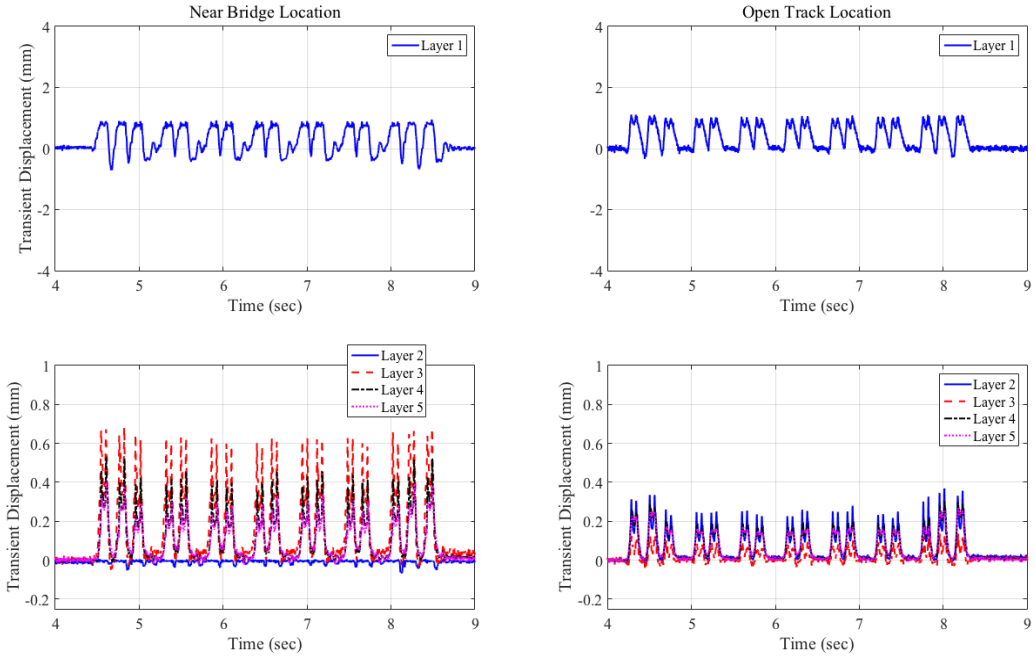

Figure 6.28: Displacement Time-Histories Recorded at the Madison Street Bridge Approach; Data Collected in May 2015; Train 1 (Acela Express)

Figure 6.29 shows the normalized transient displacement values recorded by LVDT 1 at the Madison Street bridge approach (all displacements normalized to a load level of 100 kN) and is an extension of Figure 4.19. Data points corresponding to January 2015 and May 2015 can be used as indicators of the effectiveness of stone-blowing in improving the overall track conditions at the Madison Street bridge approach. As seen from the figure, the normalized LVDT 1

displacements recorded in January 2015 were significantly lower than those recorded prior to the stone injection. Although the normalized transient displacements in May 2015 were higher than those in January 2015, the values were still significantly smaller than those before the stone-blowing. Note that the stone-blowing was performed in September 2014, and the resulting improvements to the tie support conditions were still evident in May 2015. This highlights the potential of stone-blowing as a long-term solution to poor tie support conditions at track transitions.

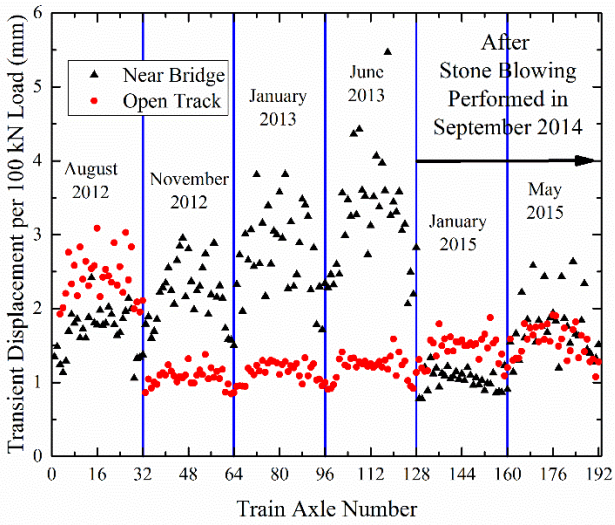

Figure 6.29: Ballast Transient Displacements Recorded at the Madison Street Bridge Approach Under the Passage of Acela Express Trains on Different Dates of Data Acquisition (Normalized to a Load of 100 kN)

Figure 6.30 shows the contribution of layer 1 at the Madison Street bridge approach to the total transient deformation under loading. As seen in the figure, the contribution of layer 1 reduced to approximately 30 percent after stone-blowing (as reflected from the data collected in January 2015). Near-bridge data could not be collected from the MDD LVDT 1 in May 2015.

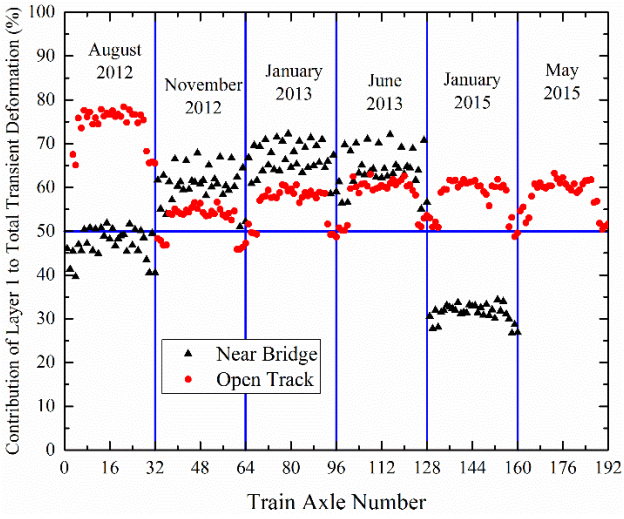

Figure 6.30: Contribution of the Ballast Layer Toward Total Transient Deformations Under Train Loading at the Madison Street Bridge Approach (South Approach; Track 2)

6.3.3 Effect of Stone-blowing on Dynamic Load Amplification

Figure 6.31 shows the percent load amplifications at the Madison Street bridge approach as calculated from the data acquired in May 2015. Note that the vertical wheel load measurement circuit at this location was broken in January 2015, hence no wheel load data could be recorded. This circuit was subsequently fixed in May 2015 and re-calibrated to facilitate the final set of data collection. As shown in Figure 6.31, negative percent amplification factors were calculated for the "force on tie" circuit. As discussed in Section 4, this was probably due to larger gaps at the tie-ballast interface for the open-track location compared to the near-bridge location. The presence of larger gaps at the tie-ballast interface resulted in a given wheel registering higher load magnitudes at the open-track location compared to the near-bridge location.

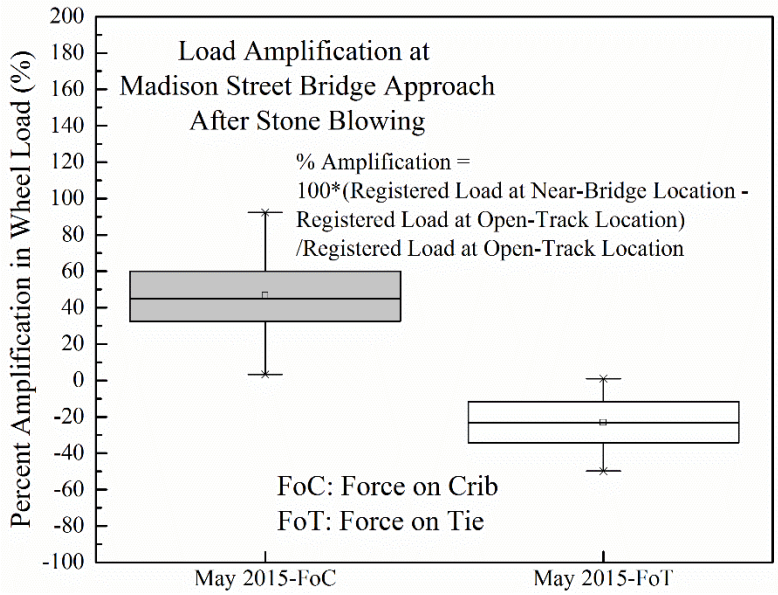

Figure 6.31: Load Amplification at the Madison Street Bridge Approach After Stone-blowing

6.3.4 Effect of Stone-blowing on the Gap at the Tie-Ballast Interface

Gaps at the tie-ballast interface were calculated for the Madison Street bridge approach after stone-blowing using the "progressive load threshold approach" (see Table 6.3). For convenience, the values corresponding to June 2013 have been included in the same table to represent values before the stone-blowing. Note that a significant reduction in the gap underneath the tie was achieved for the near-bridge location upon stone-blowing (reduction from 1.43 mm to 0.45 mm). A slight increase (to 0.61 mm) in this gap magnitude was observed in May 2015. However, the gap was still significantly smaller than the value (1.43 mm) corresponding to the pre-stone-blowing conditions. Note that the tie-gap calculated in May 2015 at the open-track location (60 ft from the south abutment) was larger than that at the near-bridge location (0.84 mm compared to 0.61 mm). This explains the higher wheel load magnitudes registered at the open-track location compared to the near-bridge location.

Table 6.3: Gap Quantification at the Tie-Ballast Interface Using the Progressive Load Threshold Approach: Madison Street Bridge Approach (After Stone-blowing)

	12 ft from South Abutment		60 ft from South Abutment	
	Gap (mm)	Load Threshold (kN)	Gap (mm)	Load Threshold (kN)
June 2013	1.43	12	0.76	17
January 2015	0.45	30	0.76	32
May 2015	0.61	18	0.84	28

6.3.5 Effect of Stone-blowing on Layer Accelerations Analyzed in Time and Frequency Domains

As discussed in Section 5, layer accelerations calculated through double differentiation of the displacement time-histories can be used to make inferences regarding track dynamic response under loading. Figure 6.32 shows the load and acceleration time-histories for the Madison Street bridge approach after stone injection (data collected in January 2015). As shown in the figure, the layer 1 accelerations at the near-bridge location were lower than 0.25 g and were comparable to those for the open-track location. This was a direct consequence of better tie support conditions accomplished through stone-blowing.

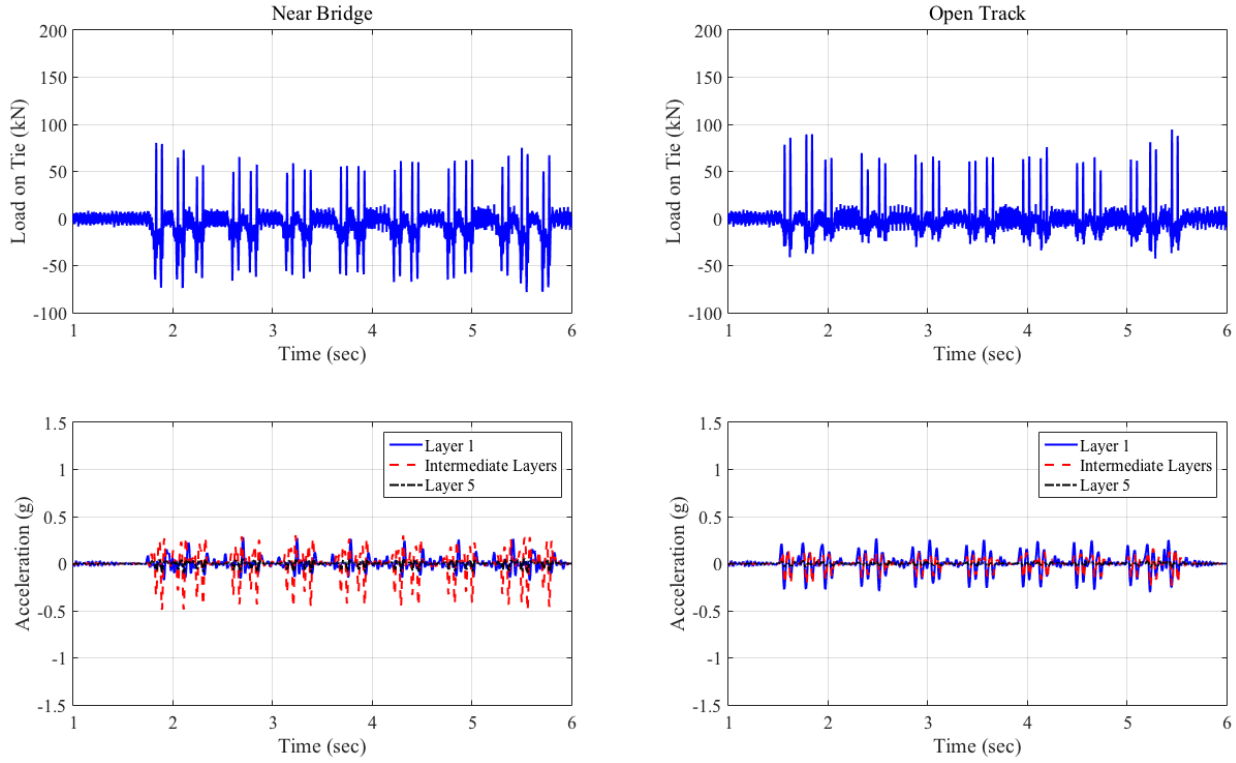

Figure 6.32: Load and Acceleration Time-Histories for the Madison Street Bridge Approach (Data Collected in January 2015) – After Stone Injection (Acela Express)

Figure 6.33 shows layer 1 accelerations for the Madison Street bridge approach presented in the frequency domain. The predominant waveform contributions for both the near-bridge and open-track locations occurred at frequency levels of 11 Hz and 16.5 Hz. Moreover, the near-bridge location comprised contributions from waveforms in the 22 Hz frequency range, whereas such frequencies were missing from the open-track location. Note that this was identical to the trends reported for the same approach before implementation of the stone-blowing (refer to Figure 5.20). This indicated that stone-blowing did not affect the dominant frequencies as far as dynamic response of the tie was concerned. Similar data collected in May 2015 are presented in Appendix A-3.

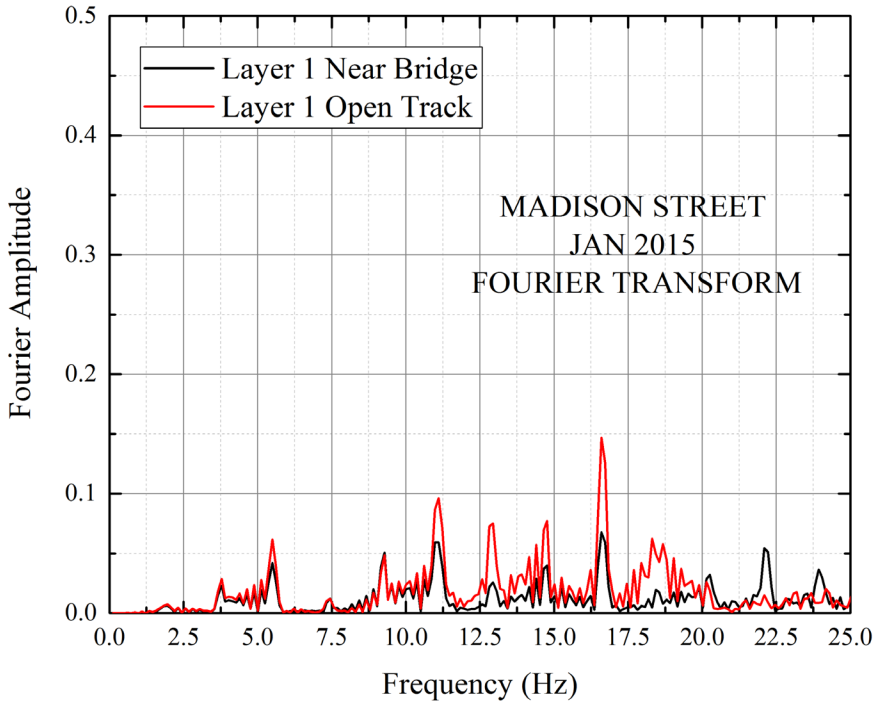

Figure 6.33: Layer 1 Accelerations for the Madison Street Bridge Approach Presented in the Frequency Domain (Data Collected in January 2015) – After Stone Injection

Figure 6.34 shows the acceleration ranges recorded at the Madison Street bridge approach immediately before and after the stone injection. As seen from the figure, peak accelerations at the near-bridge location were significantly reduced after stone-blowing (reduced from 1.2 g to 0.25 g). Although there was a slight increase to ~0.4 g in May 2015, the value was still significantly lower than pre-stone-blowing conditions. This clearly highlights the reduction in tie accelerations achieved due to the better support conditions underneath the stone-injected crossties.

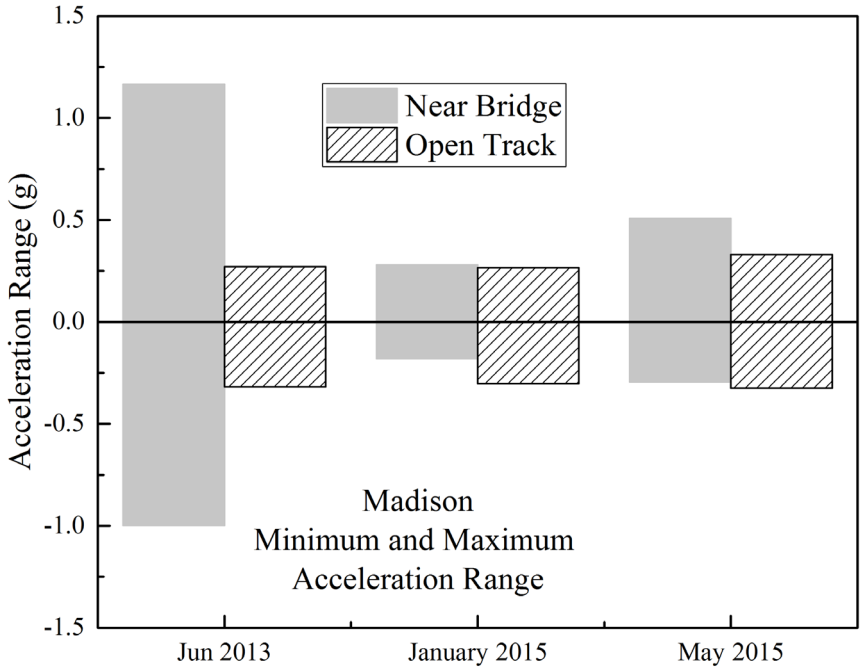

Figure 6.34: Summary of Peak Accelerations Recorded at the Madison Street Bridge Approach Under the Passage of Acela Express Trains – After Stone Injection

6.3.6 Effect of Stone-blowing on Tie Lift Off (Negative Displacement)

Figure 6.35 shows the minimum and maximum displacements recorded by the top-most LVDTs at the Madison Street bridge approach after implementation of stone injection as a remedial measure. Once again, the data corresponding to June 2013 has been included in this plot for convenience. As shown in the figure, no significant difference in the minimum and maximum transient displacement values recorded by the top LVDT at the open-track location was observed. This was expected, as the open-track location was at a distance of 60 ft from the south abutment, and the stone-blowing activity was carried out over the first 30 ft from the bridge abutment. The near-bridge location, however, registered significant changes in both the minimum and maximum transient displacement values recorded. Looking at the positive (downward) displacements, it can be seen that the value for January 2015 (three months after stone-blowing) was significantly lower than the value before stone-blowing (reduction from 1.75 mm to 0.5 mm). Although a slight increase (up to approximately 0.75 mm) in the peak positive displacement was observed in May 2015, this value was still significantly lower than that corresponding to the conditions before stone-blowing. This clearly established that improved support conditions underneath the crossties resulting from the stone injection led to significant reductions in the peak transient deformations under loading.

Similar inferences can be drawn from the peak negative transient displacements for the near-bridge location reported in Figure 6.35. Lack of adequate support conditions prior to the stone-blowing resulted in significantly high magnitudes of negative displacements. However, improved support conditions achieved through stone injection led to a drastic decrease in the peak negative displacement values. The slight loss of support between January 2015 and May 2015 led to a slight increase in the magnitude of the peak negative displacement. However, this value was still

significantly lower (approximately 75 percent less in magnitude) compared to the values prior to stone injection.

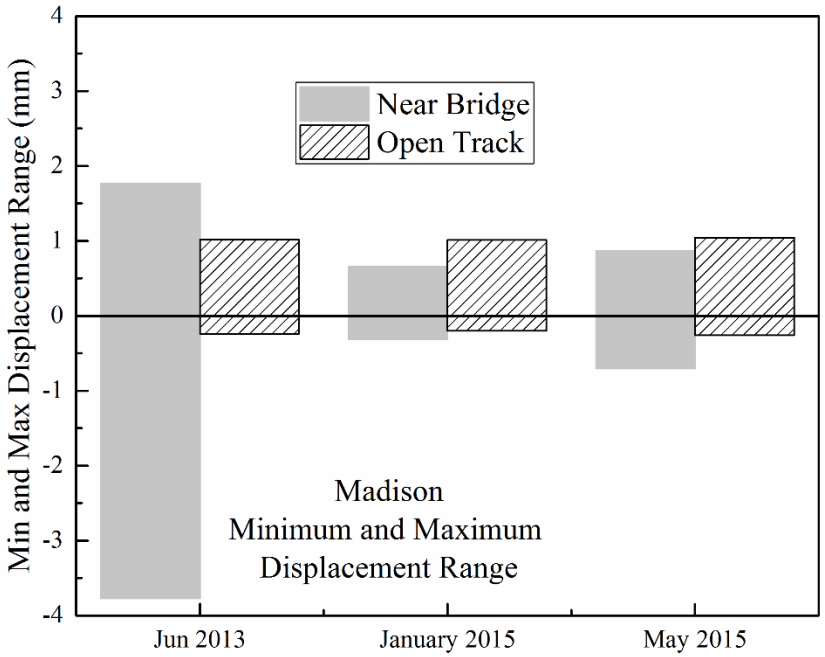

Figure 6.35: Maximum and Minimum Transient Displacements Recorded for the Instrumented Tie – Madison Street Bridge Approach – After Stone Injection

6.3.7 Effect of Stone-blowing on Track Substructure Layer Moduli

To quantify the effect of stone-blowing on track substructure layer moduli, Table 6.4 lists individual layer modulus values estimated through iterative analysis using the GeoTrack software program. The primary observation from Table 6.4 was associated with the drastic increase in the modulus values for layers 1 and 2 (ballast and fouled ballast) after stone-blowing (from 78 MPa to 117 MPa). This can be attributed primarily to the better support conditions underneath the instrumented ties achieved through stone-blowing. Elimination (or reduction) of the gap at the tie-ballast interface resulted in better "seating" of the tie on the underlying ballast layer, thus presenting increased resistance against transient deformation under loading. As already mentioned, the vertical wheel load measurement circuit was damaged at this location during the January 2015 data collection effort, hence no iterative estimation for the substructure layer moduli could be carried out corresponding to that time.

Table 6.4: Track Substructure Layer Modulus Values for the Madison Street Bridge Approach Near-Bridge Location Estimated Through Iterative Analysis Using GeoTrack – After Stone Injection

Date of Data Acquisition	Layer Modulus (MPa)				
	Layer 1	Layer 2	Layer 3	Layer 4	Layer 5
June 2013	78	78	40	39	35
May 2015	117	117	23	29	42

6.3.8 Summary

Layer settlement trends, track geometry car records, and transient displacement data collected at the Madison Street bridge approach after stone-blowing highlighted its effectiveness in improving the overall track response under loading. No significant deterioration in the improved support conditions was observed even 1 year after the stone injection. This indicated that stone-blowing can prove to be a long-lasting remedial measure to mitigate the differential movement at track transitions. Note that stone injection does not affect future tamping and resurfacing activities and is therefore likely to be well-accepted by railroad practitioners as a favorable maintenance approach.

6.4 Under Tie Pads

UTPs are essentially elastic pads placed underneath the crossties on top of the ballast. They have been found to reduce the level of vibration caused in the ballast layers under train loading and increase the damping effect of the track substructure. Moreover, UTPs can reduce the influence of varying track stiffness on the wheel/rail contact force, and as a result distribute the load of the train over a wider area within the ballast layer. Several successful research and implementation efforts involving the use of UTPs are discussed in Section 2.

A block of 30 crossties with UTPs attached to the bottom of the ties was installed on the Upland Street Bridge south approach (Track 2). The work was performed with a pre-approved 36-hour outage that began at 10:00 p.m. on Friday, August 29, 2014 (Labor Day holiday). Tracks 1 and 4 were kept active but Tracks 2 and 3 were out of service to complete the installation. A pre-constructed concrete tie track panel was brought on site for installation. The installation was performed by Amtrak work crews and involved removing the old track, installing the new track panel, unloading ballast and compacting the track substructure, surfacing and aligning the track, and thermite welding the rail joints. Work was completed by midnight on Saturday August 30, 2014.

According to the manufacturer, Pandrol-CDM Track/Novitec, UTPs are made from polyurethane elastomers manufactured in France from recycled materials (ground tires), with a shore hardness of 65 to 75. These pads have on average 10 percent void content to allow better ballast fit. Based on track geometry records at the Upland Street south approach (Track 2), researchers decided that 30 new ties with UTPs would be installed to reduce the train-induced vibrations and subsequent ballast migration. UTPs with desired engineering properties were shipped to the Amtrak Wilmington Yard facility. To ensure full adherence of the pads to the bottom of the newly fabricated concrete ties, the surface was prepared to eliminate all fines or dust. A special adhesive was placed on the bottom of the crosstie, then the pads were glued and set to dry for 8 to 12 hours. The elastomers were cut and installed with a .5 inch offset from the edge of the tie. The ties were stacked while the adhesive cured. Figure 6.36 shows photographs of the newly manufactured concrete ties mounted with the UTPs.

(a) (b)

Figure 6.36: Newly Manufactured Concrete Ties Mounted with UTPs

The first step in the installation process was cutting the rail at four locations to remove the 30 tie panels from Track 2. The new track panel was approximately 60 ft in length and constructed with 30 concrete ties and 136 RE rail. A crane was used to remove the old track panel. Once the space was cleared, a front-end loader excavated the old ballast from Track 2. Ballast was removed to a depth of 27 inches from the TOR, coinciding with the layer of asphalt that had previously been placed under the tracks. A small amount of ballast was left to support the new panel. Next, the new track panel was installed, the rail was cut in order to have staggered welds, and finally the joint bars were fastened. A photograph of the tie panel after installation is shown in Figure 6.37.

Figure 6.37: Final View of the New Tie Panel After Installation

6.4.1 Conclusions Based on Track Geometry Records

A panel comprising 30 crossties mounted with UTPs was installed along the south approach of Upland Street bridge along Track 2. This approach was not instrumented using MDDs and strain gauges in August 2012. Hence, detailed data pertaining to the layer settlement and transient deformation trends prior to implementation of any remedial measure were not available for this approach. However, based on the simplifying assumptions discussed at the beginning of this section, it was safe to assume that the pre-remediation response of this approach would be similar to that diagonally across it (Upland Track 3, north approach).

Figure 6.38 shows the space curve and running roughness data for the Upland Street south approach (Track 2) immediately before and after installation of the track panel with the UTP-mounted crossties. As shown in the figure, installation of the UTPs in late August 2014 resulted in an immediate increase in the running roughness, as was represented by an upward shift in the space curve. This can be attributed to uneven resurfacing of the track immediately after installation of the track panels. However, the space curve attained a stable configuration within 2 weeks after installation of the track panel with UTP-mounted ties. A reduction in the running roughness was observed in December 2014. No significant shift in the space curve or increase in the roughness was observed through November 2015. This indicated that the track attained a stable configuration after an initial settlement and installation of the UTPs led to a relatively consistent track geometry profile.

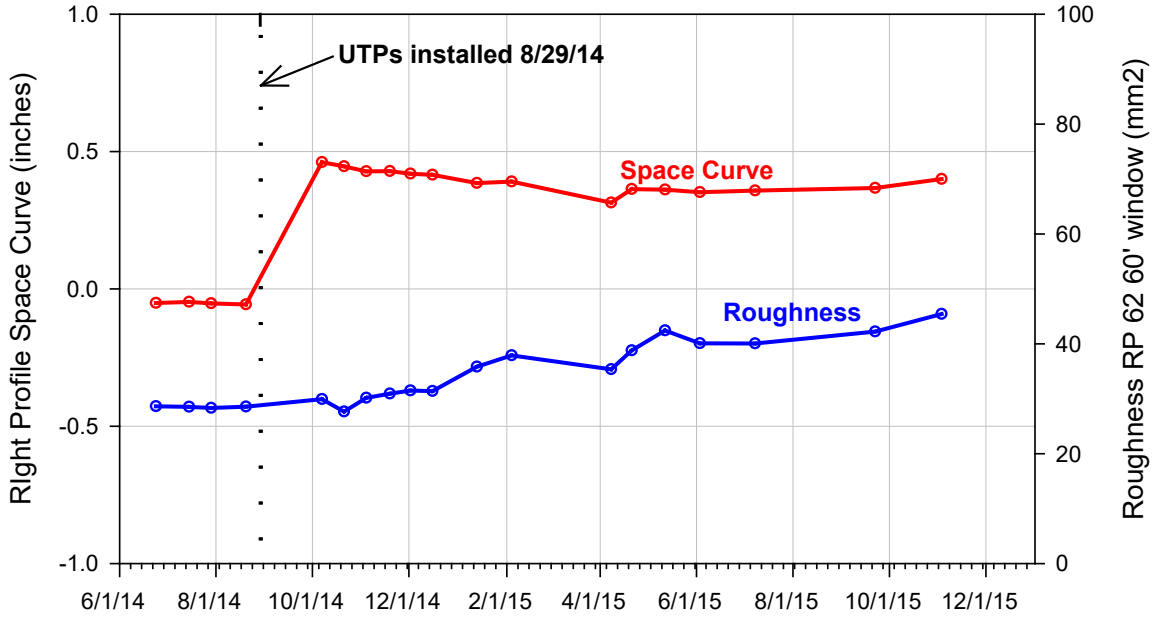

Figure 6.38: Space Curve and Running Roughness Data for the Upland Street Bridge Approach (South Approach; Track 2) Showing the Effect of UTP Installation

6.4.2 Conclusions Based on Transient Response Data

Due to the absence of MDDs and strain gauges at this location, no transient response data could be obtained prior to installation of the track panel with UTP mounted ties. However, a separate instrumentation effort was carried out in August 2015 to measure the transient response of the track panel under train loading. Note that this instrumentation effort was carried out 11 months

after installation of the track panel with UTP mounted ties, and therefore could be used as an indicator of long-term performance of the UTPs.

Figure 6.39 shows a schematic of the instrumentation layer to measure the transient response under train loading for this bridge approach. As shown in the figure, the instrumentation was mounted on the tenth and eleventh tie from the bridge abutment. Considering a 24 inch tie spacing, these ties were located at distances of approximately 20 and 22 ft from the bridge abutment, respectively. This was the same instrumentation layout as discussed in Section 5.2. One primary difference between measuring the transient displacements using this instrumentation approach and the one discussed using MDDs was that this approach measured transient deformation of the ballast layer only. However, the ballast layer accounted for a major portion of the total track transient deformations for all instrumented approaches. Hence, it was reasonable to focus on transient response of the ballast layer to make conclusions about the overall track substructure performance. Figure 6.40 shows photographs of the instrumentation types and locations used in this bridge approach.

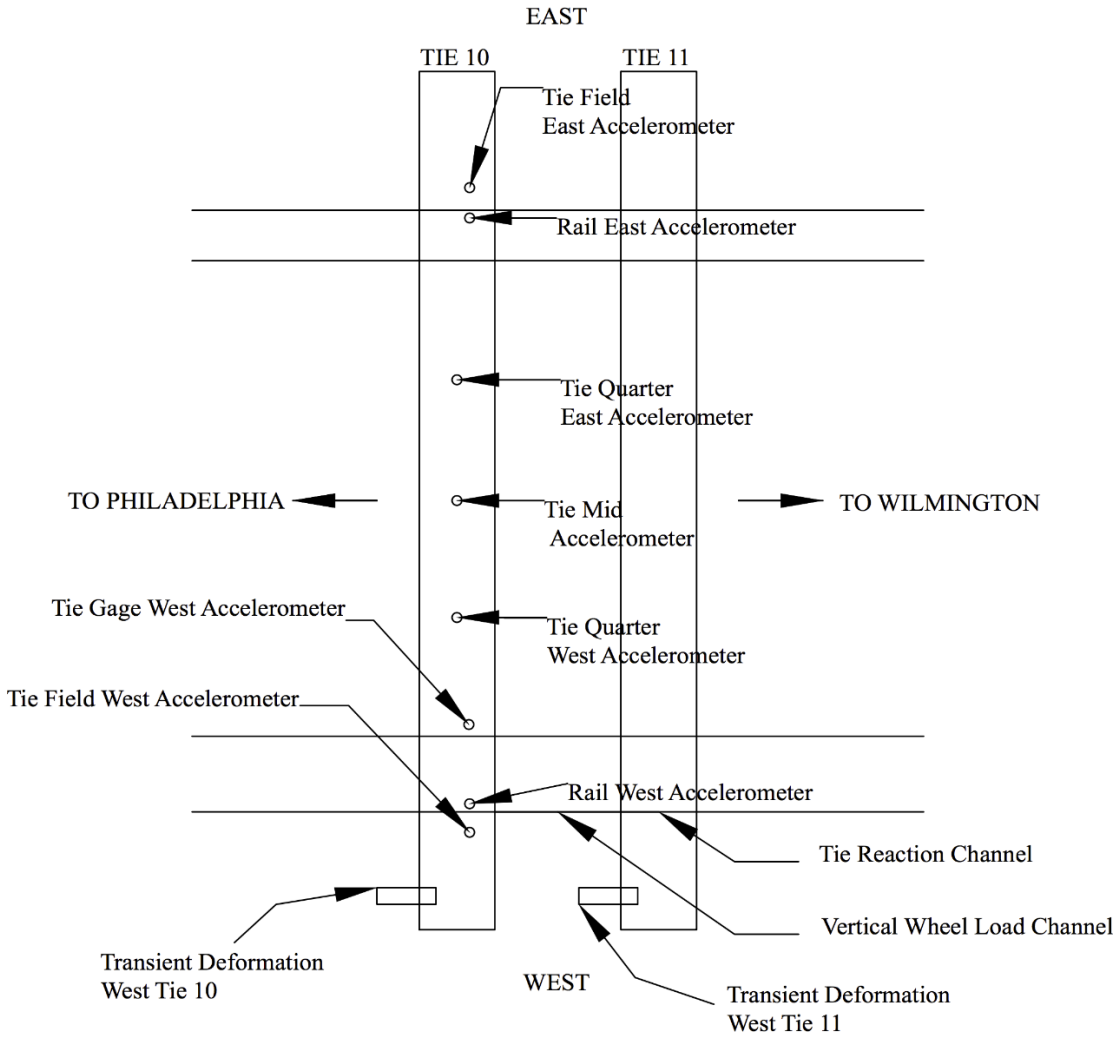

Figure 6.39: Schematic of Instrumentation Layout to Measure Transient Response of Ties Fitted With UTPs

(a)

(b)

Figure 6.40: Instrumentation Types and Locations to Measure Track Transient Response Under Loading

Figure 6.41 presents load and displacement time-histories measured at this bridge approach during the passage of an Acela Express train. As shown in the figure, peak transient displacements of approximately 1.5 mm were measured for both Tie 10 and Tie 11. Considering that this measurement was done almost a year after installation of the track panel with UTP-mounted ties, the low peak transient displacement magnitudes indicated adequate long-term performance of UTPs as a remedial measure. It should also be noted that no negative transient deformations were recorded for either tie. This indicated adequate support conditions underneath both ties.

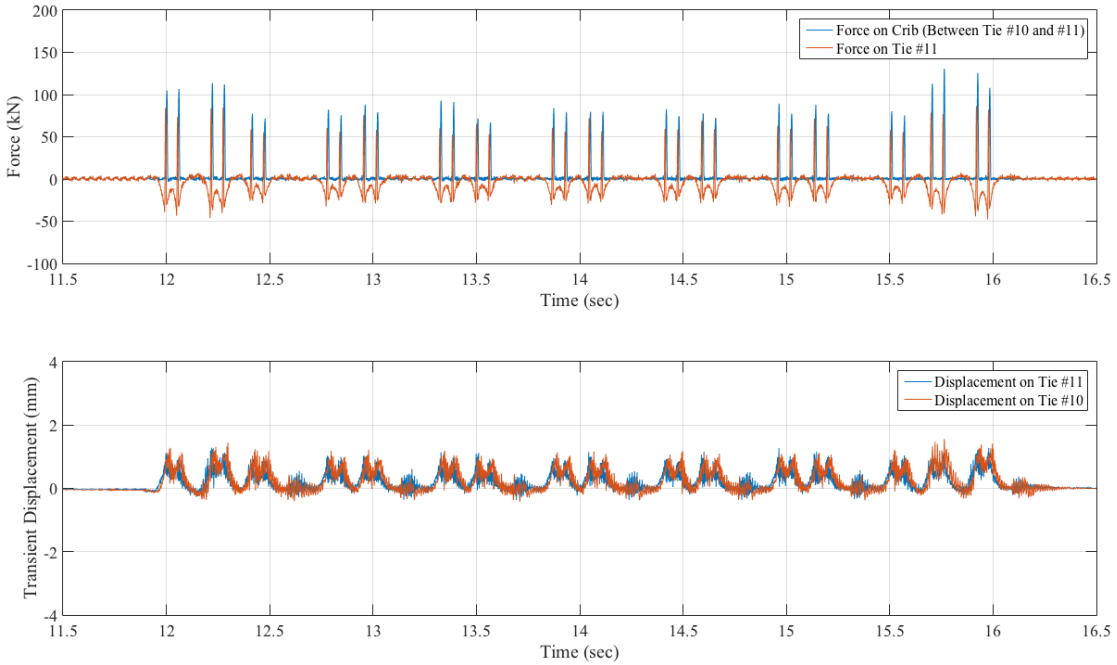

Figure 6.41: Force and Displacement Time-Histories Measured at Upland Street Bridge – Track 2 South Approach; Data Collected in August 2015; Train 1 (Acela Express)

Figure 6.42 shows the acceleration time-histories for the two ties established through double differentiation of the measured transient displacement data. Peak acceleration values lower than 0.25 g indicate adequate support conditions underneath the ties. No significant negative accelerations representing tie lift-off were detected.

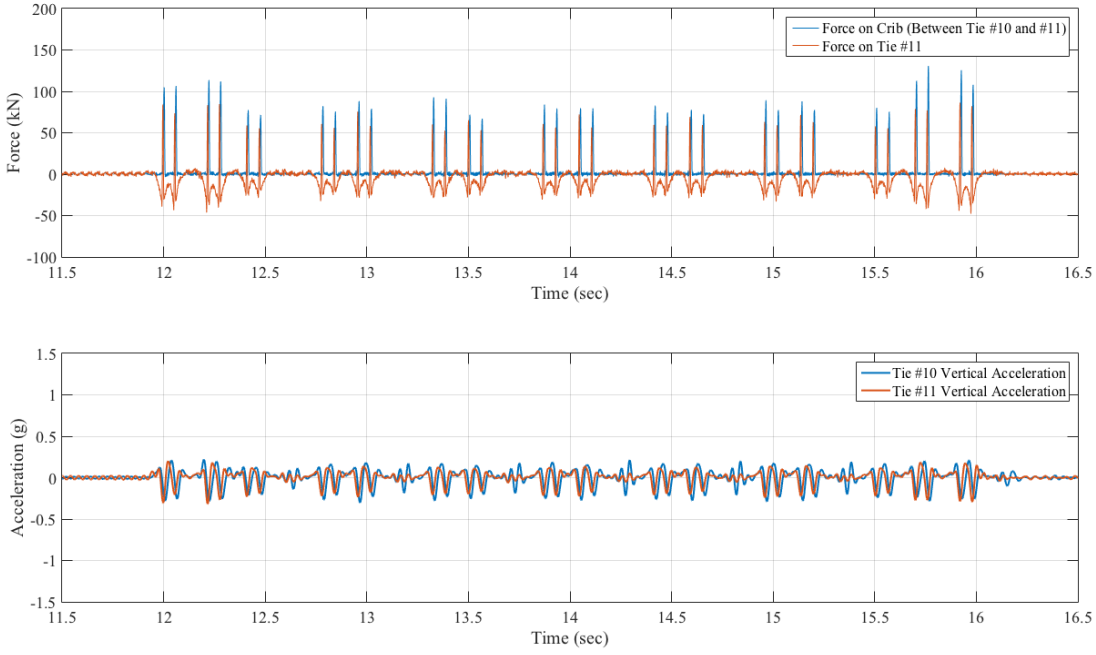

Figure 6.42: Acceleration Time-Histories Calculated from Transient Displacement Measurements at Upland Street Bridge – Track 2 – South Approach; Data Collected in August 2015; Train 1 (Acela Express)

Figure 6.43 shows accelerations for the two instrumented ties presented in the frequency domain. From the figure, dominant waveforms corresponding to 11 Hz, 12.5 Hz, and 16.5 Hz could be identified. These were similar to the dominant frequencies observed for the Madison Street bridge approach after stone-blowing (see Figure 6.33). This indicated that similar dynamic transient responses of the ties were observed after the stone-blowing and UTP remedial measure applications, both of which resulted in improved support conditions at the tie-ballast interface.

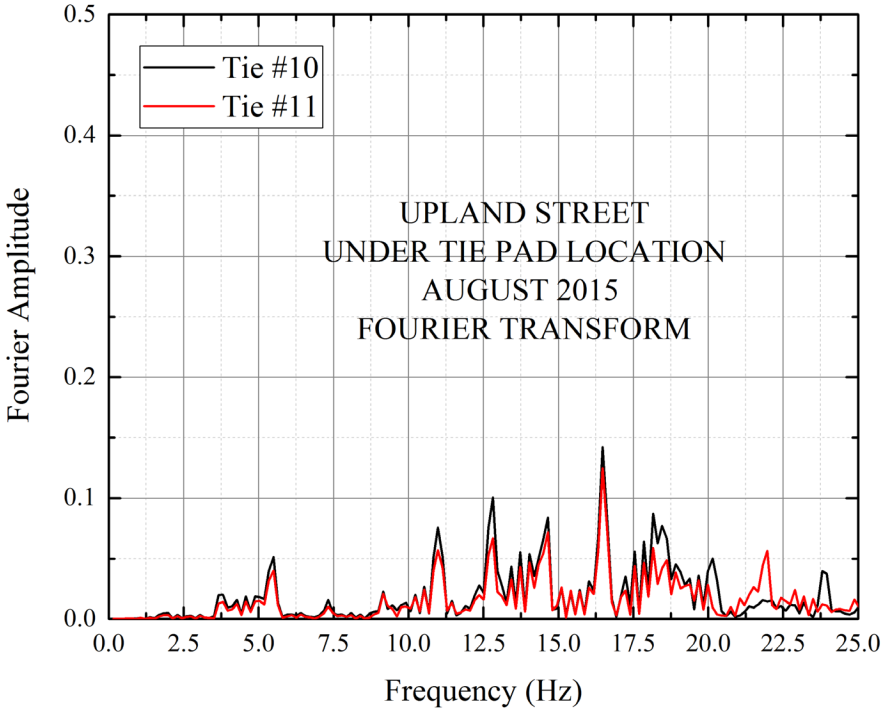

Figure 6.43: Tie Accelerations for Upland Street Bridge – Track 2 – South Approach – Presented in the Frequency Domain (Data Collected in August 2015)

6.5 Summary

This section presented details on the selection and implementation of relevant remedial measures to mitigate the problem of differential movement at the instrumented railroad track transition sites at the Amtrak NEC line. Three different remedial measures were selected based on a review of published literature and discussion with railroad industry partners: (1) chemical (polyurethane) grouting; (2) stone-blowing; and (3) installation of UTPs. The primary objective was to reduce excessive ballast layer deformations reported through the instrumentation and performance monitoring tasks. Chemical grouting of the ballast proved to be effective in the short-term, but its effectiveness as a remedial measure diminished rapidly after a few months. Close inspection of the track conditions indicated that excessive fouling of the ballast layer may have led to inadequate bonding between the grout and individual ballast particles. Grout application at another bridge approach comprising a clean ballast layer indicated better performance. However, performance of this particular bridge approach needs to be continuously monitored to draw relevant inferences based on effectiveness of the chemical grout as a feasible remedial measure. Both stone-blowing and installation of UTPs proved to be effective remedial measures to mitigate differential movement at the track transitions. Better support conditions at the tie-ballast interface could be ensured through both of these remedial measures, which in turn

led to significantly improved track response and “stable” track geometry profiles. Section 7 of this report presents details on advanced numerical modeling approaches that can be used to study the behavior of railroad track transitions.

7. Numerical Modeling of Track Transitions

This section presents in detail the numerical modeling efforts undertaken to better understand the bridge approach problem. Research activities focused on the numerical modeling of the monitored railway transitions to develop calibrated track models, understanding factors contributing to the measured differential movements, and predicting the performance of the applied rehabilitation techniques and future performance. The calibrated numerical models developed for the monitored railway transitions can accommodate various design and repair techniques, determine effects of track location and various conditions on differential movement, and evaluate effects of ballast characteristics and layer stiffness on the total differential movement using numerical modeling.

Transition zones have been the subject of 3D track model development, but the great deal of calculation time required can make it prohibitive in a design process. This is why researchers commonly use longitudinal and transverse track symmetry to reduce the calculation time as much as possible. The lack of homogeneity in layer materials (e.g., particulate and porous nature of ballast and sub-ballast) may also limit the meaningfulness of a 3D analysis, which mainly assumes continuum layer behavior. The track is treated as a group of layers (multilayer system) supporting elements with certain known characteristics of elasticity and damping which reflect the viscoelastic behavior of the track embankment, subbase, sub-ballast, ballast, tie, fastenings, and rail. Additional elements can also be introduced, such as elastic and soft pads, UTPs, ballast/sub-ballast mats, etc.

Recent efforts focused on the numerical modeling of railway transitions using 3D FEM have identified important aspects related to the bridge approach problem. Banimahd and Woodward (2007) developed a dynamic 3D coupled train-track FEM using both linear and nonlinear constitutive material models. Variables such as train speed, track stiffness, and the presence of track faults were considered in the analyses of transitions. A transition length of approximately 4 m (13 ft) was found to be sufficient for mitigating effects of dynamic load and vertical body acceleration considering no track fault in the transition zone. Nicks (2009) analyzed the track response due to the bump at the end of the bridge by creating a 3D FEM of the train, track structure, and track substructure for static and dynamic analyses considering time-history of loading. The track was modeled using beam elements. The study considered train direction, train speed, bump/dip size, subgrade/fill modulus, approach tie material, bridge tie material, bridge deck type, ballast thickness, and approach tie length. It was found that a track modulus differential alone (no bump/dip) at a bridge/approach location led to impact forces as well as increased ballast and subgrade pressures on the approach. Coelho et al. (2011) analyzed components of the track as low order isoparametric brick elements using a 3D dynamic FEM approach in time-domain. Vertical stresses and vertical displacements were predicted using an elastic material formulation including soil properties coupled with groundwater flow. When modeling the deformation behavior of the transition, the predictions were either smaller or greater than the experimental data, which included both compression and heave characteristics. Shahraki et al. (2015) also developed a 3D dynamic FEM model to take into account the time-history of loading. They studied transition response by gradually changing pad stiffness and using longer ties and auxiliary rails in the transition zone. Having auxiliary rails and modifying subgrade condition both improved dynamic behavior. For a typical low stiffness to high stiffness transition, a sensitive zone was found within 5 m (16 ft) of the slab track from the track interface.

A 3D track substructure model based on the general-purpose Abaqus software using the finite element method was developed in this section for the analyses of transient layer deformations measured at the instrumented bridge approaches. The track substructure layer moduli back calculated for the Madison, Upland, and Caldwell Street bridge locations using the GeoTrack layered elastic analysis program were used as inputs for the 3D Abaqus FEM model. Using the GeoTrack program results (obtained with linear elastic layered theory assumptions) in the development and calibration of this 3D FEM model naturally simplified the problem to transient elastic solutions. Nevertheless, this was the first step to validate the developed Abaqus model using the 3D track geometry and related material property inputs as a reliable tool. Subsequently, the 3D Abaqus model was tested for prediction accuracy when the measured transient layer deformations of two remedial measures applied at near-bridge approach locations – (1) Upland Street 15 ft location with the applied polyurethane grouting and (2) Madison 12 ft location with applied stone-blowing remediation – were compared to the FEM model predictions.

This section also includes the use of a fully coupled 3D dynamic track model developed by Huang et al. (2014). An integrated approach to dynamic modeling of railway track transitions was introduced by calibrating the fully coupled 3D dynamic track model with the track response data obtained from the instrumented bridge approaches. Loading profiles generated from this model were used as input for a numerical simulation program based on the DEM to predict individual particle accelerations within the ballast layer. Shortcomings associated with other track analysis and numerical modeling approaches based on the principles of finite element or finite difference methods to characterize the ballast layer as one continuum are highlighted. Accordingly, through the integrated approach, the importance of modeling the ballast layer as a particulate medium is mainly emphasized, and the particle-to-particle contact for load transfer within the ballast layer is demonstrated.

7.1 Development of a 3D FEM

Abaqus is a general-purpose finite element program that can provide proper analyses of various engineering problems. Although FEM-based railway track modeling has developed drastically among researchers, track response analysis with general-purpose programs has not been frequently applied in practice. The development of a calibrated 3D FEM model has the main advantage of allowing the study of new track transitions and the evaluation of success with rehabilitation designs. Therefore, to properly develop a calibrated FEM-based track response model, the selection of certain model parameters, e.g., mesh size and geometry, type of elements used, boundary conditions, loading conditions, etc., have to be made such that the developed model is validated with field measured responses. Accordingly, this section deals with such validation to be accomplished by GeoTrack program verifications for the elastic transient responses measured at the instrumented bridge approaches. In summary, the layer moduli values back calculated using GeoTrack elastic layered analysis program were used as inputs for the newly developed 3D Abaqus FEM model to accomplish such verification.

7.1.1 Geometry of the Model

Kim et al. (2009) investigated proper finite element mesh size and geometry that should be used for a 3D multilayered model to match semi-infinite axisymmetric elastic layered analysis results for pavement foundations. They concluded that the size of the mesh in FEM had be larger than 20 times the circular wheel loading radius in the horizontal direction and 140 times the wheel

loading radius in the vertical direction in order to overcome infinite boundary assumptions inherent to the layered elastic theory. Figure 7.1 displays the 3D FE mesh and the related geometry of the model Kim et al. (2009) created.

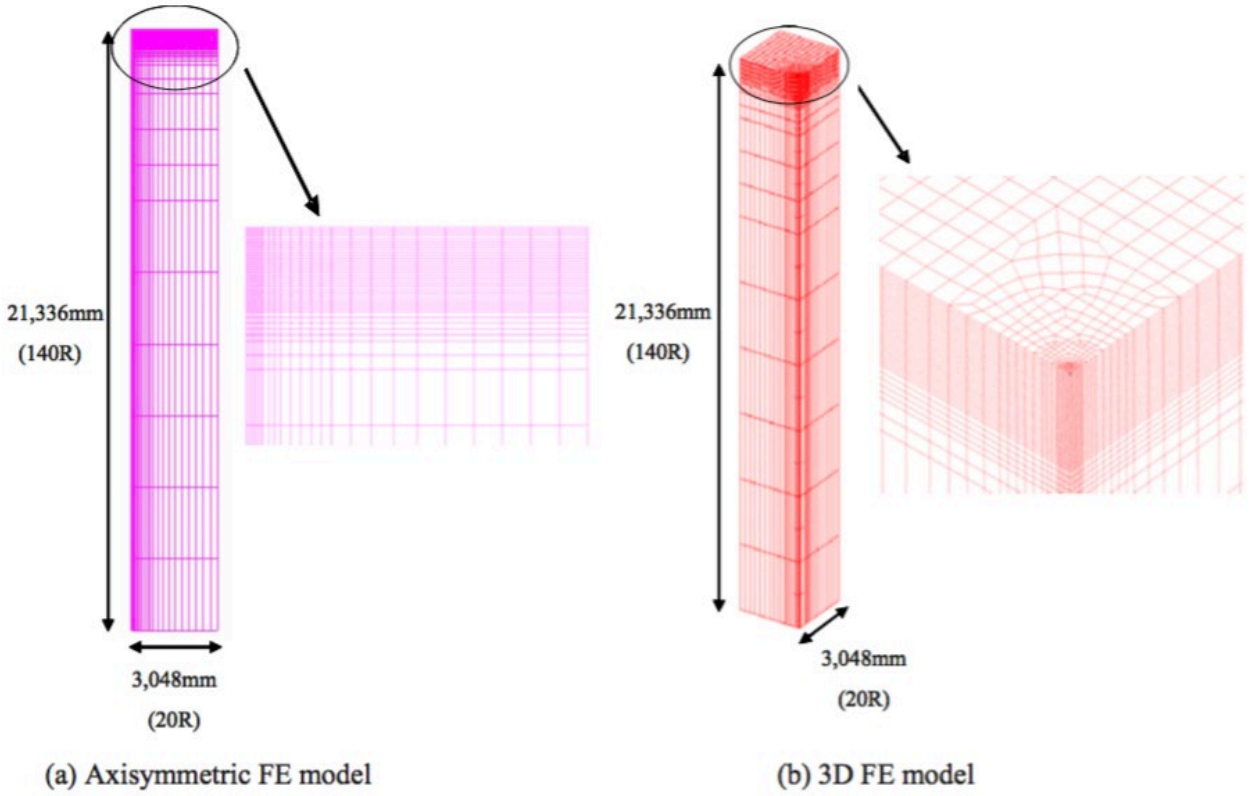

Figure 7.1: FEM Model Size Developed by Kim et. al. (2009)

In the case of the GeoTrack multilayered track response analysis, 11-tie load locations were to be represented in a 3D FEM model geometry. The distance between the centers of the first tie and the eleventh tie was 6,096 mm (240 in). The base width of each tie was 274.3 mm (10.8 in) and the half-length of the tie was 1,295.4 mm (51 in). The base of each half-tie was divided into five equal segments. Therefore, one loading configuration had a size of 274.32 mm (10.8 in) by 259.08 mm (10.2 in). When the tie group (240 in by 51 in) was placed in the center of the FE mesh, there was an additional 6,096 mm (240 in) distance to the X boundary and 6,324.6 mm (249 in) distance to the Y boundary, respectively. These distances were longer than 20 times the loading radius. As stated above, Kim et al. (2009) also reported that model depth had to be deeper than 140 times the loading radius. The total depth of five layers was taken as 2,515 mm (99 in). An extension of 17.78 m (700 in) was added to the bottom of the FE mesh to achieve the desired depth. Roller boundary conditions and half-track symmetry boundary conditions have been used in the model. Figure 7.2 and Figure 7.3 illustrate the plan and profile views, respectively, of the FE model created using the recommendation by Kim et al. (2009).

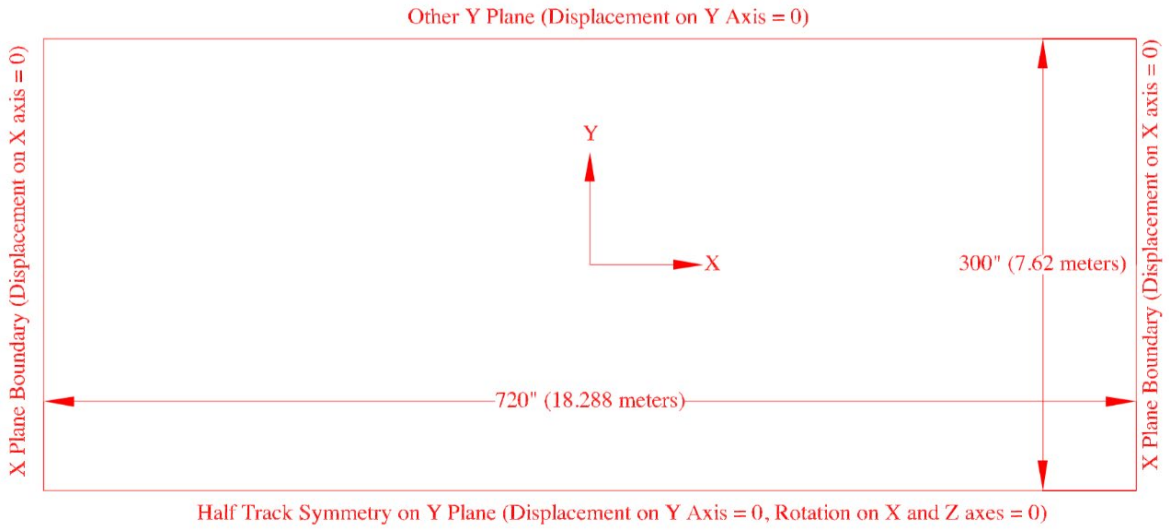

Figure 7.2: Plan View of the 3D FE Model

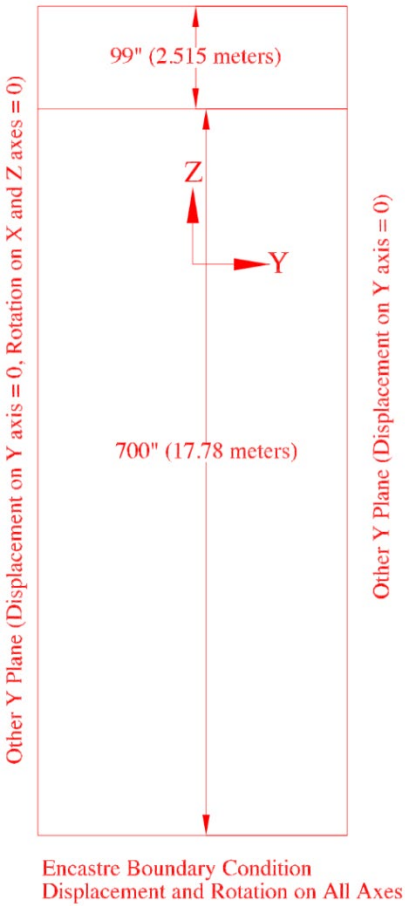

Figure 7.3: Depth of the 3D FE Model

7.1.2 Loading the Model

GeoTrack divided the bottom of the ties into 10 equal, rectangular segments and calculated the corresponding load on each segment. Since GeoTrack analysis is axisymmetric and the deepest

layer used is semi-infinite, the loads applied must be circular. Accordingly, each rectangular segment was converted into a circular area and the load was applied as uniform pressure over the circular contact area. This is illustrated for a half tie in Figure 7.4.

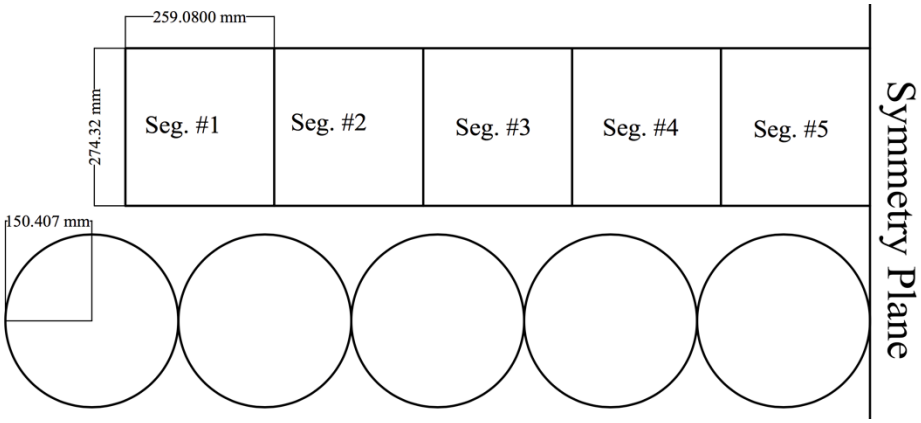

Figure 7.4: GeoTrack Half Tie Load Assignment

Note that the circle diameters added might cause longer or shorter lengths or widths than the actual tie length or tie width. As a result, this might cause slight differences in predictions by GeoTrack and the FEM model. Each circular load was obtained from the GeoTrack analyses. Figure 7.5 shows the five segments of a half tie with each segment applying uniform pressure over the circular contact area in the Abaqus FEM model.

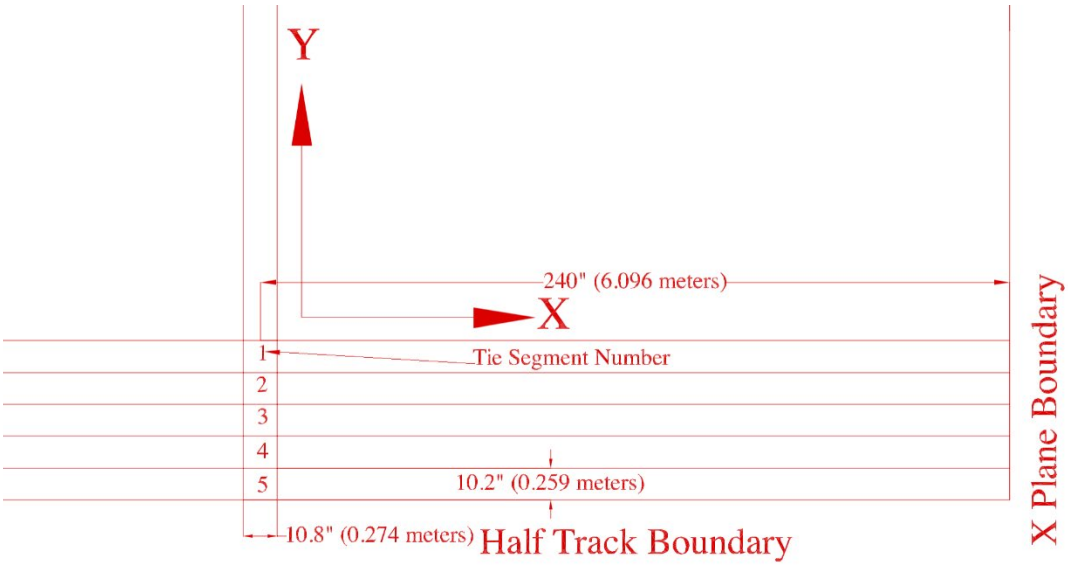

Figure 7.5: Half Tie Segment Loading Arrangement in the Model

One of the GeoTrack analysis requirements is that there should always be a load on top of tie 1. According to the wheel loads from a railroad bogie, the first axle/wheel load is applied to tie 1, and the second one is applied to ties 5 and 6 as 50-50. This load arrangement is referred to as the ties 1, 5, and 6 loading configuration, as illustrated in Figure 7.6. When this load configuration was used in GeoTrack simulations (e.g., Madison 60 ft June 2013), Table 7.1 lists the tie

segment contact pressures calculated based on the GeoTrack output. Note that these uniform pressures will need to be applied as loading in the FEM model.

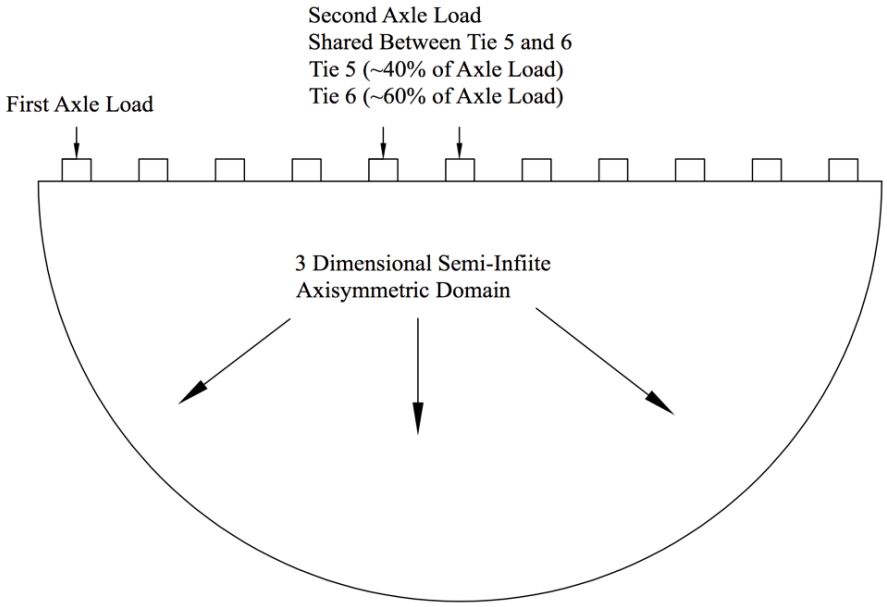

Figure 7.6: Ties 1, 5, and 6 GeoTrack Loading Configuration

Table 7.1: Tie Segment Contact Pressures Using Ties 1, 5, and 6 Loading Configuration

	Segment 1 (psi)	Segment 2 (psi)	Segment 3 (psi)	Segment 4 (psi)	Segment 5 (psi)
Tie 1	24.277	16.353	15.559	13.596	12.349
Tie 2	16.765	10.015	9.2229	8.0074	7.2849
Tie 3	10.42	5.1044	4.3691	3.6964	3.3379
Tie 4	12.209	6.5723	5.837	5.0009	4.5298
Tie 5	19.202	12.218	11.452	9.9728	9.0614
Tie 6	19.966	13.072	12.355	10.792	9.8148
Tie 7	11.942	7.1832	6.6331	5.7743	5.2633
Tie 8	4.6487	2.2195	1.8782	1.5804	1.4234
Tie 9	1.1638	0.19517	0.027233	-0.034495	-0.054466
Tie 10	-0.31409	-0.55011	-0.61547	-0.57553	-0.54012
Tie 11	-0.4793	-0.47386	-0.4902	-0.44208	-0.40759

The second load configuration consists of the main axle/wheel load applied on the sixth tie and the second axle/wheel load shared between ties 1 and 2 as 50-50. This load arrangement is illustrated in Figure 7.7. When this load configuration was used in GeoTrack simulations (e.g., Madison 60 ft June 2013), Table 7.2 lists the tie segment contact pressures calculated based on the GeoTrack output. Note that these uniform pressures will need to be applied as loading in the FEM model.

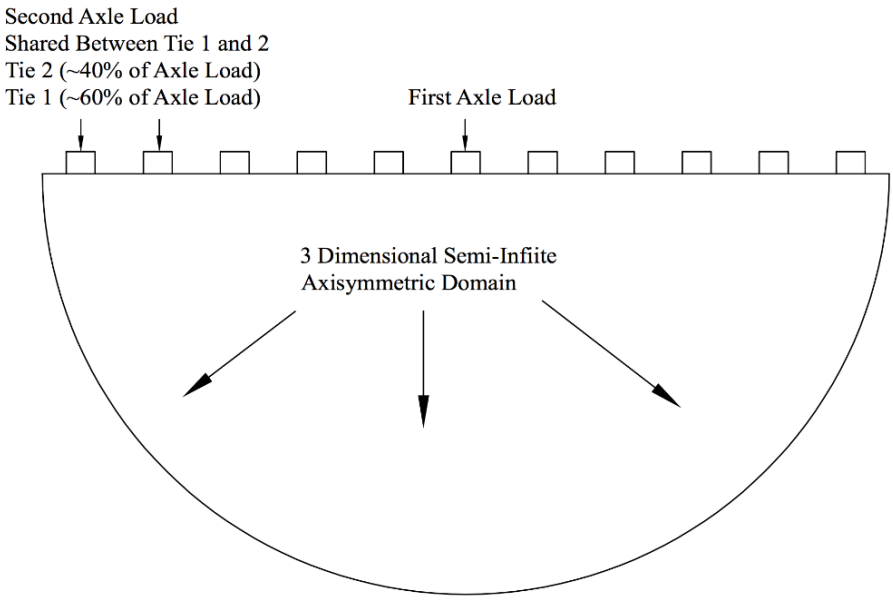

Figure 7.7: Ties 1, 2, and 6 GeoTrack Loading Configuration

Table 7.2: Tie Segment Contact Pressures Using Ties 1, 2, and 6 Loading Configuration

	Segment 1 (psi)	Segment 2 (psi)	Segment 3 (psi)	Segment 4 (psi)	Segment 5 (psi)
Tie 1	19.966	13.072	12.355	10.792	9.8148
Tie 2	19.201	12.218	11.451	9.9728	9.0614
Tie 3	12.209	6.5732	5.837	5.0009	4.5298
Tie 4	10.42	5.1044	4.3691	3.6964	3.3379
Tie 5	16.765	10.015	9.2229	8.0074	7.2849
Tie 6	24.277	16.353	15.559	13.595	12.348
Tie 7	15.631	9.6768	9.0178	7.8731	7.1814
Tie 8	6.6231	3.3978	2.9666	2.5327	2.2967
Tie 9	1.9798	0.60094	0.37582	0.26235	0.21423
Tie 10	0.025418	-0.38762	-0.48112	-0.46841	-0.44844
Tie 11	-0.82335	-0.81336	-0.8406	-0.7589	-0.69989

Since GeoTrack analysis uses the axisymmetric geometry and these two loading configurations are symmetric, the layer deformation results obtained under tie 1 for the first configuration and under tie 6 for the second configuration were exactly the same. However, when the contact pressures listed in Table 7.1 and Table 7.2 above were applied as loading in the FEM model, the results for predicted layer deformations at the Madison 60 ft location for June 2013 differed significantly from the GeoTrack results. Table 7.3 lists the percent differences between the GeoTrack and Abaqus results.

Table 7.3: Predicted Layer Deformations Compared for the Applied Tie Load Sequences

Madison 60 ft June 2013	Abaqus FEM Model Tie Loading 1, 2 and 6 Percent Difference from GeoTrack results	Abaqus FEM Model Tie Loading 1, 5 and 6 Percent Difference from GeoTrack results
Layer 1	-1.196	0.695
Layer 2	8.856	0.071
Layers 3 + 4	20.886	-0.622
Layer 5	24.543	-0.825

As listed in Table 7.3, the differences for the second load configuration (tie loading 1, 5 and 6) were typically below 1 percent. However, the differences for the first load configuration (tie loading 1, 2 and 6) were significantly higher, especially for the track substructure layers 3+4 and 5, which were of course deeper layers with low deformation values. Note that the distances between the X and Y boundaries in the FE mesh and the first tie segment 2 were approximately 240 in and 233.7 in, respectively. Considering the load radius R=5.4 in, these distances corresponded to almost 44R, more than twice the 20R recommended by Kim et al. (2009). However, these distances did not satisfy boundary conditions and/or the size of the FE mesh in the X direction, considering the wheel load interaction and overlap with the FE mesh boundaries. The solution was either to increase the FE mesh geometry or conduct analyses considering only the tie 1, 2, and 6 loading configuration for GeoTrack analysis. Since the second option was proved efficient and computationally less expensive than the first, it was adopted in this study. Accordingly, Figure 7.8 and Figure 7.9 illustrate screen shots of the 3D Abaqus FE mesh assembly indicating the boundary conditions and the loading configuration, respectively.

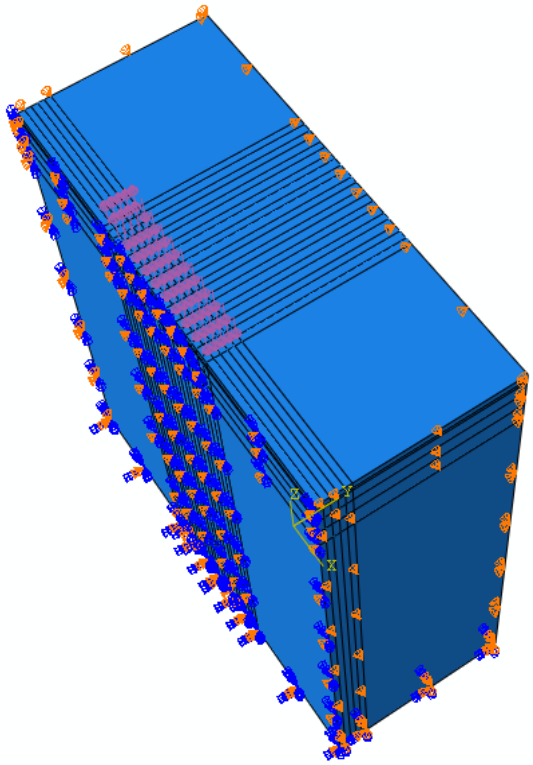

Figure 7.8: Abaqus FE Mesh and the Boundary Conditions

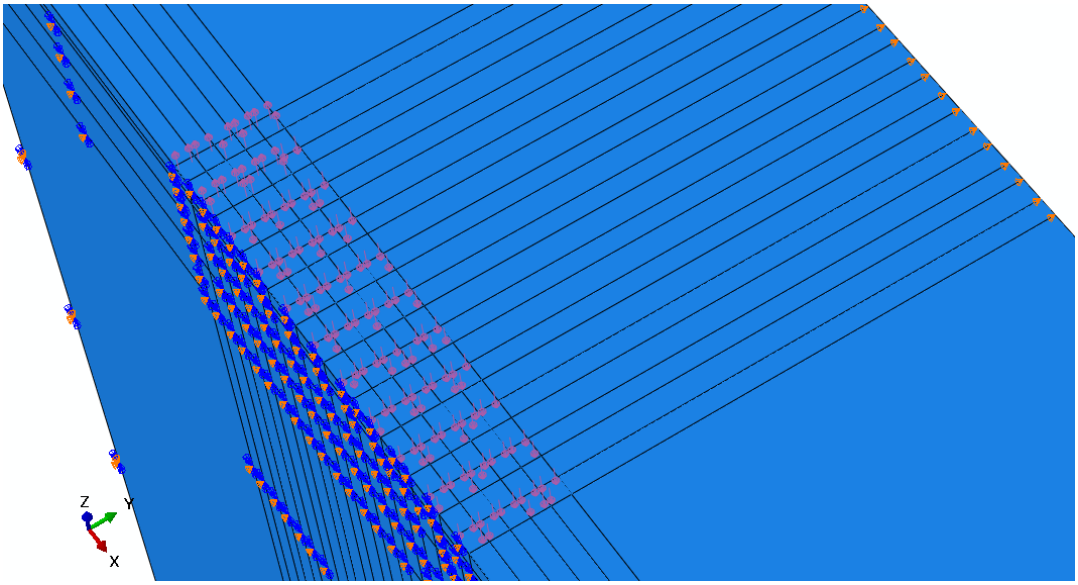

Figure 7.9: Abaqus FEM Model Zoomed to Indicate GeoTrack Loading Assembly

7.1.3 3D FEM Abaqus Element Types and Mesh Geometry

Two types of isoparametric elements used in this study were C3D8 and C3D20, available in standard Abaqus libraries. C3D8 is an 8-noded 3D brick element while C3D20 is a 20-noded 3D brick element. Figure 7.10 illustrates the element types with the node locations indicated.

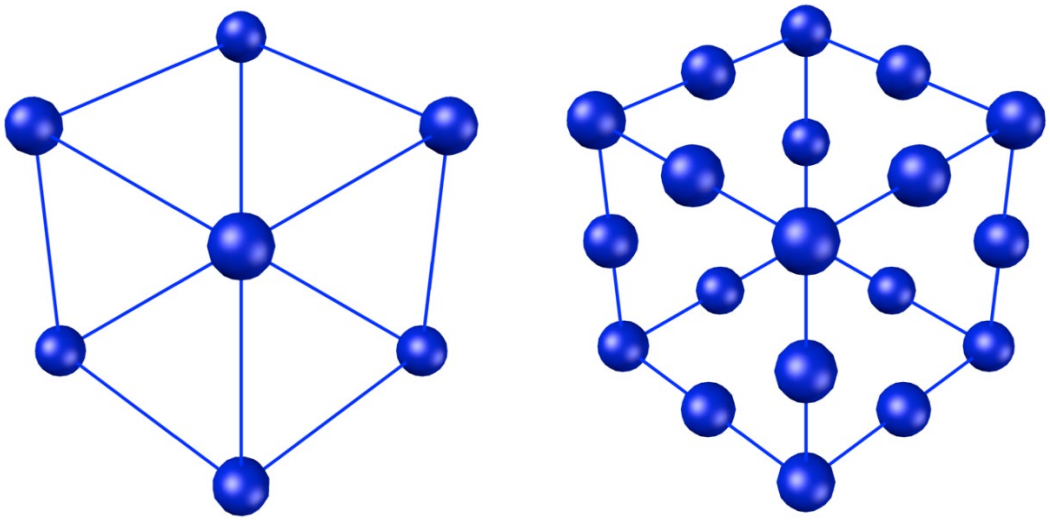

(a) (b)

Figure 7.10: Element Types: (a) C3D8 Element; (b) C3D20 Element

Two mesh scales, coarse and fine, were adopted in this study. Coarse scale mesh contains around 5,000 elements, while fine scale contains around 200,000 elements. Both models were meshed twice using the C3D8 and C3D20 elements. The predicted layer deformations at the Madison 60 ft location for June 2013 are presented in Table 7.4 for comparison with the GeoTrack results. The FEM model with 50,400 C3D20 elements and 2,046,000 C3D20 elements displayed similar

results. For better computational efficiency with less run times, coarse meshing with the C3D20 elements was used in the Abaqus FEM model simulations.

Table 7.4: Predicted Layer Deformations Compared for Different Meshing and Elements

Madison 60 ft June 2013	50400 C3D8 Percent Difference (GeoTrack)	50400 C3D20 Percent Difference (GeoTrack)	204600 C3D8 Percent Difference (GeoTrack)	204600 C3D20 Percent Difference (GeoTrack)
Layer 1	-8.932	0.695	0.216	0.720
Layer 2	1.510	0.071	0.647	0.018
Layers 3 + 4	-0.068	-0.622	-0.267	-0.625
Layer 5	-0.541	-0.825	-0.599	-0.825

Figure 7.11 and Figure 7.12 present the plan view and Y-Z view of the FEM model after meshing, respectively. Moreover, Figure 7.13 displays the 3D view of the meshed model for the coarse meshing with the C3D20 elements. The zoomed view illustrated in Figure 7.13(b) shows the refined mesh in the middle zone where the 11 ties applied the wheel loading.

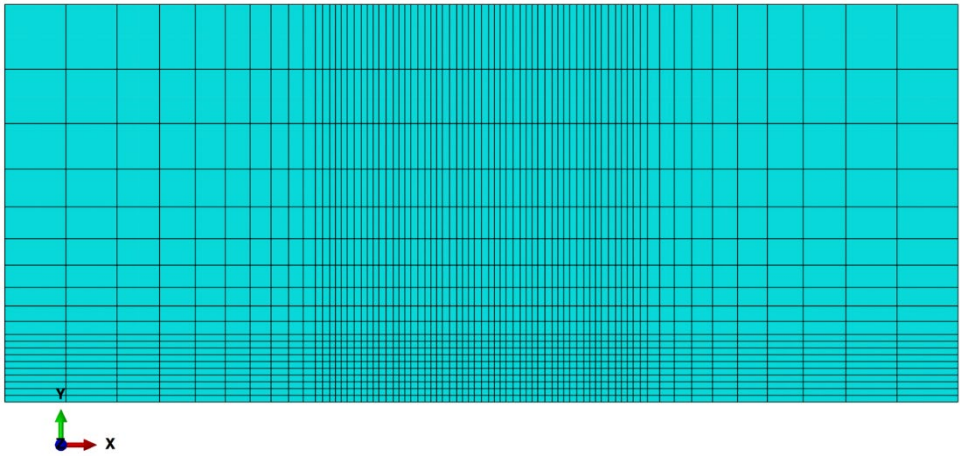

Figure 7.11: Plan View of the FE Mesh

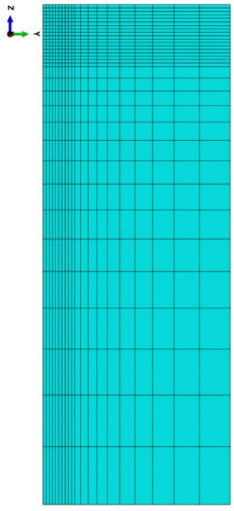

Figure 7.12: Y-Z View of the FE Mesh

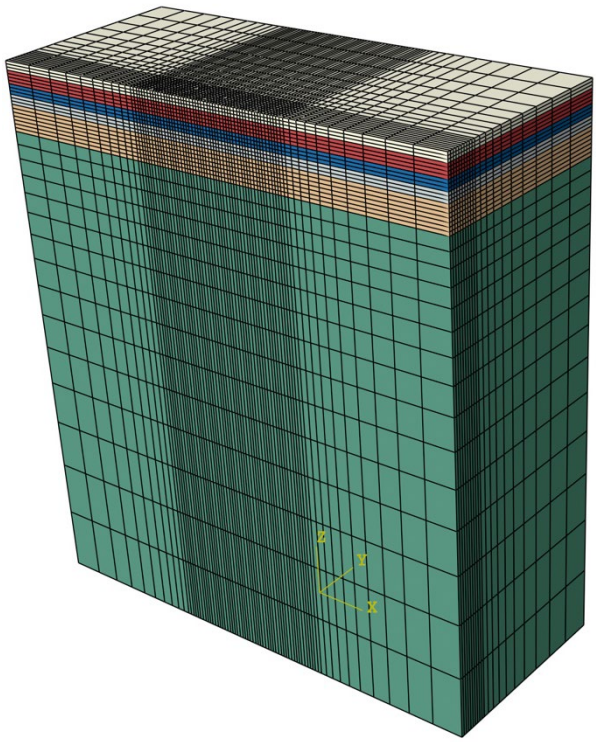

(a)

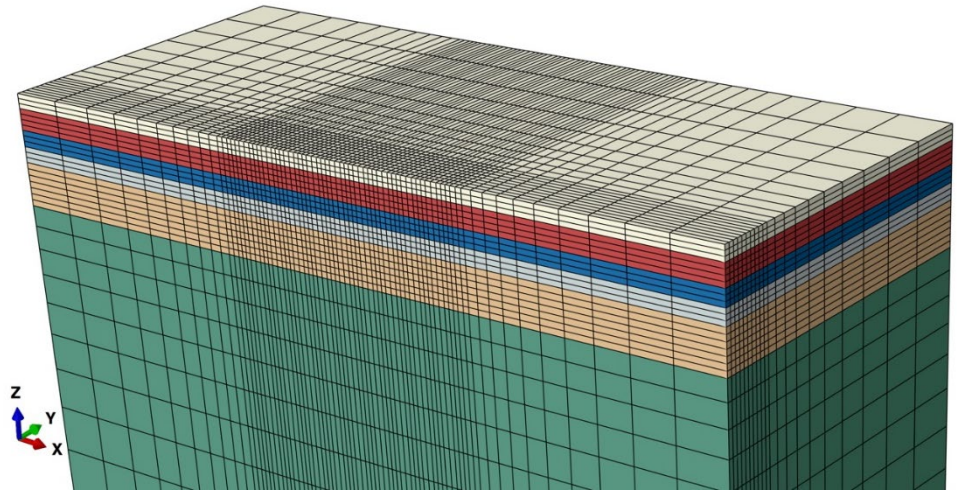

(b)

Figure 7.13: 3D View of the FE Mesh: (a) Geometry; (b) Zoomed View of the Model

The elasticity modulus and Poisson's ratio values obtained from GeoTrack backcalculation results were assigned to the Abaqus model and the loads corresponding to each GeoTrack simulation are applied to the top of layer 1 as described above. Comparisons between the GeoTrack-predicted layer displacements and those obtained by the Abaqus FEM model were made in the following section to validate the developed Abaqus model.

7.2 Validation of the 3D FEM Model

In this section layer deformation prediction results of the developed Abaqus FEM model are presented and compared to the GeoTrack results for verification. Figure 7.14 displays a typical view of the deformed track after simulation. Note the higher deformations indicated under the first tie and the fifth and sixth ties corresponding to the tie 1, 5 and 6 loading configuration (see Table 7.3)

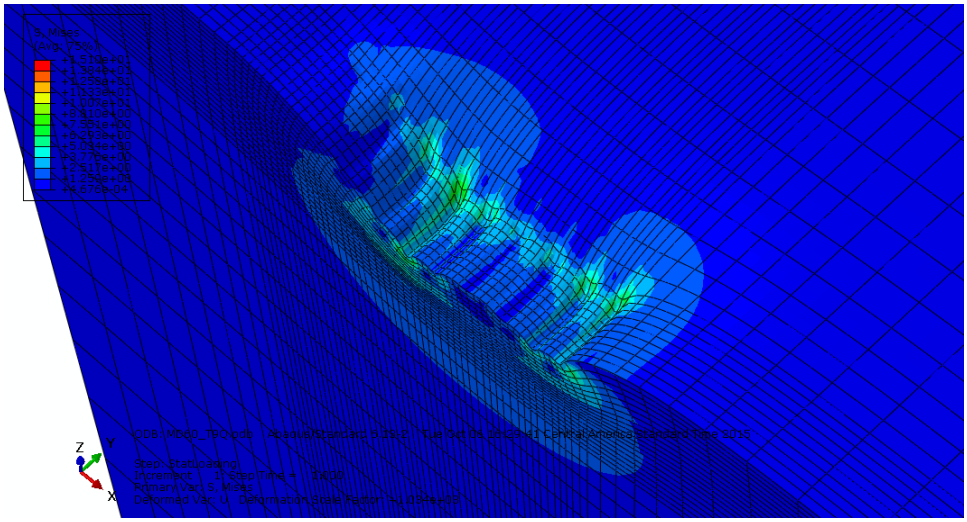

Figure 7.14: Deformation View of Abaqus FEM Model Subjected to Tie 1, 5, and 6 Loading Configuration

7.2.1 Numerical Modeling of Upland Street Bridge Approach

Near-Bridge Location (Upland 15 ft)

Table 7.5 lists layer material properties back calculated using GeoTrack for the Upland 15 ft near-bridge location. These material properties were used as inputs in Abaqus simulations. The loads calculated were applied to the FEM model created and comparison results with negligible percentage differences are displayed in Figure 7.15.

Table 7.5: Upland Street Near-Bridge Track Location Elastic Layer Modulus Values Back calculated Using GeoTrack

Track	UPLAND 15-FT							
Substructure	Aug-12		Nov-12		Jan-13		Jun-13	
	E (MPa)	ν	E (MPa)	ν	E (MPa)	ν	E (MPa)	ν
Layer 1	153	0.35	40	0.35	100	0.35	34	0.35
Layer 2	80	0.35	111	0.35	87	0.35	77	0.35
Layer 3	33	0.4	43	0.4	39	0.4	42	0.4
Layer 4	33	0.4	43	0.4	39	0.4	42	0.4
Layer 5	123	0.4	110	0.4	118	0.4	111	0.4

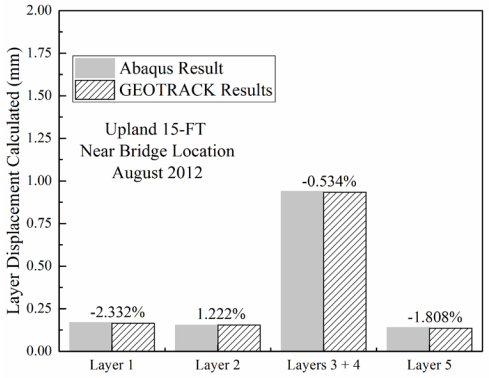

(a) UPLAND 15 ft August 2012

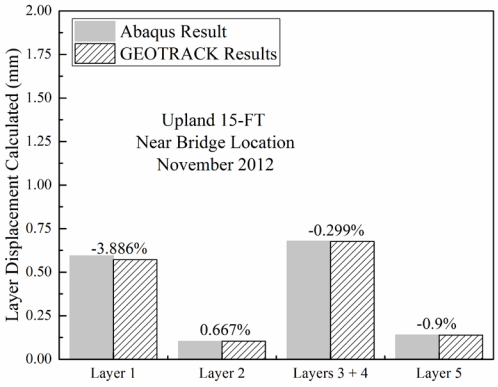

(b) UPLAND 15 ft November 2012

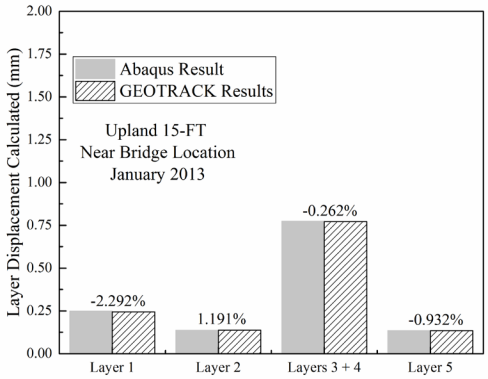

(c) UPLAND 15 ft January 2013

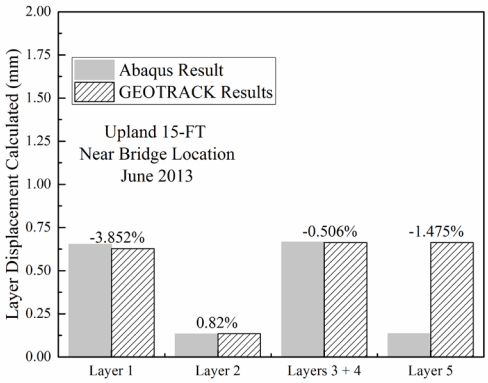

(d) UPLAND 15 ft June 2013

Figure 7.15: Upland 15 ft Predicted Layer Deformations and Percent Differences

Figure 7.15 presents almost perfect matches between the Abaqus FEM model-predicted layer deformations and the GeoTrack results. The maximum absolute percent difference was 3.886 for the November 2012 layer 1 displacement. Most comparison results were either below or around 1 percent.

Open-Track Location (Upland 60 ft)

Table 7.6 presents layer material properties back calculated using GeoTrack for the Upland 60 ft open-track location. These material properties were used in Abaqus simulations as inputs. The loads calculated were applied to the FEM model created and comparison results with negligible percentage differences are displayed in Figure 7.15.

Table 7.6: Upland Street Open-Track Location Elastic Layer Modulus Values Back calculated Using GeoTrack

Track	UPLAND 60-FT							
Substructure	Aug-12		Nov-12		Jan-13		Jun-13	
	E (MPa)	ν	E (MPa)	ν	E (MPa)	ν	E (MPa)	ν
Layer 1	184	0.35	205	0.35	180	0.35	230	0.35
Layer 2	19	0.35	57	0.35	60	0.35	54	0.35
Layer 3	31	0.4	30	0.4	31	0.4	31	0.4
Layer 4	37	0.4	33	0.4	31	0.4	32	0.4
Layer 5	70	0.4	70	0.4	64	0.4	70	0.4

When comparing predictions with the GeoTrack results, Figure 7.16 again shows almost perfect matches. Note that percent differences were slightly higher than those calculated for the Upland 15 ft location, possibly because the actual deformation values were smaller. The maximum absolute percent difference was 8.604 percent for the January 2013 layer 1 displacement. Most of the higher difference values were observed in layer 1 for ballast.

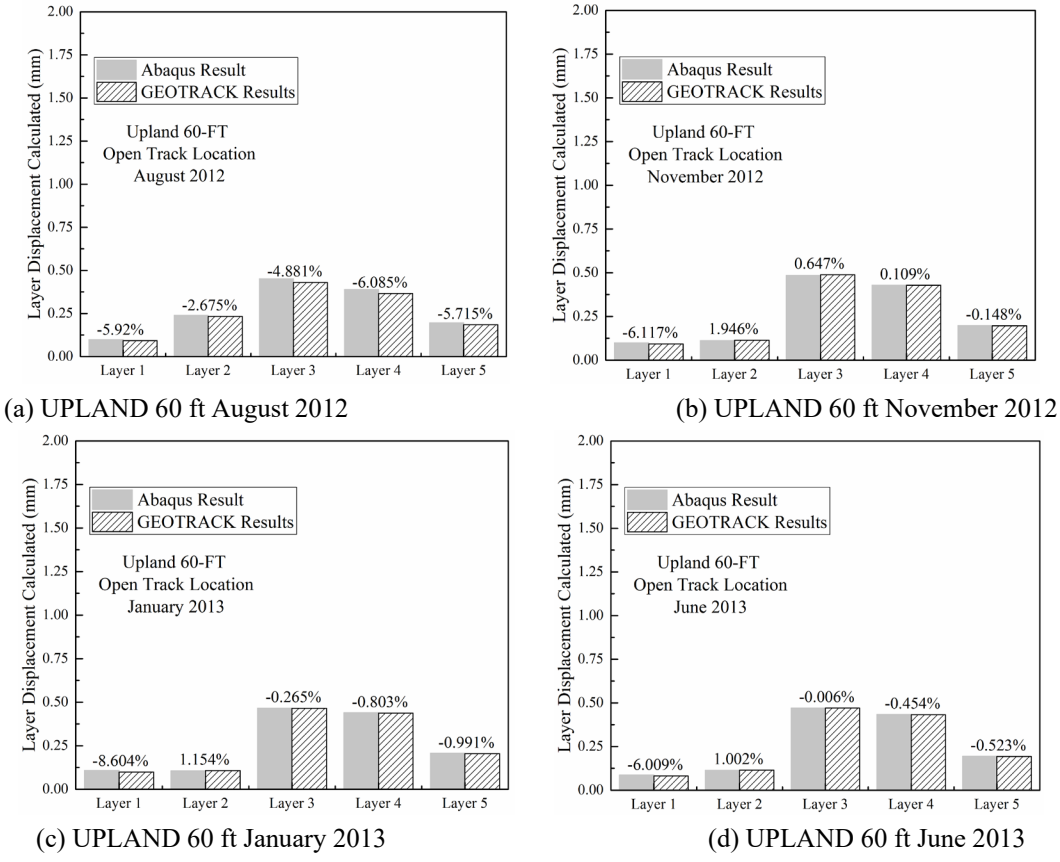

(a) UPLAND 60 ft August 2012

(b) UPLAND 60 ft November 2012

(c) UPLAND 60 ft January 2013

(d) UPLAND 60 ft June 2013

Figure 7.16: Upland 60 ft Predicted Layer Deformations and Percent Differences

7.2.2 Numerical Modeling of Madison Street Bridge Approach

Near-Bridge Location (Madison 12 ft)

Table 7.7 lists layer material properties back calculated using GeoTrack for the Madison 12 ft near-bridge location. These material properties were used as inputs in Abaqus simulations. The

loads calculated were applied to the FEM model created and comparison results with percentage differences are shown in Figure 7.16 (above).

Table 7.7: Madison Street Near-Bridge Track Location Elastic Layer Modulus Values Back calculated Using GeoTrack

Track	MADISON 12-FT							
Substructure	Aug-12		Nov-12		Jan-13		Jun-13	
	E (MPa)	ν	E (MPa)	ν	E (MPa)	ν	E (MPa)	ν
Layer 1	70	0.35	94	0.35	102	0.35	78	0.35
Layer 2	70	0.35	94	0.35	102	0.35	78	0.35
Layer 3	37	0.4	51	0.4	57	0.4	40	0.4
Layer 4	41	0.4	60	0.4	42	0.4	39	0.4
Layer 5	36	0.4	36	0.4	38	0.4	35	0.4

When comparing predictions with the GeoTrack results, Figure 7.17 in general shows close matches, although some of the Abaqus FEM predictions indicated up to 30 percent differences. These larger differences were primarily for layers 3 and 4 and from the January 2013 and June 2013 MDD data collected. However, such discrepancies were not observed for the November 2012 predictions, which showed excellent matches.

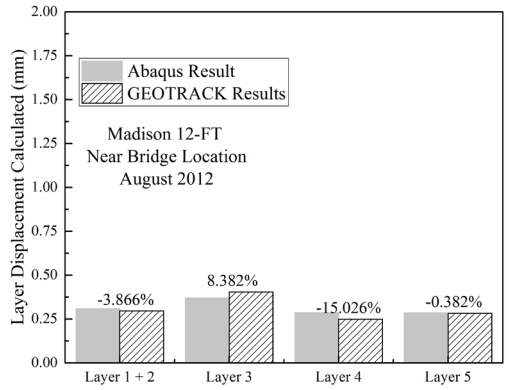

(a) MADISON 12 ft August 2012

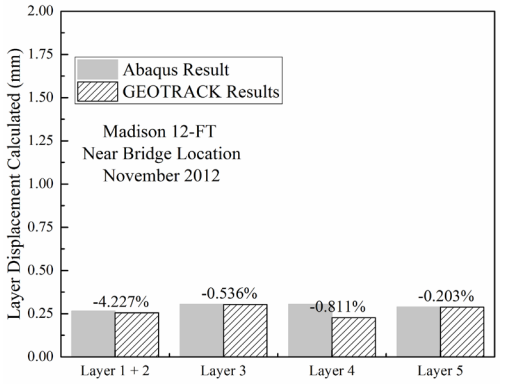

(b) MADISON 12 ft November 2012

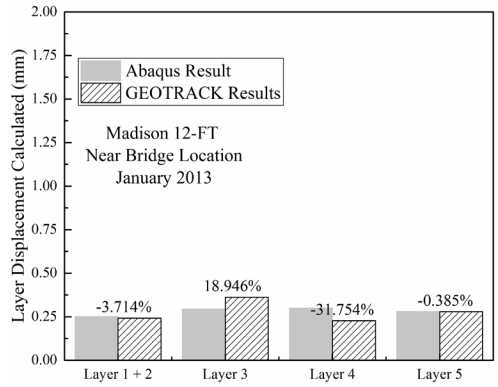

(c) MADISON 12 ft January 2013

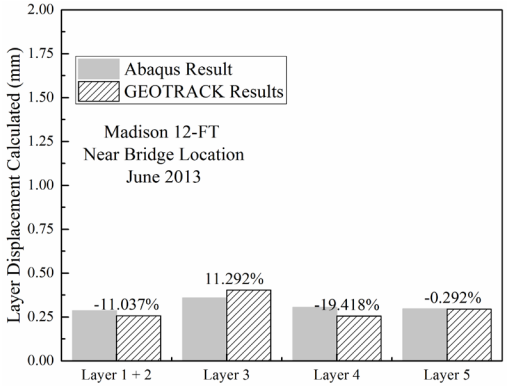

(d) MADISON 12 ft June 2013

Figure 7.17: Madison 12 ft Predicted Layer Deformations and Percent Differences

Open-Track Location (Madison 60 ft)

Table 7.8 presents layer material properties back calculated using GeoTrack for the Madison 60 ft open-track location. These material properties were used as inputs in Abaqus simulations. The loads calculated were applied to the FEM model created and comparison results with percentage differences are shown in Figure 7.18. The best comparison results were obtained in this location. Except for two values (2.47 percent and -1.216 percent), the differences were below 1 percent.

Table 7.8: Madison Street Open-Track Location Elastic Layer Modulus Values Back calculated Using GeoTrack

Track	MADISON 60-FT							
Substructure	Aug-12		Nov-12		Jan-13		Jun-13	
	E (MPa)	ν	E (MPa)	ν	E (MPa)	ν	E (MPa)	ν
Layer 1	32	0.35	155	0.35	96	0.35	105	0.35
Layer 2	56	0.35	80	0.35	80	0.35	60	0.35
Layer 3	35	0.4	39	0.4	41	0.4	34	0.4
Layer 4	35	0.4	39	0.4	41	0.4	34	0.4
Layer 5	54	0.4	50	0.4	54	0.4	49	0.4

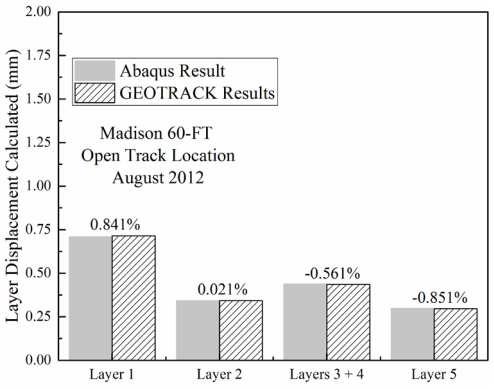

(a) MADISON 60 ft August 2012

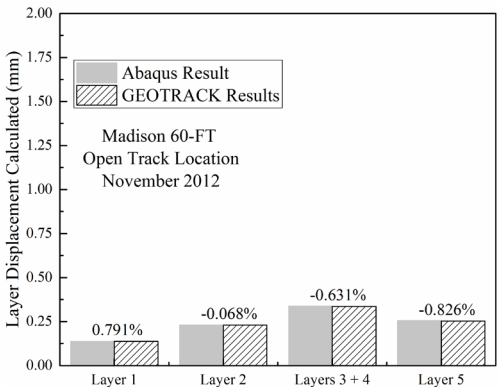

(b) MADISON 60 ft November 2012

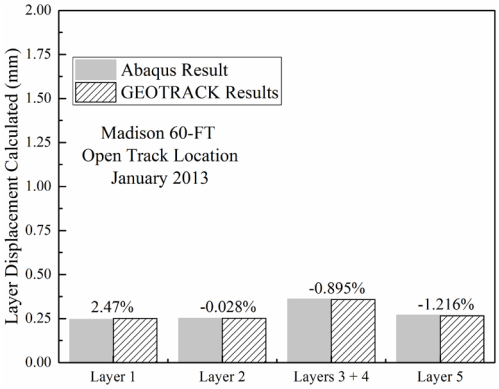

(c) MADISON 60 ft January 2013

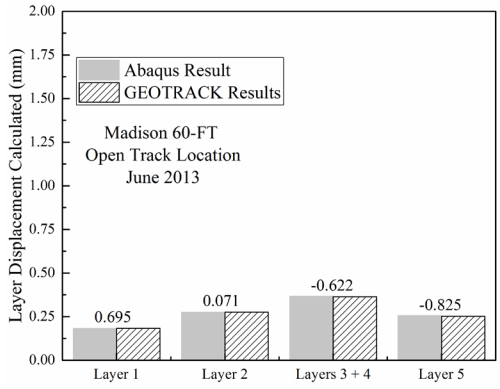

(d) MADISON 60 ft June 2013

Figure 7.18: Madison 60 ft Predicted Layer Deformations and Percent Differences

7.2.3 *Numerical Modeling of Caldwell Street Bridge Approach*

Table 7.9 lists layer material properties back calculated using GeoTrack for the Caldwell Street west end of tie location. These material properties were used as inputs in Abaqus simulations. The loads calculated were applied to the FEM model and results compared in Figure 7.19. The comparisons indicate most differences to be below 1 percent, with the absolute maximum percent difference of 3.42 percent observed in ballast layers for the June 2013 data.

Table 7.9: Caldwell Street West End of Tie Track Location Elastic Layer Modulus Values Back calculated Using GeoTrack

Track	CALDWELL WEST END OF TIE					
Substructure	Nov-12		Jan-13		Jun-13	
	E (MPa)	ν	E (MPa)	ν	E (MPa)	ν
Layer 1	52	0.35	57	0.35	50	0.35
Layer 2	52	0.35	57	0.35	50	0.35
Layer 3	126	0.4	130	0.4	130	0.4
Layer 4	38	0.4	39	0.4	35	0.4
Layer 5	80	0.4	75	0.4	80	0.4

Table 7.10 presents layer material properties back calculated using GeoTrack for the Caldwell Street east end of tie location. These material properties were used as inputs in Abaqus simulations. The loads calculated were applied to the FEM model and results compared in Figure 7.20. The largest percent differences of up to 6 percent are found to be in layers 1 and 4.

Table 7.10: Caldwell Street East End of Tie Track Location Elastic Layer Moduli Values Back calculated Using GeoTrack

Track	CALDWELL WEST END OF TIE					
Substructure	Nov-12		Jan-13		Jun-13	
	E (MPa)	ν	E (MPa)	ν	E (MPa)	ν
Layer 1	80	0.35	80	0.35	125	0.35
Layer 2	60	0.35	49	0.35	50	0.35
Layer 3	65	0.4	70	0.4	75	0.4
Layer 4	27	0.4	27	0.4	27	0.4
Layer 5	55	0.4	50	0.4	55	0.4

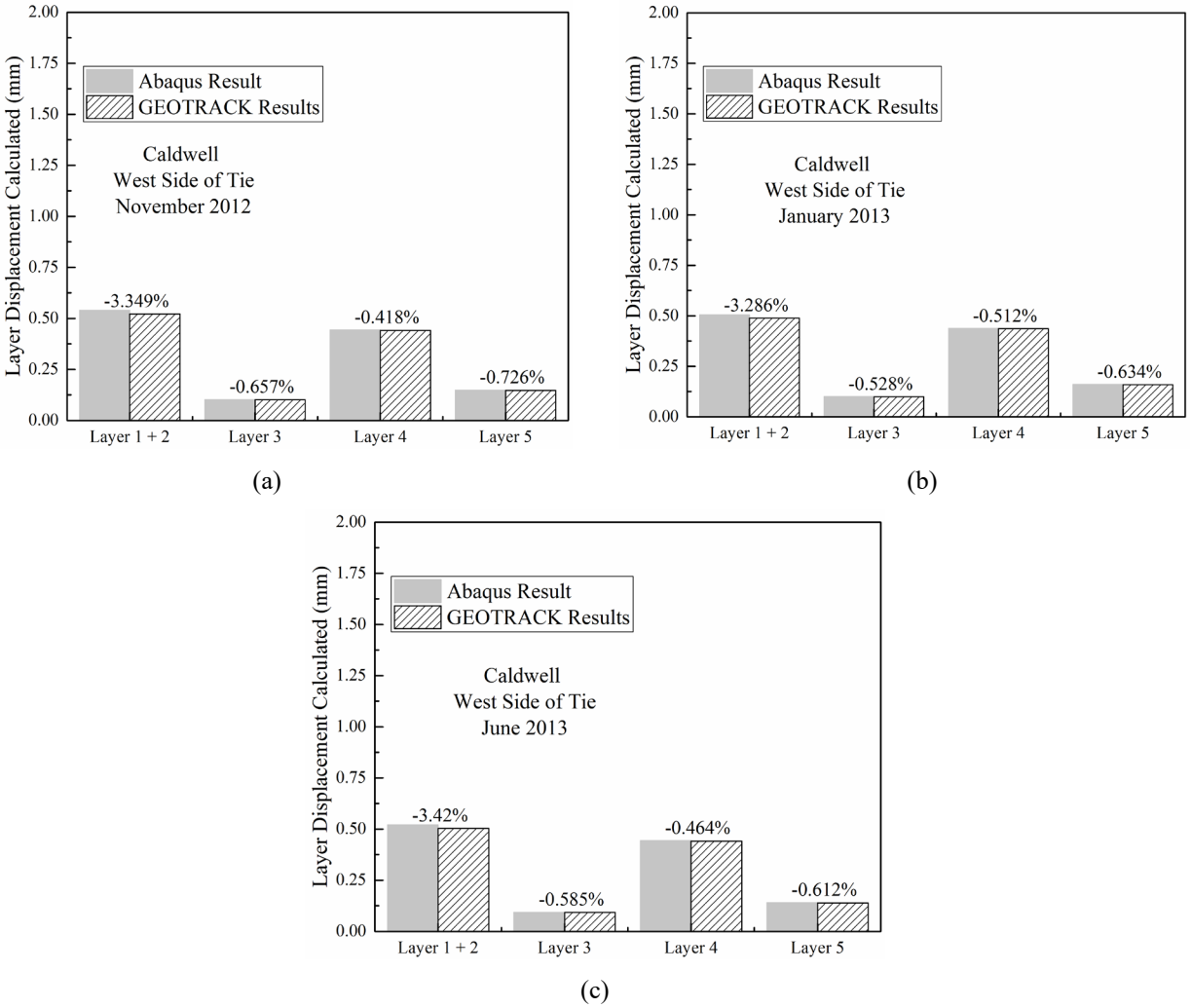

Figure 7.19: Caldwell West End of Tie Predicted Layer Deformations and Percent Differences: (a) Caldwell West – November 2012; (b) Caldwell West – January 2013; (c) Caldwell West June 2013

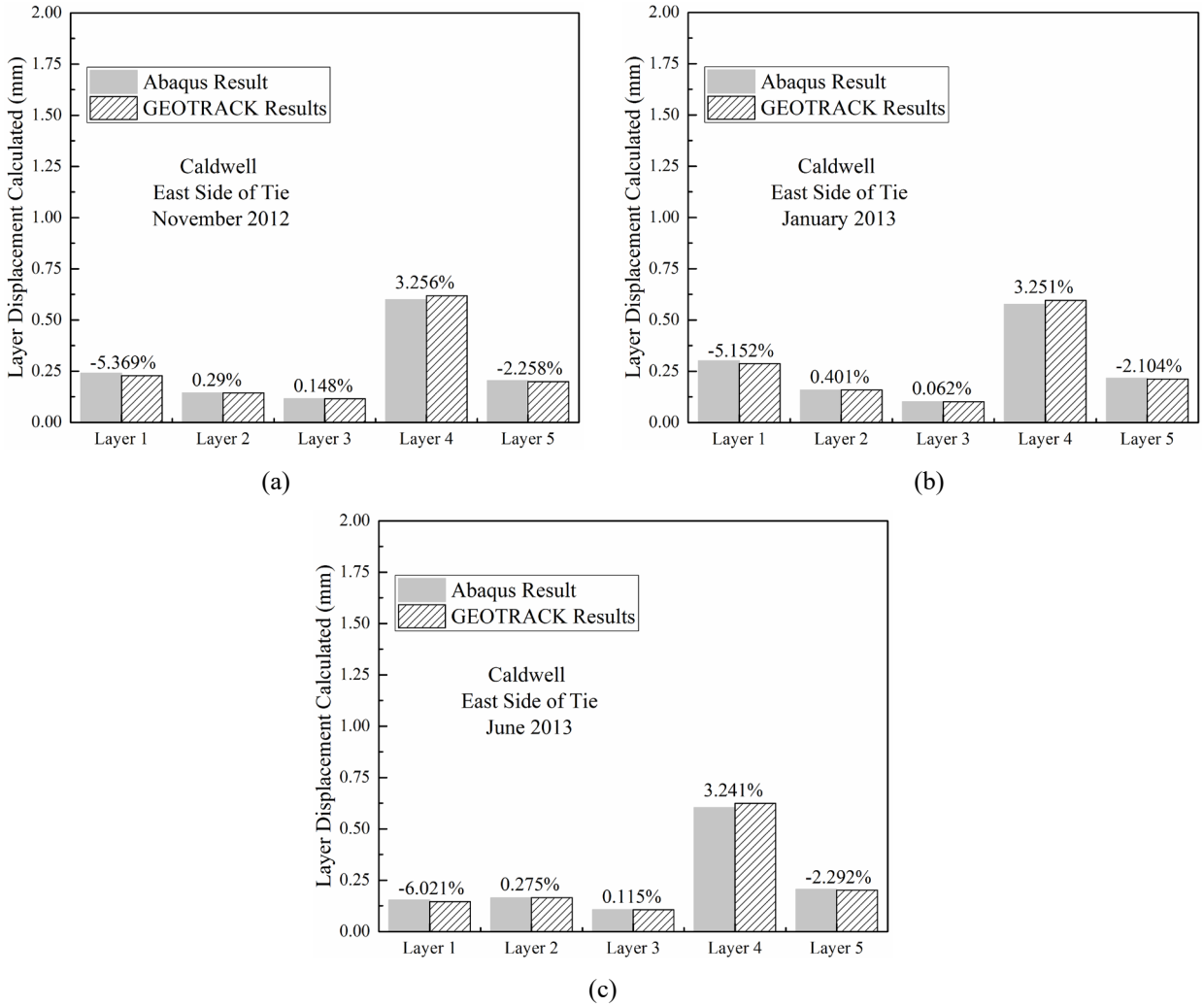

Figure 7.20: Caldwell East End of Tie Predicted Layer Deformations and Percent Differences: (a) Caldwell East November 2012; (b) Caldwell East January 2013; (c) Caldwell East June 2013

7.3 3D FEM Model to Predict Performances of Remedial Measures

In the previous sections, GeoTrack elastic layered program results were used to check against and verify the Abaqus 3D FEM model-predicted layer displacements. This helped to ensure the validity of the FE mesh and the geometry adopted, applied tie loading configuration, and the material input properties selected in the development of the 3D FEM model. Note that due to the GeoTrack input and geometry requirements, e.g., uniform pressure applied over circular area, etc., no ties and rails, which are the main load transfer components in the track structure, were created in the FEM model. In this section, a few changes are made to the model to include the ties and rail, which are described in detail. Moreover, by using GeoTrack back calculated layer material properties in the 3D FEM model, track substructure conditions related to the effects of remedial measures applied on Madison and Upland Street locations are investigated for the measured field performance.

The 3D FEM model considered segmentation of the tie loads according to the assumptions made in GeoTrack analyses, as illustrated in Figure 7.4 and Figure 7.5. Since the new model would include the actual concrete tie geometry and the associated contact areas for loading, the center of the rail was aligned with element boundaries in meshing so that accurate layer displacement results could be predicted. Standard rail gauge used in north America and most regions in the world is 1,435.1 mm. This gauge value indicates the distance between the inner edges of the surface of rail heads. The distance between the center of the rail would then vary with the width of the railhead. The standard 136 lb/yard rail has a head width of approximately 74.613 mm. Therefore, the distance between rail centers is around 1,510 mm. This value has also been used in GeoTrack. Therefore, the distance between the center of the tie (half symmetry plane) and the rail center is approximately 755 mm. In order to adjust the rail lineup, segmentation of tie contact surfaces was adjusted, as indicated in Figure 7.21. Accordingly, segments 1, 4, and 5 had equal dimensions. However, the line separating segments 2 and 3 were adjusted according to the rail lineup.

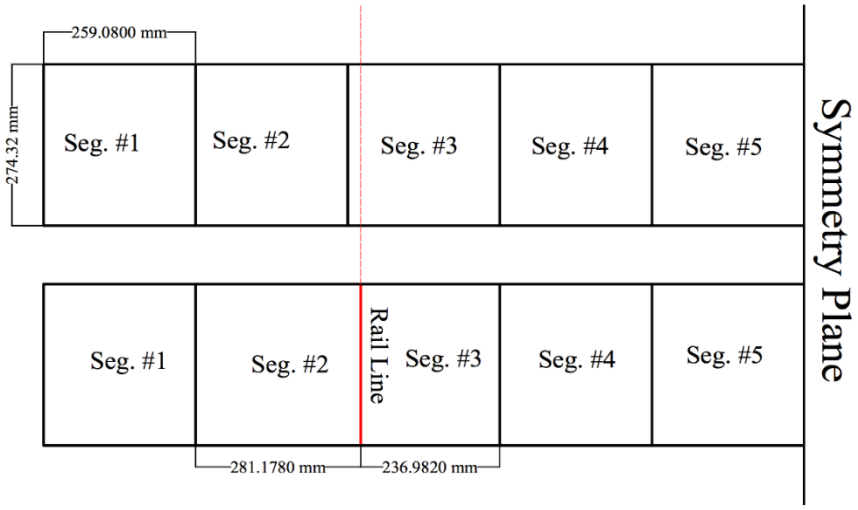

Figure 7.21: Adjusted Tie Segments in the New 3D FEM Model to Include Rails and Ties

A new FE mesh with half tie representation was created and included in the 3D FEM model. Accordingly, the half-track boundary was placed on the center planes of the ties. An elasticity modulus value of 2.07E+4 MPa and Poisson's ratio of 0.15 were assigned to ties. The half-tie dimensions used were 1,295.4 mm length, 274.32 mm base width, 228.6 mm top surface width, and 177.8 mm height. A 3D view of the half tie discretization is shown in Figure 7.22.

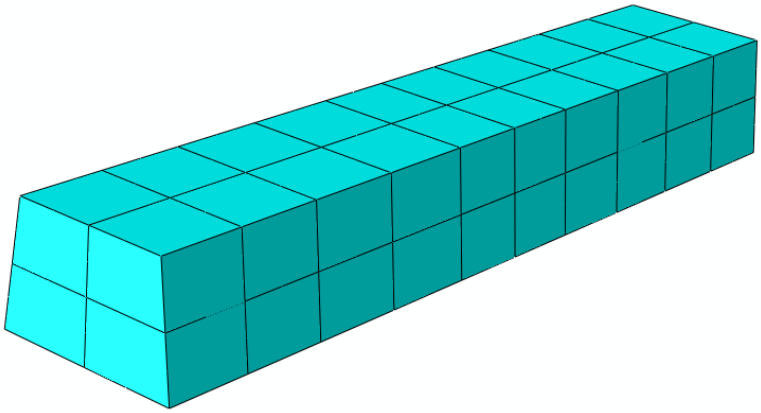

Figure 7.22: 3D View of Half Tie Created

Rail was created using a wire geometry with a length of 6324.6 mm that spans 11 ties. Three-node quadratic beam elements (B32 in Abaqus libraries) were used to mesh the rail. An elasticity modulus value of 2.07E+5 MPa and Poisson's ratio of 0.25 were assigned to the rail. A rectangular section having a width of 152.4 mm and a height of approximately 145.35 mm was assigned to the rail, which had a similar moment of inertia to the 136 lb/yard rail. The ties and rails were inserted in the model. A 3D view of FEM model assembly is shown in Figure 7.23.

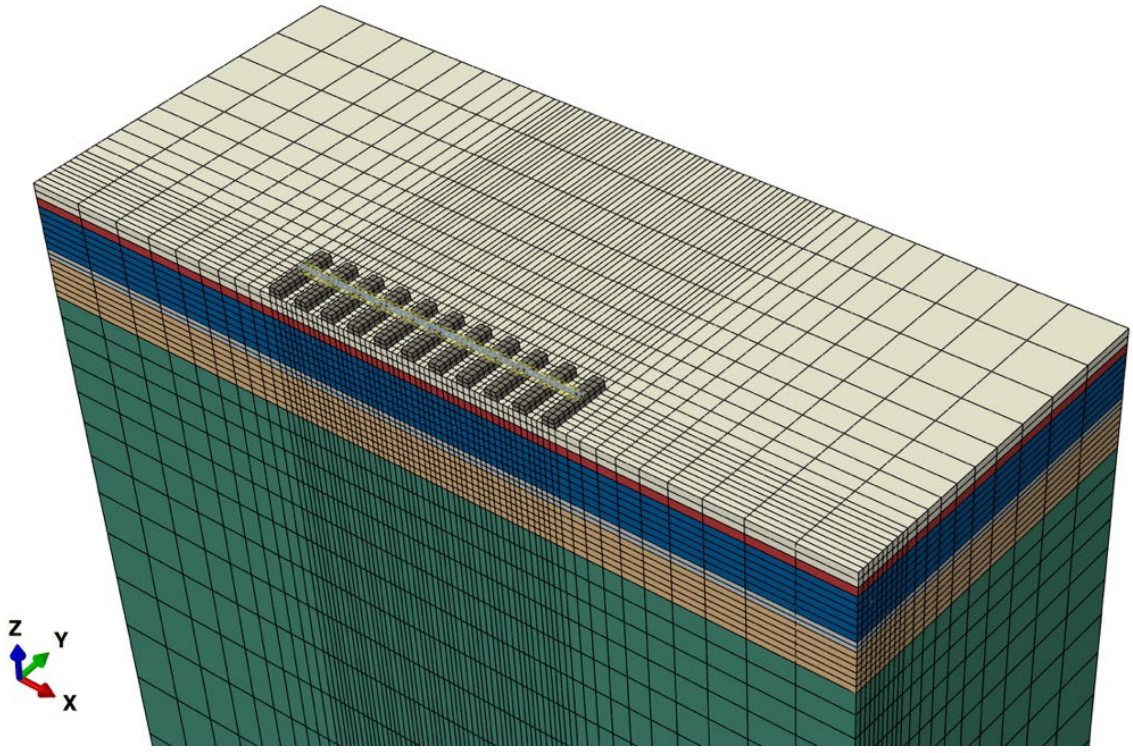

Figure 7.23: 3D View of the FEM Model Showing Half Ties and Rail Assembly

Two loads recorded from the field measurements on the rail representing front and rear axle/wheel loads of an ACELA locomotive bogie were used in the FEM analyses. The distance between the front and rear loads was 2,844.8 mm. The front axle/wheel load was applied to the sixth (center) tie and the rear load was applied between the tenth and eleventh ties. Figure 7.24

displays loads applied on rail. Table 7.11 lists the layer material properties back calculated using GeoTrack and used to predict before and after polyurethane injection behavior. Comparisons between Abaqus predictions and the field-measured layer displacements are given in Figure 7.25. Although the FEM predictions differed somewhat from the field measurements by up to 26 percent – as expected due to certain assumptions and limitations in the 3D FEM model – the typical layer displacement trends still matched fairly closely.

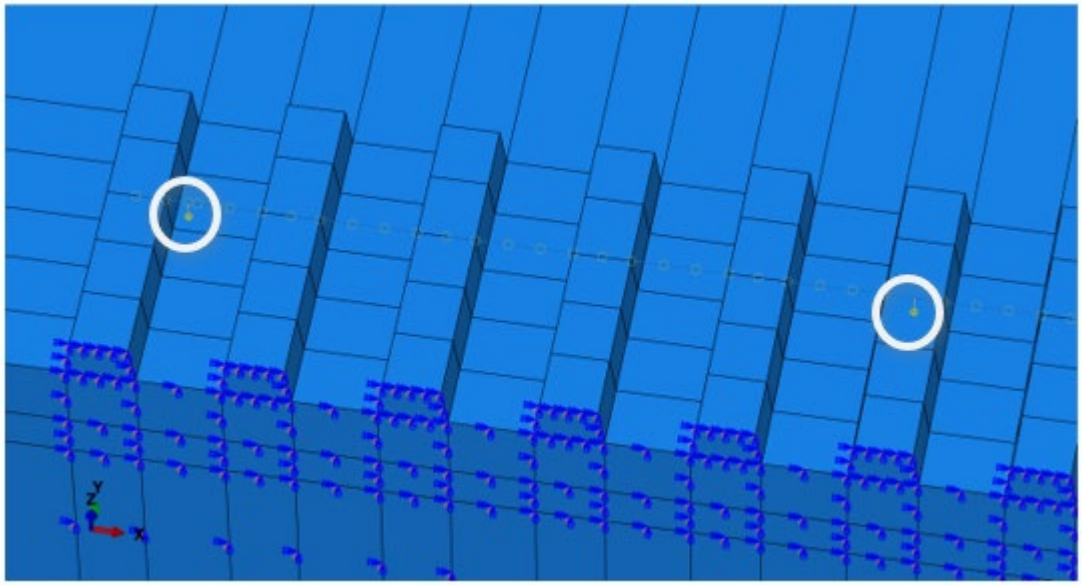

Figure 7.24: Loads Applied on Rail by an Acela Locomotive Bogie

Table 7.11: Upland Street Near-Bridge Track Location after Polyurethane Remedial Measure – Elastic Layer Modulus Values Back calculated Using GeoTrack

Track	UPLAND 15-FT before and after Application of Polyurethane							
Substructure	July 1st 2014		July 22nd 2014		January 2015		May 2015	
	E (MPa)	ν	E (MPa)	ν	E (MPa)	ν	E (MPa)	ν
Layer 1	44	0.35	90	0.35	39	0.35	14	0.35
Layer 2	58	0.35	80	0.35	84	0.35	79	0.35
Layer 3	40	0.4	31	0.4	43	0.4	80	0.4
Layer 4	40	0.4	31	0.4	43	0.4	80	0.4
Layer 5	164	0.4	114	0.4	150	0.4	231	0.4

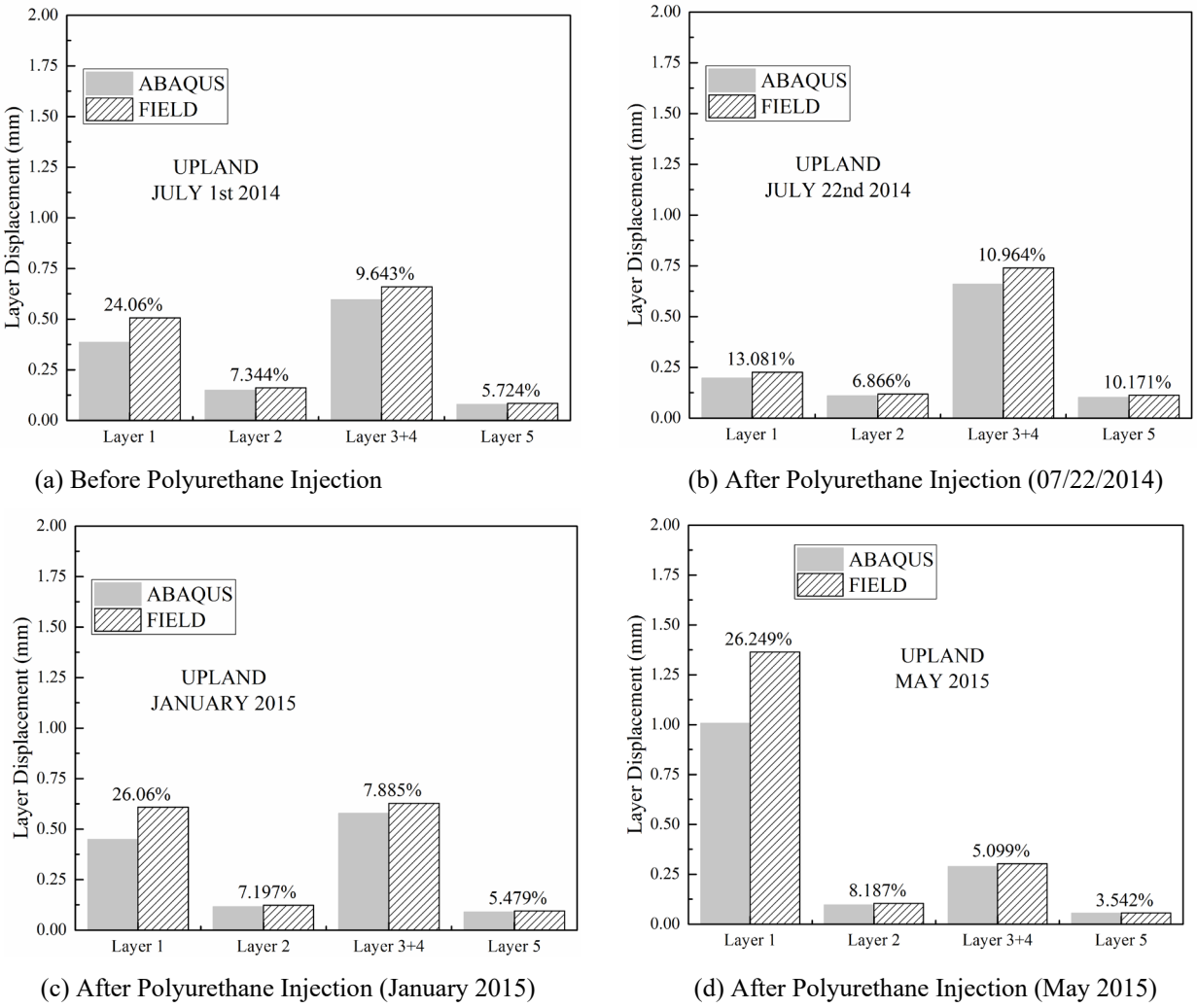

Figure 7.25: Predicted Layer Deformations and Percent Differences – Before and After Polyurethane Injection (Upland 15 ft)

Figure 7.26 shows the predicted ballast layer (layer 1) deformations at different measurement times – before and after polyurethane injection. The percent differences between the field-measured and the Abaqus FEM model-predicted values are also indicated in the figure. Interestingly, the deformation trends were adequately predicted by the FEM model. Furthermore, Figure 7.26 also shows the ballast deformations without tie-gap extraction to illustrate the development of the tie-ballast gap before and after polyurethane injection in this location.

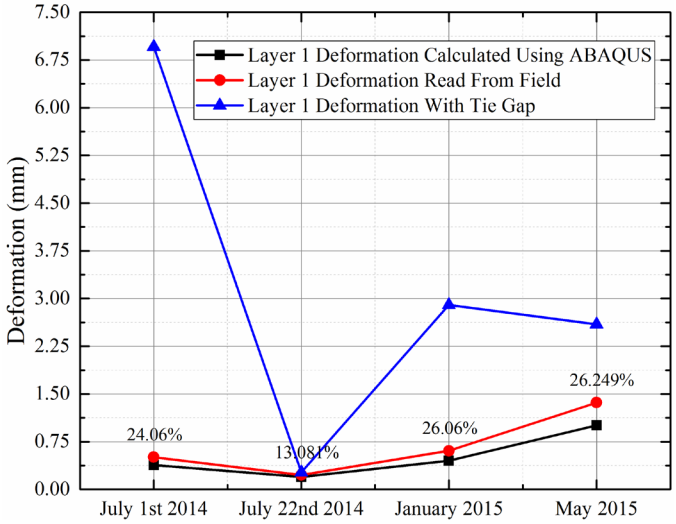

Figure 7.26: Layer 1 Ballast Deformations – Before and After Polyurethane Injection (Upland 15 ft)

To predict layer deformations after the application of stone-blowing remedial measures at the Madison Street 12 ft location for May 2015, the layer material properties back calculated using GeoTrack were again used as inputs for the Abaqus FEM model (see Table 7.12). Note that for this specific MDD data measurement taken in May 2015, LVDT 2 recordings were faulty. Therefore, LVDT 1 recorded values were used for both layers 1 and 2 to back calculate the modulus input into the FEM model. The layer deformation predictions are presented in Figure 7.27 with comparisons to those measured. As can be seen in Figure 7.27, an adequate match was observed between the field-measured values and Abaqus predictions.

Table 7.12: Madison Street 12 ft (Near-Bridge Location) after Stone-blowing Remedial Measure May 2015 – GeoTrack Backcalculation Results

	Layers 1+2	Layer 3	Layer 4	Layer 5
E (MPa), ν	117, 0.35	23, 0.4	29, 0.4	42, 0.4

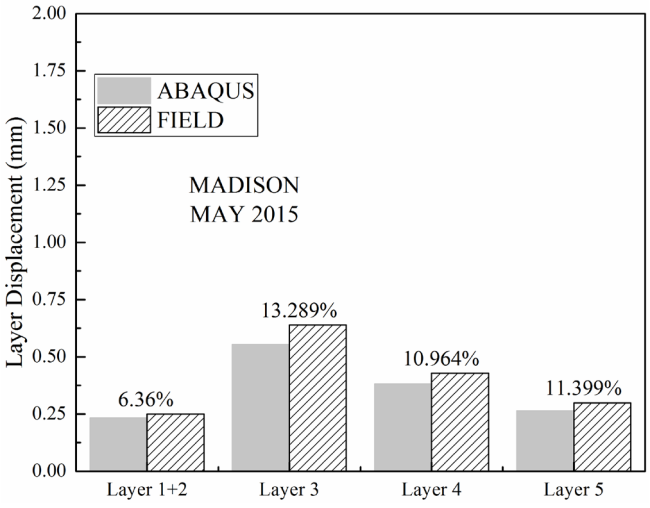

Figure 7.27: Predicted Layer Deformations and Percent Differences – After Stone-blowing (Madison 12 ft, May 2015)

7.4 Modeling for Moving Wheel Loads

The Abaqus FEM models created to this point were limited to concentrated static force and/or pressure loadings. Therefore, no moving wheel simulations could be made. It is crucial to understand the actual nature of the railroad track loading environment; it involves moving wheel loads and is the very essence of railroad dynamics. To consider such dynamic, moving load considerations, some modifications had to be made to the FEM model used in the previous section. This was accomplished by applying moving loads using a quasi-static approach. Accordingly, some additions to the FE mesh in terms of additional sectioning was needed to extend the problem domain and add more ties to the track model.

In the previous model, an 11-tie loading assembly was used to primarily accommodate GeoTrack geometry and analysis requirements. However, 11 ties were simply not enough to simulate moving wheel loads. For example, if one considers the center tie (the sixth tie in an 11-tie model) as tie number 0, when the first axle/wheel of an Acela locomotive bogie is placed on top of this tie, the second axle/wheel must be placed 2,844.8 mm behind the first. Therefore, the rear axle/wheel load is placed between the tenth and eleventh ties. For the sake of argument, these ties would be called Tie No. -4 and Tie No. -5, respectively. If first axle/wheel load is placed on Tie No. -1, which is right behind the center tie, rear axle/wheel load must now be placed between Tie No. -5 and Tie No. -6. Obviously, for an 11-tie model, Tie No. -6 does not exist, and accordingly, even a simple one-tie approach to the center tie cannot be achieved. To remedy this limitation, 10 more ties were added to the FEM model, five behind Tie No. -5, and five in front of Tie No. 5. In what follows, the geometry was re-sectioned accordingly and rail length was increased in the model. Figure 7.28 displays a 3D view of the new 3D FEM model created with 21 ties.

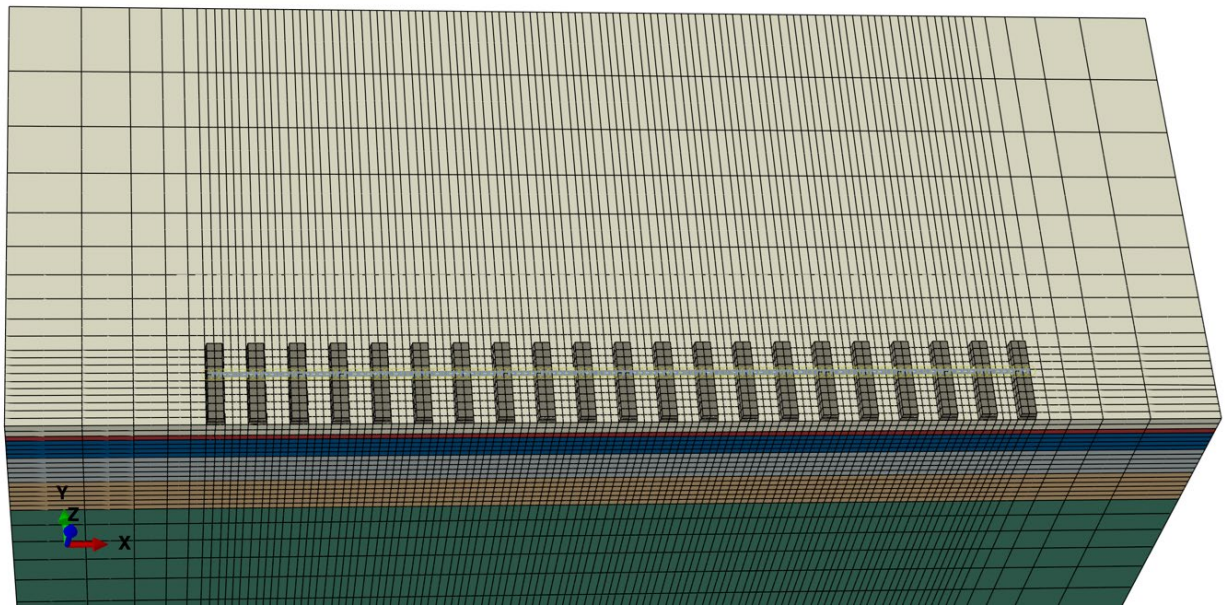

Figure 7.28: New 3D FEM Model Created with 21 Ties to Simulate Quasi-Static Moving Wheel Loads

Note that all the previous assumptions regarding material formulation, boundary conditions, layer interfaces, ballast and tie interface, and rail and tie interface were also used in this new model. To achieve a quasi-static moving wheel load, 16 + 16 concentrated point loads

representing the first and the last axles/wheels of the last bogie of an Acela train were applied to rail nodes. These loads were activated in a certain order to achieve a quasi-static movement. To further explain, the center tie was called Tie No. 0, and ties next to Tie No. 0 were called Tie No. -1 or (-1) and (1), then (-2) and (2), etc. Locations of these concentrated point loads are listed in Table 7.13.

Note that since the material formulation used thus far had linear elastic behavior, the speed of the load movement or simply train speed did not have any effect on predictions. Therefore, for convenience, a 0.1 second time step was used for each load set displayed in Table 7.13. A tabular amplification was used to activate the loads. For instance, at 0.1 second in simulation time, load set one in Table 7.13 was assigned an amplitude of 1, while the other load sets were assigned amplitudes of 0. Similarly, in 0.2 second of simulation time, load set two was assigned an amplitude of 1, while the rest was assigned an amplitude of 0. By such assignments of amplification, the previously assigned loads were activated in certain times, therefore simulating a moving wheel load effect.

For the new FEM model predictions, the Upland Street 60 ft location and the August 2012 GeoTrack back calculated layer properties presented in Table 7.6 were used. The layer deformation measurements were previously collected under the second segment of the center tie, as illustrated in Figure 7.21. The two peak wheel loads calculated for the first and last axles of the Acela bogie were 125.76 kN and 123.91 kN, respectively. An average value of 124.835 kN was used for both the front and rear axles/wheels of the loading sets. To be able to compare the FEM predictions with the field measurements, a 0.2 second timeframe that displayed the approach and departure of the last bogie of an Acela train for the simulated time and location was plotted and is presented in Figure 7.29(b). Abaqus FEM model layer deformation predictions for the front axle load location are presented in Figure 7.29(a).

Table 7.13: Concentrated Point Load Locations

Load Set	Location of Front Axle / Wheel Load	Location of Rear Axle / Wheel Load
Load Set One	On Tie (-5)	Between Ties (-9) and (-10)
Load Set Two	On Tie (-4)	Between Ties (-8) and (-9)
Load Set Three	On Tie (-3)	Between Ties (-7) and (-8)
Load Set Four	On Tie (-2)	Between Ties (-6) and (-7)
Load Set Five	On Tie (-1)	Between Ties (-5) and (-6)
Load Set Six	On Tie (0)	Between Ties (-4) and (-5)
Load Set Seven	On Tie (1)	Between Ties (-3) and (-4)
Load Set Eight	On Tie (2)	Between Ties (-2) and (-3)
Load Set Nine	On Tie (3)	Between Ties (-1) and (-2)
Load Set Ten	On Tie (4)	Between Ties (0) and (-1)
Load Set Eleven	On Tie (5)	Between Ties (1) and (0)
Load Set Twelve	On Tie (6)	Between Ties (2) and (1)
Load Set Thirteen	On Tie (7)	Between Ties (3) and (2)
Load Set Fourteen	On Tie (8)	Between Ties (4) and (3)
Load Set Fifteen	On Tie (9)	Between Ties (5) and (4)
Load Set Sixteen	On Tie (10)	Between Ties (6) and (5)

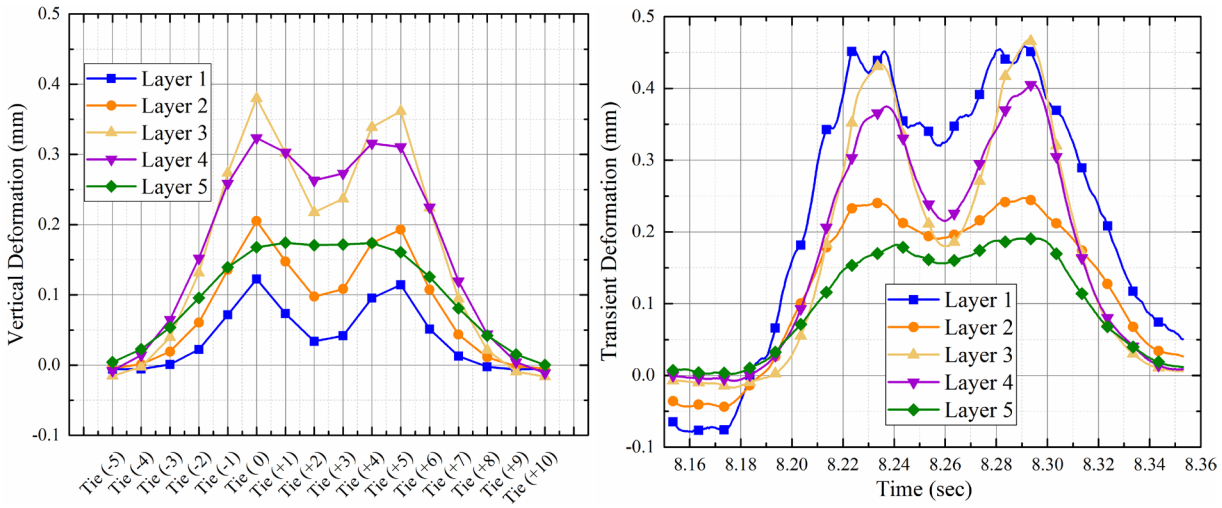

Figure 7.29: Predicted Layer Deformations from the Moving Wheel Load Simulation and the Field Measurements (Upland 60 ft August 2012); (a) Abaqus Prediction for the Front Axle/Wheel Location (Upland 60 ft August 2012 Acela); (b) Field MDD Measurements (Layer 1 with ~ 0.3435 mm Tie-Gap)

As shown in Figure 7.29, while layer 1 predictions were smaller from the Abaqus FEM model, they were in fact the largest from the field MDD measurements. The simple reason for this was the existence of a tie-gap from the field data; the tie-gap consideration was not dealt with in the Abaqus FEM model predictions. As presented in Section 5, the tie-gap for this location was approximately 0.3435 mm. If this tie-gap is extracted from the field measurement results, then layer 1 deformations match with those computed using the 3D FEM model. Moreover, quite a high elasticity modulus (184 MPa) was back calculated using GeoTrack for this layer, thus causing it to be the smallest layer deformation predicted by the Abaqus model. Apart from layer 1 for the ballast, the other layer deformations exhibited similar trends when compared to the model predictions.

To overcome this tie-gap issue, a new set of material properties, as listed in Table 7.14, were assigned to the substructure layers in the Abaqus model.

Table 7.14: Upland Street Open-Track Location Elastic Layer Modulus Values Back calculated Using GeoTrack

Track	UPLAND 60 ft	
Substructure	Aug 12	
	E (MPa)	ν
Layer 1	48	0.35
Layer 2	19	0.35
Layer 3	33	0.4
Layer 4	38	0.4
Layer 5	73	0.4

Note that Poisson's ratios used in GeoTrack to back calculate before tie-gap elimination were 0.3 for the first layer and 0.4 for the other layers. For several reasons, such as the combination of layer 1 and layer 2 in some simulations, Poisson's ratio was changed to 0.35 for layer 1 and layer

2. Since Poisson's ratio was set to 0.35 for layers 1 and 2 in the previous simulation, it was also assigned as 0.35 for layers 1 and 2. Accordingly, the new predictions are given in Figure 7.30. Note that layer 1 ballast deformations were no longer the smallest.

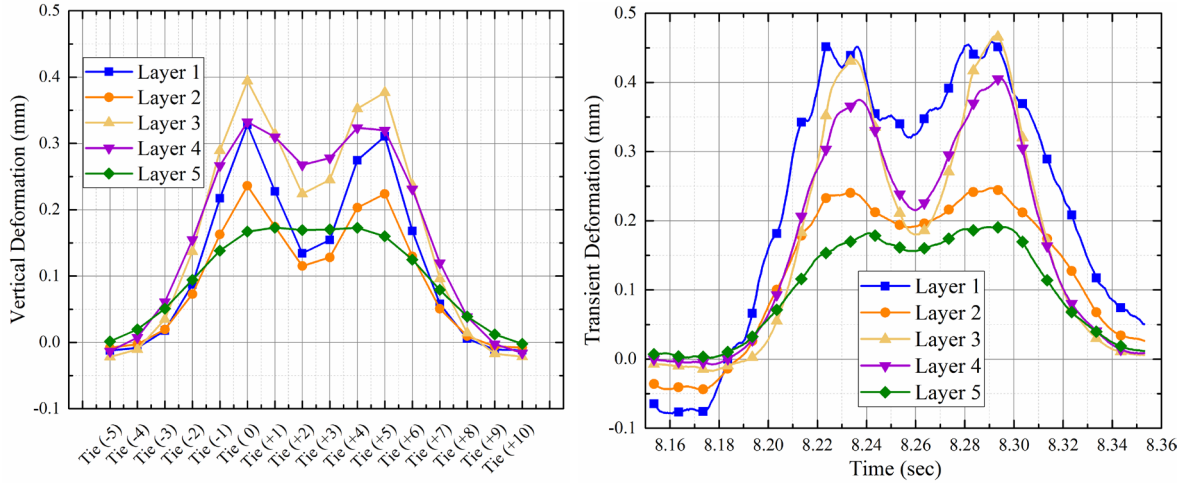

Figure 7.30: Predicted Layer Deformations from Moving Wheel Load Simulation (After Considering Tie-Gap) and Field Measurements (Upland 60 ft August 2012); (a) Abaqus Prediction for the Front Axle/Wheel Location (Upland 60 ft August 2012 ACELA) – Using Lower Ballast Layer Modulus Due to Tie-Gap; (b) Field MDD Measurements (Layer 1 with ~ 0.3435 mm Tie-Gap)

The team observed the effect of multiple wheel load interaction or individual wheel load overlaps seen in deeper layers. Although multiple peaks of the wheel load-related deformations are commonly observed in shallow depth, these peaks became smoother as layer deformations were obtained from deeper locations. This phenomenon is called multiple wheel load interaction (Kim and Tutumluer, 2008). Such an effect is clearly seen in Figure 7.30(a) where layer 5 predicted deformations exhibit one peak.

7.5 Development of an Integrated Approach for Analyzing Track Transition Behavior

Although the developed 3D Abaqus FEM model exhibited reasonable predictions in comparison to the field measured deformations, the 3D model still lacked important features such as: nonlinear material behavior for the soil and ballast layers (only linear elastic formulation had been used thus far); proper interaction at layer interfaces (layers were assumed to be fully bonded); the separation of ties from the ballast layer (ties were always in full contact with the ballast layer); the particulate nature of the movements and dynamic load-deformation behavior of individual ballast particles; the existence of a rail pad between rail and ties (rail was fully coupled to ties); and dynamic load-response behavior including vibrations and calculation of acceleration (models created thus far were static and quasi-static, preventing accelerations). To overcome some of these limitations, an integrated modeling approach was also developed.

Field instrumentation data collected from the multi-depth deflectometers and strain gauges were used to determine individual track substructure layer deformations and dynamic wheel loads, respectively. Track response data from the instrumented bridge approaches could be used to calibrate a fully coupled 3D track dynamic model. Loading profiles generated from this model

could then be used as input for a numerical simulation program based on the DEM to predict individual particle accelerations within the ballast layer. Shortcomings associated with other track analysis and numerical modeling approaches based on the principles of finite element or finite difference methods to characterize the ballast layer as one continuum were compensated in this way. Accordingly, through the integrated approach, the importance of modeling the ballast layer as a particulate medium can be emphasized, and the particle-to-particle nature of the load transfer within the ballast layer could be demonstrated.

The integrated approach introduced in this section presents the combined application of field instrumentation along with analytical and numerical track modeling. Wheel load and transient layer deformation values collected from the instrumented bridge approaches under train loading were first used to calibrate a fully coupled three dimensional train-track-soil model developed by Huang et al. (2014). This model is a modified version of the 3D Sandwich model developed by Huang et al. (2010), and characterizes the subgrade as a 3D plane stress finite element mesh. Additionally, the rail was modeled as an Euler beam discretely supported at points corresponding to the tie locations. Each rail pad, tie, and ballast system was modeled using a combination of mass, spring, and damper. The train was modeled as a simplified Type I vehicle with both primary and secondary suspensions having 10 degrees of freedom.

7.5.1 Analytical Representation of Train Loading

The governing equation for the train loading can be expressed as:

$$\left[K-\omega^2 M\right]\left\{dV(w)\right\}=\left\{f(w)\right\} \tag{7.1}$$

where "K" and "M" are the stiffness matrix and mass (including mass moment of inertia) matrices of the car, respectively. "{dV(ω)}" is the nodal displacement vector. "f(ω)" is the nodal external force vector. Since $\left\{f(\omega)\right\}=\begin{bmatrix}0\\I\end{bmatrix}\left\{P(\omega)\right\}$ where "{P(ω)}" is the nodal wheel force vector and {dW(ω)} = [0 I] {dV(ω)}, Equation (7.1) can be rewritten as:

$$\left\{dW(\omega)\right\}=\left[GV\right]\left\{P(\omega)\right\} \tag{7.2}$$

where $\left[GV\right]=\begin{bmatrix}0 & I\end{bmatrix}\left[K-\omega^2 M\right]^{-1}\begin{bmatrix}0 & I\end{bmatrix}^T$ is called "Green Function of the Vehicle." Note that Equation (7.2) is the relationship between the wheel displacement and the wheel-rail contact forces in the frequency domain. By applying forces {P} on the wheels at a frequency "ω", those wheels will vibrate with magnitudes of "dW".

7.5.2 Analytical Representation of Discrete Tie Support

The discrete nature of tie support can be analytically modeled by the following set of equations, as explained in detail by Huang and Brennecke (2013).

$$a_m(t) = \left(U_r(x_m,t) - U_t(x_m,t)\right)K_p(m) + \left(\dot{U}_r(x_m,t) - \dot{U}_t(x_m,t)\right)D_p(m) \tag{7.3}$$

$$b_m(t) = \left(U_b(x_m,t) - U_a(x_m,t)\right)K_b(m) + \left(\dot{U}_b(x_m,t) - \dot{U}_a(x_m,t)\right)D_b(m) \tag{7.2}$$

$$\begin{aligned}&\left(U_r(x_m,t) - U_t(x_m,t)\right)K_p(m) + \left(\dot{U}_r(x_m,t) - \dot{U}_t(x_m,t)\right)D_p(m) - \\ &\left(U_t(x_m,t) - U_b(x_m,t)\right)K_b(m) + \left(\dot{U}_t(x_m,t) - \dot{U}_b(x_m,t)\right)D_b(m) = \\ &M_t(m)\ddot{U}_t(x_m,t)\end{aligned} \tag{7.5}$$

$$\begin{aligned}&\left(U_t(x_m,t) - U_b(x_m,t)\right)K_b(m) + \left(\dot{U}_t(x_m,t) - \dot{U}_b(x_m,t)\right)D_b(m) - \\ &\left(U_b(x_m,t) - U_a(x_m,t)\right)K_b(m) + \left(\dot{U}_b(x_m,t) - \dot{U}_a(x_m,t)\right)D_b(m) = \\ &M_b(m)\ddot{U}_b(x_m,t)\end{aligned} \tag{7.6}$$

where

$a_m(t)$ = compression force at m^{th} tie between rail and support as a function of time;

$b_m(t)$ = compression force at the m^{th} tie between support and soil foundation as a function of time;

$U_r(x_m, t)$ = rail deflection at m^{th} tie as a function of time;

$U_t(x_m, t)$ = tie deflection at m^{th} tie as a function of time;

$U_b(x_m, t)$ = ballast top vertical displacement at m^{th} tie as a function of time;

$U_a(x_m, t)$ = soil surface deflection at m^{th} tie as a function of time;

$K_p(m)$ = stiffness of m^{th} pad;

$D_p(m)$ = damping of m^{th} pad;

$K_b(m)$ = stiffness of ballast at m^{th} tie position;

$D_b(m)$ = damping of ballast at m^{th} tie position;

$M_t(m)$ = mass of m^{th} tie; and

$M_b(m)$ = equivalent mass of ballast under the m^{th} tie.

7.5.3 Analytical Representation of Rail

The rail is modeled as an Euler Bernoulli beam, and can be represented by the following equation:

$$EIU_r(x,t)'''' + \rho U_r(\ddot{x},t) + \varepsilon U_r(\dot{x},t) + TU_r(x,t)'' = f(t)\delta(x - vt) - \sum_m a_m(t)\delta(x - x_m) \tag{7.7}$$

where

EI = bending stiffness of rail;

$U_r(x,t)$ = rail deflection as a function of time;

ρ = unit mass of rail;

ε = damping of rail (set to zero for convenience);

T = rail axial force caused by temperature increase;

f(t) = wheel load function;

δ = Dirac delta function;

x_m = location of the m^{th} tie; and

v = wheel speed.

7.5.4 Analytical Representation of 3D Soil Support

The subgrade underneath the ballast layer was represented using a 3D finite element model. The following conceptual equation can be used for representing the 3D soil layer:

$$\left\{U_a(x_m,\omega)\right\} = [GS] \times \left\{b_m(\omega)\right\} \tag{7.8}$$

where ω represents the frequency, and [GS] is Green's function of the soil and can be solved by the following equation:

$$\left([K_s] - (\omega - \lambda v)^2 \times [M]\right) \times \left[\bar{dS}\right] = [\bar{F}] \tag{7.9}$$

where

$[K_s]$ = stiffness matrix of the soil;

λ = wave number;

v = train speed;

$\left[\bar{dS}\right]$ = soil displacement vector; and

$\left[\bar{F}\right]$ = force acting on top of the soil.

7.5.5 Analytical Representation of Train-Track Soil Coupling

The contact between the wheel and the track was modeled using a Hertzian contact spring with Stiffness = HK. The mathematical representation of the wheel-rail contact is illustrated below:

$$-\left\{dW(\omega)\right\} - \left\{dR(\omega)\right\} - \left\{ds(\omega)\right\} = \left\{P(\omega)\right\} \Big/ [HK] \tag{7.10}$$

where

{dR(ω)} is the downward rail displacement in the frequency domain; and

{ds(ω)} is the combination of rail surface roughness and train speed, which induces vibrations in the vehicle (obtained through field measurements).

The overall track deflection and wheel-rail contact forces can be represented by the equation:

$$\{dR(\omega)\} = [GT]\{P(\omega)\} \tag{7.11}$$

where [GT] is the Green Function of the track, Accordingly, the wheel-rail contact force can be expressed by using the rail surface roughness and train speed:

$$\{P(\omega)\} = -([HK][GV] + [HK][GT] + [I])^{-1}\{ds(\omega)\} \tag{7.12}$$

Validation and verification of results obtained from the fully coupled 3D analytical track model have been presented in previous publications by Huang et al. (2009, 2014) and Huang and Brennecke (2013). Figure 7.31 shows a schematic representation of the dynamic track model used in the current study.

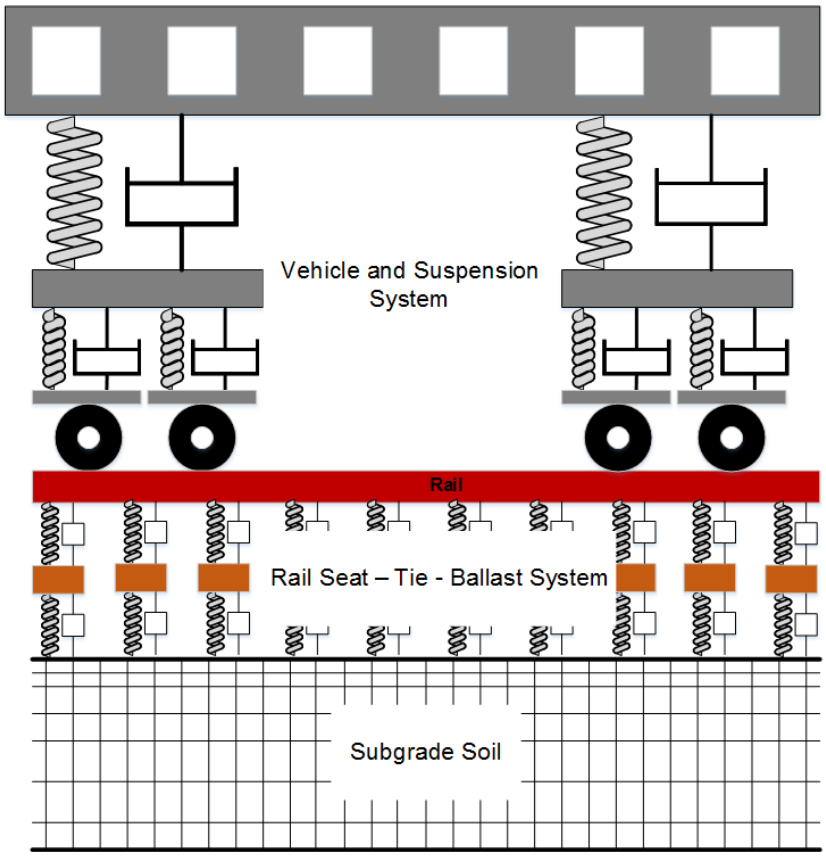

Figure 7.31: Schematic Representation of Fully Coupled 3D Track Model Used in the Current Study (Model Developed by Huang et al. 2014)

The track substructure profile presented in previous sections as the Upland 60 ft location was used in the dynamic track modeling approach to model all the layers underlying the ballast layer.

Accordingly, the modulus values for these layers were adjusted until the layer deformations predicted by the analytical model closely corresponded to those measured in the field. This final combination of layer modulus values was then used to determine the load levels transmitted to the ballast layer. Figure 7.32 shows the load levels applied on top of the ballast layer, as predicted by the analytical track model. As expected, the load levels on top of the ballast were significantly lower than those measured on the rail using strain gauges. Moreover, the analytical track model also predicted higher load levels corresponding to the power car compared to the passenger cars. The maximum load level applied on the ballast layer was 23.3 kN, which was 17 percent of the maximum load value measured on the rail (134 kN).

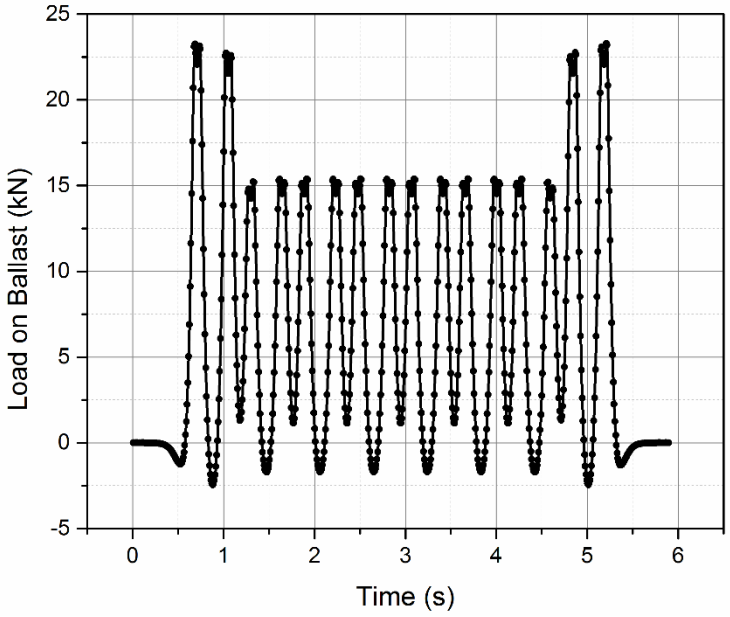

Figure 7.32: Load Levels Applied on the Ballast Layer as Predicted by the Fully Coupled 3D Dynamic Track Model

7.5.6 Image Aided Discrete Element Method

The load levels predicted by the dynamic track model on top of the ballast layer were used as inputs to an image-aided DEM program to predict ballast layer behavior. This image-aided DEM simulation approach developed at the University of Illinois has the capability to create actual ballast aggregate particles as 3D polyhedron elements having the same particle size distributions and imaging-quantified average shapes and angularities. Ghaboussi and Barbosa (1990) developed the first polyhedral 3D DEM code BLOKS3D for particle flow and Nezami et al. (2006) enhanced the program with new, fast contact detection algorithms. Tutumluer et al. (2006) combined the DEM program and the aggregate image analysis to simulate ballast behavior more accurately and realistically by using polyhedral elements regenerated from the image analysis results of ballast materials. This DEM approach was first calibrated by laboratory large-scale direct shear test results for ballast size aggregate application (Huang and Tutumluer, 2011). The calibrated DEM model was then used to model strength and settlement behavior of railroad ballast for the effects of multi-scale aggregate morphological properties (Tutumluer et al., 2006, 2007). A successful field validation study was also conducted using the ballast DEM simulation approach through constructing and monitoring field settlement records of four ballast

test sections and then comparing the measured ballast settlements under monitored train loadings to DEM model predictions (Tutumluer et al., 2011).

The first step using the image-aided DEM modeling approach in this study involved collecting representative ballast materials from the instrumented bridge approaches. The typical particle size distribution of the ballast material was first established in the laboratory through sieving, as shown in Figure 7.33. The ballast material corresponded to U.S. AREMA 3 gradation. Besides sieving, ballast particles corresponding to different sieve sizes were also scanned using the University of Illinois Aggregate Image Analyzer (UIAIA) to establish imaging-based particle morphological indices such as the Angularity Index (Rao et al., 2002), Flat & Elongated Ratio (Rao et al., 2001), and the Surface Texture Index (Rao et al., 2003). The average values for these imaging-based morphological indices were found to be 384, 2.2, and 1.4, respectively. Figure 7.34 illustrates the steps involved in creating 3D polyhedron elements corresponding to individual ballast particles to be used in discrete element modeling of railroad track structures.

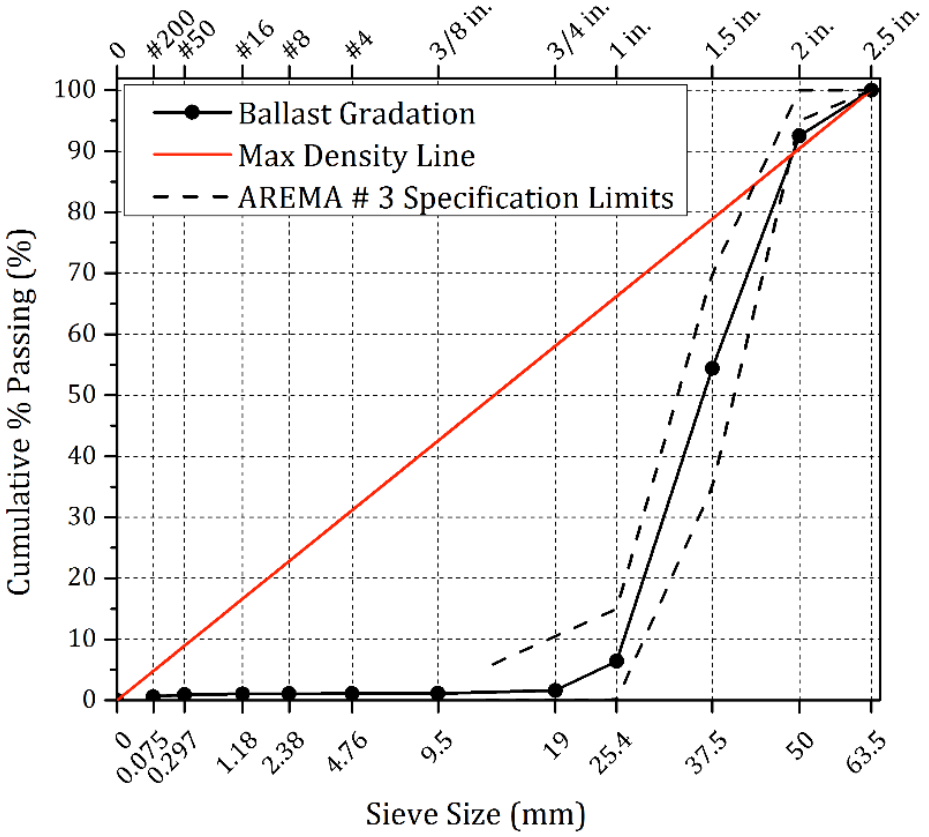

Figure 7.33: Particle Size Distribution of Ballast Material Used on Site

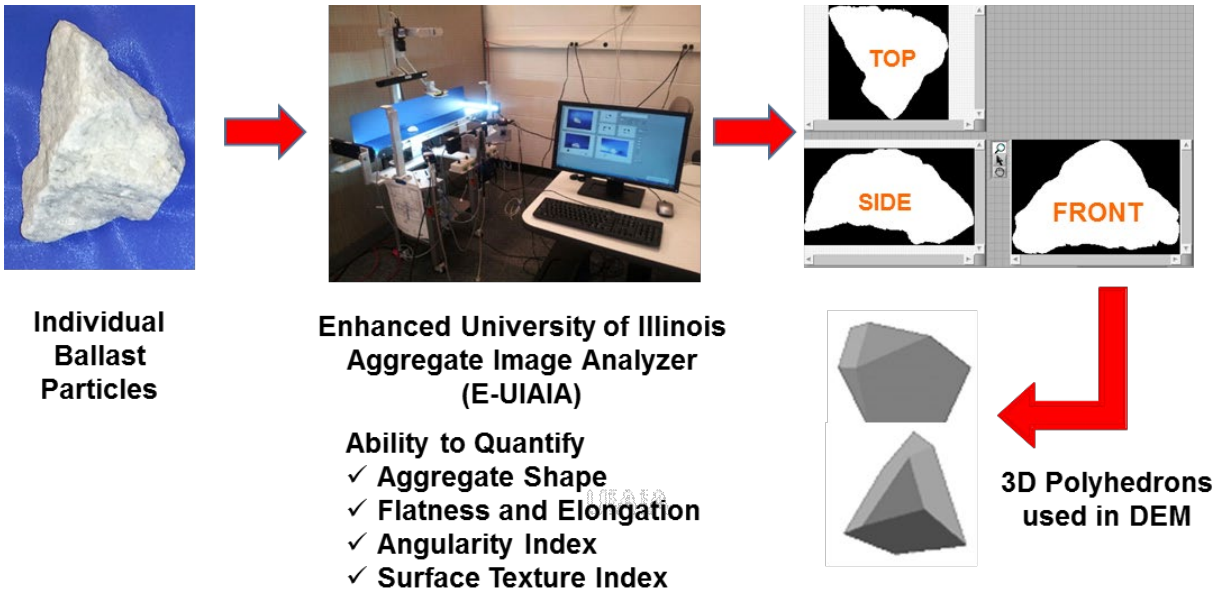

Figure 7.34: Steps Involved in Creating 3D Polyhedrons for Individual Ballast Particles to be Used in DEM of Railroad Track Structures

These morphological indices were subsequently used to select representative polyhedral ballast particles to constitute the track model using a discrete element program (BLOKS3D) developed at the University of Illinois. Figure 7.35 shows the dimensions of the half-track model generated by the BLOKS3D program used in this study.

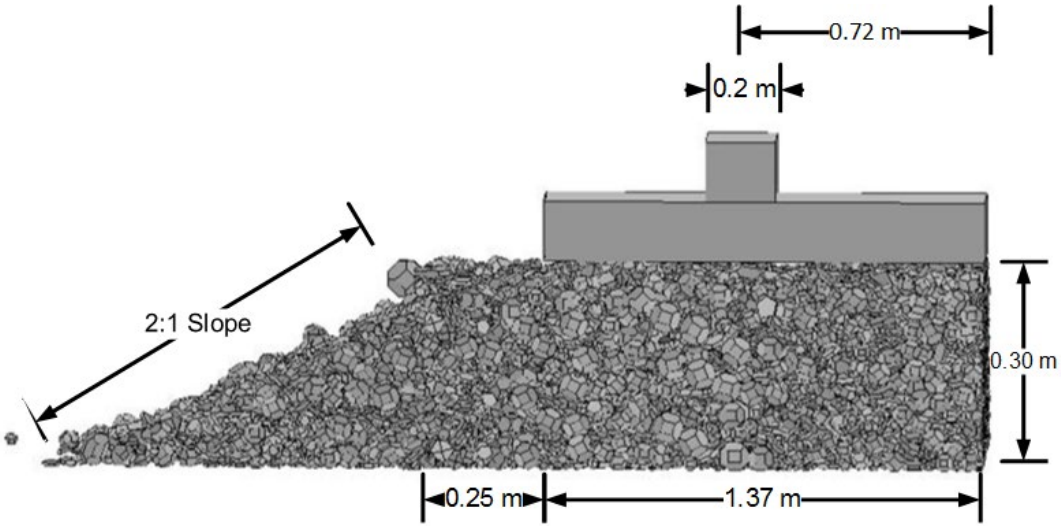

Figure 7.35: Half-Track Model Generated Using DEM

The steps followed to create the half-track model using the BLOKS3D program are listed below: (1) create a particle library to match the aggregate morphological properties established through image analysis; (2) drop the particles to form a cuboid section; (3) compaction Stage I: use one top platen to compact the ballast particles by pressing downwards – all the side and bottom boundaries simulated as rigid during this stage; (4) release the rigid boundary on the left-hand side of the model to form the ballast shoulder slope; (5) compaction Stage II: use one top platen and one side platen (on a 2:1 slope) to compact the section without changing its shape; (6) delete

the compaction platens and extra particles from the model; (7) set the tie and rail on top of the compacted ballast layer at the appropriate location; (8) modify the boundary properties to have the same contact stiffness as the ballast to ballast particle contact; (9) apply the load history determined from the analytical track model.

Note that the boundary immediately underneath the ballast layer was also assigned a stiffness value equal to the inter-particle contact stiffness. Accordingly, the boundary underneath the ballast layer was assumed to be rigid and non-deformable; therefore, the primary area of interest for the DEM modeling approach was the individual particle behavior within the ballast layer. The acceleration time-histories for individual ballast particles at different positions within the ballast layers were monitored and inferences regarding the layer behavior were drawn.

7.5.7 Results and Discussions

Figure 7.36 presents individual ballast particle acceleration levels determined at different positions within the ballast layer using the BLOKS3D program. As shown in the figure, the acceleration levels imposed on individual ballast particles under train loading can be significantly different, depending on the position of the ballast particle with respect to the load position. Two important observations can be made from the data presented in Figure 7.36. First, the acceleration levels for the individual particles reduced significantly as the distance of the particle increased from the bottom of the tie. Accordingly, the acceleration levels observed for a particle 30 cm below the bottom of the tie **(**Figure 7.36**(**d**))** was significantly lower than particles located 15 cm below the bottom of the tie (see Figure 7.36**(**a) and Figure 7.36**(**b)). Note that this was expected, since the boundary underneath the ballast layer was assumed to be rigid and non-deformable. Second, particle acceleration can change significantly with lateral position, even at the same depth from the bottom of the tie. This was clearly apparent when two different particles at 15 cm below the bottom of the tie were compared (see Figure 7.36**(**a) and Figure 7.36**(**b)). Although both particles were at the same depth, the acceleration time-histories for the two particles were quite different from each other. This difference could be attributed to the mechanism of load transfer within a particulate layer. According to previous research (Oda, 1974; Tutumluer, 1995), the load transfer within a granular material is usually along a continuous column of particles. Hence, the acceleration induced on an individual particle is largely dependent on its position with respect to the load transfer column.

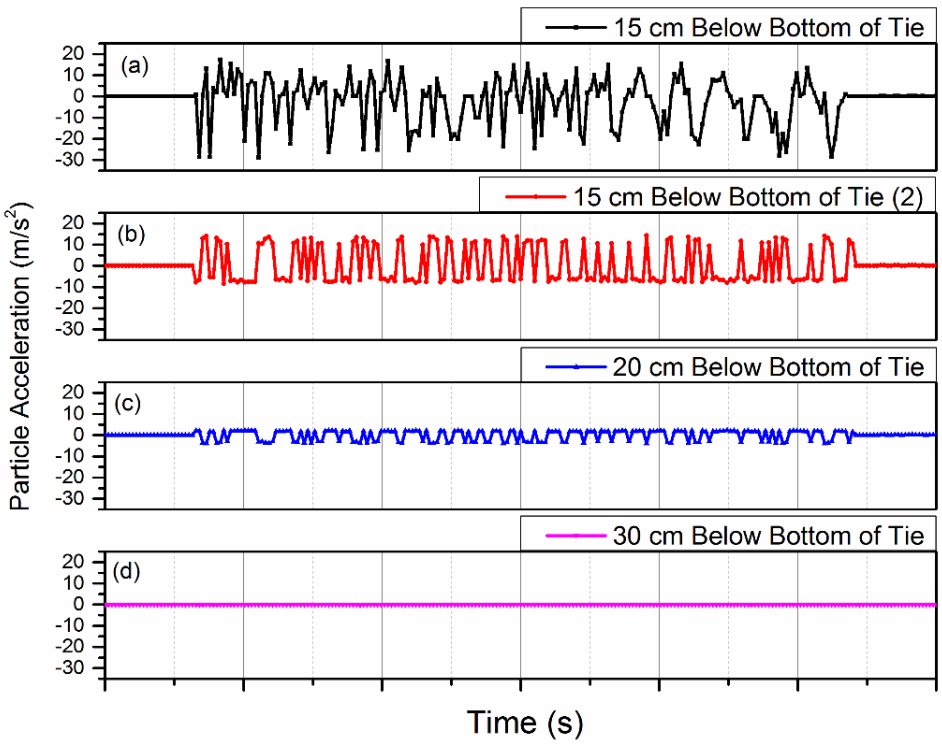

Figure 7.36: Comparing the Particle Acceleration Levels at Different Positions Within the Ballast Layer: (a) 15 cm Below Bottom of Tie – Position 1; (b) 15 cm Below Bottom of Tie – Position 2; (c) 20 cm Below Bottom of Tie; (d) 30 cm Below Bottom of Tie

Particles between the load transfer columns provide lateral support but do not carry much load. Therefore, the vertical accelerations induced in these particles can be significantly lower compared to those lying directly along the load transfer columns. For example, the particle corresponding to the acceleration levels reported in Figure 7.36(a) lay directly along a load transfer column, thus showing distinctive peaks corresponding to each load pulse. However, the particle represented in Figure 7.36(b) lay adjacent to the load transfer column, resulting in lower peaks corresponding to each load pulse. Similarly, the acceleration values gradually decreased as the distance of a particle from the load transfer column was increased. A similar decrease in particle acceleration values was noticed as the vertical distance from the bottom of the tie was increased. The acceleration values approached zero at a distance of 30 cm from the bottom of the tie, since the boundary underneath the ballast layer was assumed to be rigid and non-deformable.

Figure 7.37 presents a vector plot illustrating the load concentration within the ballast layer directly underneath the rail. It can clearly be seen that the magnitude of inter-particle force distribution in vertical direction within the ballast layer was largely dependent on the position of the particle of interest with respect to the load position (rails).

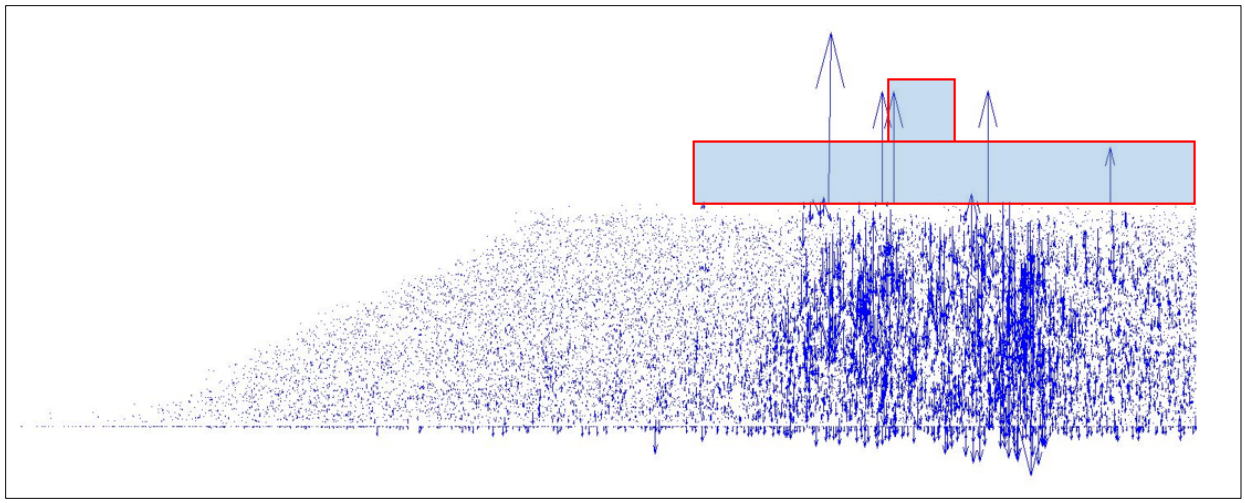

Figure 7.37: Vector Plot Showing Vertical Load Concentration Underneath the Rail as Predicted From the Discrete Element Simulation

From the above-reported results, it was evident that particle acceleration values within a ballast layer could be significantly different, depending on the location of the ballast particle with respect to the load position. Using one acceleration value for the entire layer was therefore erroneous and can be misleading as far as characterizing the dynamic behavior of individual layers is concerned. This highlights a major shortcoming of analysis approaches based on the principles of finite element or finite difference methods that characterize the ballast layer as one continuum and assign one acceleration value to the entire layer.

7.5.8 Limitations of the Integrated Approach in Its Current Form

Although the integrated approach presented in this section marks a significant improvement over continuum-based approaches, its current implementation has the following limitations:

1. The top LVDT was installed within the concrete crosstie just above the top of the ballast layer. Therefore, non-uniform support conditions underneath the crosstie can lead to different displacement time-histories for the crosstie and the ballast layer.
2. The current implementation of the dynamic track model reported here did not account for missing and/or disintegrated ties. Consideration of the missing and/or disintegrated ties can lead to a different load time-history on top of the ballast layer, thus changing the results in this report.
3. The boundary immediately underneath the ballast layer was modeled as non-deformable within the BLOKS3D DEM program. This may have led to different damping characteristics near the bottom boundary, thus affecting the predicted acceleration values.
4. Particle acceleration values reported in this section were obtained from just one simulation run. Repeated simulations using the BLOKS3D program are currently being performed to account for different initial conditions during the ballast layer compaction.
5. Particle accelerations reported in this section need to be verified through additional instrumentation comprising the placement of accelerometers at different positions within the ballast layer.

7.6 Summary

A 3D Abaqus numerical analysis model was developed based on the FEM using a certain mesh size and the geometry requirements needed to accurately predict load-deformation response behavior of a multilayered linear elastic layered system. An 11-tie FEM model was created to validate the developed model for prediction accuracy using the GeoTrack program-back calculated layer moduli as the FEM model inputs and matching predicted layer deformations due to transient train loading deflections in GeoTrack results. This was accomplished by the use of proper geometry and FE mesh sizing, element types, loading configuration, and material property inputs. Reasonably accurate matches were obtained between the developed 3D FEM model layer deformation predictions and the GeoTrack results. The calibrated 3D FEM model was then used to incorporate realistic rail and tie elements to successfully predict individual layer deformation trends of the instrumented bridge approaches with the applied polyurethane injection and stone-blowing remedial measures.

To simulate moving wheel load and dynamic loading considerations, the 11-tie model was extended to a 21-tie FEM model. A quasi-static approach was then used to simulate the wheel movement. When the individual layer deformation predictions were compared with the field measurements, similar deformation trends were observed.

Finally, an integrated approach to dynamic analysis of railway track transitions was presented through a combined application of the field instrumentation results along with analytical and numerical modeling. Track deformation and load data from the instrumented bridge approaches were used to calibrate a fully-coupled 3D track dynamic model. Loading profiles generated from this model were used as input for a numerical simulation program based on the DEM to predict individual particle accelerations within the ballast layer. Analysis results clearly indicated that particle acceleration values within a ballast layer could be significantly different, depending on the location of the ballast particle with respect to the load position. Accordingly, characterizing the ballast layer as a continuum and assigning one acceleration value to the entire layer may lead to erroneous predictions of dynamic track behavior. The ballast layer is a particulate medium and the particle-to-particle nature of wheel load transfer within the ballast layer needs to be carefully considered in dynamic track vehicle interaction modeling.

8. Conclusion

Railway transitions experience differential movements due to differences in track system stiffness, impact loads and vibration, track damping characteristics, foundation type, ballast settlement from fouling and/or degradation, as well as fill and subgrade settlement. This differential movement is especially problematic for high-speed rail infrastructure, as the bump at the transition is accentuated at high speeds. Identification of different factors contributing to this differential movement, as well as development of design and maintenance strategies to mitigate the problem, is imperative for the safe and economical operation of both freight and passenger rail networks.

To address the need to minimize differential movement at railway transitions for joint high-speed passenger and freight routes in the U.S., this FRA-supported research study was undertaken at the UIUC in collaboration with several railroad and industry research partners. The main objectives of the project were to identify major causes of differential movement at track transitions and to develop design methodologies for new railway transitions and maintenance or rehabilitation strategies for existing transitions to improve high-speed operation, safety, and passenger comfort. These inter-connected objectives were achieved by: (1) field instrumentation of several problematic bridge approaches to quantify the dynamic wheel loads and contributions of individual substructure layers to the differential movement or bump development at bridge-ends, (2) identification of mechanisms and rehabilitation techniques for mitigating the recurring settlement and geometry defects at these instrumented transition sites, and (3) development of modeling and analysis techniques for investigating the settlement and transient response behavior of the instrumented bridge approaches.

The research tasks in this project mainly targeted a direct and positive impact on both passenger rail and general freight operations in the U.S. Identified problematic bridge approaches were studied with the support and significant involvement of Amtrak and NS as Class I railroad partners in this project. Selected bridge approaches near Chester, PA, along Amtrak's NEC, and NS's N-Line mainline near Ingleside, WV, were monitored to identify root causes of differential settlement, formulate design solutions, and apply the selected remedial measures. The field instrumentation used in the current study comprised MDDs for measuring track substructure layer deformations and strain gauges mounted on the rail for measuring the vertical wheel loads and quantifying tie support conditions. The rehabilitation techniques selected focused primarily on the problematic ballast layer and included: (1) polyurethane injection and stabilization of existing ballast, (2) the use of stone-blowing to add a thin layer of clean stone to the ballast under the tie, and (3) the use of UTPs glued under new ties that were installed to decrease pressure on ballast and hence improve seating and load transfer beneath the tie.

Research project highlights and key findings on the causes of differential movement and transient response trends under train loading are summarized first in this section according to the field instrumentation results and advanced analyses of the field data from the monitored bridge approach sites. Performances of the selected remedial measures applied to the instrumented bridge approaches are discussed next with inferences made on their effectiveness for mitigating the differential movement problem. Finally, recommendations for improved bridge approach designs and future research needs are given based on the project findings.

8.1 Study Highlights and Key Findings

The key findings of this comprehensive multi-year research study are summarized in this section.

Bridge Selection

- Three problematic bridge approaches along Amtrak's NEC near Chester, PA, i.e., Upland Street (Track 3), Madison Street (Track 2), and Caldwell Street (Track 3), were selected for instrumentation and monitoring based on analyses of 60 months of track geometry records indicating recurrent bump problems both on the entrance and exit ends of these bridges.
- NS undergrade bridges located at mileposts MP352.2 (ballast-deck) and MP352.8 (open-deck) at the east Mega Site near Ingleside, WV, were selected due to recurrent track geometry degradation and required frequent tamping and alignment work.

Instruments and Performance Monitoring

- The installed MDD systems using an independent anchoring technology allowed instrumenting 10 ft and 18 ft depth profiles at the Amtrak and NS sites, respectively. The track substructure layer profiles established through visual inspection of soil samples obtained during drilling determined the locations of individual LVDT modules at the layer interfaces.
- The MDD systems installed through crossties were successful in recording both permanent (plastic) and transient deformations of individual track substructure layers. Strain gauges mounted on the rail were also effective in measuring vertical wheel loads applied during the passage of a train as well as monitoring the support conditions underneath the instrumented crossties.

Data Analysis and Root Cause Determinations

- Analyses of the track settlement (or permanent deformation) data from all three instrumented Amtrak bridge approaches established the ballast layer to be the primary source of differential movement contributing to recurrent settlement and geometry problems in the track:
    - Upland Street near-bridge location (15 ft from abutment) indicated up to 12 mm settlement in the first 250 days, whereas the accumulated settlement was only 1.5 mm for Upland Street open-track location (60 ft from abutment) in that same period before resurfacing activities. The settlement in the ballast layer was much more significant for the near-bridge location compared to the open-track location.
    - Madison Street near-bridge location (12 ft from abutment) was tamped and corrected for high track settlement after the first 20 days of instrumentation. Until the next resurfacing at approximately 355 days, the total settlement was little over 8 mm. For the open-track location at the Madison Street bridge approach (60 ft from abutment), the total settlement at 375 days was approximately 6 mm.
    - Caldwell Street bridge approach had only one crosstie instrumented on east and west ends, located 80 ft from abutment. The two ends of the tie exhibited more-or-less similar settlement behavior, with the ballast layer again contributing to a major portion of the total track settlement, which was approximately 9 mm at 375 days.

- Wheel load levels recorded at the Upland Street near-bridge locations were consistently higher than those recorded at the open-track location. This could be attributed to the dynamic amplification induced at the near-bridge location compared to the open-track location.
- At the Upland Street bridge approach site, transient deformations recorded in the ballast layer were significantly higher than those recorded in the deeper substructure layers. Note that transient displacements recorded by the top-most LVDT in a particular MDD string corresponded to the movement of the crosstie, and the magnitude of the deformation may include both: (1) the movement of the tie before it comes in contact with the underlying ballast layer and (2) deformation of the ballast layer.
- A normalization approach was adopted to compare transient layer deformations under a standard value of wheel load magnitude. Accordingly, transient displacements recorded at the Upland Street and Madison Street near-bridge locations were consistently higher than those at the open-track location.
- At the Caldwell Street bridge site, where trains moved from the bridge deck onto the approach embankment, the west end of the instrumented tie recorded consistently higher load magnitudes compared to the east end. This indicated the presence of higher dynamic amplification on the west end of the tie compared to the east end due to the presence of larger transient deformations and a larger tie-ballast gap determined under the west end.
- Analyses of the load displacement time-histories at the NS MP352.2 bridge approach indicated that the ballast layer again contributed a large portion of the total track transient deformations at the near-bridge location. The transient displacements registered by the LVDT in layer 2 at the open-track location were of comparable magnitude to those registered by the ballast layer. At both of the NS MP352.8 near-bridge and open-track locations, transient deformations recorded for the ballast layer were significantly higher (approximately 2–3 times in magnitude) compared to those recorded for layers 2 and 3.
- A novel approach was adopted to assess the tie support conditions based on wheel loads recorded by the dual-element shear strain gauges mounted at the neutral axis of the rails.
    - At the Upland Street bridge approach, the percentages of load carried by the instrumented tie at the open-track location were consistently higher than those for the near-bridge location.
    - At the Madison Street bridge approach open-track location, wheel loads carried by the instrumented tie were less in magnitude due to the presence of the large gaps underneath the tie.
    - Unlike the instrumented Amtrak bridge approaches, the percentages of the wheel load carried by the instrumented ties were similar at both the near-bridge and open-track locations for the NS instrumented bridge approaches.
- Dynamic load amplifications were more than 100 percent at the Upland Street near-bridge location (when compared to open-track wheel loads), which resulted in doubling the wheel loads on the rail. Such high dynamically amplified loads on top of the ties were likely to cause excessive vibrations and settlement, impact loading in the presence of ballast-tie-gaps, and migration of ballast particles surrounding the tie, leading to severe hanging tie

conditions. This mechanism was likely to cause progressive deterioration of the track support conditions and track geometry.

- A practical approach, named the Progressive Load Threshold Approach, was successfully adopted to quantify significant gaps underneath the instrumented crossties at the Amtrak bridge approach sites based on checking changes in load magnitude and slope of the load-deflection curve to indicate whether there was full contact at the tie-ballast interface. Tie-gaps consistently increased with time at the near-bridge locations of Upland Street and Madison Street, whereas tie-gaps did not change much for the open-track locations in these bridge approaches.
- Significant amounts of peak negative transient displacements, indicating the lifting off of the instrumented tie, or tie-lifting, were recorded after peak loads under the passage of Acela Express trains at both Upland Street and Madison Street near-bridge locations. The tie-lifting was followed by an impact load on the ballast as the rail-tie system was pushed downward under the next axle/wheel load, thereby causing an oscillatory motion.
- Negligible negative tie displacements were recorded for the open-track locations of the Upland Street and Madison Street bridge approach sites. This also corresponded to relatively low tie-gaps calculated at these locations for the same time periods.
- For the near-bridge locations of the Upland Street and Madison Street bridge approaches, calculated ballast layer accelerations were consistently higher than those for the open-track locations. Frequency-domain representations of the layer 1 accelerations at the near-bridge locations indicated significant contributions at the 11 Hz, 16.5 Hz, and 22 Hz frequency levels. The contributions from waveforms in the 22 Hz frequency range were missing from the open-track locations. This finding clearly indicated the higher-frequency, excessive vibration modes generated due to complex dynamic loads and stress waves interacting with the rigid bridge abutment.

<u>Remedial Measure Experiments</u>

- Three different remedial measures – chemical (polyurethane) grouting, stone-blowing or stone injection, and UTPs – were successfully applied on the entrance sides of the Upland and Madison Street bridges primarily targeting the ballast layer condition and tie-ballast contact improvements.
    - Chemical grouting of the ballast proved to be effective in the short-term, but its effectiveness as a remedial measure diminished rapidly after a few months. Close inspection of the track conditions indicated that excessive fouling of the ballast layer may have led to inadequate bonding between the grout and individual ballast particles. Grout application at another bridge approach comprising a clean ballast layer indicated better performance.
    - Both stone-blowing and UTPs proved to be effective remedial measures regarding sustained performance in mitigating differential movement at the track transitions. Better support conditions at the tie-ballast interface could be ensured through both of these remedial measures, which in turn led to significantly improved track response and “stable” track geometry profiles.

Numeric Modeling

- The GeoTrack software program was used as a tool for applying an iterative process to back calculate track substructure layer moduli based on the field-measured transient layer deformation results. Comparing the estimated track substructure layer moduli before and after the consideration of the tie-gap magnitudes indicated a significant increase in the estimated ballast and sub-ballast layer moduli for the latter case, which was more representative of values reported in the literature. The estimated substructure layer moduli were particularly useful for comparing the effectiveness of the applied remedial measures and during advanced numerical modeling of railroad track transitions as initial modulus estimates.
- A 3D numerical analysis model was developed based on the FEM and was successfully validated for prediction accuracy. Using the GeoTrack-back calculated layer moduli (from the transient response data collected at the Amtrak bridge approaches) as the inputs, the FEM model predicted closely matching layer deformations with GeoTrack results. The calibrated 3D FEM model was then used to incorporate realistic rail and tie elements to successfully predict individual layer deformation trends of the instrumented bridge approaches when (1) a quasi-static approach was used to simulate moving wheel loads and (2) remedial measures of the applied polyurethane injection and stone-blowing cases were considered.
- An integrated approach to dynamic analysis of railway track transition behavior was also introduced using the field instrumentation, analytical modeling, and numerical ballast simulations using the DEM. Track response data from instrumented Amtrak bridge approaches were used to determine track substructure layer properties using the GeoTrack program and then calibrate a fully coupled 3D track dynamic model. Loading profiles generated from this model were then used as inputs for a ballast aggregate imaging-based 3D DEM program to predict individual particle accelerations within the ballast layer. The importance of modeling the ballast layer as a particulate medium was emphasized, and the particle-to-particle nature of load transfer within the ballast layer was successfully demonstrated.

8.2 Recommendations for Improved Bridge Approach Designs and Future Research

Based on performance monitoring of the instrumented bridge approaches along Amtrak's NEC and NS's N-Line mainline as well as advanced analyses of the field data, the ballast layer was identified as the major contributor of differential movement at these bridge approaches. Although the permanent deformation accumulation trends alone were sufficient to show the ballast layer movement as the major cause for recurring settlements at the near-bridge locations, one should note that the MDD instrumentation installed in the open-track locations also indicated similar trends of larger ballast layer deformations than those of other substructure layers. Note that even the ballast layer transient deformations in the NS bridge approaches were two to three times higher than those of other deeper layers. This did not produce meaningful comparisons from dynamic data analyses between the open-track and near-bridge locations. The advanced analyses of the dynamic data from the Amtrak bridge approach sites under high-speed passenger traffic were very effective in highlighting significant dynamic load effects and making inferences which may be relevant to many important design aspects of such track transition zones.

Excessive vibrations within the ballast layer recorded at the Upland and Madison Street near-bridge locations led to a loss of support underneath the ties, creating tie-ballast gaps (growing progressively higher in magnitudes with time) and hanging tie conditions. Note that certain higher-frequency vibration modes were measured only at the near-bridge locations. Such inadequate support underneath ties was shown to possibly double the dynamic load levels applied to the track structure, which in turn would lead to increased layer settlements over time. Regarding the ballast layer or tie accelerations, the swinging motion of ties was also indicated to start immediately after the passage of the first bogie of the locomotive onto the bridge and was interrupted by the arrival of the second bogie, which potentially caused a heavy, hammering-type impact load on the ballast layer. This phenomenon could potentially lead to the rapid breakage of the ballast particles, thus causing increased ballast fouling and localized movement associated with tie settlement. Moreover, this hammering effect could also cause damage to the crossties, fastening systems, and the rails. Overall, this is the contributing mechanism to increase the tie-ballast gap when such oscillatory motion of the "dancing" tie at the near-bridge location causes ballast degradation and/or pulverization, associated mud pumping when the track gets wet (due to ballast fouling), and differential settlement.

The following factors were identified by the current research study as contributing to bump development at the instrumented railway bridge approaches: (1) tie-ballast contact condition and gap, (2) train speed, (3) impact loads and vibration, and (4) ballast material. All remedial measures should aim to reduce the tie-ballast gap and train/crosstie vertical acceleration at the transition zones. Future research efforts to study bridge approach transitions zone designs should target minimizing ballast degradation and differential movement by providing proper ballast contact underneath the crosstie at all times, preferably by the use of stone-blowing and UTPs as well as through increased confinement and lateral restraint (e.g., geogrids have been used for this purpose to reinforce ballast and minimize its movement).

Among the three remedial measures applied at the Upland and Madison Street near-bridge locations, the use of stone-blowing and UTPs were found to be the most effective in mitigating differential movement at the instrumented bridge approaches. A significant reduction in the gap underneath the tie was achieved for the Madison Street near-bridge location upon stone-blowing, resulting in better seating of the tie on the underlying ballast layer. Stone-blowing lowered the ballast layer accelerations and did not affect the dominant frequencies regarding dynamic response of the tie. Further, a significant reduction in tie lift-off was observed after stone-blowing. The modulus values for ballast and fouled ballast layers increased after stone-blowing. The effectiveness of stone-blowing at the Madison Street near-bridge location did not diminish over time; no significant increase in peak ballast layer transient displacement was observed even one year after the stone injection. This highlights the potential of stone-blowing as a long-term solution to poor tie support conditions at track transitions.

A track panel comprising 30 crossties mounted with UTPs was installed along the south approach of Upland Street bridge along Track 2. A separate instrumentation effort carried out 11 months after installation of the track panel measured low (1.5 mm) peak transient ballast displacements at two of the instrumented ties approximately 20 ft away from bridge abutment. No negative transient displacements were recorded for either tie, and no significant negative accelerations representing tie lift-off were detected. Computed peak acceleration values of lower than 0.25 g clearly indicated adequate support conditions underneath the ties.

The observed short lifespan of chemical grouting as a remedial measure at the Upland Street bridge approach can be attributed to the presence of high amounts of fines (fouling material) in the ballast layer at this location. The presence of the fouling material (predominantly dust generated from degraded ballast particles) most likely prevented the grout from developing strong bonds with individual ballast particles. This led to the grout-ballast bond breaking upon repeated loading, leading to diminishing effects of the remedial measure and the resumption of high rates of track settlement. Accordingly, large tie-ballast gaps, high magnitudes of acceleration, and negative displacements (including tie lift-off conditions) were recorded for the near-bridge approach location several months after the chemical grouting was applied.

The authors believe that chemical grouting can prove to be an effective remedial measure to mitigate the problem of differential movement at track transitions, given adequate ballast layer conditions and well-designed grouting operations. Future research should investigate factors contributing to successful field applications, possibly by providing adequate bonding between the grout and the ballast particles (e.g., in the case of a clean ballast layer). Advanced numerical modeling approaches such as the DEM can be used to extensively study the inter-particle bond strength achieved through grouting and its comparative magnitude to the force exerted by tamping tines.

9. References

Alves Ribeiro, C., Paixão, A., Fortunato, E., & Calçada, R. (2015). Under sleeper pads in transition zones at railway underpasses: numerical modelling and experimental validation. *Structure and Infrastructure Engineering, 11*(11), 1432-1449.

Auersch, L. (2006). Ground vibration due to railway traffic—the calculation of the effects of moving static loads and their experimental verification. *Journal of Sound and Vibration, 293*(3), 599-610.

Banimahd, M., & Woodward, P.K. (2007). 3-Dimensional finite element modelling of railway transitions. In *Proceedings of 9 th International Conference on Railway Engineering*.

Banimahd, M., Woodward, P.K., Kennedy, J., & Medero, G.M. (2012). Behaviour of train–track interaction in stiffness transitions. In *Proceedings of the Institution of Civil Engineers-Transport, 165*(3), 205-214. Thomas Telford Ltd.

Basu, D., & Kameswara Rao, N.S.V. (2013). Analytical solutions for Euler–Bernoulli beam on visco-elastic foundation subjected to moving load. *International Journal for Numerical and Analytical Methods in Geomechanics, 37*(8), 945-960.

Bian, X., Chen, Y., & Hu, T. (2008). Numerical simulation of high-speed train induced ground vibrations using 2.5 D finite element approach. *Science in China Series G: Physics, Mechanics and Astronomy, 51*(6), 632-650.

Bilow, D., & Li, D. (2005). Concrete slab track test on the high tonnage loop at the Transportation Technology Center. In *Proceedings of the 2005 AREMA Annual Conference.*

Biondi, B., Muscolino, G., & Sofi, A. (2005). A substructure approach for the dynamic analysis of train–track–bridge system. *Computers & Structures, 83*(28), 2271-2281.

Boler, H. (2012). On the shear strength of polyurethane coated railroad ballast (Master's thesis). University of Illinois at Urbana-Champaign.

Briaud, J.L., James, R. W., & Hoffman, S. B. (1997). Settlement of bridge approaches: (the bump at the end of the bridge) (Vol. 234). Transportation Research Board.

Briaud, J. L., Nicks, J.E., & Smith, B.J. (2006). The bump at the end of the railway bridge: final report. Texas A&M University.

Chang, C.S., Selig, E.T., & Adegoke, C.W. (1980). Geotrack model for railroad truck performance. *Journal of the Geotechnical Engineering Division, 106*(11), 1201-1218.

Chrismer, S. (1990). Track surfacing with conventional tamping and stone injection. Association of American Railroads Research Report No. R-719. AAR Technical Center, Chicago.

Coelho, B., Hölscher, P., Priest, J., Powrie, W., & Barends, F. (2011). An assessment of transition zone performance. *Proceedings of the Institution of Mechanical Engineers, Part F: Journal of Rail and Rapid Transit, 225*(2), 129-139.

Coelho, B., Priest, J., Holscher, P., & Powrie, W. (2009). Monitoring of transition zones in railways. Engineering Technics Press.

De Beer, M., Horak, E., & Visser, A.T. (1989). The multi-depth deflectometer (MDD) system for determining the effective elastic moduli of pavement layers. In *Nondestructive Testing of Pavements and Backcalculation of Moduli.* ASTM International.

Dersch, M.S., Tutumluer, E., Peeler, C. T., & Bower, D. K. (2010). Polyurethane coating of railroad ballast aggregate for improved performance. In *2010 Joint Rail Conference,* 337-342. American Society of Mechanical Engineers.

Dunnicliff, J. (1993). *Geotechnical instrumentation for monitoring field performance.* New York: John Wiley & Sons.

Ebersöhn, W., & Selig, E. T. (1994). Use of track geometry measurements for maintenance planning. *Transportation Research Record, 1470,* 84-92.

Ebersöhn, W., & Selig, E. T. (1994). Track modulus measurements on a heavy haul line. *Transportation Research Record, 1470*.

ERRI (1999). State of the art report-bridge ends embankment structure interaction. ERRI Project No. D230.1. Utrecht, the Netherlands.

Feng, H. (2011). 3D-models of railway track for dynamic analysis (Master's thesis). Royal Institute of Technology, Sweden.

FIMOR (2015). Fimor products for track superstructure. In *Railway Engineering 13th International Conference & Exhibition.* Edinburgh, U.K.

Frohling, R.D., Scheffel, H., & Ebersöhn, W. (1996). The vertical dynamic response of a rail vehicle caused by track stiffness variations along the track. *Vehicle System Dynamics, 25*(S1), 175-187.

Ghaboussi, J., & Barbosa, R. (1990). Three-dimensional discrete element method for granular materials. *International Journal for Numerical and Analytical Methods in Geomechanics, 14*(7), 451-472.

Giner, I.G., López Pita, A., Vieira Chaves, E.W., & Rivas Álvarez, A.M. (2012). Design of embankment–structure transitions for railway infrastructure. In *Proceedings of the Institution of Civil Engineers-Transport, 165*(1), 27-37. Thomas Telford Ltd.

Gräbe, P.J., Clayton, C., and F.J. Shaw (2005). Deformation measurement on a heavy haul track formation. Presented at the Eighth International Heavy Haul Conference.

Gräbe, P.J., & Shaw, F.J. (2010). Design life prediction of a heavy haul track foundation. *Proceedings of the Institution of Mechanical Engineers, Part F: Journal of Rail and Rapid Transit, 224*(5), 337-344.

Gräbe, P.J., Mtshotana, B.F, Sebati, M.M., & Thunemann, E.Q. (2015). The effects of under-sleeper pads on ballast contact pressure, settlement and breakdown. Transportation Research Board 94th Annual Meeting. Washington, DC.

Hayano, K., Ishii, K., & Muramoto, K. (2013). Effects of ballast thickness and tie-tamper repair on settlement characteristics of railway ballasted tracks. Railway Technical Research Institute. Geotechnical Pavement Research in Japan II, final report WG4.

Hayano, K., Hoshi, S., & Kumara, J.J. (2013). Soil mass density test on railway ballasts with using a 3D digital camera. Railway Technical Research Institute. Geotechnical Pavement

Research in Japan II, final report WG4.

Holm, G., Andréasson, B., Bengtsson, P.E., Bodare, A., & Eriksson, H. (2002). Mitigation of track and ground vibrations by high-speed trains at Ledsgard, Sweden. Swedish Deep Stabilization Research Centre Report, 10.

Huang, H., Shen, S., & Tutumluer, E. (2009). Sandwich model to evaluate railroad asphalt trackbed performance under moving loads. *Transportation Research Record: Journal of the Transportation Research Board, 2117,* 57-65.

Huang, H., & Brennecke, B. (2013). Track stiffness transition zone studied with three-dimensional sandwich track model. *Transportation Research Record: Journal of the Transportation Research Board, 2374,* 136-142.

Huang, H., Gao, Y., & Stoffels, S. (2014). A fully coupled 3D train-track-soil model for high-speed model. *Transportation Research Record: Journal of the Transportation Research Board,* 1–13.

Huang, H., & Tutumluer, E. (2011). Discrete element modeling for fouled railroad ballast. *Construction and Building Materials, 25*(8), 3306-3312.

Huang, H., Shen, S., & Tutumluer, E. (2010). Moving load on track with Asphalt trackbed. *Vehicle System Dynamics, 48*(6), 737-749.

Huang, Y.H., Lin, C., Deng, X.J., & Rose, J. (1984). KENTRACK, A computer program for hot-mix asphalt and conventional ballast railway trackbeds, Asphalt Institute (Publication RR-84-1) and National Asphalt Pavement Association (Publication QIP-105), 164.

Huang, H., Gao, Y., & Stoffels, S. (2014). Fully coupled three-dimensional train-track-soil model for high-speed rail. *Transportation Research Record: Journal of the Transportation Research Board, 2448,* 87-93.

Hyslip, J.P. (2002). Fractal analysis of geometry data for railway track condition assessment (Doctoral dissertation). Department of Civil Engineering, University of Massachusetts, Amherst.

Hyslip, J.P., Li, D., & McDaniel, C.R. (2009). Railway bridge transition case study. In *Bearing Capacity of Roads, Railways and Airfields.* 8th International Conference (BCR2A'09).

Insa, R., Salvador, P., Inarejos, J., & Roda, A. (2011). Analysis of the influence of under sleeper pads on the railway vehicle/track dynamic interaction in transition zones. *Proceedings of the Institution of Mechanical Engineers, Part F: Journal of Rail and Rapid Transit,* 0954409711430174.

Johansson, A., Nielsen, J.C., Bolmsvik, R., Karlström, A., & Lundén, R. (2008). Under sleeper pads—Influence on dynamic train–track interaction. *Wear, 265*(9), 1479-1487.

Kaewunruen, S., Remennikov, A., & Aikawa, A. (2011). A numerical study to evaluate dynamic responses of voided concrete railway sleepers to impact loading.

Kalker, J. J. (1996). Discretely supported rails subjected to transient loads. *Vehicle System Dynamics, 25*(1), 71-88.

Keene, A., & Edil, T. B. (2012). Mitigating Ballast Fouling Impact and Enhancing Rail Freight Capacity. National Center for Freight & Infrastructure Research & Education, University

of Wisconsin-Madison.

Kennedy, J., Woodward, P. K., Medero, G., & Banimahd, M. (2013). Reducing railway track settlement using three-dimensional polyurethane polymer reinforcement of the ballast. *Construction and Building Materials, 44,* 615-625.

Kerr, A., Bathurst, L. (2001). Upgrading track transitions for high-speed service. Report No. DOT/FRA/RDV-02/05. Washington, DC: U.S. Department of Transportation, Federal Railroad Administration.

Kerr, A., Moroney, B. (1993). Track transition problems and remedies. *Proceedings of the American Railway Engineering Association (AREA), 94,* 267-298.

Kim, M., & Tutumluer, E. (2008). Multiple wheel-load interaction in flexible pavements. *Transportation Research Record: Journal of the Transportation Research Board, 2068,* 49-60.

Kim, M., Tutumluer, E., & Kwon, J. (2009). Nonlinear pavement foundation modeling for three-dimensional finite-element analysis of flexible pavements. *International Journal of Geomechanics, 9*(5), 195-208.

Koch, K. (2007). Measurement of coal hopper dynamic load environment 286,000-pound gross rail load unit train service-August 2004 to May 2006. Research Report R-984, Transportation Technology Center Inc., Association of American Railroads.

Krylov, V.V. (1995). Generation of ground vibrations by superfast trains. *Applied Acoustics, 44*(2), 149-164.

Lee, H.P. (1998). Dynamic response of a Timoshenko beam on a Winkler foundation subjected to a moving mass. *Applied Acoustics, 55*(3), 203-215.

Lei, X., & Rose, J.G. (2008). Track vibration analysis for railways with mixed passenger and freight traffic. *Proceedings of the Institution of Mechanical Engineers, Part F: Journal of Rail and Rapid Transit, 222*(4), 413-421.

Lei, X., & Noda, N.A. (2002). Analyses of dynamic response of vehicle and track coupling system with random irregularity of track vertical profile. *Journal of Sound and Vibration, 258*(1), 147-165.

Li, D., & Selig, E.T. (1998). Method for railroad track foundation design. I: Development. Journal of Geotechnical and Geoenvironmental Engineering, 124(4), 316-322.

Li, D., & Davis, D. (2005). Transition of railroad bridge approaches. Journal of Geotechnical Engineering, 131(11):1392-1398.

Li, D., Otter, D. & Carr G. (2010). Railway bridge approaches under heavy axle load traffic: problems, causes, and remedies. Journal of Rail and Rapid Transit 224(5), 383-390.

Li, D., & Maal, L. (2015). Heavy axle load revenue service bridge approach problems and remedies. In 2015 Joint Rail Conference (pp. V001T01A020-V001T01A020). American Society of Mechanical Engineers.

Lundqvist, A., Larsson, R., & Dahlberg, T. (2006). Influence of railway track stiffness variations on wheel/rail contact force. Track for High-Speed Railways, Porto, Portugal.

McMichael, P., & McNaughton, A. (2003). The stoneblower–delivering the promise:

development, testing and operation of a new track maintenance system. In TRB 2003 Annual Meeting CD-ROM.

Mise, K., & Kunii, S. (1956). A theory for the forced vibrations of a railway bridge under the action of moving loads. *The Quarterly Journal of Mechanics and Applied Mathematics, 9*(2), 195-206.

Mishra, D., Tutumluer, E., Stark, T. D., Hyslip, J.P., Chrismer, S.M., & Tomas, M. (2012). Investigation of differential movement at railroad bridge approaches through geotechnical instrumentation. *Journal of Zhejiang University SCIENCE A, 13*(11), 814-824.

Mishra, D., Tutumluer, E., Boler, H., Hyslip, J., & Sussmann, T. (2014). Railroad track transitions with multi-depth deflectometers and strain gauges. *Transportation Research Record: Journal of the Transportation Research Board, 2448,* 105-114.

Muramoto, K. (2013). Geotechnical challenges for railway tracks & substructures including transition zone. Railway Technical Research Institute. Geotechnical Pavement Research in Japan II, final report WG4.

Namura, A. & Suzuki, T. (2007). Evaluation of countermeasures against differential settlement at track transitions. *Quarterly Report of RTRI 48*(3), 176-182.

Namura, A., & Suzuki, T. (2013). Evaluation of countermeasures against differential settlement at track transitions. Railway Technical Research Institute. Geotechnical Pavement Research in Japan II, final report WG4.

Nielsen, J.C., & Oscarsson, J. (2004). Simulation of dynamic train–track interaction with state-dependent track properties. *Journal of sound and vibration, 275*(3), 515-532.

Nicks, J. (2009). The bump at the end of the railway bridge (Doctoral dissertation). Texas A&M University, College Station, TX.

Nezami, E., Hashash, Y., Zhao, D., and J. Ghaboussi, J. (2006). Shortest link method for contact detection in discrete element method. *International Journal for Numerical and Analytical Methods in Geomechanics, 30*(8), 783–801.

Oda, M (1974). A mechanical and statistical model of granular material. *Soils and Foundations, 14*(1), 13–27.

Paixão, A., Alves Ribeiro, C., Pinto, N., Fortunato, E., & Calçada, R. (2015). On the use of under sleeper pads in transition zones at railway underpasses: experimental field testing. *Structure and Infrastructure Engineering, 11*(2), 112-128.

Pen, L.L., Abadi, T., Hudson, A., Zervos, A., Powrie, W. (2015). The use of under sleeper pads to improve the performance of ballasted railway track at switches and crossings: a case study.
https://www.researchgate.net/publication/283017313_ALERT2014_01_LePen

Pinto, N., Ribeiro, C.A., Gabriel, J. & Calçada, R. (2015). Dynamic monitoring of railway track displacement using an optical system. *Journal of Rail and Rapid Transit, 229*(3), 280-290.

Plotkin, D., & Davis, D. (2008). Bridge approaches and track stiffness [DOT/FRA/ORD-08-01].

Washington, DC: U.S. Department of Transportation.

Priest, J.A., Powrie, W., Yang, L., Grabe, P.J., & Clayton, C.R.I. (2010). Measurements of transient ground movements below a ballasted railway line. *Géotechnique, 60*(9), 667-677.

Puppala, A.J., Saride, S., Archeewa, E., Hoyos, L.R., & Nazarian, S. (2009). Recommendations for design, construction, and maintenance of bridge approach slabs: Synthesis report (No. FHWA/TX-09/0-6022-1). University of Texas at Arlington.

Rao, C., Tutumluer, E., & Stefanski, J.A. (2001). Coarse aggregate shape and size properties using a new image analyzer. *Journal of Testing and Evaluation, 29*(5), 461–471.

Rao, C., Tutumluer, E., & Kim, I.T. (2002). Quantification of coarse aggregate angularity based on image analysis. *Transportation Research Record: Journal of the Transportation Research Board, 1787,* 117–124.

Rao, K.R., Kim, D.N., & Hwang, J.J. (2010). Fast Fourier transform-algorithms and applications. Springer Science & Business Media.

Rao, C., Pan, T., & Tutumluer, E. (2003). Determination of coarse aggregate surface texture using image analysis. 16th ASCE Engineering Mechanics Conference, University of Washington, Seattle.

Read, D., & Li, D. (2006). Design of track transitions. Transit cooperative research program: research results digest 79. Federal Transit Administration.

Ribeiro, Alves. C., Paixão, A., Fortunato, E., & Calçada, R. (2015). Under sleeper pads in transition zones at railway underpasses: numerical modelling and experimental validation. *Structure and Infrastructure Engineering, 11*(11), 1432-1449.

Rose, J., & Anderson, J. (2006). Long-term performance of asphalt underlayment trackbeds for Maintenance-of-Way Association (AREMA) Annual Conference and Exposition.

Sakuri, T., Nakamura, T., & Muramoto, K. (2013). Cyclic loading test with full-scale model for pre-stressed ballast track. Railway Technical Research Institute. Geotechnical Pavement Research in Japan II, final report WG4.

Sasaoka, C.D., & Davis, D. (2005). Implementing track transition solutions for heavy axle load service. In Proceedings, AREMA 2005 Annual Conference, Chicago, IL.

Sasaoka, C., Davis, D., Koch, K., Reiff, R., & GeMeiner, W. (2005). Implementing track transition solutions. *Technology Digest* TD-05-001, Transportation Technology Center Inc., Pueblo, CO.

Schneider, P., Bolmsvik, R., & Nielsen, J.C. (2011). In situ performance of a ballasted railway track with under sleeper pads. *Proceedings of the Institution of Mechanical Engineers, Part F: Journal of Rail and Rapid Transit, 225*(3), 299-309.

Scullion, T., Briggs, R.C., & Lytton, R.L. (1989). Using the multi-depth deflectometer to verify modulus backcalculation procedures. In *Nondestructive Testing of Pavements and Backcalculation of Moduli.* ASTM International.

Selig, E., & Li, D. (1994). Track modulus: Its meaning and factors influencing it. *Transportation Research Record: Journal of the Transportation Research Board, 1470,* 47-54.

Selig, E. T., & Waters, J. M. (1994). Track geotechnology and substructure management. Thomas Telford.

Shahraki, M., Warnakulasooriya, C., & Witt, K.J. (2015). Numerical study of transition zone between ballasted and ballastless railway track. *Transportation Geotechnics, 3,* 58-67.

Sharpe, P. et al. (2002). Design of transition zones. *Proceedings Railway Eng.* ECS Publications, London.

Smith, M.E., Bengtsson, P.E., & Holm, G. (2006). Three-dimensional analyses of transition zones at railway bridges. Numerical methods in geotechnical engineering, 237-242.

Stewart, H.E., & Selig, E.T. (1982a). Predicted and measured resilient response of track. *Journal of the Geotechnical Engineering Division, 108*(11), 1423-1442.

Stewart, H.E., & Selig, E.T. (1982). Predicted and measured resilient response of track. *Journal of the Geotechnical Engineering Division, 108*(11), 1423-1442.

Stewart, H.E., & Selig, E.T. (1982b). Predictions of track settlement under traffic loading. Presented at the Second International Heavy Haul Railway Conference.

Sussmann, T., & Selig, E. (1998). Evaluation of increased axle loading on northeast corridor track substructure. Test Report for Amtrak. Ernest T. Selig Inc., Hadley, MA.

Sussmann, T.R., & Selig, E.T. (2000). Resilient modulus backcalculation techniques for track. In *Performance Confirmation of Constructed Geotechnical Facilities,* 401-411, ASCE.

Szycher, M. (Ed.). (1999). Szycher's handbook of polyurethanes. CRC Press.

Tanabe, M., Wakui, H., Matsumoto, N., Okuda, H., Sogabe, M., & Komiya, S. (2003). Computational model of a Shinkansen train running on the railway structure and the industrial applications. *Journal of Materials Processing Technology, 140*(1), 705-710.

Tutumluer, E. (1995). Predicting behavior of flexible pavements with granular bases. Georgia Institute of Technology, Atlanta, Georgia.

Tutumluer, E., Huang, H., Hashash, Y., & Ghaboussi, J. (2006). Aggregate shape effects on ballast tamping and railroad track stability. Presented at the AREMA 2006 Annual Conference, Louisville, Kentucky.

Tutumluer, E., Huang, H., Hashash, Y., & Ghaboussi, J. (2007). Discrete element modeling of railroad ballast settlement. Presented at the AREMA 2007 Annual Conference.

Tutumluer, E., Stark, T.D., Mishra, D., & Hyslip, J.P. (2012). Investigation and mitigation of differential movement at railway transitions for US high-speed passenger rail and joint passenger/freight corridors. In *2012 Joint Rail Conference,* 75-84. American Society of Mechanical Engineers.

Tutumluer, E., Qian, Y., Hashash, Y., Ghaboussi, J., & Davis, D.D. (2011). Field validated discrete element model for railroad ballast. Presented at the AREMA 2007 Annual Conference.

Varandas, J. (2013). Long-term behaviour of railway transitions under dynamic loading (Doctoral dissertation). Faculdade de Cieˆncias e Tecnologia da Universidade Nova de Lisboa, Portugal.

Varandas, J.N., Hölscher, P., & Silva, M.A. (2011). Dynamic behaviour of railway tracks on transitions zones. *Computers & Structures, 89*(13), 1468-1479.

Vorster, D.J., & Gräbe, P.J. (2013, February). The effect of axle load on track and foundation resilient deformation under heavy haul conditions. In *10th International Heavy Haul Association Conference.* New Delhi, India.

Wang, H., Markine, V.L., Shevtsov, I.Y., & Dollevoet, R. (2015). Analysis of the dynamic behaviour of a railway track in transition zones with differential settlement. In *2015 Joint Rail Conference.* American Society of Mechanical Engineers.

Warren, B.J. (2015). Field application of expanding rigid polyurethane stabilization of railway track substructure (Master's thesis). University of Wisconsin-Madison.

Weinmann, T.L., Lewis, A.E., & Tayabji, S.D. (2004). Pavement sensors used at accelerated pavement test facilities. In *Proceedings of 2nd International Conference on Accelerated Pavement Testing,* Minneapolis, MN.

Woodward, P.K., Kennedy, J., & Medero, G. (2009). Improving the safety of the railway track infrastructure using insitu polyurethane geocomposites. In *Proceedings of AREMA Annual Meeting.*

Woodward, P.K., Kennedy, J., Medero, G. M., & Banimahd, M. (2012). Maintaining absolute clearances in ballasted railway tracks using in situ three-dimensional polyurethane GeoComposites. In *Proceedings of the Institution of Mechanical Engineers, Part F: Journal of Rail and Rapid Transit, 226*(3), 257-271.

Woodward, P.K., Thompson, D., & Banimahd, M. (2007), Geocomposite technology: reducing railway maintenance. *Proceedings of the ICE-Transport, 160*(3), 109-115.

White, D., Sritharan, S., Suleiman, M., Mekkawy, M., & Chetlur, S. (2005). Identification of the Best Practices for Design, Construction, and Repair of Bridge Approaches. Final Report, Iowa DOT Project TR-481. Center for Transportation Research and Education, Iowa State University.

Witt, S. (2008). The influence of under sleeper pads on railway track dynamics. Sweden.

Yang, Y.B., Yau, J.D., & Hsu, L.C. (1997). Vibration of simple beams due to trains moving at high speeds. *Engineering Structures, 19*(11), 936-944.

Yin, C., & Wei, B. (2013). Numerical simulation of a bridge-subgrade transition zone due to moving vehicle in Shuohuang heavy haul railway. *Journal of Vibroengineering, 15*(2).

Zaman, M., Gopalasingam, A., & Laguros, J. (1991). Consolidation settlement of bridge approach foundation. *Journal of Geotechnical Engineering, 117*(2), 219-240.

Zhai, W., & Sun, X. (1994). A detailed model for investigating vertical interaction between railway vehicle and track. *Vehicle System Dynamics, 23*(S1), 603-615.

Zhai, W., Xia, H., Cai, C., Gao, M., Li, X., Guo, X., & Wang, K. (2013). High-speed train–track–bridge dynamic interactions–Part I: theoretical model and numerical simulation. *International Journal of Rail Transportation, 1*(1-2), 3-24.

ACRONYM	DEFINITION
AAR	Association of American Railroads
BR	Bridge
CPT	Cone Penetrometer Test
DAQ	Data Acquisition
DB	German Federal Railways
DEM	Discrete Element Method
DFT	Discrete Fourier Transform
DOFs	Degrees of Freedom
ERRI	European Rail Research Institute
FEM	Finite Element Modeling
FFT	Fast Fourier Transform
FRA	Federal Railroad Administration
GPR	Ground Penetrating Radar
GRMS	Gage Restraint Measurement System
HMA	Hot-Mix-Asphalt
Hz	Hertz
km/h	Kilometers Per Hour
kN	Kilonewton
LVDT	Linear Variable Differential Transformer
MCO	Mid-Chord Offset
MDDs	Multi-Depth Deflectometers
MGT	Million Gross Tons
MP	Milepost
MPa	Megapascal
MPa	Megapascals
NEC	Northeast Corridor
NS	Norfolk Southern
PSB	Pre-Stressed Ballast Track

ACRONYM	DEFINITION
TGMV	Track Geometry Measurement Vehicle
TLV	Track Loading Vehicle
TOR	Top-Of-Rail
TTC	Transportation Technology Center
UI	University of Illinois
UIAIA	UI Aggregate Image Analyzer
UIC	International Union of Railways
UIUC	University Of Illinois at Urbana-Champaign
UTPs	Under Tie Pads

Appendix A-1: Transient Responses of Instrumented Bridge Approaches

Upland Street Bridge Approach Load and Displacement Time Histories

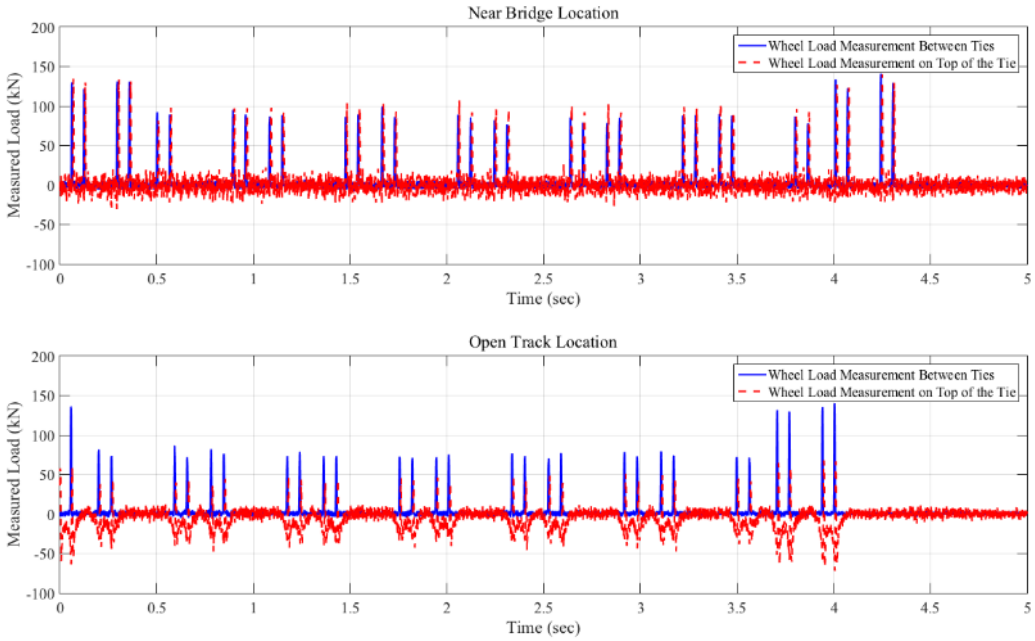

Figure A-1-1: Load Time History Recorded at Upland Street Bridge Approach; Data Collected in November 2012; Train # 1 (ACELA)

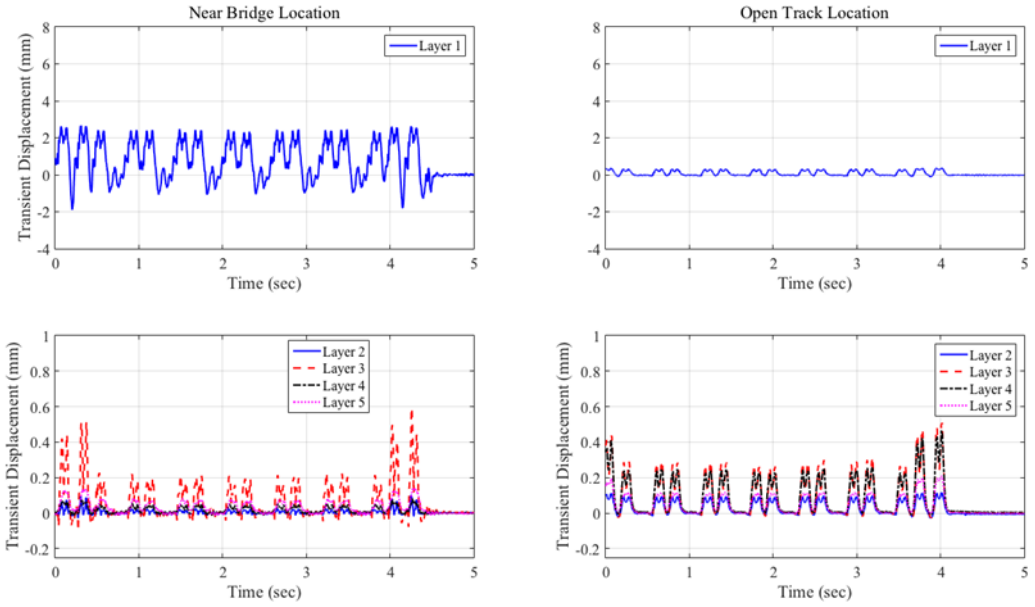

Figure A-1-2: Upland Street Bridge – November 2012 – Train # 1 (ACELA)

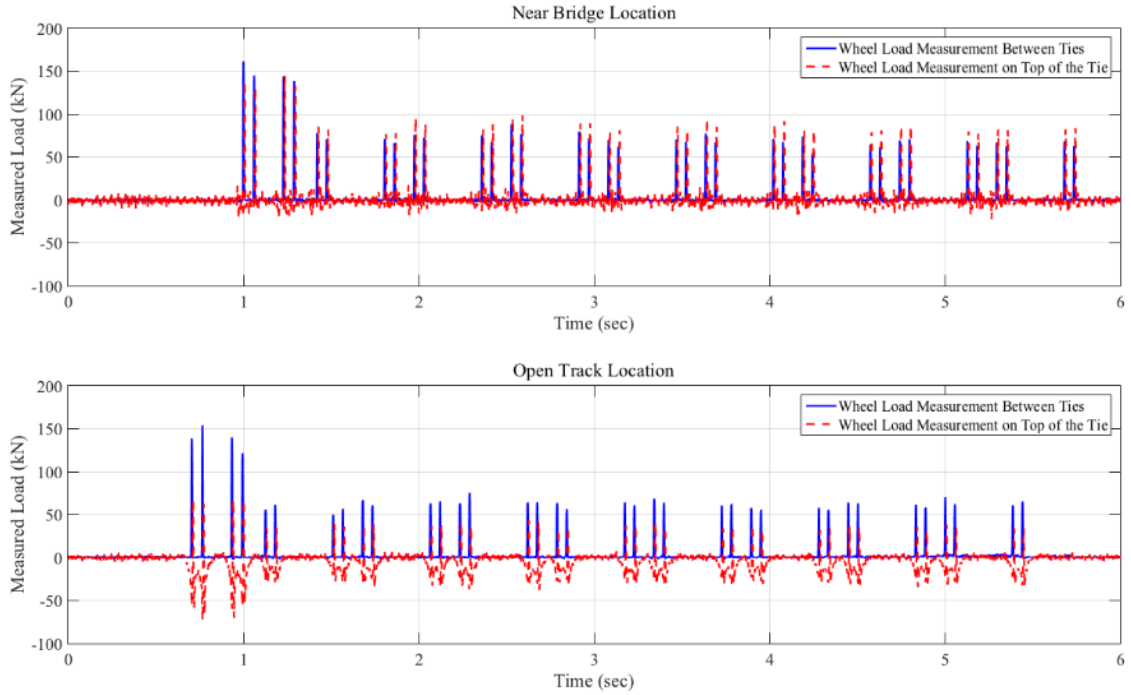

Figure A-1-3: Load Time History Recorded at Upland Street Bridge Approach; Data Collected in November 2012; Train # 2

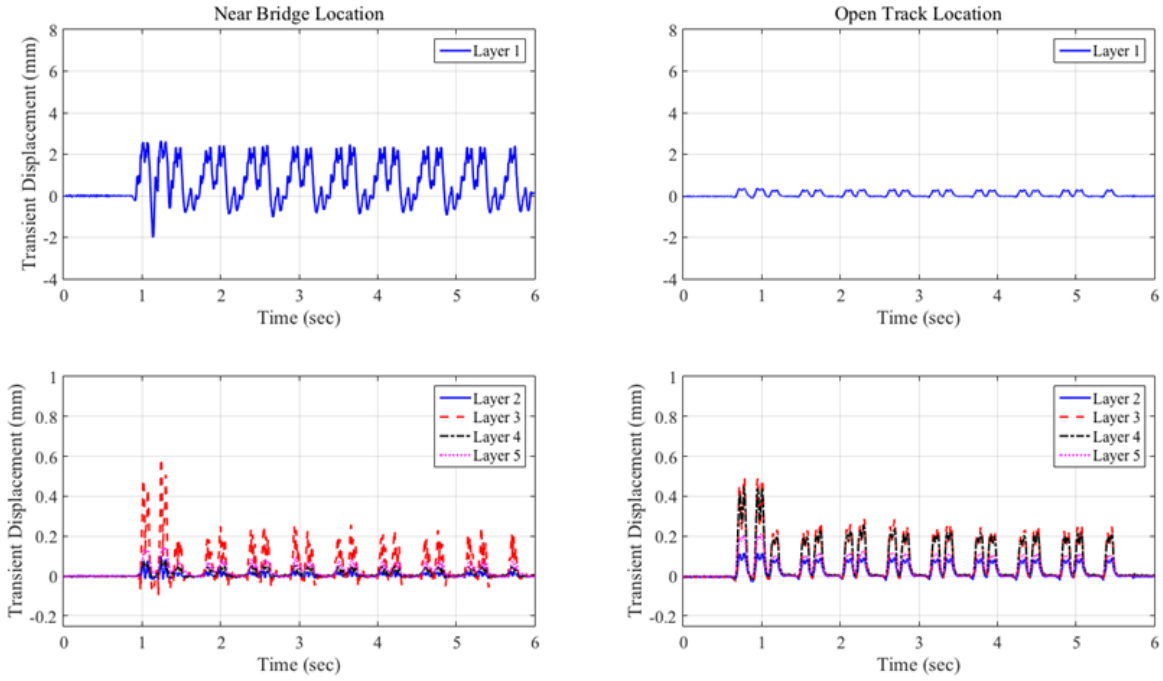

Figure A-1-4: Upland Street Bridge – November 2012 – Train # 2

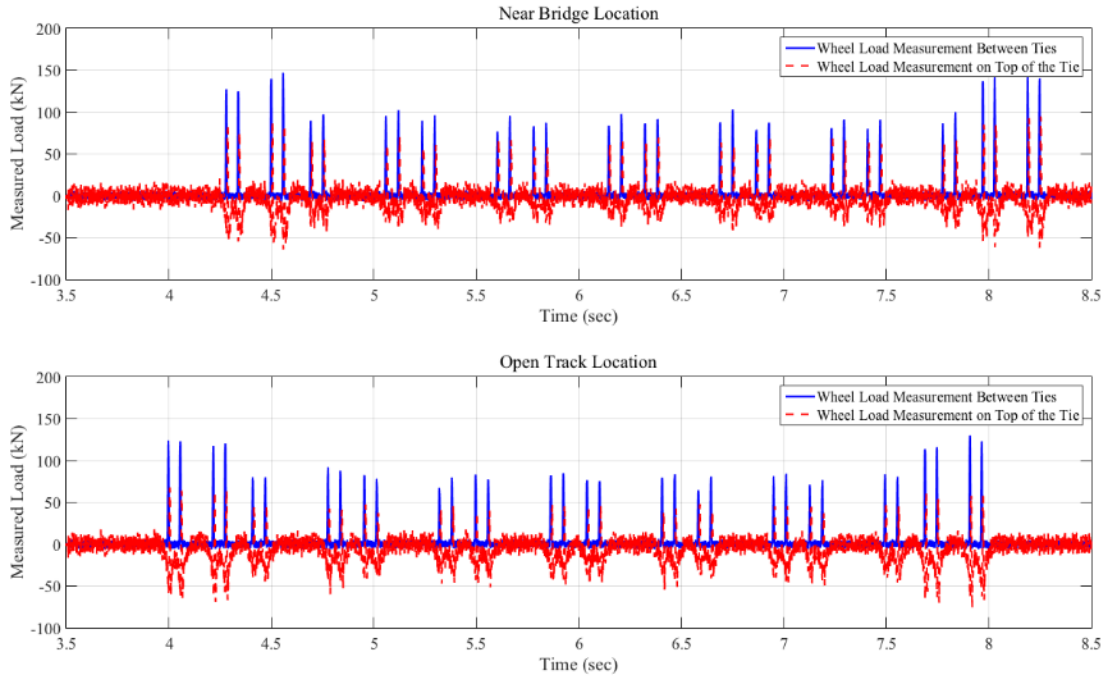

Figure A-1-5: Load Time History Recorded at Upland Street Bridge Approach; Data Collected in January 2013; Train # 1 (ACELA)

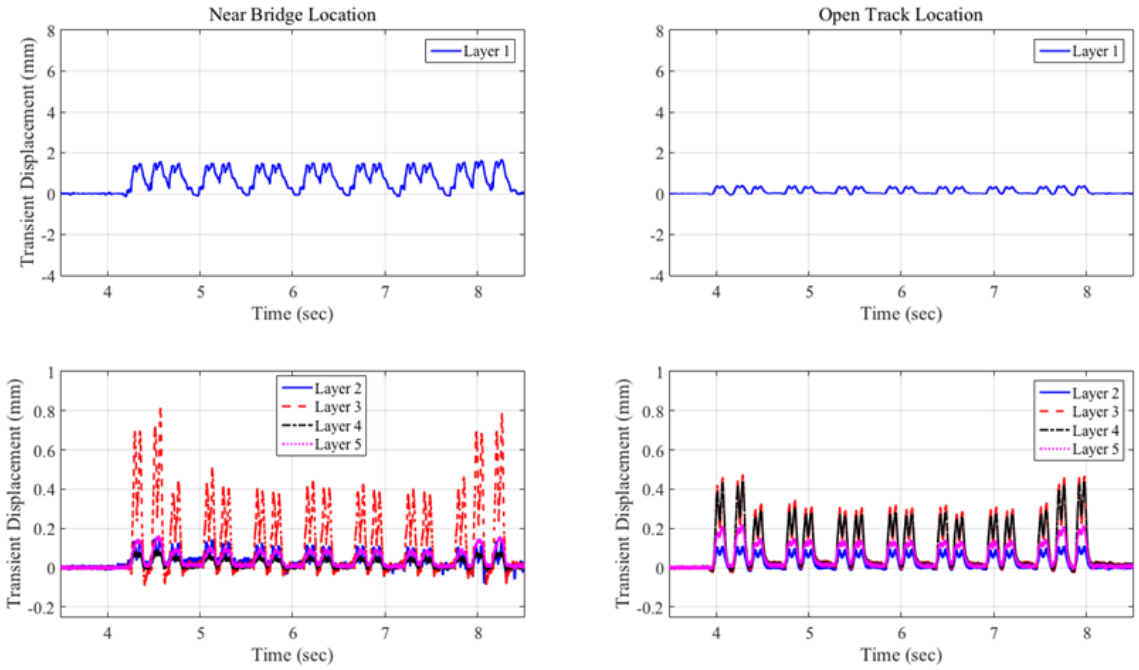

Figure A-1-6: Upland Street Bridge – January 2013 – Train # 1 (ACELA)

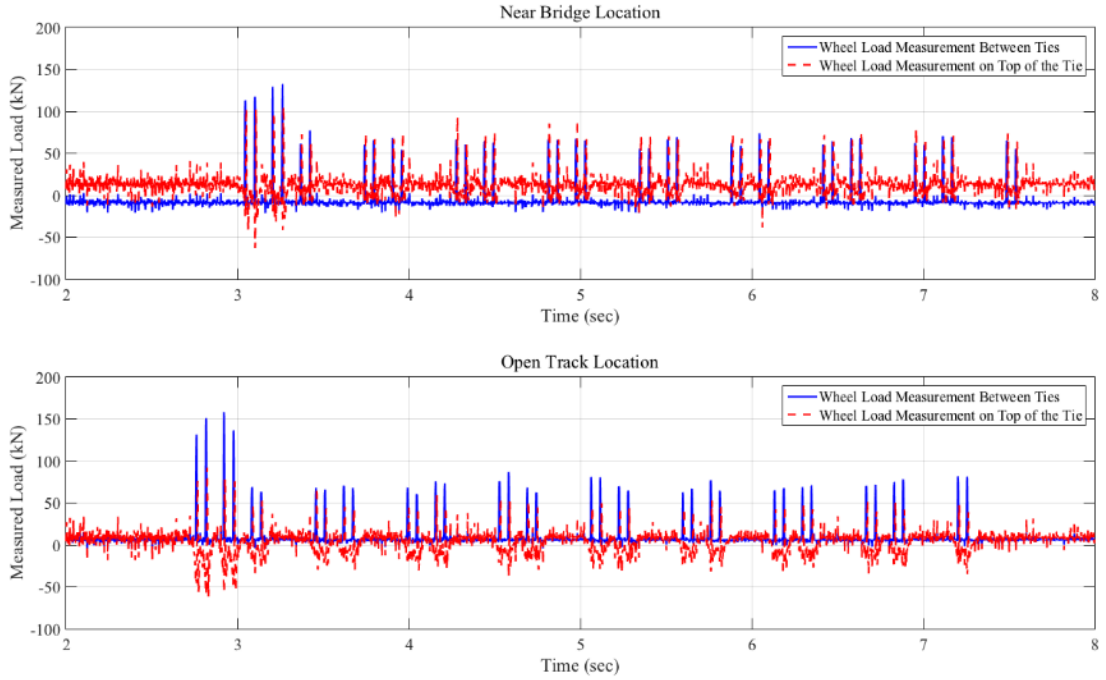

Figure A-1-7: Load Time History Recorded at Upland Street Bridge Approach; Data Collected in January 2013; Train # 2

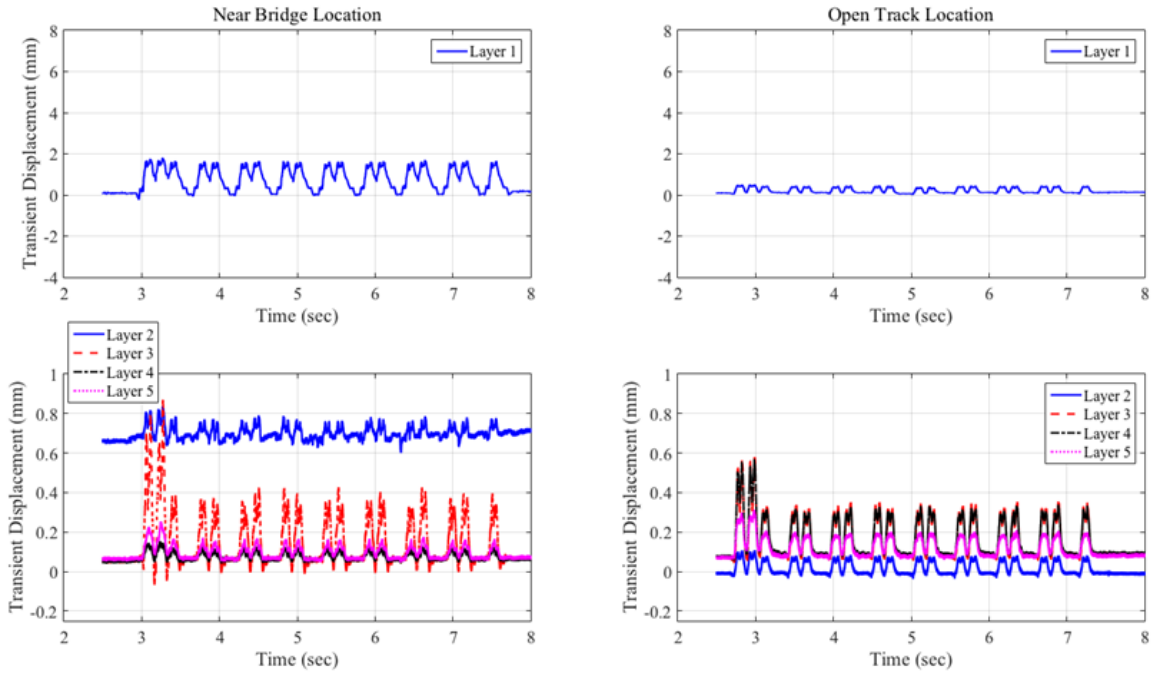

Figure A-1-8: Upland Street Bridge – January 2013 – Train # 2

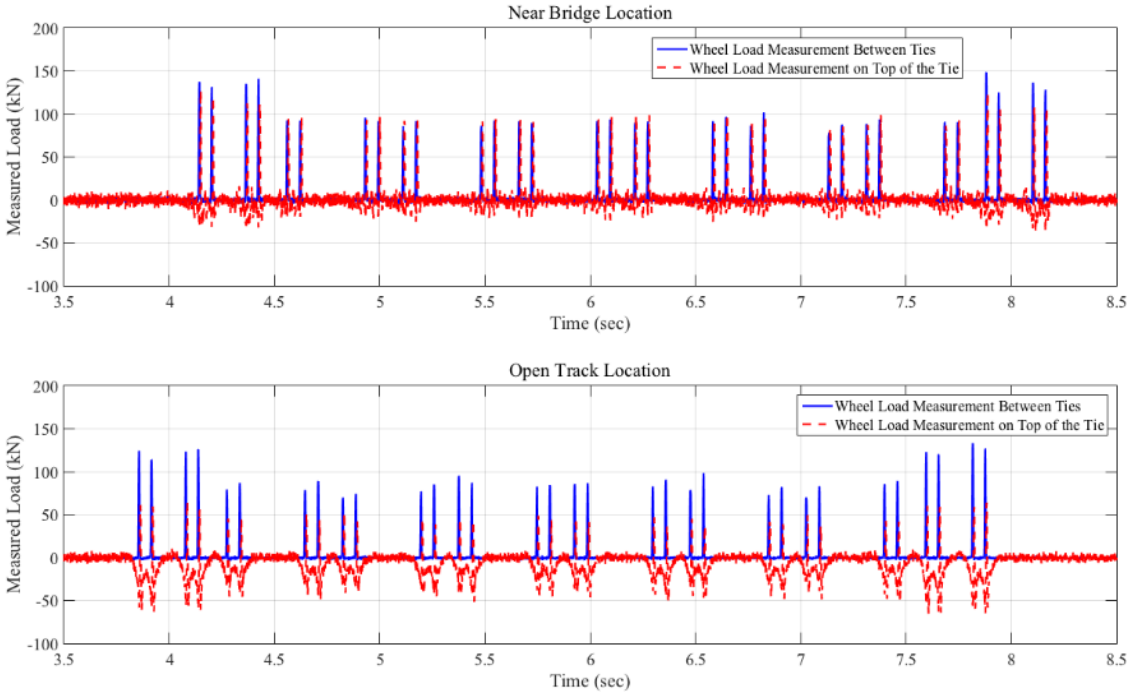

Figure A-1-9: Load Time History Recorded at Upland Street Bridge Approach; Data Collected in June 2013; Train # 1 (ACELA)

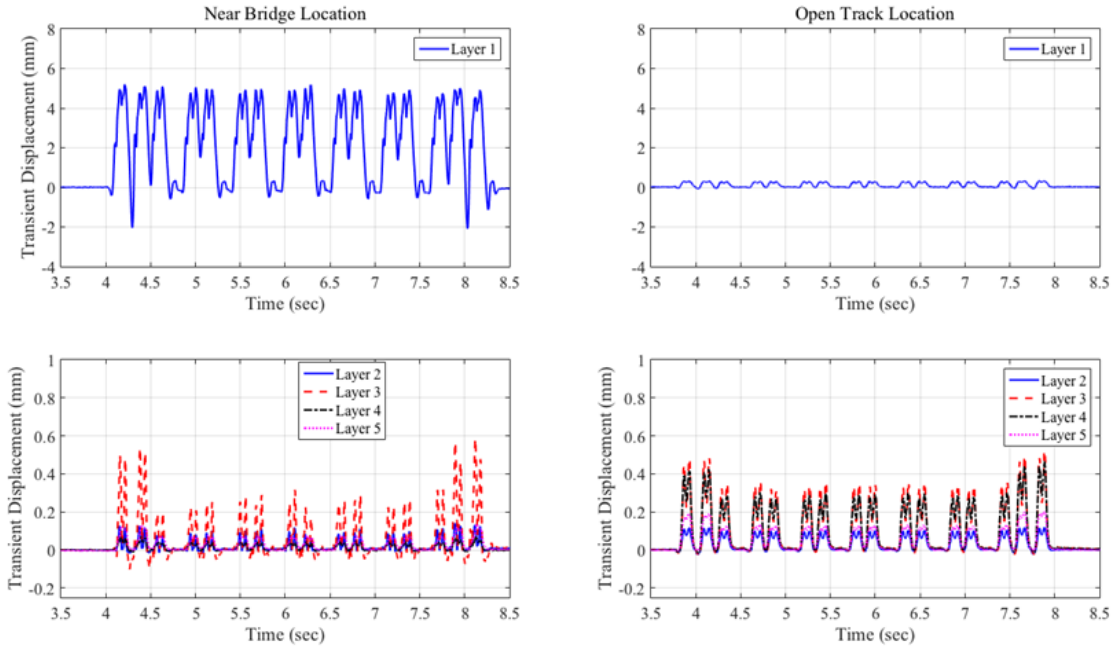

Figure A-1-10: Upland Street Bridge – June 2013 – Train # 1 (ACELA)

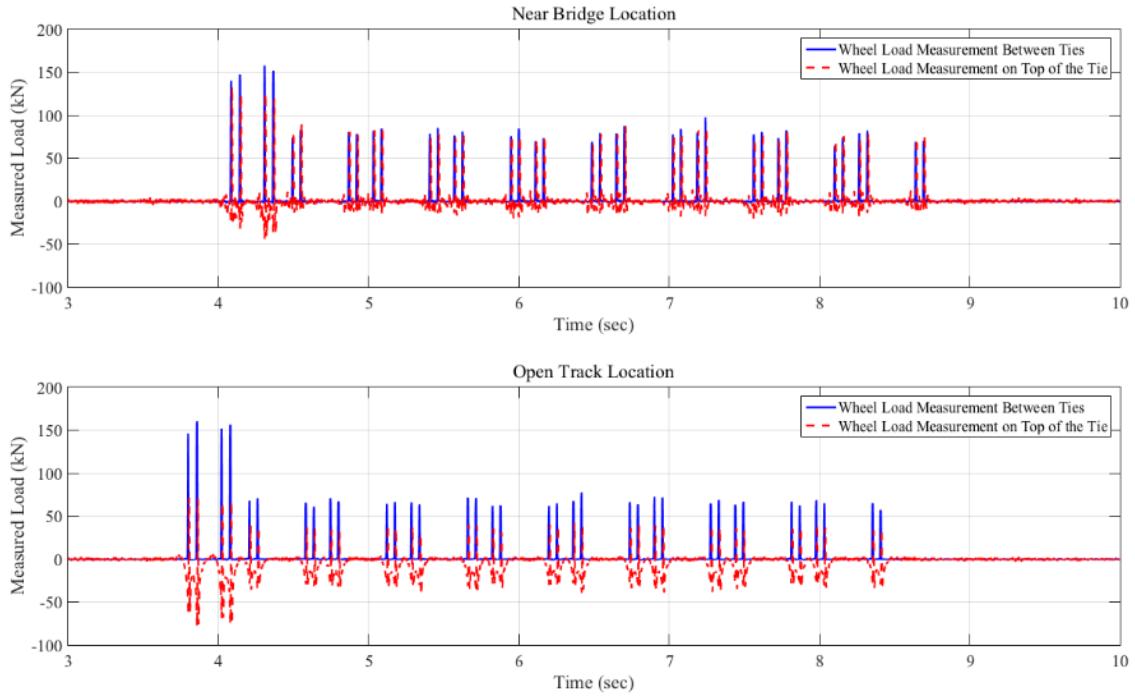

Figure A-1-11: Load Time History Recorded at Upland Street Bridge Approach; Data Collected in June 2013; Train # 2

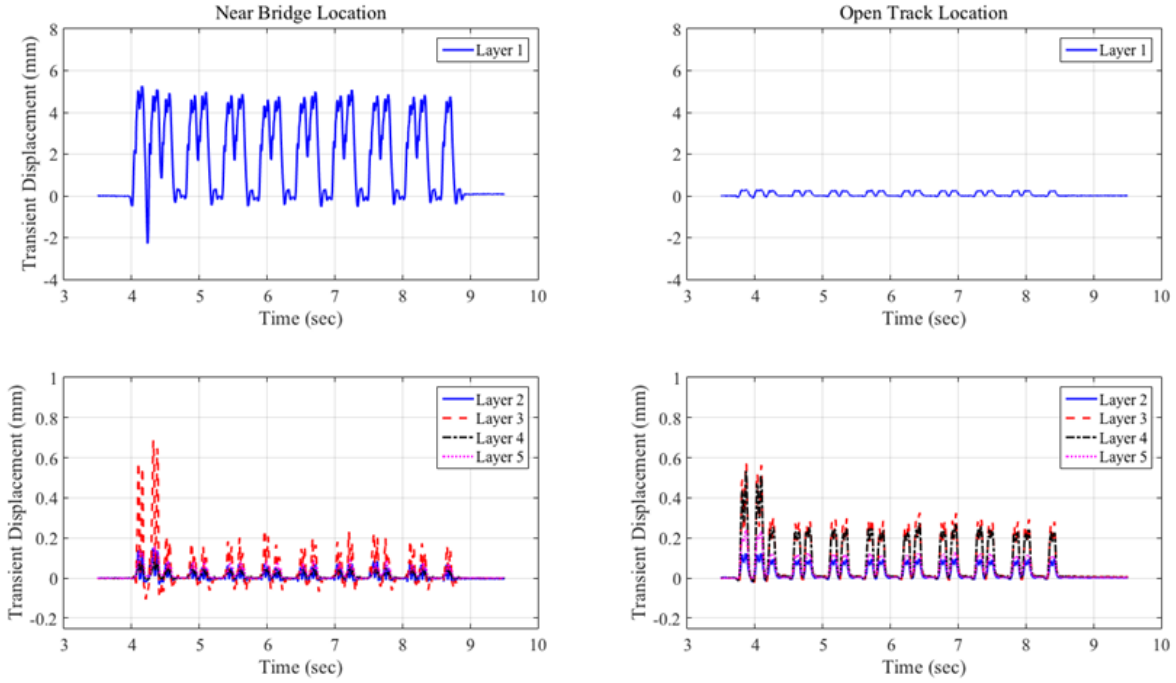

Figure A-1-12: Upland Street Bridge – June 2013 – Train # 2

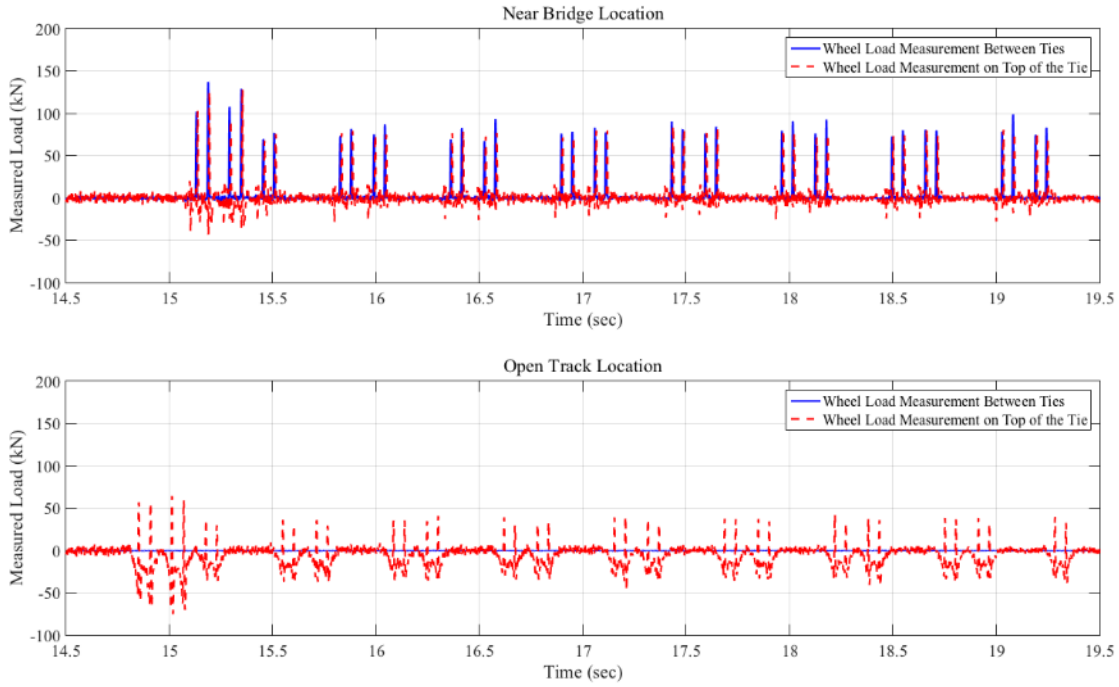

Figure A-1-13: Load Time History Recorded at Upland Street Bridge Approach; Data Collected on July 1, 2014; Train # 1

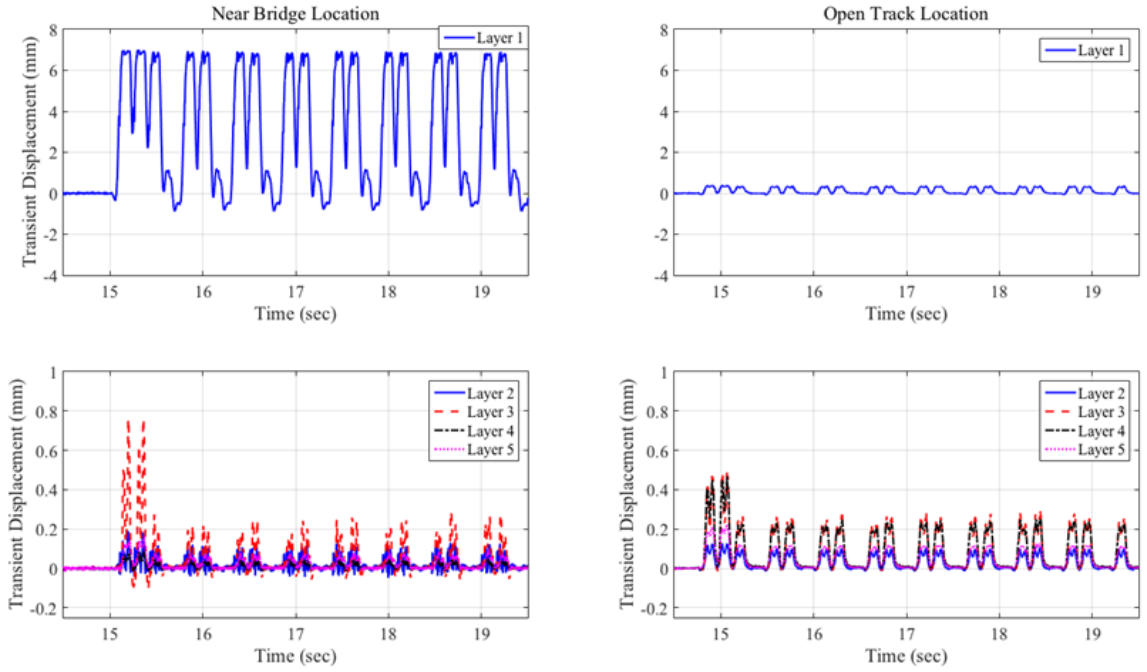

Figure A-1-14: Upland Street Bridge – July 1, 2014 – Train # 1

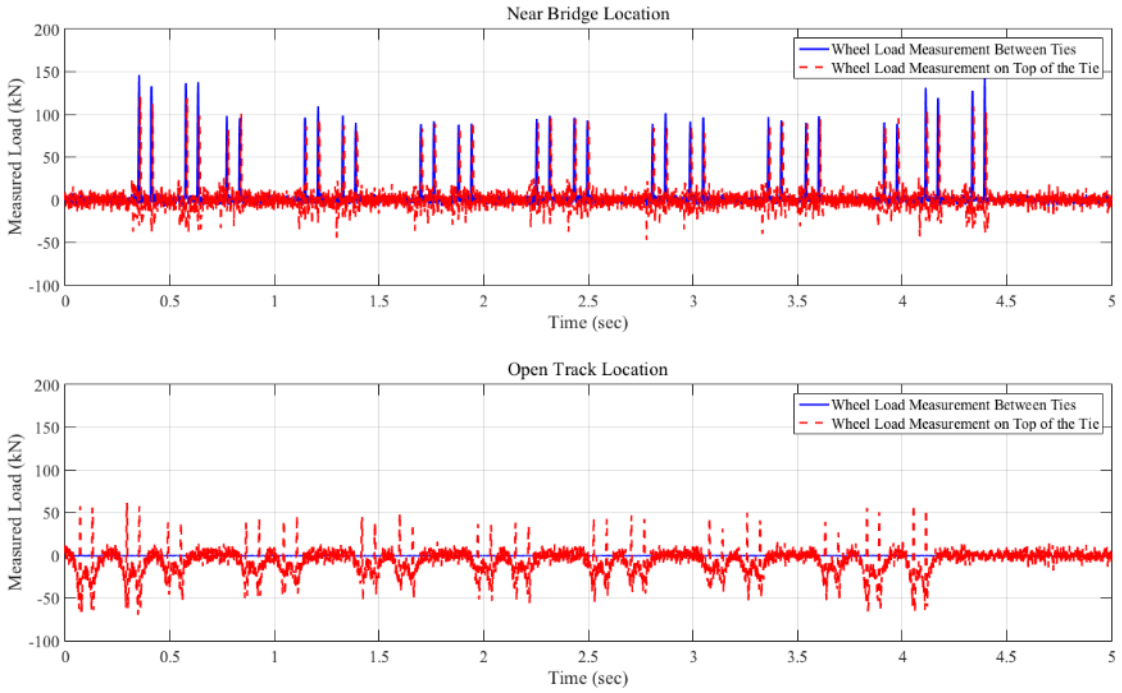

Figure A-1-15: Load Time History Recorded at Upland Street Bridge Approach; Data Collected on July 1, 2014; Train # 2 (ACELA)

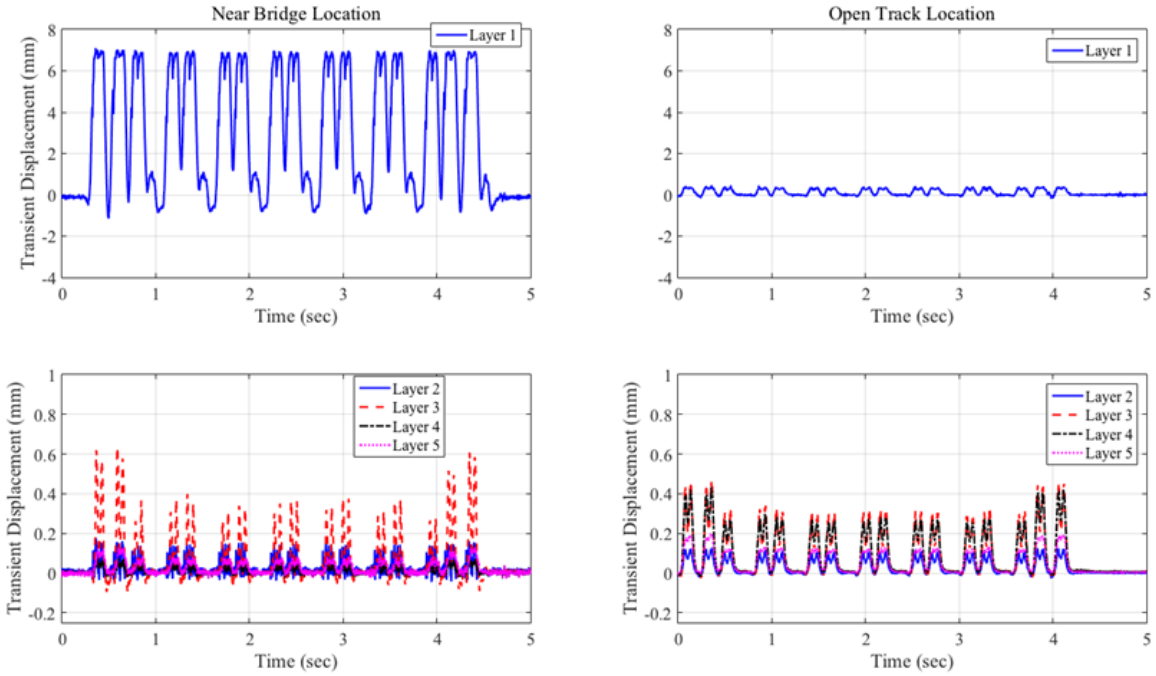

Figure A-1-16: Upland Street Bridge – July 1, 2014 – Train # 2 (ACELA)

Madison Street Bridge Approach Load and Displacement Time Histories

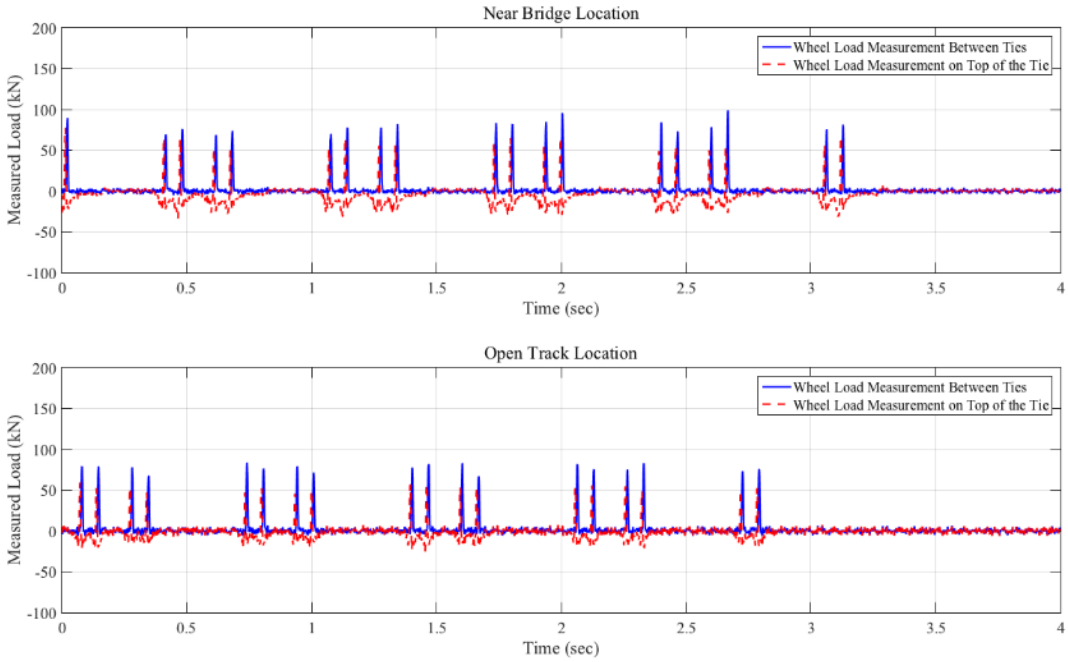

Figure A-1-17: Load Time History Recorded at Madison Street Bridge Approach; Data Collected in November 2012; Train # 1

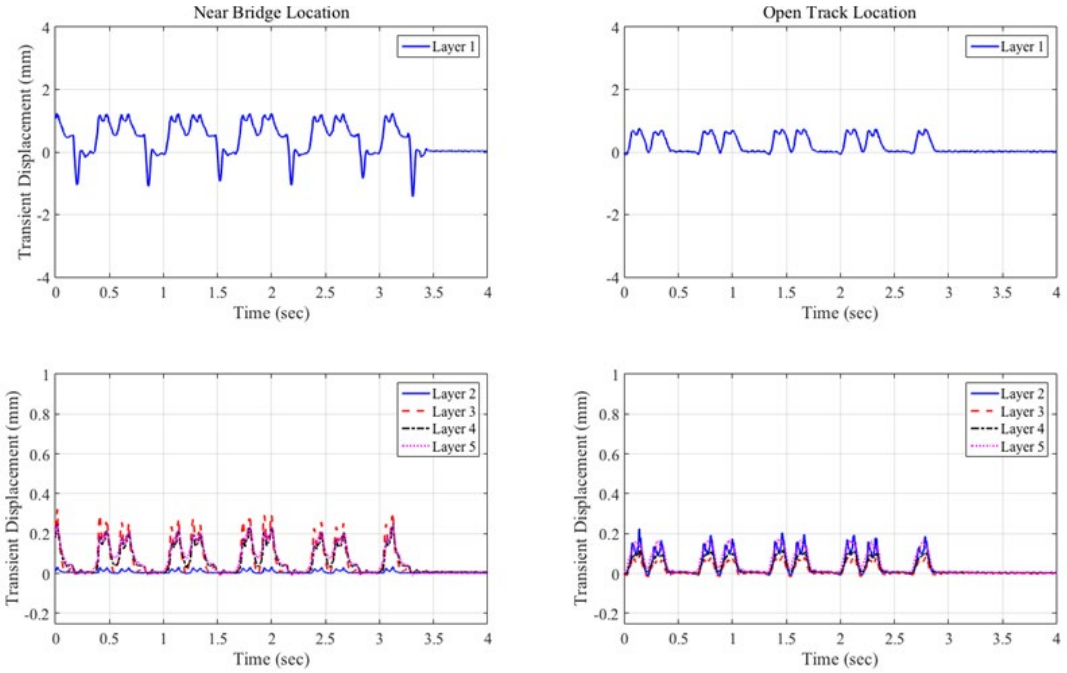

Figure A-1-18: Madison Street Bridge – November 2012 Train # 1

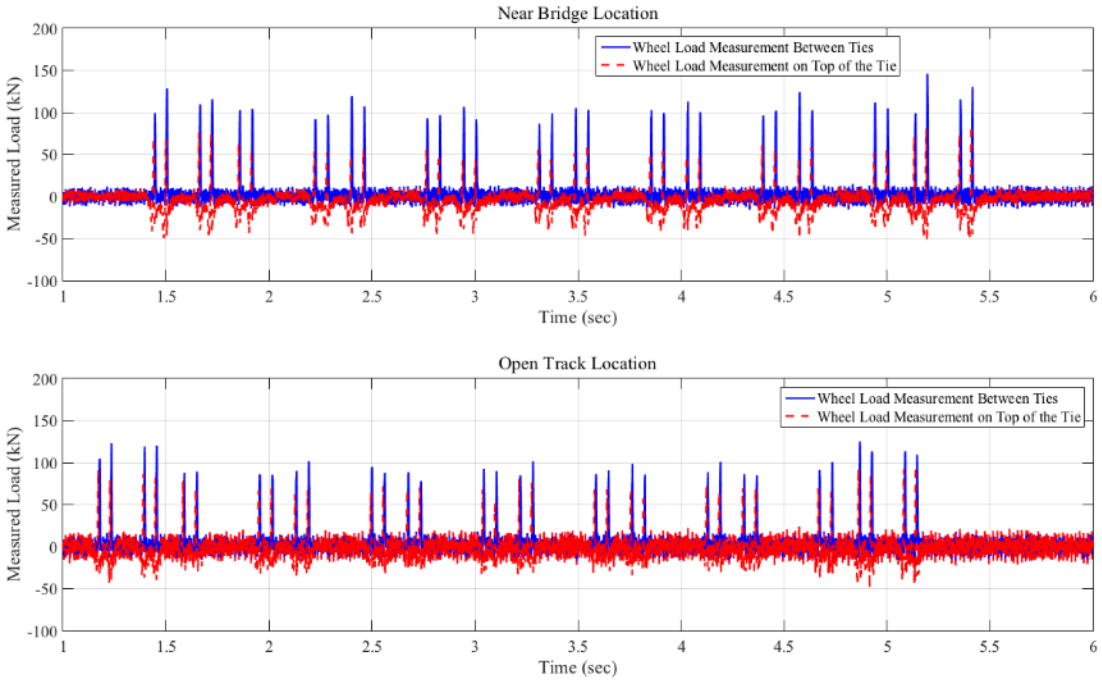

Figure A-1-19: Load Time History Recorded at Madison Street Bridge Approach; Data Collected in November 2012; Train # 2 (ACELA)

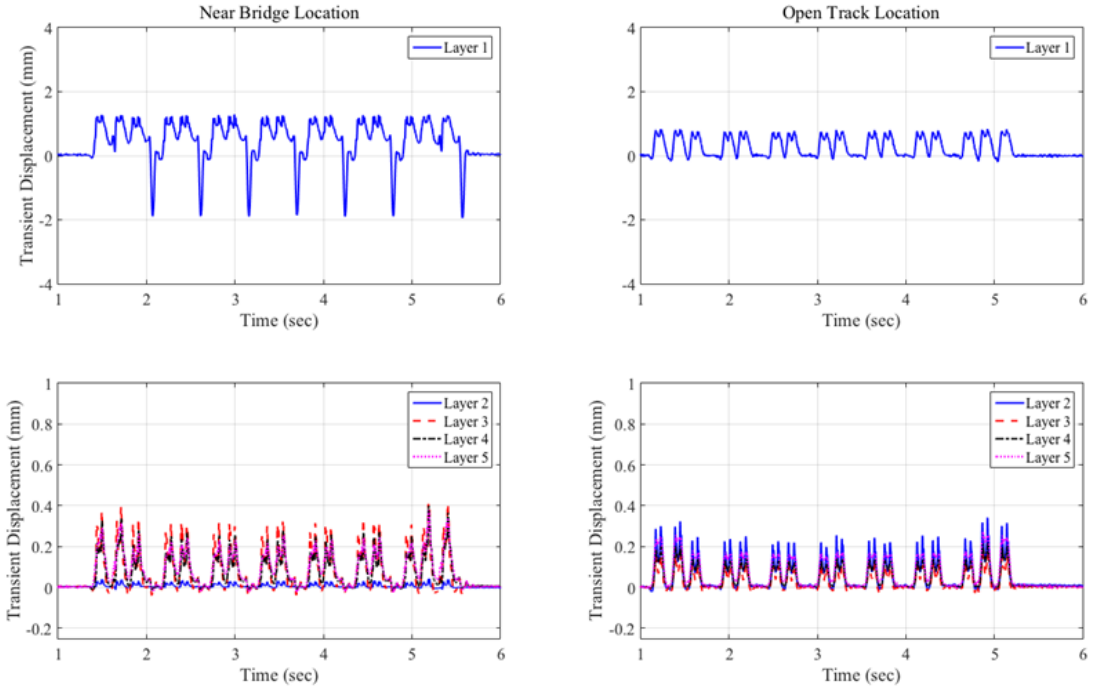

Figure A-1-20: Madison Street Bridge – November 2012 Train # 2 (ACELA)

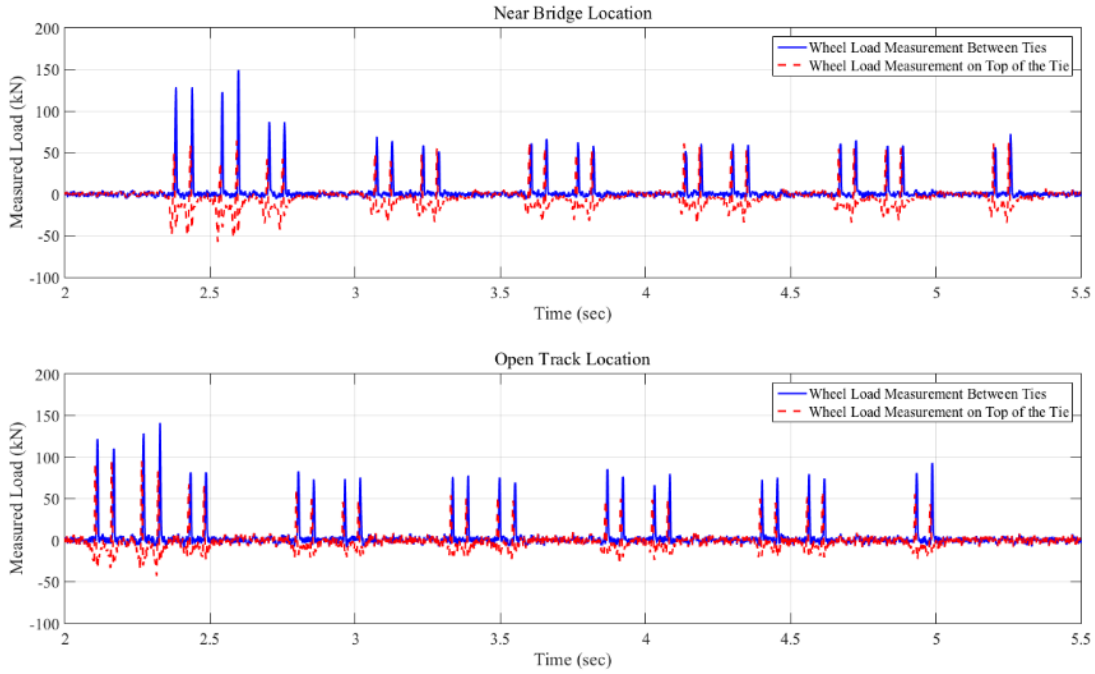

Figure A-1-21: Load Time History Recorded at Madison Street Bridge Approach; Data Collected in November 2012; Train # 3

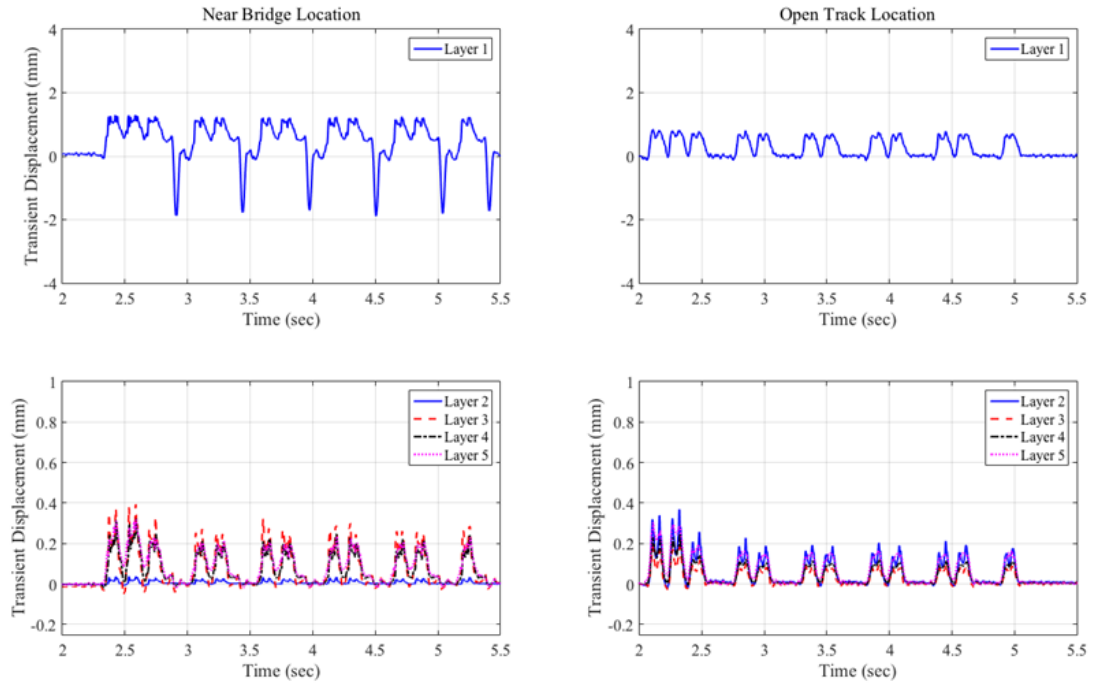

Figure A-1-22: Madison Street Bridge – November 2012 – Train # 3

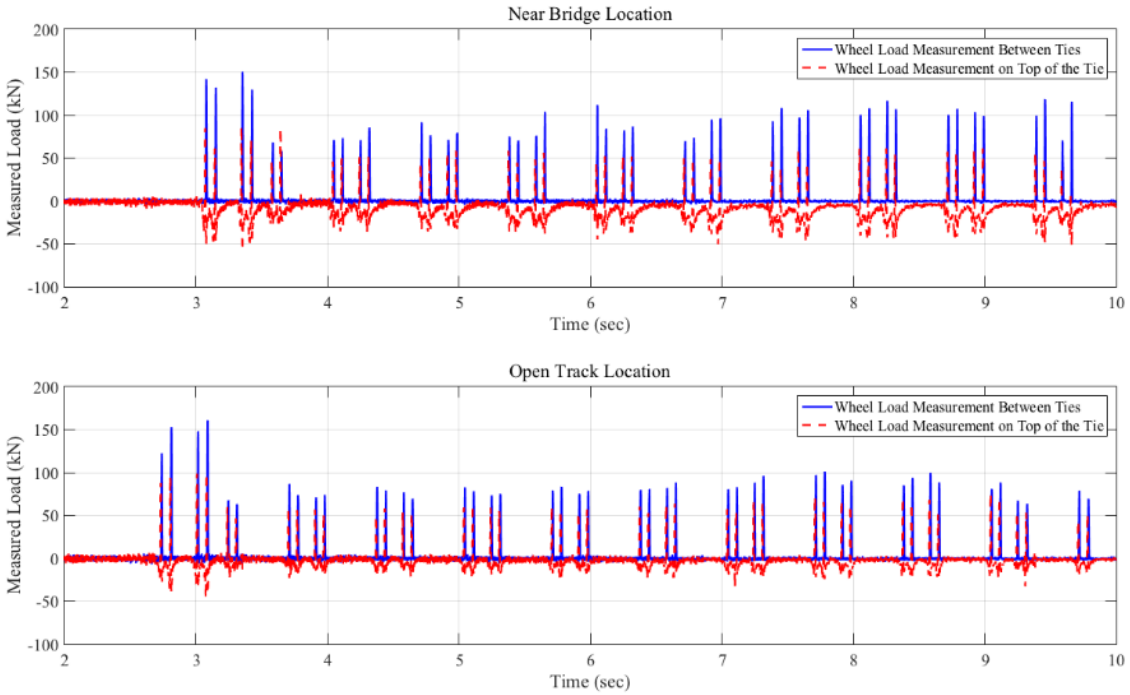

Figure A-1-23: Load Time History Recorded at Madison Street Bridge Approach; Data Collected in January 2013; Train # 1

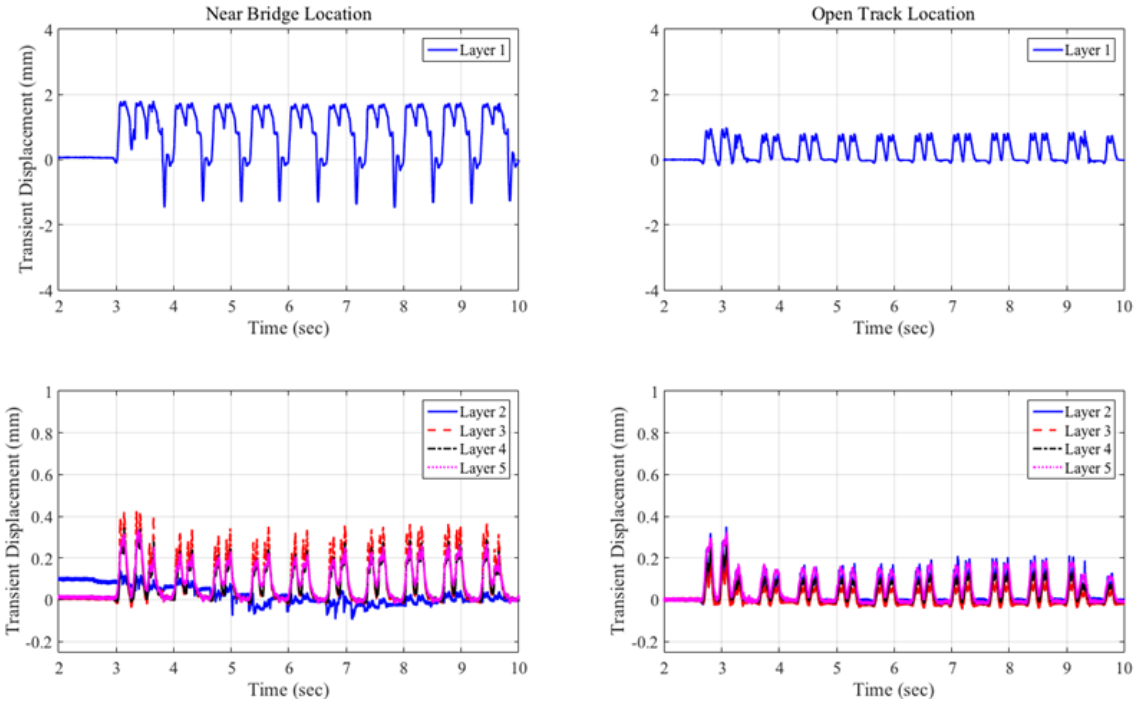

Figure A-1-24: Madison Street Bridge – January 2013 – Train # 1

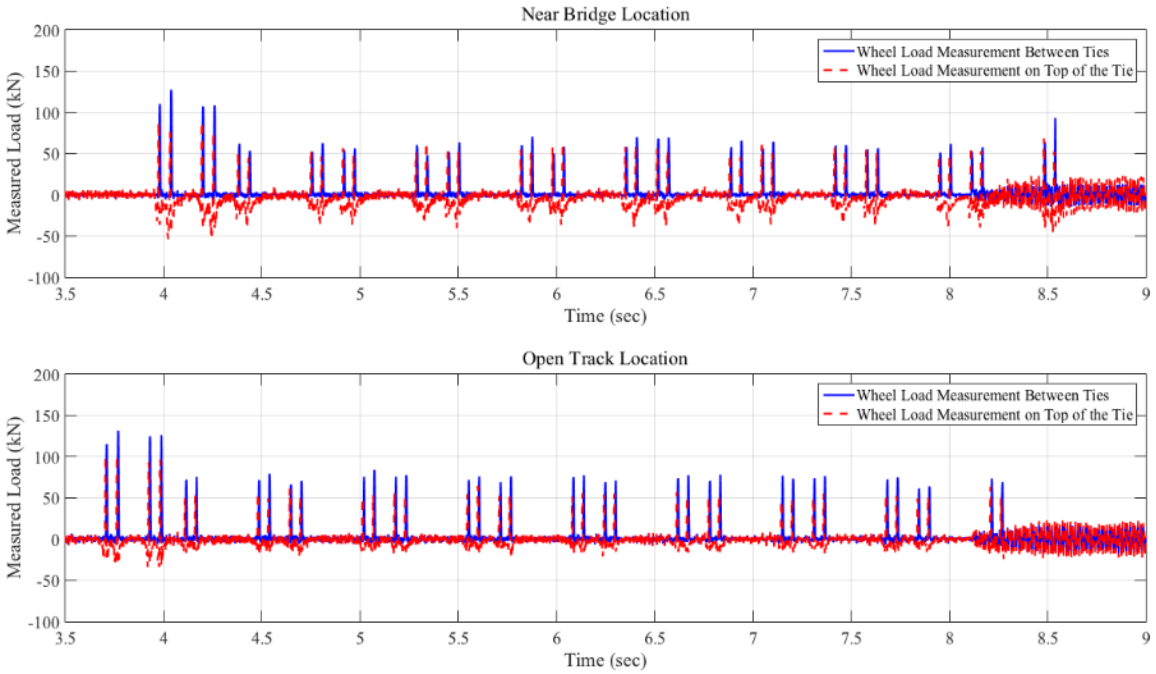

Figure A-1-25: Load Time History Recorded at Madison Street Bridge Approach; Data Collected in January 2013; Train # 2

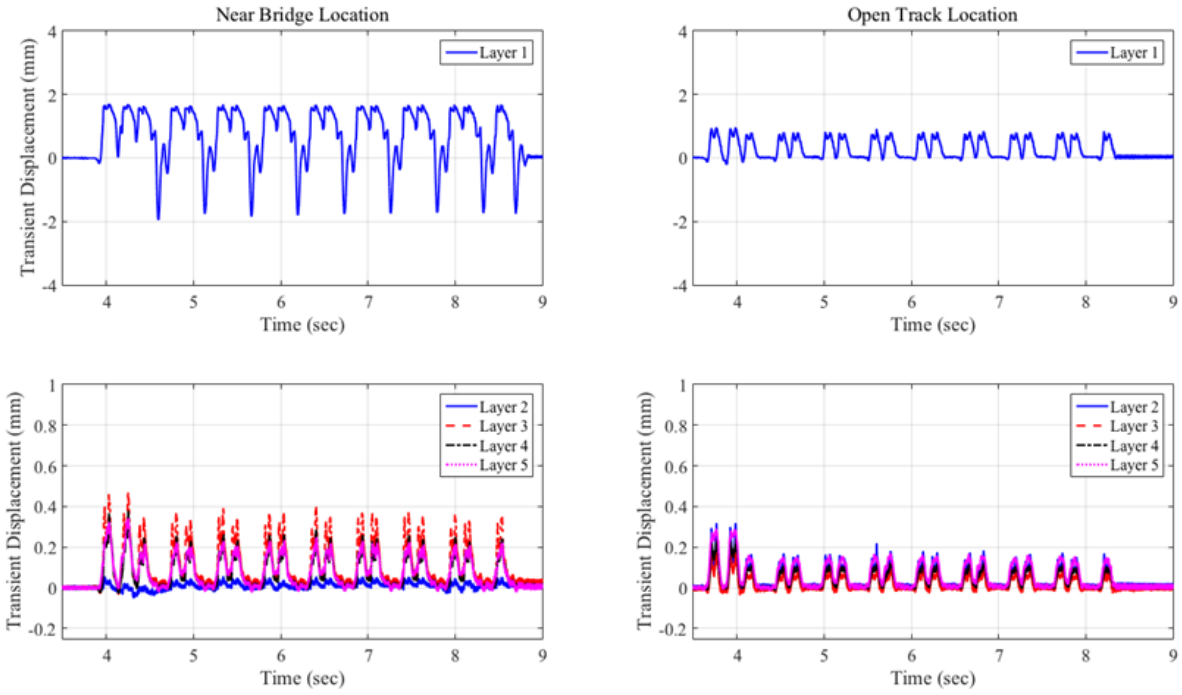

Figure A-1-26: Madison Street Bridge – January 2013 – Train # 2

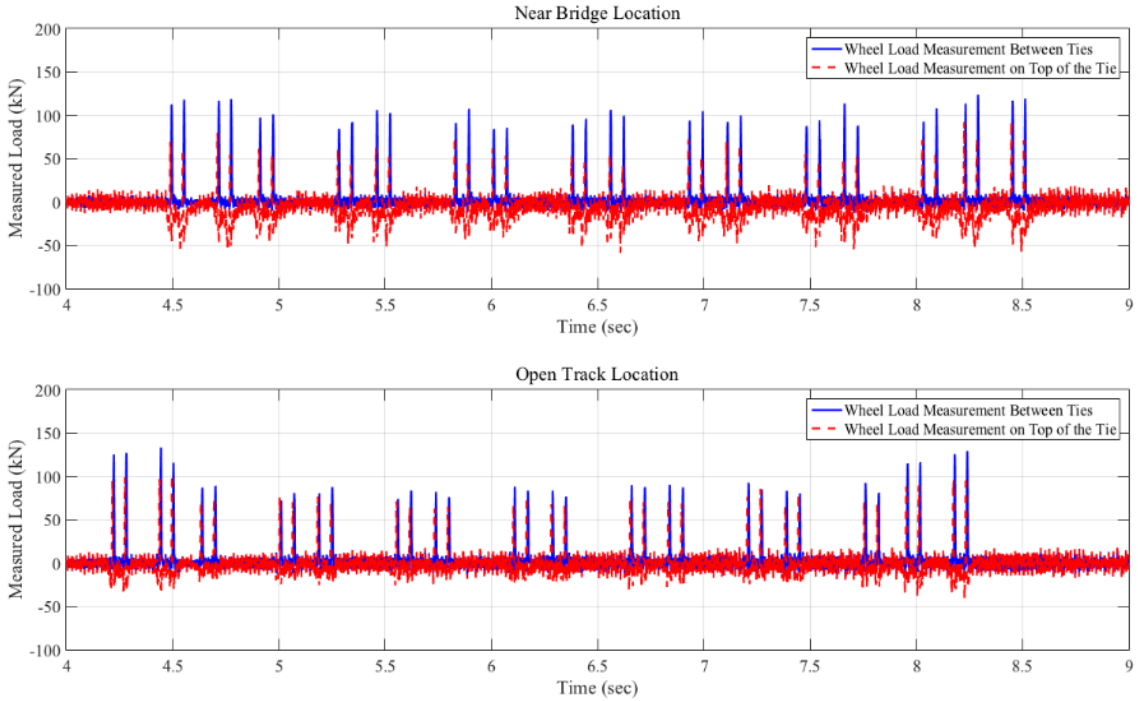

Figure A-1-27: Load Time History Recorded at Madison Street Bridge Approach; Data Collected in January 2013; Train # 3 (ACELA)

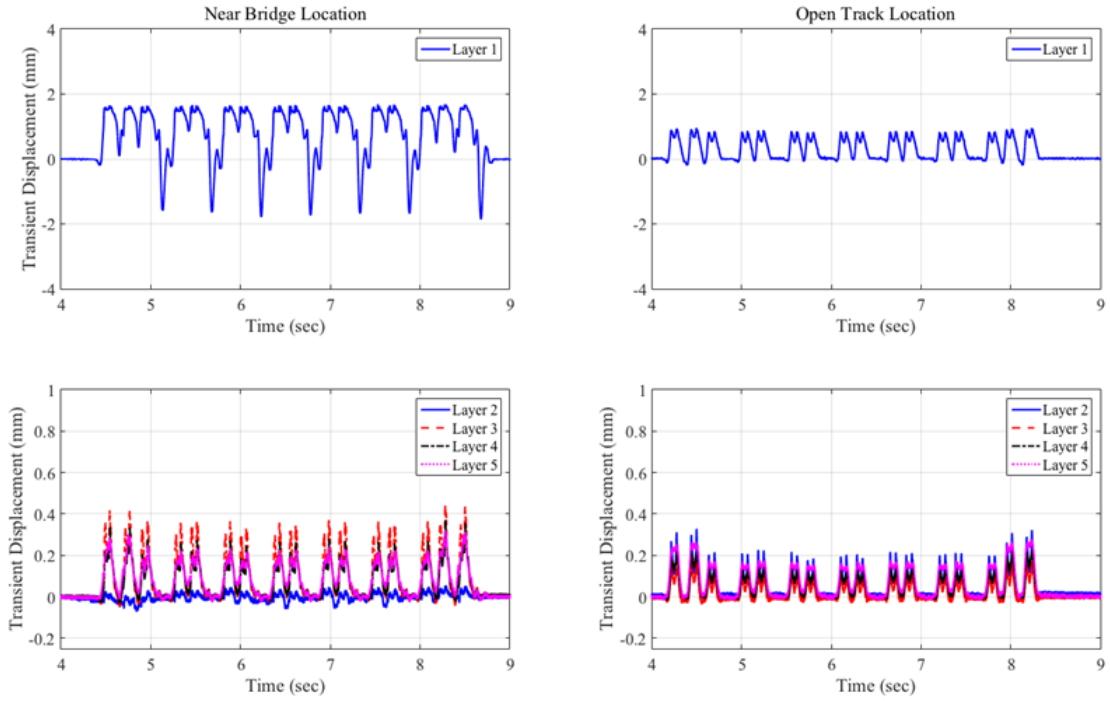

Figure A-1-28: Madison Street Bridge – January 2013 – Train # 3 (ACELA)

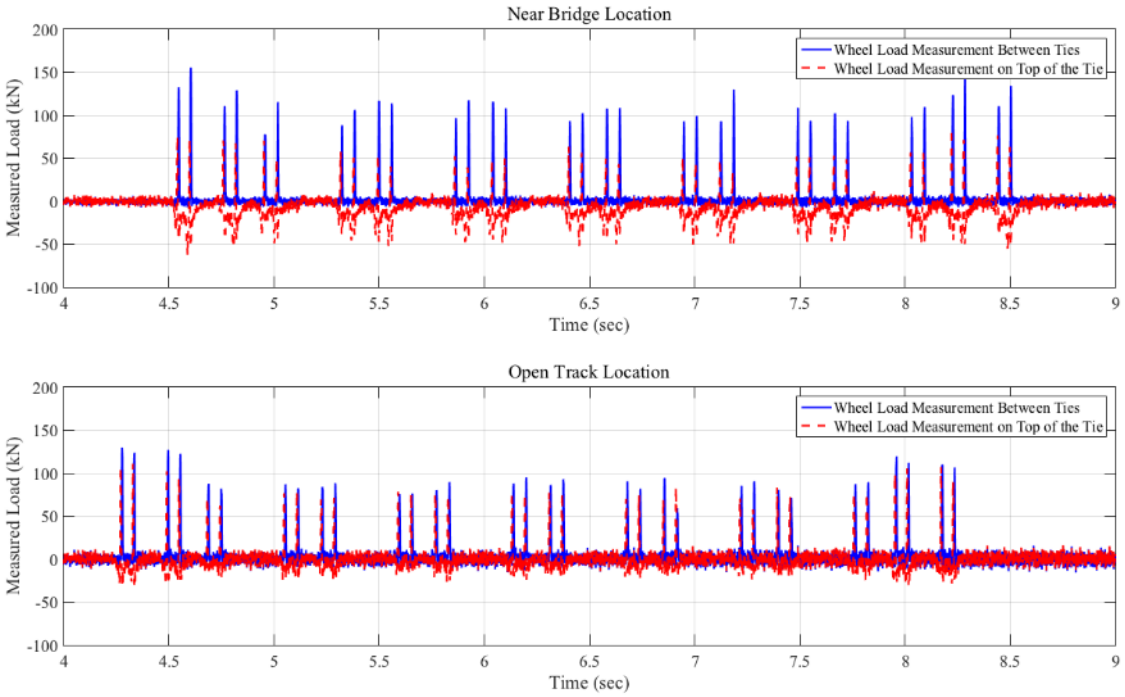

Figure A-1-29: Load Time History Recorded at Madison Street Bridge Approach; Data Collected in June 2013; Train # 1 (ACELA)

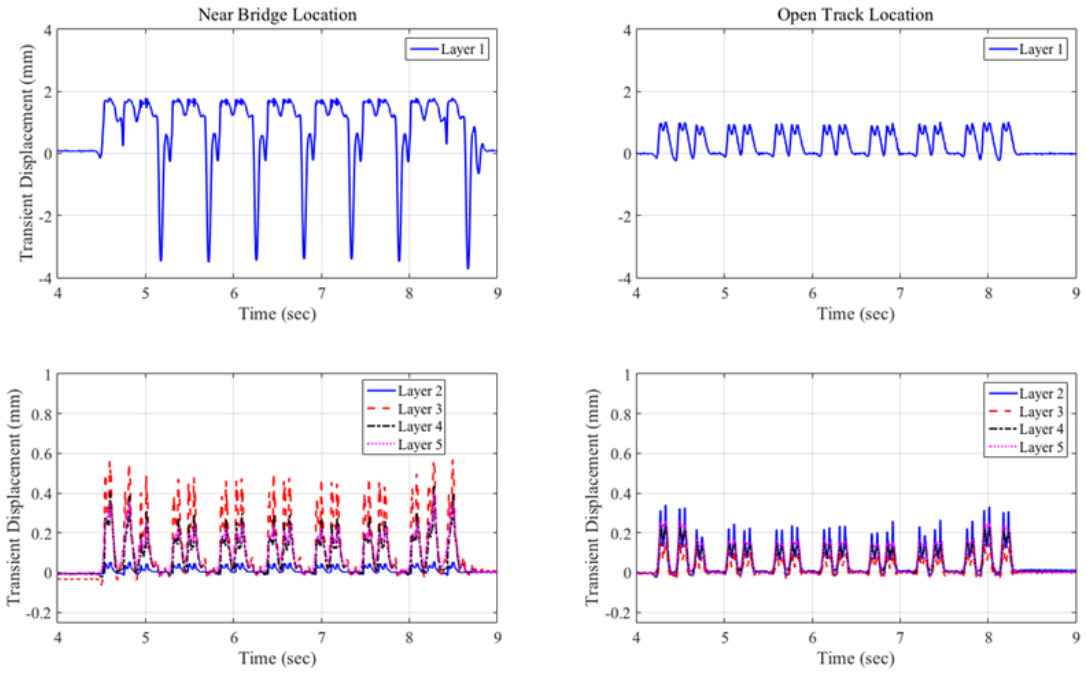

Figure A-1-30: Madison Street Bridge – June 2013 – Train # 1 (ACELA)

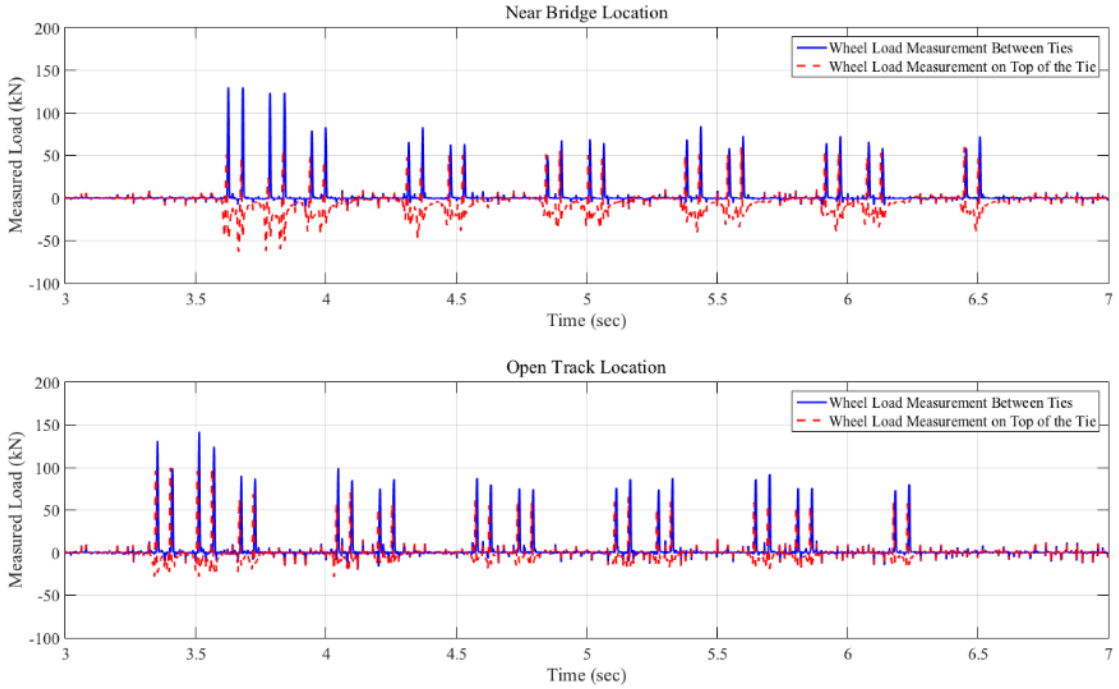

Figure A-1-31: Load Time History Recorded at Madison Street Bridge Approach; Data Collected in June 2013; Train # 2

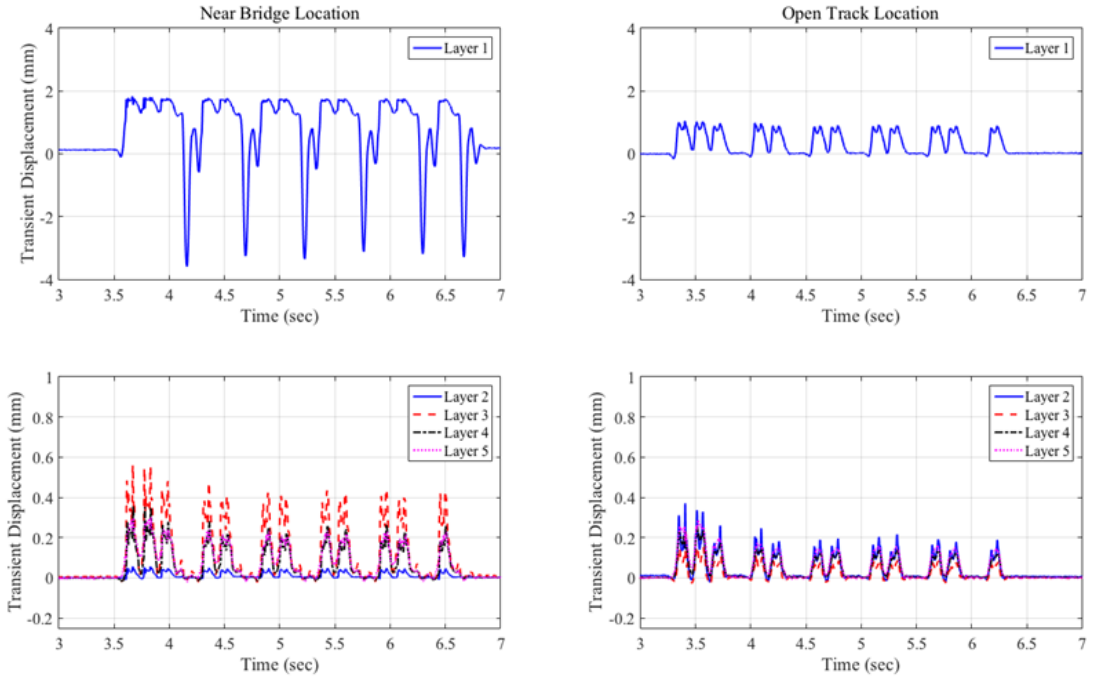

Figure A-1-32: Madison Street Bridge – June 2013 – Train # 2

Caldwell Street Bridge Approach Load and Displacement Time Histories

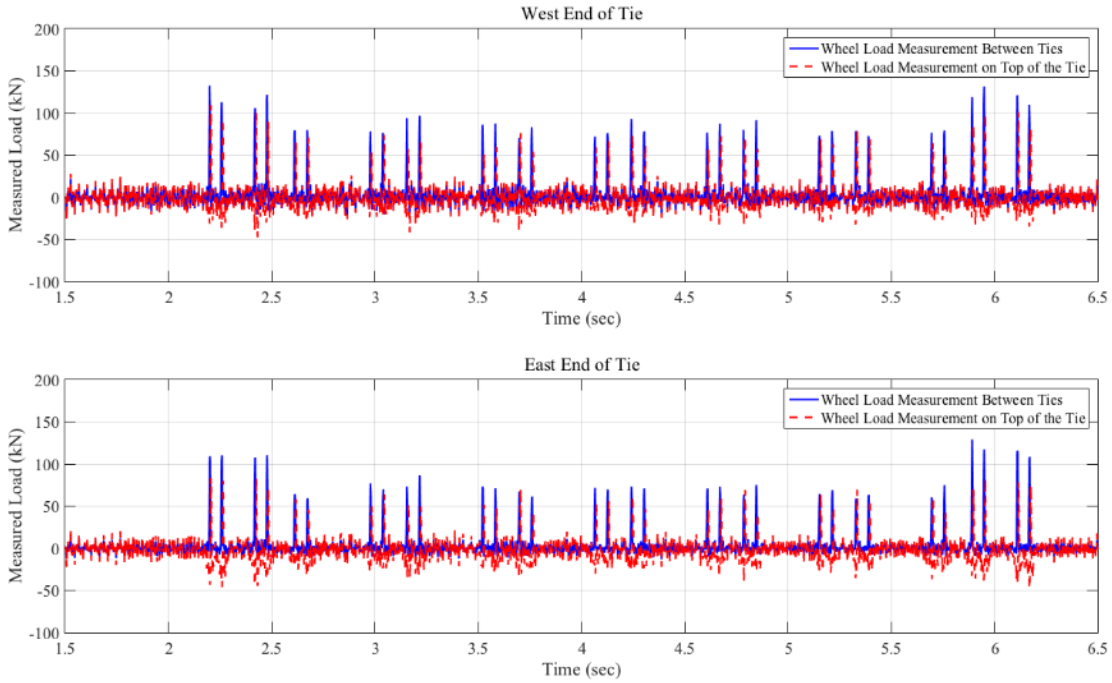

Figure A-1-33: Load Time History Recorded at Caldwell Street Bridge Approach; Data Collected in November 2012; Train # 1 (ACELA)

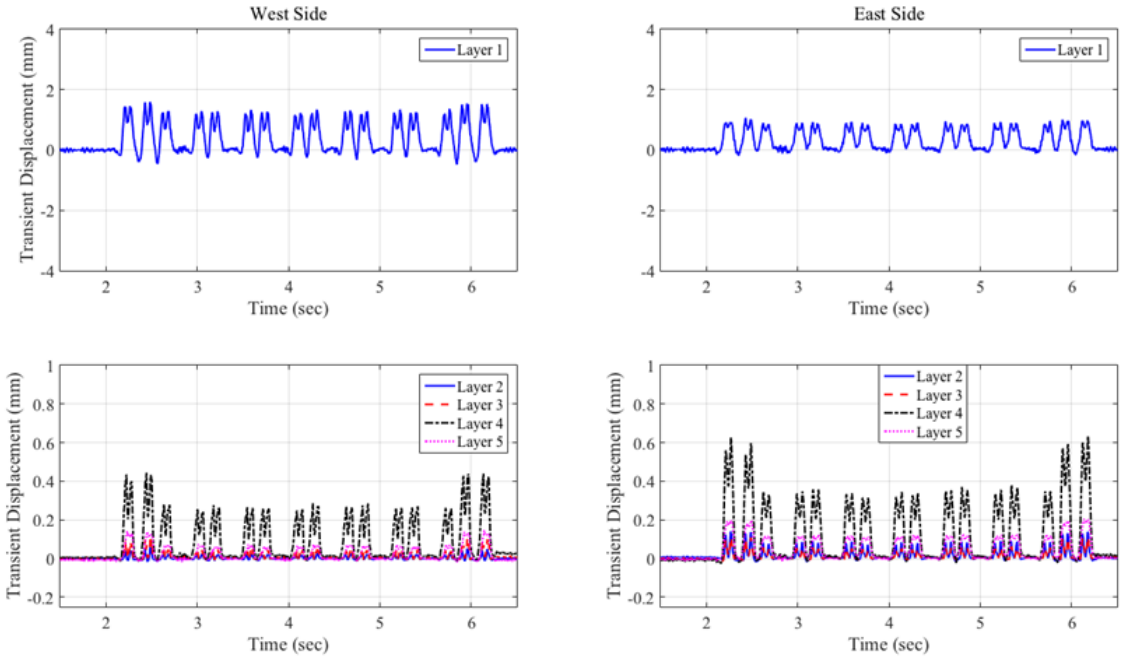

Figure A-1-34: Caldwell Street Bridge – November 2012 – Train # 1 (ACELA)

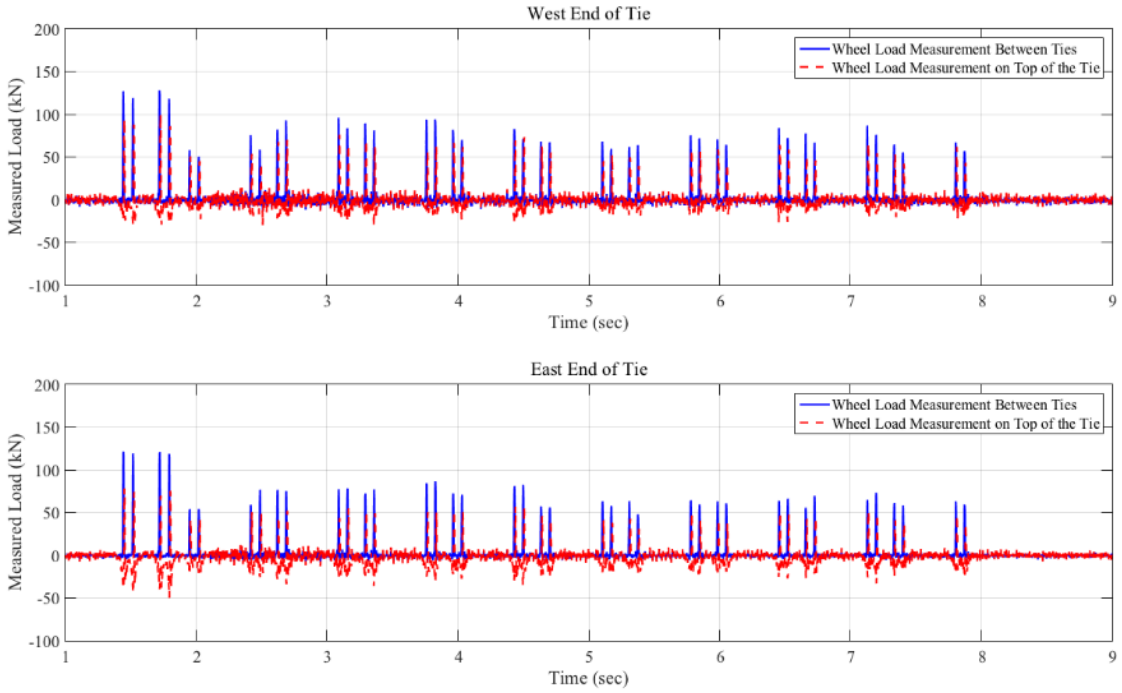

Figure A-1-35: Load Time History Recorded at Caldwell Street Bridge Approach; Data Collected in November 2012; Train # 2

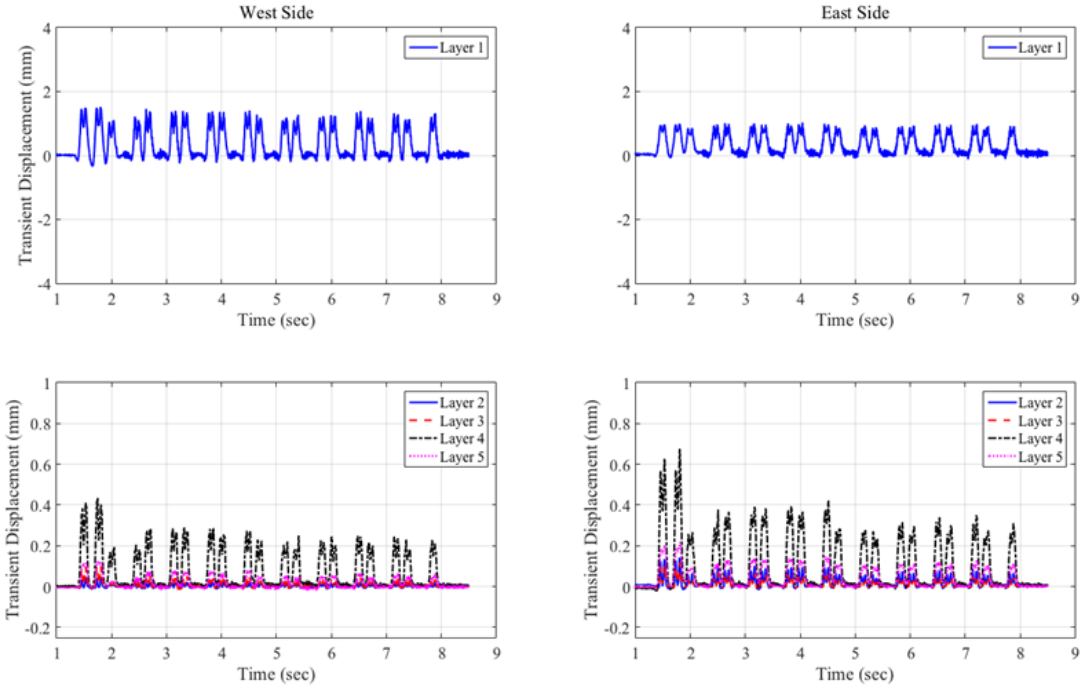

Figure A-1-36: Caldwell Street Bridge – November 2012 – Train # 2

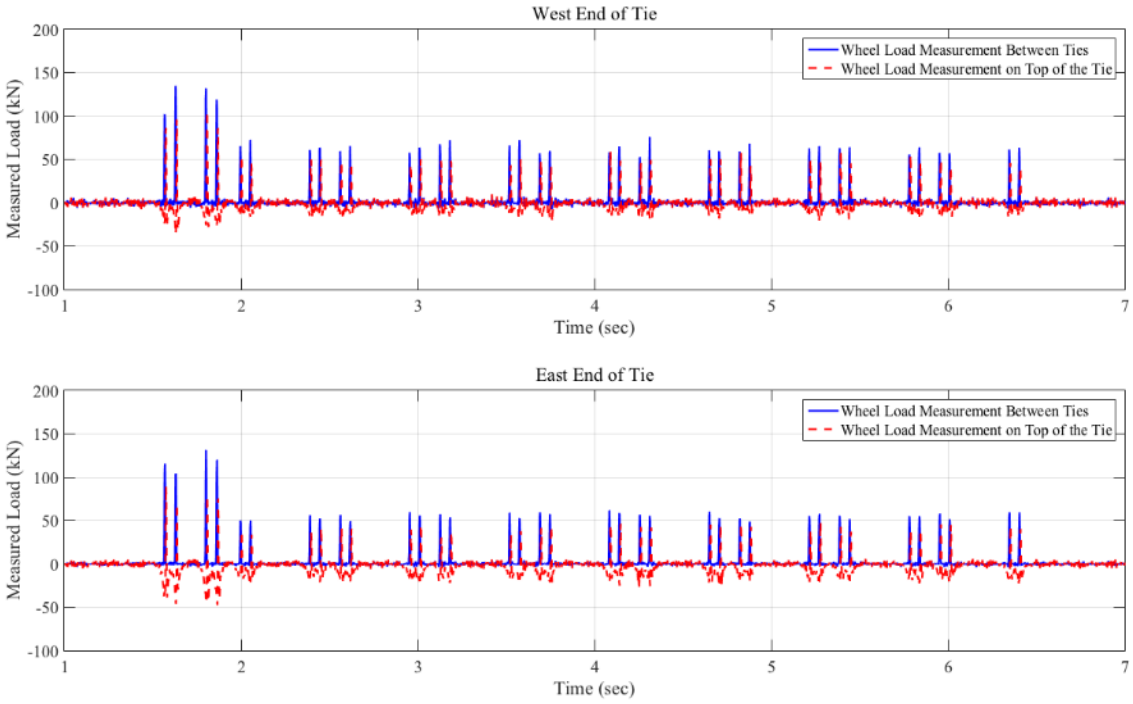

Figure A-1-37: Load Time History Recorded at Caldwell Street Bridge Approach; Data Collected in January 2013; Train # 1

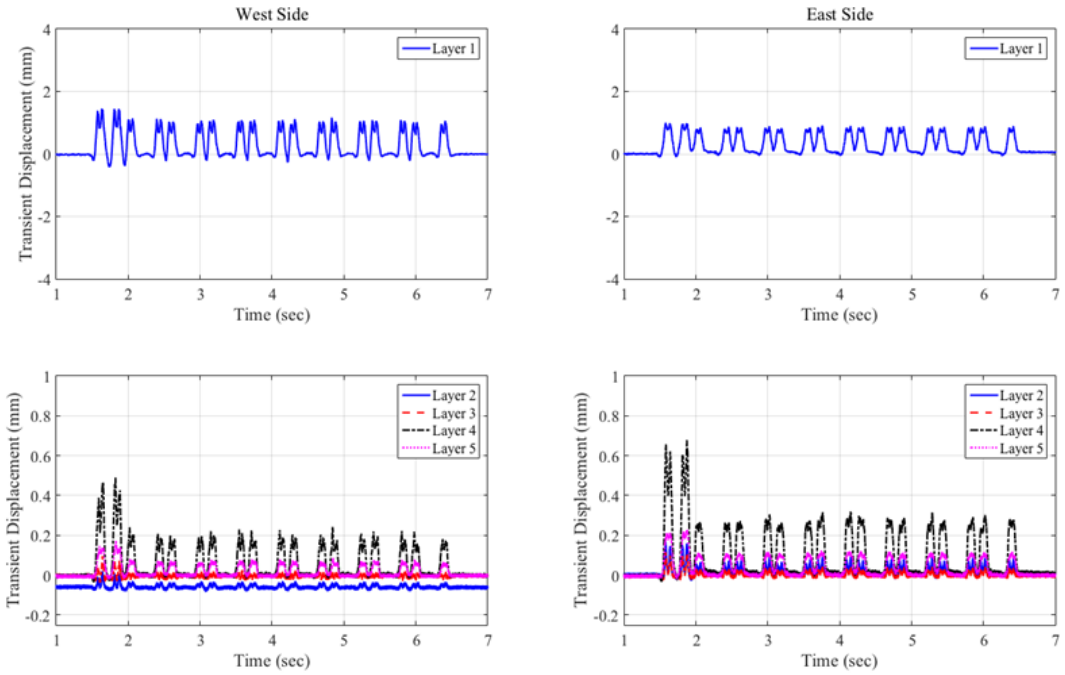

Figure A-1-38: Caldwell Street Bridge – January 2013 Train # 1

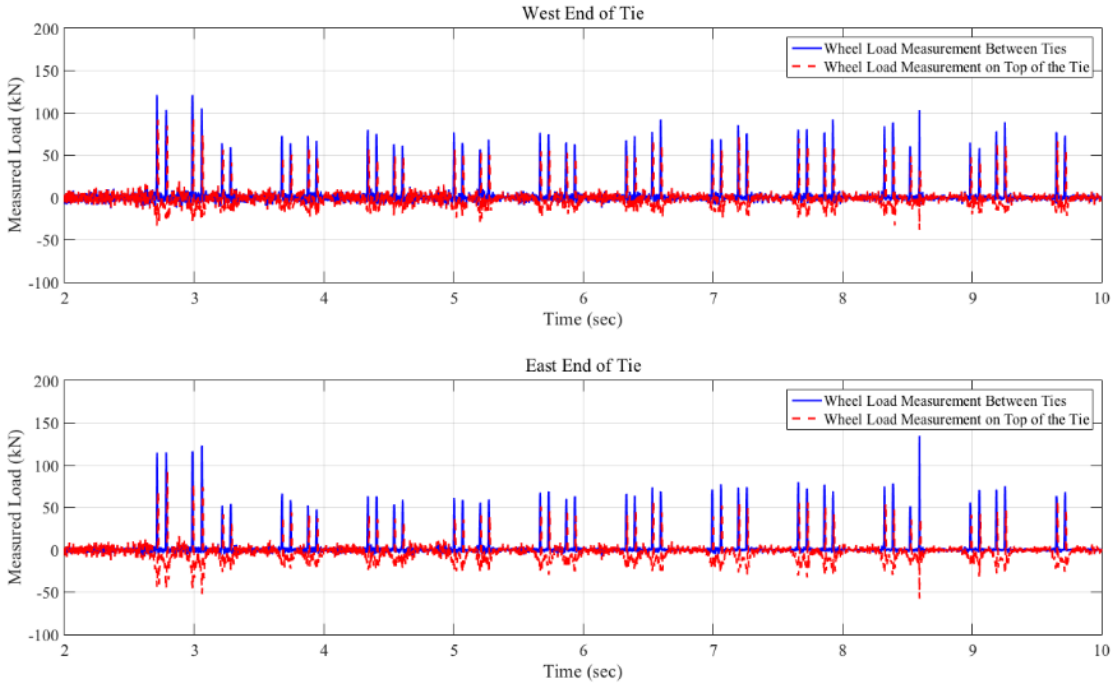

Figure A-1-39: Load Time History Recorded at Caldwell Street Bridge Approach; Data Collected in January 2013; Train # 2

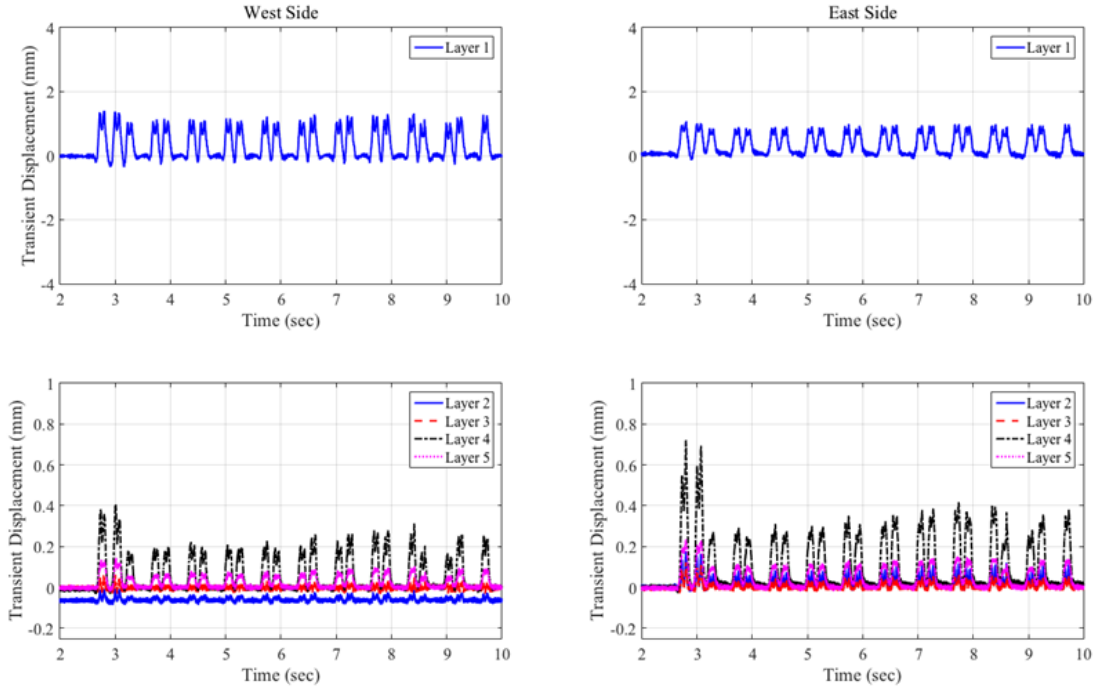

Figure A-1-40: Caldwell Street Bridge – January 2013 – Train # 2

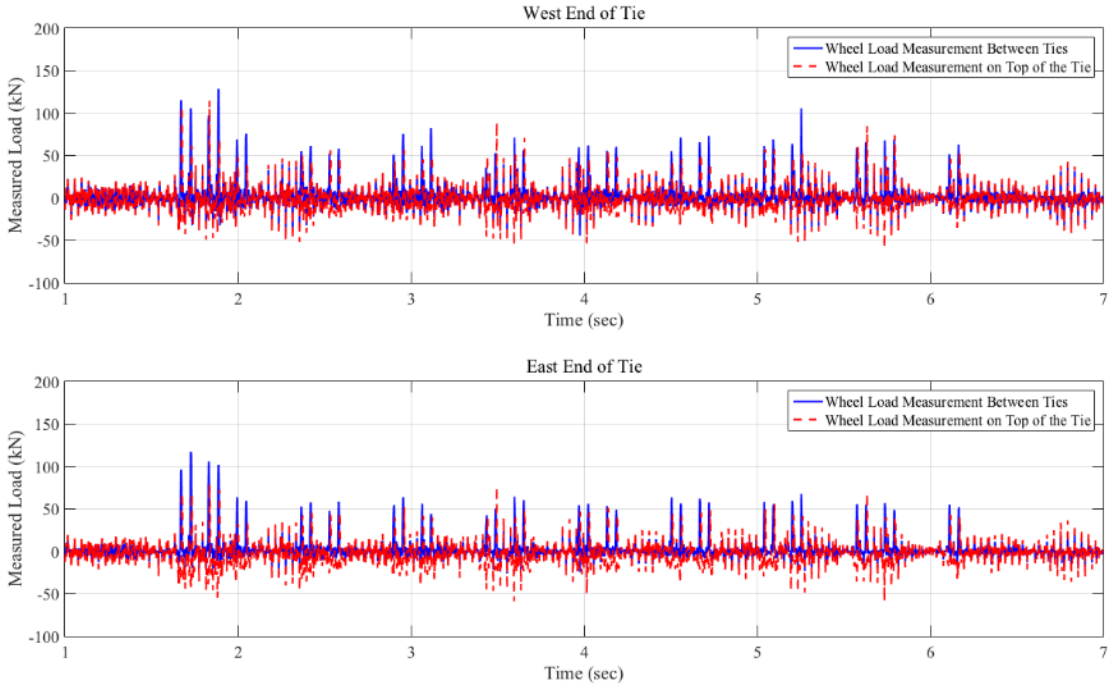

Figure A-1-41: Load Time History Recorded at Caldwell Street Bridge Approach; Data Collected in January 2013; Train # 3

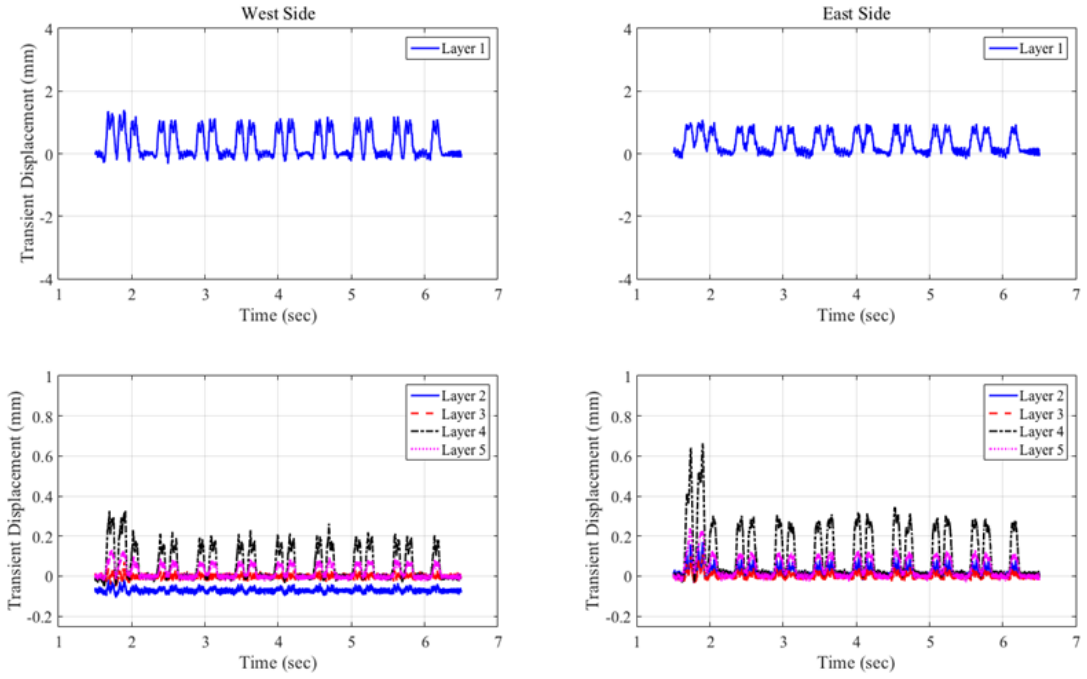

Figure A-1-42: Caldwell Street Bridge – January 2013 – Train # 3

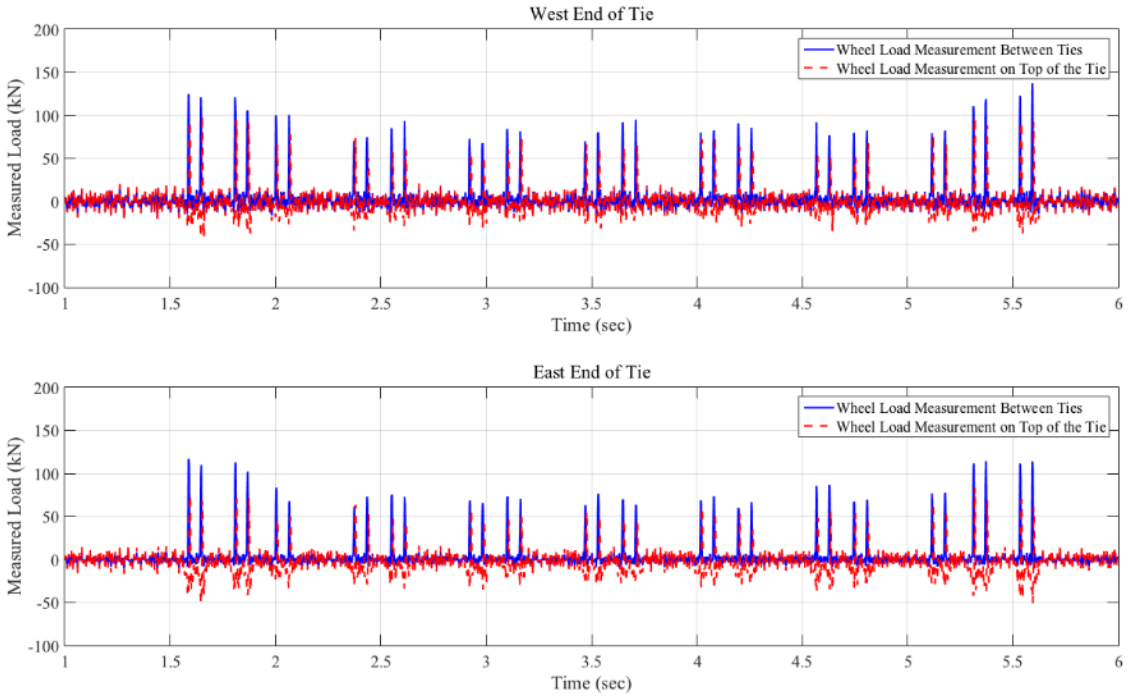

Figure A-1-43: Load Time History Recorded at Caldwell Street Bridge Approach; Data Collected in January 2013; Train # 4 (ACELA)

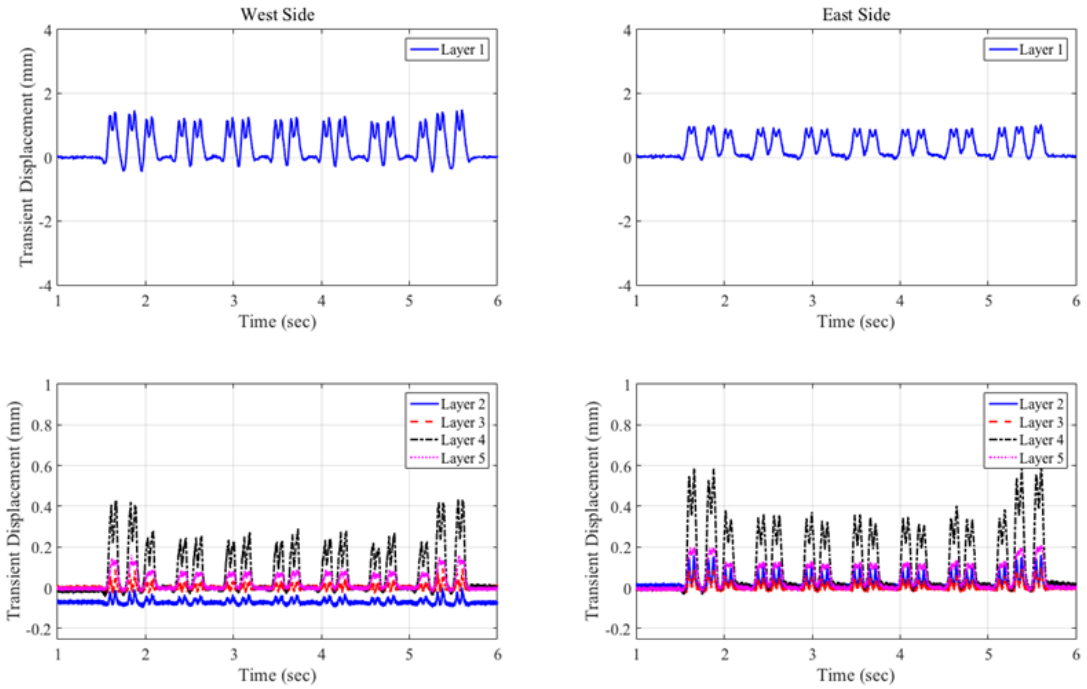

Figure A-1-44: Caldwell Street Bridge – January 2013 – Train # 4 (ACELA)

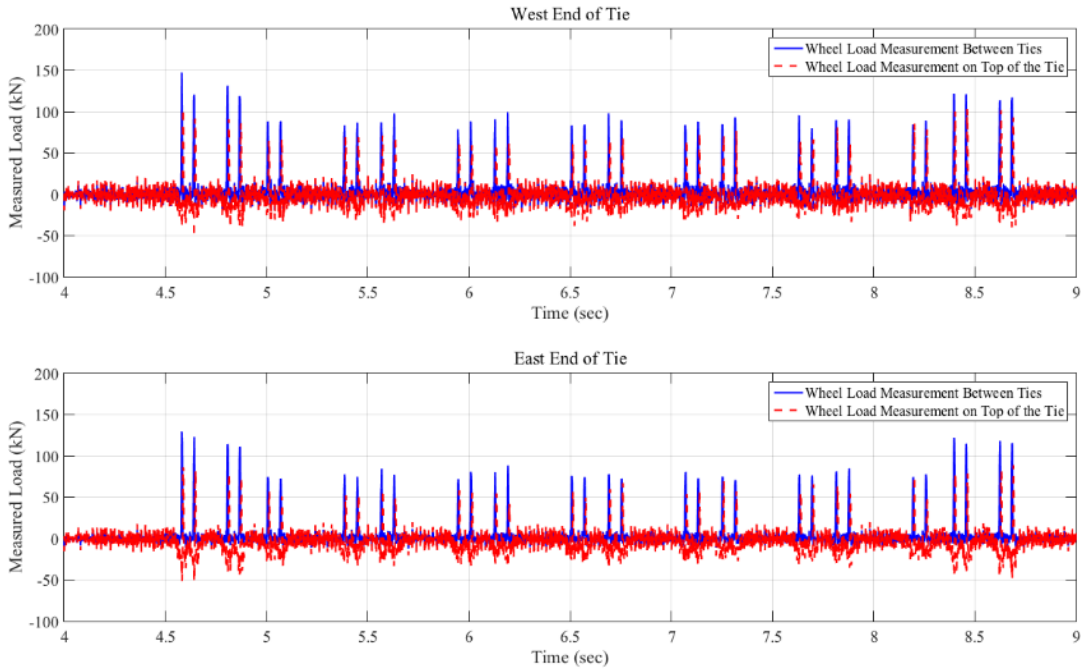

Figure A-1-45: Load Time History Recorded at Caldwell Street Bridge Approach; Data Collected in June 2013; Train # 1 (ACELA)

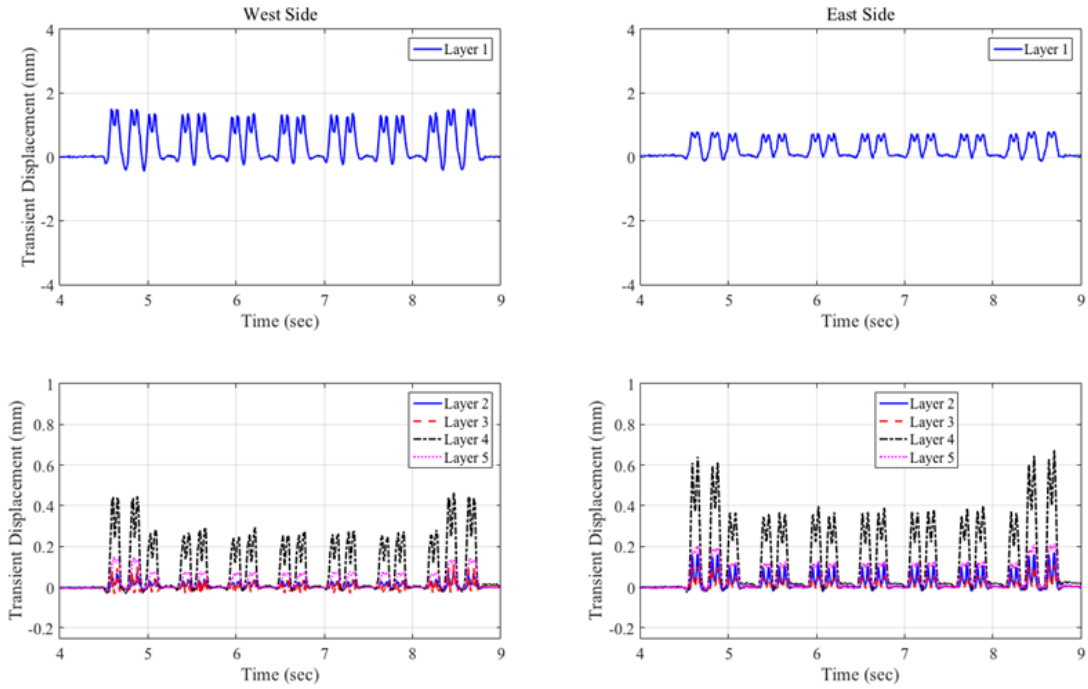

Figure A-1-46: Caldwell Street Bridge – June 2013 – Train # 1 (ACELA)

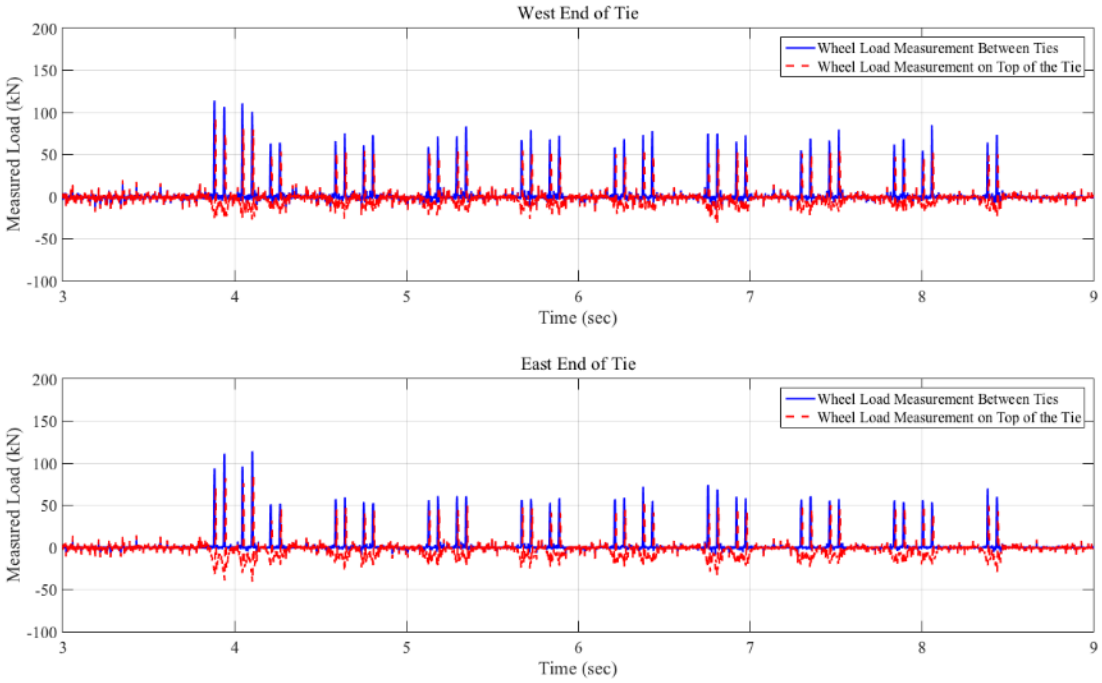

Figure A-1-47: Load Time History Recorded at Caldwell Street Bridge Approach; Data Collected in June 2013; Train # 2

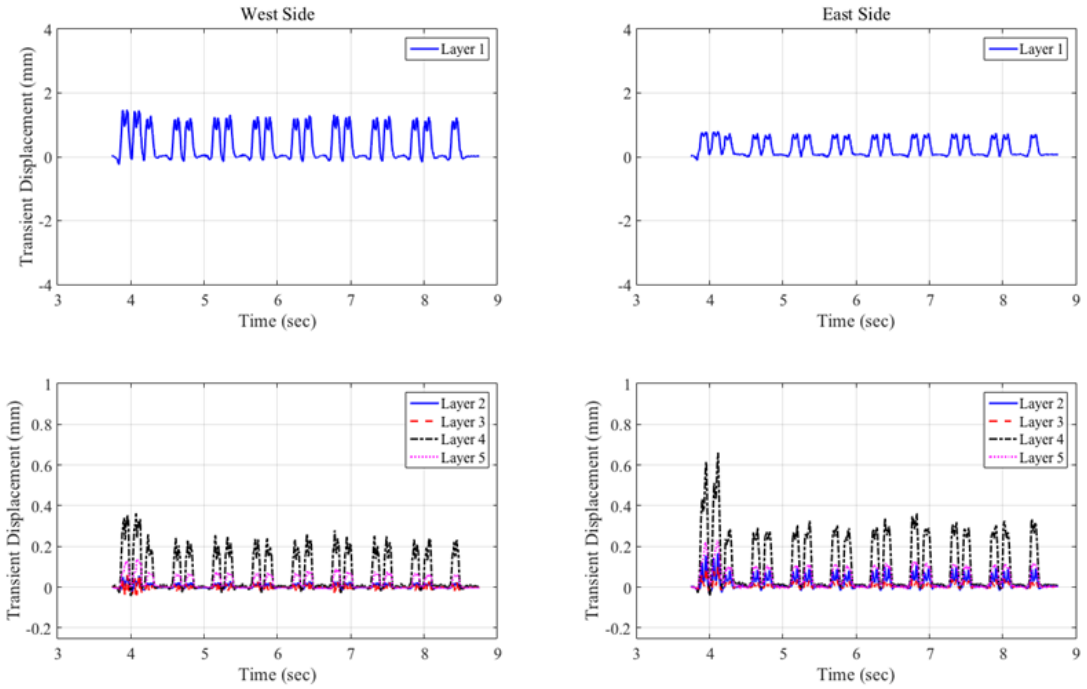

Figure A-1-48: Caldwell Street Bridge – June 2013 – Train # 2

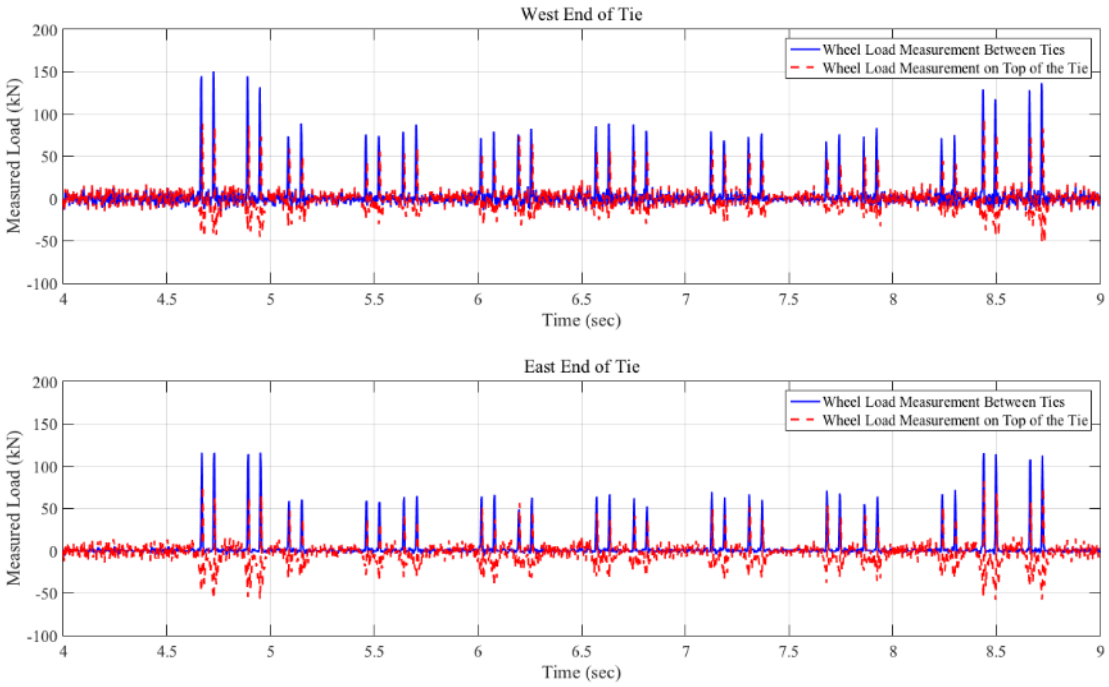

Figure A-1-49: Load Time History Recorded at Caldwell Street Bridge Approach; Data Collected in May 2015; Train # 1 (ACELA)

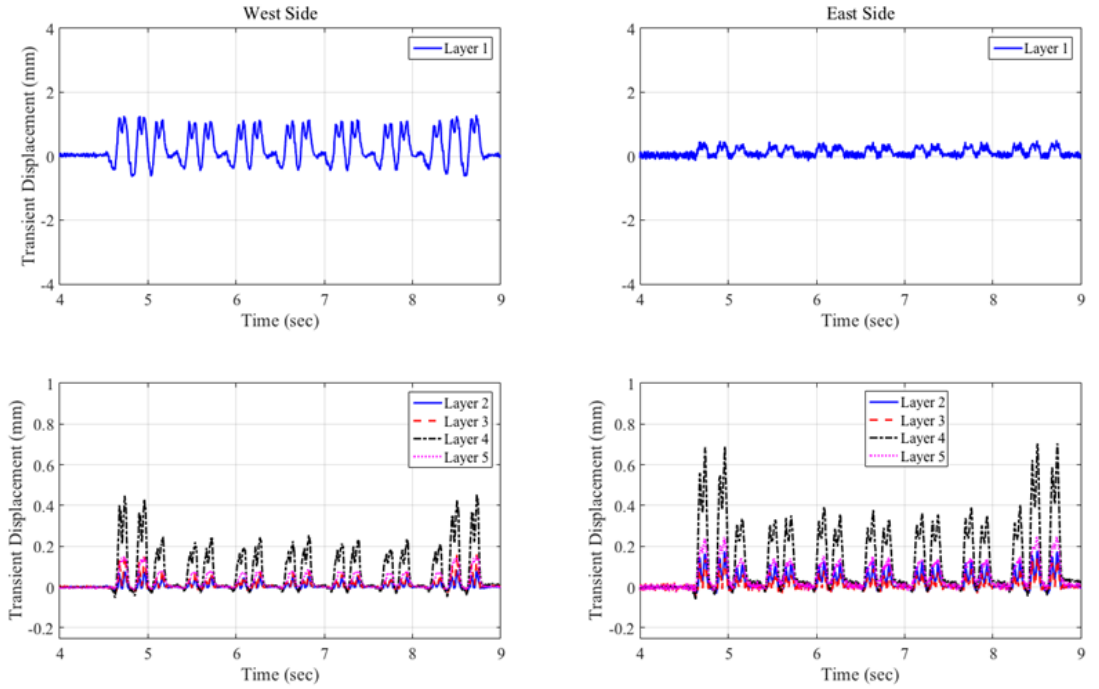

Figure A-1-50: Caldwell Street Bridge – May 2015 Train # 1 (ACELA)

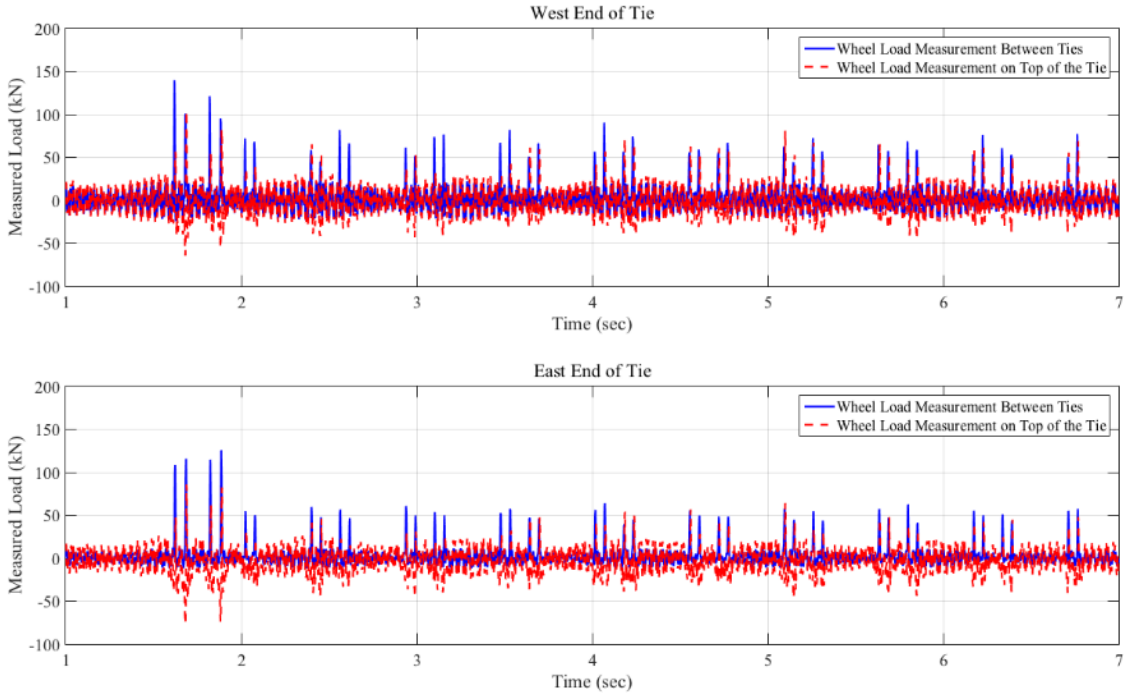

Figure A-1-51: Load Time History Recorded at Caldwell Street Bridge Approach; Data Collected in May 2015; Train # 2

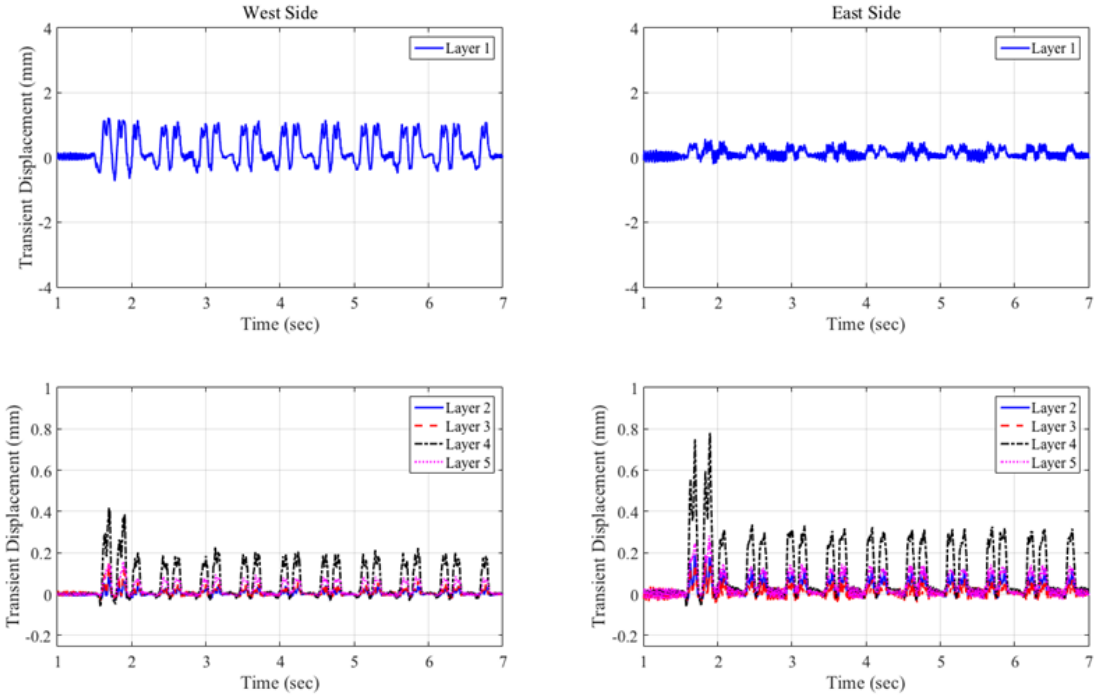

Figure A-1-52: Caldwell Street Bridge – May 2015 – Train # 2

Norfolk Southern (NS) Mile Post 352:2 Load and Time Histories

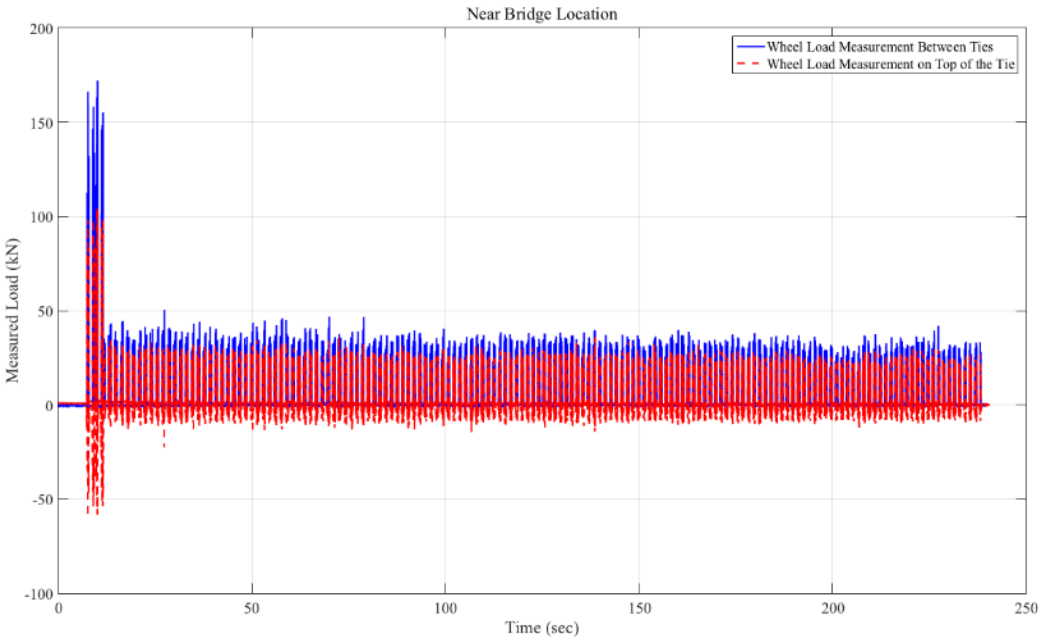

Figure A-1-53: Load Time History Recorded at the Bridge 352:2 – March 2014 – Near Bridge Location

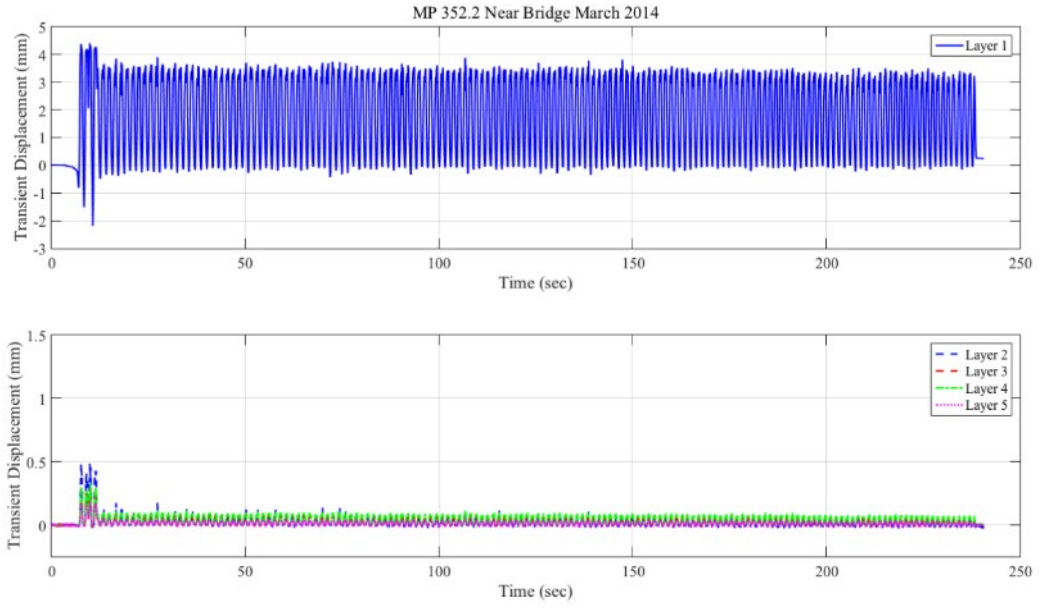

Figure A-1-54: Bridge 352:2 – March 2014 – Near Bridge Location

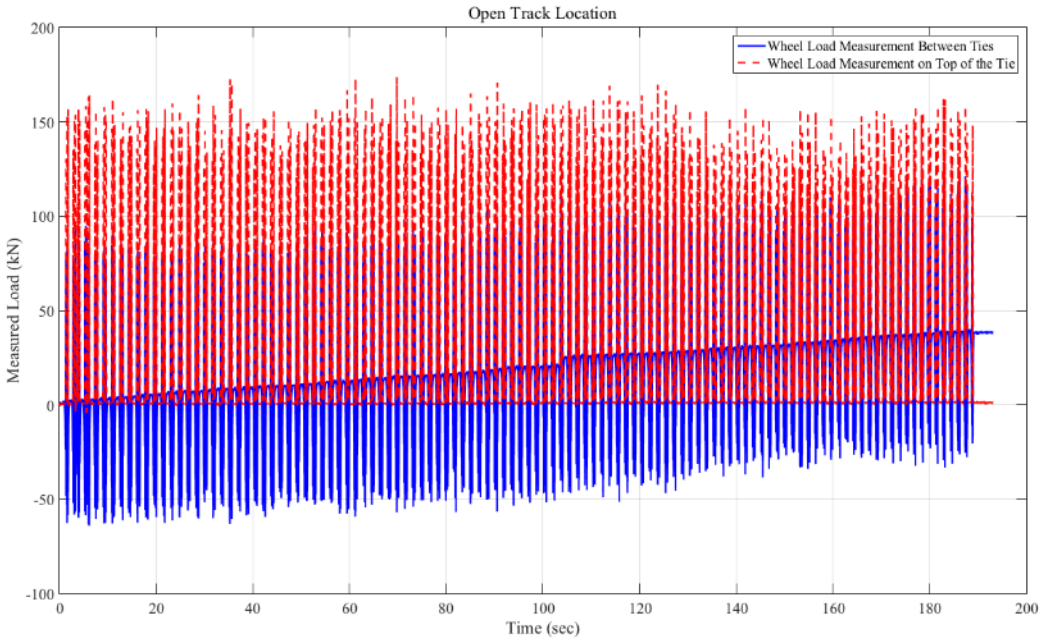

Figure A-1-55: Load Time History Recorded at the Bridge 352:2 – March 2014 – Open Track Location

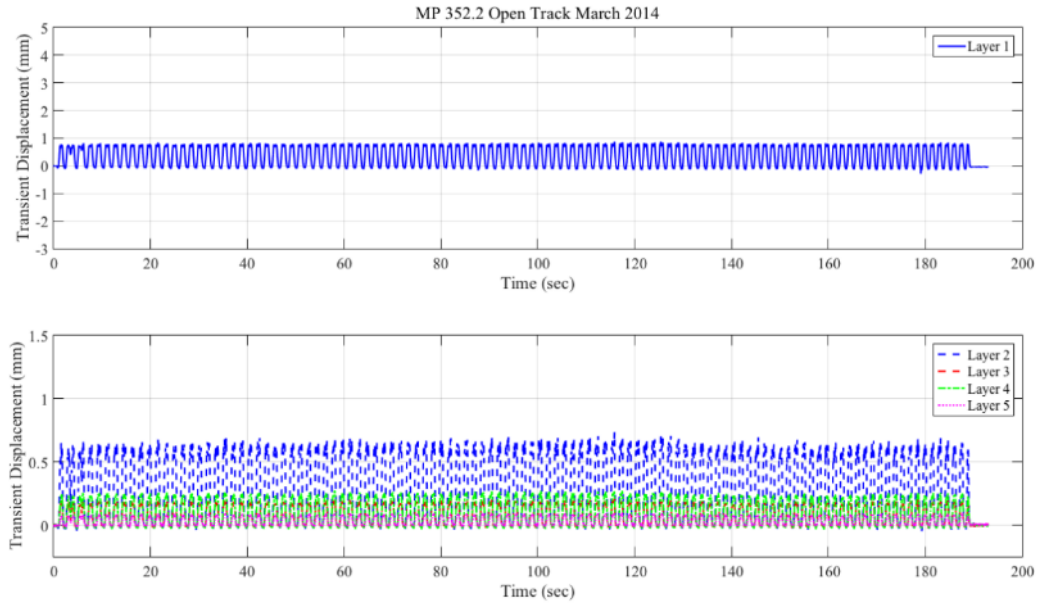

Figure A-1-56: Bridge 352:2 – March 2014 – Open Track Location

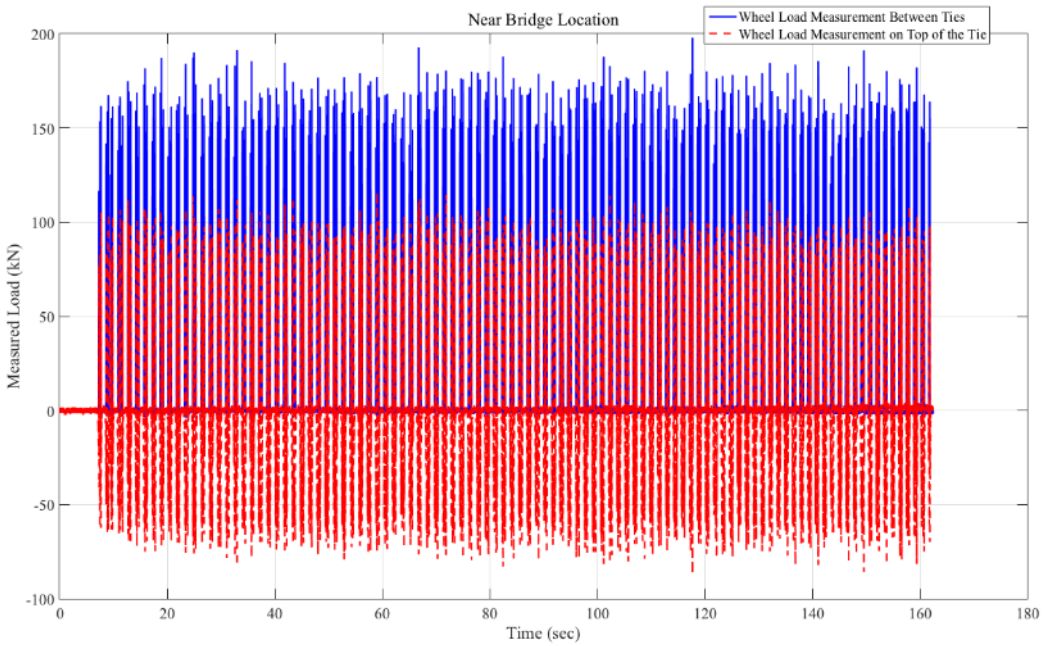

Figure A-1-57: Load Time History Recorded at the Bridge 352:2 – December 2014 – Near Bridge Location

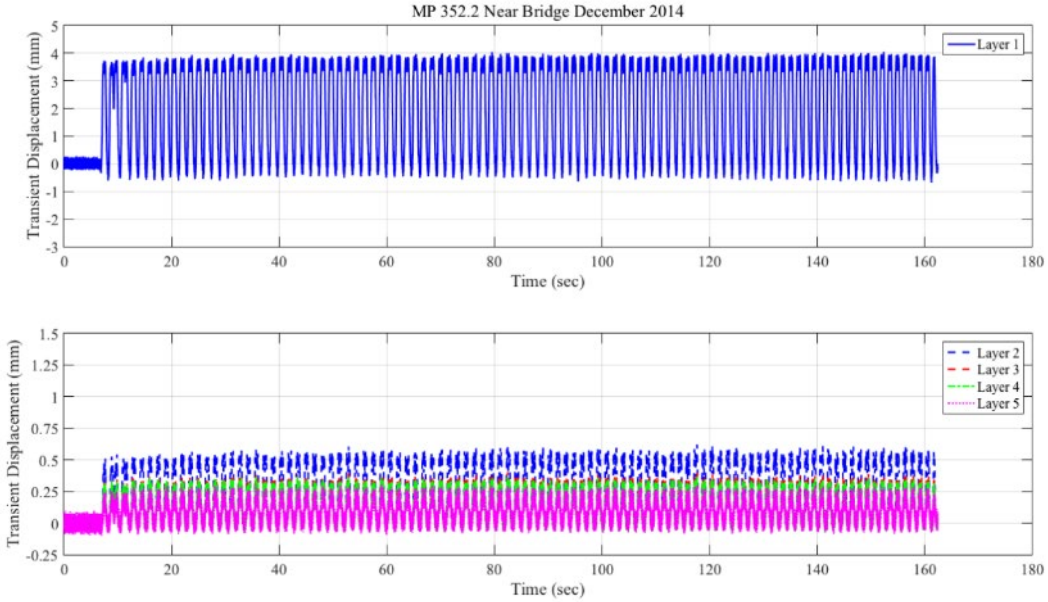

Figure A-1-58: Bridge 352:2 – December 2014 – Near Bridge Location

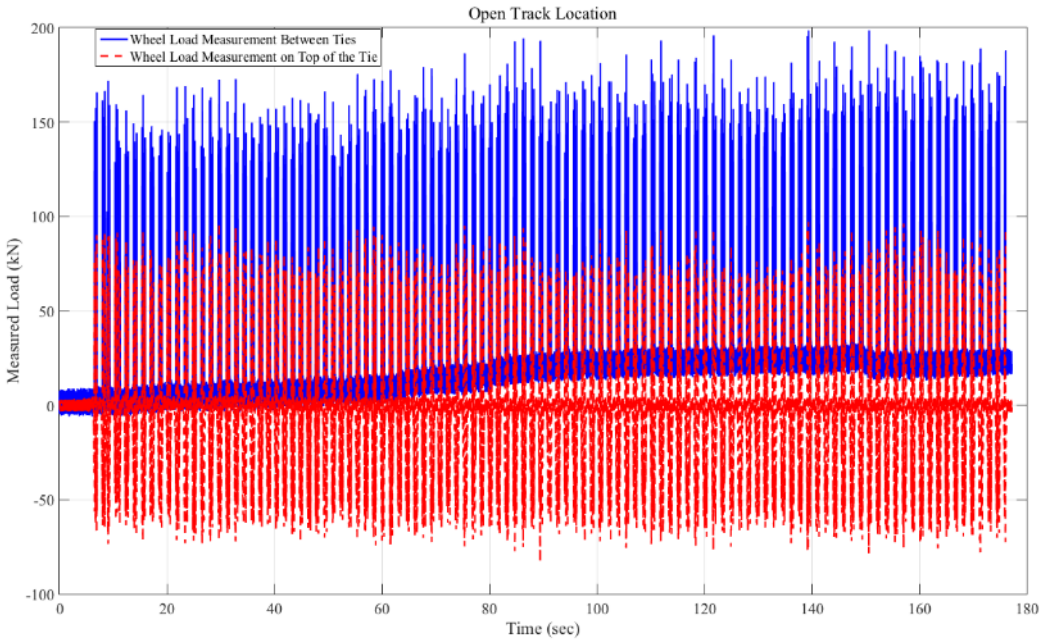

Figure A-1-59: Load Time History Recorded at the Bridge 352:2 – December 2014 – Open Track Location

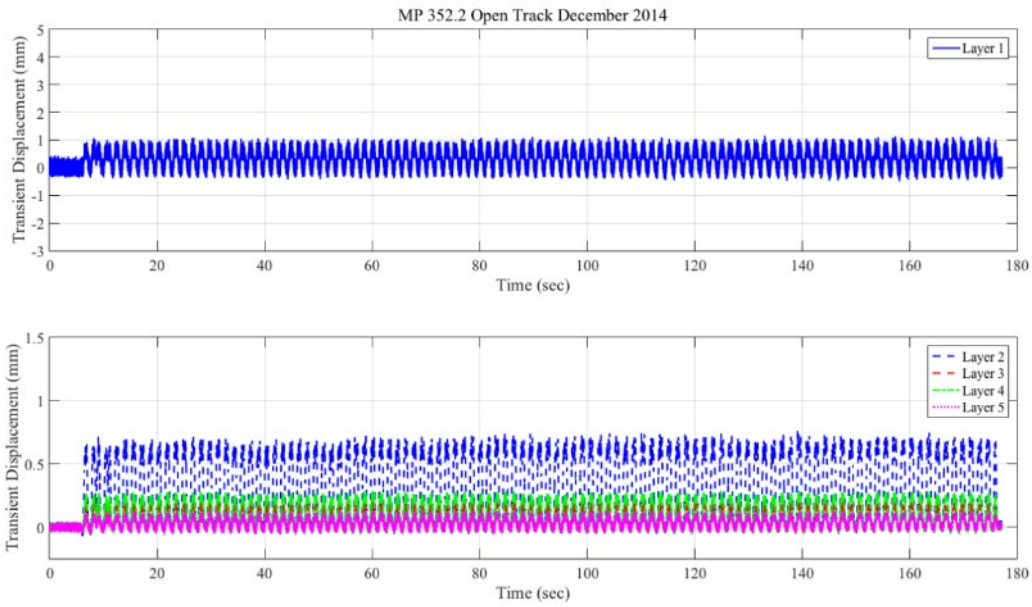

Figure A-1-60: Bridge 352:2 – December 2014 – Open Track Location

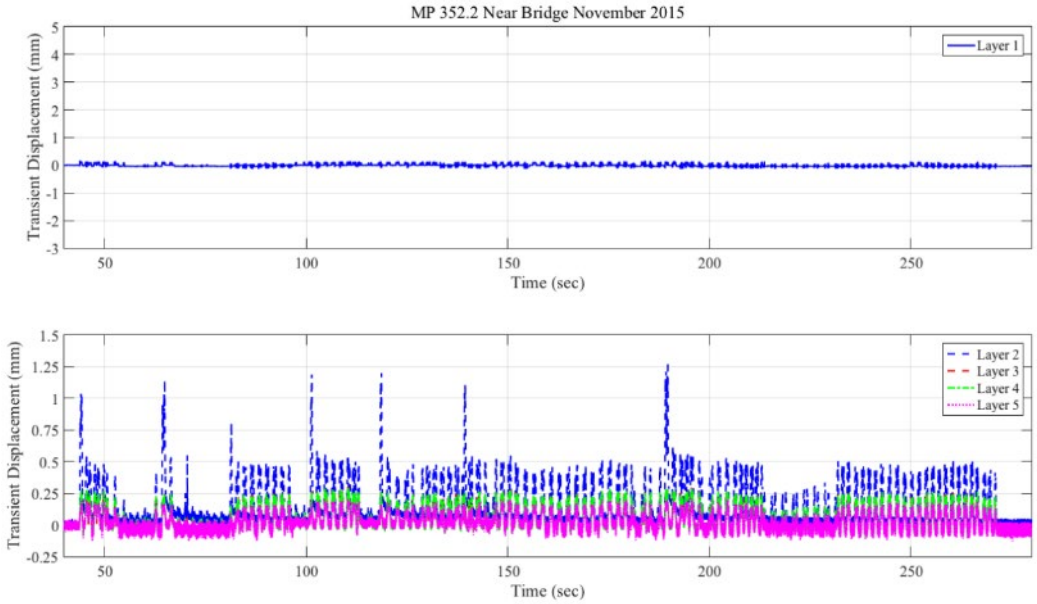

Figure A-1-61: Bridge 352:2 – November 2015 – Near Bridge Location

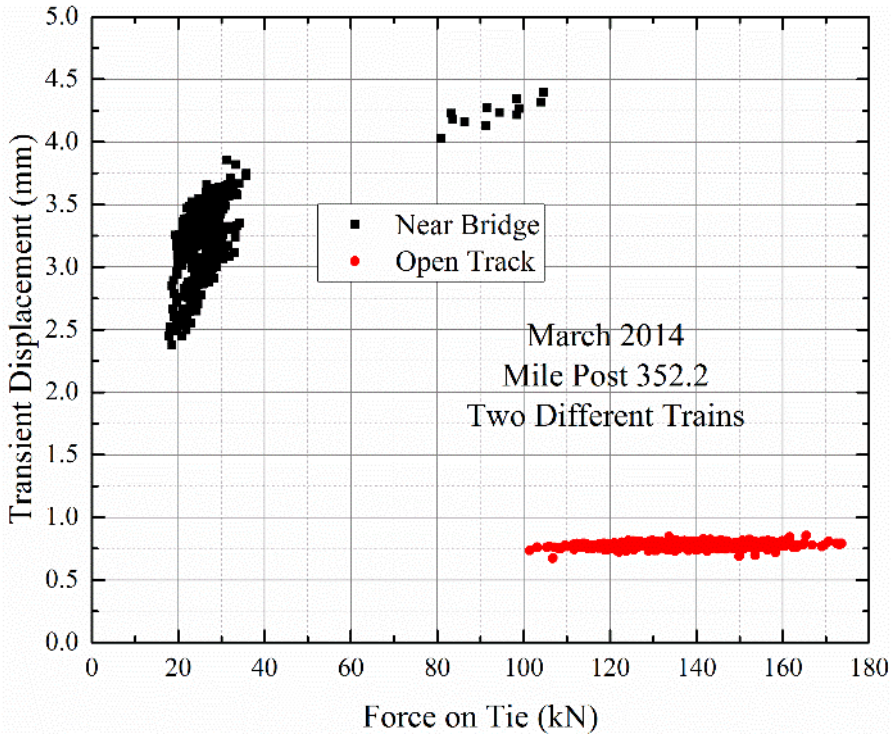

Figure A-1-62: Bridge 352:2 – March 2014 – Layer 1 Comparison

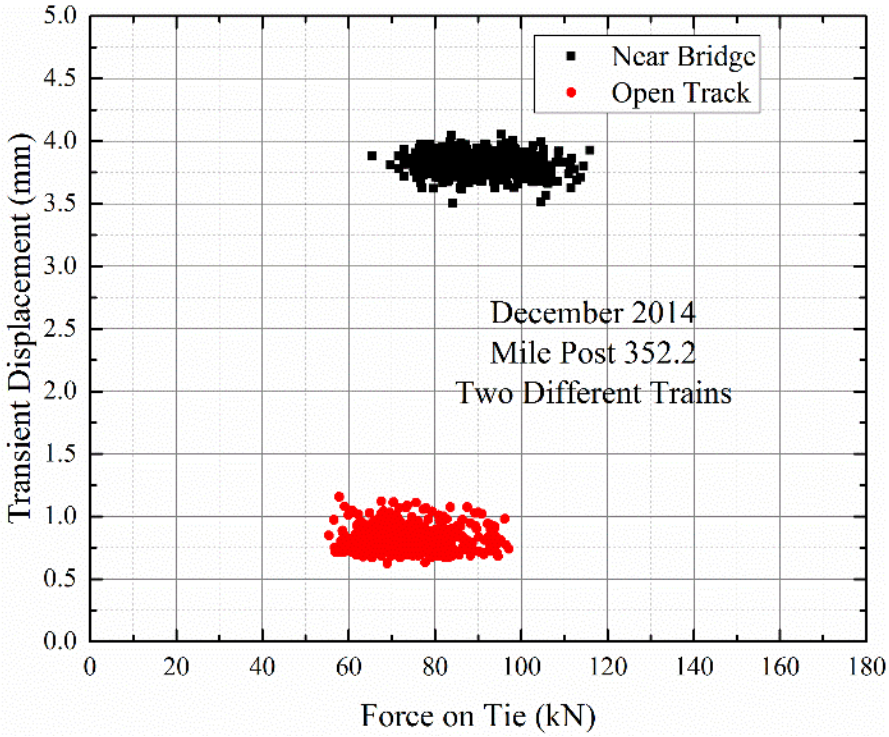

Figure A-1-63: Bridge 352:2 – December 2014 – Layer 1 Comparison

Norfolk Southern (NS) Mile Post 352:8 Load and Time Histories

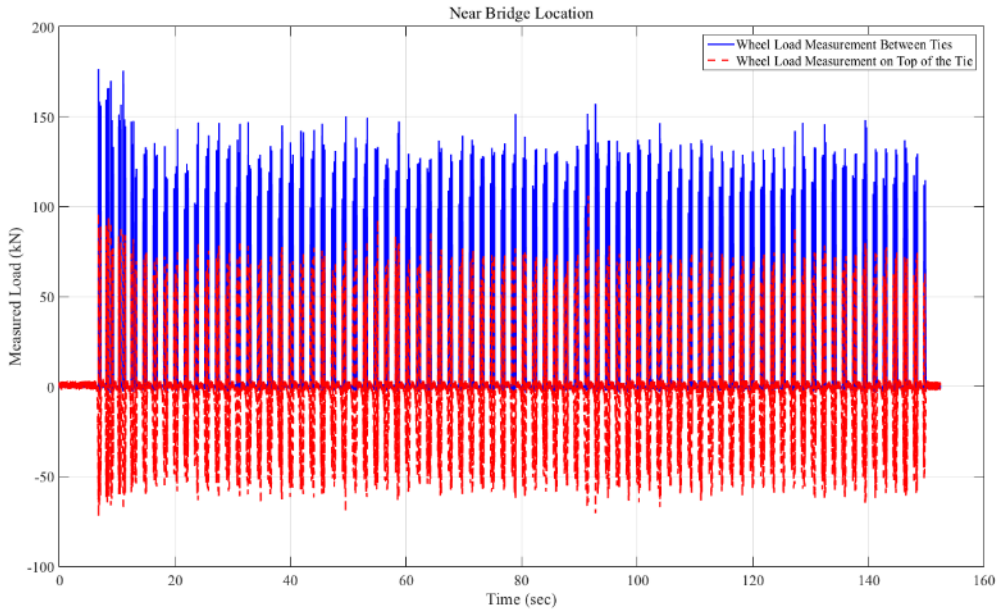

Figure A-1-64: Load Time History Recorded at the Bridge 352:8 – March 2014 – Near Bridge Location

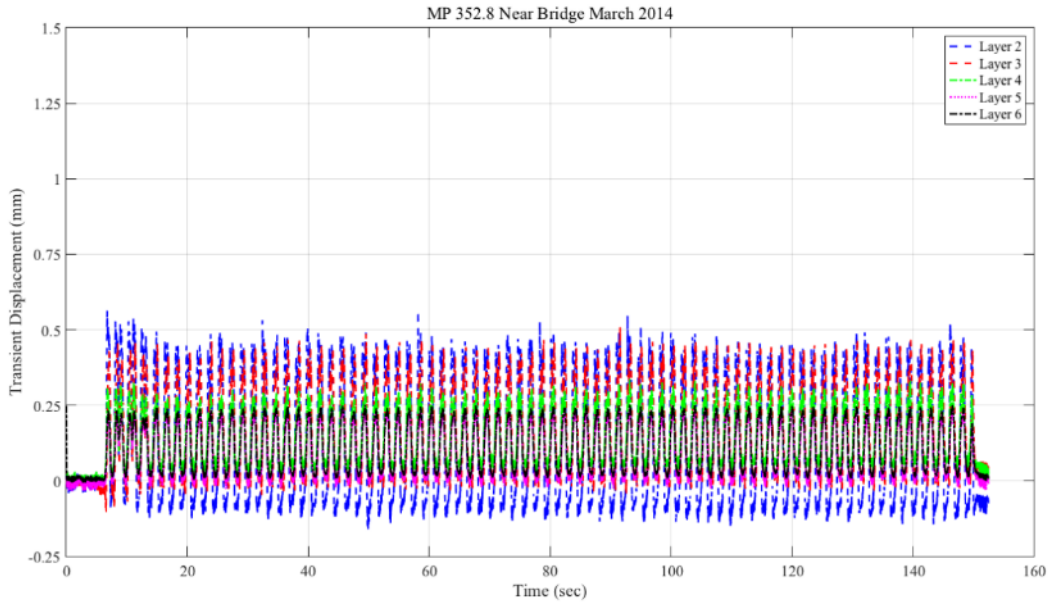

Figure A-1-65: Bridge 352:8 – March 2014 – Near Bridge Location

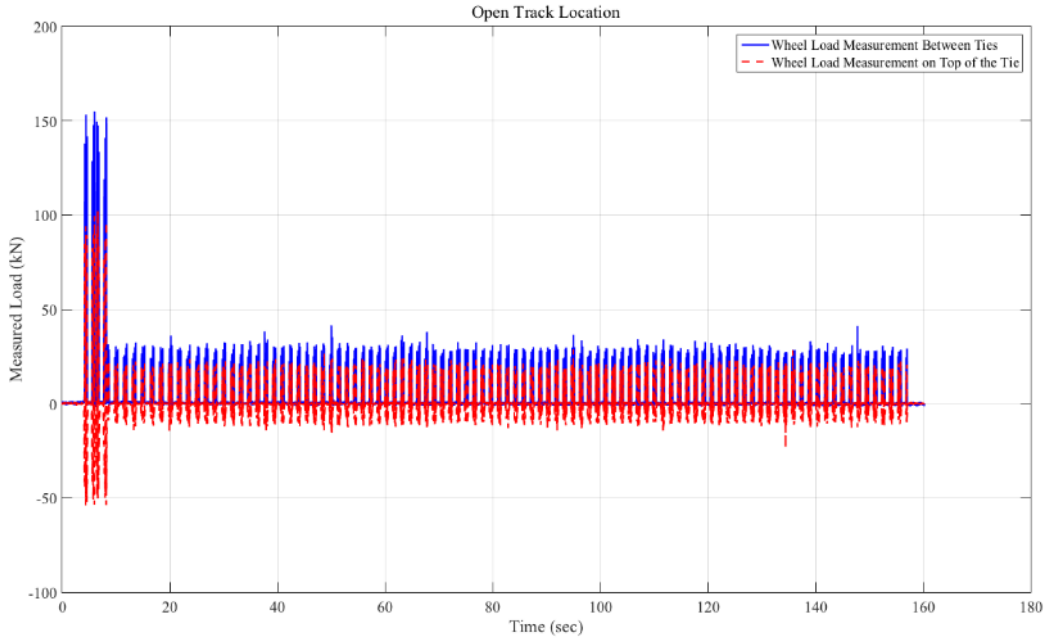

Figure A-1-66: Load Time History Recorded at the Bridge 352:8 – March 2014 – Open Track Location – Train # 1

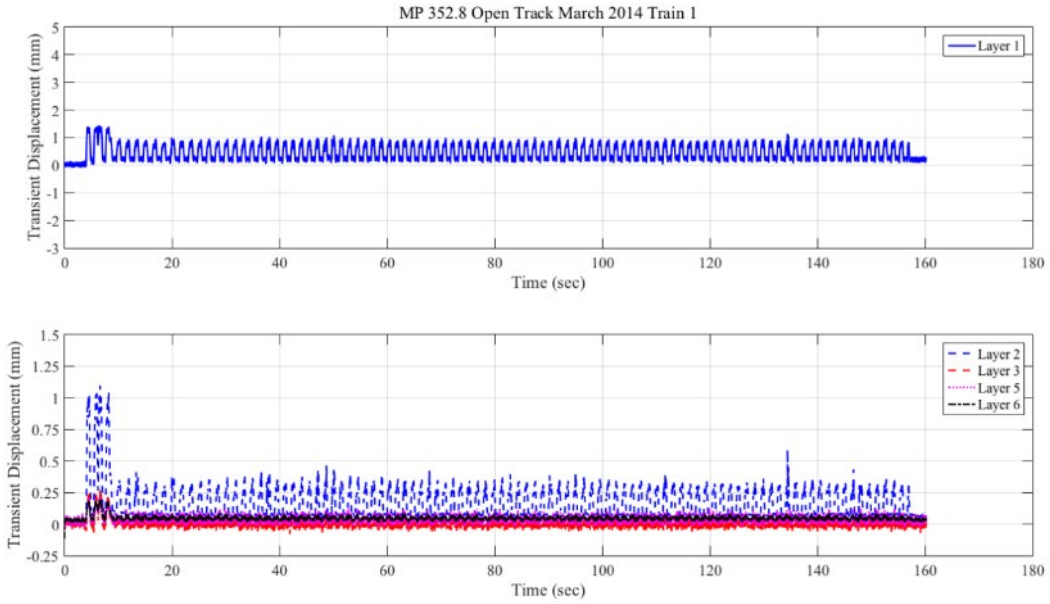

Figure A-1-67: Bridge 352:8 – March 2014 – Open Track Location – Train # 1

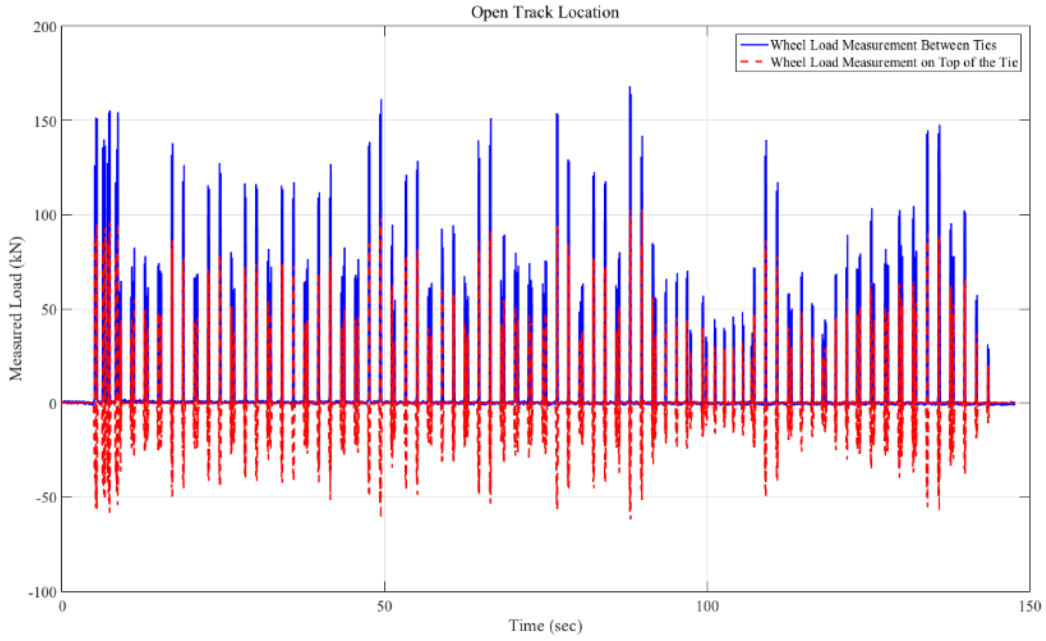

Figure A-1-68: Load Time History Recorded at the Bridge 352:8 – March 2014 – Open Track Location – Train # 2

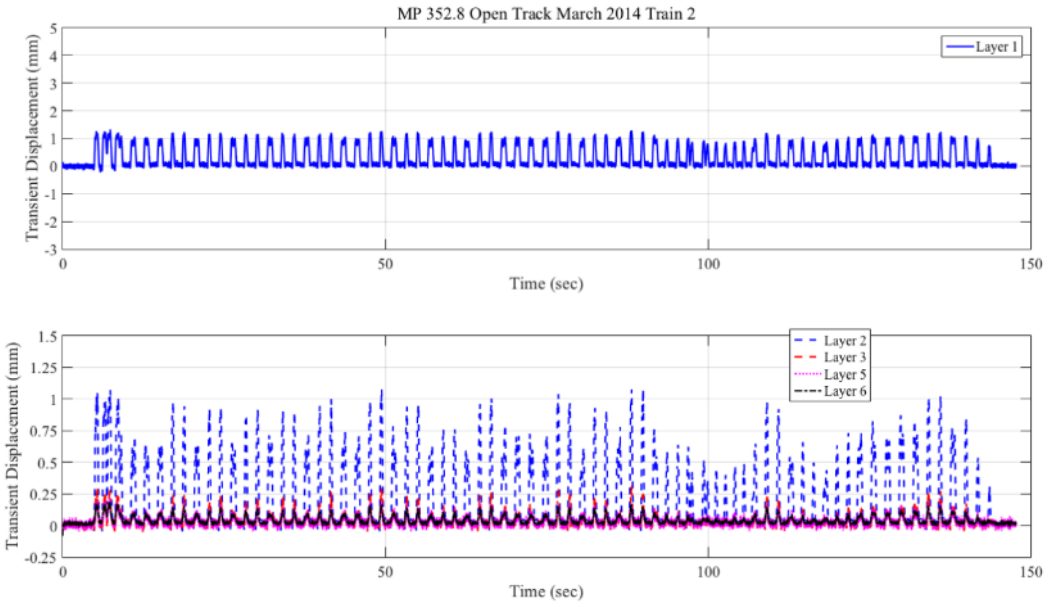

Figure A-1-69: Bridge 352:8 - March 2014 – Open Track Location – Train # 2

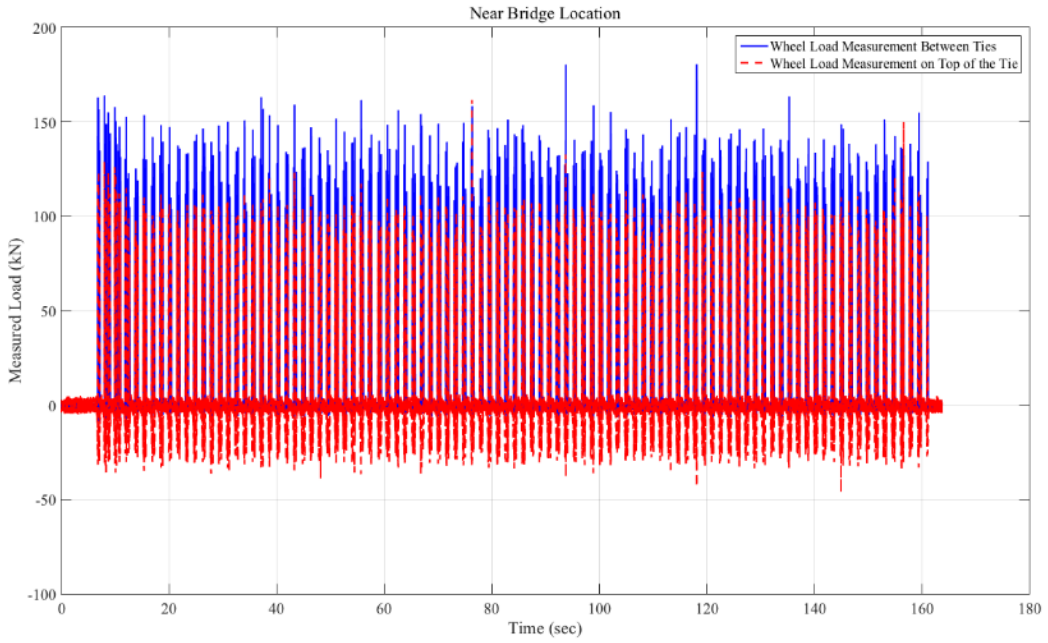

Figure A-1-70: Load Time History Recorded at the Bridge 352:8 – December 2014 – Near Bridge Location

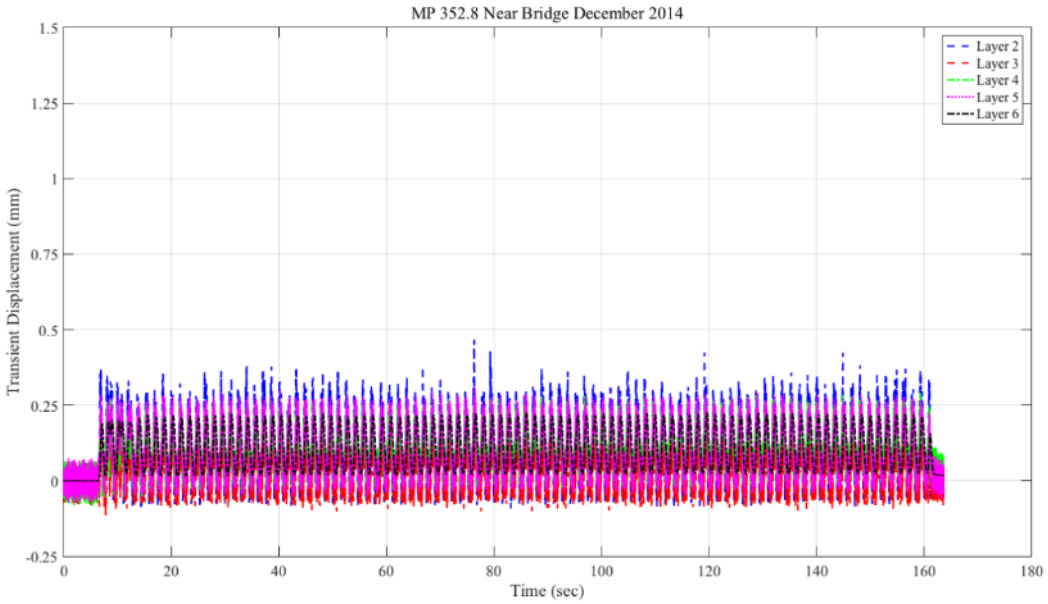

Figure A-1-71: Bridge 352:8 – December 2014 – Near Bridge Location

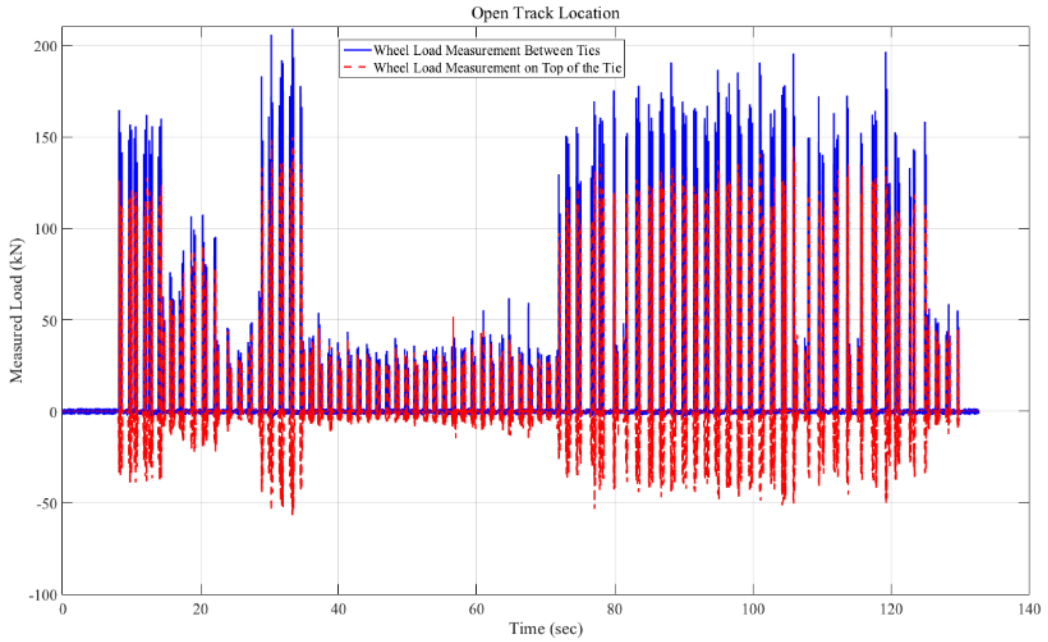

Figure A-1-72: Load Time History Recorded at the Bridge 352:8 – December 2014 – Open Track Location

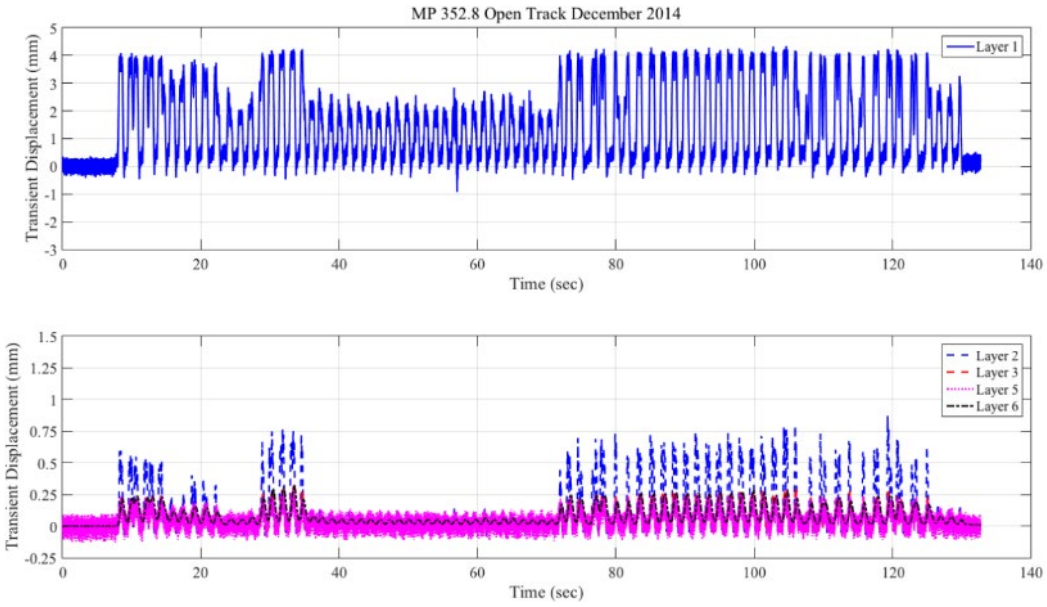

Figure A-1-73: Bridge 352:8 – December 2014 – Open Track Location

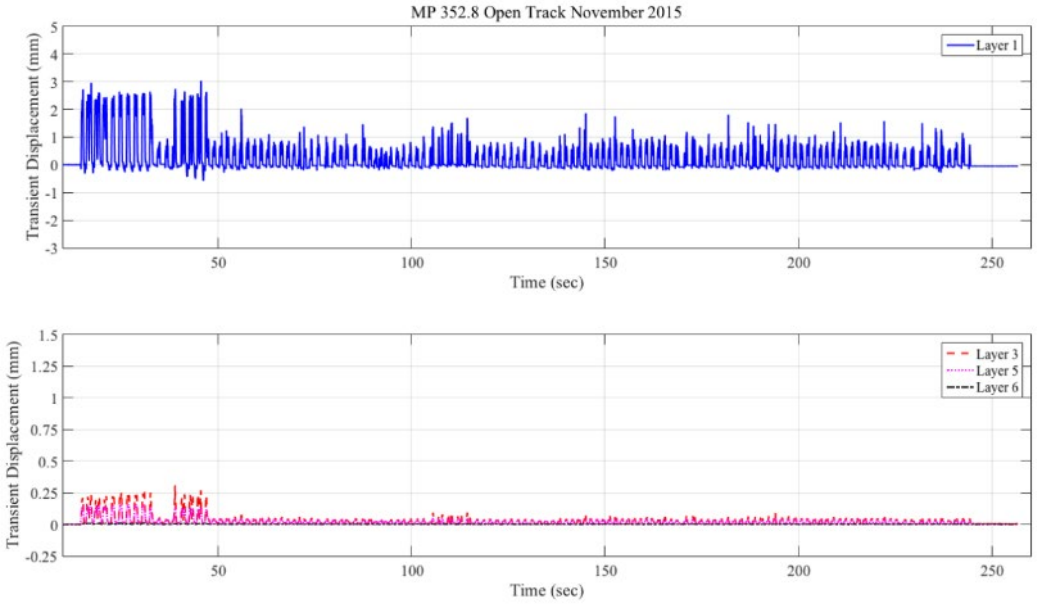

Figure A-1-74: Bridge 352:8 – November 2015 – Open Track Location – (Note LVDT 2 and 4 were broken)

Appendix A-2: Advanced Analyses of Field Instrumentation Data

Madison Street Bridge Vertical Accelerations in Time and Frequency Domain

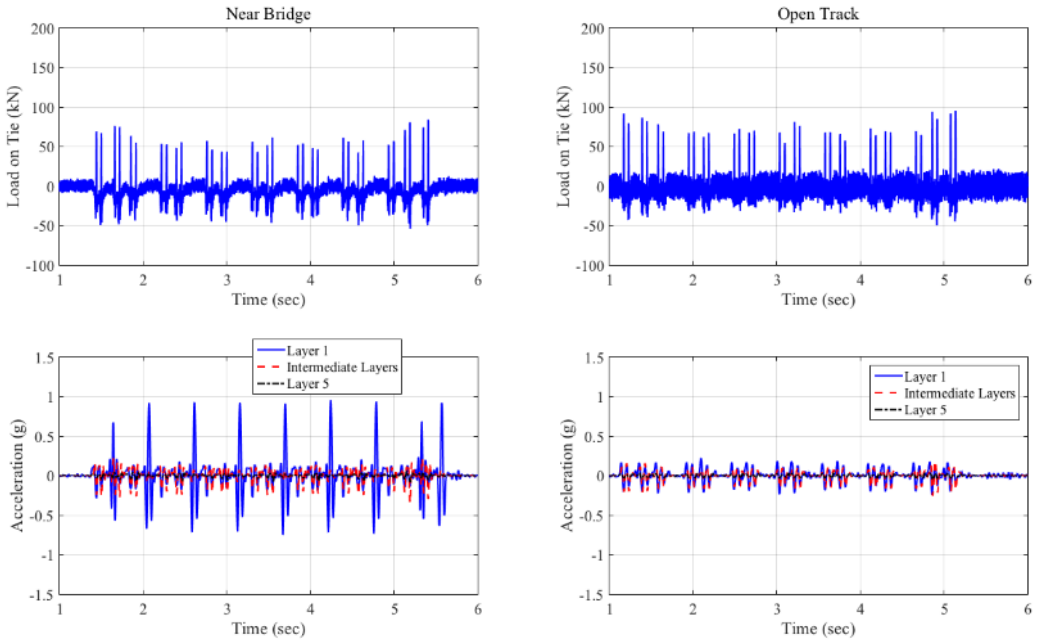

Figure A-2-1: November 2012 ACELA Train Measurement

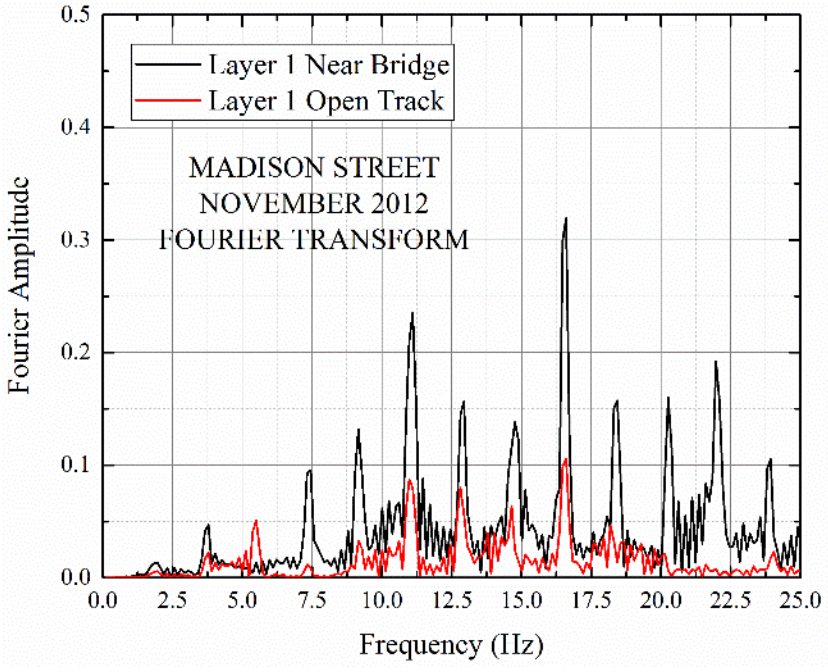

Figure A-2-2: November 2012 ACELA Train Measurement

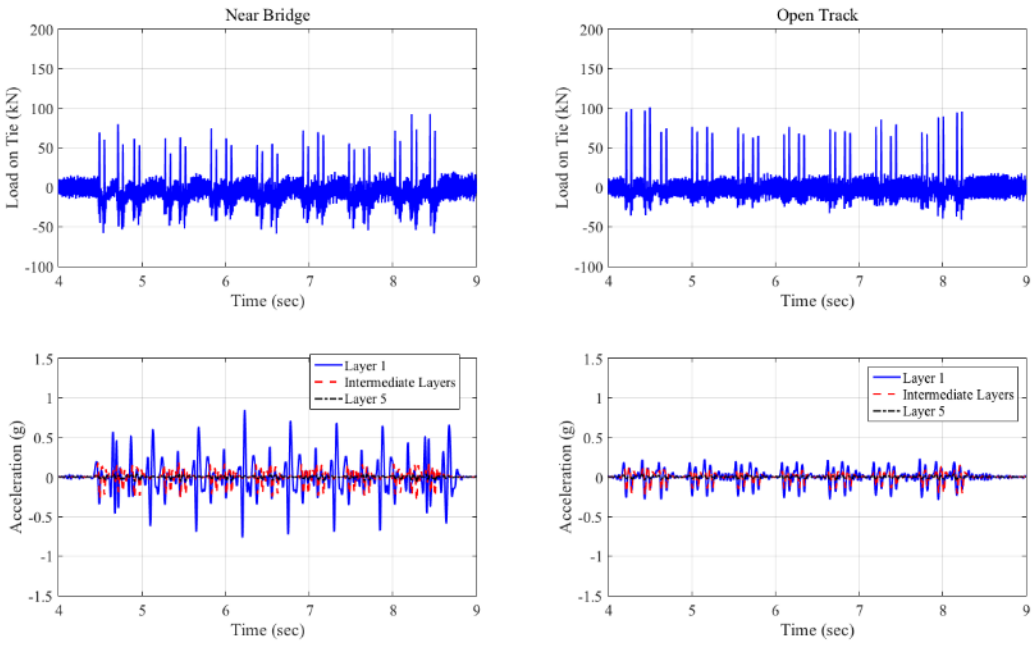

Figure A-2-3: January 2013 ACELA Train Measurement

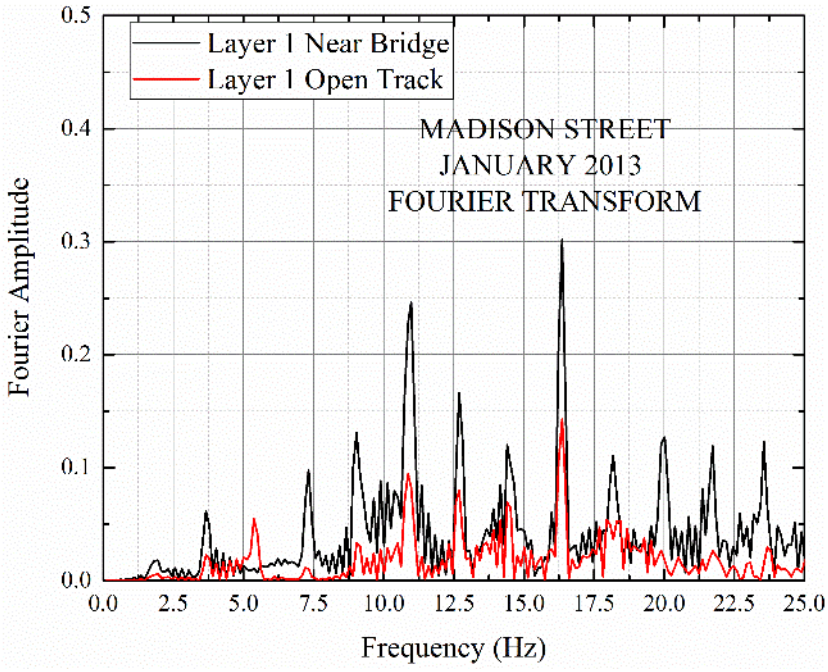

Figure A-2-4: January 2013 ACELA Train Measurement Fourier Transform

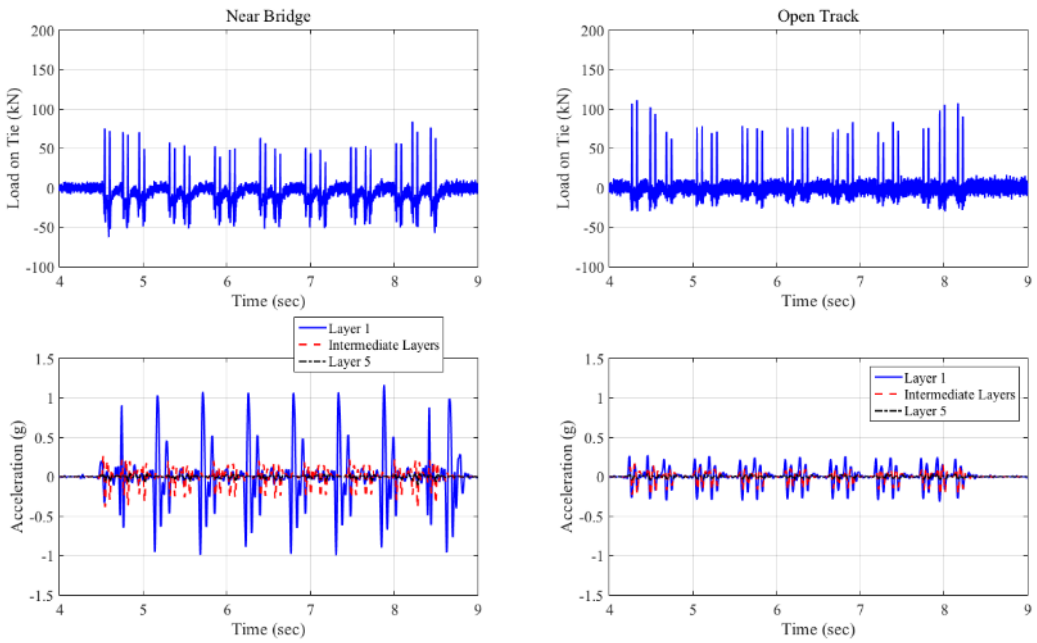

Figure A-2-5: June 2013 ACELA Train Measurement

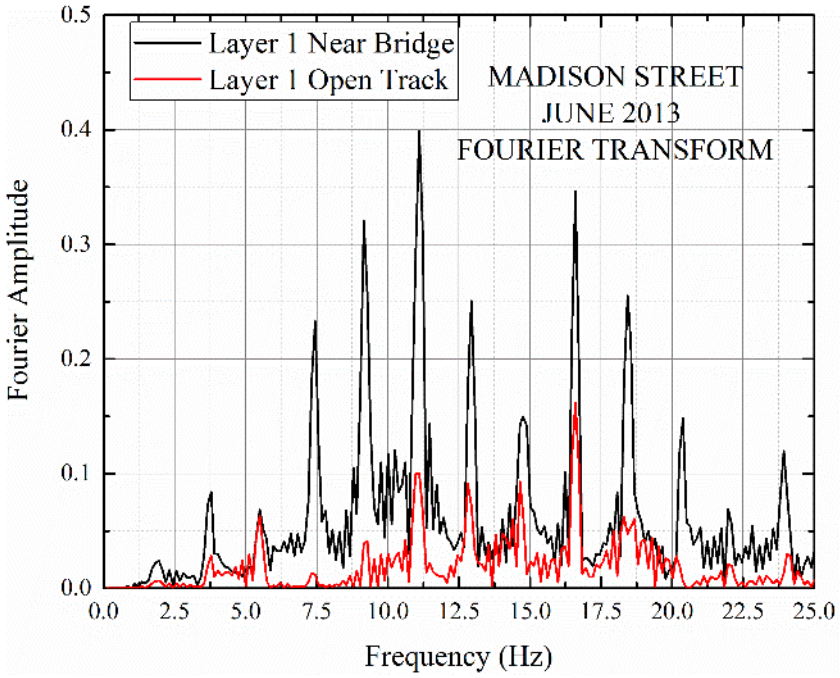

Figure A-2-6: June 2013 ACELA Train Measurement

Upland Street Bridge Vertical Accelerations in Time and Frequency Domain

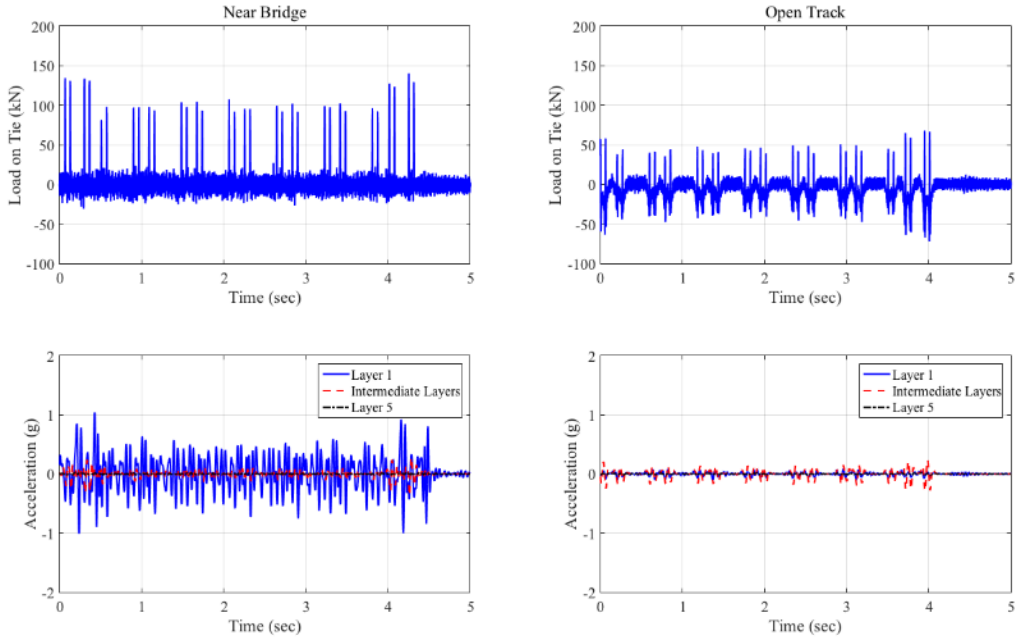

Figure A-2-7: November 2012 ACELA Train Measurement

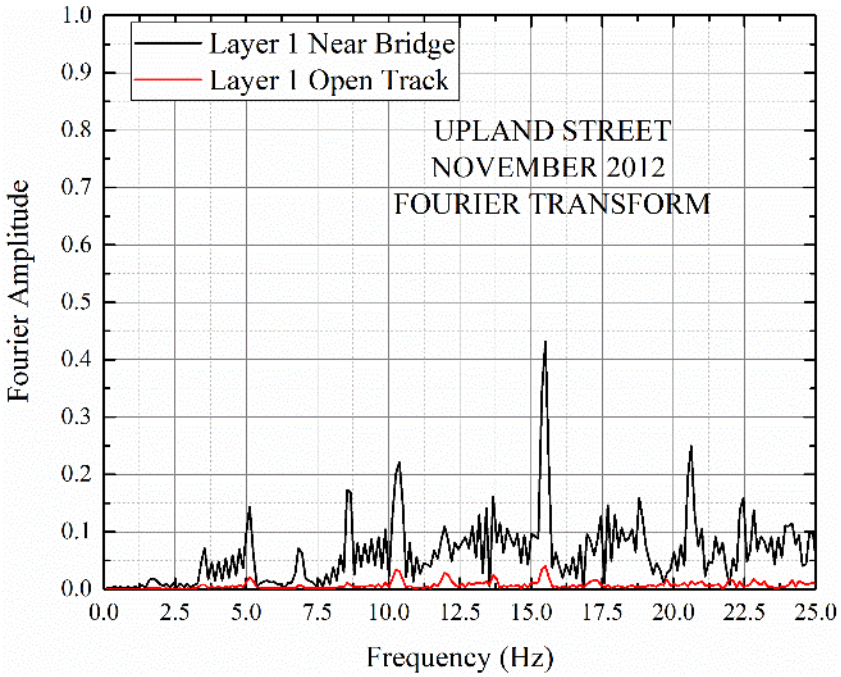

Figure A-2-8: November 2012 ACELA Train Measurement Fourier Transform

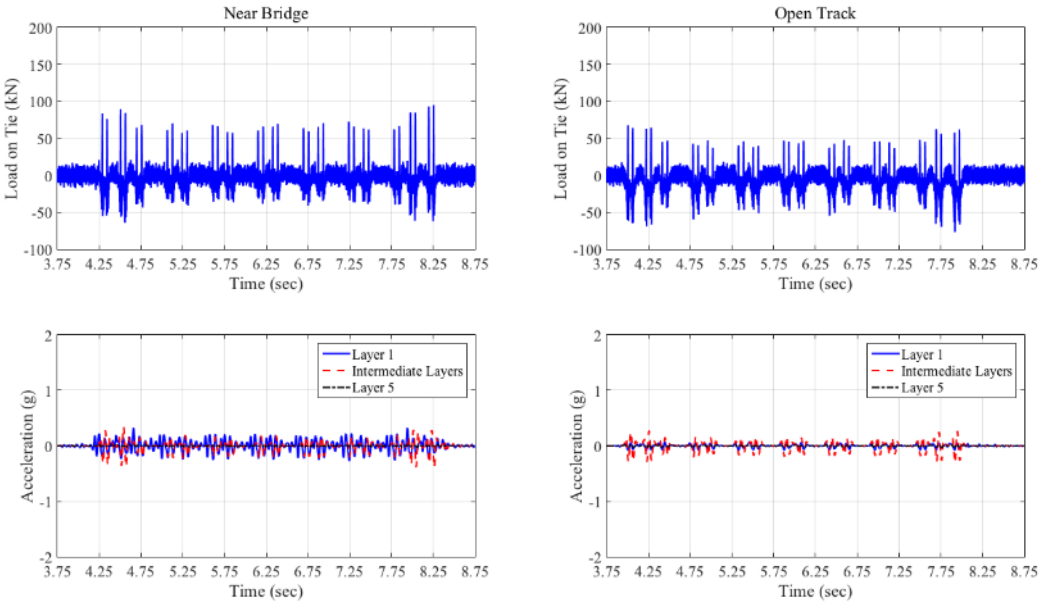

Figure A-2-9: January 2013 ACELA Train Measurement

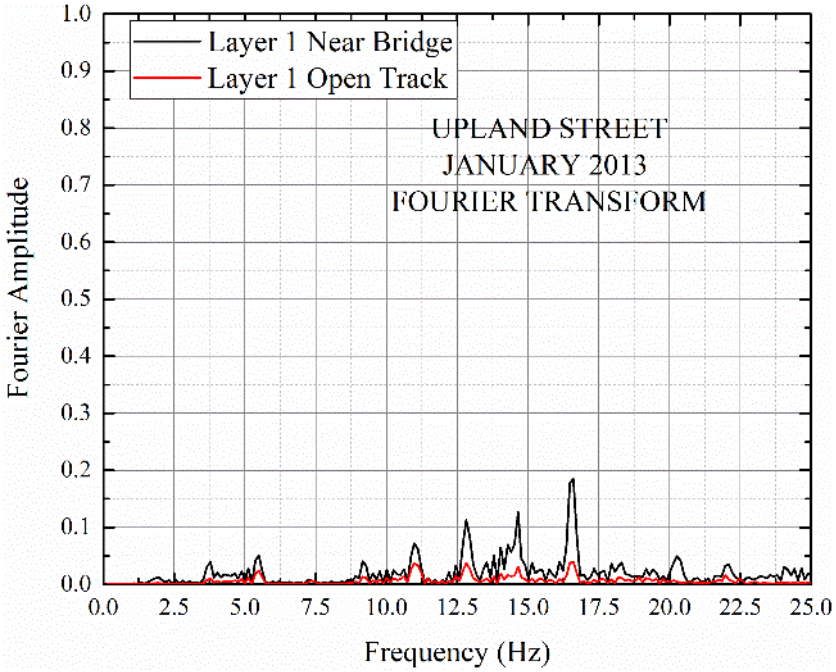

Figure A-2-10: January 2013 ACELA Train Measurement

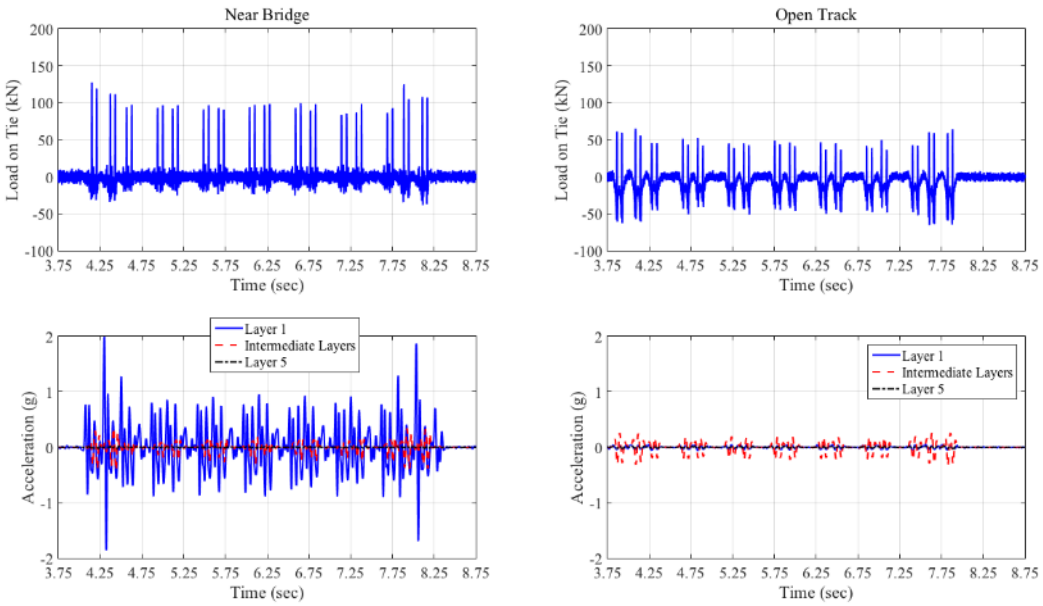

Figure A-2-11: June 2013 ACELA Train Measurement

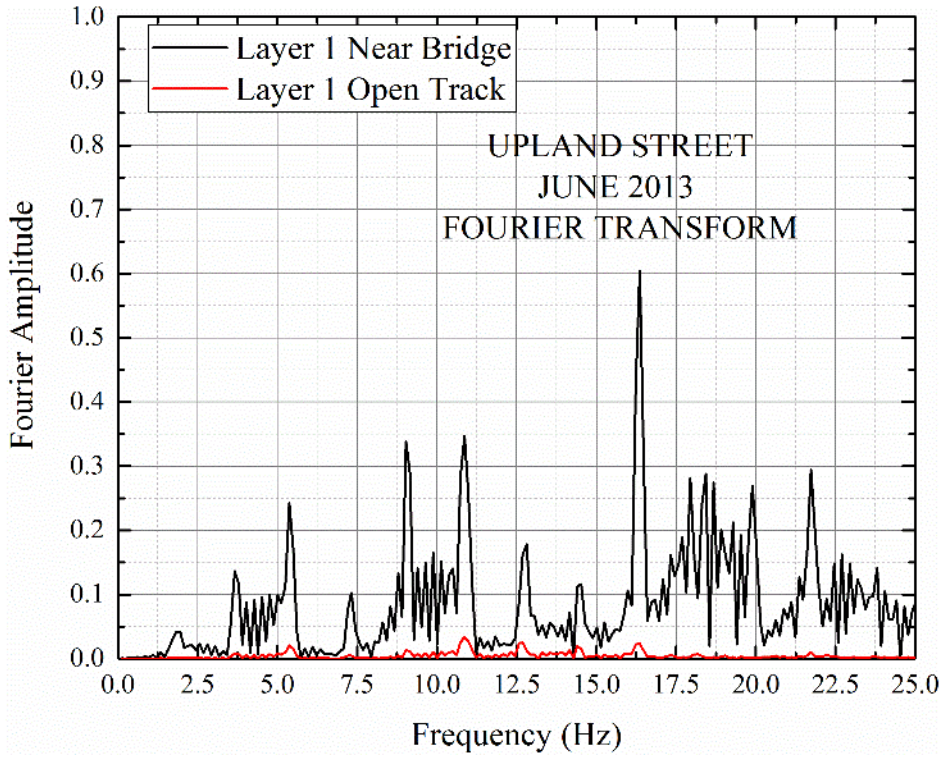

Figure A-2-12: June 2013 ACELA Train Measurement

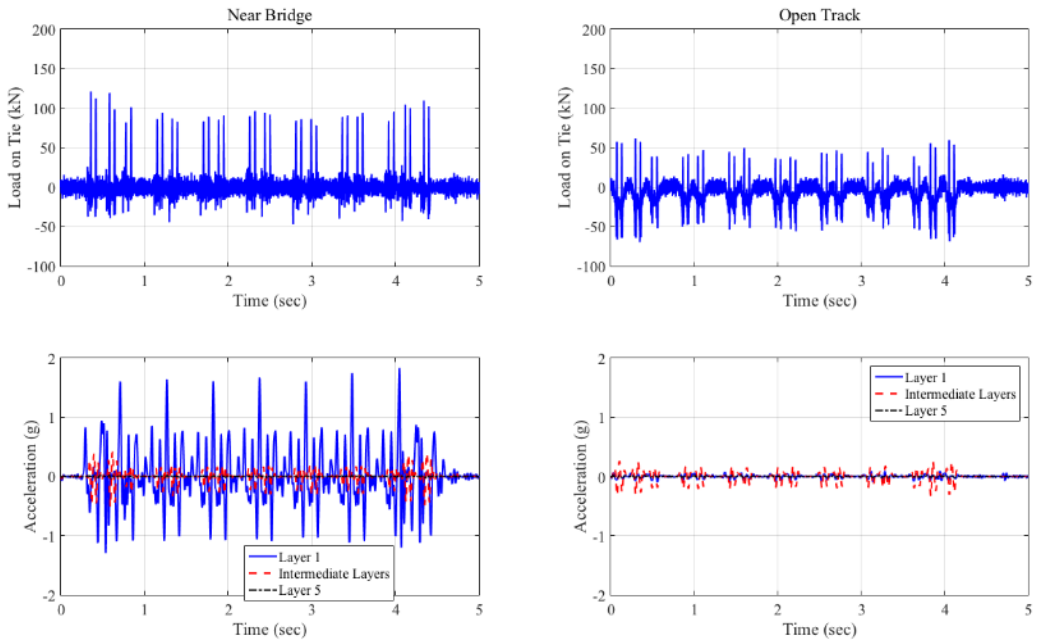

Figure A-2-13: July 1, 2014, ACELA Train Measurement

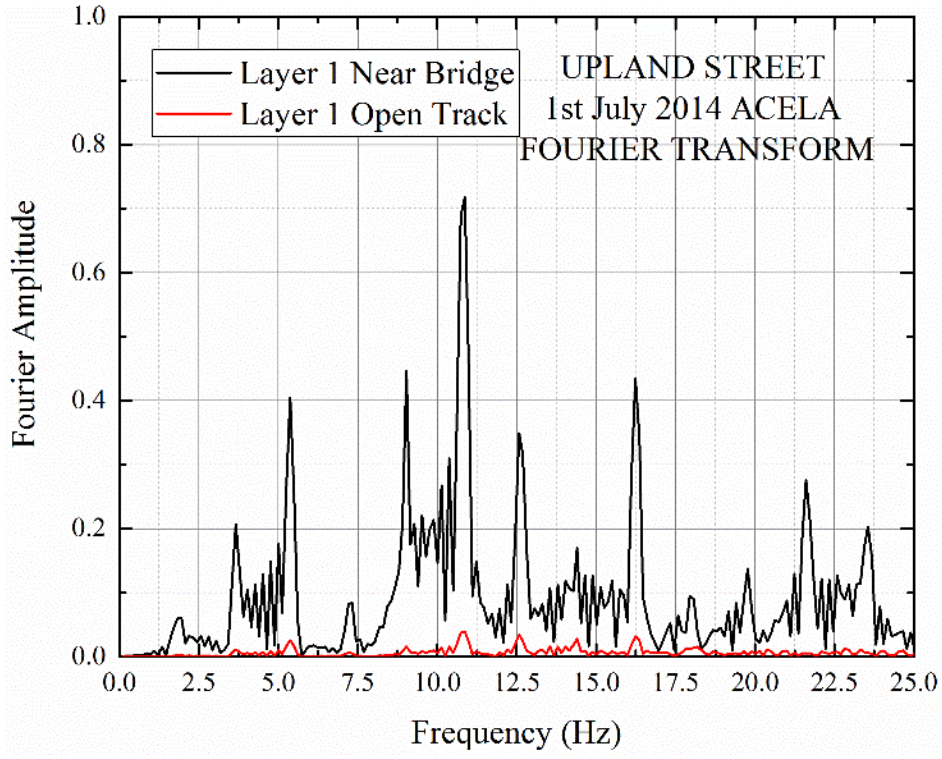

Figure A-2-14: July 1, 2014, ACELA Train Measurement

Caldwell Street Bridge Vertical Accelerations in Time and Frequency Domain

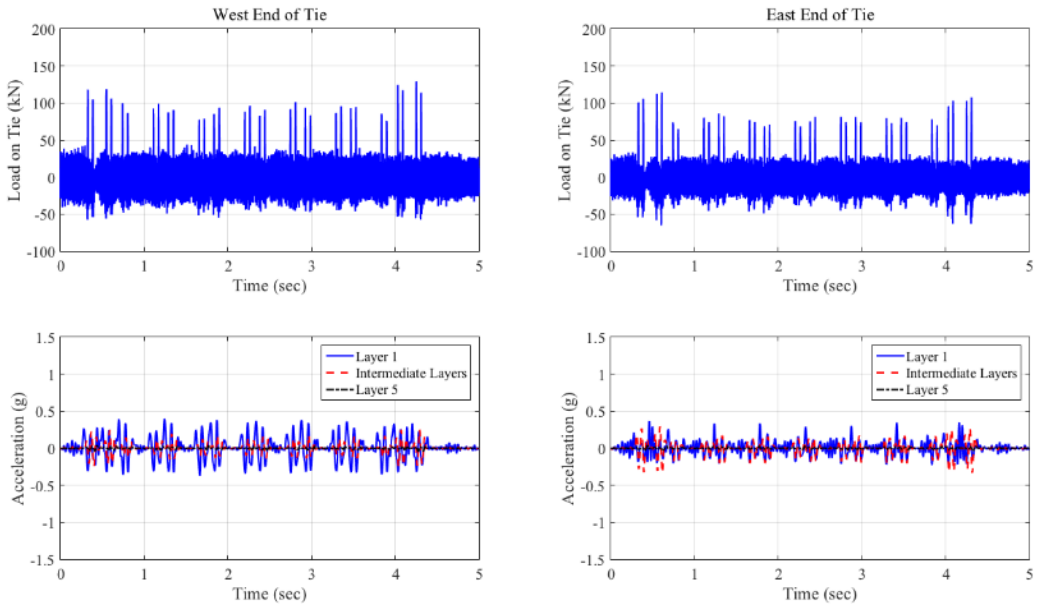

Figure A-2-15: August 2012 Train 2 ACELA Train Measurement

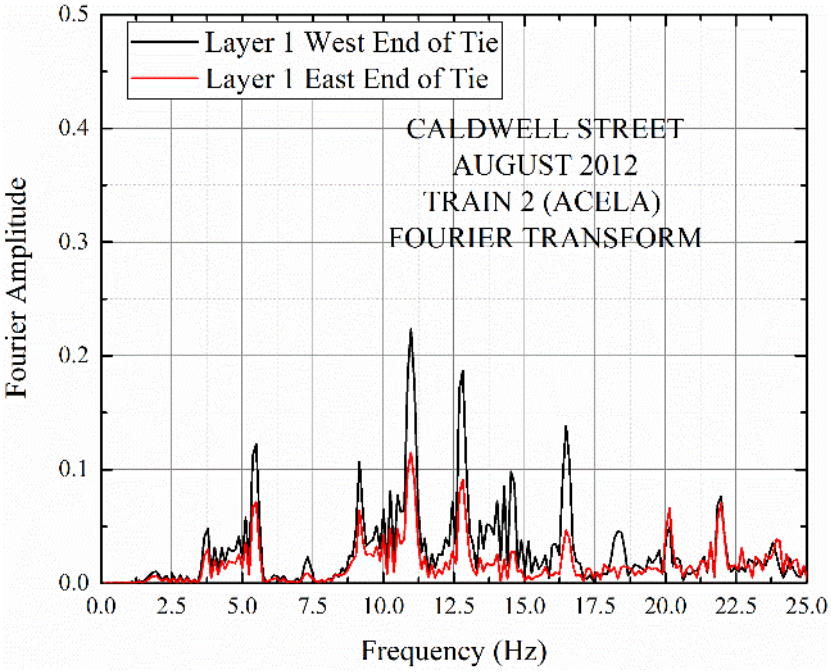

Figure A-2-16: Caldwell August 2012 ACELA Train # 2 Layer 1 Measurement Fast Fourier Transform

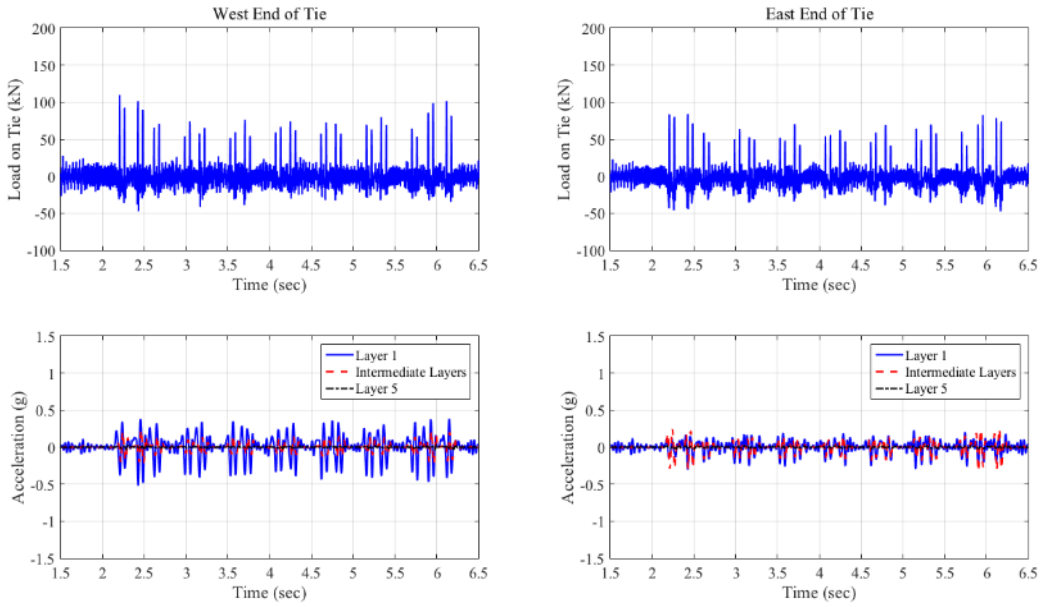

Figure A-2-17: November 2012 ACELA Train Measurement

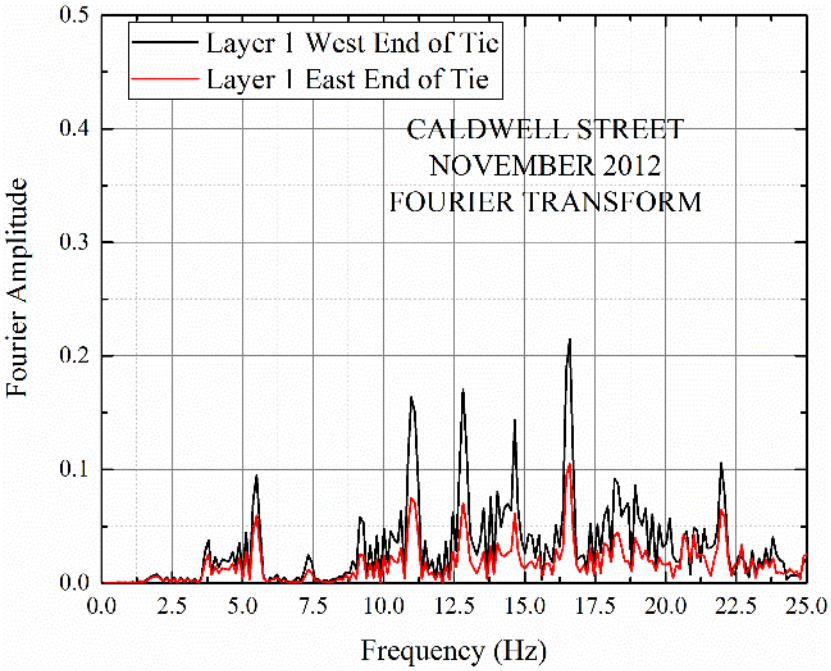

Figure A-2-18: November 2012 ACELA Train Measurement

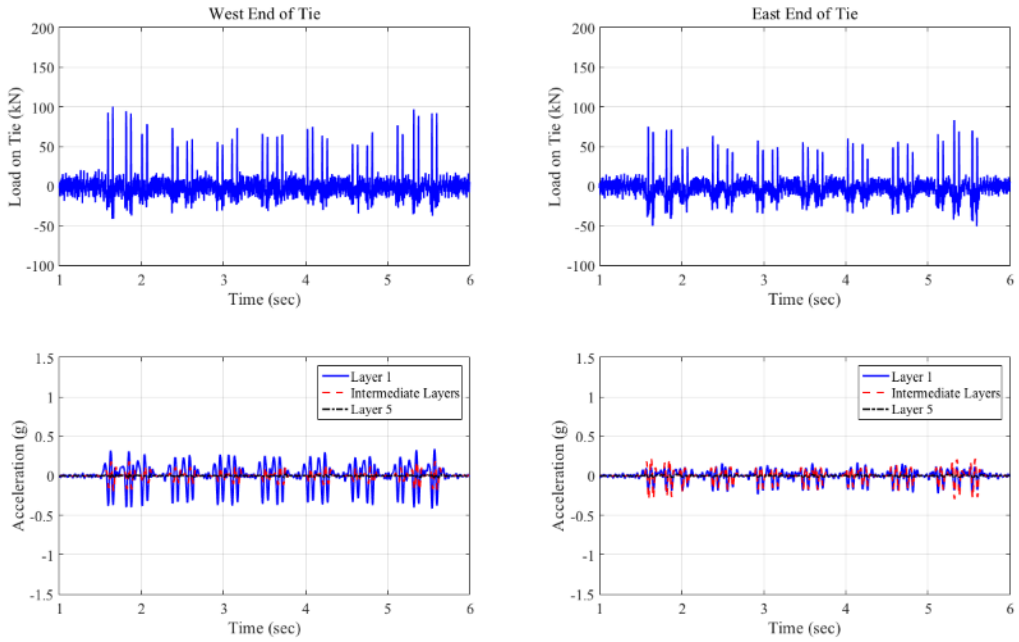

Figure A-2-19: January 2013 ACELA Train Measurement

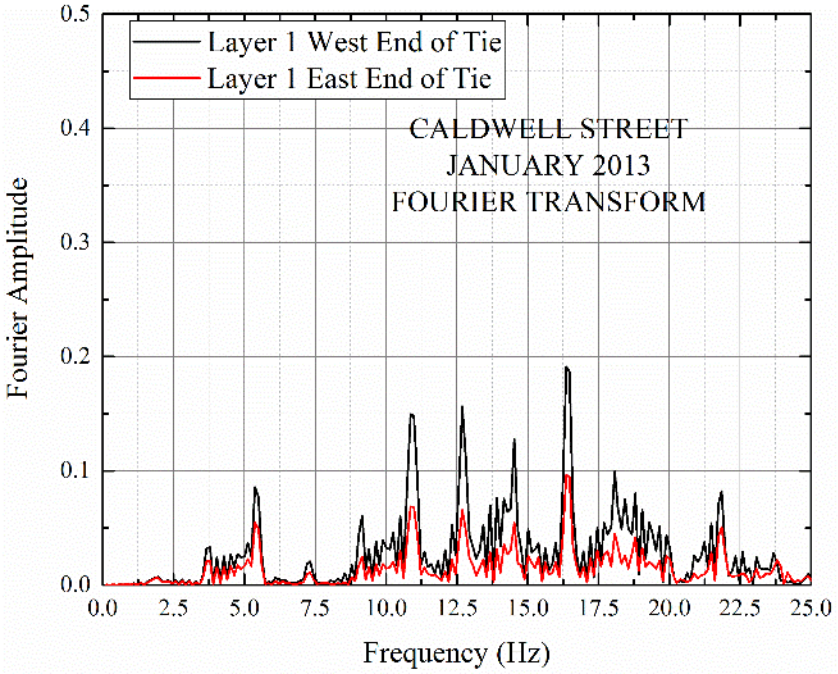

Figure A-2-20: January 2013 ACELA Train Measurement

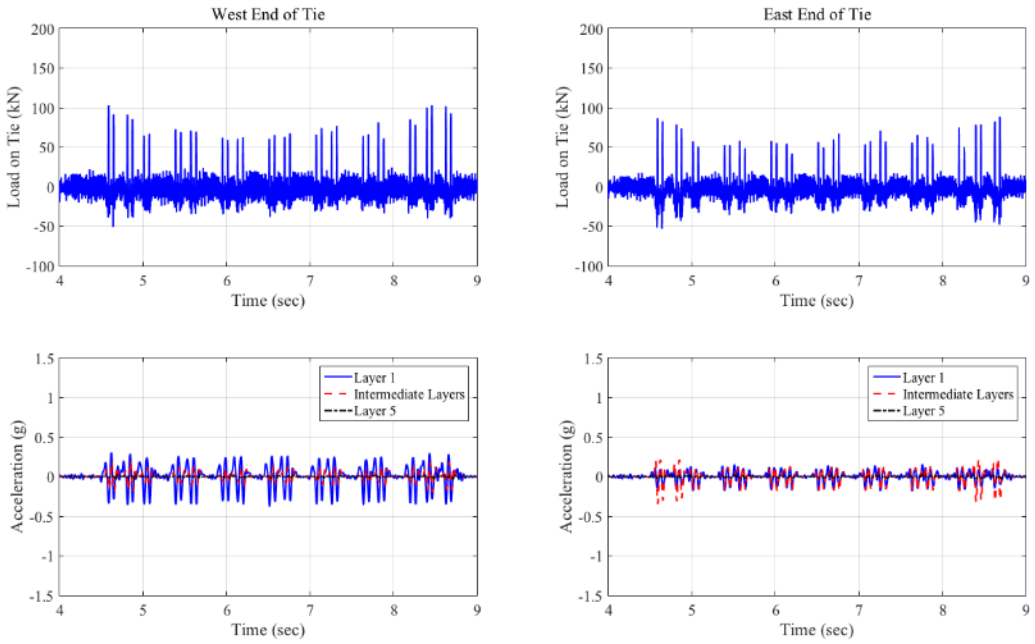

Figure A-2-21: June 2013 ACELA Train Measurement

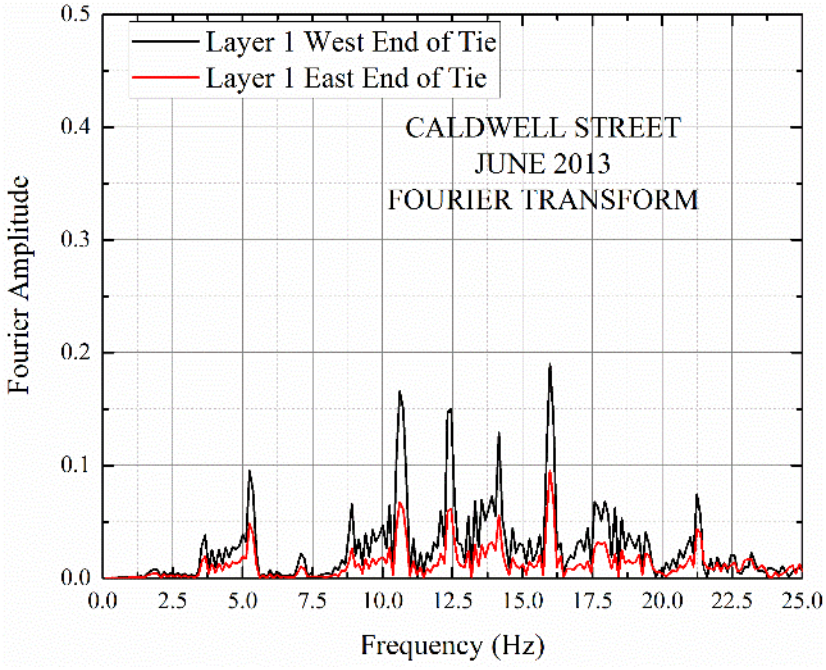

Figure A-2-22: June 2013 ACELA Train Measurement

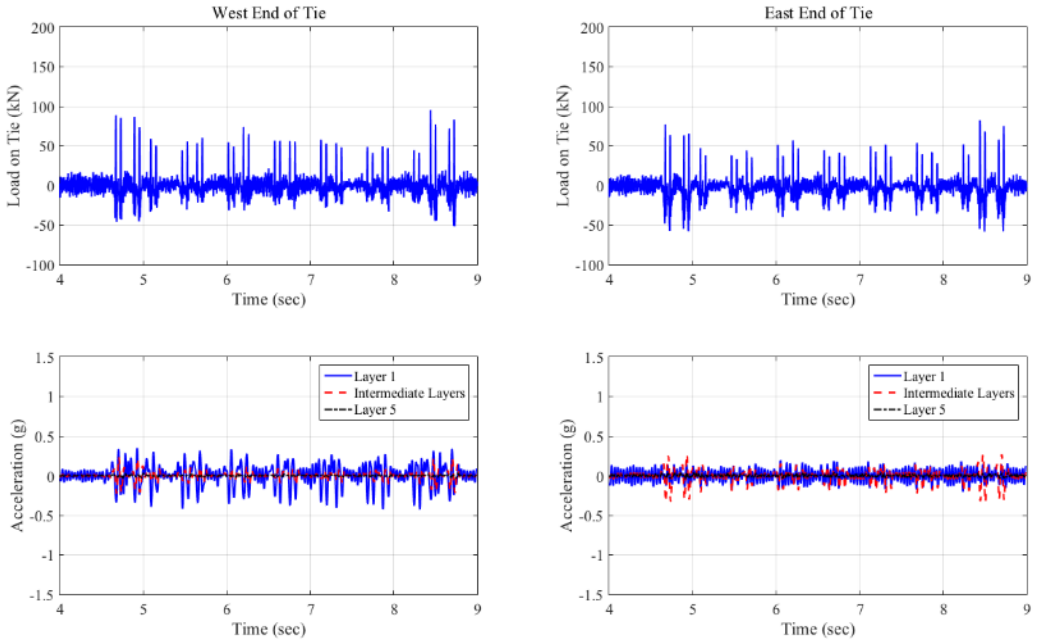

Figure A-2-23: May 2015 ACELA Train Measurement

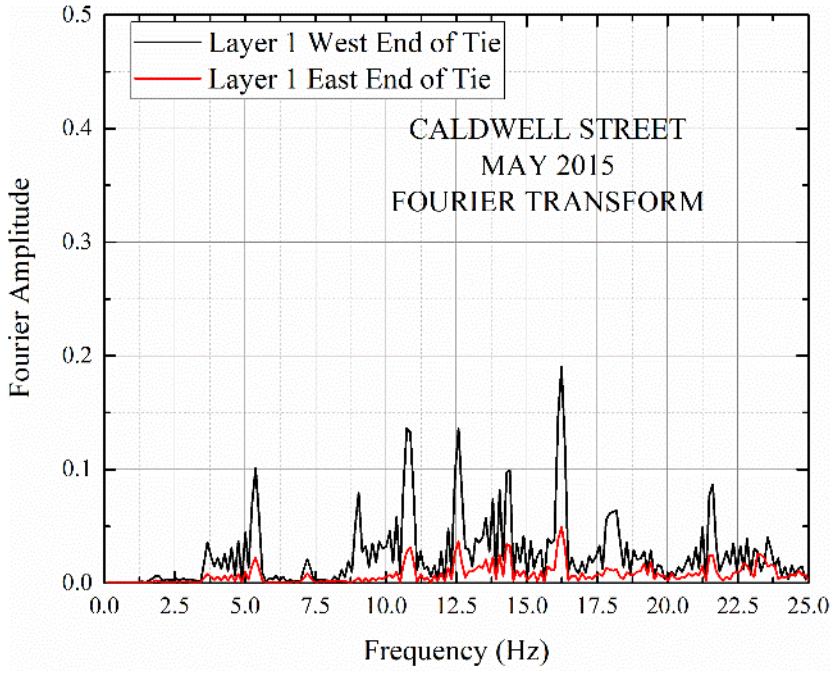

Figure A-2-24: May 2015 ACELA Train Measurement

Norfolk Southern North Line Approach Mile Post 352:2 Accelerations in Time and Frequency Domain

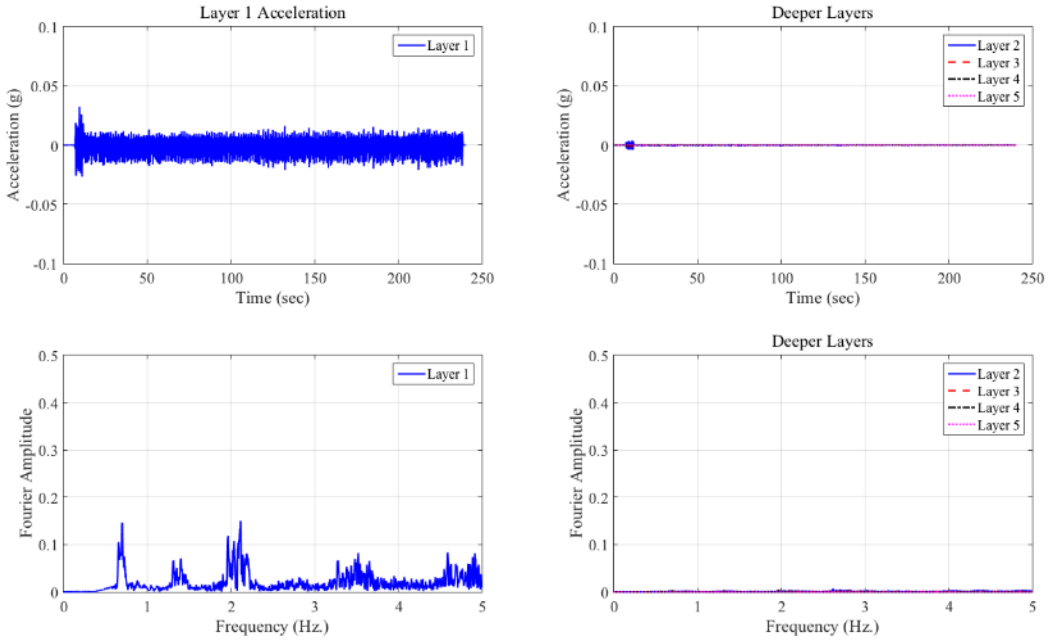

Figure A-2-25: March 2014 Near Bridge Accelerations

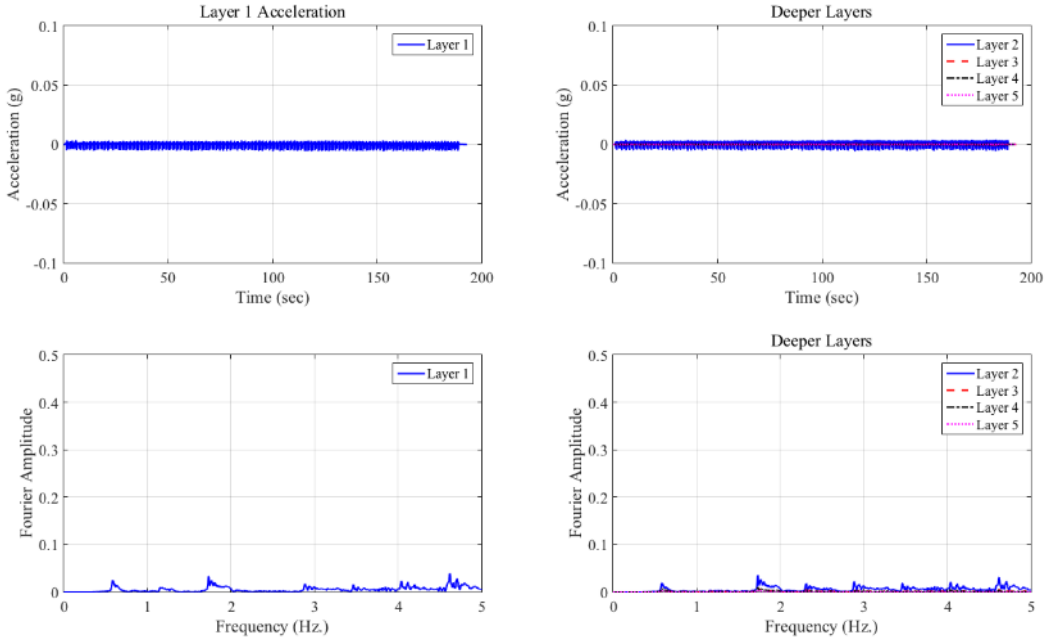

Figure A-2-26: March 2014 Open Track Accelerations

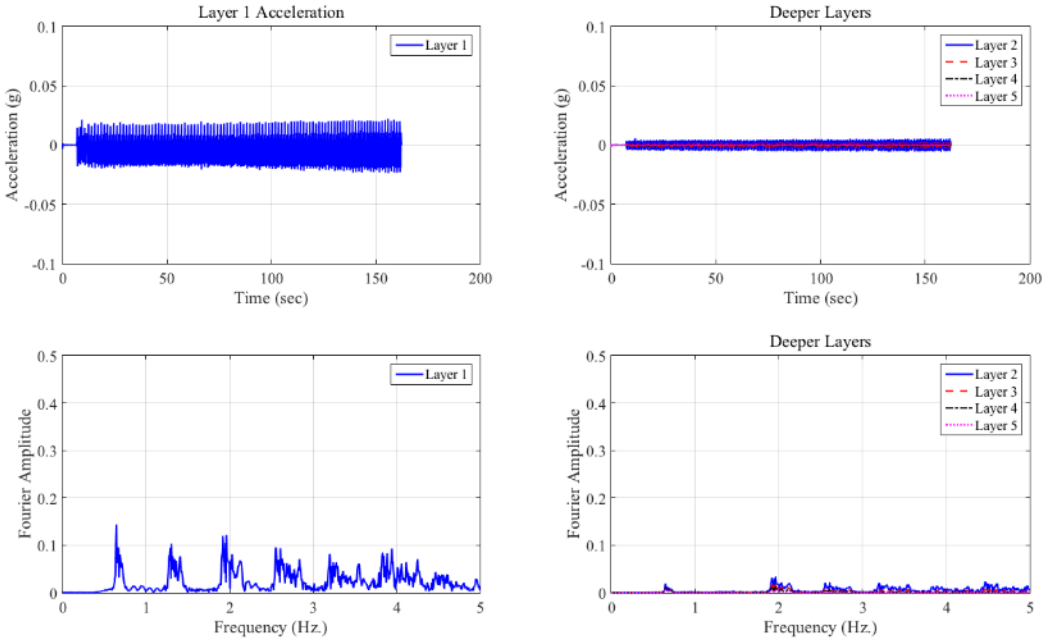

Figure A-2-27: December 2014 Near Bridge Accelerations

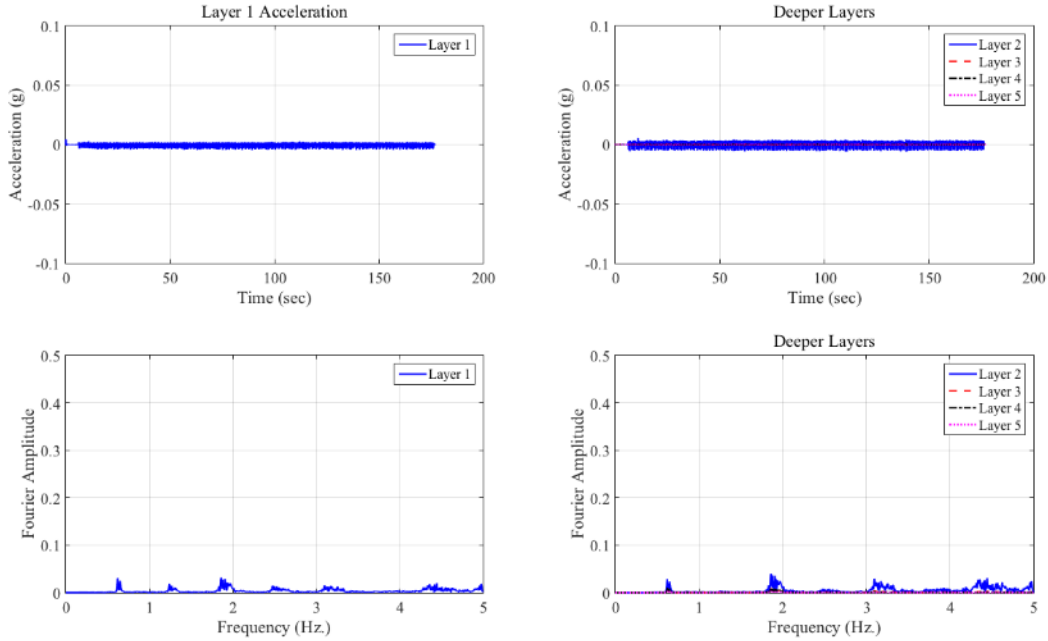

Figure A-2-28: December 2014 Open Track Accelerations

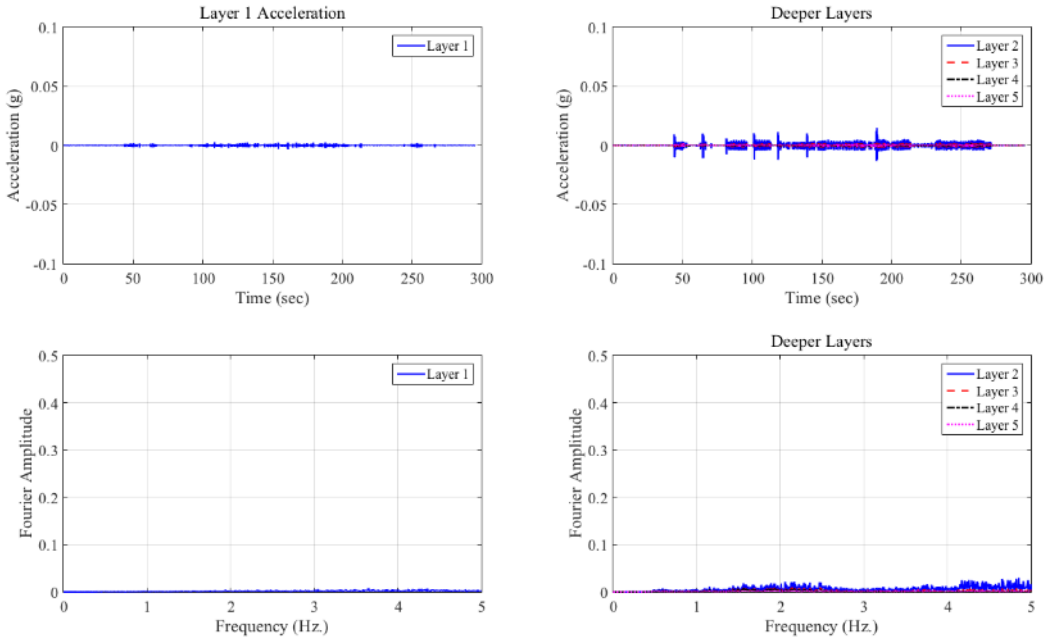

Figure A-2-29: November 2015 Near Bridge Accelerations

Norfolk Southern North Line Approach Mile Post 352:8 Accelerations in Time and Frequency Domain

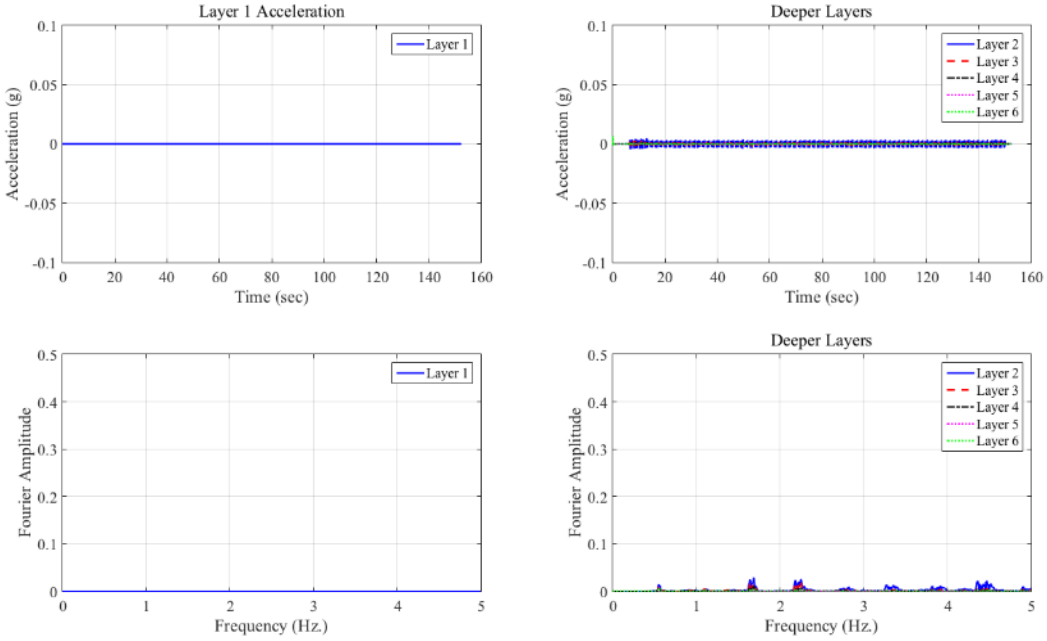

Figure A-2-30: March 2014 Near Bridge Accelerations

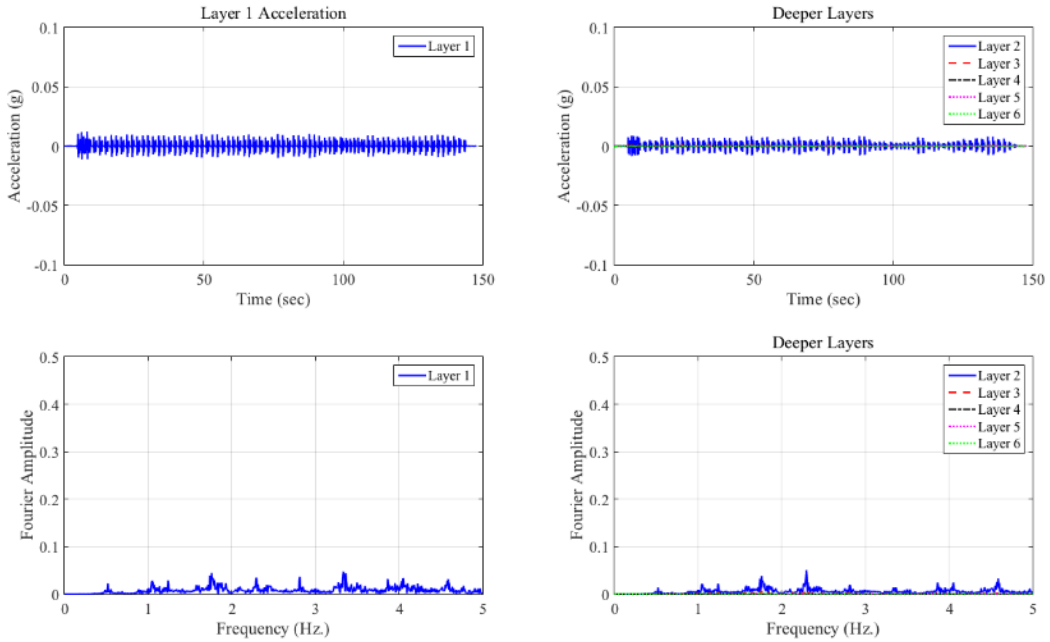

Figure A-2-31: March 2014 Open Track Train # 2 Accelerations

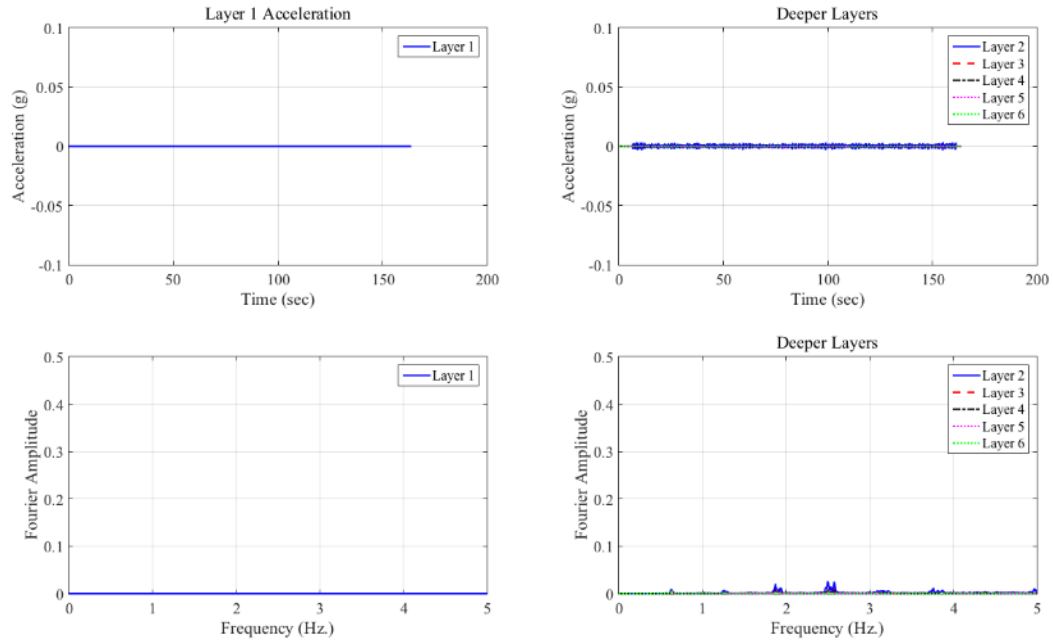

Figure A-2-32: December 2014 Near Bridge Accelerations

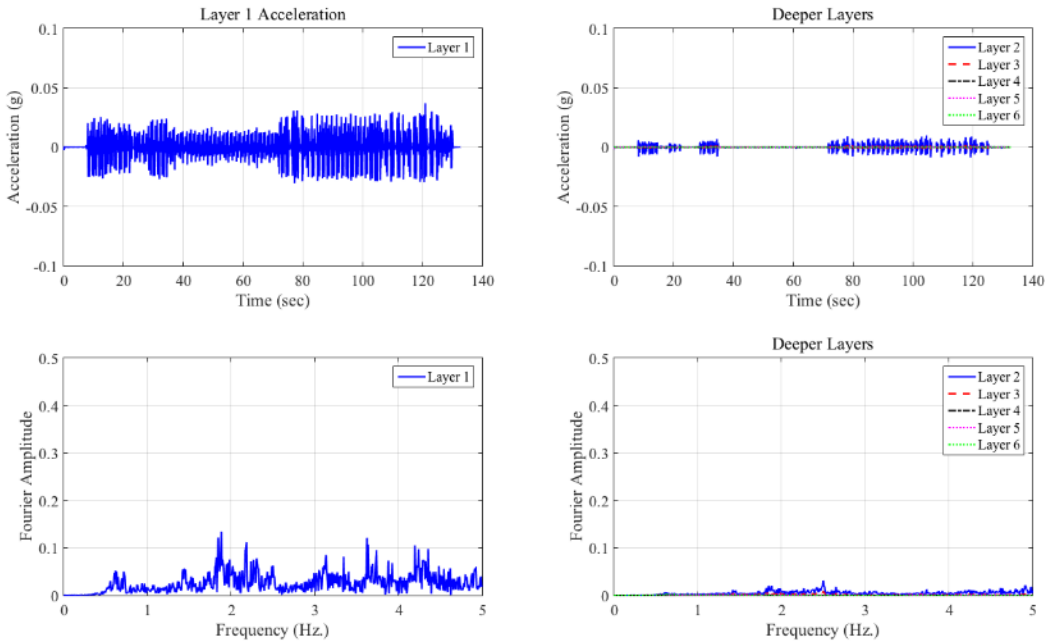

Figure A-2-33: December 2014 Open Track Accelerations

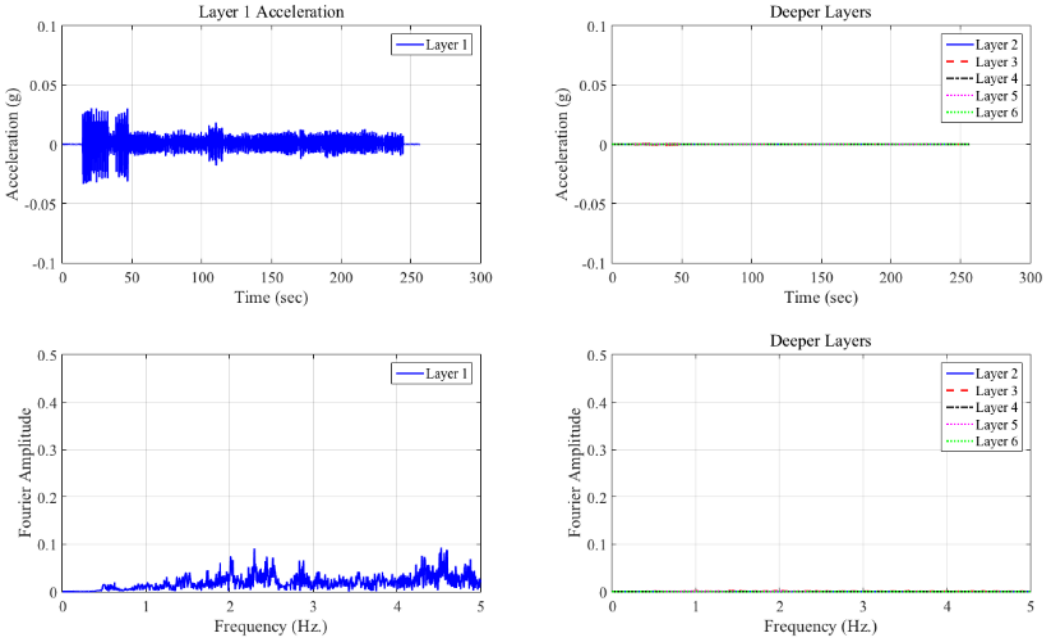

Figure A-2-34: November 2015 Open Track Accelerations

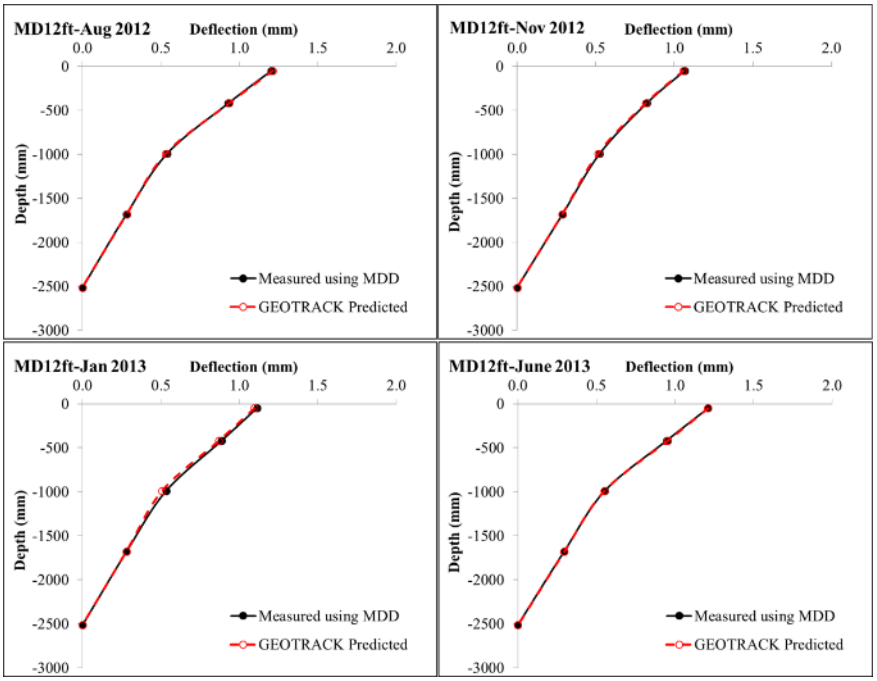

(a)

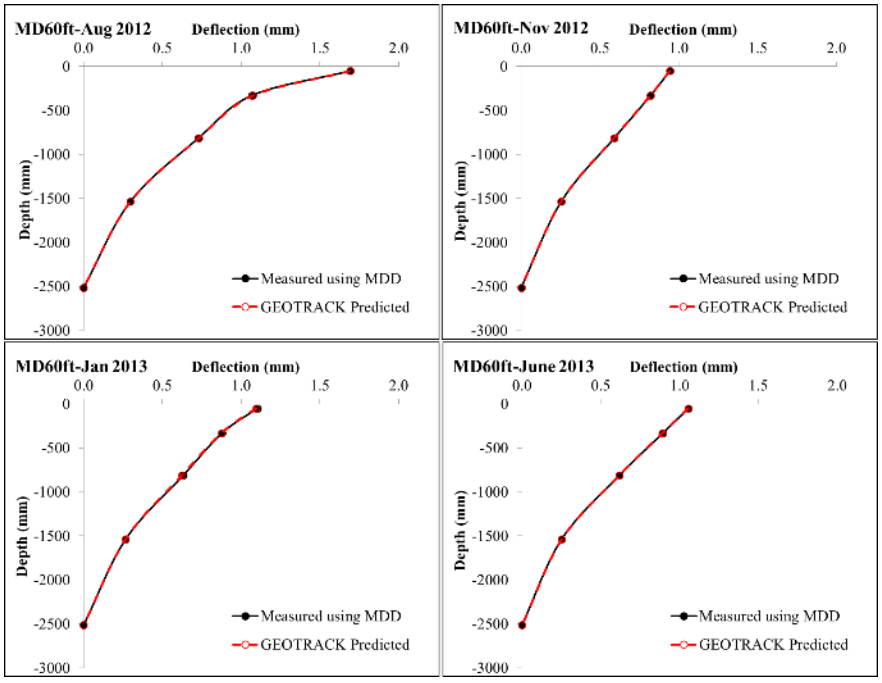

(b)

Figure A-2-35: Comparison of Calculated Deformation with Field Measured Data (a) Madison 12ft near bridge location (b) Madison 60ft open track location

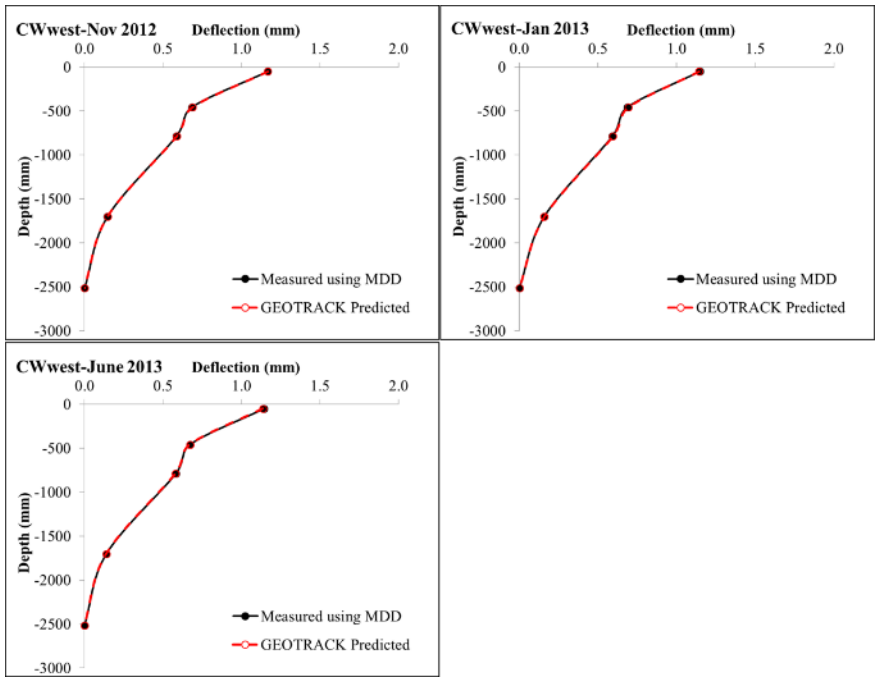

(a)

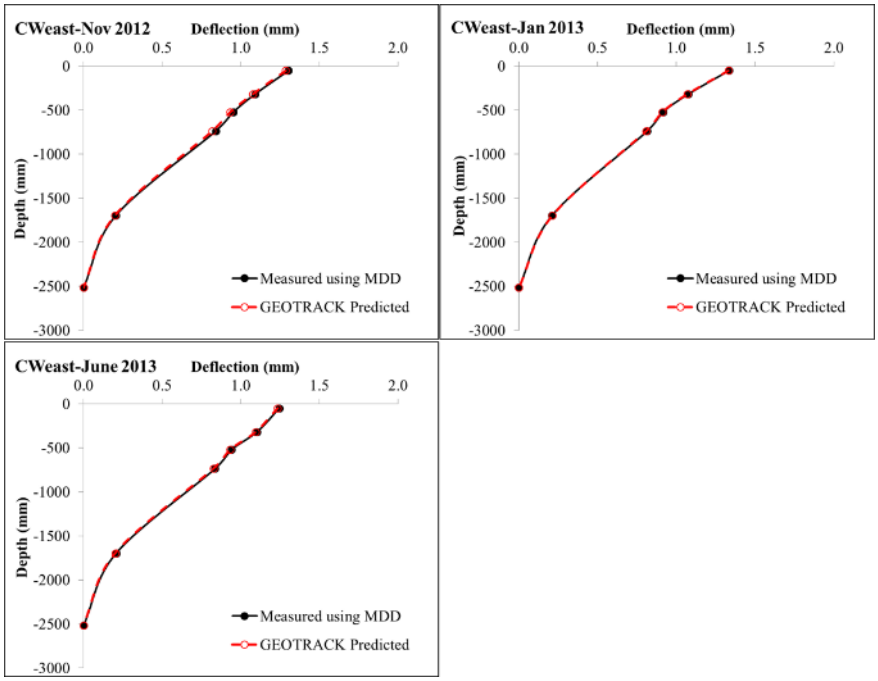

(b)

Figure A-2-36: Comparison of Calculated Deformation with Field Measured Data (a) Caldwell west location (b) Caldwell east location

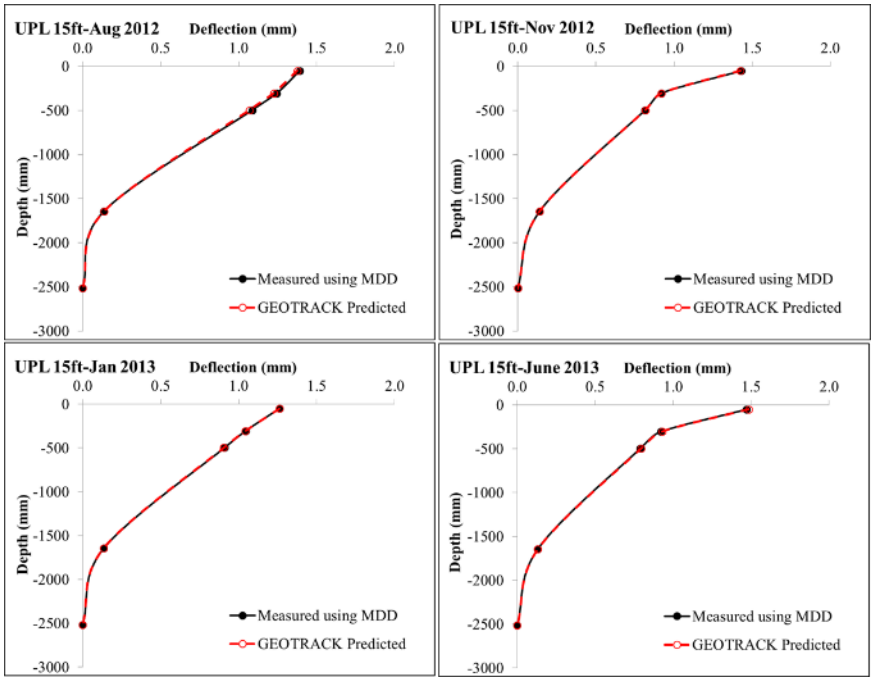

(a)

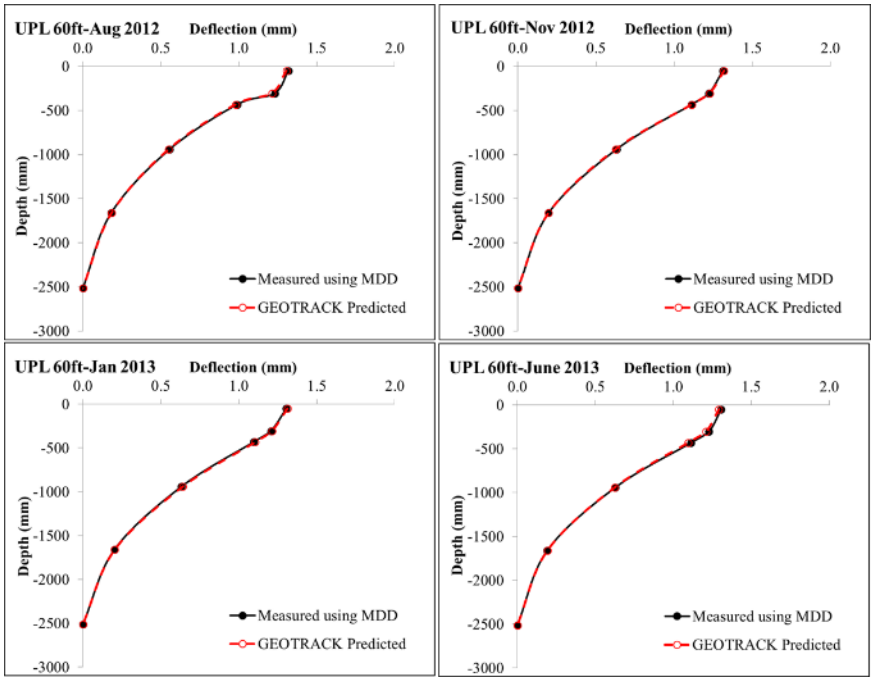

(b)

Figure A-2-37: Comparison of Calculated Deformation with Field Measured Data (a) Upland 15ft near bridge location (b) Upland 60ft open track location

Appendix A-3: Implementation of Remedial Measures and Performance Monitoring of Remediated Bridge Approaches

Upland Street Bridge Approach Displacement Time Histories

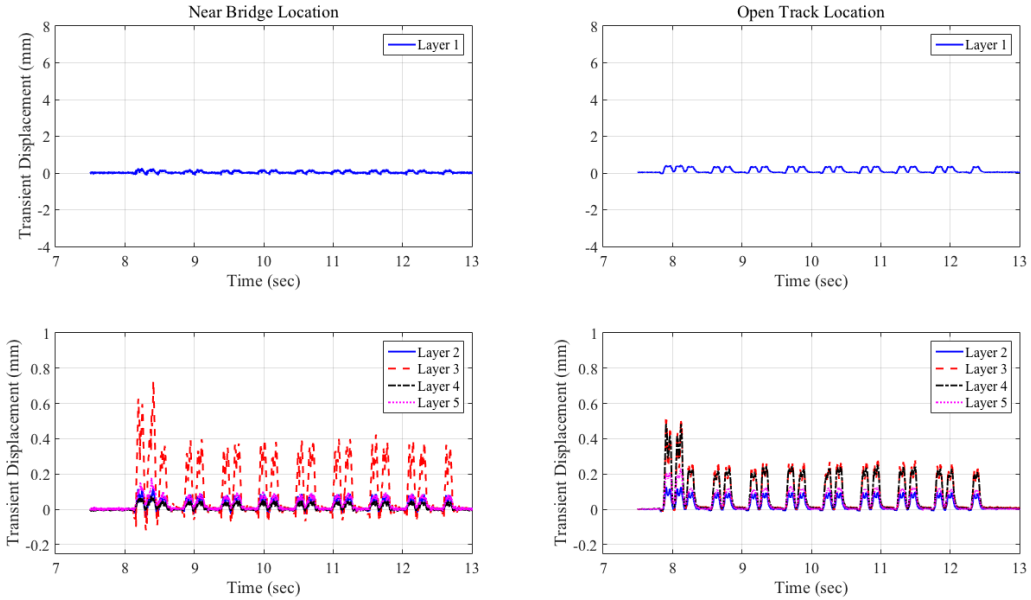

Figure A-3-1: Displacement Time History Recorded at Upland Street Bridge Approach; Data Collected on July 22, 2014; Train # 2 (Acela Express)

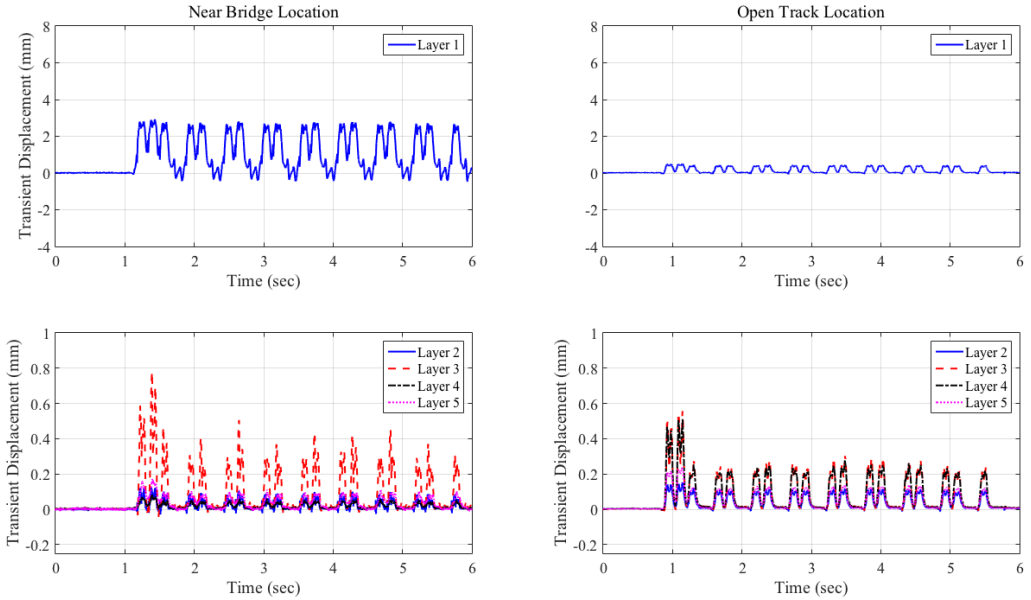

Figure A-3-2: Displacement Time History Recorded at Upland Street Bridge Approach; Data Collected in January 2015; Train # 2

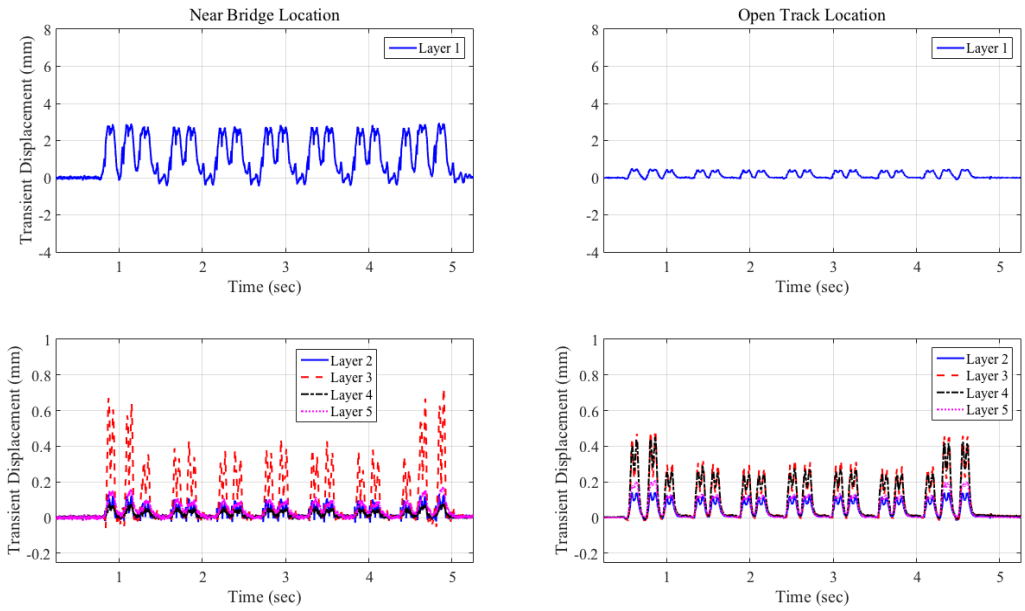

Figure A-3-3: Displacement Time History Recorded at Upland Street Bridge Approach; Data Collected in January 2015; Train # 3 (Acela Express)

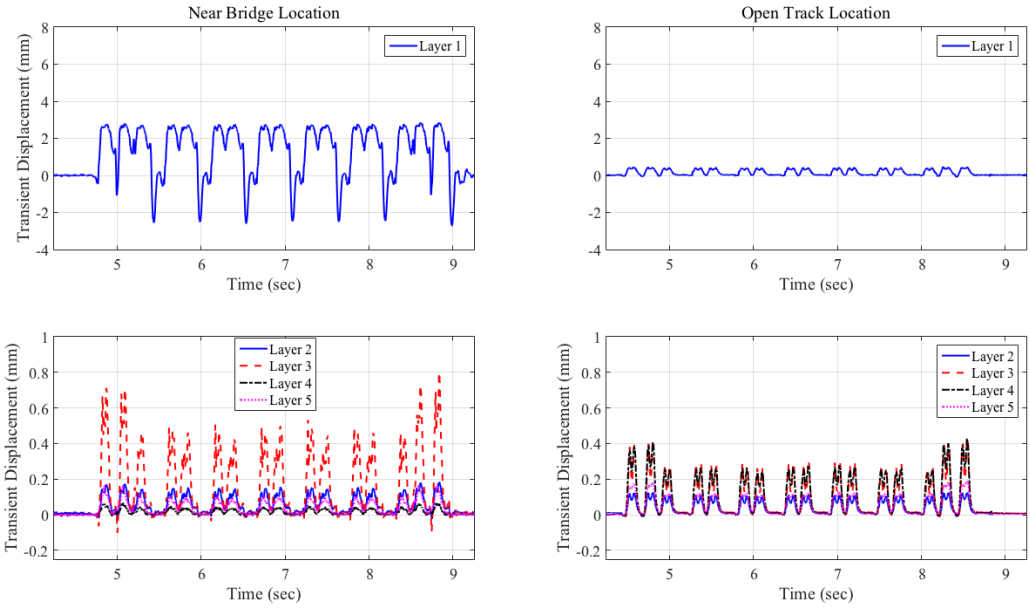

Figure A-3-4: Displacement Time History Recorded at Upland Street Bridge Approach; Data Collected in May 2015; Train # 2 (Acela Express)

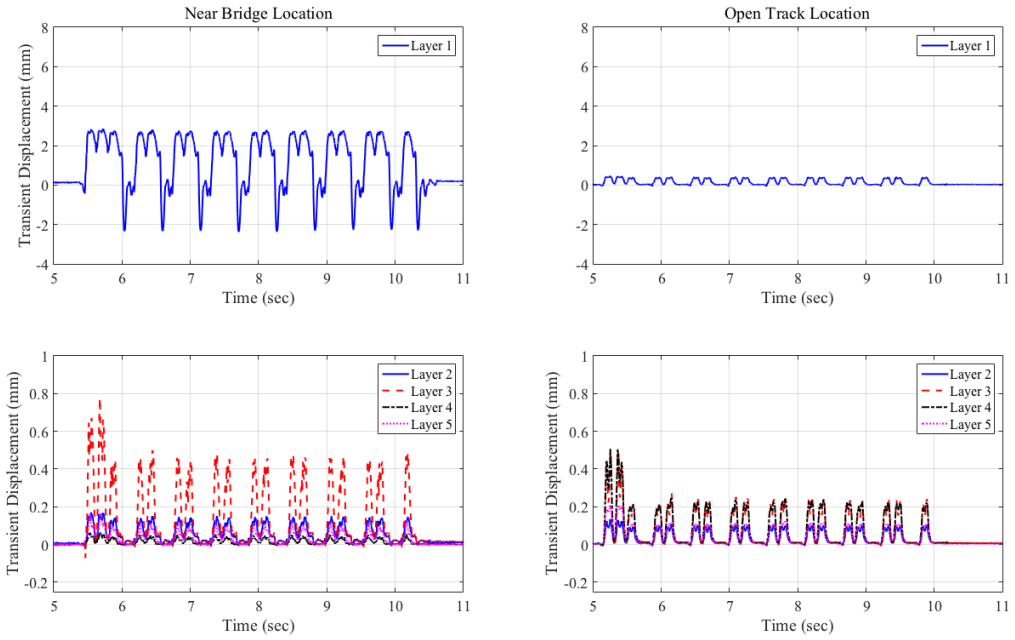

Figure A-3-5: Displacement Time History Recorded at Upland Street Bridge Approach; Data Collected in May 2015; Train # 3

Madison Street Bridge Approach Displacement Time Histories

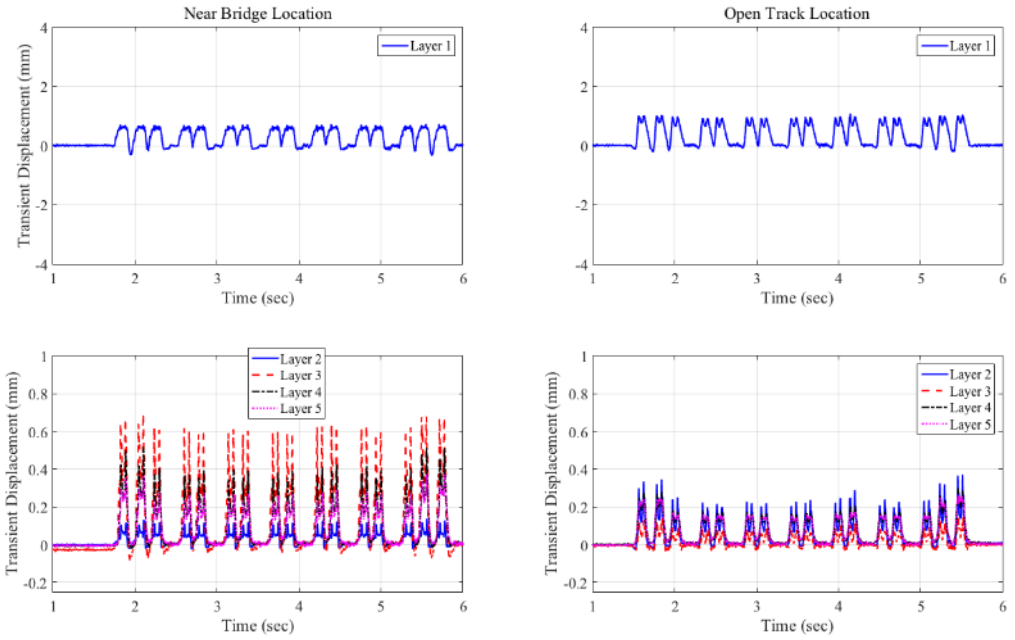

Figure A-3-6: Displacement Time History Recorded at Madison Street Bridge Approach; Data Collected in January 2015; Train # 2 (Acela Express)

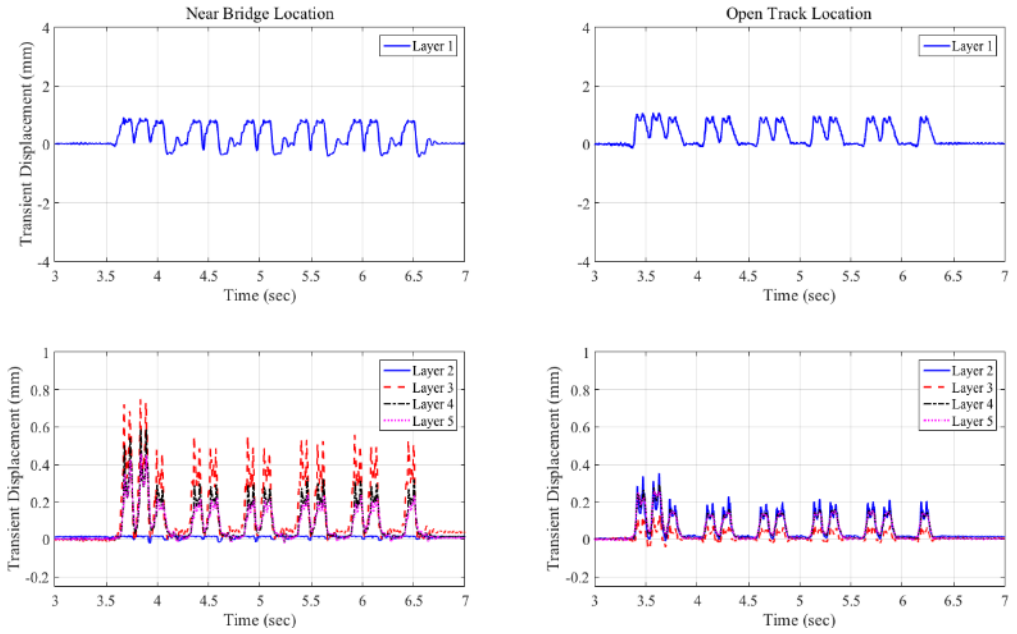

Figure A-3-7: Displacement Time History Recorded at Madison Street Bridge Approach; Data Collected in May 2015; Train # 2

Upland Street – Track 2 – South Approach (Post UTP Installation) Displacement Time Histories

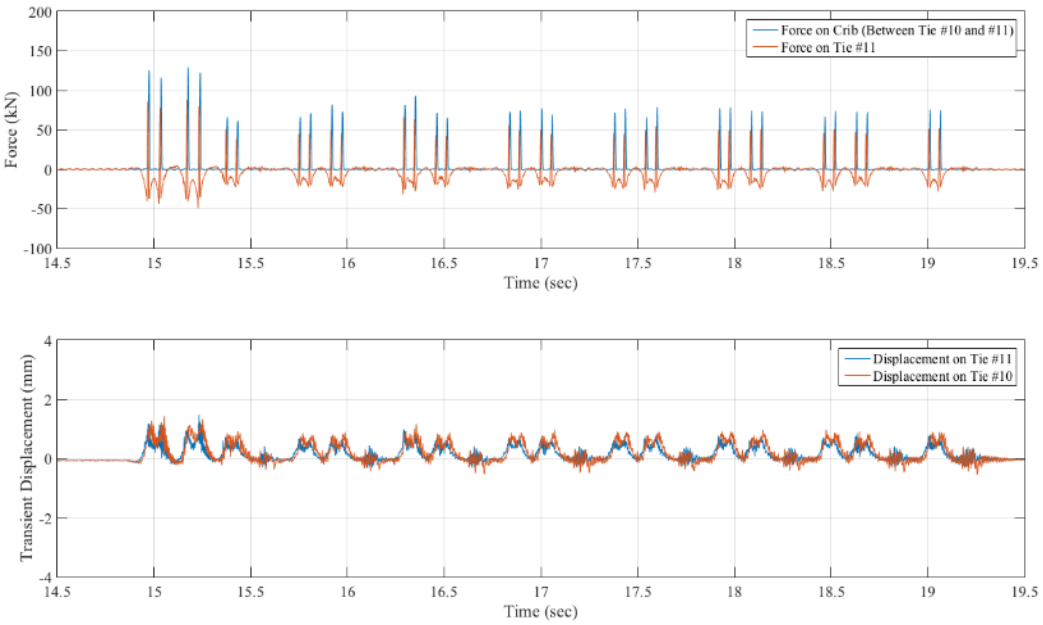

Figure A-3-8: Train # 2

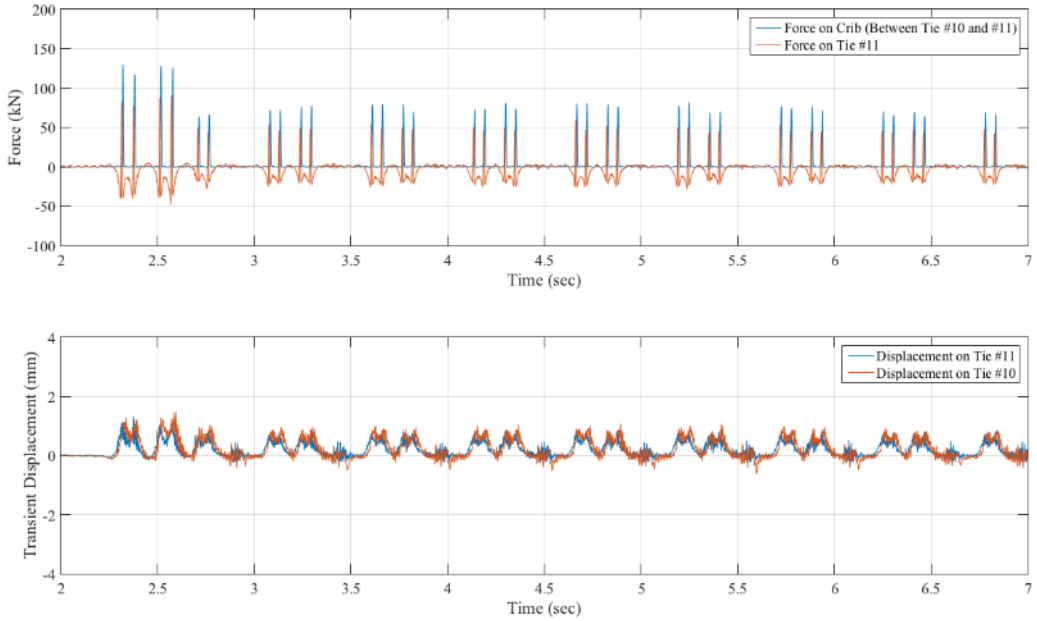

Figure A-3-9: Train # 3

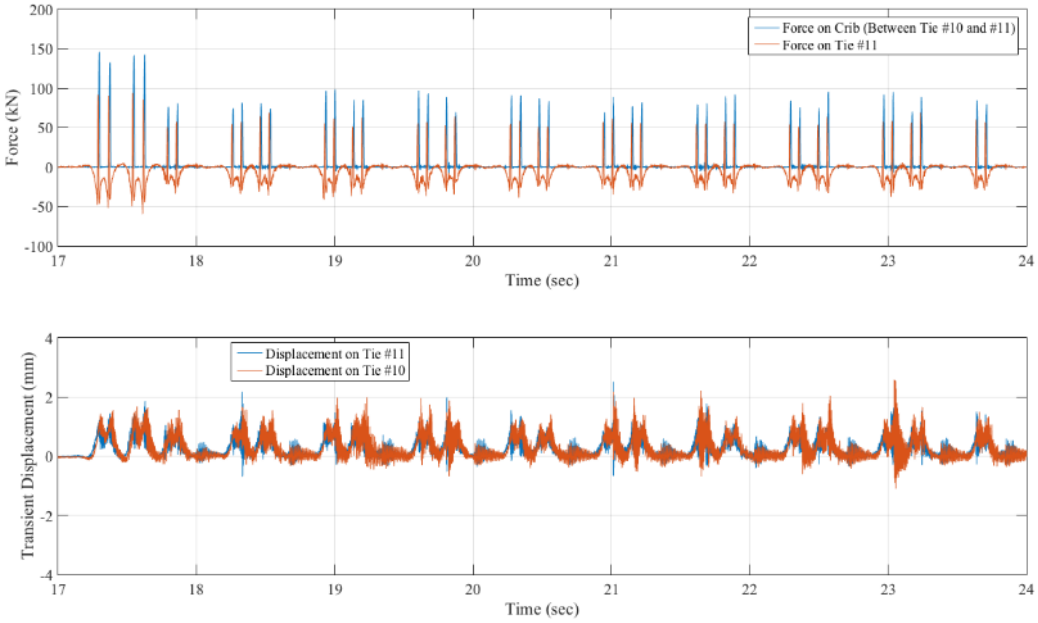

Figure A-3-10: Train # 4

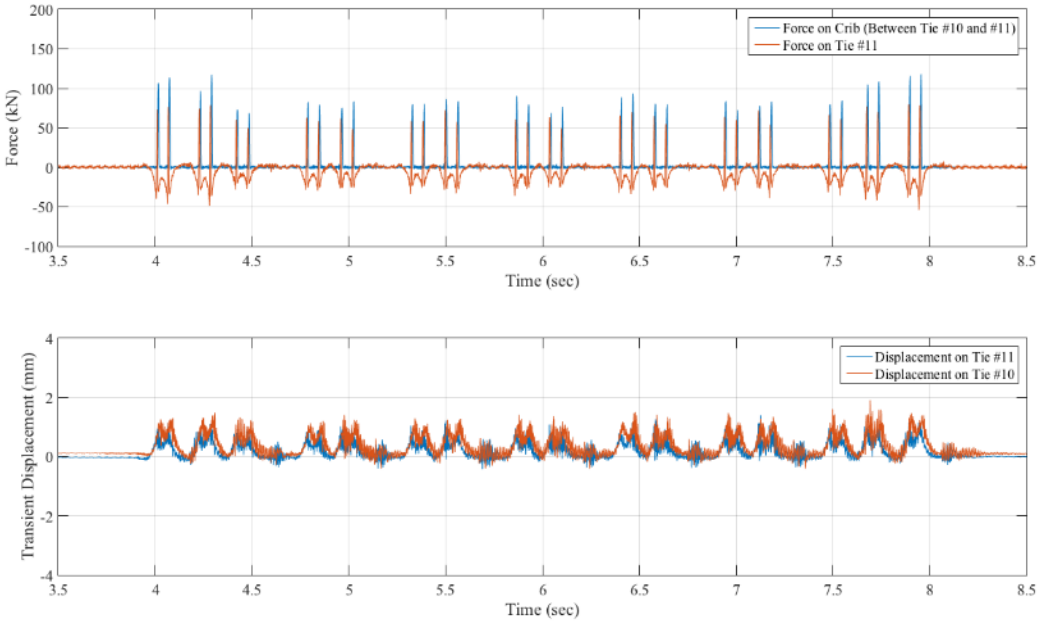

Figure A-3-11: Train # 5 (ACELA)

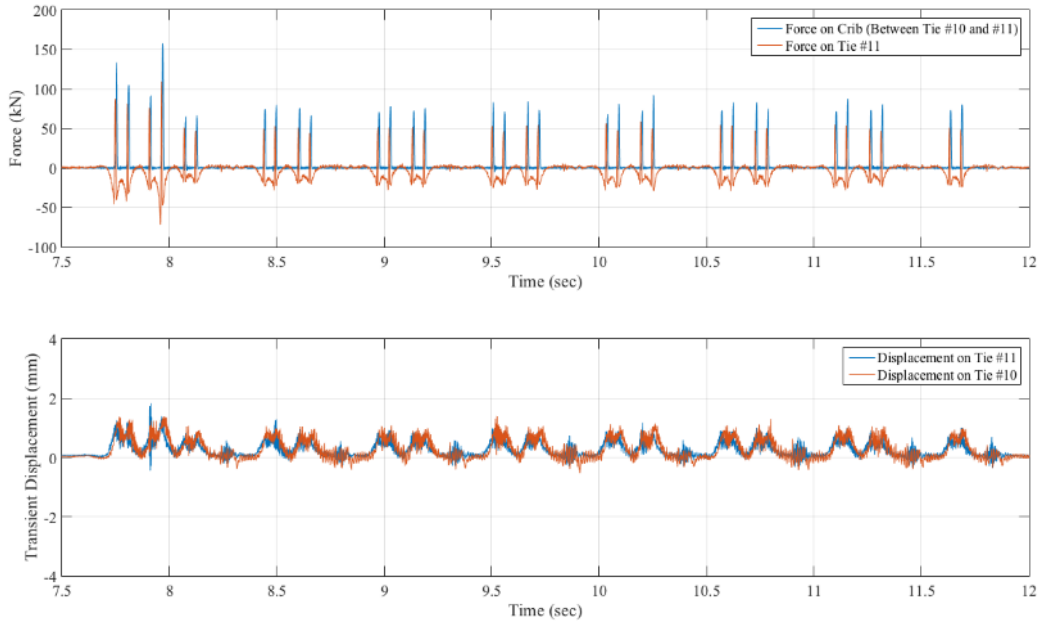

Figure A-3-12: Train # 6

Upland Street – Track 2 – South Approach (Post UTP Installation) Accelerations in Time and Frequency Domain

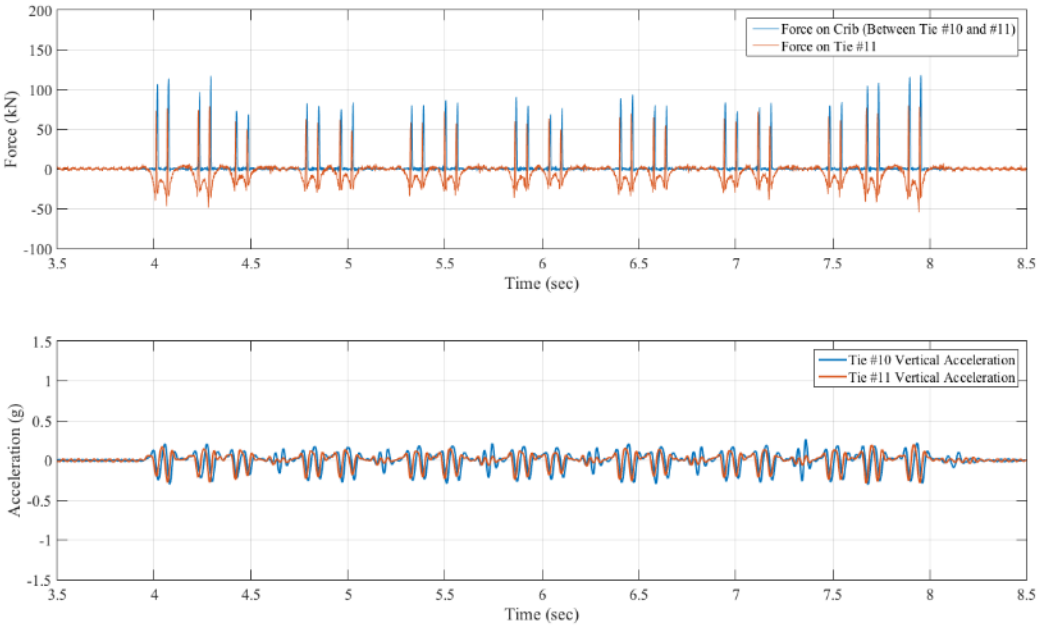

Figure A-3-13: Acceleration Time History Derived from Displacement (Train # 5 ACELA)

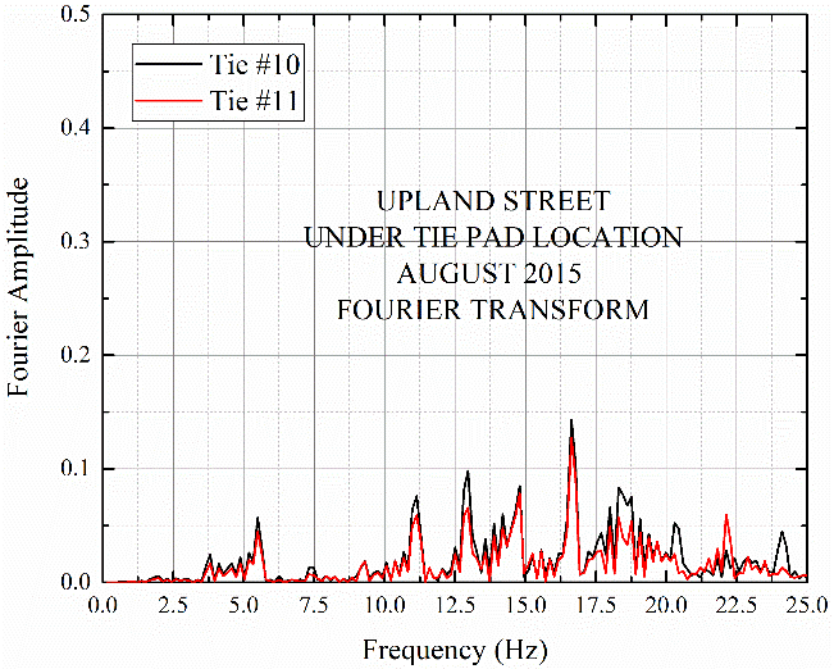

Figure A-3-14: Acceleration FFT Derived from Displacement (Train # 5 ACELA)

Upland Street – Track 2 – South Approach (Post UTP Installation) Acceleration Time History Comparison between Accelerometers and Accelerations Derived from Displacement Time Histories

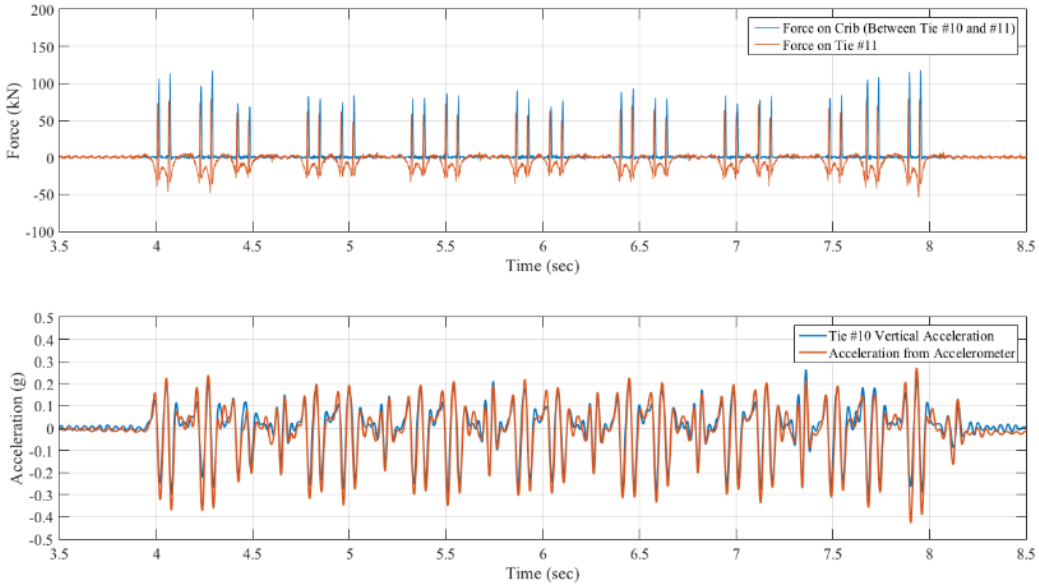

Figure A-3-15: Acceleration Comparison (Train # 5 ACELA)